High-order space and time discretization scheme applied to problems of finite thermo-viscoelasticity

Doctoral Thesis
(Dissertation)

to be awarded the degree

Doctor of Engineering (Dr.-Ing.)

submitted by

Dipl.-Ing. Torben Netz

from Wolfhagen

(place of birth)

approved by the Faculty of
Mathematics/Computer Science and Mechanical Engineering,
Clausthal University of Technology

Date of oral examination
16.08.2013

Chairperson of the Board of Examiners
Prof. Dr.-Ing. habil. Gunther Brenner

Chief Reviewer
Prof. Dr.-Ing. habil. Stefan Hartmann

Reviewer
Prof. Dr.-Ing. habil. Alexander Düster, Technische Universität Hamburg-Harburg

Foreword and Acknowledgements

This thesis took shape during my term as research associate at the Institute of Applied Mechanics (Institut für Technische Mechanik) belonging to the Clausthal University of Technology, from 15.08.2008 to 31.04.2013. I wish to take this opportunity of expressing my sincere thanks to my supervisor Prof. Dr.-Ing. habil. Stefan Hartmann for his commitment and mentorship, his support, advice and recommendations.

Throughout this period I had countless opportunities to exchange views and ideas with my colleagues. I would particularly like to thank Dr.-Ing. Karsten Jens Quint and Dr.-Ing. Ahmad-Wahadj Hamkar for providing every imaginable assistance during the initial phase of my research. I also wish to thank my colleagues Dipl.-Ing. Steffen Rothe, Dipl.-Phys. Stephan Krämer, M.Sc. Raad Al-Kinani, Dipl.-Ing. Matthias Grafenhorst and Dr.-Ing. Carmen Sguazzo for the extremely amiable, constructive working atmosphere and team spirit. I am indebted to Dipl.-Ing. Steffen Rothe for the many enlightening talks we had about the Finite Element method and various administrative matters, and I am particularly grateful to Dipl.-Phys. Stephan Krämer for our numerous inspirational discussions and his helpful, cooperative manner, while M. Sc. Raad Al-Kinani always had an open ear for questions relating to tensor analysis and continuum mechanics. I also wish to make special mention of the valuable support provided by Dipl.-Ing. Matthias Grafenhorst, which contributed to the much appreciated, pleasant working environment.

I also wish to gratefully acknowledge the support provided by Prof. Dr.-Ing. habil. Alexander Düster in incorporating the p-version of the Finite Element method, the excellent research collaboration and, in particular, for agreeing to act as co-supervisor.

May I also express my gratitude to Dipl.-Ing. Peng Xin, Dipl.-Ing. Shufei Xie and especially to Ada Böhme, for all the highly stimulating discussions we had in connection with their diploma theses, which also served to promote the development of my own ideas.

Torben Netz

Abstract

In today's engineering practice crucial decisions are based on predictions about the behavior of physical systems. The automotive and aircraft industries, for example, tend to prefer lightweight components in order to produce more fuel efficient vehicles. It is nevertheless imperative that these components satisfy the desired safety requirements, so that there is obviously a need for highly accurate predictions regarding the behavior of physical systems exposed to some external load.

The forecasting process is unfortunately prone to error. First of all, it is necessary to describe the physical reality by means of a mathematical model. To this end, the analyst has to decide which characteristics of the physical reality are conducive to the desired conclusions and accordingly need to be incorporated into the mathematical model. Thus, one possibility for an inaccuracy in the prediction is identified. Since this mathematical model cannot be solved analytically, approximate solutions are used. Now the question about the accuracy of the approximate solution, which is addressed in this work, arises. The finite element method is widespread in the context of geometrically and physically nonlinear solid mechanics employing constitutive equations of evolutionary type. The h-version of the finite element method is usually used for carrying out the spatial discretization in conjunction with the Backward-Euler method for the temporal discretization. In the last three decades, however, a very competitive approach for carrying out the spatial discretization has come up, which is known as the p-version of the finite element method. In contrast to the h-version, where a huge number of elements with a linear or at most quadratic ansatz for the displacement field is used, the p-version employs only a few elements with a high polynomial degree for the ansatz. In addition, high-order time integration schemes of DIRK-type, for instance, have been investigated in connection with h-version finite elements, exhibiting a superior performance when compared to the commonly applied Backward-Euler method. Due to the promising properties of both the p-version for the spatial discretization and the high-order time integration schemes of DIRK-type, this treatise investigates the combination of these two approaches. Isothermal as well as thermo-mechanically coupled problems are investigated, from the point of view of finite strain viscoelastic or finite strain thermo-viscoelastic material behavior.

Having discussed the material model in question, which describes the finite thermo-viscoelastic material behavior, we then proceed to set out the mathematical model and subsequently discuss the application of the vertical method of lines to the mathematical model. Firstly, the spatial discretization is carried out by means of the p-version, yielding a system of differential algebraic equations. Its algebraic part consists of the weak form of the quasistatic balance of momentum and the differential part originates from the evolution equations for the internal variables and the time-dependent temperature field. The application of high-order time integration schemes of DIRK-type leads to a system of nonlinear equations, which is solved by means of the Multilevel-Newton Algorithm for the unknown internal variables, the displacement and temperature coefficients.

In the context of isothermal solid mechanics, we compare different variations of the h-version - like pure displacement formulations or mixed elements employing an ansatz for the displacements, pressure and volumetric strains - with the p-version, highlighting the competitiveness of the p-version. Among the spatial discretization techniques under consideration these approaches generally prove to be the most efficient choice, followed by mixed finite elements, whereas elements with a purely linear ansatz for the displacement field exhibit the worst performance. The p-version exhibits particularly favorable characteristics when investigating large strains. We demonstrate that, for finite viscoelastic material behavior, the favorable characteristics of high-order DIRK-type time integration schemes, known in the context of h-version finite elements, transfer to the p-version. This approach allows an embedded step-size control monitoring the local integration error, for example. We then discuss the evidence that the superior accuracy and efficiency properties of high-order time integration schemes, employing p-version finite elements for the spatial discretization, also hold true for thermo-mechanically coupled problems. Combining high-order time integration schemes and the p-version of the finite element method accordingly delivers very accurate results reasonably economically, which renders this approach ideally suited for verification purposes.

Contents

1 Introduction

The prediction of the behavior of physical systems is of interest in all fields of engineering. These predictions often serve as basis for answering questions like “Will the components of the reality of interest under consideration meet the safety requirements they are supposed to meet?”. Some examples of what happens if this question is not answered correctly include:

- The collapse of the Tacoma Narrows bridge on 7th September 1940, see (von Karman, 2005) or
- ’The Sleipner Platform Accident’, which occurred offshore of Stavanger, Norway, in August 1991 causing a financial loss of 700 million dollars, see (Jakobsen and Rosendahl, 1994).

Besides the need for components to satisfy safety requirements, components are also required to be as cost effective as possible addressing the efficient usage of raw materials during production process. Moreover, there is a tendency to prefer lightweight components in the automobile or aircraft industry, for instance, in order to reduce fuel consumption in vehicles and aircrafts. This demonstrates the need for reliable, highly accurate predictions.

1.1 Scope of Thesis

Nowadays, it is common practice in various engineering disciplines to apply software packages for making predictions about the state of deformation and stress of a structure that has been subjected to some external load. Since the outcome of these numerical simulations is the basis for further decision-making, the analyst needs to know about its degree of reliability. According to (Szabo and Actis, 2009) the main elements of numerical simulation are the conceptualization of the physical reality, the derived mathematical model and its numerical solution. Due to the complexity of the physical reality, the derived mathematical model is generally based on assumptions leading to a simplified physical reality. The errors caused by these simplifications are called modeling errors. To illustrate this point, let us cite the reason for the failure of the Tacoma Narrows bridge, which collapsed because its mathematical model did not properly describe the aerodynamical forces and the effect of the von Karman vortices, see (von Karman, 2005). Besides theses modeling errors, the numerical solution of the mathematical model, which cannot normally be solved analytically, leads to errors of discretization. A well known example of an error in discretization is the Sleipner Platform, which sank due to an 47% underestimation of the shear forces in a critical part of the base structure of the platform, see (Jakobsen and Rosendahl, 1994; Selby et al., 1997). Controlling the errors of discretization is associated with the notion of verification (Am I solving the equations correctly?) whereas the term validation (Am I solving the right equations?) is used for comparing the outcome of a numerical simulation with the underlying physical reality. Fig. 1.1 depicts the general concept of validation and verification.

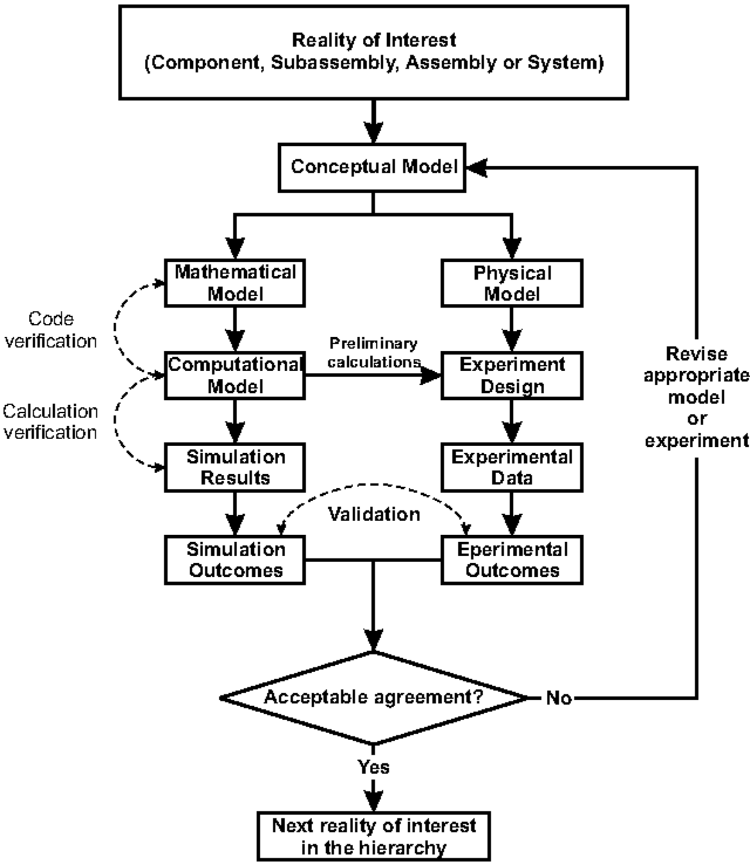

Figure 1.1: Diagram of the validation and verification procedure according to (Schwer, 2007)

We begin by deriving a conceptual model for the reality of interest, which may be a single component of a structure. The resulting mathematical model needs to be discretized to produce the computational model. The simulation outcomes now need to be validated against the experimental outcomes. In the event that no acceptable agreement is reached, we need to establish a new conceptual model, otherwise the next reality of interest in the hierarchy has to be addressed until all components of the structure under consideration are validated and verified. For further information on the general framework for validation and verification as well as the reliability of computer predictions see (Babuska et al., 2007; Babuska and Oden, 2003, 2005). This thesis addresses the topic of verification in the context of quasistatic solid mechanics, whereas validation aspects are not taken into consideration.

In commercial finite-element codes, designed for solving problems of quasistatic solid mechanics, the spatial discretization is commonly carried out using the h-version of the finite element method, meaning that linear or quadratic elements based on Lagrange polynomials are applied, see (Hughes, 2000), for instance. During the course of the last 3 decades shape functions based on integrated Legendre polynomials, as proposed in (Szabo and Babuska, 1991), have been investigated for small strain problems of linear elasticity, see (Düster et al., 2001; Szabo et al., 2004), for example, and for elastoplastic material behavior assuming small strains, see (Düster et al., 2002; Düster and Rank, 2001, 2002), among others. With respect to the large strain regime, investigations based on hyperelastic material behavior, see (Düster, 2001; Düster et al., 2003; Krause et al., 1995), for instance, as well as investigations based on powder plasticity allowing large strains, see (Heisserer, 2007; Heisserer et al., 2008a), have been carried out. The successful application of these shape functions to problems of finite thermo-elastic material behavior is demostrated in (Erbts and Düster, 2012), among other treatises. These shape functions, which are associated with the notion of the p-version of the finite element method, exhibit exponential convergence rates for smooth and even for non-smooth problems in the case of a geometric mesh refinement, see (Szabo, 1986). The hierarchic sequences of finite element spaces associated with the p-version of the finite element method, in particular, are ideally suited for the purpose of verification as shown in (Szabo and Actis, 2009; Szabo et al., 2010).

If constitutive models of evolutionary type are considered, the temporal discretization is usually carried out by the Backward-Euler method even though the applicability, efficiency and superiority of diagonally-implicit Runge-Kutta (DIRK) methods of higher order, see (Hairer and Wanner, 1996), for example, has been demonstrated in (Hartmann, 2002, 2003) etc. The constitutive model employed in this treatise describes finite thermo-viscoelastic material behavior, see (Holzapfel and Simo, 1996b), for instance. For small strain thermo-viscoelasticity see Holzapfel and Reiter (1995), for instance. Another advantageous property of DIRK-methods of higher order is that they can easily be implemented into existing finite-element codes. This is due to the fact that the structure of a finite element code making use of Backward-Euler time integration is preserved if high-order time integartion of DIRK-type is added. The aim of this thesis, which is to apply high-order time discretization schemes of DIRK-type to problems of finite thermo-viscoelasticity in conjunction with the p-version of the finite element method, promises to result in a very powerful tool, with the help of which it is possible to achieve highly accurate solutions for problems of quasistatic solid mechanics.

1.2 State of Research

In (Ellsiepen, 1999; Ellsiepen and Hartmann, 2001; Fritzen, 1997; Wittekindt, 1991) the common approach in nonlinear finite elements, employing constitutive equations of evolutionary type, like viscoelasticity, viscoplasticity or elastoplasticity, is interpreted as the application of the vertical method of lines, see (Großmann and Roos, 2005; Schiesser, 1991), to partially differential equations in space and time. In the context of structural mechanics, the spatial discretization of the weak form of the balance of momentum is carried out first, resulting in a system of nonlinear equations, which, together with ordinary differential equations, describing the evolution of the internal variables, has to be solved for the displacement coefficients. Formally these ordinary differential equations can be arranged as a system of ordinary differential equations which, in combination with the spatially discretized weak form of the balance of momentum, describes a system of differential-algebraic equations (DAE-system). (Hartmann, 1998) points out that the system of nonlinear equations, which has to be solved in each step of the time discretization scheme applied to the DAE-system, is solved by means of the Multilevel-Newton Algorithm (Rabbat et al., 1979) leading to the notions of a global and a local level as well as the consistent tangent operator. With this insight, it is possible to characterize the problem under consideration and employ efficient numerical methods, other than the one-step methods of Backward-Euler type. One important category of time integration methods comprises multistep methods exploiting information from several preceding time-steps, thus yielding efficient high-order methods, see (Hairer and Wanner, 1996). One way of constructing higher order time integration schemes is to apply backward difference formulas (BDF), see (Hairer and Wanner, 1996). The application of a BDF-method of second order to problems of small strain elasto-plasticity, based on step-size control, is discussed in (Eckert et al., 2004). But according to (Wittekindt, 1991), preference should be given to one-step methods, especially those of Runge-Kutta-type (Hairer et al., 1988), since multistep methods suffer from several drawbacks such as requiring several restarts due to the elastic-plastic case distinction when applied to problems of plasticity. In contrast to multistep methods, one-step methods make use of nothing but quantities from the previous time-step. The application of stiffly accurate diagonally-implicit Runge-Kutta methods (Alexander, 1977) to geometrically linear problems is investigated in (Ellsiepen and Hartmann, 2001). Problems of finite strain viscoelasticity have been studied in (Hartmann, 2002, 2003; Hartmann et al., 2008b), problems of finite strain powder plasticity in (Bier, 2007; Hartmann and Bier, 2008) and problems of finite strain von Mises-type viscoplasticity in (Hartmann et al., 2008a), for example. Time-adaptive DIRK-type time integration schemes coupled with h-version finite elements for the spatial discretization have also been employed for the solution of the heat conduction equation, see (Quint et al., 2011). (Rothe et al., 2012) investigates half-explicit Runge-Kutta methods (HERK-methods), see (Hairer and Wanner, 1996), for problems of small and finite strain viscoelasticity. The basic idea of HERK-methods is to apply an explicit time integration scheme to the differential part of the DAE-system and to make use of a Newton-Raphson method in order to solve the algebraic part of the spatially discretized DAE-system. In (Rothe et al., 2012) it turns out that only very small step-sizes are allowed, due to stability properties encountered with the method. From the point of view of efficiency, HERK-methods are, moreover, just as good as DIRK-methods based on a Multilevel-Newton Algorithm for solving the nonlinear equations that crop up with problems involving large strains. They are only found to be more efficient for problems of small strain viscoelasticity. (Hartmann and Wensch, 2007) discusses the application of time-adaptive Rosenbrock-type time integration schemes, see (Hairer and Wanner, 1996), to problems of viscoelasticity assuming small strains. For the application of Rosenbrock-type methods in the context of large strain viscoelasticity see (Hartmann and Hamkar, 2010).

Besides the temporal discretization, it is also necessary to carry out the spatial discretization of the weak form of the balance of momentum, leading to the algebraic part of the DAE-system. The following section summarizes the most widespread concepts for the spatial discretization. When considering pure displacement methods, we create an ansatz for the displacement field. There are several possibilities for increasing the number of degrees of freedom of the structure under consideration. One way is to vary the number of elements with which the structure is discretized, or the polynomial degree of the finite elements can be changed. Alternatively, both the number of elements *and* the polynomial degree of the elements can be varied. Increasing the number of elements, while leaving the ansatz for the displacement field constant, is associated with the notion of the h-version of the finite element method. Increasing the polynomial degree of the finite element, leaving the element size constant, is referred to as the p-version of the finite element method. Varying the element size *and* the polynomial degrees of the elements is referred to as the hp-version of the finite element method. The means of spatial discretization employed in this thesis is the p-version, going back to (Peano, 1976), where hierarchic shape functions for tetrahedral elements are introduced. For an early survey of the p-version see (Szabo, 1979). There is a wealth of scientific literature dealing with the investigation of problems of linear elasticity. (Szabo and Babuska, 1991) point out that, for many problems, the p-version proves to be more advantageous than the h-version of finite elements. In addition, (Szabo and Babuska, 1991) demonstrate numerically that applying p-version discretizations causes the error in the energy norm to approach zero at a rate which is independent of Poisson's ratio when small strain elasticity is assumed. For theoretical contemplations see (Vogelius, 1983). Further references pointing out that the p-version is locking-free for a moderate polynomial order in such cases where linear elastic material behavior is assumed are (Babuska and Suri, 1992; Suri, 1996; Szabo et al., 1989). In the context of problems of quasistatic solid mechanics, the notion of locking is characterized by the fact that the approximate displacement field (resulting from a finite element approximation, for instance) is smaller than the analytical solution of the underlying problem would suggest, see (Koschnick, 2004, p. 60). For a definition and subdivision of the term "locking", as well as remedies to overcome it, see (Koschnick, 2004) and the literature cited therein. Further investigations addressing small strain linear elasticity and the p-version are given in (Actis et al., 1999; Babuska and Strouboulis, 2001; Babuska and Szabo, 1982; Düster et al., 2001; Holzer, 1999; Rank et al., 1998). (Actis et al., 1999) investigate the p-version in the context of hierarchic models for laminated plates and shells assuming small strain elastic material behavior. They point out that the p-version is not prone to mesh distortion and is free from locking. (Babuska and Szabo, 1982) comprises theoretical knowledge about rates of convergence of the h- and p-version of the finite element method and presents examples of two-dimensional problems of linear elasticity. (Düster et al., 2001) provides an implementation of the p-version for curved thin- and thick-walled structures. Making use of the blending function method, it is possible to discretize almost arbitrarily shaped regions with only few high-order finite elements, leading to efficient discretizations even though the aspect ratio of the elements involved is very large. (Holzer, 1999) discusses the successful application of the p-version in the context of supporting formworks. Discussions concerning small strain elastoplasticity can be found in (Düster et al., 2002; Düster and Rank, 2001, 2002; Holzer and Yosibash, 1996; Jeremic and Xenophontos, 1999; Rank et al., 2005; Szabo et al., 1993), for example. (Düster et al., 2002) compares the accuracy of h- and p-extensions for elastoplastic problems and shows that a moderately fine mesh suffices for constructing p-extensions for the benchmark problem under consideration, yielding acceptably accurate results. It also investigates a structural joint and demonstrates that a strictly three-dimensional high-order finite element approach allows the consistent computation of thin-walled structures instead of applying dimensionally reduced low order elements, which are notoriously prone to difficulties. (Düster and Rank, 2001) points out that the p-version turns out to be significantly more accurate than the h-version for many problems, even if an adaptive h-refinement is taken into consideration. Further references demonstrating that the p-version is an efficient and accurate discretization strategy for physically non-linear problems include (Düster and Rank, 2002; Rank et al., 2005). Investigations into the hyperelastic material behavior are given in (Düster et al., 2003; Heisserer et al., 2008b; Netz et al., 2013a; Noel and Szabo, 1997; Yosibash et al., 2007). (Düster et al., 2003) deals with the applications of p-version finite elements for nearly incompressible hyperelastic material behavior, focussing particularly on the question of robustness to distortion and the efficiency of anisotropic p-version finite elements for thin-walled structures. (Heisserer et al., 2008b) demonstrates that the locking-free behavior of p-version finite elements observed in the geometrically linear case also applies to problems involving finite deformations when taking semi-analytic solutions into consideration. (Netz et al., 2013a) compares the p-version with mixed element formulations making an ansatz for the displacement, pressure and volumetric deformation, see (Hartmann, 2002) and the literature cited therein. The competitiveness of the p-version is backed up by numerical examples. Further means of accelerating finite element computations are contemplated, such as extrapolating the starting vector within the non-linear solution procedure and the Newton-Raphson-Chord method, keeping the tangential stiffness matrix constant for several iterations. A discussion on anisotropic hyperelastic material behavior is given in (Al-Kinani et al., 2012; Yosibash and Priel, 2012). (Heisserer, 2007; Heisserer et al., 2008a) discuss applying the p-version to problems of large strain powder plasticity while (Netz et al., 2013b; Netz and Hartmann, 2010) discuss the topic of finite strain viscoelasticity for problems of quasistatic solid mechanics using the p-version for the spatial discretization and high-order DIRK- or Rosenbrock-type schemes for the temporal discretization.

But, alongside pure displacement methods, a variety of low-order elements have been developed in order to overcome the locking phenomenon, discretizing not only the displacement field, but also other quantities, such as the pressure or the volumetric strains. In this context, we would mention the mixed element formulations contained in (Hartmann, 2002). A further well-established class of element formulations are enhanced assumed strain elements (EAS-elements) based on the Hu-Washizu principle, discretizing the strains, enhanced strains and the stresses, which are an extension of the method of incompatible modes, see (Taylor et al., 1976).

Mixed element formulations were first developed for the h-version of the finite element method for small strains, such as the B-bar method or EAS-elements, see (Hughes, 2000) or (Andelfinger and Ramm, 1993; Simo and Rifai, 1990). These ideas were then extended to finite strain applications, where EAS-elements are proposed in (Glaser and Armero, 1997; Simo and Armero, 1992) or particular pressure/volumetric-deformation formulations in (Bonet and Wood, 2000; Hartmann, 2002; Liu et al., 1994; Simo and Taylor, 1991; Simo et al., 1985), to name a few. See (Brink and Stein, 1996) for a comparison. Other proposals make use of reduced integration techniques, see (Malkus and Hughes, 1978; Zienkiewicz et al., 1971), which means that, say, a linear hexahedral element is integrated with just one Gauss point instead of eight, resulting in a considerable saving in computational time. Moreover, the error introduced by a reduced integration scheme counteracts the locking effect shown by pure low-order displacement elements. But then stabilization techniques (Belytschko et al., 1984; Flanagan and Belytschko, 1981) are required to offset the rank deficiency of the stiffness matrix introduced by the reduced integration scheme. Other proposals based on reduced integration techniques include (Reese, 2003; Reese and Wriggers, 2000, 2005; Reese et al., 2000). Some of these formulations require stabilization factors adapted to the underlying problem that are, to a certain extent, artificial, thus, leading to a direct dependency of the finite element solution on the stabilization parameters. In (Reese, 2003; Reese and Wriggers, 2005), for instance, the underlying variational formulation contains an artificial parameter on whose choice the solution depends. Since the influence of this parameter only vanishes where the finite element solution corresponds to the exact solution, it is not possible to disregard the influence of the parameter. This results in a mixture of the formulation of the mathematical model (basically determined by the constitutive model) and the numerical solution technique rendering a verification procedure practically impossible. The influence of an artificial parameter on the solution has also been mentioned by (Wriggers, 2008). A recent development in the field of stabilized mixed finite elements is the introduction of stabilized mixed finite triangular and tetrahedral elements, as presented in (Caylak, 2011), which serve to avoid locking and stress oscillatory effects. A survey of spatial discretization strategies can be found in (Bonet and Wood, 2000; Wriggers, 2008), for instance.

The topic of finite strain thermo-elasticity is addressed in (Hamkar and Hartmann, 2012), for example, where Rosenbrock-type time integration schemes are employed together with mixed finite elements for the spatial discretization. A thermo-viscoelastic material model for large strain applications is discussed in (Reese and Govindjee, 1998). A monolithic approach employing a Backward-Euler time integration scheme is used to solve the governing equations. In (Erbts and Düster, 2012) the p-version is applied to problems of finite strain thermo-elasticity, making use of a fully implicit partitioned coupling scheme combined with a Backward-Euler time integration scheme. We would cite (Hartmann et al., 2009b) with respect to thermo-mechanically coupled problems employing constitutive equation of evolutionary type. In this publication, a combination of DIRK-type time integration schemes and the h-version of the finite element method is applied to the thermo-mechanically coupled problem, which is based on a material model of small strain thermo-viscoplasticity. (Quint, 2012) uses the same approach to solve problems of large strain thermo-viscoplasticity. At this juncture, we wish to cite (Glaser, 1992), where the radial return method for problems of large strain plasticity is combined with the Backward-Euler method for the temproal discretization. Applying the h-version of finite elements in the context of small strain thermo-viscoelasticity is discussed in (Holzapfel and Reiter, 1995). For the derivation of a constitutive model of thermo-viscoelasticity at finite strains see (Holzapfel and Simo, 1996b). (Reese, 2003) presents computations based on finite thermo-viscoelastic material behavior. The spatial discretization is carried out by means of finite elements based on a stabilization technique which is suitable for various kinds of inelastic, thermo-mechanical material models. The Backward-Euler method is employed for the temporal discretization. For the general structure of various coupled systems, i.e. electro-thermal, electro-thermo-mechanical or thermo-mechanical, see (Hartmann and Rothe, 2013) pointing out that DIRK-type time integration schemes also perform well in electro-thermal coupling.

1.3 Outline of this Thesis

We have so far discussed the aim of this thesis and the current state of research. The *second chapter* introduces the fundamentals of Continuum Mechanics, beginning with the description of the motion of a material body. In addition we also take a look at the balance equations of mass, both linear and angular momentum, energy and entropy. Finally, a material model for finite thermo-viscoelasticity, which serves as the basis for several numerical examples, is presented in this treatise. Having discussed the decomposition of the deformation gradient, we will now proceed to the resulting dissection of the free energy, followed by the dissipation inequality with a view to deriving the constitutive equations required with the numerical solution procedure. The heat conduction equation and the elastic and inelastic coupling terms are derived at the end of the second chapter.

The *third chapter* deals with the strong and weak forms of the thermo-mechanically coupled problem, which consists of the heat conduction equation, the balance of momentum, constitutive equations, as well as initial and boundary values. The weak form serves as the starting point for a subsequent spatial and temporal discretization.

The *fourth chapter* discusses the solution procedure of the Initial Boundary Value Problem (IBVP), beginning with different coupling strategies for solving the coupled problem. According to the vertical method of lines, the spatial discretization is carried out first, followed by the temporal discretization in a second step. Since a refinement of the discretization of the structure under consideration in the p-version is obtained by increasing the polynomial degree of the finite element, while the number of elements remains constant, importance must be attached to the mapping from the natural coordinates $\boldsymbol{\xi}$ to the geometrical coordinates. For this reason we dedicate the following sections to the blending function method and the quasi-regional mapping, which are commonly applied for this purpose. This is followed by a discussion on incorporating the geometric modeling package GiD (Ribo et al., 2008) into the finite element code TASA-FEM (Hartmann, 2006) and details of the hierarchic shape functions that are applied for the spatial discretization of the IBVP in the case of one- two- and three-dimensional problems. We also address the pitfalls encountered when implementing these aspects into a finite element code. Having discussed the shape functions that are employed, the next step is to perform a spatial discretization of the weak form of the heat conduction equation and the weak form of the balance of momentum. Section 4.3 looks at the temporal discretization of the IBVP, which allows a very efficient step-size control when employing DIRK-methods. Section 4.4 deals with the process of solving the system of nonlinear equations, resulting from the temporal discretization, by means of the Multilevel-Newton Algorithm, as well as deriving the necessary tangents. This involves discussing the extrapolation of the vector of unknown displacement and temperature coefficients within the Multilevel-Newton Algorithm (MLNA) and another means of accelerating the Newton process, the Chord-Multilevel-Newton Algorithm (CMLNA). Section 4.6 deals with the incorporation of the linear solver PARDISO, see (Schenk and Gärtner, 2004; Schenk et al., 1999).

Chapter five presents some numerical examples and, finally, *chapter six* winds up this thesis with a conclusion and an outlook for future research in this field. The appendix contains the shape functions associated with the p-version of the finite element method, the blending function terms, the Butcher-arrays of the employed DIRK-methods, abscissas and weights for the Gaussian integration, the Babuska-Chen points and all the tangents necessary for a finite element implementation.

2 Fundamentals of Continuum Mechanics

Continuum mechanics rests upon three cornerstones. Firstly, there is the kinematical description of a material body. Secondly, there are balance relations describing the interaction of the material body with the outside world. And thirdly, there is the theory of materials that deals with the modeling of individual material behavior by introducing constitutive equations.

2.1 Kinematics

2.1.1 Motion of a Material Body

Continuum mechanics is based on the concept that matter is continuously distributed within a material body $\mathcal{B} = \{\mathcal{P}\}$. According to (Haupt, 2000) matter is defined as a set of material points $\mathcal{P}$ for which there is a set $\mathcal{K} = \{\boldsymbol{\chi}\}$ of one-to-one mappings

$$\boldsymbol{\chi}\colon \begin{cases} \mathcal{B} & \to \boldsymbol{\chi}[\mathcal{B}] \subset \mathbb{R}^3 \\ \mathcal{P} & \mapsto \boldsymbol{\chi}(\mathcal{P}) = (x_1, x_2, x_3) \Longleftrightarrow \mathcal{P} = \boldsymbol{\chi}^{-1}(x_1, x_2, x_3) \end{cases} \tag{2.1}$$

on the one hand, while the composition of two configurations $\boldsymbol{\chi}_1 \in \mathcal{K}$ and $\boldsymbol{\chi}_2 \in \mathcal{K}$

$$\boldsymbol{\chi}_2 \circ \boldsymbol{\chi}_1^{-1}\colon \begin{cases} \boldsymbol{\chi}_1[\mathcal{B}] & \to \boldsymbol{\chi}_2[\mathcal{B}] \subset \mathbb{R}^3 \\ (x_1, x_2, x_3) & \mapsto (y_1, y_2, y_3) = \boldsymbol{\chi}_2\big(\boldsymbol{\chi}_1^{-1}(x_1, x_2, x_3)\big) \end{cases} \tag{2.2}$$

is differentiable. This property leads to the fact that two neighboring material points remain neighbors. Since $\boldsymbol{\chi}$ is a unique map there is only one material point which, for a given point in time, can be located at one point in space. The motion of a material point can be regarded as a sequence of configurations assigning to each point in time t a configuration $\boldsymbol{\chi}_t$

$$t \mapsto \boldsymbol{\chi}_t\colon \begin{cases} \mathcal{B} & \to \boldsymbol{\chi}_t[\mathcal{B}] \subset \mathbb{R}^3 \\ \mathcal{P} & \mapsto (x_1, x_2, x_3) = \boldsymbol{\chi}_t(\mathcal{P}) \Longleftrightarrow \mathcal{P} = \boldsymbol{\chi}_t^{-1}(x_1, x_2, x_3). \end{cases} \tag{2.3}$$

As it is inappropriate to consider the motion of a material point as a sequence of configurations χ_t being a map from the material body to the Eucleadian vector space for each point in time, we introduce a reference configuration

$$\boldsymbol{\mathcal{R}}\colon \begin{cases} \mathcal{B} & \to \boldsymbol{\mathcal{R}}[\mathcal{B}] \subset \mathbb{R}^3 \\ \mathcal{P} & \mapsto \boldsymbol{\mathcal{R}}(\mathcal{P}) = (X_1, X_2, X_3) \Longleftrightarrow \mathcal{P} = \boldsymbol{\mathcal{R}}^{-1}(X_1, X_2, X_3). \end{cases} \tag{2.4}$$

Making use of the arbitrary reference configuration $\boldsymbol{\mathcal{R}}(\mathcal{P})$, it is possible to define

$$\boldsymbol{\chi}_{\mathrm{R}}\colon \begin{cases} \boldsymbol{\mathcal{R}} \times \mathbb{R}^{+} & \rightarrow \boldsymbol{\chi}_t[\mathcal{B}] \\ (\boldsymbol{X}, t) & \mapsto \boldsymbol{x} = \boldsymbol{\chi}_{\mathrm{R}}(\boldsymbol{X}, t) := \boldsymbol{\chi}_t\big(\boldsymbol{\mathcal{R}}^{-1}(\boldsymbol{X})\big) \end{cases} \tag{2.5}$$

which assigns to each point $\boldsymbol{X}$ a vector $\boldsymbol{x}$ containing its position for each point in time. With the map $\boldsymbol{\chi}_{\mathrm{R}}$ at hand, we can describe the motion by means of the displacement vector

$$\boldsymbol{u}(\boldsymbol{X}, t) = \boldsymbol{x} - \boldsymbol{X} = \boldsymbol{\chi}_{\mathrm{R}}(\boldsymbol{X}, t) - \boldsymbol{X}. \tag{2.6}$$

The deformation gradient

$$\mathbf{F}(\boldsymbol{X}, t) = \operatorname{Grad} \boldsymbol{\chi}_{\mathrm{R}}(\boldsymbol{X}, t) \tag{2.7}$$

measures the difference in motion of neighboring material points. Since the composition of two configurations is differentiable, there is a Taylor expansion for (2.5)

$$\boldsymbol{x} = \boldsymbol{\chi}_{\mathrm{R}}(\boldsymbol{X}, t) = \boldsymbol{\chi}_{\mathrm{R}}(\boldsymbol{X}_0 + \mathrm{d}\boldsymbol{X}, t) = \boldsymbol{\chi}_{\mathrm{R}}(\boldsymbol{X}_0, t) + \mathbf{F}\,\mathrm{d}\boldsymbol{X} + \|\mathrm{d}\boldsymbol{X}\|\boldsymbol{r}(\boldsymbol{X}_0, t, \mathrm{d}\boldsymbol{X}), \tag{2.8}$$

with the property

$$\lim_{\|\mathrm{d}\boldsymbol{X}\| \to 0} \|\boldsymbol{r}(\boldsymbol{X}_0, t, \mathrm{d}\boldsymbol{X})\| = 0. \tag{2.9}$$

The norm of a vector is given by $\|\boldsymbol{a}\| = \sqrt{\boldsymbol{a} \cdot \boldsymbol{a}}$. By stating

$$\mathbf{F} = \mathbf{1} + \mathbf{H}\,(\boldsymbol{u}) \qquad \text{with} \qquad \mathbf{H}\,(\boldsymbol{u}) = \operatorname{Grad} \boldsymbol{u} \tag{2.10}$$

the dependence of the deformation gradient $\mathbf{F}$ on the displacement $\boldsymbol{u}$ becomes obvious. In order to illustrate the geometrical meaning of the deformation gradient, we consider a material line in a reference

$$\boldsymbol{X} = \boldsymbol{C}(\alpha) \tag{2.11}$$

and current

$$\boldsymbol{x} = \boldsymbol{c}(\alpha) = \boldsymbol{\chi}_{\mathrm{R}}(\boldsymbol{C}(\alpha), t) \tag{2.12}$$

configuration with α as curve parameter. The tangent vector of the material line in current configuration yields

$$\mathrm{d}\boldsymbol{x} = \boldsymbol{c}'(\alpha)\,\mathrm{d}\alpha. \tag{2.13}$$

Inserting (2.12) into (2.13) leads to

$$\mathrm{d}\boldsymbol{x} = \boldsymbol{c}'(\alpha)\,\mathrm{d}\alpha = \frac{\mathrm{d}}{\mathrm{d}\alpha}\boldsymbol{\chi}_{\mathrm{R}}(\boldsymbol{C}(\alpha), t)\,\mathrm{d}\alpha = \big(\operatorname{Grad} \boldsymbol{\chi}_{\mathrm{R}}(\boldsymbol{X}, t)|_{\boldsymbol{X}=\boldsymbol{C}(\alpha)}\big)\,\boldsymbol{C}'(\alpha)\,\mathrm{d}\alpha \tag{2.14}$$

with

$$\mathrm{d}\boldsymbol{X} = \boldsymbol{C}'(\alpha)\,\mathrm{d}\alpha \tag{2.15}$$

being the tangent vector of the material line in the reference configuration and

$$\mathbf{F} = \operatorname{Grad} \boldsymbol{\chi}_{\mathrm{R}}(\boldsymbol{X}, t)|_{\boldsymbol{X}=\boldsymbol{C}(\alpha)} \tag{2.16}$$

being the deformation gradient evaluated at point $\boldsymbol{C}(\alpha)$. Thus, the deformation gradient maps the tangent of a material line element in reference configuration

$$\mathrm{d}\boldsymbol{x} = \mathbf{F}\,\mathrm{d}\boldsymbol{X} \tag{2.17}$$

to the current configuration. Further geometrical properties such as

$$\mathrm{d}\boldsymbol{a} = (\det \mathbf{F})\,\mathbf{F}^{-\mathrm{T}}\,\mathrm{d}\boldsymbol{A} \tag{2.18}$$

and

$$\mathrm{d}v = (\det \mathbf{F})\,\mathrm{d}V = J\,\mathrm{d}V \tag{2.19}$$

describe the deformation of a material surface and volume element from reference to current configuration, respectively. For proof see (Haupt, 2000, p. 28). Since it is beneficial to have a strain measure that disregards rigid body motions, we introduce the right and left Cauchy-Green tensor

$$\mathbf{C} = \mathbf{F}^{\mathrm{T}}\mathbf{F} \quad \text{and} \quad \mathbf{B} = \mathbf{F}\mathbf{F}^{\mathrm{T}}. \tag{2.20}$$

The Green strain tensor

$$\mathbf{E} = \frac{1}{2}\,(\mathbf{C} - \mathbf{1}) \tag{2.21}$$

is likewise of interest. According to (Flory, 1961) the deformation gradient

$$\mathbf{F} = \hat{\mathbf{F}}\bar{\mathbf{F}} \tag{2.22}$$

is split into a volume changing $\hat{\mathbf{F}}$ and a volume preserving part $\bar{\mathbf{F}}$ having the properties

$$\hat{\mathbf{F}} = J^{1/3}\mathbf{1}, \qquad \det \hat{\mathbf{F}} = \det \mathbf{F} = J, \tag{2.23}$$

$$\bar{\mathbf{F}} = J^{-1/3}\mathbf{F}, \qquad \det \bar{\mathbf{F}} = 1. \tag{2.24}$$

Using the unimodular right Cauchy-Green tensor $\bar{\mathbf{C}}$

$$\bar{\mathbf{C}} = \bar{\mathbf{F}}^{\mathrm{T}}\bar{\mathbf{F}}, \tag{2.25}$$

we obtain the invariants

$$\mathrm{I}_{\bar{\mathbf{C}}} = \mathrm{tr}\,\bar{\mathbf{C}}, \tag{2.26}$$

$$\mathrm{II}_{\bar{\mathbf{C}}} = \frac{1}{2}((\mathrm{tr}\,\bar{\mathbf{C}})^2 - \mathrm{tr}\,\bar{\mathbf{C}}^2) \tag{2.27}$$

and

$$\mathrm{III}_{\bar{\mathbf{C}}} = \det \bar{\mathbf{C}}, \tag{2.28}$$

necessary in Section 2.3. The time derivative of the determinant of the deformation gradient reads

$$\dot{J} = J\mathbf{F}^{-\mathrm{T}} \cdot \dot{\mathbf{F}} = J\mathrm{div}\,\boldsymbol{v}. \tag{2.29}$$

Furthermore, the norm $\|.\|$ of a tensor $\mathbf{A}$ is given by

$$\|\mathbf{A}\| = \sqrt{\mathbf{A} \cdot \mathbf{A}}. \tag{2.30}$$

2.1.2 Deformation Velocities

Material line, area and volume elements change in time according to

$$(\mathrm{d}\boldsymbol{x})^{\cdot} = (\mathbf{F}\,\mathrm{d}\boldsymbol{X})^{\cdot} = \dot{\mathbf{F}}\mathbf{F}^{-1}\,\mathrm{d}\boldsymbol{x} = \mathbf{L}\,\mathrm{d}\boldsymbol{x}, \tag{2.31}$$

$$(\mathrm{d}\boldsymbol{a})^{\cdot} = \left(J\mathbf{F}^{-\mathrm{T}}\,\mathrm{d}\boldsymbol{A}\right)^{\cdot} = J\left(\mathbf{F}^{-\mathrm{T}}\cdot\dot{\mathbf{F}}\right)\mathbf{F}^{-\mathrm{T}}\,\mathrm{d}\boldsymbol{A} - J\mathbf{F}^{-\mathrm{T}}\dot{\mathbf{F}}^{\mathrm{T}}\mathbf{F}^{-\mathrm{T}}\,\mathrm{d}\boldsymbol{A} = \left[(\operatorname{div}\boldsymbol{v})\mathbf{1} - \mathbf{L}^{\mathrm{T}}\right]\mathrm{d}\boldsymbol{a}, \tag{2.32}$$

$$(\mathrm{d}v)^{\cdot} = \dot{J}\,\mathrm{d}V = (\operatorname{div}\boldsymbol{v})\,\mathrm{d}v, \tag{2.33}$$

where use is made of the spatial velocity gradient

$$\mathbf{L} = \operatorname{grad}\boldsymbol{v}(\boldsymbol{x},t) = \dot{\mathbf{F}}\mathbf{F}^{-1}, \tag{2.34}$$

(2.18), (2.19) and (2.29). The spatial velocity gradient decomposes additively into a symmetric part $\mathbf{D}$, called strain rate tensor, and a skew symmetric part $\mathbf{W}$, called vorticity or spin tensor

$$\mathbf{L} = \mathbf{D} + \mathbf{W}, \tag{2.35}$$

with

$$\mathbf{W} = \frac{1}{2}\left(\mathbf{L} - \mathbf{L}^{T}\right) \tag{2.36}$$

and

$$\mathbf{D} = \frac{1}{2}\left(\mathbf{L} + \mathbf{L}^{T}\right). \tag{2.37}$$

2.2 Balance Equations

The interaction of the outside world with the material body $\mathcal{B}$ is described by balance equations. There are the balance of mass, momentum, angular momentum and energy. In the spatial representation they generally take the form of

$$\frac{\mathrm{d}}{\mathrm{d}t}\int_{\omega}\varrho\,(\boldsymbol{x},t)\,\boldsymbol{\Psi}(\boldsymbol{X},t)\,\mathrm{d}v = \int_{\omega}\varrho\,(\boldsymbol{x},t)\,[\varphi(\boldsymbol{x},t) + z(\boldsymbol{x},t)]\,\mathrm{d}v + \int_{\partial\omega}\boldsymbol{\Phi}(\boldsymbol{x},t)\,\boldsymbol{n}\,\mathrm{d}a, \tag{2.38}$$

whereas

$$\begin{aligned}\frac{\mathrm{d}}{\mathrm{d}t}\int_{\Omega}\varrho_{\mathrm{R}}\,(\boldsymbol{X},t)\,\boldsymbol{\Psi}_{\mathrm{R}}\,\mathrm{d}V = &\int_{\Omega}\varrho_{\mathrm{R}}(\boldsymbol{X},t)\,\left[\varphi_{\mathrm{R}}\,(\boldsymbol{X},t) + z_{\mathrm{R}}(\boldsymbol{X},t)\right]\mathrm{d}V\\ &+\int_{\partial\Omega}\boldsymbol{\Phi}_{\mathrm{R}}(\boldsymbol{X},t)\,\boldsymbol{n}_{\mathrm{R}}\,\mathrm{d}A\end{aligned} \tag{2.39}$$

is the more common formulations in the material representation. ω and Ω refer to an integration over the volume in current and reference configuration, respectively. $\partial\omega$ and $\partial\Omega$ are related to an integration over a surface in current and reference configuration. The quantity to be balanced is denoted by $\boldsymbol{\Psi}$ or $\boldsymbol{\Psi}_{\mathrm{R}}$ depending on whether it is associated with the current or reference configuration. Their temporal change equals the sum of the flux over the surface of the material body $\boldsymbol{\Phi}$ ($\boldsymbol{\Phi}_{\mathrm{R}}$), the volume distributed exchange with the outside world φ (φ_{R}) and the production term z (z_{R}).

2.2.1 Balance of Mass

The mass $m(\mathcal{B}, t)$ of a material body $\mathcal{B}$ is a scalar quantity that measures a material body's resistance to acceleration and the strength of its gravitational interactions with other masses. Since a mass density ϱ is assigned to each material point, the mass of a material body can be given in either spatial or in material configuration as

$$(\mathcal{B}, t) \mapsto m(\mathcal{B}, t) = \int\limits_{\omega} \varrho(\boldsymbol{x}, t) \, \mathrm{d}v = \int\limits_{\Omega} \varrho_{\mathrm{R}}(\boldsymbol{X}, t) \, \mathrm{d}V. \tag{2.40}$$

The conservation of mass

$$\frac{\mathrm{d}m}{\mathrm{d}t} = \frac{\mathrm{d}}{\mathrm{d}t} \int\limits_{\omega} \varrho(\boldsymbol{x}, t) \, \mathrm{d}v = \frac{\mathrm{d}}{\mathrm{d}t} \int\limits_{\Omega} \varrho_{\mathrm{R}}(\boldsymbol{X}, t) \, \mathrm{d}V = 0 \tag{2.41}$$

states that mass remains constant with respect to time. Since it is possible to exchange the derivative with respect to time and the integration via the volume in reference configuration, the local form of the balance of mass in the material representation

$$\frac{\partial}{\partial t} \varrho_{\mathrm{R}}(\boldsymbol{X}, t) = 0 \Longleftrightarrow \varrho_{\mathrm{R}} = \varrho_{\mathrm{R}}(\boldsymbol{X}) \tag{2.42}$$

follows. It is possible to switch from the reference to the current configuration by inserting (2.19) into the conservation of mass (2.41) yielding

$$\frac{\mathrm{d}m}{\mathrm{d}t} = \frac{\mathrm{d}}{\mathrm{d}t} \int\limits_{\omega} \varrho(\boldsymbol{x}, t) \, \mathrm{d}v = \int\limits_{\Omega} \frac{\mathrm{d}}{\mathrm{d}t} \left(\varrho \det \mathbf{F} \right) \mathrm{d}V \tag{2.43}$$

$$= \int\limits_{\Omega} \left(\dot{\varrho} \det \mathbf{F} + \varrho \left(\det \mathbf{F} \right) \, \mathbf{F}^{-T} \cdot \dot{\mathbf{F}} \right) \mathrm{d}V. \tag{2.44}$$

Making use of the velocity gradient (2.34) and the definition of the transpose of a tensor

$$\operatorname{div} \boldsymbol{v} = \operatorname{tr} \mathbf{L} = \mathbf{1} \cdot \dot{\mathbf{F}} \mathbf{F}^{-1} = \mathbf{F}^{-1} \cdot \dot{\mathbf{F}}^{T} = \mathbf{F}^{-T} \cdot \dot{\mathbf{F}} \tag{2.45}$$

follows. Using (2.45) (2.44) can be reformulated as

$$0 = \int\limits_{\Omega} \left(\dot{\varrho} + \varrho \operatorname{div} \boldsymbol{v} \right) \mathrm{d}v \tag{2.46}$$

yielding the local balance of mass

$$\frac{\mathrm{d}}{\mathrm{d}t} \varrho + \varrho \operatorname{div} \boldsymbol{v} = 0. \tag{2.47}$$

(2.41) and (2.19) lead to

$$\varrho_{\mathrm{R}} = \varrho \det \mathbf{F}. \tag{2.48}$$

2.2.2 Balance of Linear Momentum

The momentum of the material body $\mathcal{B}$ is defined as the product of the density of a material point with its velocity

$$\boldsymbol{p}(\mathcal{B},t) = \int\limits_{\omega} \boldsymbol{v}(\boldsymbol{x},t)\,\varrho(\boldsymbol{x},t)\,\mathrm{d}v = \int\limits_{\Omega} \boldsymbol{v}(\boldsymbol{X},t)\,\varrho_{\mathrm{R}}(\boldsymbol{X})\,\mathrm{d}V \tag{2.49}$$

integrated via the volume of the material body. The balance of momentum in the spatial

$$\frac{\mathrm{d}\boldsymbol{p}}{\mathrm{d}t} = \frac{\mathrm{d}}{\mathrm{d}t}\int\limits_{\omega} \boldsymbol{v}\left(\boldsymbol{x},t\right)\varrho\left(\boldsymbol{x},t\right)\mathrm{d}v = \int\limits_{\partial\omega} \boldsymbol{t}\left(\boldsymbol{x},t\right)\mathrm{d}a + \int\limits_{\omega} \boldsymbol{k}\left(\boldsymbol{x},t\right)\varrho\left(\boldsymbol{x},t\right)\mathrm{d}v, \tag{2.50a}$$

and the material representation

$$\frac{\mathrm{d}\boldsymbol{p}}{\mathrm{d}t} = \frac{\mathrm{d}}{\mathrm{d}t}\int\limits_{\Omega} \boldsymbol{v}\left(\boldsymbol{X},t\right)\varrho_{\mathrm{R}}\left(\boldsymbol{X},t\right)\mathrm{d}V = \int\limits_{\partial\Omega} \boldsymbol{t}_{\mathrm{R}}\left(\boldsymbol{X},t\right)\mathrm{d}A + \int\limits_{\Omega} \boldsymbol{k}\left(\boldsymbol{X},t\right)\varrho_{\mathrm{R}}\left(\boldsymbol{X},t\right)\mathrm{d}V \tag{2.50b}$$

states that the temporal change of momentum of a material body equals the sum of the forces acting on the surface of the material body and the volume-distributed force density induced, say, by gravity. Via Cauchy's theorem

$$\boldsymbol{t}\left(\boldsymbol{x},t,\boldsymbol{n}\right) = \mathbf{T}\left(\boldsymbol{x},t\right)\boldsymbol{n} \tag{2.51}$$

the stress vector $\boldsymbol{t}$ is related to the stress tensor $\mathbf{T}$. Similarly, the first Piola-Kirchhoff stress tensor

$$\mathbf{T}_{\mathrm{R}} = (\det\mathbf{F})\mathbf{T}\mathbf{F}^{-\mathrm{T}} \tag{2.52}$$

is related to the stress vector in the reference configuration

$$\boldsymbol{t}_{\mathrm{R}} = \mathbf{T}_{\mathrm{R}}\boldsymbol{n}_{\mathrm{R}}. \tag{2.53}$$

Making use of (2.19), (2.51) and the divergence theorem, the global balance of momentum (2.50a) results in

$$\int\limits_{\omega} \frac{\mathrm{d}}{\mathrm{d}t}\left(\boldsymbol{v}\left(\boldsymbol{x},t\right)\varrho\left(\boldsymbol{x},t\right)J\right)\mathrm{d}V = \int\limits_{\omega} \operatorname{div}\mathbf{T}\,\mathrm{d}v + \int\limits_{\omega} \boldsymbol{k}\left(\boldsymbol{x},t\right)\varrho\left(\boldsymbol{x},t\right)\mathrm{d}v. \tag{2.54}$$

With the time derivative of the determinant of the deformation gradient (2.29), the local balance of mass (2.47) and (2.19), we can formulate

$$\begin{aligned}\int\limits_{\omega} \frac{\mathrm{d}}{\mathrm{d}t}\left(\boldsymbol{v}\varrho J\right)\mathrm{d}V &= \int\limits_{\omega}\left(\frac{\mathrm{d}}{\mathrm{d}t}(\varrho\boldsymbol{v})J + \varrho\boldsymbol{v}\dot{J}\right)\mathrm{d}V \\ &= \int\limits_{\omega}\left(\dot{\varrho}\boldsymbol{v} + \varrho\dot{\boldsymbol{v}} + \varrho\boldsymbol{v}\operatorname{div}\boldsymbol{v}\right)J\,\mathrm{d}V = \int\limits_{\omega}\varrho\frac{\mathrm{d}}{\mathrm{d}t}\boldsymbol{v}\,\mathrm{d}v\end{aligned}$$

and the local balance of momentum expressed in terms of quantities of the current configuration yields

$$\varrho\frac{\mathrm{d}}{\mathrm{d}t}\boldsymbol{v}\left(\boldsymbol{x},t\right)=\operatorname{div}\mathbf{T}\left(\boldsymbol{x},t\right)+\varrho\left(\boldsymbol{x},t\right)\boldsymbol{k}\left(\boldsymbol{x},t\right). \tag{2.55a}$$

With respect to quantities of the reference configuration, we obtain

$$\varrho_{\mathrm{R}}\frac{\mathrm{d}}{\mathrm{d}t}\boldsymbol{v}\left(\boldsymbol{X},t\right)=\operatorname{Div}\mathbf{T}_{\mathrm{R}}\left(\boldsymbol{X},t\right)+\varrho_{\mathrm{R}}\left(\boldsymbol{X}\right)\boldsymbol{k}\left(\boldsymbol{X},t\right). \tag{2.55b}$$

2.2.3 Balance of Angular Momentum

The angular momentum of a material body expressed by means of quantities operating on the material and spatial representation, respectively, is given by

$$\boldsymbol{m}(\mathcal{B},t)=\int\limits_{\omega}(\boldsymbol{x}-\boldsymbol{c})\times\boldsymbol{v}\varrho(\boldsymbol{x},t)\,\mathrm{d}v=\int\limits_{\Omega}(\boldsymbol{\chi}_{\mathrm{R}}(\boldsymbol{X},t)-\boldsymbol{c})\times\boldsymbol{v}\varrho_{\mathrm{R}}(\boldsymbol{X})\,\mathrm{d}V. \tag{2.56}$$

Both the balance of momentum and the balance of angular momentum characterize the kinetic state of the material body. Its temporal change with respect to a fixed point $\boldsymbol{c}$ equals the external angular momentum acting on the material body. This external angular momentum consists of a sum representing the external angular momentum exerted by surface traction and a sum representing the external angular momentum resulting from a volume-distributed force density. Together with (2.47), (2.55a) the balance of angular momentum

$$\frac{\mathrm{d}\boldsymbol{m}}{\mathrm{d}t}=\frac{\mathrm{d}}{\mathrm{d}t}\int\limits_{\omega}(\boldsymbol{x}-\boldsymbol{c})\times\boldsymbol{v}\varrho\,\mathrm{d}v=\int\limits_{\partial\omega}(\boldsymbol{x}-\boldsymbol{c})\times\boldsymbol{t}\,\mathrm{d}a+\int\limits_{\omega}(\boldsymbol{x}-\boldsymbol{c})\times\boldsymbol{k}\varrho\,\mathrm{d}v \tag{2.57}$$

yields the symmetry of the Cauchy stress tensor

$$\mathbf{T}=\mathbf{T}^{\mathrm{T}}. \tag{2.58}$$

In order to express the specific stress power in terms of quantities operating on the material or the spatial representation, respectively, see (2.72a) and (2.72b) for instance, we introduce the second Piola-Kirchhoff stress tensor

$$\tilde{\mathbf{T}}:=(\det\mathbf{F})\,\mathbf{F}^{-1}\mathbf{T}\mathbf{F}^{-\mathrm{T}}. \tag{2.59}$$

It ensures the equality of the specific stress power in material and spatial representation, since

$$\frac{1}{\varrho}\mathbf{T}\cdot\mathbf{D}=\frac{\det\mathbf{F}}{\varrho_{\mathrm{R}}}\mathbf{T}\cdot\mathbf{F}^{-\mathrm{T}}\dot{\mathbf{E}}\mathbf{F}^{-1}=\frac{1}{\varrho_{\mathrm{R}}}\tilde{\mathbf{T}}\cdot\dot{\mathbf{E}} \tag{2.60}$$

holds. For the second Piola-Kirchhoff stress tensor the property

$$\tilde{\mathbf{T}}=\tilde{\mathbf{T}}^{\mathrm{T}} \tag{2.61}$$

also holds. But with (2.58), $\mathbf{T}=\frac{1}{J}\mathbf{T}_{\mathrm{R}}\mathbf{F}^{\mathrm{T}}$ and $\mathbf{T}^{\mathrm{T}}=\frac{1}{J}\mathbf{F}\mathbf{T}_{\mathrm{R}}^{\mathrm{T}}$

$$\mathbf{T}_{\mathrm{R}}=\mathbf{F}\mathbf{T}_{\mathrm{R}}^{\mathrm{T}}\mathbf{F}^{-\mathrm{T}} \tag{2.62}$$

is derived meaning that the first Piola-Kirchhoff stress tensor is not symmetric.

2.2.4 First Law of Thermodynamics - Balance of Energy

The total energy content of a material body is given by the sum of the kinetic

$$K(\mathcal{B},t) = \int\limits_{\omega} \tfrac{1}{2}\boldsymbol{v}\cdot\boldsymbol{v}\varrho\,\mathrm{d}v \tag{2.63}$$

and internal energy

$$E(\mathcal{B},t) = \int\limits_{\omega} e\varrho\,\mathrm{d}v \tag{2.64}$$

where e is the mass specific internal energy. The total energy content of a material body can be changed by the power of external forces

$$L(\mathcal{B},t) = \int\limits_{\partial\omega} \mathbf{T}\boldsymbol{n}\cdot\boldsymbol{v}\,\mathrm{d}a + \int\limits_{\omega} \boldsymbol{k}\cdot\boldsymbol{v}\varrho\,\mathrm{d}v \tag{2.65}$$

including the action of the surface and volume forces, and by a non-mechanical energy exchange such as the heat flux

$$Q(\mathcal{B},t) = -\int\limits_{\partial\omega} \boldsymbol{q}\cdot\boldsymbol{n}\,\mathrm{d}a + \int\limits_{\omega} r\varrho\,\mathrm{d}v. \tag{2.66}$$

$\boldsymbol{q}$ denotes the Cauchy heat flux vector and r a volume-distributed heat supply. Thus, the balance of energy can be formulated as

$$\dot{K}(\mathcal{B},t) + \dot{E}(\mathcal{B},t) = L(\mathcal{B},t) + Q(\mathcal{B},t). \tag{2.67}$$

Inserting (2.63) - (2.66) into (2.67) yields the global form of the energy balance in spatial representation

$$\frac{\mathrm{d}}{\mathrm{d}t}\int\limits_{\omega} \left(\tfrac{1}{2}\boldsymbol{v}\cdot\boldsymbol{v} + e\right)\varrho\,\mathrm{d}v = \int\limits_{\partial\omega} \mathbf{T}\boldsymbol{n}\cdot\boldsymbol{v}\,\mathrm{d}a + \int\limits_{\omega} \boldsymbol{k}\cdot\boldsymbol{v}\varrho\,\mathrm{d}v - \int\limits_{\partial\omega} \boldsymbol{q}\cdot\boldsymbol{n}\,\mathrm{d}a + \int\limits_{\omega} r\varrho\,\mathrm{d}v. \tag{2.68}$$

Based on the result of the balance of angular momentum (2.58), the definition of the transpose of a tensor $\mathbf{T}\boldsymbol{n}\cdot\boldsymbol{v} = \mathbf{T}^{T}\boldsymbol{v}\cdot\boldsymbol{n}$ and the divergence theorem

$$\int\limits_{\omega} \left(\boldsymbol{v}\cdot\dot{\boldsymbol{v}} + \dot{e}\right)\varrho\,\mathrm{d}v = \int\limits_{\omega} \left[\mathrm{div}\,\left(\mathbf{T}^{\mathrm{T}}\boldsymbol{v}\right) + \boldsymbol{k}\cdot\boldsymbol{v}\varrho - \mathrm{div}\,\boldsymbol{q} + r\varrho\right]\mathrm{d}v \tag{2.69}$$

follows. Inserting the product rule

$$\mathrm{div}\,\left(\mathbf{T}^{\mathrm{T}}\boldsymbol{v}\right) = \mathrm{div}\,\mathbf{T}\cdot\boldsymbol{v} + \mathbf{T}\cdot\,\mathrm{grad}\,\boldsymbol{v} = \left(\mathrm{div}\,\mathbf{T}\right)\,\cdot\boldsymbol{v} + \mathbf{T}\cdot\mathbf{D} \tag{2.70}$$

leads to

$$\int\limits_{\omega} \left[\left(\varrho\dot{\boldsymbol{v}} - \mathrm{div}\,\mathbf{T} - \varrho\boldsymbol{k}\right)\,\cdot\boldsymbol{v} + \varrho\dot{e} - \mathbf{T}\cdot\mathbf{D} + \mathrm{div}\,\boldsymbol{q} - r\varrho\right]\mathrm{d}v = 0. \tag{2.71}$$

With the help of (2.55a) we are able to simplify (2.71) to produce the local form of the energy balance in the spatial representation

$$\frac{\mathrm{d}e}{\mathrm{d}t} = \frac{1}{\varrho}\mathbf{T}\cdot\mathbf{D} - \frac{1}{\varrho}\mathrm{div}\,\boldsymbol{q} + r. \tag{2.72a}$$

For the material representation

$$\frac{\mathrm{d}e}{\mathrm{d}t} = \frac{1}{\varrho_{\mathrm{R}}}\tilde{\mathbf{T}}\cdot\dot{\mathbf{E}} - \frac{1}{\varrho_{\mathrm{R}}}\,\mathrm{Div}\,\boldsymbol{q}_{\mathrm{R}} + r \tag{2.72b}$$

follows analogously. The heat flux in the material representation is related to the heat flux in the spatial representation by means of

$$\boldsymbol{q}_{\mathrm{R}} = (\det\mathbf{F})\,\mathbf{F}^{-1}\boldsymbol{q} \qquad \leftrightarrow \qquad \boldsymbol{q} = \frac{1}{\det\mathbf{F}}\mathbf{F}\boldsymbol{q}_{\mathrm{R}}, \tag{2.73}$$

see (Haupt, 2000).

2.2.5 Second Law of Thermodynamics - Balance of Entropy

The balance of energy states that in an isolated system the total energy is conserved and can be transformed from one type of energy to another. The missing information on the direction of the transformation is provided by the second law of thermodynamics, which states that it is possible to create entropy but never to annihilate it. Entropy is a scalar quantity measuring the amount of energy that has been transformed irreversibly. The mere ideal limit case of a reversible process is accordingly labeled by zero entropy. Together with the balance of entropy, the second law of thermodynamics yields the Clausius-Duhem inequality which is the basis for a thermo-mechanically consistent material model. The entropy content of a material body is given by

$$S(\mathcal{B},t) = \int_{\omega} s\varrho\,\mathrm{d}v. \tag{2.74}$$

The integrand s is called specific entropy per unit mass, see (Haupt, 2000). The exchange between the entropy of a material body and its surroundings H can either be a volume-distributed exchange or an exchange which goes through the surface of the material body

$$H(\mathcal{B},t) = \int_{\partial\omega} \phi\,\mathrm{d}a + \int_{\omega} \sigma\varrho\,\mathrm{d}v. \tag{2.75}$$

We also introduce a volume-distributed production term

$$\Gamma(\mathcal{B},t) = \int_{\omega} \gamma\varrho\,\mathrm{d}v. \tag{2.76}$$

The balance of entropy, stating that the sum of the entropy supply and entropy production is equal to the temporal change of entropy, can now be formulated as

$$\dot{S}(\mathcal{B},t)=H(\mathcal{B},t)+\Gamma(\mathcal{B},t). \tag{2.77}$$

According to (Haupt, 2000) the entropy flux vector

$$\boldsymbol{\phi}=\frac{1}{\theta}\boldsymbol{q}, \tag{2.78}$$

where θ denotes the absolute temperature, is a good approximation for the entropy supply where processes close to equilibrium are considered. Based on (2.78), the entropy flux through the surface

$$\phi=-\boldsymbol{\phi}\cdot\boldsymbol{n} \tag{2.79}$$

and the volume-distributed entropy supply

$$\sigma=\frac{1}{\theta}r, \tag{2.80}$$

the second law of thermodynamics, stating that the entropy production is never negative,

$$\Gamma(\mathcal{B},t)=\dot{S}(\mathcal{B},t)-H(\mathcal{B},t)\geq 0 \tag{2.81}$$

yields

$$\Gamma=\frac{\mathrm{d}}{\mathrm{d}t}\int\limits_{\omega}s\varrho\,\mathrm{d}v+\int\limits_{\partial\omega}\frac{1}{\theta}\boldsymbol{q}\cdot\boldsymbol{n}\,\mathrm{d}a-\int\limits_{\omega}\frac{1}{\theta}r\varrho\,\mathrm{d}v\geq 0. \tag{2.82}$$

With the help of the divergence theorem, (2.82) yields

$$\Gamma=\frac{\mathrm{d}}{\mathrm{d}t}\int\limits_{\omega}s\varrho\,\mathrm{d}v-\int\limits_{\omega}\frac{1}{\theta}r\varrho\,\mathrm{d}v+\int\limits_{\omega}\left(\frac{1}{\theta}\mathrm{div}\,\boldsymbol{q}-\frac{1}{\theta^2}\,\mathrm{grad}\,\theta\cdot\boldsymbol{q}\right)\mathrm{d}v\geq 0. \tag{2.83}$$

It is now possible to derive the local form of the Clausius-Duhem inequality in spatial representation

$$\gamma=\dot{s}-\frac{r}{\theta}+\frac{1}{\theta\varrho}\mathrm{div}\,\boldsymbol{q}-\frac{1}{\varrho\theta^2}\,\mathrm{grad}\,\theta\cdot\boldsymbol{q}\geq 0, \tag{2.84}$$

where use is made of

$$\frac{\mathrm{d}}{\mathrm{d}t}\int\limits_{\omega}s\varrho\,\mathrm{d}v=\int\limits_{\omega}\frac{\mathrm{d}}{\mathrm{d}t}(s\varrho J)\,\mathrm{d}V=\int\limits_{\omega}(\dot{s}\varrho+s(\dot{\varrho}+\varrho\mathrm{div}\,\boldsymbol{v}))\,\mathrm{d}v=\int\limits_{\omega}\dot{s}\varrho\,\mathrm{d}v \tag{2.85}$$

with (2.19) and (2.47). Assuming the internal dissipation $d=\gamma\theta$ and (2.72a), (2.84) can be rewritten as

$$d=\theta\dot{s}-\dot{e}+\frac{1}{\varrho}\mathbf{T}\cdot\mathbf{D}-\frac{1}{\theta\varrho}\,\mathrm{grad}\,\theta\cdot\boldsymbol{q}\geq 0.$$

With the Helmholtz free energy

$$\psi := e - \theta s \tag{2.86}$$

and assuming

$$\theta\dot{s} - \dot{e} = \frac{\mathrm{d}}{\mathrm{d}t}\left(\theta s - e\right) - s\dot{\theta} \tag{2.87}$$

the Clausius-Duhem inequality can either be formulated in the spatial

$$d = -\dot{\psi} - s\dot{\theta} + \frac{1}{\varrho}\mathbf{T}\cdot\mathbf{D} - \frac{1}{\theta\varrho}\,\mathrm{grad}\,\theta\cdot\boldsymbol{q} \geq 0 \tag{2.88}$$

or in the material representation

$$d = -\dot{\psi} - s\dot{\theta} + \frac{1}{\varrho_{\mathrm{R}}}\tilde{\mathbf{T}}\cdot\dot{\mathbf{E}} - \frac{1}{\theta\varrho_{\mathrm{R}}}\,\mathrm{Grad}\,\theta\cdot\boldsymbol{q}_{\mathrm{R}} \geq 0. \tag{2.89}$$

2.3 A Material Model of finite Thermo-Viscoelasticity

Elastomers, also called rubber-like solids, are part of the polymer group and their behavior is considerably influenced by temperature. Under the glass transition temperature θ_{G} they exhibit a brittle, glass-like behavior, whereas for $\theta_{\mathrm{G}} < \theta$ an entropic elastic behavior enabling finite reversible deformations can be observed. Above θ_{G} a linear dependence of the equilibrium stresses on the temperature and a nonlinear dependence on the strain is visible. Elastomers exhibit nearly incompressible material behavior, as discussed in (Hartmann et al., 2001, 2003; Sedlan, 2000) and the stress-strain curve shows a dependence on the strain rate, see (Lion, 1997). The material model of finite thermo-viscoelasticity, whose derivation is sketched below, is based on (Hamkar, 2013). According to (Lion, 2000) the rheological model given in Fig. 2.1 is used to motivate the material model. Similar proposals have already been put foreward in (Heimes, 2005) and for isothermal material behavior in (Sedlan, 2000) and (Haupt and Sedlan, 2001). The free energy ψ is split into one part $\bar{\psi}_{\mathrm{M}}^{\mathrm{eq}}$, which is associated with the nonlinear spring accounting for

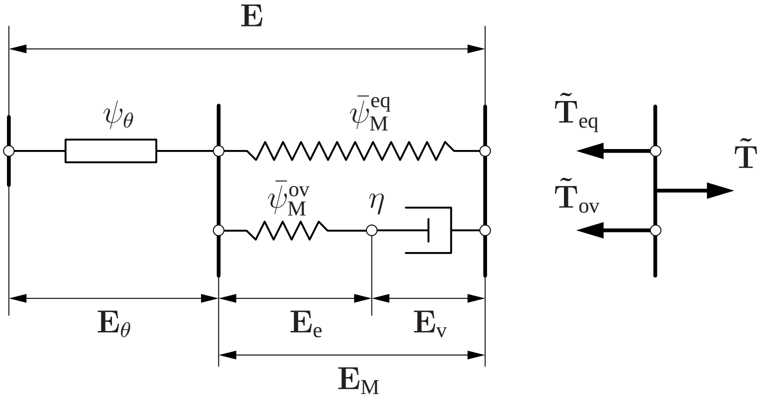

Figure 2.1: Rheological model of thermo-viscoelastic material model

the equilibrium stresses, one part $\bar{\psi}_{\mathrm{M}}^{\mathrm{ov}}$ accounting for the overstresses and one part ψ_θ which is associated with thermal deformation. The rate dependence of the damping elements is modeled via a nonlinear viscosity function η.

2.3.1 Multiplicative Decomposition of the Deformation Gradient and Choice of Free Energy

In the field of finite strains it is common to apply a multiplicative decomposition of the deformation gradient $\mathbf{F}$, see (Lubliner, 1985), for instance, in order to split the motion of a material point into different parts. According to (Lu and Pister, 1975) the deformation gradient is decomposed into an isothermal $\mathbf{F}_{\mathrm{M}}$ and a thermal part $\mathbf{F}_\theta$

$$\mathbf{F} = \mathbf{F}_\theta \mathbf{F}_{\mathrm{M}}. \tag{2.90}$$

This proposal is taken up in (Heimes, 2005; Holzapfel and Simo, 1996a; Lion, 1997; Miehe, 1988), among others. Since a thermal expansion can be considered to be purely volumetric in the case of elastomers, we choose the ansatz

$$\mathbf{F}_\theta = \varphi^{1/3}\mathbf{1} \quad \text{with} \quad \varphi := \hat{\varphi}(\theta - \theta_0) = 1 + \alpha_\theta(\theta - \theta_0), \tag{2.91}$$

see (Lion, 2000; Treloar, 1975), α_θ being the thermal expansion coefficient determining the volume change resulting from an increase in temperature. θ denotes the current temperature of a material point and θ_0 the reference temperature. For the mechanical part of the deformation gradient $\mathbf{F}_{\mathrm{M}}$ we introduce a decomposition into a volume-preserving $\bar{\mathbf{F}}_{\mathrm{M}}$ and a volume-changing $\hat{\mathbf{F}}_{\mathrm{M}}$ with the properties

$$\bar{\mathbf{F}}_{\mathrm{M}} = J_{\mathrm{M}}^{-\frac{1}{3}}\mathbf{F}_{\mathrm{M}}, \quad \det\bar{\mathbf{F}}_{\mathrm{M}} = 1, \quad \hat{\mathbf{F}}_{\mathrm{M}} = J_{\mathrm{M}}^{\frac{1}{3}}\mathbf{1} \quad \text{and} \quad \det\hat{\mathbf{F}}_{\mathrm{M}} = J_{\mathrm{M}},$$

see (Flory, 1961).We then proceed to split the volume-preserving mechanical part of the deformation gradient into an elastic $\bar{\mathbf{F}}_{\mathrm{e}}$ and a viscous part $\bar{\mathbf{F}}_{\mathrm{v}}$. Thus, the whole decomposition is described by

$$\mathbf{F} = \mathbf{F}_\theta\mathbf{F}_{\mathrm{M}} = \mathbf{F}_\theta\hat{\mathbf{F}}_{\mathrm{M}}\bar{\mathbf{F}}_{\mathrm{M}} = \mathbf{F}_\theta\hat{\mathbf{F}}_{\mathrm{M}}\bar{\mathbf{F}}_{\mathrm{e}}\bar{\mathbf{F}}_{\mathrm{v}} = \mathbf{F}_\theta\check{\mathbf{F}}_{\mathrm{e}}\bar{\mathbf{F}}_{\mathrm{v}} \tag{2.92}$$

where the elastic reversible deformation is given by

$$\check{\mathbf{F}}_{\mathrm{e}} = \hat{\mathbf{F}}_{\mathrm{M}}\bar{\mathbf{F}}_{\mathrm{e}}. \tag{2.93}$$

Fig. 2.2 illustrates the configurations involved and the deformation gradients mediating between them. Besides the reference $\boldsymbol{\mathcal{R}}$ and current configuration $\boldsymbol{\chi}_t$, we also introduce three intermediate configurations $\bar{\boldsymbol{\chi}}_t$, $\check{\boldsymbol{\chi}}_t$ and $\hat{\boldsymbol{\chi}}_t$. A material line element corresponding to the different configurations is also depicted. We consider this material line element in order to obtain the strain measures required. Based on the decomposition of the deformation gradient $\mathbf{F} = \mathbf{F}_\theta\check{\mathbf{F}}_{\mathrm{e}}\bar{\mathbf{F}}_{\mathrm{v}}$, given in (2.92), it can be expressed as

$$\mathrm{d}\boldsymbol{x} = \mathbf{F}_\theta\,\mathrm{d}\hat{\boldsymbol{x}}, \quad \mathrm{d}\hat{\boldsymbol{x}} = \check{\mathbf{F}}_{\mathrm{e}}\,\mathrm{d}\bar{\boldsymbol{x}}, \quad \mathrm{d}\bar{\boldsymbol{x}} = \bar{\mathbf{F}}_{\mathrm{v}}\,\mathrm{d}\boldsymbol{X} \tag{2.94}$$

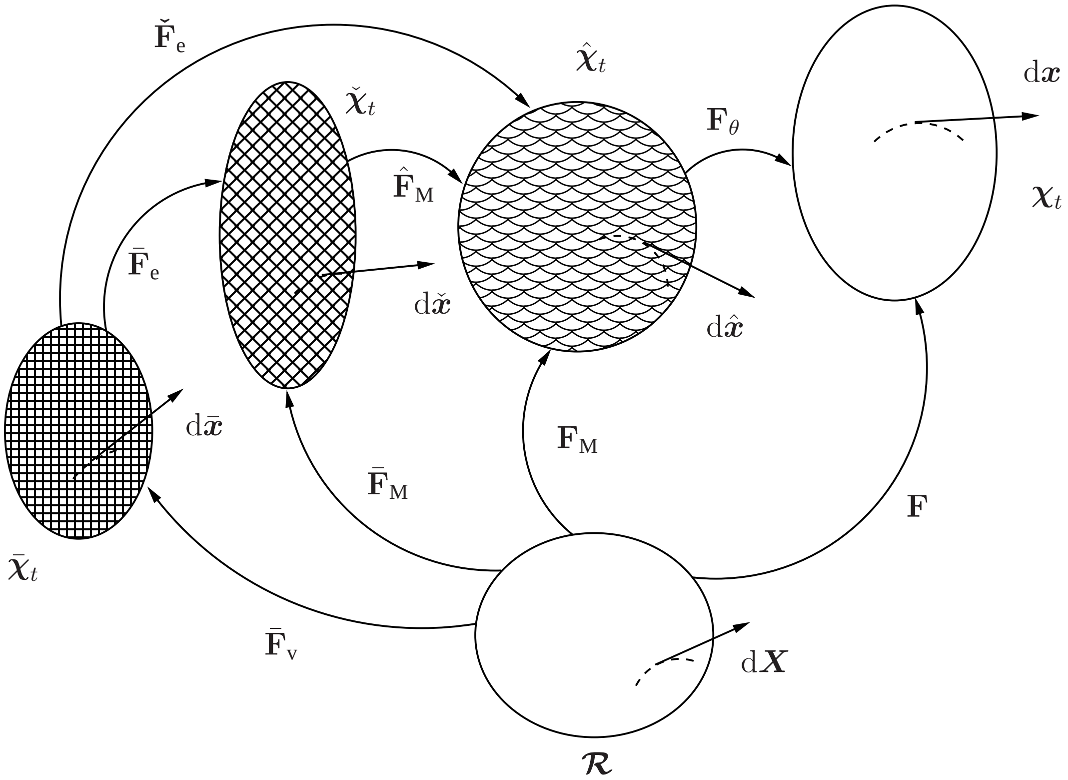

Figure 2.2: Decomposition of the deformation gradient

and

$$\mathrm{d}\boldsymbol{x} = \mathbf{F}_\theta \check{\mathbf{F}}_{\mathrm{e}} \bar{\mathbf{F}}_{\mathrm{v}} \, \mathrm{d}\boldsymbol{X} = \mathbf{F} \, \mathrm{d}\boldsymbol{X} . \tag{2.95}$$

Employing (2.17) and (2.21), one half of the difference between the squared material line element in the current and the reference configuration can be expressed as

$$\frac{1}{2}\left(\mathrm{d}\boldsymbol{x}^2 - \mathrm{d}\boldsymbol{X}^2\right) = \frac{1}{2}\left(\mathbf{F}\,\mathrm{d}\boldsymbol{X}\cdot\mathbf{F}\,\mathrm{d}\boldsymbol{X} - \mathrm{d}\boldsymbol{X}\cdot\,\mathrm{d}\boldsymbol{X}\right) = \mathrm{d}\boldsymbol{X}\cdot\mathbf{E}\,\mathrm{d}\boldsymbol{X} . \tag{2.96}$$

We accordingly obtain

$$\frac{1}{2}\left(\mathrm{d}\bar{\boldsymbol{x}}^2 - \mathrm{d}\boldsymbol{X}^2\right) = \mathrm{d}\boldsymbol{X}\cdot\mathbf{E}_{\mathrm{v}}\,\mathrm{d}\boldsymbol{X} , \tag{2.97}$$

$$\frac{1}{2}\left(\mathrm{d}\hat{\boldsymbol{x}}^2 - \mathrm{d}\bar{\boldsymbol{x}}^2\right) = \mathrm{d}\bar{\boldsymbol{x}}\cdot\check{\boldsymbol{\Gamma}}_{\mathrm{e}}\,\mathrm{d}\bar{\boldsymbol{x}} \quad \text{and} \tag{2.98}$$

$$\frac{1}{2}\left(\mathrm{d}\boldsymbol{x}^2 - \mathrm{d}\hat{\boldsymbol{x}}^2\right) = \mathrm{d}\hat{\boldsymbol{x}}\cdot\boldsymbol{\Gamma}_\theta\,\mathrm{d}\hat{\boldsymbol{x}} \tag{2.99}$$

which employs the viscous Green strain tensor

$$\mathbf{E}_{\mathrm{v}} = \frac{1}{2}\left(\bar{\mathbf{F}}_{\mathrm{v}}^{\mathrm{T}}\bar{\mathbf{F}}_{\mathrm{v}} - \mathbf{1}\right) \tag{2.100}$$

operating on $\boldsymbol{\mathcal{R}}$,

$$\check{\mathbf{\Gamma}}_{\mathrm{e}} = \frac{1}{2}\left(\check{\mathbf{F}}_{\mathrm{e}}^{\mathrm{T}}\check{\mathbf{F}}_{\mathrm{e}} - \mathbf{1}\right) \tag{2.101}$$

representing the elastic, reversible part of the total strains, operating on $\bar{\chi}_t$ and

$$\mathbf{\Gamma}_{\theta} = \frac{1}{2}\left(\mathbf{F}_{\theta}^{\mathrm{T}}\mathbf{F}_{\theta} - \mathbf{1}\right) = \frac{1}{2}\left(\varphi^{\frac{2}{3}} - 1\right)\mathbf{1}, \tag{2.102}$$

operating on $\hat{\chi}_t$. With (2.96), (2.97), (2.98) and (2.99) this leads to

$$\begin{aligned} \mathrm{d}\boldsymbol{X}\cdot\mathbf{E}\,\mathrm{d}\boldsymbol{X} &= \mathrm{d}\boldsymbol{X}\cdot\mathbf{E}_{\mathrm{v}}\,\mathrm{d}\boldsymbol{X} + \mathrm{d}\bar{\boldsymbol{x}}\cdot\check{\mathbf{\Gamma}}_{\mathrm{e}}\,\mathrm{d}\bar{\boldsymbol{x}} + \mathrm{d}\hat{\boldsymbol{x}}\cdot\mathbf{\Gamma}_{\theta}\,\mathrm{d}\hat{\boldsymbol{x}} \\ &= \mathrm{d}\boldsymbol{X}\cdot\mathbf{E}_{\mathrm{v}}\,\mathrm{d}\boldsymbol{X} + \mathrm{d}\boldsymbol{X}\cdot\bar{\mathbf{F}}_{\mathrm{v}}^{\mathrm{T}}\check{\mathbf{\Gamma}}_{\mathrm{e}}\bar{\mathbf{F}}_{\mathrm{v}}\,\mathrm{d}\boldsymbol{X} + \mathrm{d}\boldsymbol{X}\cdot\bar{\mathbf{F}}_{\mathrm{v}}^{\mathrm{T}}\check{\mathbf{F}}_{\mathrm{e}}^{\mathrm{T}}\mathbf{\Gamma}_{\theta}\check{\mathbf{F}}_{\mathrm{e}}\bar{\mathbf{F}}_{\mathrm{v}}\,\mathrm{d}\boldsymbol{X} \\ &= \mathrm{d}\boldsymbol{X}\cdot\left(\mathbf{E}_{\mathrm{v}} + \bar{\mathbf{F}}_{\mathrm{v}}^{\mathrm{T}}\check{\mathbf{\Gamma}}_{\mathrm{e}}\bar{\mathbf{F}}_{\mathrm{v}} + \bar{\mathbf{F}}_{\mathrm{v}}^{\mathrm{T}}\check{\mathbf{F}}_{\mathrm{e}}^{\mathrm{T}}\mathbf{\Gamma}_{\theta}\check{\mathbf{F}}_{\mathrm{e}}\bar{\mathbf{F}}_{\mathrm{v}}\right)\mathrm{d}\boldsymbol{X} \\ &= \mathrm{d}\boldsymbol{X}\cdot\left(\mathbf{E}_{\mathrm{v}} + \mathbf{E}_{\mathrm{e}} + \mathbf{E}_{\theta}\right)\mathrm{d}\boldsymbol{X} \end{aligned} \tag{2.103}$$

with the elastic Green strain tensor

$$\mathbf{E}_{\mathrm{e}} = \bar{\mathbf{F}}_{\mathrm{v}}^{\mathrm{T}}\check{\mathbf{\Gamma}}_{\mathrm{e}}\bar{\mathbf{F}}_{\mathrm{v}} = \frac{1}{2}\left(\mathbf{F}_{\mathrm{M}}^{\mathrm{T}}\mathbf{F}_{\mathrm{M}} - \bar{\mathbf{F}}_{\mathrm{v}}^{\mathrm{T}}\bar{\mathbf{F}}_{\mathrm{v}}\right), \tag{2.104}$$

the thermal Green strain tensor

$$\mathbf{E}_{\theta} = \bar{\mathbf{F}}_{\mathrm{v}}^{\mathrm{T}}\check{\mathbf{F}}_{\mathrm{e}}^{\mathrm{T}}\mathbf{\Gamma}_{\theta}\check{\mathbf{F}}_{\mathrm{e}}\bar{\mathbf{F}}_{\mathrm{v}} = \frac{1}{2}\left(\mathbf{F}^{\mathrm{T}}\mathbf{F} - \mathbf{F}_{\mathrm{M}}^{\mathrm{T}}\mathbf{F}_{\mathrm{M}}\right) = \mathbf{E} - \mathbf{E}_{\mathrm{M}}, \tag{2.105}$$

see (Hamkar and Hartmann, 2012) and (2.100). The mechanical strain tensor is defined as the sum of the elastic and the viscous Green strains

$$\mathbf{E}_{\mathrm{M}} := \mathbf{E}_{\mathrm{e}} + \mathbf{E}_{\mathrm{v}} = \lim_{\theta\to\theta_0}\mathbf{E} = \frac{1}{2}\left(\mathbf{F}_{\mathrm{M}}^{\mathrm{T}}\mathbf{F}_{\mathrm{M}} - \mathbf{1}\right). \tag{2.106}$$

In order to determine the transformation of strain measures expressed by quantities operating on the reference and quantities operating on the mechanical intermediate configuration, we look at the difference in the squared material line elements

$$\begin{aligned} \frac{1}{2}\left(\mathrm{d}\hat{\boldsymbol{x}}^2 - \mathrm{d}\boldsymbol{X}^2\right) &= \mathrm{d}\boldsymbol{X}\cdot\frac{1}{2}\left(\mathbf{F}_{\mathrm{M}}^{\mathrm{T}}\mathbf{F}_{\mathrm{M}} - \mathbf{1}\right)\mathrm{d}\boldsymbol{X} = \mathrm{d}\boldsymbol{X}\cdot\mathbf{E}_{\mathrm{M}}\,\mathrm{d}\boldsymbol{X} \\ &= \frac{1}{2}\left(\mathrm{d}\hat{\boldsymbol{x}}^2 - \mathbf{F}_{\mathrm{M}}^{-1}\,\mathrm{d}\hat{\boldsymbol{x}}\cdot\mathbf{F}_{\mathrm{M}}^{-1}\,\mathrm{d}\hat{\boldsymbol{x}}\right) = \frac{1}{2}\left(\mathrm{d}\hat{\boldsymbol{x}}^2 - \mathrm{d}\hat{\boldsymbol{x}}\cdot\mathbf{F}_{\mathrm{M}}^{-\mathrm{T}}\mathbf{F}_{\mathrm{M}}^{-1}\,\mathrm{d}\hat{\boldsymbol{x}}\right) \\ &= \mathrm{d}\hat{\boldsymbol{x}}\cdot\frac{1}{2}\left(\mathbf{1} - \mathbf{F}_{\mathrm{M}}^{-\mathrm{T}}\mathbf{F}_{\mathrm{M}}^{-1}\right)\mathrm{d}\hat{\boldsymbol{x}} = \mathrm{d}\hat{\boldsymbol{x}}\cdot\mathbf{\Gamma}_{\mathrm{M}}\,\mathrm{d}\hat{\boldsymbol{x}} = \mathrm{d}\boldsymbol{X}\cdot\mathbf{F}_{\mathrm{M}}^{\mathrm{T}}\mathbf{\Gamma}_{\mathrm{M}}\mathbf{F}_{\mathrm{M}}\,\mathrm{d}\boldsymbol{X} \end{aligned}$$

resulting in the relations

$$\mathbf{\Gamma}_{\mathrm{M}} = \frac{1}{2}\left(\mathbf{1} - \mathbf{F}_{\mathrm{M}}^{-\mathrm{T}}\mathbf{F}_{\mathrm{M}}^{-1}\right) \tag{2.107}$$

and

$$\mathbf{E}_{\mathrm{M}} = \mathbf{F}_{\mathrm{M}}^{\mathrm{T}}\mathbf{\Gamma}_{\mathrm{M}}\mathbf{F}_{\mathrm{M}} \quad \leftrightarrow \quad \mathbf{\Gamma}_{\mathrm{M}} = \mathbf{F}_{\mathrm{M}}^{-\mathrm{T}}\mathbf{E}_{\mathrm{M}}\mathbf{F}_{\mathrm{M}}^{-1}. \tag{2.108}$$

In a similar way, it is possible to motivate

$$\mathbf{E}_\mathrm{v} = \bar{\mathbf{F}}_\mathrm{v}^\mathrm{T}\bar{\boldsymbol{\Gamma}}_\mathrm{v}\bar{\mathbf{F}}_\mathrm{v} \quad \leftrightarrow \quad \bar{\boldsymbol{\Gamma}}_\mathrm{v} = \bar{\mathbf{F}}_\mathrm{v}^{-\mathrm{T}}\mathbf{E}_\mathrm{v}\bar{\mathbf{F}}_\mathrm{v}^{-1}. \tag{2.109}$$

Thus, by means of $\mathbf{F}_\mathrm{M}^{-\mathrm{T}}\,(.)\,\mathbf{F}_\mathrm{M}^{-1}$ strain tensors are transformed from $\boldsymbol{\mathcal{R}}$ to $\hat{\chi}_t$ and by $\bar{\mathbf{F}}_\mathrm{v}^{-\mathrm{T}}\,(.)\,\bar{\mathbf{F}}_\mathrm{v}^{-1}$ from $\boldsymbol{\mathcal{R}}$ to $\bar{\chi}_t$. The same relations hold true for the rates of the strain tensors resulting in

$$\begin{aligned}
\overset{\triangle}{\boldsymbol{\Gamma}} = \mathbf{F}_\mathrm{M}^{-\mathrm{T}}\dot{\mathbf{E}}\mathbf{F}_\mathrm{M}^{-1} &= \frac{1}{2}\left(\mathbf{F}_\mathrm{M}^{-\mathrm{T}}\dot{\mathbf{F}}^\mathrm{T}\mathbf{F}\mathbf{F}_\mathrm{M}^{-1} + \mathbf{F}_\mathrm{M}^{-\mathrm{T}}\mathbf{F}^\mathrm{T}\dot{\mathbf{F}}\mathbf{F}_\mathrm{M}^{-1}\right)\\
&= \frac{1}{2}\left(\mathbf{F}_\mathrm{M}^{-\mathrm{T}}\left(\mathbf{F}_\mathrm{M}^\mathrm{T}\dot{\mathbf{F}}_\theta^\mathrm{T} + \dot{\mathbf{F}}_\mathrm{M}^\mathrm{T}\mathbf{F}_\theta^\mathrm{T}\right)\mathbf{F}_\theta + \mathbf{F}_\theta^\mathrm{T}\left(\dot{\mathbf{F}}_\theta\mathbf{F}_\mathrm{M} + \mathbf{F}_\theta\dot{\mathbf{F}}_\mathrm{M}\right)\mathbf{F}_\mathrm{M}^{-1}\right)\\
&= \frac{1}{2}\left(\dot{\mathbf{F}}_\theta^\mathrm{T}\mathbf{F}_\theta + \mathbf{F}_\mathrm{M}^{-\mathrm{T}}\dot{\mathbf{F}}_\mathrm{M}^\mathrm{T}\mathbf{F}_\theta^\mathrm{T}\mathbf{F}_\theta + \mathbf{F}_\theta^\mathrm{T}\dot{\mathbf{F}}_\theta + \mathbf{F}_\theta^\mathrm{T}\mathbf{F}_\theta\dot{\mathbf{F}}_\mathrm{M}\mathbf{F}_\mathrm{M}^{-1}\right)\\
&= \frac{1}{2}\left(\frac{2}{3}\varphi^{-\frac{1}{3}}\varphi'\dot{\theta}\mathbf{1} + \left(\mathbf{F}_\mathrm{M}^{-\mathrm{T}}\dot{\mathbf{F}}_\mathrm{M}^\mathrm{T} + \dot{\mathbf{F}}_\mathrm{M}\mathbf{F}_\mathrm{M}^{-\mathrm{T}}\right)\varphi^{\frac{2}{3}}\right)\\
&= \left(\frac{1}{3}\varphi^{-\frac{1}{3}}\varphi'\dot{\theta}\mathbf{1} + \frac{1}{2}\left(\mathbf{L}_\mathrm{M}^\mathrm{T} + \mathbf{L}_\mathrm{M}\right)\varphi^{\frac{2}{3}}\right)\\
&= \left(\frac{1}{3}\varphi^{-\frac{1}{3}}\varphi'\dot{\theta}\mathbf{1} + \overset{\triangle}{\boldsymbol{\Gamma}}_\mathrm{M}\varphi^{\frac{2}{3}}\right)
\end{aligned} \tag{2.110}$$

based on $\dot{\mathbf{F}}_\theta = \frac{1}{3}\varphi^{-\frac{2}{3}}\varphi'\dot{\theta}\mathbf{1}$, $\mathbf{L}_\mathrm{M} = \dot{\mathbf{F}}_\mathrm{M}\mathbf{F}_\mathrm{M}^{-1}$ and

$$\overset{\triangle}{\boldsymbol{\Gamma}}_\mathrm{M} = \mathbf{F}_\mathrm{M}^{-\mathrm{T}}\dot{\mathbf{E}}_\mathrm{M}\mathbf{F}_\mathrm{M}^{-1} = \frac{1}{2}\left(\mathbf{F}_\mathrm{M}^{-\mathrm{T}}\dot{\mathbf{F}}_\mathrm{M}^\mathrm{T} + \dot{\mathbf{F}}_\mathrm{M}\mathbf{F}_\mathrm{M}^{-1}\right) = \frac{1}{2}\left(\mathbf{L}_\mathrm{M}^\mathrm{T} + \mathbf{L}_\mathrm{M}\right).$$

Another quantity that is of interest is

$$\begin{aligned}
\overset{\triangle}{\check{\boldsymbol{\Gamma}}} = \bar{\mathbf{F}}_\mathrm{v}^{-\mathrm{T}}\dot{\mathbf{E}}\bar{\mathbf{F}}_\mathrm{v}^{-1} &= \frac{1}{2}\bar{\mathbf{F}}_\mathrm{v}^{-\mathrm{T}}\left(\dot{\mathbf{F}}^\mathrm{T}\mathbf{F} + \mathbf{F}^\mathrm{T}\dot{\mathbf{F}}\right)\bar{\mathbf{F}}_\mathrm{v}^{-1}\\
&= \frac{1}{2}\Big(\check{\mathbf{F}}_\mathrm{e}^\mathrm{T}\dot{\mathbf{F}}_\theta^\mathrm{T}\mathbf{F}_\theta\check{\mathbf{F}}_\mathrm{e} + \dot{\check{\mathbf{F}}}_\mathrm{e}^\mathrm{T}\mathbf{F}_\theta^\mathrm{T}\mathbf{F}_\theta\check{\mathbf{F}}_\mathrm{e} + \bar{\mathbf{F}}_\mathrm{v}^{-\mathrm{T}}\dot{\bar{\mathbf{F}}}_\mathrm{v}^\mathrm{T}\check{\mathbf{F}}_\mathrm{e}^\mathrm{T}\mathbf{F}_\theta^\mathrm{T}\mathbf{F}_\theta\check{\mathbf{F}}_\mathrm{e}\\
&\qquad + \check{\mathbf{F}}_\mathrm{e}^\mathrm{T}\mathbf{F}_\theta^\mathrm{T}\dot{\mathbf{F}}_\theta\check{\mathbf{F}}_\mathrm{e} + \check{\mathbf{F}}_\mathrm{e}^\mathrm{T}\mathbf{F}_\theta^\mathrm{T}\mathbf{F}_\theta\dot{\check{\mathbf{F}}}_\mathrm{e} + \check{\mathbf{F}}_\mathrm{e}\mathbf{F}_\theta^\mathrm{T}\mathbf{F}_\theta\check{\mathbf{F}}_\mathrm{e}\dot{\bar{\mathbf{F}}}_\mathrm{v}\bar{\mathbf{F}}_\mathrm{v}^{-\mathrm{T}}\Big)\\
&= \frac{1}{2}\left(\frac{1}{3}\varphi^{-\frac{1}{3}}\varphi'\dot{\theta}\check{\mathbf{C}}_\mathrm{e} + \varphi^{\frac{2}{3}}\dot{\check{\mathbf{F}}}_\mathrm{e}^\mathrm{T}\check{\mathbf{F}}_\mathrm{e} + \varphi^{\frac{2}{3}}\mathbf{L}_\mathrm{v}^\mathrm{T}\check{\mathbf{C}}_\mathrm{e} + \frac{1}{3}\varphi^{-\frac{1}{3}}\varphi'\dot{\theta}\check{\mathbf{C}}_\mathrm{e} + \varphi^{\frac{2}{3}}\check{\mathbf{F}}_\mathrm{e}^\mathrm{T}\dot{\check{\mathbf{F}}}_\mathrm{e} + \varphi^{\frac{2}{3}}\check{\mathbf{C}}_\mathrm{e}\mathbf{L}_\mathrm{v}\right)\\
&= \frac{1}{2}\left(\frac{2}{3}\varphi^{-\frac{1}{3}}\varphi'\dot{\theta}\check{\mathbf{C}}_\mathrm{e} + \varphi^{\frac{2}{3}}\left(\dot{\check{\mathbf{C}}}_\mathrm{e} + \mathbf{L}_\mathrm{v}^\mathrm{T}\check{\mathbf{C}}_\mathrm{e} + \check{\mathbf{C}}_\mathrm{e}\mathbf{L}_\mathrm{v}\right)\right)
\end{aligned} \tag{2.111}$$

which is based on

$$\varphi' = \frac{\mathrm{d}\varphi}{\mathrm{d}\theta}, \quad \dot{\mathbf{F}}_\theta = \frac{1}{3}\varphi^{-\frac{2}{3}}\varphi'\dot{\theta}\mathbf{1}, \quad \check{\mathbf{C}}_\mathrm{e} = \check{\mathbf{F}}_\mathrm{e}^\mathrm{T}\check{\mathbf{F}}_\mathrm{e} \quad \text{and} \quad \mathbf{L}_\mathrm{v} = \dot{\bar{\mathbf{F}}}_\mathrm{v}\bar{\mathbf{F}}_\mathrm{v}^{-1}. \tag{2.112}$$

With the derivative of the elastic

$$\overset{\triangle}{\check{\boldsymbol{\Gamma}}}_\mathrm{e} = \bar{\mathbf{F}}_\mathrm{v}^{-\mathrm{T}}\dot{\mathbf{E}}_\mathrm{e}\bar{\mathbf{F}}_\mathrm{v}^{-1} = \dot{\check{\boldsymbol{\Gamma}}}_\mathrm{e} + \mathbf{L}_\mathrm{v}^\mathrm{T}\check{\boldsymbol{\Gamma}}_\mathrm{e} + \check{\boldsymbol{\Gamma}}_\mathrm{e}\mathbf{L}_\mathrm{v}, \quad \dot{\check{\boldsymbol{\Gamma}}}_\mathrm{e} = \frac{1}{2}\left(\dot{\check{\mathbf{F}}}_\mathrm{e}^\mathrm{T}\check{\mathbf{F}}_\mathrm{e} + \check{\mathbf{F}}_\mathrm{e}^\mathrm{T}\dot{\check{\mathbf{F}}}_\mathrm{e}\right) \tag{2.113}$$

and viscous strain tensor

$$\overset{\triangle}{\bar{\boldsymbol{\Gamma}}}_{\mathrm{v}} = \frac{1}{2}\bar{\mathbf{F}}_{\mathrm{v}}^{-\mathrm{T}}\dot{\mathbf{C}}_{\mathrm{v}}\bar{\mathbf{F}}_{\mathrm{v}}^{-1} = \frac{1}{2}\left(\bar{\mathbf{F}}_{\mathrm{v}}^{-\mathrm{T}}\dot{\bar{\mathbf{F}}}_{\mathrm{v}}^{\mathrm{T}} + \dot{\bar{\mathbf{F}}}_{\mathrm{v}}\bar{\mathbf{F}}_{\mathrm{v}}^{-1}\right) = \frac{1}{2}\left(\mathbf{L}_{\mathrm{v}} + \mathbf{L}_{\mathrm{v}}^{\mathrm{T}}\right) \tag{2.114}$$

(2.111) finally yields

$$\overset{\triangle}{\check{\boldsymbol{\Gamma}}} = \frac{1}{3}\varphi^{-\frac{1}{3}}\varphi'\dot{\theta}\check{\mathbf{C}}_{\mathrm{e}} + \varphi^{\frac{2}{3}}\left(\overset{\triangle}{\check{\boldsymbol{\Gamma}}}_{\mathrm{e}} + \overset{\triangle}{\bar{\boldsymbol{\Gamma}}}_{\mathrm{v}}\right). \tag{2.115}$$

We discuss the choice of the free energy in terms of these strain measures to serve as a basis for deriving a thermodynamically consistent material model. According to (Lion, 2000) and (Heimes, 2005), we introduce a decomposition of the free energy into a mechanical part ψ_{M} and a part that depends on the temperature

$$\psi\left(\mathbf{E}_{\mathrm{M}}, \check{\boldsymbol{\Gamma}}_{\mathrm{e}}, \theta\right) = \psi_{\mathrm{M}}\left(\mathbf{E}_{\mathrm{M}}, \check{\boldsymbol{\Gamma}}_{\mathrm{e}}, \theta\right) + \psi_{\theta}(\theta). \tag{2.116}$$

For the definition of ψ_θ see (2.216). The former is dissected into

$$\psi_{\mathrm{M}}\left(\mathbf{E}_{\mathrm{M}}, \check{\boldsymbol{\Gamma}}_{\mathrm{e}}, \theta\right) = \frac{\theta}{\theta_0}\bar{\psi}_{\mathrm{M}}^{\mathrm{eq}}(J_{\mathrm{M}}, \mathbf{C}_{\mathrm{M}}) + \bar{\psi}_{\mathrm{M}}^{\mathrm{ov}}(\check{\boldsymbol{\Gamma}}_{\mathrm{e}}, \theta) \tag{2.117}$$

where $\bar{\psi}_{\mathrm{M}}^{\mathrm{eq}}(J_{\mathrm{M}}, \mathbf{C}_{\mathrm{M}})$ represents the energy stored in the nonlinear spring accounting for the elastic energy contribution of the rheoligical model given in Fig. 2.1 and $\bar{\psi}_{\mathrm{M}}^{\mathrm{ov}}(\check{\boldsymbol{\Gamma}}_{\mathrm{e}}, \theta)$ represents the energy stored in the nonlinear spring of the Maxwell-element. As proposed in (Hartmann, 2003) and (Hartmann and Neff, 2003) $\bar{\psi}_{\mathrm{M}}^{\mathrm{eq}}$ is further divided into

$$\bar{\psi}_{\mathrm{M}}^{\mathrm{eq}} = U(J_{\mathrm{M}}) + \bar{v}(\bar{\mathbf{C}}_{\mathrm{M}}) \tag{2.118}$$

with

$$U(J_{\mathrm{M}}) = \frac{K}{50\varrho_{\mathrm{R}}}\left(J_{\mathrm{M}}^{5} + J_{\mathrm{M}}^{-5} - 2\right) \tag{2.119}$$

and

$$\begin{aligned} \bar{v}(\bar{\mathbf{C}}_{\mathrm{M}}) &= \bar{v}(\bar{\mathbf{C}}) = w\left(\mathrm{I}_{\bar{\mathbf{C}}}, \mathrm{II}_{\bar{\mathbf{C}}}\right) \\ &= (1/\varrho_{\mathrm{R}})\left(c_{10}\left(\mathrm{I}_{\bar{\mathbf{C}}} - 3\right) + c_{01}\left(\mathrm{II}_{\bar{\mathbf{C}}}^{3/2} - 3\sqrt{3}\right) + \alpha\left(\mathrm{I}_{\bar{\mathbf{C}}}^{3} - 27\right)\right) \end{aligned} \tag{2.120}$$

which is based on

$$\bar{\mathbf{C}}_{\mathrm{M}} = J_{\mathrm{M}}^{-\frac{2}{3}}\bar{\mathbf{C}} = \left(\frac{J}{\varphi}\right)^{-\frac{2}{3}}\varphi^{-\frac{2}{3}}\mathbf{C} = J^{-\frac{2}{3}}\mathbf{C} = \bar{\mathbf{C}}. \tag{2.121}$$

$U(J_{\mathrm{M}})$ is related to a volume-changing and $\bar{v}(\bar{\mathbf{C}}_{\mathrm{M}})$ to a volume-preserving deformation. For a discussion about the ansatz (2.119) see (Hamkar and Hartmann, 2012; Hartmann and Neff, 2003). Employing the definition of the heat capacity

$$c = \theta\frac{\partial s}{\partial \theta} \tag{2.122}$$

we identify ψ_θ, see (Haupt, 2000). Since a relation for the entropy s and heat capacity is called for in (2.122), we discuss the derivation of ψ_θ in Section 2.4. For the free energy related to the spring accounting for the overstresses, we assume

$$\bar{\psi}_{\mathrm{M}}^{\mathrm{ov}}(\check{\boldsymbol{\Gamma}}_{\mathrm{e}}, \theta) = \bar{w}_{\mathrm{ov}}\left(\bar{\mathbf{C}}_{\mathrm{e}}\left(\check{\mathbf{C}}_{\mathrm{e}}\right)\right) = \bar{w}_{\mathrm{ov}}\left(\mathrm{I}_{\bar{\mathbf{C}}_{\mathrm{e}}}\right) = \frac{\mu}{\varrho_{\mathrm{R}}}\left(\mathrm{I}_{\bar{\mathbf{C}}_{\mathrm{e}}} - 3\right) \tag{2.123}$$

with $\check{\mathbf{C}}_{\mathrm{e}} = \check{\mathbf{F}}_{\mathrm{e}}^{\mathrm{T}}\check{\mathbf{F}}_{\mathrm{e}}$, $\bar{\mathbf{C}}_{\mathrm{e}} = \left(\det \check{\mathbf{C}}_{\mathrm{e}}\right)^{-\frac{1}{3}}\check{\mathbf{C}}_{\mathrm{e}}$ and $\mathrm{I}_{\bar{\mathbf{C}}_{\mathrm{e}}} = \operatorname{tr}\bar{\mathbf{C}}_{\mathrm{e}}$, see (Lion, 2000).

2.3.2 Exploitation of the Dissipation Inequality

The stress power is reformulated employing quantities operating on the intermediate configuration according to the concept of dual variables, see (Haupt and Tsakmakis, 1989, 1996),

$$\tilde{\mathbf{T}} \cdot \dot{\mathbf{E}} = \mathbf{S}_{\mathrm{M}}^{\mathrm{eq}} \cdot \mathbf{F}_{\mathrm{M}}^{-\mathrm{T}}\dot{\mathbf{E}}\mathbf{F}_{\mathrm{M}}^{-1} + \check{\mathbf{S}}_{\mathrm{ov}} \cdot \bar{\mathbf{F}}_{\mathrm{v}}^{-\mathrm{T}}\dot{\mathbf{E}}\bar{\mathbf{F}}_{\mathrm{v}}^{-1} = \mathbf{S}_{\mathrm{M}}^{\mathrm{eq}} \cdot \overset{\triangle}{\hat{\boldsymbol{\Gamma}}} + \check{\mathbf{S}}_{\mathrm{ov}} \cdot \overset{\triangle}{\check{\boldsymbol{\Gamma}}}. \tag{2.124}$$

$\mathbf{S}_{\mathrm{M}}^{\mathrm{eq}}$ denotes the equilibrium stress tensor operating on $\hat{\boldsymbol{\chi}}_t$ and $\check{\mathbf{S}}_{\mathrm{ov}}$ the overstresses operating on $\check{\boldsymbol{\chi}}_t$. Inserting (2.110) and (2.115) into (2.124) leads to

$$\tilde{\mathbf{T}} \cdot \dot{\mathbf{E}} = \varphi^{2/3}\mathbf{S}_{\mathrm{M}}^{\mathrm{eq}} \cdot \overset{\triangle}{\boldsymbol{\Gamma}}_{\mathrm{M}} + \frac{\varphi'}{3\varphi^{1/3}}\left(\operatorname{tr}\mathbf{S}_{\mathrm{M}}^{\mathrm{eq}}\right)\dot{\theta} + \varphi^{2/3}\check{\mathbf{S}}_{\mathrm{ov}} \cdot \left(\overset{\triangle}{\check{\boldsymbol{\Gamma}}}_{\mathrm{e}} + \overset{\triangle}{\bar{\boldsymbol{\Gamma}}}_{\mathrm{v}}\right) + \frac{1}{3}\varphi^{-\frac{1}{3}}\varphi'\dot{\theta}\check{\mathbf{S}}_{\mathrm{ov}} \cdot \check{\mathbf{C}}_{\mathrm{e}} \tag{2.125}$$

which with

$$\check{\mathbf{S}}_{\mathrm{ov}} \cdot \check{\mathbf{C}}_{\mathrm{e}} = \check{\mathbf{S}}_{\mathrm{ov}} \cdot \check{\mathbf{F}}_{\mathrm{e}}^{\mathrm{T}}\check{\mathbf{F}}_{\mathrm{e}} = \check{\mathbf{F}}_{\mathrm{e}}\check{\mathbf{S}}_{\mathrm{ov}}\check{\mathbf{F}}_{\mathrm{e}}^{\mathrm{T}} \cdot \mathbf{1} = \mathbf{1} \cdot \mathbf{S}_{\mathrm{M}}^{\mathrm{ov}} = \operatorname{tr}\mathbf{S}_{\mathrm{M}}^{\mathrm{ov}} \tag{2.126}$$

and

$$\mathbf{S}_{\mathrm{M}} = \mathbf{S}_{\mathrm{M}}^{\mathrm{eq}} + \mathbf{S}_{\mathrm{M}}^{\mathrm{ov}} \tag{2.127}$$

finally yields

$$\tilde{\mathbf{T}} \cdot \dot{\mathbf{E}} = \varphi^{2/3}\mathbf{S}_{\mathrm{M}}^{\mathrm{eq}} \cdot \overset{\triangle}{\boldsymbol{\Gamma}}_{\mathrm{M}} + \frac{\varphi'}{3\varphi^{1/3}}\left(\operatorname{tr}\mathbf{S}_{\mathrm{M}}\right)\dot{\theta} + \varphi^{2/3}\check{\mathbf{S}}_{\mathrm{ov}} \cdot \left(\overset{\triangle}{\check{\boldsymbol{\Gamma}}}_{\mathrm{e}} + \overset{\triangle}{\bar{\boldsymbol{\Gamma}}}_{\mathrm{v}}\right). \tag{2.128}$$

In order to guarantee the thermodynamical consistency of the material model, we demonstrate below that the constitutive relations fulfill the second law of thermodynamics. Inserting the time derivative of the free energy

$$\dot{\psi} = \frac{\partial\psi}{\partial\mathbf{E}_{\mathrm{M}}} \cdot \dot{\mathbf{E}}_{\mathrm{M}} + \frac{\partial\psi}{\partial\check{\boldsymbol{\Gamma}}_{\mathrm{e}}} \cdot \dot{\check{\boldsymbol{\Gamma}}}_{\mathrm{e}} + \frac{\partial\psi}{\partial\theta}\dot{\theta} \tag{2.129}$$

and the stress power (2.128) into the Clausius-Duhem inequality (2.89) yields

$$\begin{aligned} &\left(-\mathbf{F}_{\mathrm{M}}\frac{\partial\psi}{\partial\mathbf{E}_{\mathrm{M}}}\mathbf{F}_{\mathrm{M}}^{\mathrm{T}} + \frac{1}{\varrho_{\mathrm{R}}}\varphi^{\frac{2}{3}}\mathbf{S}_{\mathrm{M}}^{\mathrm{eq}}\right) \cdot \overset{\triangle}{\boldsymbol{\Gamma}}_{\mathrm{M}} + \left(-s - \frac{\partial\psi}{\partial\theta} + \frac{\varphi'}{3\varrho_{\mathrm{R}}\varphi^{\frac{1}{3}}}\operatorname{tr}\mathbf{S}_{\mathrm{M}}\right)\dot{\theta} \\ &- \frac{\partial\psi}{\partial\check{\boldsymbol{\Gamma}}_{\mathrm{e}}} \cdot \dot{\check{\boldsymbol{\Gamma}}}_{\mathrm{e}} + \frac{1}{\varrho_{\mathrm{R}}}\varphi^{\frac{2}{3}}\check{\mathbf{S}}_{\mathrm{ov}} \cdot \left(\overset{\triangle}{\check{\boldsymbol{\Gamma}}}_{\mathrm{e}} + \overset{\triangle}{\bar{\boldsymbol{\Gamma}}}_{\mathrm{v}}\right) - \frac{1}{\varrho_{\mathrm{R}}\theta}\operatorname{Grad}\theta \cdot \boldsymbol{q}_{\mathrm{R}} \geq 0 \end{aligned} \tag{2.130}$$

based on

$$\frac{\partial\psi}{\partial\mathbf{E}_{\mathrm{M}}}\cdot\dot{\mathbf{E}}_{\mathrm{M}}=\frac{\partial\psi}{\partial\mathbf{E}_{\mathrm{M}}}\cdot\mathbf{F}_{\mathrm{M}}^{\mathrm{T}}\overset{\triangle}{\boldsymbol{\Gamma}}_{\mathrm{M}}\mathbf{F}_{\mathrm{M}}=\mathbf{F}_{\mathrm{M}}\frac{\partial\psi}{\partial\mathbf{E}_{\mathrm{M}}}\mathbf{F}_{\mathrm{M}}^{\mathrm{T}}\cdot\overset{\triangle}{\boldsymbol{\Gamma}}_{\mathrm{M}}. \tag{2.131}$$

In order to fulfill (2.130) for arbitrary $\overset{\triangle}{\boldsymbol{\Gamma}}_{\mathrm{M}}$ and $\dot{\theta}$ we achieve a relation for the weighted Cauchy stress tensor operating on the mechanical intermediate configuration

$$\mathbf{S}_{\mathrm{M}}^{\mathrm{eq}}=\varrho_{\mathrm{R}}\varphi^{-\frac{2}{3}}\mathbf{F}_{\mathrm{M}}\frac{\partial\psi}{\partial\mathbf{E}_{\mathrm{M}}}\mathbf{F}_{\mathrm{M}}^{\mathrm{T}}\quad\text{and for the entropy}\quad s=-\frac{\partial\psi}{\partial\theta}+\frac{\varphi'}{3\varrho_{\mathrm{R}}\varphi^{\frac{1}{3}}}\operatorname{tr}\mathbf{S}_{\mathrm{M}}. \tag{2.132}$$

Using the Oldroyd derivative

$$\overset{\triangle}{\check{\boldsymbol{\Gamma}}}_{\mathrm{e}}=\dot{\check{\boldsymbol{\Gamma}}}_{\mathrm{e}}+\mathbf{L}_{\mathrm{v}}^{\mathrm{T}}\check{\boldsymbol{\Gamma}}_{\mathrm{e}}+\check{\boldsymbol{\Gamma}}_{\mathrm{e}}\mathbf{L}_{\mathrm{v}} \tag{2.133}$$

the residual inequality reads

$$\begin{aligned}&\left(\frac{1}{\varrho_{\mathrm{R}}}\varphi^{\frac{2}{3}}\check{\mathbf{S}}_{\mathrm{ov}}-\frac{\partial\psi}{\partial\check{\boldsymbol{\Gamma}}_{\mathrm{e}}}\right)\cdot\overset{\triangle}{\check{\boldsymbol{\Gamma}}}_{\mathrm{e}}+\frac{1}{\varrho_{\mathrm{R}}}\varphi^{\frac{2}{3}}\check{\mathbf{S}}_{\mathrm{ov}}\cdot\overset{\triangle}{\bar{\boldsymbol{\Gamma}}}_{\mathrm{v}}\\&+\frac{\partial\psi}{\partial\check{\boldsymbol{\Gamma}}_{\mathrm{e}}}\cdot\left(\mathbf{L}_{\mathrm{v}}^{\mathrm{T}}\check{\boldsymbol{\Gamma}}_{\mathrm{e}}+\check{\boldsymbol{\Gamma}}_{\mathrm{e}}\mathbf{L}_{\mathrm{v}}\right)-\frac{1}{\varrho_{\mathrm{R}}\theta}\operatorname{Grad}\theta\cdot\boldsymbol{q}_{\mathrm{R}}\geq 0.\end{aligned} \tag{2.134}$$

With the stress tensor operating on the inelastic intermediate configuration $\bar{\chi}_t$, see Fig. 2.2,

$$\check{\mathbf{S}}_{\mathrm{ov}}=\varrho_{\mathrm{R}}\varphi^{-\frac{2}{3}}\frac{\partial\psi}{\partial\check{\boldsymbol{\Gamma}}_{\mathrm{e}}} \tag{2.135}$$

we can now formulate the residual inequality

$$\frac{\partial\psi}{\partial\check{\boldsymbol{\Gamma}}_{\mathrm{e}}}\cdot\overset{\triangle}{\bar{\boldsymbol{\Gamma}}}_{\mathrm{v}}+\frac{\partial\psi}{\partial\check{\boldsymbol{\Gamma}}_{\mathrm{e}}}\cdot\left(\mathbf{L}_{\mathrm{v}}^{\mathrm{T}}\check{\boldsymbol{\Gamma}}_{\mathrm{e}}+\check{\boldsymbol{\Gamma}}_{\mathrm{e}}\mathbf{L}_{\mathrm{v}}\right)-\frac{1}{\varrho_{\mathrm{R}}\theta}\operatorname{Grad}\theta\cdot\boldsymbol{q}_{\mathrm{R}}\geq 0. \tag{2.136}$$

Reformulating the first part of (2.136) according to

$$\begin{aligned}\frac{\partial\psi}{\partial\check{\boldsymbol{\Gamma}}_{\mathrm{e}}}\cdot\overset{\triangle}{\bar{\boldsymbol{\Gamma}}}_{\mathrm{v}}+\frac{\partial\psi}{\partial\check{\boldsymbol{\Gamma}}_{\mathrm{e}}}\cdot\left(\mathbf{L}_{\mathrm{v}}^{\mathrm{T}}\check{\boldsymbol{\Gamma}}_{\mathrm{e}}+\check{\boldsymbol{\Gamma}}_{\mathrm{e}}\mathbf{L}_{\mathrm{v}}\right)&=\frac{\partial\psi}{\partial\check{\boldsymbol{\Gamma}}_{\mathrm{e}}}\cdot\frac{1}{2}\left(\mathbf{L}_{\mathrm{v}}^{\mathrm{T}}+\mathbf{L}_{\mathrm{v}}\right)+\frac{\partial\psi}{\partial\check{\boldsymbol{\Gamma}}_{\mathrm{e}}}\cdot\left(\mathbf{L}_{\mathrm{v}}^{\mathrm{T}}\check{\boldsymbol{\Gamma}}_{\mathrm{e}}+\check{\boldsymbol{\Gamma}}_{\mathrm{e}}\mathbf{L}_{\mathrm{v}}\right)\\&=\frac{\partial\psi}{\partial\check{\boldsymbol{\Gamma}}_{\mathrm{e}}}\cdot\frac{1}{2}\left(\left(\mathbf{1}+2\check{\boldsymbol{\Gamma}}_{\mathrm{e}}\right)\mathbf{L}_{\mathrm{v}}+\mathbf{L}_{\mathrm{v}}^{\mathrm{T}}\left(\mathbf{1}+2\check{\boldsymbol{\Gamma}}_{\mathrm{e}}\right)\right)\\&=\frac{\partial\psi}{\partial\check{\boldsymbol{\Gamma}}_{\mathrm{e}}}\cdot\frac{1}{2}\left(\check{\mathbf{C}}_{\mathrm{e}}\mathbf{L}_{\mathrm{v}}+\mathbf{L}_{\mathrm{v}}^{\mathrm{T}}\check{\mathbf{C}}_{\mathrm{e}}\right)=\check{\mathbf{C}}_{\mathrm{e}}\frac{\partial\psi}{\partial\check{\boldsymbol{\Gamma}}_{\mathrm{e}}}\cdot\frac{1}{2}\left(\mathbf{L}_{\mathrm{v}}+\mathbf{L}_{\mathrm{v}}^{\mathrm{T}}\right)\\&=\check{\mathbf{C}}_{\mathrm{e}}\frac{\partial\psi}{\partial\check{\boldsymbol{\Gamma}}_{\mathrm{e}}}\cdot\overset{\triangle}{\bar{\boldsymbol{\Gamma}}}_{\mathrm{v}} &&(2.137)\\&=\frac{\varphi^{\frac{2}{3}}}{\varrho_{\mathrm{R}}}\check{\mathbf{C}}_{\mathrm{e}}\check{\mathbf{S}}_{\mathrm{ov}}\cdot\overset{\triangle}{\bar{\boldsymbol{\Gamma}}}_{\mathrm{v}} &&(2.138)\end{aligned}$$

using (2.135) and (2.114) results in

$$\frac{\varphi^{\frac{2}{3}}}{\varrho_{\mathrm{R}}}\check{\mathbf{C}}_{\mathrm{e}}\check{\mathbf{S}}_{\mathrm{ov}}\cdot\overset{\triangle}{\bar{\boldsymbol{\Gamma}}}_{\mathrm{v}}-\frac{1}{\varrho_{\mathrm{R}}\theta}\operatorname{Grad}\theta\cdot\boldsymbol{q}_{\mathrm{R}}\geq 0. \tag{2.139}$$

In order to fulfill the first part of the inequality (2.139) adequately, we assume

$$\frac{\varphi^{\frac{2}{3}}}{\varrho_{\mathrm{R}}}\check{\mathbf{C}}_{\mathrm{e}}\check{\mathbf{S}}_{\mathrm{ov}} \cdot \overset{\vartriangle}{\bar{\mathbf{\Gamma}}}_{\mathrm{v}} \geq 0 \tag{2.140}$$

which is guaranteed for

$$\overset{\vartriangle}{\bar{\mathbf{\Gamma}}}_{\mathrm{v}} = \frac{1}{\eta}\check{\mathbf{C}}_{\mathrm{e}}\check{\mathbf{S}}_{\mathrm{ov}}, \quad \eta > 0, \tag{2.141}$$

where the proportionality factor η is the viscosity function. Inserting

$$\operatorname{grad}\theta = \mathbf{F}^{-\mathrm{T}} \operatorname{Grad}\theta \tag{2.142}$$

into the Cauchy heat flux vector

$$\boldsymbol{q} = -\lambda \operatorname{grad}\theta \tag{2.143}$$

yields

$$\boldsymbol{q} = -\lambda\mathbf{F}^{-\mathrm{T}} \operatorname{Grad}\theta. \tag{2.144}$$

With (2.73) we obtain the Piola-Kirchhoff heat flux vector

$$\boldsymbol{q}_{\mathrm{R}} = -\boldsymbol{\lambda}_{\mathrm{R}} \operatorname{Grad}\theta, \tag{2.145}$$

where the heat conductivity of the material is denoted by

$$\boldsymbol{\lambda}_{\mathrm{R}} = \lambda(\det\mathbf{F})\mathbf{F}^{-1}\mathbf{F}^{-\mathrm{T}}. \tag{2.146}$$

We accordingly propose a linear relation between the temperature gradient and the heat flux vector, which is called Fourier's law. This proposal satisfies the heat conduction inequality

$$-\frac{1}{\theta}\operatorname{Grad}\theta \cdot \boldsymbol{q}_{\mathrm{R}} \geq 0. \tag{2.147}$$

2.3.3 Derivation of Constitutive Equations

In order to concretize constitutive equations, we use (2.132), (2.135) and (2.141). To begin with, we calculate the equilibrium stress

$$\mathbf{S}_{\mathrm{M}}^{\mathrm{eq}} = \varrho_{\mathrm{R}}\varphi^{-\frac{2}{3}}\mathbf{F}_{\mathrm{M}}\frac{\partial\psi}{\partial\mathbf{E}_{\mathrm{M}}}\mathbf{F}_{\mathrm{M}}^{\mathrm{T}} = \varrho_{\mathrm{R}}\varphi^{-\frac{2}{3}}\frac{\theta}{\theta_0}\mathbf{F}_{\mathrm{M}}\frac{\mathrm{d}\bar{\psi}_{\mathrm{M}}^{\mathrm{eq}}}{\mathrm{d}\mathbf{E}_{\mathrm{M}}}\mathbf{F}_{\mathrm{M}}^{\mathrm{T}}. \tag{2.148}$$

Due to the free energy (2.116) the derivative necessary in (2.148) reads

$$\frac{\mathrm{d}\bar{\psi}_{\mathrm{M}}^{\mathrm{eq}}}{\mathrm{d}\mathbf{E}_{\mathrm{M}}} = 2\frac{\mathrm{d}U(J_{\mathrm{M}}(\mathbf{C}_{\mathrm{M}}))}{\mathrm{d}\mathbf{C}_{\mathrm{M}}} + 2\frac{\mathrm{d}\bar{v}(\bar{\mathbf{C}}_{\mathrm{M}}(\mathbf{C}_{\mathrm{M}}))}{\mathrm{d}\mathbf{C}_{\mathrm{M}}} \tag{2.149}$$

yielding a decomposition of the stress state into one part resulting from a volumetric deformation

$$\begin{aligned}\hat{\mathbf{S}}_{\mathrm{M}}^{\mathrm{eq}} &= \varrho_{\mathrm{R}}\varphi^{-\frac{2}{3}}\frac{\theta}{\theta_0}\mathbf{F}_{\mathrm{M}}\frac{\mathrm{d}U(J_{\mathrm{M}}(\mathbf{C}_{\mathrm{M}}))}{\mathrm{d}\mathbf{C}_{\mathrm{M}}}\mathbf{F}_{\mathrm{M}}^{\mathrm{T}} \\ &= \varrho_{\mathrm{R}}\varphi^{-\frac{2}{3}}J_{\mathrm{M}}\frac{\theta}{\theta_0}U'(J_{\mathrm{M}})\mathbf{1},\end{aligned} \tag{2.150}$$

based on

$$\frac{\mathrm{d}U(J_{\mathrm{M}}(\mathbf{C}_{\mathrm{M}}))}{\mathrm{d}\mathbf{C}_{\mathrm{M}}} = \frac{1}{2} J_{\mathrm{M}} U'(J_{\mathrm{M}}) \mathbf{C}_{\mathrm{M}}^{-1} \tag{2.151}$$

and one part

$$\bar{\mathbf{S}}_{\mathrm{M}}^{\mathrm{eq}} = 2\varrho_{\mathrm{R}} \varphi^{-\frac{2}{3}} \frac{\theta}{\theta_0} \mathbf{F}_{\mathrm{M}} \frac{\mathrm{d}\bar{v}(\bar{\mathbf{C}}_{\mathrm{M}}(\mathbf{C}_{\mathrm{M}}))}{\mathrm{d}\mathbf{C}_{\mathrm{M}}} \mathbf{F}_{\mathrm{M}}^{\mathrm{T}} \tag{2.152}$$

which is induced by a volume-preserving deformation. With

$$\frac{\mathrm{d}\bar{v}(\bar{\mathbf{C}}_{\mathrm{M}}(\mathbf{C}_{\mathrm{M}}))}{\mathrm{d}\mathbf{C}_{\mathrm{M}}} = \left[\frac{\mathrm{d}\bar{\mathbf{C}}_{\mathrm{M}}}{\mathrm{d}\mathbf{C}_{\mathrm{M}}}\right]^{\mathrm{T}} \frac{\mathrm{d}\bar{v}}{\mathrm{d}\bar{\mathbf{C}}_{\mathrm{M}}} \tag{2.153}$$

and

$$\left[\frac{\mathrm{d}\bar{\mathbf{C}}_{\mathrm{M}}}{\mathrm{d}\mathbf{C}_{\mathrm{M}}}\right]^{\mathrm{T}} = J_{\mathrm{M}}^{-\frac{2}{3}} \left(\mathcal{I} - \frac{1}{3}\left[\mathbf{C}_{\mathrm{M}}^{-1} \otimes \mathbf{C}_{\mathrm{M}}\right]\right), \tag{2.154}$$

where $\mathcal{I} = [\mathbf{1} \otimes \mathbf{1}]^{T_{23}}$ denotes the fourth order identity tensor, it follows that

$$\begin{aligned}
\bar{\mathbf{S}}_{\mathrm{M}}^{\mathrm{eq}} &= 2\varrho_{\mathrm{R}} \varphi^{-\frac{2}{3}} J_{\mathrm{M}}^{-\frac{2}{3}} \frac{\theta}{\theta_0} \mathbf{F}_{\mathrm{M}} \left(\mathcal{I} - \frac{1}{3}\left[\mathbf{C}_{\mathrm{M}}^{-1} \otimes \mathbf{C}_{\mathrm{M}}\right]\right) \frac{\mathrm{d}\bar{v}}{\mathrm{d}\bar{\mathbf{C}}_{\mathrm{M}}} \mathbf{F}_{\mathrm{M}}^{\mathrm{T}} \\
&= 2\varrho_{\mathrm{R}} \varphi^{-\frac{2}{3}} J_{\mathrm{M}}^{-\frac{2}{3}} \frac{\theta}{\theta_0} [\mathbf{F}_{\mathrm{M}} \otimes \mathbf{F}_{\mathrm{M}}]^{T_{23}} \left(\mathcal{I} - \frac{1}{3}\left[\mathbf{C}_{\mathrm{M}}^{-1} \otimes \mathbf{C}_{\mathrm{M}}\right]\right) \frac{\mathrm{d}\bar{v}}{\mathrm{d}\bar{\mathbf{C}}_{\mathrm{M}}}
\end{aligned}$$

$$= 2\varrho_{\mathrm{R}} \varphi^{-\frac{2}{3}} J_{\mathrm{M}}^{-\frac{2}{3}} \frac{\theta}{\theta_0} \left([\mathbf{F}_{\mathrm{M}} \otimes \mathbf{F}_{\mathrm{M}}]^{T_{23}} - \frac{1}{3}[\mathbf{1} \otimes \mathbf{C}_{\mathrm{M}}]\right) \frac{\mathrm{d}\bar{v}}{\mathrm{d}\bar{\mathbf{C}}_{\mathrm{M}}} \tag{2.155}$$

$$= 2\varrho_{\mathrm{R}} \varphi^{-\frac{2}{3}} J_{\mathrm{M}}^{-\frac{2}{3}} \frac{\theta}{\theta_0} \left(\mathcal{I} - \frac{1}{3}[\mathbf{1} \otimes \mathbf{1}]\right) [\mathbf{F}_{\mathrm{M}} \otimes \mathbf{F}_{\mathrm{M}}]^{T_{23}} \frac{\mathrm{d}\bar{v}}{\mathrm{d}\bar{\mathbf{C}}_{\mathrm{M}}} \tag{2.156}$$

$$= 2\varrho_{\mathrm{R}} \varphi^{-\frac{2}{3}} \frac{\theta}{\theta_0} \left(\bar{\mathbf{F}}_{\mathrm{M}} \frac{\mathrm{d}\bar{v}}{\mathrm{d}\bar{\mathbf{C}}_{\mathrm{M}}} \bar{\mathbf{F}}_{\mathrm{M}}^{\mathrm{T}}\right)^{\mathrm{D}}. \tag{2.157}$$

In (2.155) we assume the identity

$$[\mathbf{A} \otimes \mathbf{B}]^{T_{23}} [\mathbf{C} \otimes \mathbf{D}] = \left[\mathbf{A}\mathbf{C}\mathbf{B}^{\mathrm{T}} \otimes \mathbf{D}\right] \tag{2.158}$$

and in (2.156) we employ

$$[\mathbf{C} \otimes \mathbf{D}] [\mathbf{A} \otimes \mathbf{B}]^{T_{23}} = \mathbf{C} \otimes \mathbf{A}^{\mathrm{T}}\mathbf{D}\mathbf{B} \tag{2.159}$$

see (Hartmann, 2003). With (2.150), (2.157), the kinematic relation

$$\bar{\mathbf{B}}_{\mathrm{M}} = J_{\mathrm{M}}^{-\frac{2}{3}} \mathbf{B}_{\mathrm{M}} = (\varphi/J)^{\frac{2}{3}} \varphi^{-\frac{2}{3}} \mathbf{B} = J^{-\frac{2}{3}} \mathbf{B} = \bar{\mathbf{B}} \tag{2.160}$$

and

$$\begin{aligned}
\left(\bar{\mathbf{F}}_{\mathrm{M}} \frac{\mathrm{d}\bar{v}}{\mathrm{d}\bar{\mathbf{C}}_{\mathrm{M}}} \bar{\mathbf{F}}_{\mathrm{M}}^{\mathrm{T}}\right)^{\mathrm{D}} &= \left(\bar{\mathbf{F}}_{\mathrm{M}} \left[\frac{\mathrm{d}\bar{\mathbf{B}}_{\mathrm{M}}}{\mathrm{d}\bar{\mathbf{C}}_{\mathrm{M}}}\right]^{\mathrm{T}} \frac{\mathrm{d}\bar{v}}{\mathrm{d}\bar{\mathbf{B}}_{\mathrm{M}}} \bar{\mathbf{F}}_{\mathrm{M}}^{\mathrm{T}}\right)^{\mathrm{D}} = \left(\bar{\mathbf{F}}_{\mathrm{M}} \left[\bar{\mathbf{F}}_{\mathrm{M}}^{-1} \otimes \bar{\mathbf{F}}_{\mathrm{M}}^{\mathrm{T}}\right]^{T_{23}} \frac{\mathrm{d}\bar{v}}{\mathrm{d}\bar{\mathbf{B}}_{\mathrm{M}}} \bar{\mathbf{F}}_{\mathrm{M}}^{\mathrm{T}}\right)^{\mathrm{D}} \\
&= \left(\frac{\mathrm{d}\bar{v}}{\mathrm{d}\bar{\mathbf{B}}_{\mathrm{M}}} \bar{\mathbf{B}}_{\mathrm{M}}\right)^{\mathrm{D}} = \left(\bar{\mathbf{B}}_{\mathrm{M}} \frac{\mathrm{d}\bar{v}}{\mathrm{d}\bar{\mathbf{B}}_{\mathrm{M}}}\right)^{\mathrm{D}}
\end{aligned} \tag{2.161}$$

based on

$$\bar{\mathbf{B}}_{\mathrm{M}} = \left[\mathbf{F}^{-\mathrm{T}} \otimes \mathbf{F}\right]^{T_{23}} \bar{\mathbf{C}}_{\mathrm{M}} = \left[\bar{\mathbf{F}}_{\mathrm{M}}^{-\mathrm{T}} \otimes \bar{\mathbf{F}}_{\mathrm{M}}\right]^{T_{23}} \bar{\mathbf{C}}_{\mathrm{M}}, \tag{2.162}$$

we arrive at an expression for the equilibrium part of the Cauchy stress tensor

$$\begin{aligned} \mathbf{T}_{\mathrm{eq}} &= \frac{1}{J}\mathbf{S}_{\mathrm{eq}} = \frac{1}{J}\mathbf{F}_{\theta}\mathbf{S}_{\mathrm{M}}^{\mathrm{eq}}\mathbf{F}_{\theta}^{\mathrm{T}} = \frac{\varphi^{\frac{2}{3}}}{J}\left(\hat{\mathbf{S}}_{\mathrm{M}}^{\mathrm{eq}} + \bar{\mathbf{S}}_{\mathrm{M}}^{\mathrm{eq}}\right) \\ &= \varrho_{\mathrm{R}}\varphi^{-1}\frac{\theta}{\theta_0}U'(J/\varphi)\mathbf{1} + 2\varrho_{\mathrm{R}}J^{-1}\frac{\theta}{\theta_0}\left(\frac{\mathrm{d}\bar{v}}{\mathrm{d}\bar{\mathbf{B}}}\bar{\mathbf{B}}\right)^{\mathrm{D}}. \end{aligned} \tag{2.163}$$

With

$$\begin{aligned} &\mathbf{F}^{-1}\left(\bar{\mathbf{F}}_{\mathrm{M}}\frac{\mathrm{d}\bar{v}}{\mathrm{d}\bar{\mathbf{C}}_{\mathrm{M}}}\bar{\mathbf{F}}_{\mathrm{M}}^{\mathrm{T}}\right)^{\mathrm{D}}\mathbf{F}^{-\mathrm{T}} = \left[\mathbf{F}^{-1} \otimes \mathbf{F}^{-1}\right]^{T_{23}}\left[\mathcal{I} - \frac{1}{3}\left[\mathbf{1} \otimes \mathbf{1}\right]\right]\left[\bar{\mathbf{F}}_{\mathrm{M}} \otimes \bar{\mathbf{F}}_{\mathrm{M}}\right]^{T_{23}}\frac{\mathrm{d}\bar{v}}{\mathrm{d}\bar{\mathbf{C}}} \\ &= J^{-\frac{2}{3}}\left[\left[\mathbf{F}^{-1} \otimes \mathbf{F}^{-1}\right]^{T_{23}} - \frac{1}{3}\left[\mathbf{C}^{-1} \otimes \mathbf{1}\right]\right]\left[\mathbf{F} \otimes \mathbf{F}\right]^{T_{23}}\frac{\mathrm{d}\bar{v}}{\mathrm{d}\bar{\mathbf{C}}}^{*} \\ &= J^{-\frac{2}{3}}\left[\mathcal{I} - \frac{1}{3}\left[\mathbf{C}^{-1} \otimes \mathbf{C}\right]\right]\frac{\mathrm{d}\bar{v}}{\mathrm{d}\bar{\mathbf{C}}} \end{aligned} \tag{2.164}$$

based on

$$\bar{\mathbf{F}}_{\mathrm{M}} = J_{\mathrm{M}}^{-\frac{1}{3}}\mathbf{F}_{\mathrm{M}} = \left(\frac{J}{\varphi}\right)^{-\frac{1}{3}}\varphi^{-\frac{1}{3}}\mathbf{F} = J^{-\frac{1}{3}}\mathbf{F} \tag{2.165}$$

and

$$\left[\mathbf{A} \otimes \mathbf{B}\right]^{T_{23}}\left[\mathbf{C} \otimes \mathbf{D}\right]^{T_{23}} = \left[\mathbf{AC} \otimes \mathbf{BD}\right]^{T_{23}}, \tag{2.166}$$

see (Hartmann, 2003), the equilibrium stress tensor can be expressed in relation to the reference configuration

$$\tilde{\mathbf{T}}_{\mathrm{eq}} = J\mathbf{F}^{-1}\mathbf{T}_{\mathrm{eq}}\mathbf{F}^{-\mathrm{T}} \tag{2.167}$$

$$= \varrho_{\mathrm{R}}J_{\mathrm{M}}\frac{\theta}{\theta_0}U'(J_{\mathrm{M}})\mathbf{C}^{-1} + 2\varrho_{\mathrm{R}}\frac{\theta}{\theta_0}J^{-\frac{2}{3}}\left[\mathcal{I} - \frac{1}{3}\left[\mathbf{C}^{-1} \otimes \mathbf{C}\right]\right]\frac{\mathrm{d}\bar{v}}{\mathrm{d}\bar{\mathbf{C}}}. \tag{2.168}$$

Assuming

$$w_1 = \frac{\partial w}{\partial \mathrm{I}_{\bar{\mathbf{C}}}} = \frac{1}{\varrho_{\mathrm{R}}}(c_{10} + 3\alpha\mathrm{I}_{\bar{\mathbf{C}}}^2), \quad w_2 = \frac{\partial w}{\partial \mathrm{II}_{\bar{\mathbf{C}}}} = \frac{3}{2\varrho_{\mathrm{R}}}c_{01}\mathrm{II}_{\bar{\mathbf{C}}}^{\frac{1}{2}},$$

$$\frac{\partial \mathrm{I}_{\bar{\mathbf{C}}}}{\partial \bar{\mathbf{C}}} = \mathbf{1} \quad \text{and} \quad \frac{\partial \mathrm{II}_{\bar{\mathbf{C}}}}{\partial \bar{\mathbf{C}}} = \mathrm{I}_{\bar{\mathbf{C}}}\mathbf{1} - \bar{\mathbf{C}}$$

the derivative of $\bar{v}$ given in (2.120) with respect to the unimodular right Cauchy-Green tensor reads

$$\frac{\mathrm{d}\bar{v}}{\mathrm{d}\bar{\mathbf{C}}} = \frac{\partial w}{\partial \mathrm{I}_{\bar{\mathbf{C}}}}\frac{\partial \mathrm{I}_{\bar{\mathbf{C}}}}{\partial \bar{\mathbf{C}}} + \frac{\partial w}{\partial \mathrm{II}_{\bar{\mathbf{C}}}}\frac{\partial \mathrm{II}_{\bar{\mathbf{C}}}}{\partial \bar{\mathbf{C}}} = (w_1 + w_2\mathrm{I}_{\bar{\mathbf{C}}})\mathbf{1} - w_2\bar{\mathbf{C}} \tag{2.169}$$

and the constitutive relation for the equilibrium stresses can be formulated in terms of

$$\begin{aligned}\tilde{\mathbf{T}}_{\mathrm{eq}} =& \varrho_{\mathrm{R}} \frac{J}{\varphi} \frac{\theta}{\theta_0} U' \left(\frac{J}{\varphi} \right) \mathbf{C}^{-1} \\ & + 2 \varrho_{\mathrm{R}} \frac{\theta}{\theta_0} J^{-\frac{2}{3}} \left((w_1 + w_2 \mathrm{I}_{\bar{\mathbf{C}}}) \mathbf{1} - w_2 \bar{\mathbf{C}} - \frac{1}{3} (w_1 \mathrm{I}_{\bar{\mathbf{C}}} + 2 w_2 \mathrm{II}_{\bar{\mathbf{C}}}) \bar{\mathbf{C}}^{-1} \right) . \end{aligned} \tag{2.170}$$

With the free energy (2.116) and (2.135) it follows that

$$\check{\mathbf{S}}_{\mathrm{ov}} = \varrho_{\mathrm{R}} \varphi^{-\frac{2}{3}} \frac{\mathrm{d}\bar{\psi}^{\mathrm{ov}}_{\mathrm{M}}(\check{\mathbf{\Gamma}}_{\mathrm{e}}, \theta)}{\mathrm{d}\check{\mathbf{\Gamma}}_{\mathrm{e}}} . \tag{2.171}$$

The examination of $\frac{\mathrm{d}\bar{\psi}^{\mathrm{ov}}_{\mathrm{M}}(\check{\mathbf{\Gamma}}_{\mathrm{e}}, \theta)}{\mathrm{d}\check{\mathbf{\Gamma}}_{\mathrm{e}}}$ yields

$$\frac{\mathrm{d}\bar{\psi}^{\mathrm{ov}}_{\mathrm{M}}}{\mathrm{d}\check{\mathbf{\Gamma}}_{\mathrm{e}}} = 2 \frac{\mathrm{d}\bar{\psi}^{\mathrm{ov}}_{\mathrm{M}}}{\mathrm{d}\check{\mathbf{C}}_{\mathrm{e}}} = 2 \left[\frac{\mathrm{d}\bar{\mathbf{C}}_{\mathrm{e}}}{\mathrm{d}\check{\mathbf{C}}_{\mathrm{e}}} \right]^{\mathrm{T}} \frac{\mathrm{d}\bar{w}_{\mathrm{ov}}}{\mathrm{d}\bar{\mathbf{C}}_{\mathrm{e}}} \tag{2.172}$$

with

$$\frac{\mathrm{d}\bar{\mathbf{C}}_{\mathrm{e}}}{\mathrm{d}\check{\mathbf{C}}_{\mathrm{e}}} = \left(\det \check{\mathbf{C}}_{\mathrm{e}} \right)^{-\frac{1}{3}} \left[\mathcal{I} - \frac{1}{3} \left[\check{\mathbf{C}}_{\mathrm{e}} \otimes \check{\mathbf{C}}_{\mathrm{e}}^{-1} \right] \right] \tag{2.173}$$

so the overstresses can be formulated as

$$\check{\mathbf{S}}_{\mathrm{ov}} = 2 \varrho_{\mathrm{R}} \varphi^{-\frac{2}{3}} \left(\det \check{\mathbf{C}}_{\mathrm{e}} \right)^{-\frac{1}{3}} \left[\mathcal{I} - \frac{1}{3} \left[\check{\mathbf{C}}_{\mathrm{e}}^{-1} \otimes \check{\mathbf{C}}_{\mathrm{e}} \right] \right] \frac{\mathrm{d}\bar{w}_{\mathrm{ov}}}{\mathrm{d}\bar{\mathbf{C}}_{\mathrm{e}}} . \tag{2.174}$$

We base these calculations on the relations

$$\check{\mathbf{C}}_{\mathrm{e}} = \check{\mathbf{F}}_{\mathrm{e}}^{\mathrm{T}} \check{\mathbf{F}}_{\mathrm{e}} = \bar{\mathbf{F}}_{\mathrm{e}}^{\mathrm{T}} \hat{\mathbf{F}}_{\mathrm{M}}^{\mathrm{T}} \hat{\mathbf{F}}_{\mathrm{M}} \bar{\mathbf{F}}_{\mathrm{e}} = J_{\mathrm{M}}^{\frac{2}{3}} \bar{\mathbf{C}}_{\mathrm{e}} \quad \leftrightarrow \quad \bar{\mathbf{C}}_{\mathrm{e}} = J_{\mathrm{M}}^{-\frac{2}{3}} \check{\mathbf{C}}_{\mathrm{e}} \tag{2.175}$$

and

$$J_{\mathrm{M}}^{\frac{2}{3}} = \left(\frac{J}{\varphi} \right)^{\frac{2}{3}} = \left(\det \check{\mathbf{F}}_{\mathrm{e}} \right)^{\frac{2}{3}} \left(\det \bar{\mathbf{F}}_{\mathrm{v}} \right)^{\frac{2}{3}} = \left(\det \check{\mathbf{C}}_{\mathrm{e}} \right)^{\frac{1}{3}} \tag{2.176}$$

with the assumption

$$\det \bar{\mathbf{F}}_{\mathrm{v}} = 1, \tag{2.177}$$

see (Hartmann, 2002). Expressed by quantities relative to the reference configuration we obtain

$$\tilde{\mathbf{T}}_{\mathrm{ov}} = \bar{\mathbf{F}}_{\mathrm{v}}^{-1} \check{\mathbf{S}}_{\mathrm{ov}} \bar{\mathbf{F}}_{\mathrm{v}}^{-\mathrm{T}} \tag{2.178}$$

$$\begin{aligned} &= 2 \varrho_{\mathrm{R}} \varphi^{-\frac{2}{3}} \left(\det \check{\mathbf{C}}_{\mathrm{e}} \right)^{-\frac{1}{3}} \left[\bar{\mathbf{F}}_{\mathrm{v}}^{-1} \otimes \bar{\mathbf{F}}_{\mathrm{v}}^{-1} \right]^{T_{23}} \left[\mathcal{I} - \frac{1}{3} \left[\check{\mathbf{C}}_{\mathrm{e}}^{-1} \otimes \check{\mathbf{C}}_{\mathrm{e}} \right] \right] \frac{\mathrm{d}\bar{w}_{\mathrm{ov}}}{\mathrm{d}\bar{\mathbf{C}}_{\mathrm{e}}} \\ &= 2 \varrho_{\mathrm{R}} \varphi^{-\frac{2}{3}} \left(\det \check{\mathbf{C}}_{\mathrm{e}} \right)^{-\frac{1}{3}} \left[\left[\bar{\mathbf{F}}_{\mathrm{v}}^{-1} \otimes \bar{\mathbf{F}}_{\mathrm{v}}^{-1} \right]^{T_{23}} - \frac{1}{3} \left[\bar{\mathbf{F}}_{\mathrm{v}}^{-1} \check{\mathbf{C}}_{\mathrm{e}}^{-1} \bar{\mathbf{F}}_{\mathrm{v}}^{-\mathrm{T}} \otimes \check{\mathbf{C}}_{\mathrm{e}} \right] \right] \frac{\mathrm{d}\bar{w}_{\mathrm{ov}}}{\mathrm{d}\check{\mathbf{C}}_{\mathrm{e}}} \\ &= 2 \varrho_{\mathrm{R}} \varphi^{-\frac{2}{3}} \left(\det \check{\mathbf{C}}_{\mathrm{e}} \right)^{-\frac{1}{3}} \left[\left[\bar{\mathbf{F}}_{\mathrm{v}}^{-1} \otimes \bar{\mathbf{F}}_{\mathrm{v}}^{-1} \right]^{T_{23}} - \frac{1}{3} \left[\mathbf{C}^{-1} \otimes \bar{\mathbf{F}}_{\mathrm{v}}^{-\mathrm{T}} \mathbf{C} \bar{\mathbf{F}}_{\mathrm{v}}^{-1} \right] \right] \frac{\mathrm{d}\bar{w}_{\mathrm{ov}}}{\mathrm{d}\check{\mathbf{C}}_{\mathrm{e}}} \\ &= 2 \varrho_{\mathrm{R}} \varphi^{-\frac{2}{3}} \left(\det \check{\mathbf{C}}_{\mathrm{e}} \right)^{-\frac{1}{3}} \left[\mathcal{I} - \frac{1}{3} \left[\mathbf{C}^{-1} \otimes \mathbf{C} \right] \right] \left[\bar{\mathbf{F}}_{\mathrm{v}}^{-1} \otimes \bar{\mathbf{F}}_{\mathrm{v}}^{-1} \right]^{T_{23}} \frac{\mathrm{d}\bar{w}_{\mathrm{ov}}}{\mathrm{d}\check{\mathbf{C}}_{\mathrm{e}}} \end{aligned} \tag{2.179}$$

where (2.159) and the relations

$$\mathbf{C} = \varphi^{\frac{2}{3}} \bar{\mathbf{F}}_{\mathrm{v}}^{\mathrm{T}} \check{\mathbf{C}}_{\mathrm{e}} \bar{\mathbf{F}}_{\mathrm{v}} \quad \text{and} \quad \mathbf{C}^{-1} = \varphi^{-\frac{2}{3}} \bar{\mathbf{F}}_{\mathrm{v}}^{-1} \check{\mathbf{C}}_{\mathrm{e}}^{-1} \bar{\mathbf{F}}_{\mathrm{v}}^{-\mathrm{T}} \tag{2.180}$$

are applied. With the free energy (2.123) it follows that

$$\left[\bar{\mathbf{F}}_{\mathrm{v}}^{-1} \otimes \bar{\mathbf{F}}_{\mathrm{v}}^{-1}\right]^{T_{23}} \frac{\mathrm{d}\bar{w}_{\mathrm{ov}}}{\mathrm{d}\bar{\mathbf{C}}_{\mathrm{e}}} = \frac{\mu}{\varrho_{\mathrm{R}}} \mathbf{C}_{\mathrm{v}}^{-1} \tag{2.181}$$

so the overstresses with respect to quantities of the reference configuration read

$$\begin{aligned}
\tilde{\mathbf{T}}_{\mathrm{ov}} &= 2\varrho_{\mathrm{R}} \varphi^{-\frac{2}{3}} \left(\det \check{\mathbf{C}}_{\mathrm{e}}\right)^{-\frac{1}{3}} \left[\mathcal{I} - \frac{1}{3}\left[\mathbf{C}^{-1} \otimes \mathbf{C}\right]\right] \frac{\mu}{\varrho_{\mathrm{R}}} \mathbf{C}_{\mathrm{v}}^{-1} \\
&= 2\mu J^{-\frac{2}{3}} \left(\mathbf{C}_{\mathrm{v}}^{-1} - \frac{1}{3}\left(\mathbf{C}_{\mathrm{v}}^{-1} \cdot \mathbf{C}\right) \mathbf{C}^{-1}\right).
\end{aligned} \tag{2.182}$$

Making use of

$$\frac{\mathrm{d}\bar{w}_{\mathrm{ov}}}{\mathrm{d}\bar{\mathbf{C}}_{\mathrm{e}}} = \left[\frac{\mathrm{d}\bar{\mathbf{B}}_{\mathrm{e}}}{\mathrm{d}\bar{\mathbf{C}}_{\mathrm{e}}}\right]^{\mathrm{T}} \frac{\mathrm{d}\bar{w}_{\mathrm{ov}}}{\mathrm{d}\bar{\mathbf{B}}_{\mathrm{e}}} = \left[\bar{\mathbf{F}}_{\mathrm{e}}^{\mathrm{T}} \otimes \bar{\mathbf{F}}_{\mathrm{e}}^{-1}\right]^{T_{23}} \frac{\mathrm{d}\bar{w}_{\mathrm{ov}}}{\mathrm{d}\bar{\mathbf{B}}_{\mathrm{e}}} \tag{2.183}$$

the overstresses expressed relative to the intermediate configuration $\bar{\chi}_t$, given in (2.174), can be expressed by means of quantities operating on the intermediate configuration $\hat{\chi}_t$

$$\begin{aligned}
\mathbf{S}_{\mathrm{ov}} &= \varphi^{\frac{2}{3}} \check{\mathbf{F}}_{\mathrm{e}} \check{\mathbf{S}}_{\mathrm{ov}} \check{\mathbf{F}}_{\mathrm{e}}^{\mathrm{T}} \\
&= 2\varrho_{\mathrm{R}} \left(\det \check{\mathbf{C}}_{\mathrm{e}}\right)^{-\frac{1}{3}} \left[\check{\mathbf{F}}_{\mathrm{e}} \otimes \check{\mathbf{F}}_{\mathrm{e}}\right]^{T_{23}} \left[\mathcal{I} - \frac{1}{3}\check{\mathbf{C}}_{\mathrm{e}}^{-1} \otimes \check{\mathbf{C}}_{\mathrm{e}}\right] \left[\bar{\mathbf{F}}_{\mathrm{e}}^{\mathrm{T}} \otimes \bar{\mathbf{F}}_{\mathrm{e}}^{-1}\right]^{T_{23}} \frac{\mathrm{d}\bar{w}_{\mathrm{ov}}}{\mathrm{d}\bar{\mathbf{B}}_{\mathrm{e}}} \\
&= 2\varrho_{\mathrm{R}} \left(\det \check{\mathbf{C}}_{\mathrm{e}}\right)^{-\frac{1}{3}} \left[\left[\check{\mathbf{F}}_{\mathrm{e}} \otimes \check{\mathbf{F}}_{\mathrm{e}}\right]^{T_{23}} - \frac{1}{3}\mathbf{1} \otimes \check{\mathbf{C}}_{\mathrm{e}}\right] \left[\bar{\mathbf{F}}_{\mathrm{e}}^{\mathrm{T}} \otimes \bar{\mathbf{F}}_{\mathrm{e}}^{-1}\right]^{T_{23}} \frac{\mathrm{d}\bar{w}_{\mathrm{ov}}}{\mathrm{d}\bar{\mathbf{B}}_{\mathrm{e}}} \\
&= 2\varrho_{\mathrm{R}} \left(\det \check{\mathbf{C}}_{\mathrm{e}}\right)^{-\frac{1}{3}} \left[J_{\mathrm{M}}^{\frac{2}{3}} \left[\bar{\mathbf{B}}_{\mathrm{e}} \otimes \mathbf{1}\right]^{T_{23}} - \frac{1}{3} J_{\mathrm{M}}^{\frac{2}{3}} \mathbf{1} \otimes \bar{\mathbf{B}}_{\mathrm{e}}\right] \frac{\mathrm{d}\bar{w}_{\mathrm{ov}}}{\mathrm{d}\bar{\mathbf{B}}_{\mathrm{e}}} \\
&= 2\varrho_{\mathrm{R}} \left(\det \check{\mathbf{C}}_{\mathrm{e}}\right)^{-\frac{1}{3}} \left(\frac{J}{\varphi}\right)^{2/3} \left[\left[\bar{\mathbf{B}}_{\mathrm{e}} \otimes \mathbf{1}\right]^{T_{23}} - \frac{1}{3}\mathbf{1} \otimes \bar{\mathbf{B}}_{\mathrm{e}}\right] \frac{\mathrm{d}\bar{w}_{\mathrm{ov}}}{\mathrm{d}\bar{\mathbf{B}}_{\mathrm{e}}} \\
&= 2\varrho_{\mathrm{R}} \bar{\mathbf{B}}_{\mathrm{e}} \frac{\mathrm{d}\bar{w}_{\mathrm{ov}}}{\mathrm{d}\bar{\mathbf{B}}_{\mathrm{e}}} - \frac{1}{3}\left(\frac{\mathrm{d}\bar{w}_{\mathrm{ov}}}{\mathrm{d}\bar{\mathbf{B}}_{\mathrm{e}}} \cdot \bar{\mathbf{B}}_{\mathrm{e}}\right) \mathbf{1} = 2\varrho_{\mathrm{R}} \bar{\mathbf{B}}_{\mathrm{e}} \frac{\mathrm{d}\bar{w}_{\mathrm{ov}}}{\mathrm{d}\bar{\mathbf{B}}_{\mathrm{e}}} - \frac{1}{3}\left(\mathbf{1} \cdot \bar{\mathbf{B}}_{\mathrm{e}} \frac{\mathrm{d}\bar{w}_{\mathrm{ov}}}{\mathrm{d}\bar{\mathbf{B}}_{\mathrm{e}}}\right) \mathbf{1} \\
&= 2\varrho_{\mathrm{R}} \left[\mathcal{I} - \frac{1}{3}\mathbf{1} \otimes \mathbf{1}\right] \bar{\mathbf{B}}_{\mathrm{e}} \frac{\mathrm{d}\bar{w}_{\mathrm{ov}}}{\mathrm{d}\bar{\mathbf{B}}_{\mathrm{e}}} = 2\varrho_{\mathrm{R}} \left(\bar{\mathbf{B}}_{\mathrm{e}} \frac{\mathrm{d}\bar{w}_{\mathrm{ov}}}{\mathrm{d}\bar{\mathbf{B}}_{\mathrm{e}}}\right)^{\mathrm{D}}.
\end{aligned} \tag{2.184}$$

Making use of the free energy (2.123) finally yields

$$\mathbf{T}_{\mathrm{ov}} = 2\mu \bar{\mathbf{B}}_{\mathrm{e}}^{\mathrm{D}}. \tag{2.185}$$

In order to derive the evolution equations, we use $\overset{\triangle}{\bar{\mathbf{\Gamma}}} = \frac{1}{2}\bar{\mathbf{F}}_\mathrm{v}^{-\mathrm{T}}\dot{\mathbf{C}}_\mathrm{v}\bar{\mathbf{F}}_\mathrm{v}^{-1}$, (2.141) and the stress-strain relation (2.174) leading to

$$
\begin{aligned}
\dot{\mathbf{C}}_\mathrm{v} &= \frac{2}{\eta}\bar{\mathbf{F}}_\mathrm{v}^\mathrm{T}\check{\mathbf{C}}_\mathrm{e}\check{\mathbf{S}}_\mathrm{ov}\bar{\mathbf{F}}_\mathrm{v} = \frac{4}{\eta}\varrho_\mathrm{R}\varphi^{-\frac{2}{3}}\left(\det\check{\mathbf{C}}_\mathrm{e}\right)^{-\frac{1}{3}}\left[\bar{\mathbf{F}}_\mathrm{v}^\mathrm{T}\otimes\bar{\mathbf{F}}_\mathrm{v}^\mathrm{T}\right]^{T_{23}}\check{\mathbf{C}}_\mathrm{e}\left[\mathcal{I}-\frac{1}{3}\left[\check{\mathbf{C}}_\mathrm{e}^{-1}\otimes\check{\mathbf{C}}_\mathrm{e}\right]\right]\frac{\mathrm{d}\bar{w}_\mathrm{ov}}{\mathrm{d}\bar{\mathbf{C}}_\mathrm{e}} \\
&= \frac{4}{\eta}\varrho_\mathrm{R}\varphi^{-\frac{2}{3}}\left(\det\check{\mathbf{C}}_\mathrm{e}\right)^{-\frac{1}{3}}\left[\bar{\mathbf{F}}_\mathrm{v}^\mathrm{T}\otimes\bar{\mathbf{F}}_\mathrm{v}^\mathrm{T}\right]^{T_{23}}\left[\check{\mathbf{C}}_\mathrm{e}\frac{\mathrm{d}\bar{w}_\mathrm{ov}}{\mathrm{d}\bar{\mathbf{C}}_\mathrm{e}}-\frac{1}{3}\left(\check{\mathbf{C}}_\mathrm{e}\cdot\frac{\mathrm{d}\bar{w}_\mathrm{ov}}{\mathrm{d}\bar{\mathbf{C}}_\mathrm{e}}\right)\mathbf{1}\right] \\
&= \frac{4\mu}{\eta}\varphi^{-\frac{2}{3}}\left(\det\check{\mathbf{C}}_\mathrm{e}\right)^{-\frac{1}{3}}\left[\bar{\mathbf{F}}_\mathrm{v}^\mathrm{T}\check{\mathbf{C}}_\mathrm{e}\bar{\mathbf{F}}_\mathrm{v}-\frac{1}{3}\left(\bar{\mathbf{F}}_\mathrm{v}^\mathrm{T}\check{\mathbf{C}}_\mathrm{e}\bar{\mathbf{F}}_\mathrm{v}\cdot\mathbf{C}_\mathrm{v}^{-1}\right)\mathbf{C}_\mathrm{v}\right] \\
&= \frac{4\mu}{\eta}\varphi^{-\frac{4}{3}}\left(\det\check{\mathbf{C}}_\mathrm{e}\right)^{-\frac{1}{3}}\left[\mathbf{C}-\frac{1}{3}\left(\mathbf{C}\cdot\mathbf{C}_\mathrm{v}^{-1}\right)\mathbf{C}_\mathrm{v}\right] && (2.186) \\
&= \frac{4\mu}{\eta}\frac{\varphi^{-\frac{2}{3}}}{J^{\frac{2}{3}}}\left[\mathbf{C}-\frac{1}{3}\left(\mathbf{C}\cdot\mathbf{C}_\mathrm{v}^{-1}\right)\mathbf{C}_\mathrm{v}\right] && (2.187)
\end{aligned}
$$

based on

$$
\frac{\mathrm{d}\bar{w}_\mathrm{ov}}{\mathrm{d}\bar{\mathbf{C}}_\mathrm{e}} = \frac{\mu}{\varrho_\mathrm{R}}\mathbf{1} = \frac{\mu}{\varrho_\mathrm{R}}\bar{\mathbf{F}}_\mathrm{v}\mathbf{C}_\mathrm{v}^{-1}\bar{\mathbf{F}}_\mathrm{v}^\mathrm{T}. \tag{2.188}
$$

According to (Lion, 2000), we assume an exponential dependence for the viscosity

$$
\eta = \eta_0\exp\left(-\frac{\|\check{\mathbf{C}}_\mathrm{e}\check{\mathbf{S}}_\mathrm{ov}\|}{s_0\left(\frac{1}{\sqrt{3}}\|\mathbf{C}_\mathrm{v}^{-1}\|\right)^{r_0}}\right) \tag{2.189}
$$

with

$$
\eta_0(\theta) = \bar{\eta}_0\exp\left(\frac{\kappa}{\theta}-\frac{\kappa}{\theta_0}\right) \tag{2.190}
$$

and

$$
s_0(\theta) = s_\infty + \left(\bar{s}_0 - s_\infty\right)\exp\left(-w_s(\theta-\theta_0)\right). \tag{2.191}
$$

By means of

$$
\begin{aligned}
\|\check{\mathbf{C}}_\mathrm{e}\hat{\mathbf{S}}_\mathrm{v}\| &= \sqrt{\check{\mathbf{C}}_\mathrm{e}\hat{\mathbf{S}}_\mathrm{ov}\cdot\check{\mathbf{C}}_\mathrm{e}\hat{\mathbf{S}}_\mathrm{ov}} = \sqrt{\check{\mathbf{C}}_\mathrm{e}\hat{\mathbf{S}}_\mathrm{ov}\cdot\hat{\mathbf{S}}_\mathrm{ov}\check{\mathbf{C}}_\mathrm{e}} \\
&= \sqrt{\varphi^{-\frac{4}{3}}\bar{\mathbf{F}}_\mathrm{v}^{-\mathrm{T}}\mathbf{C}\bar{\mathbf{F}}_\mathrm{v}^{-1}\hat{\mathbf{S}}_\mathrm{ov}\cdot\hat{\mathbf{S}}_\mathrm{ov}\bar{\mathbf{F}}_\mathrm{v}^{-\mathrm{T}}\mathbf{C}\bar{\mathbf{F}}_\mathrm{v}^{-1}} = \sqrt{\varphi^{-\frac{4}{3}}\mathbf{C}\bar{\mathbf{F}}_\mathrm{v}^{-1}\hat{\mathbf{S}}_\mathrm{ov}\bar{\mathbf{F}}_\mathrm{v}^{-\mathrm{T}}\cdot\bar{\mathbf{F}}_\mathrm{v}^{-1}\hat{\mathbf{S}}_\mathrm{ov}\bar{\mathbf{F}}_\mathrm{v}^{-\mathrm{T}}\mathbf{C}} \\
&= \sqrt{\varphi^{-\frac{4}{3}}\mathbf{C}\tilde{\mathbf{T}}_\mathrm{ov}\cdot\tilde{\mathbf{T}}_\mathrm{ov}\mathbf{C}} = \sqrt{\varphi^{-\frac{4}{3}}\mathbf{C}\tilde{\mathbf{T}}_\mathrm{ov}\cdot\mathbf{C}\tilde{\mathbf{T}}_\mathrm{ov}} = \|\varphi^{-\frac{2}{3}}\mathbf{C}\tilde{\mathbf{T}}_\mathrm{ov}\|,
\end{aligned}
$$

based on (2.180), it is possible to reformulate (2.189) using quantities relative to the reference configuration

$$
\eta = \eta_0\exp\left(-\frac{\|\varphi^{-\frac{2}{3}}\mathbf{C}\tilde{\mathbf{T}}_\mathrm{ov}\|}{s_0\left(\frac{1}{\sqrt{3}}\|\mathbf{C}_\mathrm{v}^{-1}\|\right)^{r_0}}\right). \tag{2.192}
$$

The material model stated in the reference configuration is summarized in Tab. 2.1. Now the balance relations introduced in Section 2.2, which are insufficient for determining the field variables, can be closed by means of the constitutive equations presented in this section.

Table 2.1: Material model of finite thermo-viscoelasticity expressed in terms of quantities of the reference configuration

(1) **2nd Piola-Kirchhoff stresses**

$$\tilde{\mathbf{T}} = \tilde{\mathbf{T}}_{\text{eq}} + \tilde{\mathbf{T}}_{\text{ov}} = \tilde{\mathbf{T}}_{\text{eq}}^{\text{vol}} + \tilde{\mathbf{T}}_{\text{eq}}^{\text{iso}} + \tilde{\mathbf{T}}_{\text{ov}} := \mathbf{h}\left(\mathbf{C}, \theta, \mathbf{C}_{\text{v}}\right)$$

(2) **equilibrium stresses**

$$\begin{aligned} \tilde{\mathbf{T}}_{\text{eq}}^{\text{vol}} &= \varrho_{\text{R}} \frac{\theta}{\theta_0} \frac{J}{\varphi} U'(J/\varphi) \mathbf{C}^{-1}, \quad U'(J/\varphi) = \frac{K}{10 \varrho_{\text{R}}} ((J/\varphi)^4 - (J/\varphi)^{-6}) \\ \tilde{\mathbf{T}}_{\text{eq}}^{\text{iso}} &= 2 \varrho_{\text{R}} \frac{\theta}{\theta_0} J^{-\frac{2}{3}} \left((w_1 + w_2 \mathrm{II}_{\bar{\mathbf{C}}}) \mathbf{1} - w_2 \bar{\mathbf{C}} - \frac{1}{3} (w_1 \mathrm{I}_{\bar{\mathbf{C}}} + 2 w_2 \mathrm{II}_{\bar{\mathbf{C}}}) \bar{\mathbf{C}}^{-1} \right) \end{aligned}$$

$$w_1 = \frac{1}{\varrho_{\text{R}}} \left(c_{10} + 3 \alpha \mathrm{I}_{\bar{\mathbf{C}}}^2 \right), \quad w_2 = \frac{3}{2 \varrho_{\text{R}}} c_{01} \mathrm{II}_{\bar{\mathbf{C}}}^{1/2}$$

(3) **overstresses**

$$\begin{aligned} \tilde{\mathbf{T}}_{\text{ov}} &= 2 \mu J^{-\frac{2}{3}} (\mathbf{C}_{\text{v}}^{-1} - \frac{1}{3} (\mathbf{C} \cdot \mathbf{C}_{\text{v}}^{-1}) \mathbf{C}^{-1}) \\ \dot{\mathbf{C}}_{\text{v}} &= 4 \frac{\mu}{\eta} \varphi^{-\frac{2}{3}} J^{-\frac{2}{3}} (\mathbf{C} - \frac{1}{3} (\mathbf{C}_{\text{v}}^{-1} \cdot \mathbf{C}) \mathbf{C}_{\text{v}}) := \tilde{\boldsymbol{r}}(\theta, \mathbf{C}, \mathbf{C}_{\text{v}}) \\ \varphi &= 1 + \alpha_\theta (\theta - \theta_0) \\ \eta &= \eta_0 \exp \left(- \frac{\| \varphi^{-\frac{2}{3}} \mathbf{C} \tilde{\mathbf{T}}_{\text{ov}} \|}{s_0 \left(\frac{1}{\sqrt{3}} \| \mathbf{C}_{\text{v}}^{-1} \| \right)^{r_0}} \right) \\ \eta_0(\theta) &= \bar{\eta}_0 \exp \left(\frac{\kappa}{\theta} - \frac{\kappa}{\theta_0} \right) \\ s_0(\theta) &= s_\infty + (\bar{s}_0 - s_\infty) \exp(-w_s (\theta - \theta_0)) \end{aligned}$$

2.3.4 Isothermal Contemplation of the Constitutive Equations

Since this thesis not only addresses thermo-mechanically coupled problems but also isothermal examples, this section deals with the changes needed to derive an isothermal material model from the one discussed above. Disregarding the temperature dependence of the stress-strain relations by stating $\theta/\theta_0 = 1$ yields

$$\varphi = 1 + \alpha_\theta (\theta - \theta_0) = 1 \tag{2.193}$$

and thus, with $\mathbf{F}_\theta = \mathbf{1}$, the decomposition of the deformation gradient (2.92) reads

$$\mathbf{F} = \hat{\mathbf{F}}_\mathrm{M}\bar{\mathbf{F}}_\mathrm{e}\bar{\mathbf{F}}_\mathrm{v} = \check{\mathbf{F}}_\mathrm{e}\bar{\mathbf{F}}_\mathrm{v}. \tag{2.194}$$

In this way the deformation gradient is split into an elastic part $\check{\mathbf{F}}_\mathrm{e}$ and a viscous, volume-preserving part $\bar{\mathbf{F}}_\mathrm{v}$. Based on this decomposition, we write the free energy as follows:

$$\psi_\mathrm{M}\left(\mathbf{E}_\mathrm{M}, \check{\mathbf{\Gamma}}_\mathrm{e}\right) = \bar{\psi}^\mathrm{eq}_\mathrm{M}(J_\mathrm{M}, \mathbf{C}_\mathrm{M}) + \bar{\psi}^\mathrm{ov}_\mathrm{M}(\check{\mathbf{\Gamma}}_\mathrm{e}). \tag{2.195}$$

Following the procedure employed in Section 2.3.2, we insert (2.195) into the dissipation inequality which, in the isothermal case, reads

$$d = -\dot{\psi} + \frac{1}{\varrho_\mathrm{R}}\tilde{\mathbf{T}} \cdot \mathbf{E} \geq 0, \tag{2.196}$$

cf. (2.89), yielding potential relations for the constitutive equations. Based on (2.118) - (2.120) and (2.123) the constitutive equations for the equilibrium stress state read

$$\tilde{\mathbf{T}}_\mathrm{eq} = \varrho_\mathrm{R} J U'(J)\mathbf{C}^{-1} + 2\varrho_\mathrm{R} J^{-2/3}\left[\mathcal{I} - \frac{1}{3}\mathbf{C}^{-1} \otimes \mathbf{C}\right]\frac{\mathrm{d}\bar{v}}{\mathrm{d}\bar{\mathbf{C}}} \tag{2.197}$$

with

$$\frac{\mathrm{d}\bar{v}}{\mathrm{d}\bar{\mathbf{C}}} = (w_1 + w_2 \mathrm{I}_{\bar{\mathbf{C}}})\mathbf{1} - w_2\bar{\mathbf{C}} \tag{2.198}$$

and those for the overstresses read

$$\tilde{\mathbf{T}}_\mathrm{ov} = 2\varrho_\mathrm{R}\mu J^{-\frac{2}{3}}\left(\mathbf{C}_\mathrm{v}^{-1} - \frac{1}{3}\left(\mathbf{C}\cdot\mathbf{C}_\mathrm{v}^{-1}\right)\mathbf{C}^{-1}\right). \tag{2.199}$$

Exploiting the residual inequality suggests the evolution equations for the internal variables

$$\dot{\mathbf{C}}_\mathrm{v} = \frac{4\varrho_\mathrm{R}\mu}{\eta}\frac{(\det\mathbf{C}_\mathrm{v})^{1/3}}{(\det\mathbf{C})^{1/3}}\left(\mathbf{C} - \frac{1}{3}\left(\mathbf{C}\cdot\mathbf{C}_\mathrm{v}^{-1}\right)\mathbf{C}_\mathrm{v}\right) \tag{2.200}$$

where the viscosity

$$\eta = \eta_0 \exp\left(-s_0\sqrt{\mathbf{C}\tilde{\mathbf{T}}_\mathrm{ov}\cdot\tilde{\mathbf{T}}_\mathrm{ov}\mathbf{C}}\right) \tag{2.201}$$

is chosen according to (Hartmann, 2002).

2.4 Derivation of the Heat Conduction Equation

In order to derive evolution equations for the temperature field, the Helmholtz free energy (2.86) is inserted into (2.72b) leading to

$$\dot{\psi} + \dot{\theta}s + \theta\dot{s} = \frac{1}{\varrho_\mathrm{R}}\tilde{\mathbf{T}}\cdot\dot{\mathbf{E}} - \frac{1}{\varrho_\mathrm{R}}\operatorname{Div}\boldsymbol{q}_\mathrm{R} + r. \tag{2.202}$$

Inserting the time derivative of the free energy (2.129), the stress power (2.128), the entropy (2.132) and (2.135) into (2.202) yields

$$\begin{aligned}
&\frac{\partial\psi}{\partial\mathbf{E}_{\mathrm{M}}}\cdot\dot{\mathbf{E}}_{\mathrm{M}}+\frac{\partial\psi}{\partial\check{\boldsymbol{\Gamma}}_{\mathrm{e}}}\cdot\dot{\check{\boldsymbol{\Gamma}}}_{\mathrm{e}}+\theta\dot{s}+\frac{1}{\varrho_{\mathrm{R}}}\operatorname{Div}\boldsymbol{q}_{\mathrm{R}}-\frac{1}{\varrho_{\mathrm{R}}}\varphi^{\frac{2}{3}}\mathbf{S}_{\mathrm{M}}^{\mathrm{eq}}\cdot\overset{\triangle}{\boldsymbol{\Gamma}}_{\mathrm{M}}-\frac{\partial\psi}{\partial\check{\boldsymbol{\Gamma}}_{\mathrm{e}}}\cdot\left(\overset{\triangle}{\check{\boldsymbol{\Gamma}}}_{\mathrm{e}}+\overset{\triangle}{\bar{\bar{\boldsymbol{\Gamma}}}}_{\mathrm{v}}\right)-r\\
&=\frac{\partial\psi}{\partial\mathbf{E}_{\mathrm{M}}}\cdot\dot{\mathbf{E}}_{\mathrm{M}}-\frac{\partial\psi}{\partial\check{\boldsymbol{\Gamma}}_{\mathrm{e}}}\cdot\left(\mathbf{L}_{\mathrm{v}}^{\mathrm{T}}\check{\boldsymbol{\Gamma}}_{\mathrm{e}}+\check{\boldsymbol{\Gamma}}_{\mathrm{e}}\mathbf{L}_{\mathrm{v}}-\overset{\triangle}{\bar{\bar{\boldsymbol{\Gamma}}}}_{\mathrm{v}}\right)+\theta\dot{s}+\frac{1}{\varrho_{\mathrm{R}}}\operatorname{Div}\boldsymbol{q}_{\mathrm{R}}-\frac{1}{\varrho_{\mathrm{R}}}\varphi^{\frac{2}{3}}\mathbf{S}_{\mathrm{M}}^{\mathrm{eq}}\cdot\overset{\triangle}{\boldsymbol{\Gamma}}_{\mathrm{M}}-r\\
&=\frac{\partial\psi}{\partial\mathbf{E}_{\mathrm{M}}}\cdot\dot{\mathbf{E}}_{\mathrm{M}}-\frac{\varphi^{\frac{2}{3}}}{\varrho_{\mathrm{R}}}\check{\mathbf{C}}_{\mathrm{e}}\check{\mathbf{S}}_{\mathrm{ov}}\cdot\overset{\triangle}{\bar{\bar{\boldsymbol{\Gamma}}}}_{\mathrm{v}}+\theta\dot{s}+\frac{1}{\varrho_{\mathrm{R}}}\operatorname{Div}\boldsymbol{q}_{\mathrm{R}}-\frac{1}{\varrho_{\mathrm{R}}}\varphi^{\frac{2}{3}}\mathbf{S}_{\mathrm{M}}^{\mathrm{eq}}\cdot\overset{\triangle}{\boldsymbol{\Gamma}}_{\mathrm{M}}-r\\
&=-\frac{\varphi^{\frac{2}{3}}}{\varrho_{\mathrm{R}}}\check{\mathbf{C}}_{\mathrm{e}}\check{\mathbf{S}}_{\mathrm{ov}}\cdot\overset{\triangle}{\bar{\bar{\boldsymbol{\Gamma}}}}_{\mathrm{v}}+\theta\dot{s}+\frac{1}{\varrho_{\mathrm{R}}}\operatorname{Div}\boldsymbol{q}_{\mathrm{R}}-r=0\\
&\rightarrow\quad\theta\dot{s}=-\frac{1}{\varrho_{\mathrm{R}}}\operatorname{Div}\boldsymbol{q}_{\mathrm{R}}+d+r\quad\text{with}\quad d=\frac{\varphi^{\frac{2}{3}}}{\varrho_{\mathrm{R}}}\check{\mathbf{C}}_{\mathrm{e}}\check{\mathbf{S}}_{\mathrm{ov}}\cdot\overset{\triangle}{\bar{\bar{\boldsymbol{\Gamma}}}}_{\mathrm{v}}.
\end{aligned}\tag{2.203}$$

In addition, we also employ the relations (2.133), (2.137) and

$$\begin{aligned}
&\frac{\partial\psi}{\partial\mathbf{E}_{\mathrm{M}}}\cdot\dot{\mathbf{E}}_{\mathrm{M}}=\frac{\varphi^{\frac{2}{3}}}{\varrho_{\mathrm{R}}}\mathbf{F}_{\mathrm{M}}^{-1}\mathbf{S}_{\mathrm{M}}^{\mathrm{eq}}\mathbf{F}_{\mathrm{M}}^{-\mathrm{T}}\cdot\dot{\mathbf{E}}_{\mathrm{M}}=\frac{\varphi^{\frac{2}{3}}}{\varrho_{\mathrm{R}}}\mathbf{S}_{\mathrm{M}}^{\mathrm{eq}}\cdot\mathbf{F}_{\mathrm{M}}^{-\mathrm{T}}\dot{\mathbf{E}}_{\mathrm{M}}\mathbf{F}_{\mathrm{M}}^{-1}\\
&=\frac{\varphi^{\frac{2}{3}}}{\varrho_{\mathrm{R}}}\mathbf{S}_{\mathrm{M}}^{\mathrm{eq}}\cdot\mathbf{F}_{\mathrm{M}}^{-\mathrm{T}}\frac{1}{2}\left(\dot{\mathbf{F}}_{\mathrm{M}}^{\mathrm{T}}\mathbf{F}_{\mathrm{M}}+\mathbf{F}_{\mathrm{M}}^{\mathrm{T}}\dot{\mathbf{F}}_{\mathrm{M}}\right)\mathbf{F}_{\mathrm{M}}^{-1}=\frac{\varphi^{\frac{2}{3}}}{\varrho_{\mathrm{R}}}\mathbf{S}_{\mathrm{M}}^{\mathrm{eq}}\cdot\frac{1}{2}\left(\mathbf{L}_{\mathrm{M}}^{\mathrm{T}}+\mathbf{L}_{\mathrm{M}}\right)=\frac{\varphi^{\frac{2}{3}}}{\varrho_{\mathrm{R}}}\mathbf{S}_{\mathrm{M}}^{\mathrm{eq}}\cdot\overset{\triangle}{\boldsymbol{\Gamma}}_{\mathrm{M}}.
\end{aligned}$$

In order to derive from (2.203) an evolution equation for the temperature, we contemplate the time derivative of the entropy (2.132) with the free energy (2.116)

$$\dot{s}=-\frac{1}{\theta_0}\frac{\partial\bar{\psi}_{\mathrm{M}}^{\mathrm{eq}}}{\partial\mathbf{E}_{\mathrm{M}}}\cdot\dot{\mathbf{E}}_{\mathrm{M}}-\frac{\partial^2\psi_\theta}{\partial\theta^2}\dot{\theta}+\frac{1}{\varrho_{\mathrm{R}}}\frac{\mathrm{d}}{\mathrm{d}t}\left(\tilde{\varphi}(\mathbf{1}\cdot\mathbf{S}_{\mathrm{M}})\right).\tag{2.204}$$

By means of

$$\begin{aligned}
&\frac{\mathrm{d}}{\mathrm{d}t}\left(\tilde{\varphi}(\theta)(\mathbf{1}\cdot\mathbf{S}_{\mathrm{M}})\right)=\frac{\mathrm{d}}{\mathrm{d}t}\left(\tilde{\varphi}(\theta)(\mathbf{1}\cdot\hat{\mathbf{S}}_{\mathrm{M}}^{\mathrm{eq}})\right)=\frac{\mathrm{d}}{\mathrm{d}t}\left(\varrho_{\mathrm{R}}\frac{\varphi'}{\varphi^2}\frac{\theta}{\theta_0}JU'\left(\frac{J}{\varphi}\right)\right)\\
&=\varrho_{\mathrm{R}}\frac{\varphi'}{\varphi^2}\frac{1}{\theta_0}\left(1-2\theta\frac{\varphi'}{\varphi}\right)\dot{\theta}JU'+\varrho_{\mathrm{R}}\frac{\varphi'}{\varphi^2}\frac{\theta}{\theta_0}\left[\left(\frac{\partial J}{\partial\mathbf{C}}U'+J\frac{\partial U'}{\partial\mathbf{C}}\right)\cdot\dot{\mathbf{C}}+J\frac{\partial U'}{\partial\theta}\dot{\theta}\right]\\
&=\varrho_{\mathrm{R}}\frac{\varphi'}{\varphi^2}\frac{1}{\theta_0}\left(1-2\theta\frac{\varphi'}{\varphi}\right)\dot{\theta}JU'+\varrho_{\mathrm{R}}\frac{\varphi'}{\varphi^2}\frac{\theta}{\theta_0}\left[\frac{1}{2}J(U'+\frac{J}{\varphi}U'')\mathbf{C}^{-1}\cdot\dot{\mathbf{C}}-\frac{\varphi'}{\varphi}\frac{J^2}{\varphi}U''\dot{\theta}\right]\\
&=\varrho_{\mathrm{R}}\left(\frac{\varphi'}{\varphi^2}\frac{1}{\theta_0}\left(1-2\theta\frac{\varphi'}{\varphi}\right)JU'-\frac{\varphi'}{\varphi^2}\frac{\theta}{\theta_0}\frac{\varphi'}{\varphi}\frac{J^2}{\varphi}U''\right)\dot{\theta}+\varrho_{\mathrm{R}}\frac{\varphi'}{\varphi^2}\frac{\theta}{\theta_0}J(U'+\frac{J}{\varphi}U'')\mathbf{C}^{-1}\cdot\dot{\mathbf{E}}\\
&=\left(\tilde{\varphi}'(\mathbf{1}\cdot\hat{\mathbf{S}}_{\mathrm{M}}^{\mathrm{eq}})+\tilde{\varphi}\left(\mathbf{1}\cdot\frac{\partial\hat{\mathbf{S}}_{\mathrm{M}}^{\mathrm{eq}}}{\partial\theta}\right)\right)\dot{\theta}+\tilde{\varphi}J\left(\mathbf{1}\cdot\frac{\partial\hat{\mathbf{S}}_{\mathrm{M}}^{\mathrm{eq}}}{\partial J}\right)\mathbf{C}^{-1}\cdot\dot{\mathbf{E}}
\end{aligned}\tag{2.205}$$

where the short notation

$$\tilde{\varphi}(\theta)=\frac{\varphi'}{3\varphi^{\frac{1}{3}}}\tag{2.206}$$

and the relations

$$\mathbf{1}\cdot\frac{\partial\hat{\mathbf{S}}^{\mathrm{eq}}_{\mathrm{M}}}{\partial J} = 3\varrho_{\mathrm{R}}\varphi^{-\frac{5}{3}}\frac{\theta}{\theta_0}(U' + \frac{J}{\varphi}U''), \tag{2.207}$$

$$\mathbf{1}\cdot\frac{\partial\hat{\mathbf{S}}^{\mathrm{eq}}_{\mathrm{M}}}{\partial \theta} = 3\varrho_{\mathrm{R}}J\varphi^{-\frac{5}{3}}\left(\left(\frac{1}{\theta_0} - \frac{5}{3}\frac{\varphi'}{\varphi}\frac{\theta}{\theta_0}\right)U' - \frac{\theta}{\theta_0}\frac{\varphi'}{\varphi}\frac{J}{\varphi}U''\right), \tag{2.208}$$

$$\mathbf{1}\cdot\hat{\mathbf{S}}^{\mathrm{eq}}_{\mathrm{M}} = 3\varrho_{\mathrm{R}}\varphi^{-\frac{2}{3}}\frac{J}{\varphi}\frac{\theta}{\theta_0}U' \tag{2.209}$$

are employed, the kinematic relation

$$\dot{\mathbf{E}}_{\mathrm{M}} = \varphi^{-\frac{2}{3}}\dot{\mathbf{E}} - \frac{1}{3}\frac{\varphi'}{\varphi}\dot{\theta}\mathbf{C}_{\mathrm{M}} \tag{2.210}$$

and relation (2.148), the time derivative of the entropy $\dot{s}$ yields

$$\begin{aligned}
\dot{s} &= \left(-\frac{\partial^2\psi_\theta}{\partial\theta^2} + \frac{1}{\varrho_{\mathrm{R}}}\tilde{\varphi}'(\mathbf{1}\cdot\hat{\mathbf{S}}^{\mathrm{eq}}_{\mathrm{M}}) + \frac{1}{\varrho_{\mathrm{R}}}\tilde{\varphi}\left(\mathbf{1}\cdot\frac{\partial\hat{\mathbf{S}}^{\mathrm{eq}}_{\mathrm{M}}}{\partial\theta}\right) + \frac{1}{\varrho_{\mathrm{R}}}\frac{1}{3}\frac{\varphi'}{\varphi^{\frac{1}{3}}}\frac{1}{\theta}\mathbf{F}^{-1}_{\mathrm{M}}\mathbf{S}^{\mathrm{eq}}_{\mathrm{M}}\mathbf{F}^{-\mathrm{T}}_{\mathrm{M}}\cdot\mathbf{C}_{\mathrm{M}}\right)\dot{\theta} \\
&\quad + \left(\frac{1}{\varrho_{\mathrm{R}}}\tilde{\varphi}J\left(\mathbf{1}\cdot\frac{\partial\hat{\mathbf{S}}^{\mathrm{eq}}_{\mathrm{M}}}{\partial J}\right)\mathbf{C}^{-1} - \frac{1}{\varrho_{\mathrm{R}}}\frac{1}{\theta}\mathbf{F}^{-1}_{\mathrm{M}}\mathbf{S}^{\mathrm{eq}}_{\mathrm{M}}\mathbf{F}^{-\mathrm{T}}_{\mathrm{M}}\right)\cdot\dot{\mathbf{E}} \\
&= \frac{1}{\varrho_{\mathrm{R}}}\left(-\varrho_{\mathrm{R}}\frac{\partial^2\psi_\theta}{\partial\theta^2} + \tilde{\varphi}'(\mathbf{1}\cdot\hat{\mathbf{S}}^{\mathrm{eq}}_{\mathrm{M}}) + \tilde{\varphi}\left(\mathbf{1}\cdot\frac{\partial\hat{\mathbf{S}}^{\mathrm{eq}}_{\mathrm{M}}}{\partial\theta}\right) + \tilde{\varphi}\frac{1}{\theta}(\mathbf{1}\cdot\hat{\mathbf{S}}^{\mathrm{eq}}_{\mathrm{M}})\right)\dot{\theta} \\
&\quad + \frac{1}{\varrho_{\mathrm{R}}}\left(\tilde{\varphi}J\left(\mathbf{1}\cdot\frac{\partial\hat{\mathbf{S}}^{\mathrm{eq}}_{\mathrm{M}}}{\partial J}\right)\mathbf{C}^{-1} - \frac{1}{\theta}\tilde{\mathbf{T}}_{\mathrm{eq}}\right)\cdot\dot{\mathbf{E}} \\
&= \frac{1}{\varrho_{\mathrm{R}}}\left(-\varrho_{\mathrm{R}}\frac{\partial^2\psi_\theta}{\partial\theta^2} + (\tilde{\varphi}' + \frac{\tilde{\varphi}}{\theta})(\mathbf{1}\cdot\hat{\mathbf{S}}^{\mathrm{eq}}_{\mathrm{M}}) + \tilde{\varphi}\left(\mathbf{1}\cdot\frac{\partial\hat{\mathbf{S}}^{\mathrm{eq}}_{\mathrm{M}}}{\partial\theta}\right)\right)\dot{\theta} \\
&\quad + \frac{1}{\varrho_{\mathrm{R}}}\left(\left(\tilde{\varphi}J\left(\mathbf{1}\cdot\frac{\partial\hat{\mathbf{S}}^{\mathrm{eq}}_{\mathrm{M}}}{\partial J}\right) - \frac{\varphi^{\frac{2}{3}}}{3\theta}(\mathbf{1}\cdot\hat{\mathbf{S}}^{\mathrm{eq}}_{\mathrm{M}}))\right)\mathbf{C}^{-1} - \frac{1}{\theta}\tilde{\mathbf{T}}^{\mathrm{iso}}_{\mathrm{eq}}\right)\cdot\dot{\mathbf{E}}.
\end{aligned}$$

We now obtain an evolution equation for the temperature field

$$c_{\mathrm{d}}\dot{\theta} = -\frac{1}{\varrho_{\mathrm{R}}}\operatorname{Div}\boldsymbol{q}_{\mathrm{R}} + r + d + p \tag{2.211}$$

where

$$\begin{aligned}
p(J,\mathbf{C},\theta) &:= \frac{\theta}{\varrho_{\mathrm{R}}}\left(\left(\frac{\varphi^{\frac{2}{3}}}{3\theta}(\mathbf{1}\cdot\hat{\mathbf{S}}^{\mathrm{eq}}_{\mathrm{M}})) - \tilde{\varphi}J\left(\mathbf{1}\cdot\frac{\partial\hat{\mathbf{S}}^{\mathrm{eq}}_{\mathrm{M}}}{\partial J}\right)\right)\mathbf{C}^{-1} + \frac{1}{\theta}\tilde{\mathbf{T}}^{\mathrm{iso}}_{\mathrm{eq}}\right)\cdot\dot{\mathbf{E}} \\
&= \left(\theta\beta J\mathbf{C}^{-1} + \frac{1}{\varrho_{\mathrm{R}}}\tilde{\mathbf{T}}^{\mathrm{iso}}_{\mathrm{eq}}\right)\cdot\dot{\mathbf{E}}
\end{aligned} \tag{2.212}$$

with

$$\beta = \frac{\theta}{\theta_0}\frac{\varphi'}{\varphi^2}\left(\left(\frac{\varphi}{\theta\varphi'} - 1\right)U'(J/\varphi) - \frac{J}{\varphi}U''(J/\varphi)\right) \tag{2.213}$$

describes the thermoelastic coupling and

$$c_{\mathrm{d}}(J,\theta) := \frac{\theta}{\varrho_{\mathrm{R}}}\left(-\varrho_{\mathrm{R}}\frac{\partial^2\psi_\theta}{\partial\theta^2} + (\tilde{\varphi}' + \frac{\tilde{\varphi}}{\theta})(\mathbf{1}\cdot\hat{\mathbf{S}}^{\mathrm{eq}}_{\mathrm{M}}) + \tilde{\varphi}\left(\mathbf{1}\cdot\frac{\partial\hat{\mathbf{S}}^{\mathrm{eq}}_{\mathrm{M}}}{\partial\theta}\right)\right) \tag{2.214}$$

the heat capacity of the material body. The thermoelastic coupling term p represents the heat production of the material body which is induced by elastic deformation, see(Haupt, 2000), for example. The heat capacity given by (2.214) generally depends on the deformation as well as on the temperature. According to (Heimes, 2005), however, once the glass transition temperature is exceeded, elastomers exhibit an approximately linear relation between the heat capacity and the temperature. It is also possible to disregard the dependence of the heat capacity on the deformation, see (Jansohn, 1997). We therefore choose the linear ansatz

$$c_{\mathrm{d}} = c_{\mathrm{d0}}(1 + c_{\mathrm{dk}}(\theta - \theta_0)) \tag{2.215}$$

for the specific heat capacity c_{d} as proposed in (Heimes, 2005). With the common approximation $c_{\mathrm{d}} \approx \theta\dfrac{\mathrm{d}^2\psi_\theta}{\mathrm{d}\theta^2}$ and the boundary conditions $\dfrac{\mathrm{d}\psi_\theta}{\mathrm{d}\theta} = 0$ and $\psi_\theta = 0$ the thermal part of the free energy reads

$$\psi_\theta = \varrho_{\mathrm{R}}c_{\mathrm{d0}}\left(\left(\theta - \theta_0 - \theta\ln\frac{\theta}{\theta_0}\right)(1 - c_{\mathrm{dk}}\theta_0) - \frac{1}{2}c_{\mathrm{dk}}(\theta - \theta_0)^2\right). \tag{2.216}$$

The internal dissipation (2.203) accounting for the heat production caused by inelastic stress power reads

$$\begin{aligned}
d &= \frac{\varphi^{\frac{2}{3}}}{\varrho_{\mathrm{R}}}\check{\mathbf{C}}_{\mathrm{e}}\check{\mathbf{S}}_{\mathrm{ov}}\cdot\overset{\triangle}{\bar{\bar{\mathbf{\Gamma}}}}_{\mathrm{v}} = \frac{1}{2\varrho_{\mathrm{R}}}\varphi^{\frac{2}{3}}\check{\mathbf{C}}_{\mathrm{e}}\bar{\mathbf{F}}_{\mathrm{v}}\tilde{\mathbf{T}}_{\mathrm{ov}}\bar{\mathbf{F}}_{\mathrm{v}}^{\mathrm{T}}\cdot\bar{\mathbf{F}}_{\mathrm{v}}^{-\mathrm{T}}\dot{\mathbf{C}}_{\mathrm{v}}\bar{\mathbf{F}}_{\mathrm{v}}^{-1}\\
&= \frac{1}{2\varrho_{\mathrm{R}}}\varphi^{\frac{2}{3}}\bar{\mathbf{F}}_{\mathrm{v}}^{-1}\check{\mathbf{C}}_{\mathrm{e}}\bar{\mathbf{F}}_{\mathrm{v}}\tilde{\mathbf{T}}_{\mathrm{ov}}\cdot\dot{\mathbf{C}}_{\mathrm{v}}\\
&= \frac{\mu}{\varrho_{\mathrm{R}}}J^{-\frac{2}{3}}\left(\bar{\mathbf{F}}_{\mathrm{v}}^{-1}\bar{\mathbf{F}}_{\mathrm{v}}^{-\mathrm{T}}\mathbf{C}\mathbf{C}_{\mathrm{v}}^{-1} - \frac{1}{3}(\mathbf{C}\cdot\mathbf{C}_{\mathrm{v}}^{-1})\bar{\mathbf{F}}_{\mathrm{v}}^{-1}\bar{\mathbf{F}}_{\mathrm{v}}^{-\mathrm{T}}\right)\cdot\dot{\mathbf{C}}_{\mathrm{v}}\\
&= \frac{\mu}{\varrho_{\mathrm{R}}}J^{-\frac{2}{3}}\left(\mathbf{C}_{\mathrm{v}}^{-1}\mathbf{C}\mathbf{C}_{\mathrm{v}}^{-1} - \frac{1}{3}(\mathbf{C}\cdot\mathbf{C}_{\mathrm{v}}^{-1})\mathbf{C}_{\mathrm{v}}^{-1}\right)\cdot\dot{\mathbf{C}}_{\mathrm{v}} && (2.217)\\
&= \frac{\mu}{\varrho_{\mathrm{R}}}J^{-\frac{2}{3}}\left[\mathbf{C}_{\mathrm{v}}^{-1}\otimes\mathbf{C}_{\mathrm{v}}^{-1}\right]^{T_{23}}\mathbf{C}\cdot\dot{\mathbf{C}}_{\mathrm{v}} && (2.218)
\end{aligned}$$

based on the relations

$$\check{\mathbf{C}}_{\mathrm{e}} = \varphi^{-\frac{2}{3}}\bar{\mathbf{F}}_{\mathrm{v}}^{-\mathrm{T}}\mathbf{C}\bar{\mathbf{F}}_{\mathrm{v}}^{-1}, \tag{2.219}$$

(2.182) and (2.187). The evaluation of the latter sum in (2.217) results in

$$\begin{aligned}
\left(\mathbf{C} \cdot \mathbf{C}_{\mathrm{v}}^{-1}\right) \mathbf{C}_{\mathrm{v}}^{-1} \cdot \dot{\mathbf{C}}_{\mathrm{v}} &= \frac{4\mu}{\eta} \frac{\varphi^{-\frac{2}{3}}}{J^{\frac{2}{3}}} \left(\mathbf{C} \cdot \mathbf{C}_{\mathrm{v}}^{-1}\right) \mathbf{C}_{\mathrm{v}}^{-1} \cdot \left(\mathbf{C} - \frac{1}{3} \left(\mathbf{C} \cdot \mathbf{C}_{\mathrm{v}}^{-1}\right) \mathbf{C}_{\mathrm{v}}\right) \\
&= \frac{4\mu}{\eta} \frac{\varphi^{-\frac{2}{3}}}{J^{\frac{2}{3}}} \left(\mathbf{C} \cdot \mathbf{C}_{\mathrm{v}}^{-1}\right) \left(\left(\mathbf{C}_{\mathrm{v}}^{-1} \cdot \mathbf{C}\right) - \frac{1}{3} \left(\mathbf{C} \cdot \mathbf{C}_{\mathrm{v}}^{-1}\right) \left(\mathbf{C}_{\mathrm{v}}^{-1} \cdot \mathbf{C}_{\mathrm{v}}\right)\right) \\
&= \frac{4\mu}{\eta} \frac{\varphi^{-\frac{2}{3}}}{J^{\frac{2}{3}}} \left(\mathbf{C} \cdot \mathbf{C}_{\mathrm{v}}^{-1}\right) \left(\left(\mathbf{C}_{\mathrm{v}}^{-1} \cdot \mathbf{C}\right) - \left(\mathbf{C} \cdot \mathbf{C}_{\mathrm{v}}^{-1}\right)\right) = 0.
\end{aligned}$$

The left-hand side of (2.211) gives the energy stored in the material body due to a change of temperature. The first term on the right-hand side represents the heat flux occurring within the material body, r denotes a volume-distributed heat production such as radiation. In the current configuration, the heat conduction equation reads

$$c_{\mathrm{d}} \dot{\theta} = -\frac{1}{\varrho} \operatorname{div} \boldsymbol{q} + r + d + p. \tag{2.220}$$

3 Initial Boundary Value Problem

3.1 Local Form of the IBVP

The initial conditions of the IBVP for the temperature

$$\theta(\boldsymbol{X}, t_\mathrm{i}) = \theta_\mathrm{i}(\boldsymbol{X}) \,, \qquad \text{for all } \boldsymbol{X} \in \Omega, \tag{3.1}$$

$$\theta(\boldsymbol{x}, t_\mathrm{i}) = \theta_\mathrm{i}(\boldsymbol{x}) \,, \qquad \text{for all } \boldsymbol{x} \in \omega, \tag{3.2}$$

as well as for the internal variables

$$\mathbf{q}(\boldsymbol{X}, t_\mathrm{i}) = \mathbf{q}_\mathrm{i}(\boldsymbol{X}) \,, \qquad \text{for all } \boldsymbol{X} \in \Omega, \tag{3.3}$$

$$\mathbf{q}(\boldsymbol{x}, t_\mathrm{i}) = \mathbf{q}_\mathrm{i}(\boldsymbol{x}) \,, \qquad \text{for all } \boldsymbol{x} \in \omega, \tag{3.4}$$

can be formulated in either the material or spatial representation. They have to be specified all over the material body $\mathcal{B}$. Besides the description of the initial state of the material body $\mathcal{B}$, boundary conditions for $t \in \,]t_\mathrm{i}, t_\mathrm{e}[$ have to be applied to its surface. For the purpose of defining the boundary conditions, we split the material surface of the body $\mathcal{B}$ into disjoint subsets. For the mechanical field, we divide the boundary into a region defining the displacements (indicated by the index u) and one prescribing the stresses (indicated by the index s), stated either in the material configuration as

$$\partial\Omega = \overline{\partial_\mathrm{u}\Omega \cup \partial_\mathrm{s}\Omega}, \qquad \partial_\mathrm{u}\Omega \cap \partial_\mathrm{s}\Omega = \varnothing,$$

or in the spatial representation as

$$\partial\omega = \overline{\partial_\mathrm{u}\omega \cup \partial_\mathrm{s}\omega}, \qquad \partial_\mathrm{u}\omega \cap \partial_\mathrm{s}\omega = \varnothing.$$

The bar denotes the closure of the set, cf. Hughes (2000). In the material representation, the Dirichlet boundary condition specifies the displacement over the finite open interval $]t_\mathrm{i}, t_\mathrm{e}[\subset \mathbb{R}$ and reads

$$\boldsymbol{u} = \boldsymbol{\chi}_\mathrm{R}(\boldsymbol{X}, t) - \boldsymbol{X} = \boldsymbol{r}(\boldsymbol{X}, t) \qquad \text{for } \boldsymbol{X} \in \partial_\mathrm{u}\Omega \text{ and } t \in \,]t_\mathrm{i}, t_\mathrm{e}[. \tag{3.5}$$

As regards the specification of the thermal boundary conditions, we split the boundary into three different areas. It is possible to prescribe either the temperature field, the heat flux or a combination of both, leading to

$$\partial\Omega = \overline{\partial_\theta\Omega \cup \partial_\mathrm{q}\Omega \cup \partial_{\theta\mathrm{q}}\Omega}, \qquad \partial_\theta\Omega \cap \partial_\mathrm{q}\Omega \cap \partial_{\theta\mathrm{q}}\Omega = \varnothing,$$

with respect to the material representation or

$$\partial\omega = \overline{\partial_\theta\omega \cup \partial_{\mathrm{q}}\omega \cup \partial_{\theta\mathrm{q}}\omega}, \qquad \partial_\theta\omega \cap \partial_{\mathrm{q}}\omega \cap \partial_{\theta\mathrm{q}}\omega = \varnothing$$

for the spatial representation. The corresponding Dirichlet boundary conditions read

$$\theta(\boldsymbol{X}, t) = \hat{T}(\boldsymbol{X}, t) \qquad \text{for } \boldsymbol{X} \in \partial_\theta\Omega \text{ and } t \in]t_{\mathrm{i}}, t_{\mathrm{e}}[\tag{3.6}$$

and

$$\theta(\boldsymbol{x}, t) = \bar{T}(\boldsymbol{x}, t) \qquad \text{for } \boldsymbol{x} \in \partial_\theta\omega \text{ and } t \in]t_{\mathrm{i}}, t_{\mathrm{e}}[. \tag{3.7}$$

The Neumann boundary conditions are expressed by

$$\mathbf{T}_{\mathrm{R}}\boldsymbol{n}_{\mathrm{R}} = \boldsymbol{s}(\boldsymbol{X}, \mathbf{F}, t) \qquad \text{for } \boldsymbol{X} \in \partial_{\mathrm{s}}\Omega \text{ and } t \in]t_{\mathrm{i}}, t_{\mathrm{e}}[, \tag{3.8}$$

$$\boldsymbol{q}_{\mathrm{R}} \cdot \boldsymbol{n}_{\mathrm{R}} = f_{\theta\mathrm{q}}(\boldsymbol{X}, \theta, t) \qquad \text{for } \boldsymbol{X} \in \partial_{\theta\mathrm{q}}\Omega \text{ and } t \in]t_{\mathrm{i}}, t_{\mathrm{e}}[, \tag{3.9}$$

and

$$\boldsymbol{q}_{\mathrm{R}} \cdot \boldsymbol{n}_{\mathrm{R}} = f_{\mathrm{q}}(\boldsymbol{X}, t) \qquad \text{for } \boldsymbol{X} \in \partial_{\mathrm{q}}\Omega \text{ and } t \in]t_{\mathrm{i}}, t_{\mathrm{e}}[. \tag{3.10}$$

If the prescribed stress vector depends on the deformation gradient, see (3.8), we use the notion “follower loading”, see (Yosibash et al., 2007), for instance, meaning that the stress vector should remain normal in terms of the deformed surface. If we contemplate convective cooling, for example, the prescribed heat flux depends not only on time but also on the surface temperature, as indicated in (3.9). Often

$$f_{\theta\mathrm{q}} = \overline{q}_{\mathrm{con}} + \overline{q}_{\mathrm{rad}} \tag{3.11}$$

is assumed with

$$\overline{q}_{\mathrm{con}} = h_{\mathrm{c}}\left(\theta(\boldsymbol{x}(t)) - \theta_{\mathrm{f}}\right) \quad \text{for} \quad \boldsymbol{x} \in \partial_{\theta\mathrm{q}}\Omega \quad \text{and} \quad t \in]t_{\mathrm{i}}, t_{\mathrm{e}}[\tag{3.12}$$

accounting for a pure convection and

$$\overline{q}_{\mathrm{rad}} = \epsilon\sigma\left(\theta^4(\boldsymbol{x}(t)) - \theta_\infty^4\right) \qquad \text{for} \quad \boldsymbol{x} \in \partial_{\theta\mathrm{q}}\Omega \quad \text{and} \quad t \in]t_{\mathrm{i}}, t_{\mathrm{e}}[\tag{3.13}$$

indicating the net rate of heat transfer caused by radiation per unit surface, see (Quint, 2012). h_{c} denotes the heat transfer coefficient which reflects the mean heat transfer and θ_{f} the absolute temperature of the surrounding fluid. The term thermal radiation denotes energy emitted by matter and transported by electromagnetic waves, see (Incropera et al., 2007). Unlike heat convection, thermal radiation does not require any medium and is most efficient in a vacuum. σ is the Stefan-Boltzmann constant ($\sigma = 5.67 \times 10^{-8}\,\mathrm{W/(m^2K^4)}$), θ_∞ the absolute temperature of the surroundings and ϵ the emissivity which depends on the material and the condition, see (Quint, 2012). It ranges from 0 to 1. Apart from emitting radiation, a surface also intercepts and absorbs it. The property describing the portion of irradiation that is absorbed into the surface of a material body is called absorptivity. The absorptivity often equals the emissivity, referred to as gray surface, see (Quint, 2012, p. 28) and the literature cited therein. With (2.18) and the definition of the transpose of a tensor the norm of $\mathrm{d}a$ yields

$$\mathrm{d}a = \sqrt{\mathrm{d}\boldsymbol{a} \cdot \mathrm{d}\boldsymbol{a}} = (\det \mathbf{F}) \sqrt{\boldsymbol{n}_\mathrm{R} \cdot \mathbf{F}^{-1}\mathbf{F}^{-\mathrm{T}}\boldsymbol{n}_\mathrm{R}}\, \mathrm{d}A. \tag{3.14}$$

Since the representation of a force or a heat flux acting on the surface of the material body $\mathcal{B}$ is the same in both spatial and material representation

$$\mathbf{T}\boldsymbol{n}\, \mathrm{d}a = \mathbf{T}_\mathrm{R}\boldsymbol{n}_\mathrm{R}\, \mathrm{d}A, \tag{3.15}$$

$$\boldsymbol{q} \cdot \boldsymbol{n}\, \mathrm{d}a = \boldsymbol{q}_\mathrm{R} \cdot \boldsymbol{n}_\mathrm{R}\, \mathrm{d}A \tag{3.16}$$

the stress vector $\boldsymbol{t}$ can be formulated as

$$\begin{aligned} \boldsymbol{t} = \mathbf{T}\boldsymbol{n} = \mathbf{T}_\mathrm{R}\boldsymbol{n}_\mathrm{R}\frac{\mathrm{d}A}{\mathrm{d}a} &= \frac{1}{(\det \mathbf{F}) \sqrt{\boldsymbol{n}_\mathrm{R} \cdot \mathbf{F}^{-1}\mathbf{F}^{-\mathrm{T}}\boldsymbol{n}_\mathrm{R}}}\mathbf{T}_\mathrm{R}\boldsymbol{n}_\mathrm{R} \\ &= \hat{\boldsymbol{s}}(\boldsymbol{X}, t) = \bar{\boldsymbol{s}}(\boldsymbol{\chi}_\mathrm{R}(\boldsymbol{X}, t)\,, t) \qquad \text{for } \boldsymbol{X} \in \partial_\mathrm{s}\Omega \text{ and } t \in \,]t_\mathrm{i}, t_\mathrm{e}[, \end{aligned} \tag{3.17}$$

whereas for the heat flux

$$\begin{aligned} q_\mathrm{n} = \boldsymbol{q} \cdot \boldsymbol{n} = \boldsymbol{q}_\mathrm{R} \cdot \boldsymbol{n}_\mathrm{R}\frac{\mathrm{d}A}{\mathrm{d}a} &= \frac{1}{(\det \mathbf{F}) \sqrt{\boldsymbol{n}_\mathrm{R} \cdot \mathbf{F}^{-1}\mathbf{F}^{-\mathrm{T}}\boldsymbol{n}_\mathrm{R}}}\boldsymbol{q}_\mathrm{R} \cdot \boldsymbol{n}_\mathrm{R} \\ &= \hat{f}_\mathrm{q}(\boldsymbol{X}, t) = \bar{f}_\mathrm{q}(\boldsymbol{\chi}_\mathrm{R}(\boldsymbol{X}, t)\,, t) \qquad \text{for } \boldsymbol{X} \in \partial_\mathrm{q}\Omega \text{ and } t \in \,]t_\mathrm{i}, t_\mathrm{e}[. \end{aligned} \tag{3.18}$$

holds. This clearly shows how the prescribed stress and heat flux depends on the deformation. The strong form of the IBVP is summarized in Tab. 3.1. Since it is not generally possible to provide an analytic solution for the IBVP under consideration, we have to employ an approximate solution based on variational principles.

3.2 Variational Form of the IBVP

The finite element method is based on a variational formulation, known as the weak form. The derivation of the weak form of the mechanical or the thermal equilibrium, as given in Sections 3.2.1 and 3.2.2, is based on ansatz functions made for the displacement and temperature field as well as their virtual counterparts. The set of ansatz functions for the displacement

$$\boldsymbol{\mathcal{S}}_{u,t} := \{\, \boldsymbol{u}(\,\cdot\,, t) \mid \boldsymbol{u}\,(\boldsymbol{X}, t) = \boldsymbol{r}(\boldsymbol{X}, t) \;\text{ for } \boldsymbol{X} \in \partial_\mathrm{u}\Omega \,\} \tag{3.19}$$

and for the temperature field

$$\mathcal{S}_{\theta,t} := \left\{\, \theta(\,\cdot\,, t) \;\middle|\; \theta(\boldsymbol{X}, t) = \hat{T}(\boldsymbol{X}, t) \;\text{ for } \boldsymbol{X} \in \partial_\theta\Omega \,\right\} \tag{3.20}$$

satisfy the Dirichlet boundary conditions whereas the set of ansatz functions made for the virtual displacements

$$\boldsymbol{\mathcal{V}}_u := \left\{\, \delta\boldsymbol{u} \colon \Omega \to \mathbb{R}^3 \;\middle|\; \delta\boldsymbol{u}\,(\boldsymbol{X}) = \boldsymbol{0} \text{ for } \boldsymbol{X} \in \partial_\mathrm{u}\Omega \,\right\} \tag{3.21}$$

Table 3.1: Strong form of the coupled problem

Given the initial conditions

$$\begin{aligned} \theta(\boldsymbol{X}, t_{\mathrm{i}}) &= \theta_{\mathrm{i}}(\boldsymbol{X}) \quad \boldsymbol{X} \in \Omega, \\ \mathbf{q}(\boldsymbol{X}, t_{\mathrm{i}}) &= \mathbf{q}_{\mathrm{i}}(\boldsymbol{X}) \quad \boldsymbol{X} \in \Omega, \end{aligned}$$

and the boundary conditions

$$\begin{aligned} \boldsymbol{u}(\boldsymbol{X}, t) &= \boldsymbol{r}(\boldsymbol{X}, t) \text{ on } \partial_{\mathrm{u}}\Omega \times]t_{\mathrm{i}}, t_{\mathrm{e}}[, \\ \mathbf{T}_{\mathrm{R}}\boldsymbol{n}_{\mathrm{R}} &= \boldsymbol{s}\,(\boldsymbol{X}, \mathbf{F}, t) \text{ on } \partial_{\mathrm{s}}\Omega \times]t_{\mathrm{i}}, t_{\mathrm{e}}[, \\ \theta(\boldsymbol{X}, t) &= \hat{T}(\boldsymbol{X}, t) \text{ on } \partial_{\theta}\Omega \times]t_{\mathrm{i}}, t_{\mathrm{e}}[, \\ \boldsymbol{q}_{\mathrm{R}} \cdot \boldsymbol{n}_{\mathrm{R}} &= f_{\mathrm{q}}(\boldsymbol{X}, t) \text{ on } \partial_{\mathrm{q}}\Omega \times]t_{\mathrm{i}}, t_{\mathrm{e}}[, \\ \boldsymbol{q}_{\mathrm{R}} \cdot \boldsymbol{n}_{\mathrm{R}} &= f_{\theta\mathrm{q}}(\boldsymbol{X}, \theta, t) \text{ on } \partial_{\theta\mathrm{q}}\Omega \times]t_{\mathrm{i}}, t_{\mathrm{e}}[, \end{aligned}$$

find $(\boldsymbol{u}, \theta)\colon \overline{\Omega} \times [t_{\mathrm{i}}, t_{\mathrm{e}}] \rightarrow \mathbb{R}^3 \times \mathbb{R}$ such that

$$\begin{aligned} \mathbf{0} &= \operatorname{Div} \mathbf{T}_{\mathrm{R}} + \varrho_{\mathrm{R}}\boldsymbol{k} \quad \text{on } \Omega \times]t_{\mathrm{i}}, t_{\mathrm{e}}[, \\ c_{\mathrm{d}}\dot{\theta} &= -\frac{1}{\varrho_{\mathrm{R}}} \operatorname{Div} \boldsymbol{q}_{\mathrm{R}} + r + p + d \quad \text{on } \Omega \times]t_{\mathrm{i}}, t_{\mathrm{e}}[, \\ \dot{\mathbf{q}} &= \tilde{\boldsymbol{r}}\,(\mathbf{C}, \theta, \mathbf{q}) \text{ on } \Omega \times]t_{\mathrm{i}}, t_{\mathrm{e}}[, \end{aligned}$$

with the constitutive relations

$$\begin{aligned} \tilde{\mathbf{T}} &= \mathbf{h}\,(\mathbf{C}, \theta, \mathbf{q})\,, \\ \boldsymbol{q}_{\mathrm{R}} &= -\boldsymbol{\lambda}_{\mathrm{R}} \operatorname{Grad} \theta. \end{aligned}$$

and virtual temperatures

$$\mathcal{V}_{\theta} := \{\, \delta\theta\colon \Omega \rightarrow \mathbb{R} \mid \delta\theta(\boldsymbol{X}) = 0 \text{ for } \boldsymbol{X} \in \partial_{\theta}\Omega \,\} \tag{3.22}$$

is admissible, meaning that they vanish where Dirichlet boundary conditions are prescribed. In contrast to the Dirichlet boundary conditions the Neumann boundary conditions do not need to be enforced explicitly since they are satisfied automatically by the weak form, see Jeltsch-Fricker (2002).

3.2.1 Weak Form of the Balance of Momentum

Since the influence of inertia is disregarded, the balance of linear momentum (2.55b) reduces to the equilibrium condition

$$\mathbf{0} = \mathrm{Div}\,\mathbf{T}_{\mathrm{R}} + \varrho_{\mathrm{R}}\boldsymbol{k}. \tag{3.23}$$

One way of deriving the weak form of the balance of momentum which, under certain continuity assumptions, see Jeltsch-Fricker (2002), is equivalent to the differential form, is to multiply (3.23) by test functions given in (3.21) and to integrate it via the volume, resulting in

$$\int\limits_{\Omega} \left(\mathrm{Div}\,\mathbf{T}_{\mathrm{R}} + \varrho_{\mathrm{R}}\boldsymbol{k}\right) \cdot \delta\boldsymbol{u}\,\mathrm{d}V = 0. \tag{3.24}$$

Applying the identity

$$\left(\mathrm{Div}\,\mathbf{T}_{\mathrm{R}}\right) \cdot \delta\boldsymbol{u} = \mathrm{Div}\left(\mathbf{T}_{\mathrm{R}}^{T}\delta\boldsymbol{u}\right) - \mathbf{T}_{\mathrm{R}} \cdot \mathrm{Grad}\,\delta\boldsymbol{u} \tag{3.25}$$

yields

$$\int\limits_{\Omega} \left(\mathrm{Div}\left(\mathbf{T}_{\mathrm{R}}^{T}\delta\boldsymbol{u}\right) - \mathbf{T}_{\mathrm{R}} \cdot \mathrm{Grad}\,\delta\boldsymbol{u} + \varrho_{\mathrm{R}}\boldsymbol{k} \cdot \delta\boldsymbol{u}\right) \mathrm{d}V = 0. \tag{3.26}$$

Making use of the divergence theorem leads to

$$\int\limits_{\partial\Omega} \left(\mathbf{T}_{\mathrm{R}}^{T}\delta\boldsymbol{u}\right) \cdot \boldsymbol{n}_{\mathrm{R}}\,\mathrm{d}A - \int\limits_{\Omega} \mathbf{T}_{\mathrm{R}} \cdot \mathrm{Grad}\,\delta\boldsymbol{u}\,\mathrm{d}V + \int\limits_{\Omega} \varrho_{\mathrm{R}}\boldsymbol{k} \cdot \delta\boldsymbol{u}\,\mathrm{d}V = 0. \tag{3.27}$$

By means of the definition of the second Piola-Kirchhoff stress tensor $\mathbf{T}_{\mathrm{R}} = \mathbf{F}\tilde{\mathbf{T}}$ and the Cauchy-theorem $\mathbf{T}_{\mathrm{R}}\boldsymbol{n}_{\mathrm{R}} = \boldsymbol{t}_{\mathrm{R}}$

$$\int\limits_{\partial\Omega} \boldsymbol{t}_{\mathrm{R}} \cdot \delta\boldsymbol{u}\,\mathrm{d}A - \int\limits_{\Omega} \tilde{\mathbf{T}} \cdot \mathbf{F}^{\mathrm{T}}\,\mathrm{Grad}\,\delta\boldsymbol{u}\,\mathrm{d}V + \int\limits_{\Omega} \varrho_{\mathrm{R}}\boldsymbol{k} \cdot \delta\boldsymbol{u}\,\mathrm{d}V = 0 \tag{3.28}$$

can be formulated. Employing (2.10) the Green strain tensor (2.21) reads

$$\mathbf{E}\left(\boldsymbol{u}\right) = \frac{1}{2}\left(\mathbf{H}\left(\boldsymbol{u}\right) + \mathbf{H}^{\mathrm{T}}\left(\boldsymbol{u}\right) + \mathbf{H}^{\mathrm{T}}\left(\boldsymbol{u}\right)\mathbf{H}\left(\boldsymbol{u}\right)\right) \tag{3.29}$$

and its Gateaux derivative reads

$$\begin{aligned}
\delta\mathbf{E} &= \mathrm{D}\mathbf{E}\left(\boldsymbol{u}\right)\left[\delta\boldsymbol{u}\right] \\
&= \frac{\mathrm{d}}{\mathrm{d}\lambda}\tfrac{1}{2}\Big[\,\mathrm{Grad}((\boldsymbol{u} + \lambda\delta\boldsymbol{u}) + \mathrm{Grad}^{\mathrm{T}}\left(\boldsymbol{u} + \lambda\delta\boldsymbol{u}\right) + \\
&\qquad\qquad \mathrm{Grad}^{\mathrm{T}}\left(\boldsymbol{u} + \lambda\delta\boldsymbol{u}\right)\mathrm{Grad}\,\boldsymbol{u} + \mathrm{Grad}^{\mathrm{T}}\,\boldsymbol{u}\,\mathrm{Grad}\left(\boldsymbol{u} + \lambda\delta\boldsymbol{u}\right)\Big]_{\lambda=0} \\
&= \tfrac{1}{2}\left(\mathrm{Grad}\,\delta\boldsymbol{u} + \mathrm{Grad}^{\mathrm{T}}\,\delta\boldsymbol{u} + \mathrm{Grad}^{\mathrm{T}}\,\delta\boldsymbol{u}\,\mathrm{Grad}\,\boldsymbol{u} + \mathrm{Grad}^{\mathrm{T}}\,\boldsymbol{u}\,\mathrm{Grad}\,\delta\boldsymbol{u}\right) \\
&= \tfrac{1}{2}\left(\mathrm{Grad}\,\delta\boldsymbol{u} + \mathrm{Grad}^{\mathrm{T}}\,\delta\boldsymbol{u} + \mathrm{Grad}^{\mathrm{T}}\,\delta\boldsymbol{u}\left(\mathbf{F} - \mathbf{1}\right) + \left(\mathbf{F}^{\mathrm{T}} - \mathbf{1}\right)\mathrm{Grad}\,\delta\boldsymbol{u}\right) \\
&= \tfrac{1}{2}\left(\mathbf{F}^{\mathrm{T}}\,\mathrm{Grad}\,\delta\boldsymbol{u} + \mathrm{Grad}^{T}\delta\boldsymbol{u}\;\mathbf{F}\right).
\end{aligned} \tag{3.30}$$

Exploiting the symmetry of the second Piola-Kirchhoff stress tensor, see (2.61) and employing (3.30), the product in the second integral can be reformulated as

$$\tilde{\mathbf{T}} \cdot \mathbf{F}^{\mathrm{T}} \operatorname{Grad} \delta \boldsymbol{u} = \tilde{\mathbf{T}} \cdot \tfrac{1}{2} \left(\mathbf{F}^{\mathrm{T}} \operatorname{Grad} \delta \boldsymbol{u} + \operatorname{Grad}^{\mathrm{T}} \delta \boldsymbol{u}\, \mathbf{F} \right) = \tilde{\mathbf{T}} \cdot \delta \mathbf{E} \tag{3.31}$$

and the weak form of the balance of linear momentum in the material

$$\int\limits_{\Omega} \tilde{\mathbf{T}} \cdot \delta \mathbf{E} \, \mathrm{d}V = \int\limits_{\partial\Omega} \boldsymbol{t}_{\mathrm{R}} \cdot \delta \boldsymbol{u} \, \mathrm{d}A + \int\limits_{\Omega} \varrho_{\mathrm{R}} \boldsymbol{k} \cdot \delta \boldsymbol{u} \, \mathrm{d}V \tag{3.32}$$

or the spatial representation now reads

$$\int\limits_{\omega} \mathbf{T} \cdot \operatorname{grad} \delta \boldsymbol{u} \, \mathrm{d}v = \int\limits_{\partial\omega} \boldsymbol{t} \cdot \delta \boldsymbol{u} \, \mathrm{d}a + \int\limits_{\omega} \varrho \boldsymbol{k} \cdot \delta \boldsymbol{u} \, \mathrm{d}v. \tag{3.33}$$

3.2.2 Weak Form of the Heat Conduction Equation

The heat conduction equation (2.211) serves as a basis for determining the temperature field. In order to derive its weak form, (2.211) is multiplied by virtual temperatures introduced in (3.22). The approach presented in Section 3.2.1 yields the weak form of the heat conduction equation in the material

$$\int\limits_{\Omega} \varrho_{\mathrm{R}} c_{\mathrm{d}} \dot{\theta} \delta\theta \, \mathrm{d}V - \int\limits_{\Omega} \boldsymbol{q}_{\mathrm{R}} \cdot \operatorname{Grad} \delta\theta \, \mathrm{d}V = - \int\limits_{\partial\Omega} \boldsymbol{q}_{\mathrm{R}} \cdot \boldsymbol{n}_{\mathrm{R}} \delta\theta \, \mathrm{d}A + \int\limits_{\Omega} \varrho_{\mathrm{R}} (r + p + d) \delta\theta \, \mathrm{d}V \tag{3.34}$$

or the spatial representation

$$\int\limits_{\omega} \varrho c_{\mathrm{d}} \dot{\theta} \delta\theta \, \mathrm{d}v - \int\limits_{\omega} \boldsymbol{q} \cdot \operatorname{grad} \delta\theta \, \mathrm{d}v = - \int\limits_{\partial\omega} \boldsymbol{q} \cdot \boldsymbol{n} \delta\theta \, \mathrm{d}a + \int\limits_{\omega} \varrho (r + p + d) \delta\theta \, \mathrm{d}v. \tag{3.35}$$

Tab. 3.2 shows the weak form of the coupled problem.

Table 3.2: Weak form of the coupled problem

Given the initial conditions θ_i, $\mathbf{q}_\mathrm{i}$, the boundary conditions $\boldsymbol{r}$, $\boldsymbol{s}$, $\hat{T}$, f_q, and $f_{\theta\mathrm{q}}$, find $\boldsymbol{u} \in \boldsymbol{\mathcal{S}}_{u,t}$ and $\theta \in \mathcal{S}_{\theta,t}$ so that for any $t \in [t_\mathrm{i}, t_\mathrm{e}]$

$$\begin{aligned}\pi_\mathrm{u}\big(\boldsymbol{u}, \theta, \mathbf{q}, \delta\boldsymbol{u}\big) = \int\limits_{\Omega} \tilde{\mathbf{T}} \cdot \delta\mathbf{E} \,\mathrm{d}V \;&-\; \int\limits_{\partial_\mathrm{s}\Omega} \boldsymbol{s} \cdot \delta\boldsymbol{u} \,\mathrm{d}A \\ &-\; \int\limits_{\Omega} \varrho_\mathrm{R} \boldsymbol{k} \cdot \delta\boldsymbol{u} \,\mathrm{d}V = 0, \quad \text{for all } \delta\boldsymbol{u} \in \boldsymbol{\mathcal{V}}_u,\end{aligned}$$

$$\begin{aligned}\pi_\theta(\boldsymbol{u}, \theta, \mathbf{q}, \delta\theta) = &\int\limits_{\Omega} \varrho_\mathrm{R} \Big(c_\mathrm{d}\dot{\theta} - r - p - d\Big)\, \delta\theta \,\mathrm{d}V - \int\limits_{\Omega} \boldsymbol{q}_\mathrm{R} \cdot \operatorname{Grad}\delta\theta \,\mathrm{d}V \\ &+ \int\limits_{\partial_\mathrm{q}\Omega} f_\mathrm{q} \delta\theta \,\mathrm{d}A + \int\limits_{\partial_{\theta\mathrm{q}}\Omega} f_{\theta\mathrm{q}} \delta\theta \,\mathrm{d}A = 0, \quad \text{for all } \delta\theta \in \mathcal{V}_\theta,\end{aligned}$$

and

$$\begin{aligned}\dot{\mathbf{q}} &= \tilde{\boldsymbol{r}}(\mathbf{C}, \theta, \mathbf{q})\,, \qquad && \mathbf{q}(\boldsymbol{X}, t_\mathrm{i}) = \mathbf{q}_\mathrm{i}(\boldsymbol{X})\,, \qquad && \text{for any } \boldsymbol{X} \in \Omega, \\ \tilde{\mathbf{T}} &= \mathbf{h}\,(\mathbf{C}, \theta, \mathbf{q})\,, && && \\ \boldsymbol{q}_\mathrm{R} &= -\boldsymbol{\lambda}_\mathrm{R} \operatorname{Grad}\theta. && &&\end{aligned}$$

4 Solution Procedure

This chapter discusses the solution procedure that is applied to the weak form of the inelastic, thermo-mechanically coupled IBVP given in Tab. 3.2. Since it is not possible to derive an analytical solution, we are obliged to use numerical solution procedures. Due to the structure of the IBVP, we opt for the vertical method of lines, which means that we begin by discretizing the spatial domain and then proceed to the discretization of the temporal domain. The spatial discretization of the weak form is done using the p-version of the finite element method, proposed in (Szabo and Babuska, 1991), leading to a system of differential-algebraic equations, referred to as the DAE-system. This DAE-system in turn needs to be solved by numerical methods. The approach for the temporal discretization adopted in this thesis is to use diagonally-implicit Runge-Kutta methods, see (Hairer and Wanner, 1996), for instance. In (Wittekindt, 1991) and (Fritzen, 1997) the discretized form of the prinicple of virtual displacements coupled with ordinary differential equations, which are defined locally at the integration points and represent the behavior of the constitutive model, is interpreted as a DAE-system. Based on this result (Ellsiepen and Hartmann, 2001) show that, for isothermal considerations, applying a Backward-Euler time integration scheme to the DAE-system in conjuction with the Multilevel-Newton Algorithm (MLNA) for solving the nonlinear equation system that ensues is fully equivalent to the classical finite element approach, i.e. the application of the Backward-Euler time integration scheme at Gauss-point level. With this insight, high-order time integration schemes can be applied to the DAE-system so it is possible to use an embedded step-size control. High-order time integration schemes of DIRK-type are of special interest, since a finite element computer program based on the classical approach can easily be augmented with a high-order time integration scheme due to the algorithmic structure of diagonally-implicit Runge-Kutta methods.

4.1 Coupling Strategies

According to (Felippa and Park, 1980) there are four approaches for solving two-field coupled problems.

- **Field elimination**
  Field elimination means that one field state variable is selected as fundamental, and the other field state variables are eliminated through the interaction equations, see (Felippa and Park, 1980). Since there are only very few cases in which this approach can be applied, it is not of further interest.

- **Monolithic solution**
  The fully coupled system is treated as a computational entity, and all field state variables are simultaneously advanced in time, i.e. the balance of linear momentum and the heat conduction equation are solved concurrently at each time-step in the case of thermomechanics. The resulting coupling terms required when employing this approach, induce an unsymmetry in the global equation system. For strongly coupled problems the simultaneous solution procedure is indispensable, see (Lübbing, 1997).

- **Partitioned solution**
  For weakly coupled problems we can adopt a partitioned solution procedure, where the different field state variables of an increment are computed separately in a parallel manner, see Fig. 4.1. This means that we have to guess one field variable in order to start the alternating procedure. This approach is discussed in (Park, 1980; Park and Felippa, 1980), among others.

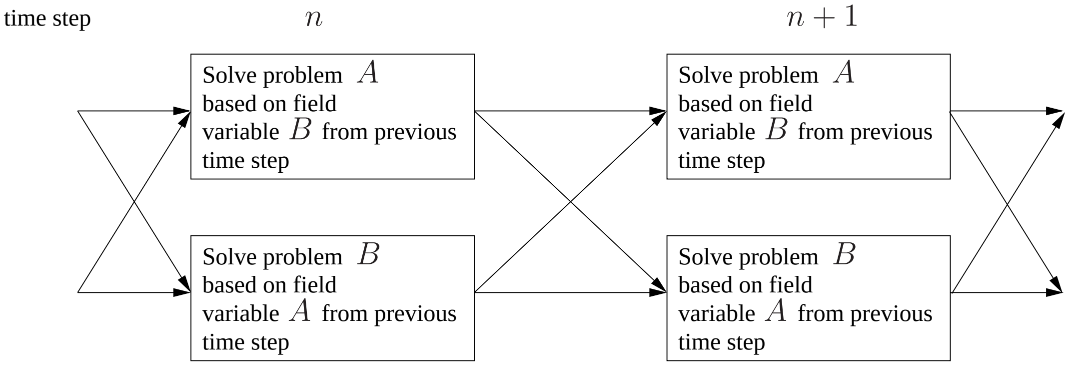

Figure 4.1: One way partitioned scheme

- **Staggered solution**
  In contrast to the partitioned solution, the fields are computed one after the other, see (Felippa and Park, 1980; Miehe, 1993, 1995b, 1996; Simo and Miehe, 1992), for example. We guess the unknown field variable and use, say, the quantity related to the beginning of the time-step. The basic approach of an iterative staggered scheme is given in Fig. 4.2. The convergence of the staggered scheme is not known a priori since it depends on the polynomial degree p and size h of the finite elements, the step-size Δt, the quotient $\Delta t/h^2$, the choice of the operator split and the predictor, see (Turska and Schrefler, 1993). (Armero and Simo, 1992) introduce a two-phase operator split, dividing the full non-linear system of thermo-elasticity into an adiabatic elastodynamic phase, followed by a heat conduction phase at a fixed configuration, which exhibits superior stability properties. See also (Armero and Simo, 1993). In (Erbts and Düster, 2012) the drawbacks of the isothermal split methodology, see (Miehe, 1995a; Simo and Miehe, 1992), for instance, such as not guaranteeing unconditional stability in the case of strong coupling, are cured by employ-

ing convergence acceleration methods. These predict the primary variables of the current time-step and apply numerical relaxation.

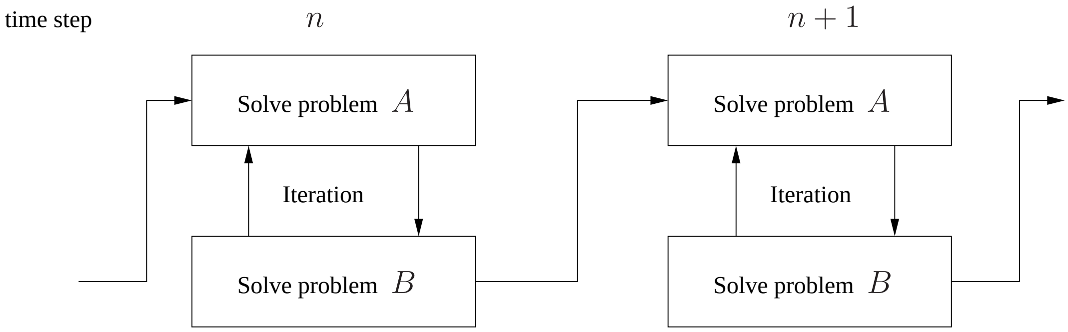

Figure 4.2: Iterative staggered scheme

A comparison between the characteristics of the simultaneous and staggered solution scheme can be found in (Lübbing, 1997). The most obvious advantage of a staggered solution scheme is the possibility to combine existing one-field codes in order to solve multi-field problems. Moreover, the systems of equations that have to be solved within the staggered scheme are smaller than the matrices resulting from a fully coupled approach. The main advantages of a simultaneous solution scheme over a staggered one are the superior stability properties of the time integration procedure and superior convergence characteristics, since the coupling terms are not linearized with the staggered approach. According to (Lübbing, 1997) a staggered solution scheme should only be employed in the case of a weak coupling between the fields under consideration. We have therefore chosen to employ a monolithic solution procedure in this treatise.

4.2 Spatial Discretization using the p-Version of the Finite Element Method

This section discusses the spatial discretization of the weak form of the coupled problem, paying particular attention to the applied mapping concept, its implementation into the finite element code TASA-FEM, the ansatz made for the displacement and temperature field and specific pitfalls concerning their implementation.

4.2.1 Mapping

In the context of finite element computations the domain of interest $\mathcal{B}$ is divided into n_{el} subdomains Ω_e, see Fig. 4.3. The map mediating between Ω_e and Ω_{st}^h is given by

$$\boldsymbol{X} = \boldsymbol{\chi}^e(\boldsymbol{\xi}) \qquad \text{and accordingly} \qquad \boldsymbol{\xi} = \boldsymbol{\varphi}^e(\boldsymbol{X}). \tag{4.1}$$

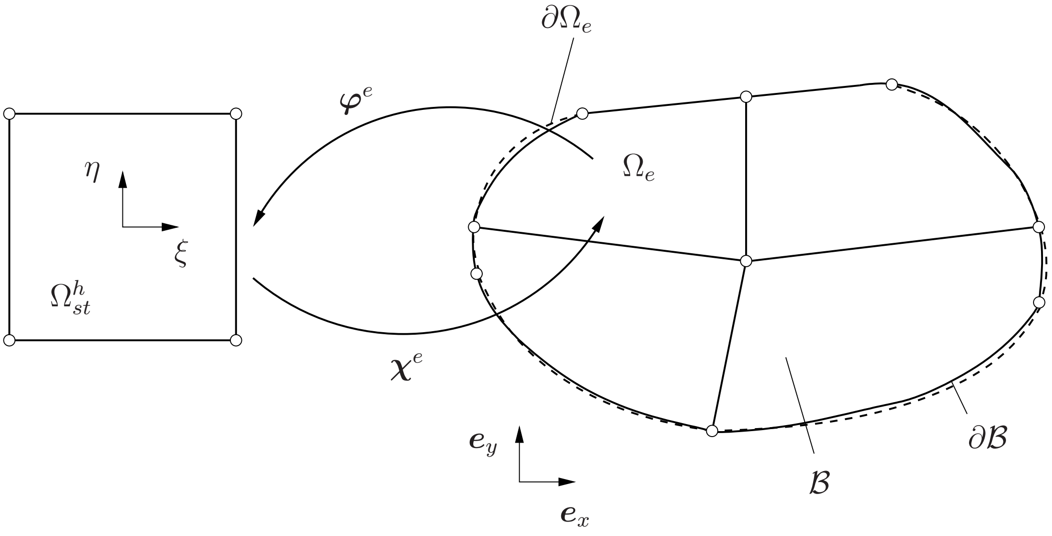

Figure 4.3: Discretization of a two-dimensional material body using blending functions

Basically, we distinguish between three different mapping concepts. Firstly, the map from the natural coordinates $\boldsymbol{\xi}$ to the geometrical coordinates can be included in the ansatz used for approximating the solution associated with the notion of a subparametric mapping. That is the case if a polynomial of lesser degree is used for the mapping than for approximating the solution meaning the map is less “complex” than the ansatz made for the approximation of the solution of the underlying mathematical problem. Secondly, the map can be as “complex” as the approximation of the solution associated with the concept of isoparametric mapping. In the h-version of the finite element method this concept is widespread. Thirdly, there are superparametric mapping concepts which are characterized either by a non-polynomial ansatz for the mapping and a polynomial ansatz for the approximation of the solution or by a mapping whose polynomial degree is higher than that of the approximation of the solution.

As with the p-version of the finite element method only few elements with a high polynomial degree are used, so a very precise approximation of the geometry is needed. One means of representing the geometry accurately is the blending function method, which is based on data containing the description of the exact geometrical model. Using a CAD (Computer Aided Design) computer program, the geometrical model is represented with the help of rational or non-rational B-splines (Rogers, 2001). Where non-rational B-splines are used in conjunction with the blending function method to carry out the mapping from global to local coordinates, the map can belong to either of the mapping concepts in question, depending on the polynomial order of the ansatz functions and the polynomial order of the B-splines. Rational B-splines always lead to superparametric mappings because they are not polynomials.

4.2.1.1 Blending Function Method

For a hexahedral element the blending function method, which was introduced by Gordon and Hall, see (Gordon and Hall, 1973a) and (Gordon and Hall, 1973b), reads

$$\boldsymbol{X} = \boldsymbol{\chi}^e(\xi,\eta,\zeta) = \sum_{i=1}^{8} N_{1,1,1}^{N_i}(\xi,\eta,\zeta)\boldsymbol{X}_i + \sum_{i=1}^{6} \boldsymbol{f}_i(\xi,\eta,\zeta) - \sum_{i=1}^{12} \boldsymbol{e}_i(\xi,\eta,\zeta), \tag{4.2}$$

see (Kiralyfalvi and Szabo, 1997). There is accordingly a link between the natural coordinates $\boldsymbol{\xi}$ and the geometrical coordinates, see Fig. 4.4. The first sum in (4.2) represents the linear coordinate transformation containing the tri-linear shape functions $N_{1,1,1}^{N_i}$ of node N_i. The second term represents the surfaces of the elements. The surface blending terms, such as the one representing surface 6

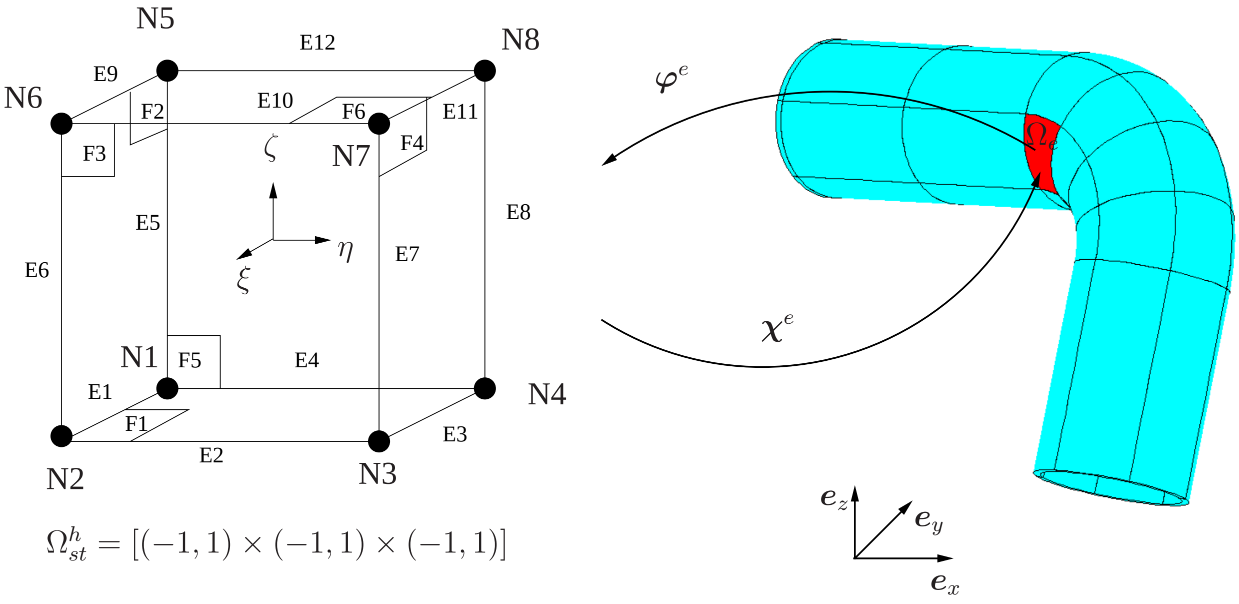

Figure 4.4: Discretized three-dimensional material body and mapping employing blending function method

$$\begin{aligned}\boldsymbol{f}_6(\xi,\eta,\zeta) = \Big[\boldsymbol{F}_6(\xi,\eta) - \frac{1}{4}\,&[(1-\xi)(1-\eta)\boldsymbol{X}_5 + (1+\xi)(1-\eta)\boldsymbol{X}_6 \\ &+ (1+\xi)(1+\eta)\boldsymbol{X}_7 + (1-\xi)(1+\eta)\boldsymbol{X}_8]\Big]\left(\frac{1+\zeta}{2}\right),\end{aligned}$$

represent the difference between the exact geometrical representation of the surface $\boldsymbol{F}_6$ and the plane spanned by the 4 nodes belonging to the surface. The geometrical representation of the surface is based on information supplied by the pre- and post-processing software GiD, see Ribo et al. (2008). This difference evens out linearly as it gets closer to the opposite surface. We proceed in the same way with the curves, see curve 1, for instance,

$$\boldsymbol{e}_1(\xi,\eta,\zeta) = \left[\boldsymbol{E}_1(\xi) - \frac{1}{2}\left[1-\xi)\boldsymbol{X}_1 + (1+\xi)\boldsymbol{X}_2\right]\right]\left(\frac{1-\eta}{2}\right)\left(\frac{1-\zeta}{2}\right).$$

The difference between the exact representation of the curve and the straight line going through the nodes of the curve evens out linearly with respect to the local directions which are orthogonal to the direction of the edge. See Appendix A.2 for a summary of all the terms of the blending function method.

4.2.1.2 Quasi-Regional Mapping

When working with superparametric maps, we have to pay attention to the representation of rigid body modes, see (Szabo and Babuska, 1991) and (Düster, 2001). A general rigid body mode can be expressed by

$$\boldsymbol{x} = \mathbf{Q}\boldsymbol{X} + \boldsymbol{c} \tag{4.3}$$

where $\mathbf{Q}$ is an orthogonal tensor with the property $\mathbf{Q}^{\mathrm{T}}\mathbf{Q} = \mathbf{1}$. This accounts for the rotational part of the rigid body mode, whereas vector $\boldsymbol{c}$ describes the translational part of the rigid body mode. Deriving the current position of the material body $\boldsymbol{x}$ with respect to $\boldsymbol{X}$ yields the deformation gradient, see (2.7), of a rigid body mode $\mathbf{F} = \mathbf{Q}$. So the Green strain tensor

$$\mathbf{E} = \frac{1}{2}\left(\mathbf{Q}^{\mathrm{T}}\mathbf{Q} - \mathbf{1}\right) = \mathbf{0} \tag{4.4}$$

does not induce any strains. With (4.3), $\boldsymbol{x} = \boldsymbol{X} + \boldsymbol{u}$ and (4.1) it follows that

$$\boldsymbol{u}_{\text{rbm}} = (\mathbf{Q} - \mathbf{1})\,\boldsymbol{X} + \boldsymbol{c} = (\mathbf{Q} - \mathbf{1})\,\boldsymbol{\chi}^e(\boldsymbol{\xi}) + \boldsymbol{c}. \tag{4.5}$$

The ansatz for the displacement field, which is given in (4.16), can only satisfy the rigid body motion (4.5) if the mapping is included in the ansatz for the displacement field. Otherwise, artificial strains will be induced, see (Bröker, 2001). One way of circumventing this is to approximate the exact geometry with the help of Lagrange polynomials, as proposed in (Kiralyfalvi and Szabo, 1997). If the polynomial degree used for the mapping is lower than that used for approximating the primary variables, no artificial strains will be introduced. An arbitrarily shaped curve $\boldsymbol{E}(\xi)$ can be approximated by

$$\boldsymbol{P}_n(\xi) = \sum_{i=0}^{n} \boldsymbol{E}(\xi_i)A_i(\xi) \tag{4.6}$$

taking n Lagrange polynomials

$$A_i(\xi) = \prod_{j=0,j\neq i}^{n} \frac{\xi-\xi_j}{\xi_i-\xi_j} \qquad i = 0,...,n \tag{4.7}$$

into consideration. Since the Lagrange polynomials have the property

$$A_i(\xi_k) = \delta_{ik} = \begin{cases} 1, & \text{for} \quad i = k \\ 0, & \text{for} \quad i \neq k \end{cases}, \tag{4.8}$$

the coefficients used for approximating the curve $\boldsymbol{E}(\xi)$ are the values of the curve evaluated at the points ξ_i. Chen and Babuska computed a set of optimal points, see (Chen and Babuska, 1995) and (Chen and Babuska, 1996), which contain details concerning the accuracy of the quasi-regional mapping. The Chen-Babuska points are given in Appendix A.4. An extension to two-dimensional functions is given by

$$\boldsymbol{B}_n(\xi,\eta) = \sum_{k=1}^{n}\sum_{j=1}^{m} \boldsymbol{F}(\xi_k,\eta_j)A_k(\xi)A_j(\eta),$$

see (Bröker, 2001, p. 64)

4.2.1.3 Incorporation of the Geometrical Modeling Package GiD

Since almost arbitrarily shaped elements can be used as a basis for deriving the Jacobian of the map $\boldsymbol{X} = \boldsymbol{\chi}^e(\xi,\eta,\zeta)$, it is important to incorporate them into a geometry modeling package, see (Bröker, 2001) and (Nübel, 2005). With regard to the incorporation into GiD, (Garcia-Donore et al., 2010) suggested that what we call "volume" in GiD terminology should be taken to be one finite element. In this way, it is then possible to find out which nodes, curves and surfaces belong to which volume along with other details of the exact geometrical description of curves and surfaces in parametric form. Fig. 4.5 depicts a curve depending on the arc length t. The origin of the curve coincides with $t = 0$ and its end with $t = 1$. This parametric curve is provided by GiD. In GiD curves are represented either as rational or as non-rational B-splines (Rogers, 2001). A non-rational B-spline representing the parametric description of curve 1, for instance, is given by

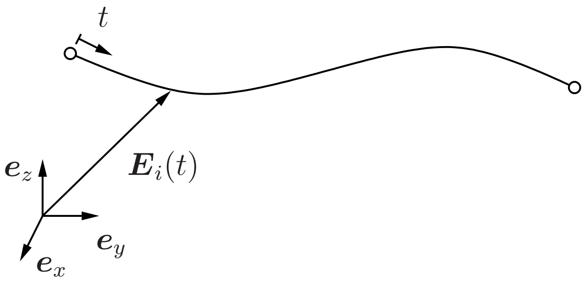

Figure 4.5: Parametric description of a curve provided by GiD

$$\boldsymbol{E}_1(t) = \sum_{i=1}^{n+1} \boldsymbol{P}_i S_{i,k}(t) \quad 0 \le t < 1, \quad 2 < k < n+1. \tag{4.9}$$

$\boldsymbol{P}_i$ is the position vector of the $n+1$ control polygon vertices and the $S_{i,k}$ are the normalized B-spline basis functions, which are defined by the Cox-de Boor recursion formulas,

$$S_{i,1}(t) = \begin{cases} 1 & \text{if} \quad x_i \le t < x_{i+1} \\ 0 & \text{otherwise} \end{cases} \tag{4.10}$$

and

$$S_{i,k}(t) = \frac{(t - x_i)S_{i,k-1}(t)}{x_{i+k-1} - x_i} + \frac{(x_{i+k} - t)S_{i+1,k-1}(t)}{x_{i+k} - x_{i+1}}. \tag{4.11}$$

Alternatively, the curve can be represented by a rational B-spline given by

$$\boldsymbol{E}_1(t) = \frac{\sum_{i=1}^{n+1} \boldsymbol{P}_i S_{i,k}(t) w_i}{\sum_{i=1}^{n+1} S_{i,k}(t) w_i}. \tag{4.12}$$

The w_i denote weights that are associated with the control vertices $\boldsymbol{P}_i$. As the relation

$$\sum_{i=1}^{n+1} S_{i,k}(t) = 1$$

holds for non-rational B-splines, inserting $w_i = 1$ in (4.12) yields (4.9). We therefore conclude that non-rational B-spline basis functions are a special case among their rational counterparts.

The geometrical modeling package GiD provides the parametric description of a surface, see Fig. 4.6, depending on the geometry, either as non-rational

$$\boldsymbol{F}_6(r, s) = \sum_{i=1}^{n+1} \sum_{j=1}^{m+1} \boldsymbol{P}_{i,j} S_{i,k}(r) R_{j,l}(s) \tag{4.13}$$

or rational

$$\boldsymbol{F}_6(r, s) = \frac{\sum_{i=1}^{n+1} \sum_{j=1}^{m+1} \boldsymbol{P}_{i,j} S_{i,k}(r) R_{j,l}(s) w_{i,j}}{\sum_{i=1}^{n+1} \sum_{j=1}^{m+1} S_{i,k}(r) R_{j,l}(s) w_{i,j}} \tag{4.14}$$

B-splines. $\boldsymbol{P}_{i,j}$ are the control vertices, $S_{i,k}(r)$ and $R_{j,l}(s)$ are the non-rational B-spline basis functions given by (4.10) and (4.11) and $w_{i,j}$ are weights associated with the control vertices.

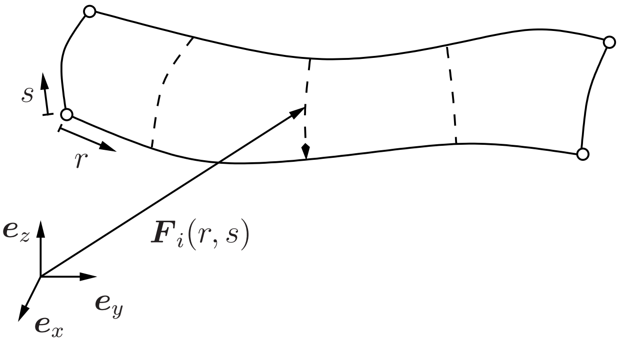

Figure 4.6: Parametric description of a surface provided by GiD

The parametric description needs to be transformed from the GiD parameter space to the parameter space of the unit element yielding

$$\boldsymbol{E}_1 = \boldsymbol{E}_1(t(\xi))$$

and

$$\boldsymbol{F}_1 = \boldsymbol{F}_1(r(\xi, \eta), s(\xi, \eta))$$

for edge 1 and face 1, for example. For $t(\xi)$ we assume a linear function

$$t(\xi) = \frac{1}{2}(\xi + 1) \quad -1 \leq \xi \leq 1 \quad \text{and} \quad 0 \leq t \leq 1.$$

In this context, we have to account for the orientation of a curve with respect to the orientation of the corresponding edge of the unit element. Since GiD provides the information as to whether the starting node or the end node of the curve belongs to $t = 0$ or to $t = 1$, this is easily dealt with. With regard to the parametric description of surfaces, which are also represented as rational or non-rational B-splines, the map from the GiD parameter space to the unit element space is given by

$$\boldsymbol{r}(\xi, \eta) = \begin{Bmatrix} r(\xi, \eta) \\ s(\xi, \eta) \end{Bmatrix} = \sum_{i=1}^{4} N_{1,1}^{N_i}(\xi, \eta) \boldsymbol{r}_i, \tag{4.15}$$

where $N_{1,1}^{N_i}$ are the bilinear shape functions given in (4.26). Since the GiD parameter space ranges from 0 to 1, the values of the GiD parameter space at the corner points of a surface denoted by $\boldsymbol{r}_i$ can be $(0, 0)$, $(1, 0)$, $(1, 1)$ and $(0, 1)$. In this context, it is crucial to deal with the orientation of the local coordinates of the surface of the unit element $\boldsymbol{\xi}$ within the parametric description of the surface supplied by GiD, see Fig. 4.7. This displays two possible orientations for the local coordinates $\boldsymbol{\xi}$ and the coordinates $\boldsymbol{r}$, pointing out the necessity to take a closer look at the the map from $\boldsymbol{\xi}$ to $\boldsymbol{r}$. In order to correctly evaluate (4.15), we need to know which corner point $\boldsymbol{r}_j$ belongs to which shape function $N_{1,1}^{N_i}$. Taking the left-hand side of Fig. 4.7 into consideration, the local node number i, indicated by the number within the unit element, belongs to the corner point $\boldsymbol{r}_i$ of the r-s-coordinate system. With the help of this information, the order of the corner points reads $\boldsymbol{r}_1 = (0, 0)$, $\boldsymbol{r}_2 = (1, 0)$, $\boldsymbol{r}_3 = (1, 1)$ and $\boldsymbol{r}_4 = (0, 1)$. This allows us to evaluate (4.15) and determine the map mediating between $\boldsymbol{\xi}$ and $\boldsymbol{r}$. Taking a closer look at the right-hand side of Fig. 4.7, we observe that the local node number 1 belongs to $\boldsymbol{r}_4$, the local node number 2 belongs to $\boldsymbol{r}_1$, 3 to $\boldsymbol{r}_2$ and 4 to $\boldsymbol{r}_3$. When evaluating (4.15) this information has to be taken into consideration, leading to a different order of the corner points, which in this case is given by $\boldsymbol{r}_1 = (0, 1)$, $\boldsymbol{r}_2 = (0, 0)$, $\boldsymbol{r}_3 = (1, 0)$ and $\boldsymbol{r}_4 = (1, 1)$. Proceeding accordingly for all possible combinations of the coordinate systems $\boldsymbol{\xi}$ and $\boldsymbol{r}$ guarantees the correct evaluation of (4.15), no matter how the local coordinates $\boldsymbol{\xi}$ are oriented within the surface.

In order to ensure a consistent map $\boldsymbol{X} = \boldsymbol{\chi}^e(\xi, \eta, \zeta)$, the continuity requirements between the nodes, curves and surfaces, such as

$$\begin{aligned} \boldsymbol{X} = \boldsymbol{X}_1 = \boldsymbol{E}_1(t(-1)) = \boldsymbol{E}_4(t(-1)) &= \boldsymbol{E}_5(t(-1)) \\ &= \boldsymbol{F}_1(r(-1, -1), s(-1, -1)) \\ &= \boldsymbol{F}_2(r(-1, -1), s(-1, -1)) \\ &= \boldsymbol{F}_5(r(-1, -1), s(-1, -1)) \end{aligned}$$

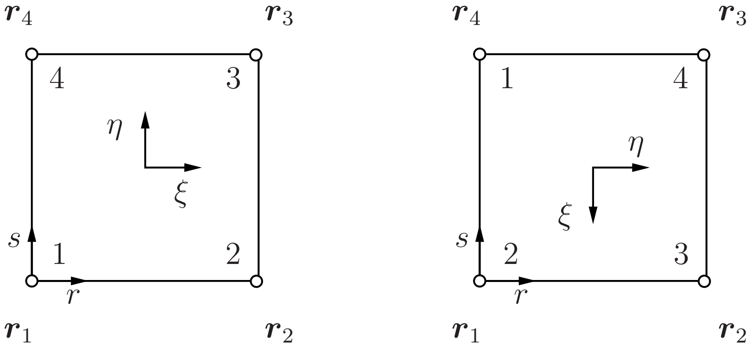

Figure 4.7: Two possible orientations of the local coordinates of the surface of the unit element within the GiD parameter space $\boldsymbol{r}$. The local node numbers are indicated by the number within the unit element.

and $\boldsymbol{X}(\xi,-1,-1) = \boldsymbol{E}_1 = \boldsymbol{F}_1(r(\xi,-1),s(\xi,-1)) = \boldsymbol{F}_4(r(\xi,-1),s(\xi,-1))$ have to be fulfilled. It is likewise imperative to ensure the continuity of the derivatives of neighboring nodes, curves and surfaces with respect to their local coordinates like

$$\frac{\partial \boldsymbol{X}(\xi,-1,-1)}{\partial \xi} = \frac{\partial \boldsymbol{E}_1(\xi)}{\partial \xi} = \frac{\partial \boldsymbol{F}_1(\xi,\eta=-1)}{\partial \xi} = \frac{\partial \boldsymbol{F}_2(\xi,\zeta=-1)}{\partial \xi}.$$

4.2.2 Hierarchic Shape Functions based on Integrated Legendre Polynomials

We define scalar valued ansatz functions N_j in order to approximate the displacements, virtual displacements, temperatures and virtual temperatures by

$$\boldsymbol{u}^h(\mathbf{x},t) = \underbrace{\left[\boldsymbol{N}_\mathrm{d}(\mathbf{x})\ \overline{\boldsymbol{N}}_\mathrm{d}(\mathbf{x})\right]}_{\boldsymbol{N}_\mathrm{ad}(\mathbf{x})} \underbrace{\left\{\begin{array}{c} \boldsymbol{u}(t) \\ \overline{\boldsymbol{u}}(t) \end{array}\right\}}_{\boldsymbol{u}_\mathrm{a}(t)} = \boldsymbol{N}_\mathrm{d}(\mathbf{x})\,\boldsymbol{u}(t) + \overline{\boldsymbol{N}}_\mathrm{d}(\mathbf{x})\,\overline{\boldsymbol{u}}(t), \tag{4.16}$$

$$\delta\boldsymbol{u}^h(\mathbf{x}) = \underbrace{\left[\boldsymbol{N}_\mathrm{d}(\mathbf{x})\ \overline{\boldsymbol{N}}_\mathrm{d}(\mathbf{x})\right]}_{\boldsymbol{N}_\mathrm{ad}(\mathbf{x})} \underbrace{\left\{\begin{array}{c} \delta\boldsymbol{u} \\ \delta\overline{\boldsymbol{u}} = \boldsymbol{0} \end{array}\right\}}_{\delta\boldsymbol{u}_\mathrm{a}} = \boldsymbol{N}_\mathrm{d}(\mathbf{x})\,\delta\boldsymbol{u}, \tag{4.17}$$

$$\theta^h(\mathbf{x},t) = \boldsymbol{N}_{\mathrm{a}\theta}^\mathrm{T}(\mathbf{x})\boldsymbol{\Theta}_\mathrm{a}(t) = \boldsymbol{N}_\theta^\mathrm{T}(\mathbf{x})\boldsymbol{\Theta}(t) + \overline{\boldsymbol{N}}_\theta^\mathrm{T}(\mathbf{x})\overline{\boldsymbol{\Theta}}(t) \tag{4.18}$$

and

$$\delta\theta^h(\mathbf{x},t) = \boldsymbol{N}_\theta^\mathrm{T}(\mathbf{x})\delta\boldsymbol{\Theta}. \tag{4.19}$$

See Section 4.2.2.5 for the arrangement of the ansatz functions N_j in the matrices containing all ansatz functions of an element for the displacement and temperature field, respectively. The displacement and temperature coefficients contained in $\boldsymbol{u}_{\mathrm{a}}$ and $\boldsymbol{\Theta}_{\mathrm{a}}$, respectively, are partitioned into $\boldsymbol{u}$ or $\boldsymbol{\Theta}$ summing up the unknown and $\overline{\boldsymbol{u}}$ or $\overline{\boldsymbol{\Theta}}$ summing up all the prescribed coefficients. Wherever displacements or temperatures are prescribed, $\delta\overline{\boldsymbol{u}} = \boldsymbol{0}$, $\delta\overline{\boldsymbol{\Theta}} = \boldsymbol{0}$ holds for their virtual counterparts. The subscript a indicates that all displacement or temperature degrees of freedom are contained in that particular vector, whereas the subscripts θ and d refer to temperature or displacement-related quantities. With n_{modes} denoting the number of modes of the whole structure $\boldsymbol{N}_{\mathrm{ad}} \in \mathbb{R}^{3\times 3n_{\mathrm{modes}}}$, $\boldsymbol{N}_{\mathrm{a}\theta} \in \mathbb{R}^{n_{\mathrm{modes}}}$, $\boldsymbol{u}_{\mathrm{a}} \in \mathbb{R}^{3n_{\mathrm{modes}}}$, $\delta\boldsymbol{u}_{\mathrm{a}} \in \mathbb{R}^{3n_{\mathrm{modes}}}$, $\boldsymbol{\Theta}_{\mathrm{a}} \in \mathbb{R}^{n_{\mathrm{modes}}}$, $\delta\boldsymbol{\Theta}_{\mathrm{a}} \in \mathbb{R}^{n_{\mathrm{modes}}}$, $\boldsymbol{N}_{\mathrm{d}} \in \mathbb{R}^{3\times n_{\mathrm{nu}}}$, $\overline{\boldsymbol{N}}_{\mathrm{d}} \in \mathbb{R}^{3\times n_{\mathrm{pu}}}$, $\boldsymbol{N}_{\theta} \in \mathbb{R}^{n_{\mathrm{n}\theta}}$ and $\overline{\boldsymbol{N}}_{\theta} \in \mathbb{R}^{n_{\mathrm{p}\theta}}$ holds, with n_{pu} and $n_{\mathrm{p}\theta}$ counting the prescribed displacement and temperature degrees of freedom and n_{nu} and $n_{\mathrm{n}\theta}$ counting the unknown displacement and temperature degrees of freedom. Making use of the map (4.1) and exploiting the element-wise definition of the shape functions, we write

$$\boldsymbol{u}^{h}(\mathbf{x},t) = \boldsymbol{N}_{\mathrm{ad}}(\mathbf{x})\,\boldsymbol{u}_{\mathrm{a}}(t) = \mathbf{N}_{\mathrm{d}}^{e}(\boldsymbol{\varphi}^{e}(\mathbf{x}))\mathbf{u}^{\mathrm{e}} \quad \text{for} \quad \mathbf{x} \in \Omega_e, \tag{4.20}$$

$$\delta\boldsymbol{u}^{h}(\mathbf{x},t) = \boldsymbol{N}_{\mathrm{ad}}(\mathbf{x})\,\delta\boldsymbol{u}_{\mathrm{a}}(t) = \mathbf{N}_{\mathrm{d}}^{e}(\boldsymbol{\varphi}^{\boldsymbol{e}}(\mathbf{x}))\delta\mathbf{u}^{\mathrm{e}} \quad \text{for} \quad \mathbf{x} \in \Omega_e, \tag{4.21}$$

$$\theta^{h}(\mathbf{x},t) = \boldsymbol{N}_{\mathrm{a}\theta}^{\mathrm{T}}(\mathbf{x})\,\boldsymbol{\Theta}_{\mathrm{a}}(t) = \mathbf{N}_{\theta}^{e\mathrm{T}}(\boldsymbol{\varphi}^{\boldsymbol{e}}(\mathbf{x}))\boldsymbol{\Theta}^{e} \quad \text{for} \quad \mathbf{x} \in \Omega_e \tag{4.22}$$

and

$$\delta\theta^{h}(\mathbf{x},t) = \boldsymbol{N}_{\mathrm{a}\theta}^{\mathrm{T}}(\mathbf{x})\,\delta\boldsymbol{\Theta}_{\mathrm{a}}(t) = \mathbf{N}_{\theta}^{e\,\mathrm{T}}(\boldsymbol{\varphi}^{\boldsymbol{e}}(\mathbf{x}))\delta\boldsymbol{\Theta}^{e} \quad \text{for} \quad \mathbf{x} \in \Omega_e \tag{4.23}$$

with $\mathbf{N}_{\mathrm{d}}^{e} \in \mathbb{R}^{3\times 3n_{\mathrm{em}}}$, $\mathbf{u}^{\mathrm{e}} \in \mathbb{R}^{3n_{\mathrm{em}}}$, $\delta\mathbf{u}^{\mathrm{e}} \in \mathbb{R}^{3n_{\mathrm{em}}}$, $\mathbf{N}_{\theta}^{e} \in \mathbb{R}^{n_{\mathrm{em}}}$, $\boldsymbol{\Theta}^{e} \in \mathbb{R}^{n_{\mathrm{em}}}$ and $\delta\boldsymbol{\Theta}^{e} \in \mathbb{R}^{n_{\mathrm{em}}}$, n_{em} denoting the number of modes belonging to an element. We introduce hierarchic shape functions for hexahedral elements contained in $\mathbf{N}_{\mathrm{d}}^{e}$ and $\mathbf{N}_{\theta}^{e}$. To begin with, we will discuss the one-dimensional basis, as it is very easy to derive the two- and three-dimensional basis from its one-dimensional counterpart. The two-dimensional basis is also necessary for evaluating the element stiffness and the right-hand side resulting from a stress or heat flux acting on the surface of the computational domain. When shape functions based on Lagrange polynomials are used for the spatial discretization, a physical meaning, such as displacements, can be assigned to each coefficient of the ansatz approximating the unknown quantities. With integrated Legendre polynomials this is different. In this case, there are not only the coefficients belonging to the nodes of the finite element mesh but also shape functions belonging to the edges, faces and volumes of the finite element. A physical meaning can be assigned to the coefficients belonging to the shape functions of the nodes because they constitute a partition of unity. This does not hold for the coefficients belonging to the shape functions of the edges, faces and volumes. The discussion of the shape functions follows (Szabo and Babuska, 1991), (Düster, 2001) and (Heisserer, 2007).

4.2.2.1 The One-Dimensional Basis

We begin by discussing the construction of the one-dimensional basis of the p-version of the finite element method. There are two kinds of shape function belonging to the one-dimensional unit element.

1. Nodal modes: Linear shape functions

$$N_1(\xi) = 1/2(1-\xi),$$
$$N_2(\xi) = 1/2(1+\xi)$$

constituting a partition of unity

$$N_1(\xi) + N_2(\xi) = 1$$

called nodal modes, are assigned to the nodes of the unit element.

2. Internal modes: Shape functions belonging to the interior of the element

$$N_i(\xi) = \phi_{i-1}(\xi), \quad i = 3, 4, ..., p+1$$

are called internal or bubble modes. As p designates the polynomial degree of the shape function, the internal modes come into play when the polynomial degree is greater than or equal to two. The internal modes are based on integrated Legendre polynomials

$$\phi_i(\xi) = \sqrt{\frac{2i-1}{2}} \int_{-1}^{\xi} L_{i-1}(x)dx \tag{4.24}$$

$$= \frac{1}{\sqrt{4i-2}}\left(L_i(\xi) - L_{i-2}(\xi)\right), \qquad i = 2, 3, ... \tag{4.25}$$

in which the Legendre polynomials can be computed by applying the Rodriguez formula

$$L_n(\xi) = \frac{1}{2^n n!}\frac{d^n}{d\xi^n}(\xi^2-1)^n, \quad \xi \in (-1, 1), \quad n = 0, 1, 2, ...$$

Within the unit element they are orthogonal

$$\int_{-1}^{+1} L_n(\xi)L_m(\xi)d\xi = \begin{cases} \frac{2}{2n+1} & \text{if} \quad n = m \\ 0 & \qquad \text{otherwise} \end{cases}$$

yielding a diagonally dominant stiffness matrix

$$\int_{-1}^{+1} \frac{d\,N_i}{d\,\xi}\frac{d\,N_j}{d\,\xi}d\xi = \delta_{ij}, \qquad i \geq 3 \quad \text{and} \quad j \geq 1 \qquad \text{or} \qquad i \geq 1 \quad \text{and} \quad j \geq 3.$$

Increasing the polynomial degree of the finite element is done by enriching the vector space spanned by the linear shape functions with the internal modes. The integrated Legendre polynomials constitute a hierarchic basis because a set of shape functions associated with a specific polyonomial degree incorporates all sets of shape functions associated with a lesser polynomial degree. The hierarchic basis does not constitute a partition of unity, so no physical meaning such as a displacement can be associated with its coefficients.

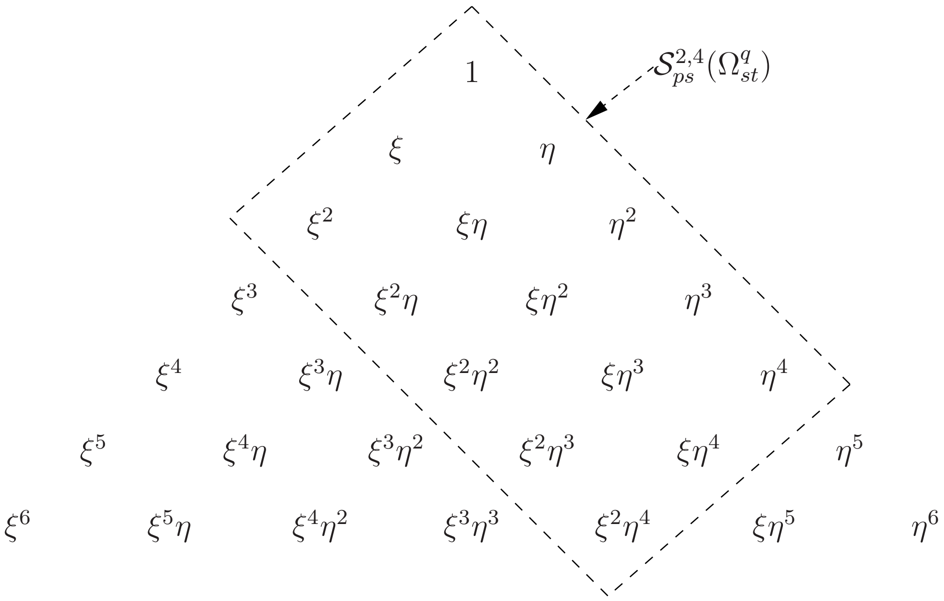

Figure 4.8: Spanning sets for the tensor product space $\boldsymbol{\mathcal{S}}_{ps}^{p_\xi,p_\eta}(\Omega_{st}^{q})$

4.2.2.2 The Two-Dimensional Basis

The two-dimensional basis is not only needed for integrating the surface traction vector via the surface of the computational domain but is also well suited for explaining the differences between the trunk $\boldsymbol{\mathcal{S}}_{ts}^{p_\xi,p_\eta}(\Omega_{st}^{q})$ and tensor product space $\boldsymbol{\mathcal{S}}_{ps}^{p_\xi,p_\eta}(\Omega_{st}^{q})$. The tensor product space comprises all the polynomials on $\Omega_{st}^{h} = [(-1,1)\times(-1,1)]$ spanned by the set of monomials

$$\xi^i\eta^j \quad \text{with} \quad i = 0,1,...,p_\xi, \quad j = 1,2,...,p_\eta,$$

see also Fig. 4.8. Certain monomials are omitted when constructing the trunk space, leading to a slower increase in the number of modes associated with a given polynomial degree when compared to the tensor product space. The trunk space $\boldsymbol{\mathcal{S}}_{ts}^{p_\xi,p_\eta}(\Omega_{st}^{q})$ on $\Omega_{st}^{h} = [(-1,1)\times(-1,1)]$ is spanned by the subset containing the monomials

$$\begin{aligned}
\xi^i\eta^j &\quad \text{with} \quad i = 0,...,p_\xi, \quad j = 0,...,p_\eta, \quad i+j = 0,...,\max(p_\xi,p_\eta)\\
\xi\eta &\quad \text{for} \quad p_\xi = p_\eta = 1\\
\xi^{p_\xi}\eta &\quad \text{for} \quad p_\xi \geq 2\\
\xi\eta^{p_\eta} &\quad \text{for} \quad p_\eta \geq 2,
\end{aligned}$$

see also Fig. 4.9. A quadrilateral element, as given in Fig. 4.10, consists of four nodes, four edges and one face. Shape functions are assigned to each of these geometrical objects.

1. Nodal modes: Bilinear shape functions

$$N_{1,1}^{N_i}(\xi,\eta) = \frac{1}{4}(1+\xi_i\xi)(1+\eta_i\eta) \quad \text{with} \quad i = 1,...,4, \tag{4.26}$$

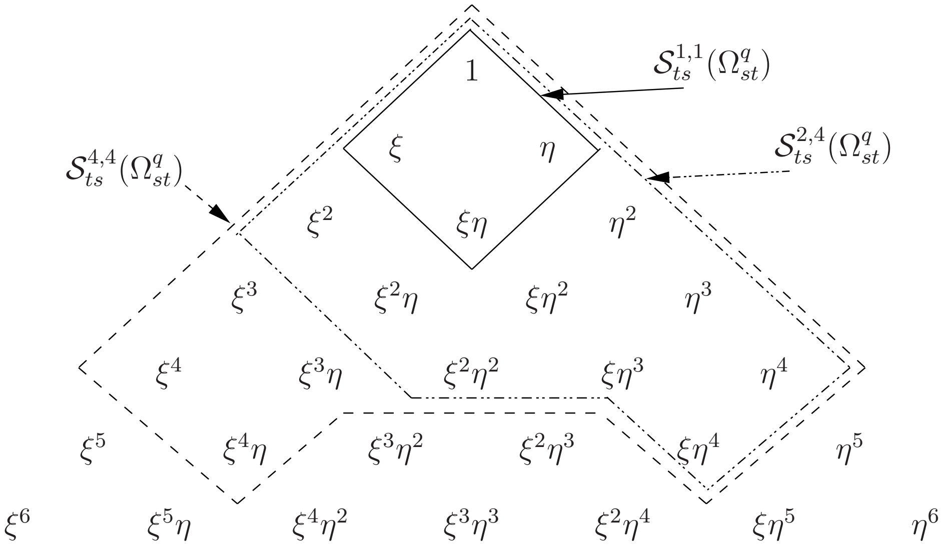

Figure 4.9: Spanning sets for the trunk space $\boldsymbol{\mathcal{S}}_{ts}^{p_\xi,p_\eta}(\Omega_{st}^q)$

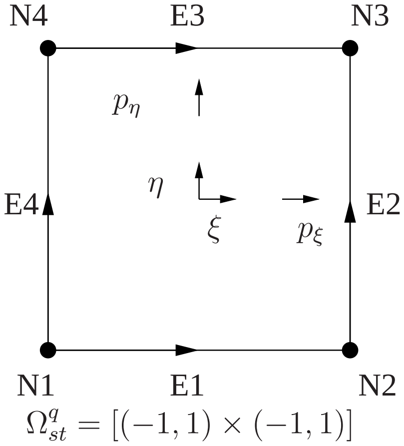

Figure 4.10: Quadrilateral unit element

for which

$$\sum_{i=1}^{4} N_{1,1}^{N_i}(\xi,\eta) = 1$$

holds, belong to the nodes of the unit element. (ξ_i, η_i) denote the local coordinates $(\pm 1, \pm 1)$ of the nodes.

2. Edge modes: We assign the shape functions

$$N_{i,1}^{E_1}(\xi,\eta) \quad = \frac{1}{2}\phi_i(\xi)(1-\eta), \qquad i = 2, ..., p_\xi \tag{4.27}$$

and

$$N_{i,1}^{E_3}(\xi,\eta) \quad = \frac{1}{2}\phi_i(\xi)(1+\eta), \qquad i = 2, ..., p_\xi \tag{4.28}$$

consisting of an ansatz of arbitrary order in ξ-direction and an ansatz of order one in η-direction to the edges oriented in the local ξ-direction. The shape functions belonging to the edges oriented in η-direction

$$N_{1,i}^{E_2}(\xi,\eta) \quad = \frac{1}{2}\phi_i(\eta)(1+\xi), \qquad i = 2, ..., p_\eta \tag{4.29}$$

and

$$N_{1,i}^{E_4}(\xi,\eta) \quad = \frac{1}{2}\phi_i(\eta)(1-\xi), \qquad i = 2, ..., p_\eta \tag{4.30}$$

consist of a linear ansatz in ξ-direction and an ansatz of arbitrary order in η-direction. These shape functions equal zero at the nodes and at all other edges of the unit element.

3. Internal modes: Shape functions with arbitrary order in both local directions

$$N_{i,j}^{int}(\xi,\eta) \quad = \quad \phi_i(\xi)\phi_j(\eta) \tag{4.31}$$

$$\text{for} \quad \begin{cases} ps & i = 2, ..., p_\xi - 2, j = 2, ..., p_\eta - 2 \\ ts & i = 2, ..., p_\xi - 4, j = 2, ..., p_\eta - 4, \\ & i + j = 4, ..., \max(p_\xi, p_\eta) \end{cases} \tag{4.32}$$

belong to the interior of the unit element. In (4.27) - (4.31) ϕ_i is given by (4.24). These shape functions, called interior or bubble modes, vanish at the nodes and edges of the unit element. Similar to the one-dimensional basis, only the shape functions belonging to the nodes constitute a partition of unity, implying that the coefficients belonging to the edges and the interior of the unit element, contained in the ansatz made for the displacement or temperature field, do not have a physical meaning such as displacement or temperature. The shape functions associated with the trunk space of the p-version of the finite element method for a polynomial degree of up to 8 are plotted in Fig. 4.11. The shape functions spanning the trunk and tensor product space can be found in Appendix A.1.1 and A.1.2, respectively.

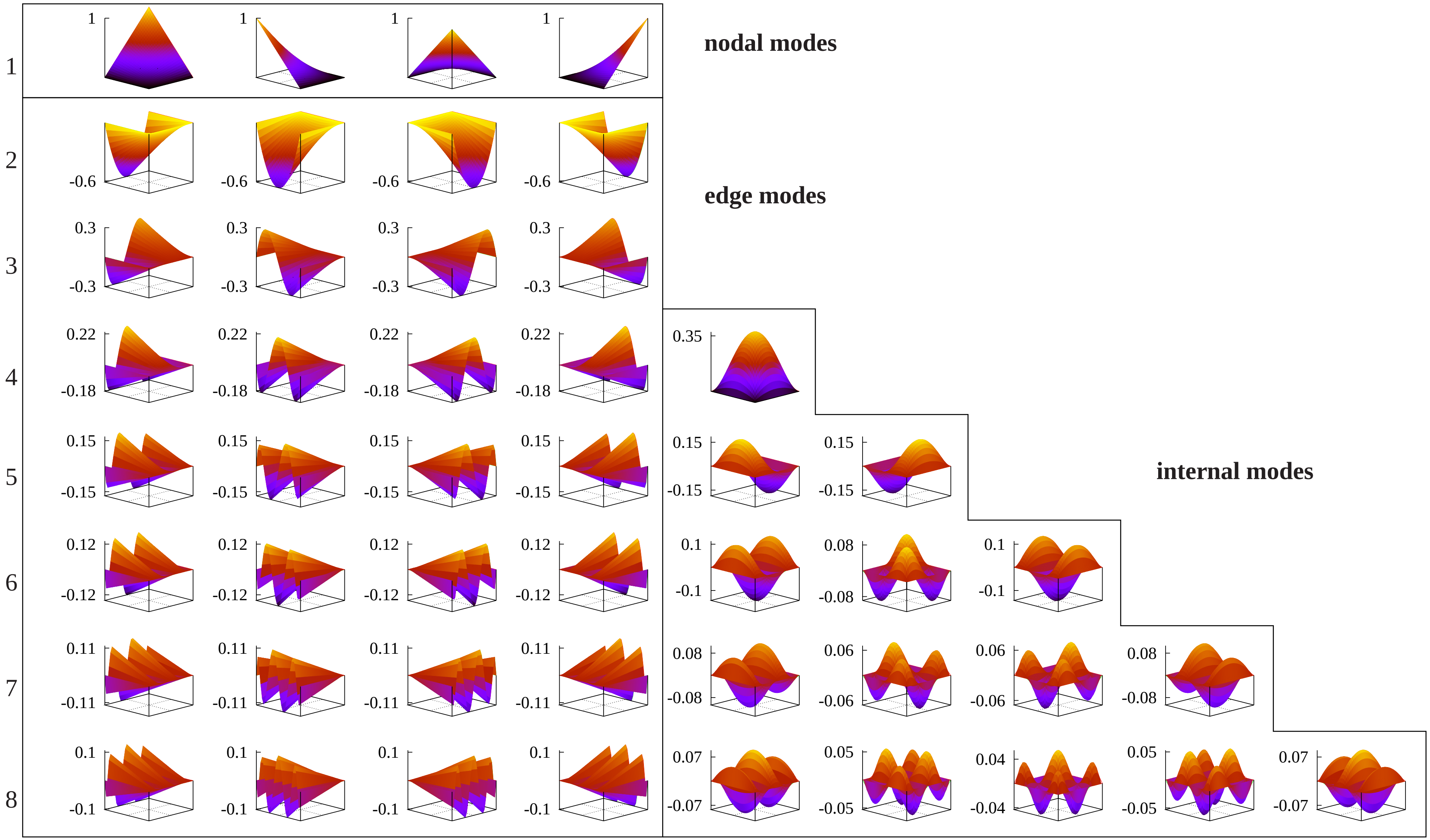

Figure 4.11: Hierarchic shape functions for $\boldsymbol{\mathcal{S}}_{ts}^{p_\xi,p_\eta}(\Omega_{st}^{q})$ according to (Szabo and Babuska, 1991)

4.2.2.3 The Three-Dimensional Basis

We will now proceed to discuss the tensor product space $\boldsymbol{\mathcal{S}}_{ps}^{p_\xi,p_\eta,p_\zeta}(\Omega_{st}^h)$ as well as the trunk space $\boldsymbol{\mathcal{S}}_{ts}^{p_\xi,p_\eta,p_\zeta}(\Omega_{st}^h)$ below. The three-dimensional ansatz of the p-version consists of four different kinds of shape functions belonging to the nodes, edges, surfaces and volume of a hexahedral unit element, see Fig. 4.12.

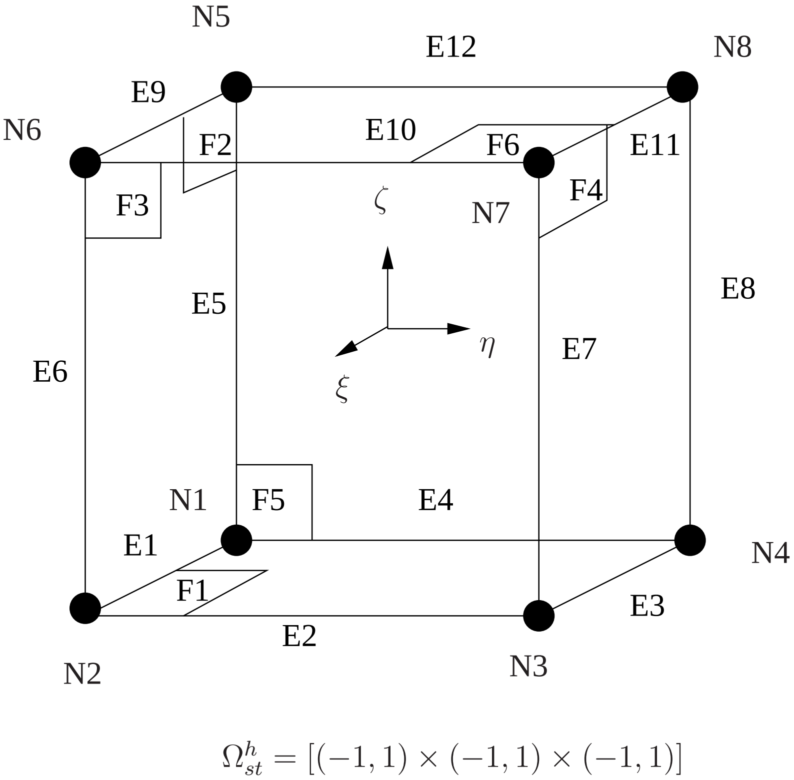

Figure 4.12: Hexahedral unit element according to (Düster, 2001)

1. Nodal modes: There are the tri-linear shape functions

$$N_{1,1,1}^{N_i}(\xi,\eta,\zeta) \quad = \quad \frac{1}{8}(1+\xi_i\xi)(1+\eta_i\eta)(1+\zeta_i\zeta) \quad \text{with} \quad i = 1,...,8,$$

belonging to the nodes of the elements which constitute a partition of unity, see (Hughes, 2000). The values (ξ_i, η_i, ζ_i) are the local coordinates of the element nodes amounting to ± 1.

2. Edge modes: In addition, there are shape functions belonging to the 12 edges of the unit element called edge modes, such as the shape function at edge 1

$$N_{i,1,1}^{E_1}(\xi,\eta,\zeta) \quad = \quad \frac{1}{4}(1-\eta)(1-\zeta)\phi_i(\xi), \qquad i = 2,...,p_\xi \tag{4.33}$$

as indicated by the superimposed E_1. The subscripts $(i,1,1)$ indicate the polynomial degree with respect to the local directions ξ, η and ζ. Thus, the shape function consists of a polynomial

p		1	2	3	4	5	6	7	8	9	10
dof	ts	24	60	96	150	222	315	432	576	750	957
	ps	24	81	192	375	648	1029	1536	2187	3000	3993
n_{ip}		8	27	64	125	216	343	512	729	1000	1331

Table 4.1: Number of degrees of freedom and number of integration points per element for the trunk and tensor product space, $\text{dof}_{ts}(p) = 3(8 + 12(p-1) + 6\sum_{i=1}^{p-3} i + \sum_{i=1}^{p-5} i(p-4-i))$, $\text{dof}_{ps}(p) = 3(8 + 12(p-1) + 6(p-1)^2 + (p-1)^3)$, $n_{\text{ip}} = (p+1)^3$

of high order $\phi_i(\xi)$ with respect to the local direction of the edge to which the shape function belongs as well as the linear terms belonging to the other local directions. The edge modes are defined separately and they vanish at all edges except the one to which they belong.

3. Face modes: On top of that, a shape function is assigned to each face of the unit element.

$$\begin{aligned} N^{F_1}_{i,j,1}(\xi,\eta,\zeta) &= \frac{1}{2}(1-\zeta)\phi_i(\xi)\phi_j(\eta) \\ \text{for} \quad & \begin{cases} ps & i = 2, ..., p_\xi, j = 2, ..., p_\eta \\ ts & i = 2, ..., p_\xi - 2, j = 2, ..., p_\eta - 2, i + j = 4, ..., \max(p_\xi, p_\eta) \end{cases} \end{aligned}$$

represents the shape function corresponding to face 1 which is oriented orthogonally to the local ζ-direction and accordingly has a polynomial of degree i and j in ξ- and η-direction, respectively.

4. Internal modes: There are, moreover, other modes which belong to the interior of the unit element. The so-called internal modes are given by

$$\begin{aligned} N^{int}_{i,j,k}(\xi,\eta,\zeta) &= \phi_i(\xi)\phi_j(\eta)\phi_k(\zeta) \\ \text{for} \quad & \begin{cases} ps & i = 2, ..., p_\xi, j = 2, ..., p_\eta, k = 2, ..., p_\zeta \\ ts & i = 2, ..., p_\xi - 4, j = 2, ..., p_\eta - 4, \\ & k = 2, ..., p_\zeta - 4, i + j + k = 6, ..., \max(p_\xi, p_\eta, p_\zeta). \end{cases} \end{aligned}$$

They vanish at all edges and faces of the unit element. Tab. 4.1 shows the number of degrees of freedom for the trunk and tensor product space formulation and the required number of Gauss points. A table containing the shape functions associated with the trunk space can be found in Appendix A.1.3. For the tensor product space see Appendix A.1.4.

4.2.2.4 Inter-Element Continuity

The continuity of the ansatz for the displacement field of two neighboring elements is not a foregone conclusion. The p-version of the finite element method is characterized by the fact that shape functions are assigned to the edges, faces and the interior of an element. That is why care has to be taken with the orientation of the edges and faces. It is unusual for the orientation of two neighboring elements to be identical, which means that the orientation of an edge induced by the orientation of the first element to which it belongs, for example, is different from its orientation induced by the second element. In order to circumvent this problem, a global orientation is assigned to each edge. The positive direction of the edge is determined by the geometrical modeling package GiD, which provides the global node number of the starting and end node for each curve. For each edge of each element, we assign either $+1$, indicating that the local and global orientation of the edge are identical, or -1, indicating that its local and global orientation are different. There is a similar problem with the faces. We select two edges of each face that are oriented in different local directions, designating its global orientation.

It is also important that the polynomial degrees of neighboring edges and faces are equal. When different polynomial degrees are assigned to different local directions, it can happen that the polynomial degree of an edge, induced by the first element to which it belongs, is different from the polynomial degree of the other elements to which it belongs. If this is the case, the higher polynomial degree is assigned to the edge. We opted for the same approach with the faces.

4.2.2.5 Arrangement of Shape Functions

In order to complete the discussion of the shape functions, the matrices $\mathbf{N}_{\mathrm{d}}^{e}$ and $\mathbf{N}_{\theta}^{e}$ containing the shape functions of one element are written as follows. They are composed of linear shape functions belonging to the nodes $\mathbf{N}_{\mathrm{d}}^{e\mathrm{N}}$, $\mathbf{N}_{\theta}^{e\mathrm{N}}$ and shape functions of arbitrary order belonging to the edges $\mathbf{N}_{\mathrm{d}}^{e\mathrm{E}}$, $\mathbf{N}_{\theta}^{e\mathrm{E}}$, faces $\mathbf{N}_{\mathrm{d}}^{e\mathrm{F}}$, $\mathbf{N}_{\theta}^{e\mathrm{F}}$ and to the volume $\mathbf{N}_{\mathrm{d}}^{e\mathrm{I}}$, $\mathbf{N}_{\theta}^{e\mathrm{I}}$ of the hexahedral element indicated by the superimposed N, E, F and I. The partitioning accordingly reads

$$\mathbf{N}_{\mathrm{d}}^{e} = \left[\mathbf{N}_{\mathrm{d}}^{e\mathrm{N}} \quad \mathbf{N}_{\mathrm{d}}^{e\mathrm{E}} \quad \mathbf{N}_{\mathrm{d}}^{e\mathrm{F}} \quad \mathbf{N}_{\mathrm{d}}^{e\mathrm{I}}\right] \tag{4.34}$$

and

$$\mathbf{N}_{\theta}^{e\,\mathrm{T}} = \left[\mathbf{N}_{\theta}^{e\mathrm{N}\,\mathrm{T}} \quad \mathbf{N}_{\theta}^{e\mathrm{E}\,\mathrm{T}} \quad \mathbf{N}_{\theta}^{e\mathrm{F}\,\mathrm{T}} \quad \mathbf{N}_{\theta}^{e\mathrm{I}\,\mathrm{T}}\right] \tag{4.35}$$

with $(.)^{\mathrm{T}}$ denoting the transposition of a matrix. The arrangement of the trilinear shape functions is given by

$$\mathbf{N}_{\mathrm{d}}^{e\mathrm{N}} = \begin{bmatrix} N_{1,1,1}^{N_1} & 0 & 0 & & N_{1,1,1}^{N_8} & 0 & 0 \\ 0 & N_{1,1,1}^{N_1} & 0 & \dots & 0 & N_{1,1,1}^{N_8} & 0 \\ 0 & 0 & N_{1,1,1}^{N_1} & & 0 & 0 & N_{1,1,1}^{N_8} \end{bmatrix} \tag{4.36}$$

and

$$\mathbf{N}_{\theta}^{e\mathrm{N}\,\mathrm{T}} = \left[N_{1,1,1}^{N_1} \quad \dots \quad N_{1,1,1}^{N_8}\right] . \tag{4.37}$$

By way of an example, the arrangement of the modes belonging to edge 1 is given by

$$\mathbf{N}_{\mathrm{d}}^{e\mathrm{E1}} = \begin{bmatrix} N_{2,1,1}^{E_1} & 0 & 0 & & N_{p_\xi,1,1}^{E_1} & 0 & 0 \\ 0 & N_{2,1,1}^{E_1} & 0 & \dots & 0 & N_{p_\xi,1,1}^{E_1} & 0 \\ 0 & 0 & N_{2,1,1}^{E_1} & & 0 & 0 & N_{p_\xi,1,1}^{E_1} \end{bmatrix} \tag{4.38}$$

and

$$\mathbf{N}_{\theta}^{e\mathrm{E1}\,\mathrm{T}} = \left[N_{2,1,1}^{E_1} \quad \dots \quad N_{p_\xi,1,1}^{E_1}\right] , \tag{4.39}$$

whereas the arrangement of all edge modes associated with the displacement and temperature field reads

$$\mathbf{N}_{\mathrm{d}}^{e\mathrm{E}} = \left[\mathbf{N}_{\mathrm{d}}^{e\mathrm{E1}} \quad \mathbf{N}_{\mathrm{d}}^{e\mathrm{E2}} \quad \ldots \quad \mathbf{N}_{\mathrm{d}}^{e\mathrm{E12}}\right] \tag{4.40}$$

and

$$\mathbf{N}_{\theta}^{e\mathrm{E\,T}} = \left[\mathbf{N}_{\theta}^{e\mathrm{E1\,T}} \quad \mathbf{N}_{\theta}^{e\mathrm{E2\,T}} \quad \ldots \quad \mathbf{N}_{\theta}^{e\mathrm{E12\,T}}\right], \tag{4.41}$$

respectively. For the shape functions belonging to the faces, we choose

$$\mathbf{N}_{\mathrm{d}}^{e\mathrm{F}} = \left[\mathbf{N}_{\mathrm{d}}^{e\mathrm{F1}} \quad \mathbf{N}_{\mathrm{d}}^{e\mathrm{F2}} \quad \ldots \quad \mathbf{N}_{\mathrm{d}}^{e\mathrm{F6}}\right] \tag{4.42}$$

and

$$\mathbf{N}_{\theta}^{e\mathrm{F\,T}} = \left[\mathbf{N}_{\theta}^{e\mathrm{F1\,T}} \quad \mathbf{N}_{\theta}^{e\mathrm{F2\,T}} \quad \ldots \quad \mathbf{N}_{\theta}^{e\mathrm{F6\,T}}\right] \tag{4.43}$$

and the modes belonging to face 1 might, for instance, be given by

$$\mathbf{N}_{\mathrm{d}}^{e\mathrm{F1}} = \begin{bmatrix} N_{2,2,1}^{F_1} & 0 & 0 & & N_{p_\xi,p_\eta,1}^{F_1} & 0 & 0 \\ 0 & N_{2,2,1}^{F_1} & 0 & \ldots & 0 & N_{p_\xi,p_\eta,1}^{F_1} & 0 \\ 0 & 0 & N_{2,2,1}^{F_1} & & 0 & 0 & N_{p_\xi,p_\eta,1}^{F_1} \end{bmatrix} \tag{4.44}$$

and

$$\mathbf{N}_{\theta}^{e\mathrm{E1\,T}} = \left[N_{2,2,1}^{F_1} \quad \ldots \quad N_{p_\xi,p_\eta,1}^{F_1}\right]. \tag{4.45}$$

The arrangement of the internal modes reads

$$\mathbf{N}_{\mathrm{d}}^{e\mathrm{I}} = \begin{bmatrix} N_{2,2,2}^{int} & 0 & 0 & & N_{p_\xi,p_\eta,p_\zeta}^{int} & 0 & 0 \\ 0 & N_{2,2,2}^{int} & 0 & \ldots & 0 & N_{p_\xi,p_\eta,p_\zeta}^{int} & 0 \\ 0 & 0 & N_{2,2,2}^{int} & & 0 & 0 & N_{p_\xi,p_\eta,p_\zeta}^{int} \end{bmatrix} \tag{4.46}$$

and

$$\mathbf{N}_{\theta}^{e\mathrm{I\,T}} = \left[N_{2,2,2}^{int} \quad \ldots \quad N_{p_\xi,p_\eta,p_\zeta}^{int}\right], \tag{4.47}$$

where the polynomial degree is initially increased with respect to the ζ-direction, then for the η-direction and finally for the ξ-direction. The arrangement of the shape functions can also be found in (Düster, 2001).

4.2.3 About the Spatial Discretization of the Weak Forms

Making use of the ansatz for the displacements (4.20), virtual displacements (4.21), temperatures (4.22) and virtual temperatures (4.23) and exploiting the symmetry of the weighted Cauchy stress tensor by arranging its components as

$$\mathbf{S}^{e\,\mathrm{T}} = \{S_{11}, S_{22}, S_{33}, S_{12}, S_{23}, S_{31}\} \tag{4.48}$$

we derive a discrete form of (3.33)

$$\pi_{\mathrm{u}}\big(\boldsymbol{u}, \theta, \boldsymbol{q}, \delta\boldsymbol{u}\big) \quad \rightarrow \quad \pi_{\mathrm{u}}^{\mathrm{h}}(\boldsymbol{u}_{\mathrm{a}}, \boldsymbol{\Theta}_{\mathrm{a}}, \boldsymbol{q}, \delta\boldsymbol{u}) \tag{4.49}$$

resulting in

$$\pi_{\mathrm{u}}^{\mathrm{h}}(\boldsymbol{u}_{\mathrm{a}}, \boldsymbol{\Theta}_{\mathrm{a}}, \boldsymbol{q}, \delta\boldsymbol{u}) = \delta\boldsymbol{u}^{\mathrm{T}} \left\{ \sum_{e=1}^{n_{\mathrm{el}}} \boldsymbol{Z}_{\mathrm{d}}^{e\mathrm{T}} \left\{ \int_{\omega_e} \mathbf{B}_{\mathrm{d}}^{e\mathrm{T}}\, \mathbf{S}^e(\mathbf{x}, t)\ \mathrm{d}v - \overline{\mathbf{p}}_{\mathrm{c}}^{e}(t) \right\} \right\} = 0 \tag{4.50}$$

with

$$\overline{\mathbf{p}}_{\mathrm{c}}^{e}(t) \equiv \int_{\omega_e} \mathbf{N}_{\mathrm{d}}^{e\mathrm{T}}(\mathbf{x})\rho(\mathbf{x})\mathbf{k}\ \mathrm{d}v + \int_{\partial_{\mathrm{s}}\omega_e} \mathbf{N}_{\mathrm{d}}^{e\mathrm{T}}(\mathbf{x})\mathbf{s}^e(\mathbf{x}, t)\ \mathrm{d}a. \tag{4.51}$$

$\boldsymbol{Z}_{\mathrm{d}}^{e} \in \mathbb{R}^{3n_{\mathrm{em}} \times n_{\mathrm{nu}}}$ is a matrix whose entries are only zeros or ones indicating the position of the unknown element displacement coefficients in the vector containing all unknown displacement coefficients, see (Hartmann, 2003). Together with $\bar{\boldsymbol{Z}}_{\mathrm{d}}^{e}$ it mediates between the vector containing all displacement coefficients $\boldsymbol{u}_{\mathrm{a}}^{\mathrm{T}} = \left\{\boldsymbol{u}^{\mathrm{T}} \quad \bar{\boldsymbol{u}}^{\mathrm{T}}\right\}$ and the vector containing all displacement coefficients of one element $\mathbf{u}^{\mathrm{e}}$ by

$$\mathbf{u}^{\mathrm{e}} = \boldsymbol{Z}_{\mathrm{d}}^{e}\boldsymbol{u} + \bar{\boldsymbol{Z}}_{\mathrm{d}}^{e}\bar{\boldsymbol{u}} \tag{4.52}$$

where $\bar{\boldsymbol{Z}}_{\mathrm{d}}^{e} \in \mathbb{R}^{3n_{\mathrm{em}} \times n_{\mathrm{pu}}}$. In order to derive the strain-displacement matrix $\mathbf{B}_{\mathrm{d}}^{e}$, we apply the differential operator matrix

$$\mathbf{L}_{\mathrm{d}} = \begin{bmatrix} \frac{\partial}{\partial x} & 0 & 0 \\ 0 & \frac{\partial}{\partial y} & 0 \\ 0 & 0 & \frac{\partial}{\partial z} \\ \frac{\partial}{\partial y} & \frac{\partial}{\partial x} & 0 \\ 0 & \frac{\partial}{\partial z} & \frac{\partial}{\partial y} \\ \frac{\partial}{\partial z} & 0 & \frac{\partial}{\partial x} \end{bmatrix} \tag{4.53}$$

to the shape functions (4.34)

$$\mathbf{B}_{\mathrm{d}}^{e}(\boldsymbol{\varphi}^{\boldsymbol{e}}(\mathbf{x})) = \mathbf{L}_{\mathrm{d}}\mathbf{N}_{\mathrm{d}}^{e} = \mathbf{L}_{\mathrm{d}}\left[\mathbf{N}_{\mathrm{d}}^{e\mathrm{N}} \quad \mathbf{N}_{\mathrm{d}}^{e\mathrm{E}} \quad \mathbf{N}_{\mathrm{d}}^{e\mathrm{F}} \quad \mathbf{N}_{\mathrm{d}}^{e\mathrm{I}}\right] \tag{4.54}$$

$$= \left[\mathbf{B}_{\mathrm{d}\,1}^{e} \ldots \mathbf{B}_{\mathrm{d}\,n_{\mathrm{em}}}^{e}\right] \in \mathbb{R}^{6 \times 3n_{\mathrm{em}}}. \tag{4.55}$$

The first integral in (4.51) characterizes a volume-distributed load and the second term tractions prescribed on the surface of the structure under consideration. In the material representation, the spatially discretized principle of virtual displacements reads

$$\pi_{\mathrm{u}}^{\mathrm{h}}(\boldsymbol{u}_{\mathrm{a}}, \boldsymbol{\Theta}_{\mathrm{a}}, \boldsymbol{q}, \delta\boldsymbol{u}) = \delta\boldsymbol{u}^{\mathrm{T}} \left\{ \sum_{e=1}^{n_{\mathrm{el}}} \boldsymbol{Z}_{\mathrm{d}}^{e\mathrm{T}} \left\{ \int_{\Omega_e} \mathbf{B}_{\mathrm{d}}^{e\mathrm{T}} \mathbf{F}_{23}^{e} \tilde{\mathbf{T}}^e(\mathbf{X}, t)\ \mathrm{d}V - \overline{\mathbf{p}}_{\mathrm{r}}^{e}(t) \right\} \right\} = 0 \tag{4.56}$$

with

$$\overline{\mathbf{p}}_{\mathrm{r}}^{e}(t) \equiv \int_{\Omega_e} \mathbf{N}_{\mathrm{d}}^{e\mathrm{T}}(\mathbf{X})\rho(\mathbf{X})\mathbf{k}\ \mathrm{d}V + \int_{\partial_{\mathrm{s}}\Omega_e} \mathbf{N}_{\mathrm{d}}^{e\mathrm{T}}(\mathbf{X})\mathbf{s}^e(\mathbf{X}, t)\ \mathrm{d}A \tag{4.57}$$

where $\tilde{\mathbf{T}}^e$ denotes the second Piola-Kirchhoff stresses. In the matrix notation, the push-forward operator $[\mathbf{F}\otimes\mathbf{F}]^{\mathrm{T}_{23}}$ reads

$$\mathbf{F}^e_{23} = \begin{bmatrix} F_{11}^2 & F_{12}^2 & F_{13}^2 & 2F_{11}F_{12} & 2F_{12}F_{13} & 2F_{13}F_{11} \\ F_{21}^2 & F_{22}^2 & F_{23}^2 & 2F_{21}F_{22} & 2F_{22}F_{23} & 2F_{23}F_{21} \\ F_{31}^2 & F_{32}^2 & F_{33}^2 & 2F_{31}F_{32} & 2F_{32}F_{33} & 2F_{33}F_{31} \\ F_{11}F_{21} & F_{12}F_{22} & F_{13}F_{23} & F_{11}F_{22}+F_{12}F_{21} & F_{12}F_{23}+F_{13}F_{22} & F_{13}F_{21}+F_{11}F_{23} \\ F_{21}F_{31} & F_{22}F_{32} & F_{23}F_{33} & F_{21}F_{32}+F_{22}F_{31} & F_{22}F_{33}+F_{23}F_{32} & F_{23}F_{31}+F_{21}F_{33} \\ F_{31}F_{11} & F_{32}F_{12} & F_{33}F_{13} & F_{31}F_{12}+F_{32}F_{11} & F_{32}F_{13}+F_{33}F_{12} & F_{33}F_{11}+F_{31}F_{13} \end{bmatrix}, \tag{4.58}$$

see (Hartmann, 2003, p. 161). The elasticity relation

$$\tilde{\mathbf{T}}^e(\mathbf{X},t) = \mathbf{h}^e(\mathbf{C}(\mathbf{X},t),\theta(\mathbf{X},t),\mathbf{q}^e(\mathbf{X},t)) \tag{4.59}$$

depends on the deformation, temperature and internal variables. Since the virtual displacements are arbitrary, the spatially discretized principle of virtual displacements (4.56) or (4.50) yields a system of nonlinear equations

$$\pi_{\mathrm{u}}^{\mathrm{h}}(\boldsymbol{u}_{\mathrm{a}},\boldsymbol{\Theta}_{\mathrm{a}},\boldsymbol{q},\delta\boldsymbol{u}) \quad \rightarrow \quad \boldsymbol{g}(\boldsymbol{u}_{\mathrm{a}},\boldsymbol{\Theta}_{\mathrm{a}},\boldsymbol{q}) \tag{4.60}$$

of the form

$$\boldsymbol{g}(\boldsymbol{u}_{\mathrm{a}},\boldsymbol{\Theta}_{\mathrm{a}},\boldsymbol{q}) = \sum_{e=1}^{n_{\mathrm{el}}} \boldsymbol{Z}_{\mathrm{d}}^{e\mathrm{T}} \left\{ \int_{\omega_e} \mathbf{B}_{\mathrm{d}}^{e\mathrm{T}}\, \mathbf{S}^e(\mathbf{x},t)\ \mathrm{d}v - \overline{\mathbf{p}}_{\mathrm{c}}^{e}(t) \right\} = \tag{4.61}$$

$$= \sum_{e=1}^{n_{\mathrm{el}}} \boldsymbol{Z}_{\mathrm{d}}^{e\mathrm{T}} \left\{ \int_{\Omega_e} \mathbf{B}_{\mathrm{d}}^{e\mathrm{T}} \mathbf{F}_{23}^{e} \tilde{\mathbf{T}}^e(\mathbf{X},t)\ \mathrm{d}V - \overline{\mathbf{p}}_{\mathrm{r}}^{e}(t) \right\} = \boldsymbol{0}. \tag{4.62}$$

Implementation into the in-house code TASA-FEM is based on (4.61). The integration required in (4.61) is carried out by means of the map (4.1), to begin with, leading to the multiplication of the integrand with the determinant of $\mathbf{j}_e$ mediating between the unit element Ω_{st}^h and the element in current configuration, see Fig. 4.13, among other things, and subsequently applying the Gaussian quadrature rule (Kim and Suri, 1993; Schwarz and Köckler, 2004), in order to approximate the integral, yielding

$$\int_{\omega_e} \mathbf{B}_{\mathrm{d}}^{e\mathrm{T}}\, \mathbf{S}^e(\mathbf{x},t)\ \mathrm{d}v = \int_{\Omega_{st}^h} \mathbf{B}_{\mathrm{d}}^{e\mathrm{T}}(\boldsymbol{\xi})\, \mathbf{S}^e(\boldsymbol{\xi},t)\ \det\mathbf{j}_e(\boldsymbol{\xi},t)\,\mathrm{d}v \tag{4.63}$$

$$= \int_{-1}^{+1}\int_{-1}^{+1}\int_{-1}^{+1} \mathbf{B}_{\mathrm{d}}^{e\mathrm{T}}(\boldsymbol{\xi})\, \mathbf{S}^e(\boldsymbol{\xi},t)\ \det\mathbf{j}_e(\boldsymbol{\xi},t)\,\mathrm{d}\xi\,\mathrm{d}\eta\,\mathrm{d}\zeta \tag{4.64}$$

$$\approx \sum_{i=1}^{n_{\mathrm{ip}}} w_i \mathbf{B}_{\mathrm{d}}^{e\mathrm{T}}(\boldsymbol{\xi}_i)\, \mathbf{S}^e(\boldsymbol{\xi}_i),t)\ \det\mathbf{j}_e(\boldsymbol{\xi}_i,t). \tag{4.65}$$

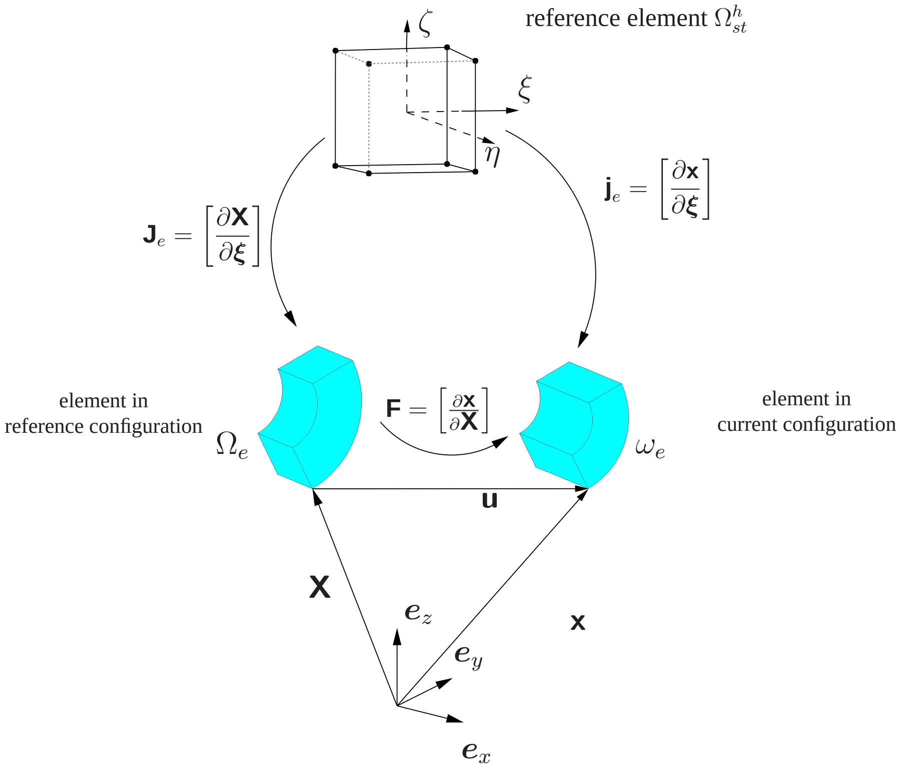

Figure 4.13: Deformation of a hexahedral element with blending functions

The abscissas and weights of the Gaussian quadrature can be found in Appendix A.3. Where the spatial discretization is done with the help of the tensor product space, it proves to be favorable to replace the Gaussian quadrature scheme by a vector quadrature scheme dissecting the integrand into two parts before integrating them separately (Hinnant, 1994; Martins-Wagner, 2003; Nübel and Rank, 2000). Own computations have shown that, the set-up of the element stiffness matrix for a polynomial degree greater than 5 is more efficient in terms of CPU-time, for small strain applications based on the tensor product space, when a vector quadrature is applied instead of a Gaussian quadrature. For a polynomial degree of 10 the set up of the element stiffness matrix is four times as fast, if vector quadrature instead of Gaussian quadrature is applied.

Once the spatially discretized principle of virtual displacements has been derived, we need to discuss the assemblage procedure of the internal variables. Summing up via the internal variables of each Gauss point $\mathbf{q}^e(\boldsymbol{\xi}_i, t)$

$$\boldsymbol{q}(t) = \sum_{e=1}^{n_{\text{el}}} \sum_{i=1}^{n_{\text{ip}}} \mathbf{Z}_{\text{q}}^{e(i)\text{T}} \mathbf{q}^e(\boldsymbol{\xi}_i, t) \quad \text{with} \quad \mathbf{q}^e(\boldsymbol{\xi}_i, t) \in \mathbb{R}^{n_{\text{q}}}, \tag{4.66}$$

see (Ellsiepen, 1999) and (Hartmann, 2002), a vector $\boldsymbol{q}(t) \in \mathbb{R}^{n_{\text{Q}}}$ containing all internal variables of the structure under consideration is assembled with the help of the matrix $\mathbf{Z}_{\text{q}}^e(\boldsymbol{\xi}_{ip}) \in \mathbb{R}^{n_{\text{q}} \times n_{\text{Q}}}$. Applying the same procedure to the differential equations that are defined separately for each

Gauss point

$$\dot{\mathbf{q}}^e(\boldsymbol{\xi}_{ip}, t) = \tilde{\mathbf{r}}^e\left(\mathbf{C}(\boldsymbol{\xi}_{ip}, t), \theta^h(\boldsymbol{\xi}_{ip}, t), \mathbf{q}^e(\boldsymbol{\xi}_{ip}, t)\right), \tag{4.67}$$

see (2.187) and Tab. 2.1, we obtain a system of ordinary differential equations of first order

$$\dot{\boldsymbol{q}}(t) - \boldsymbol{r}(\boldsymbol{u}(t), \boldsymbol{\Theta}(t), \boldsymbol{q}(t)) = \boldsymbol{0}, \quad \boldsymbol{q}(t) \in \mathbb{R}^{n_{\mathrm{Q}}}, \tag{4.68}$$

see Fig. 4.14.

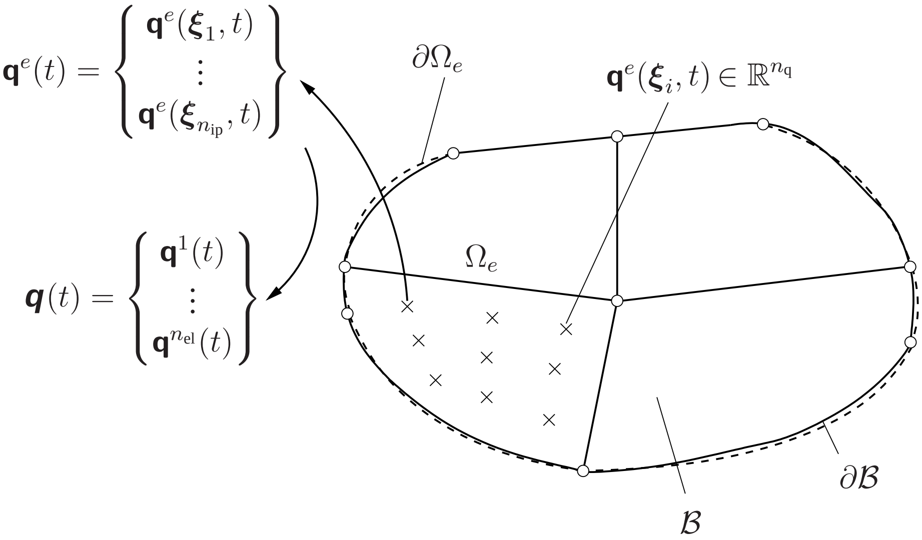

Figure 4.14: Assembly procedure for internal variables for Ω_e

Making use of the Cauchy heat flux vector (2.143), the ansatz approximating the temperatures (4.22) and virtual temperatures (4.23) and (4.35), the weak form of the heat conduction equation (3.35) leads to

$$\pi_\theta^{\mathrm{h}}(\boldsymbol{u}_{\mathrm{a}}, \dot{\boldsymbol{u}}_{\mathrm{a}}, \boldsymbol{\Theta}_{\mathrm{a}}, \dot{\boldsymbol{\Theta}}_{\mathrm{a}}, \boldsymbol{q}, \delta\boldsymbol{\Theta}) = \tag{4.69}$$

$$\delta\boldsymbol{\Theta}^{\mathrm{T}} \sum_{e=1}^{n_{\mathrm{el}}} \boldsymbol{Z}_\theta^{e\mathrm{T}} \left\{ \left[\int\limits_{\omega_e} \varrho(\mathbf{x}, t) c_{\mathrm{d}}^{\mathrm{h}}(\boldsymbol{\Theta}_{\mathrm{a}})\, \mathbf{N}_\theta^e(\mathbf{x}) \mathbf{N}_\theta^{e\mathrm{T}}(\mathbf{x})\, \mathrm{d}v \right] \dot{\boldsymbol{\Theta}}^e + \left[\int\limits_{\omega_e} \mathbf{B}_\theta^{e\mathrm{T}} \lambda \mathbf{B}_\theta\, \mathrm{d}v \right] \boldsymbol{\Theta}^e \right. \tag{4.70}$$

$$\left. + \int\limits_{\partial_{\mathrm{q}}\omega_e} f_{\mathrm{q}} \mathbf{N}_\theta^e(\mathbf{x})\, \mathrm{d}a + \int\limits_{\partial_{\theta\mathrm{q}}\omega^e} f_{\theta\mathrm{q}} \mathbf{N}_\theta^e(\mathbf{x})\, \mathrm{d}a + \int\limits_{\omega_e} \varrho(\mathbf{x})(r^{\mathrm{h}} + p^{\mathrm{h}} + d^{\mathrm{h}}) \mathbf{N}_\theta^e(\mathbf{x})\, \mathrm{d}v \right\}. \tag{4.71}$$

$(.)^{\mathrm{h}}$ indicates quantities that depend on discretized displacement or temperature coefficients. In general, the heat capacity depends on the temperature and displacement field, see (2.214), but in this case we assume a linear dependence of the heat capacity on the temperature, see (2.215).

Again, the mediation between the local and global temperature coefficient vector is carried out by

$$\boldsymbol{\Theta}^e = \boldsymbol{Z}_\theta^e\,\boldsymbol{\Theta} + \bar{\boldsymbol{Z}}_\theta^e\,\bar{\boldsymbol{\Theta}} \quad \text{with} \quad \boldsymbol{Z}_\theta^e \in \mathbb{R}^{n_\mathrm{em}\times n_{\mathrm{n}\theta}} \quad \text{and} \quad \bar{\boldsymbol{Z}}_\theta^e \in \mathbb{R}^{n_\mathrm{em}\times n_{\mathrm{p}\theta}}. \tag{4.72}$$

The thermoelastic coupling term is given by $p^\mathrm{h} = p^\mathrm{h}(\boldsymbol{u}_\mathrm{a}, \dot{\boldsymbol{u}}_\mathrm{a}, \boldsymbol{\Theta}_\mathrm{a})$, see (2.212), and the inelastic dissipation reads $d^\mathrm{h} = d^\mathrm{h}(\boldsymbol{u}_\mathrm{a}, \boldsymbol{q}, \boldsymbol{\Theta}_\mathrm{a})$, cf. (2.218). With the differential operator matrix

$$\mathbf{L}_\theta = \begin{Bmatrix} \dfrac{\partial}{\partial x} \\ \dfrac{\partial}{\partial y} \\ \dfrac{\partial}{\partial z} \end{Bmatrix} \tag{4.73}$$

it is possible to derive the matrix $\mathbf{B}_\theta^e \in \mathbb{R}^{3\times n_\mathrm{em}}$ relating the temperatures to the temperature gradients

$$\mathbf{B}_\theta^e(\boldsymbol{\varphi}^{\boldsymbol{e}}(\mathbf{x})) = \mathbf{L}_\theta\,\mathbf{N}_\theta^{e\,\mathrm{T}} = \mathbf{L}_\theta\,\begin{bmatrix}\mathbf{N}_\theta^{e\mathrm{N}\,\mathrm{T}} & \mathbf{N}_\theta^{e\mathrm{E}\,\mathrm{T}} & \mathbf{N}_\theta^{e\mathrm{F}\,\mathrm{T}} & \mathbf{N}_\theta^{e\mathrm{I}\,\mathrm{T}}\end{bmatrix}. \tag{4.74}$$

Using the short notations

$$\boldsymbol{C}_\mathrm{d}(\boldsymbol{\Theta}_\mathrm{a}, \boldsymbol{u}_\mathrm{a}, \boldsymbol{q}) = \sum_{e=1}^{n_\mathrm{el}} \boldsymbol{Z}_\theta^{e\mathrm{T}} \left[\int\limits_{\omega_e} \varrho(\mathbf{x}) c_\mathrm{d}^\mathrm{h}(\boldsymbol{\Theta}_\mathrm{a})\,\mathbf{N}_\theta^e(\mathbf{x})\mathbf{N}_\theta^{e\mathrm{T}}(\mathbf{x})\,\mathrm{d}v\right] \boldsymbol{Z}_\theta^e \tag{4.75}$$

denoting the heat capacity matrix,

$$\boldsymbol{C}_\lambda(\boldsymbol{\Theta}_\mathrm{a}, \boldsymbol{u}_\mathrm{a}, \boldsymbol{q}) = \sum_{e=1}^{n_\mathrm{el}} \boldsymbol{Z}_\theta^{e\mathrm{T}} \left[\int\limits_{\omega_e} \mathbf{B}_\theta^{e\mathrm{T}} \lambda^\mathrm{h} \mathbf{B}_\theta^e\,\mathrm{d}v\right] \boldsymbol{Z}_\theta^e \tag{4.76}$$

symbolizing the heat conductivity matrix and the right-hand sides

$$\boldsymbol{R}_\Theta(\boldsymbol{u}_\mathrm{a}, \dot{\boldsymbol{u}}_\mathrm{a}, \boldsymbol{\Theta}_\mathrm{a}, \boldsymbol{q}) = \sum_{e=1}^{n_\mathrm{el}} \boldsymbol{Z}_\theta^{e\mathrm{T}} \left\{\int\limits_{\omega_e} \varrho(\mathbf{x}, t)(r^\mathrm{h} + p^\mathrm{h} + d^\mathrm{h})\mathbf{N}_\theta^e(\mathbf{x})\,\mathrm{d}v\right\}, \tag{4.77}$$

$$\boldsymbol{R}_\Theta^\mathrm{ext}(\boldsymbol{u}_\mathrm{a}, \boldsymbol{\Theta}_\mathrm{a}) = \sum_{e=1}^{n_\mathrm{el}} \boldsymbol{Z}_\theta^{e\mathrm{T}} \left\{\int\limits_{\partial_\mathrm{q}\omega^e} f_\mathrm{q}\mathbf{N}_\theta^e(\mathbf{x})\,\mathrm{d}a + \int\limits_{\partial_{\theta\mathrm{q}}\omega^e} f_{\theta\mathrm{q}}\mathbf{N}_\theta^e(\mathbf{x})\,\mathrm{d}a\right\}, \tag{4.78}$$

describing the thermo-mechanical coupling effect and the heatflux over the surface of the structure, we obtain a system of ordinary differential equations

$$\boldsymbol{C}_\mathrm{d}(\boldsymbol{\Theta}_\mathrm{a}, \boldsymbol{u}_\mathrm{a}, \boldsymbol{q})\,\dot{\boldsymbol{\Theta}}_\mathrm{a}(t) = -\boldsymbol{C}_\lambda(\boldsymbol{\Theta}_\mathrm{a}, \boldsymbol{u}_\mathrm{a}, \boldsymbol{q})\,\boldsymbol{\Theta}_\mathrm{a} + \boldsymbol{R}_\Theta(\boldsymbol{u}_\mathrm{a}, \dot{\boldsymbol{u}}_\mathrm{a}, \boldsymbol{\Theta}_\mathrm{a}, \boldsymbol{q}) + \boldsymbol{R}_\Theta^\mathrm{ext}(\boldsymbol{u}_\mathrm{a}, \boldsymbol{\Theta}_\mathrm{a}) = \boldsymbol{r}_{\boldsymbol{\Theta}}. \tag{4.79}$$

Tab. 4.2 summarizes the resulting DAE-system.

4.3 Temporal Discretization

This section discusses the solution of the DAE-system resulting from the spatial discretization of the weak form of the coupled problem by means of the p-version of the finite element method, given in Tab. 4.2. Text books dealing with the solution of DAE-systems by numerical means include (Hairer et al., 1993; Hairer and Wanner, 1996; Strehmel and Weiner, 1995).

Table 4.2: DAE-system occuring in thermo-viscoelasticity

In order to compute $\boldsymbol{u}(t)$, $\boldsymbol{\Theta}(t)$ and $\boldsymbol{q}(t)$ for $t \in [t_0, t_e]$

$$\begin{aligned} \boldsymbol{0} &= \boldsymbol{g}(t, \boldsymbol{u}(t), \boldsymbol{\Theta}(t), \boldsymbol{q}(t)) && (4.80)\\ \boldsymbol{C}_{\mathrm{d}}(t, \boldsymbol{u}, \boldsymbol{\Theta}, \boldsymbol{q})\dot{\boldsymbol{\Theta}}(t) &= \boldsymbol{r}_{\boldsymbol{\Theta}}(t, \boldsymbol{u}(t), \dot{\boldsymbol{u}}(t), \boldsymbol{\Theta}(t), \boldsymbol{q}(t)) && (4.81)\\ \dot{\boldsymbol{q}}\,(t) &= \boldsymbol{r}(t, \boldsymbol{u}(t), \boldsymbol{\Theta}(t), \boldsymbol{q}(t)) && (4.82) \end{aligned}$$

with the initial conditions

$$\boldsymbol{q}(t_0) = \boldsymbol{q}_0, \quad \boldsymbol{\Theta}(t_0) = \boldsymbol{\Theta}_0, \quad \boldsymbol{u}(t_0) = \boldsymbol{u}_0 \qquad (4.83)$$

must be solved.

4.3.1 Diagonally-Implicit Runge-Kutta Methods

We choose diagonally-implicit Runge-Kutta methods for the temporal discretization. In this case the temporal domain is divided into time-steps which in turn are subdivided into stages. At each stage a system of nonlinear equations has to be solved which, in the context of the finite element method, is done by applying the Multilevel-Newton Algorithm, as shown in (Ellsiepen and Hartmann, 2001; Hartmann, 1998, 2005), for example. We begin by discussing the application of diagonally-implicit Runge-Kutta methods to the system of explicit ordinary differential equations

$$\dot{\boldsymbol{y}}(t) = \boldsymbol{f}(t, \boldsymbol{y}(t)) \quad \text{with} \quad \boldsymbol{y}(t_0) = \boldsymbol{y}_0, \qquad (4.84)$$

$\boldsymbol{y} \in \mathbb{R}^d$ and $t \in [t_i, t_e]$. The most obvious approach for solving (4.84) is to begin with $\boldsymbol{y}_n$ and add the function $\boldsymbol{f}(t, \boldsymbol{y}(t))$ evaluated at $t = t_n$ multiplied by a time increment $\Delta t_n = t_{n+1} - t_n$ resulting in

$$\boldsymbol{y}(t_{n+1}) \approx \boldsymbol{y}_{n+1} = \boldsymbol{y}_n + \Delta t_n \boldsymbol{f}(t_n, \boldsymbol{y}_n) \qquad (4.85)$$

which is known as the explicit Euler method. The approximate solution accordingly depends on nothing but known quantities and is obtained by a mere function evaluation. If the function $\boldsymbol{f}(t, \boldsymbol{y}(t))$ evaluated at $t = t_{n+1}$ is used to approximate the solution

$$\boldsymbol{y}(t_{n+1}) \approx \boldsymbol{y}_{n+1} = \boldsymbol{y}_n + \Delta t_n \boldsymbol{f}(t_{n+1}, \boldsymbol{y}_{n+1}), \qquad (4.86)$$

the approximate solution $\boldsymbol{y}_{n+1}$ depends on itself, so it is necessary to solve the system of nonlinear equations

$$\boldsymbol{y}_{n+1} - \boldsymbol{y}_n - \Delta t_n \boldsymbol{f}(t_{n+1}, \boldsymbol{y}_{n+1}) = \boldsymbol{0} \qquad (4.87)$$

for $\boldsymbol{y}_{n+1}$. By dividing the step-size Δt into stages, as indicated in Fig. 4.15, we obtain the

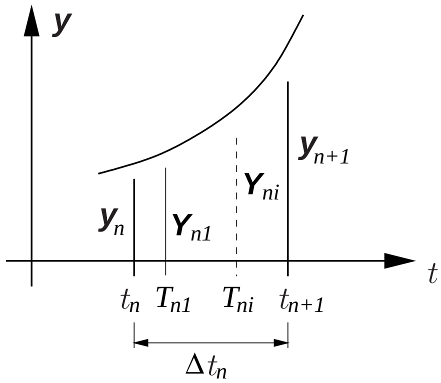

Figure 4.15: Time-steps and stages

Table 4.3: Butcher array for Runge-Kutta method: (a) Implicit Runge-Kutta method (b) Stiffly-accurate diagonally-implicit Runge-Kutta method

$$\begin{array}{c|cccc} c_1 & a_{11} & a_{12} & \dots & a_{1s} \\ c_2 & a_{21} & a_{22} & \dots & a_{2s} \\ \vdots & \vdots & & \ddots & \vdots \\ c_s & a_{1s} & a_{2s} & \dots & a_{ss} \\ \hline & b_1 & b_2 & \dots & b_s \end{array}$$

(a)

$$\begin{array}{c|cccc} c_1 & a_{11} & 0 & \dots & 0 \\ c_2 & a_{21} & a_{22} & \ddots & \vdots \\ \vdots & \vdots & & \ddots & 0 \\ c_s & b_1 & b_2 & \dots & b_s \\ \hline & b_1 & b_2 & \dots & b_s \end{array}$$

(b)

quadrature rule

$$\boldsymbol{y}(t_{n+1}) \approx \boldsymbol{y}_{n+1} = \boldsymbol{y}_n + \Delta t_n \sum_{i=1}^{s} b_i \boldsymbol{f}(T_{ni}, \boldsymbol{Y}_{ni}). \tag{4.88}$$

The next step is to evaluate the quantity $\boldsymbol{f}(T_{ni}, \boldsymbol{Y}_{ni})$, referred to as the stage derivative, at the the stages $T_{ni} = t_n + c_i \Delta t_n$. The stage derivatives, which are weighted with scalar quantities b_i, are summed up and the result, which is multiplied by Δt_n, is added to the solution of the last time-step in order to compute the approximate solution of the current time-step. It is obvious that in (4.88) the function values $\boldsymbol{y}(t_n + c_i \Delta t_n)$ still need to be determined, which is done by employing another quadrature rule

$$\boldsymbol{y}(t_n + c_i \Delta t_n) \approx \boldsymbol{Y}_{ni} = \boldsymbol{y}_n + \Delta t_n \sum_{j=1}^{s} a_{ij} \boldsymbol{f}(t_n + c_j \Delta t_n, \boldsymbol{Y}_{nj}). \tag{4.89}$$

The coefficients b_i, c_i and a_{ij} are contained in the Butcher arrays, see Tab. 4.3 and App. A.5. They are defined with respect to efficiency, stability and accuracy considerations (Hairer and Wanner, 1996). If all coefficients a_{ij} are allowed to be non-zero, a fully implicit integration method results. In this case the computation of $\boldsymbol{Y}_{ni}$ calls for the solution of a system of nonlinear equations which is coupled in the stage values $\boldsymbol{Y}_{ni}$ and is consequently of the dimension $d \times s$. If the coefficients a_{ij} are restricted to zero for $j \geq i$, the result is an explicit integration method. In this case, the solution of nonlinear equations is superfluous and the unknown stage values are obtained by function evaluations. $a_{ij} = 0$ for $j > i$ holds for diagonally-implicit methods, which leads to a partitioning of (4.89) into one part containing only quantities that are known at stage T_{ni}

$$\boldsymbol{S}_{ni} = \boldsymbol{y}_n + \Delta t_n \sum_{j=1}^{i-1} a_{ij} \boldsymbol{f}(t_n + c_j \Delta t_n\,, \boldsymbol{Y}_{nj}), \tag{4.90}$$

and one part depending on unknown quantities related to stage T_{ni} resulting in

$$\boldsymbol{Y}_{ni} = \boldsymbol{S}_{ni} + \Delta t_n\, a_{ii} \boldsymbol{f}(t_n + c_i \Delta t_n\,, \boldsymbol{Y}_{ni}) \tag{4.91}$$

for the approximate solution. Thus, the computation of the stage values $\boldsymbol{Y}_{ni}$ calls for the solution of a system of nonlinear equations

$$\boldsymbol{Y}_{ni} - \boldsymbol{S}_{ni} - \Delta t_n\, a_{ii} \boldsymbol{f}(t_n + c_i \Delta t_n\,, \boldsymbol{Y}_{ni}) = \boldsymbol{0} \tag{4.92}$$

of the dimension d. The value at time t_{n+1} is computed by evaluating the quadrature rule (4.88). The term stiffly-accurate refers to the fact that, in this case, $a_{sj} = b_j$ holds as indicated in Tab. 4.3. So $\boldsymbol{y}_{n+1} = \boldsymbol{Y}_{ns}$.

4.3.2 Application of DIRK-Methods to the Thermo-Mechanically Coupled Problem

In order to apply diagonally-implicit Runge Kutta methods to the DAE-system given in Tab. 4.2, its algebraic part (4.80) is replaced by

$$\epsilon \dot{\boldsymbol{u}} = \boldsymbol{g}(t, \boldsymbol{u}(t), \boldsymbol{\Theta}(t), \boldsymbol{q}(t)) \quad \text{with} \quad 0 < \epsilon \ll 1. \tag{4.93}$$

Applying the quadrature rule (4.89) to (4.93) yields

$$\epsilon \boldsymbol{U}_{ni} = \epsilon \boldsymbol{u}_n + \Delta t_n \sum_{j=1}^{i} a_{ij} \boldsymbol{g}(t_n + c_j \Delta t_n, \boldsymbol{U}_{nj}, \boldsymbol{\Theta}_{nj}, \boldsymbol{Q}_{nj}). \tag{4.94}$$

For $\epsilon \rightarrow 0$ the system of nonlinear equations

$$\boldsymbol{0} = \boldsymbol{g}(t_n + c_j \Delta t_n, \boldsymbol{U}_{nj}, \boldsymbol{\Theta}_{nj}, \boldsymbol{Q}_{nj}) \tag{4.95}$$

results. For the integration of the ordinary differential equations describing the behaviour of the internal variables (4.82) we write

$$\begin{aligned} \boldsymbol{Q}_{ni} &= \boldsymbol{q}_n + \Delta t_n \sum_{j=1}^{i} a_{ij} \boldsymbol{r}(t_n + c_j \Delta t, \boldsymbol{U}_{nj}, \boldsymbol{\Theta}_{nj}, \boldsymbol{Q}_{nj}) \\ &= \boldsymbol{S}^q_{ni} + \Delta t_n a_{ii} \boldsymbol{r}(t_n + c_i \Delta t_n, \boldsymbol{U}_{ni}, \boldsymbol{\Theta}_{ni}, \boldsymbol{Q}_{ni}) \end{aligned} \tag{4.96}$$

based on the starting value

$$\boldsymbol{S}^q_{ni} = \boldsymbol{q}_n + \Delta t_n \sum_{j=1}^{i-1} a_{ij}\dot{\boldsymbol{Q}}_{nj}. \tag{4.97}$$

The integration of (4.81) yields

$$\begin{aligned}\boldsymbol{C}_{\mathrm{d}}\boldsymbol{\Theta}_{ni} &= \boldsymbol{C}_{\mathrm{d}}\boldsymbol{\Theta}_n + \Delta t_n \sum_{j=1}^{i} a_{ij}\boldsymbol{r}_{\boldsymbol{\Theta}}(t_n + c_j\Delta t_n, \boldsymbol{U}_{nj}, \dot{\boldsymbol{U}}_{nj}, \boldsymbol{\Theta}_{nj}, \boldsymbol{Q}_{nj}) \\ &= \boldsymbol{C}_{\mathrm{d}}\boldsymbol{S}^{\boldsymbol{\Theta}}_{ni} + \Delta t_n a_{ii}\boldsymbol{r}_{\boldsymbol{\Theta}}(t_n + c_i\Delta t_n, \boldsymbol{U}_{ni}, \frac{\boldsymbol{U}_{ni} - \boldsymbol{S}^u_{ni}}{\Delta t_n\, a_{ii}}, \boldsymbol{\Theta}_{ni}, \boldsymbol{Q}_{ni})\end{aligned} \tag{4.98}$$

with

$$\boldsymbol{S}^{\boldsymbol{\Theta}}_{ni} = \boldsymbol{\Theta}_n + \Delta t_n \sum_{j=1}^{i-1} a_{ij}\dot{\boldsymbol{\Theta}}_{nj} \quad \text{and} \quad \boldsymbol{S}^u_{ni} = \boldsymbol{u}_n + \Delta t_n \sum_{j=1}^{i-1} a_{ij}\dot{\boldsymbol{U}}_{nj}. \tag{4.99}$$

Accordingly, the temporal discretization of the DAE-systems results in a system of nonlinear equations

$$\left\{\begin{array}{r} \boldsymbol{G}_{\mathrm{u}\,ni}(\boldsymbol{U}_{ni}, \boldsymbol{\Theta}_{ni}, \boldsymbol{Q}_{ni}) \\ \boldsymbol{G}_{\theta\ ni}(\boldsymbol{U}_{ni}, \boldsymbol{\Theta}_{ni}, \boldsymbol{Q}_{ni}) \\ \boldsymbol{L}_{ni}(\boldsymbol{U}_{ni}, \boldsymbol{\Theta}_{ni}, \boldsymbol{Q}_{ni}) \end{array}\right\} = \boldsymbol{0}, \tag{4.100}$$

comprising the spatially discretized weak form of the balance of momentum

$$\boldsymbol{G}_{\mathrm{u}\,ni}(\boldsymbol{U}_{ni}, \boldsymbol{\Theta}_{ni}, \boldsymbol{Q}_{ni}) \equiv \boldsymbol{g}(T_{ni}, \boldsymbol{U}_{ni}, \boldsymbol{\Theta}_{ni}, \boldsymbol{Q}_{ni}), \tag{4.101}$$

see (4.95), the discretized heat conduction equation

$$\begin{aligned}\boldsymbol{G}_{\theta\ ni}(\boldsymbol{U}_{ni}, \boldsymbol{\Theta}_{ni}, \boldsymbol{Q}_{ni}) \equiv& \boldsymbol{C}_{\mathrm{d}}(t, \boldsymbol{u}, \boldsymbol{\Theta}, \boldsymbol{q})\frac{\boldsymbol{\Theta}_{ni} - \boldsymbol{S}^{\boldsymbol{\Theta}}_{ni}}{\Delta t_n\, a_{ii}} \\ &- \boldsymbol{r}_{\boldsymbol{\Theta}}(T_{ni}, \boldsymbol{U}_{ni}, \frac{\boldsymbol{U}_{ni} - \boldsymbol{S}^u_{ni}}{\Delta t_n\, a_{ii}}, \boldsymbol{\Theta}_{ni}, \boldsymbol{Q}_{ni}),\end{aligned} \tag{4.102}$$

see (4.98), and the discretized evolution equations

$$\boldsymbol{L}_{ni}(\boldsymbol{U}_{ni}, \boldsymbol{\Theta}_{ni}, \boldsymbol{Q}_{ni}) \equiv \frac{\boldsymbol{Q}_{ni} - \boldsymbol{S}^q_{ni}}{\Delta t_n\, a_{ii}} - \boldsymbol{r}(T_{ni}, \boldsymbol{U}_{ni}, \boldsymbol{\Theta}_{ni}, \boldsymbol{Q}_{ni}), \tag{4.103}$$

see (4.96). This system of nonlinear equations has to be solved at each stage of the procedure. By introducing the partitioned quantities

$$\boldsymbol{y}_n = \left\{\begin{array}{c} \boldsymbol{u}_n \\ \boldsymbol{\Theta}_n \\ \boldsymbol{q}_n \end{array}\right\}, \qquad \boldsymbol{Y}_{ni} = \left\{\begin{array}{c} \boldsymbol{U}_{ni} \\ \boldsymbol{\Theta}_{ni} \\ \boldsymbol{Q}_{ni} \end{array}\right\}, \qquad \boldsymbol{S}_{ni} = \left\{\begin{array}{c} \boldsymbol{S}^u_{ni} \\ \boldsymbol{S}^{\boldsymbol{\Theta}}_{ni} \\ \boldsymbol{S}^q_{ni} \end{array}\right\} \tag{4.104}$$

(4.100) can be reformulated as

$$\boldsymbol{F}(T_{ni}, \boldsymbol{Y}_{ni}, \frac{\boldsymbol{Y}_{ni} - \boldsymbol{S}_{ni}}{\Delta t_n\, a_{ii}}) = \boldsymbol{0}. \tag{4.105}$$

The components of the starting vector $\boldsymbol{S}_{ni}$ are given in (4.97) and (4.99). In cases where stiffly-accurate DIRK-methods are used, which have the property $\boldsymbol{y}_{n+1} = \boldsymbol{Y}_{ns}$, it is not necessary to compute the function values at time-step t_{n+1}

$$\boldsymbol{y}_{n+1} = \boldsymbol{y}_n + \Delta t_n \sum_{i=1}^{s} b_i \dot{\boldsymbol{Y}}_{ni}. \tag{4.106}$$

4.3.3 Step-Size Control

For an efficient temporal discretization it is indispensable to attain an appropriate step-size. For this purpose, highly efficient methods can be derived for local error control based on embedded Runge-Kutta methods. If two s-stage methods are conducted in such a way that they use the same stages c_i, have the same coefficient matrix a_{ij}, but use different weights b_i and $\hat{b}_i$, one arrives at different accuracy orders p and $\hat{p}$. To compute an estimate of the local error, the consistency orders of the two methods must differ by one, i.e. $\hat{p} = p - 1$. Using both methods for a single step leads to

$$\boldsymbol{y}_{n+1} = \boldsymbol{y}(t_n) + \Delta t_n \, \boldsymbol{\Phi}(t_n, \boldsymbol{y}; \Delta t_n \,), \tag{4.107}$$

$$\hat{\boldsymbol{y}}_{\,n+1} = \boldsymbol{y}(t_n) + \Delta t_n \, \hat{\boldsymbol{\Phi}}\,(t_n, \hat{\boldsymbol{y}}\,; \Delta t_n \,), \tag{4.108}$$

where the solution vector $\boldsymbol{y}^{\mathrm{T}} = \{\boldsymbol{u}^{\mathrm{T}}, \boldsymbol{\Theta}^{\mathrm{T}}, \boldsymbol{q}^{\mathrm{T}}\}$ has been introduced. $\boldsymbol{\Phi}$ denotes the so-called increment function of the method, see (Hairer et al., 1993). The two different methods lead to the local errors

$$\boldsymbol{\delta} = \boldsymbol{y}(t_{n+1}) - \boldsymbol{y}_{n+1} = \Delta t_n{}^{p+1} \boldsymbol{\Phi}(t_n, \boldsymbol{y}) + \mathcal{O}(\Delta t_n{}^{p+2}), \tag{4.109}$$

$$\hat{\boldsymbol{\delta}} = \boldsymbol{y}(t_{n+1}) - \hat{\boldsymbol{y}}_{n+1} = \Delta t_n{}^{\hat{p}+1} \hat{\boldsymbol{\Phi}}(t_n, \boldsymbol{y}) + \mathcal{O}(\Delta t_n{}^{\hat{p}+2}). \tag{4.110}$$

The local integration error of the method employing the lower consistency order can therefore be stated as

$$\boldsymbol{\delta} - \hat{\boldsymbol{\delta}} = \hat{\boldsymbol{y}}_{n+1} - \boldsymbol{y}_{n+1} = \Delta t_n{}^{\hat{p}+1} \hat{\boldsymbol{\Phi}}(t_n, \boldsymbol{y}) + \mathcal{O}(\Delta t_n{}^{\hat{p}+2}) \approx \Delta t_n{}^{\hat{p}+1} \hat{\boldsymbol{\Phi}}(t_n, \boldsymbol{y}). \tag{4.111}$$

Let us now assume that the absolute value of the integration error is lower than a user-defined tolerance

$$\|\Delta t_n{}^{\hat{p}+1} \hat{\boldsymbol{\Phi}}\,(t_n, \boldsymbol{y})\| \approx \|\hat{\boldsymbol{y}}_{\,n+1} - \boldsymbol{y}_{n+1}\| \leq \epsilon_r \|\hat{\boldsymbol{y}}_{\,n}\| + \epsilon_a. \tag{4.112}$$

In order to compute an appropriate step-size for the next time-step, the integration error has to remain constant when time elapses

$$\|\hat{\boldsymbol{\Phi}}\,(t_n, \boldsymbol{y})\| \approx C, \tag{4.113}$$

yielding

$$\|\hat{\boldsymbol{y}}_{\,n+1} - \boldsymbol{y}_{n+1}\| \approx C \Delta t_n{}^{\hat{p}+1}. \tag{4.114}$$

We also obtain

$$C \Delta t_{\text{new}}{}^{\hat{p}+1} = \epsilon_r \|\hat{\boldsymbol{y}}_{\,n}\| + \epsilon_a \tag{4.115}$$

where the local error related to the new step-size is equal to that related to the current time-step size. This allows us to guess the new step-size by eliminating C in (4.114) and (4.115) resulting in

$$\Delta t_{\text{new}} = \Delta t_n \left(\frac{\epsilon_r \|\hat{\boldsymbol{y}}_n\| + \epsilon_a}{\|\hat{\boldsymbol{y}}_{n+1} - \boldsymbol{y}_{n+1}\|} \right)^{1/(\hat{p}+1)} . \tag{4.116}$$

Since the solution vector $\boldsymbol{y}$ contains quantities related to the displacement and temperature field, it is split into

$$\boldsymbol{u}_{\text{err}} = \hat{\boldsymbol{u}}_{n+1} - \boldsymbol{u}_{n+1}, \quad \boldsymbol{q}_{\text{err}} = \hat{\boldsymbol{q}}_{n+1} - \boldsymbol{q}_{n+1} \qquad \text{and} \qquad \boldsymbol{\Theta}_{\text{err}} = \hat{\boldsymbol{\Theta}}_{n+1} - \boldsymbol{\Theta}_{n+1}. \tag{4.117}$$

As it is not advisable to change the step-size (4.116) too often and according to (Diebels et al., 1998), we introduce the error measure for the displacement and temperature coefficients

$$\mathrm{e}_u \equiv \sqrt{\frac{1}{n_{\text{nu}}} \sum_{l=1}^{n_{\text{nu}}} \left(\frac{u_{\text{err},l}}{\epsilon_{\text{r}}^u |u_l| + \epsilon_{\text{a}}^u} \right)^2}, \qquad \mathrm{e}_\theta \equiv \sqrt{\frac{1}{n_{\text{n}\theta}} \sum_{l=1}^{n_{\text{n}\theta}} \left(\frac{\theta_{\text{err},l}}{\epsilon_{\text{r}}^\theta |\theta_l| + \epsilon_{\text{a}}^\theta} \right)^2} \tag{4.118}$$

and the internal variables

$$\mathrm{e}_q \equiv \max_{1 \le k \le n_{\text{q}}} \left| \frac{q_{\text{err},k}}{\epsilon_{\text{r}}^q |q_k| + \epsilon_{\text{a}}^q} \right| . \tag{4.119}$$

Having computed the error measures, the maximum $\mathrm{e}_{\max} = \max(\mathrm{e}_u, \mathrm{e}_\theta, \mathrm{e}_q)$ is used to determine the new step-size

$$\Delta t_{\text{new}} = \Delta t_n \times \begin{cases} \max\Big(f_{\min}, f_{\text{safety}} \times \mathrm{e}_{\max}^{-1/(\hat{p}+1)}\Big) & \text{if } \mathrm{e}_{\max} > 1 \\ \min\Big(f_{\max}, f_{\text{safety}} \times \mathrm{e}_{\max}^{-1/(\hat{p}+1)}\Big) & \text{if } \mathrm{e}_{\max} \le 1. \end{cases} \tag{4.120}$$

$f_{\min}$ and $f_{\max}$ keep the step-size from increasing and decreasing too fast and the safety factor $0 < f_{\text{safety}} < 1$ prevents oscillations in the step-size. Values around $0.8 < f_{\text{safety}} < 0.9$, $0.2 < f_{\min} < 0.5$, and $2 < f_{\max} < 3$ usually work best, but this can be highly problem-dependent. Since the stage quantities $\dot{\boldsymbol{Y}}_{ni}$ have already been computed by the method with the consistency order p, we can write

$$\hat{\boldsymbol{y}}_{n+1} = \boldsymbol{y}_n + \Delta t_n \sum_{i=1}^{s} \hat{b}_i \dot{\boldsymbol{Y}}_{ni}, \tag{4.121}$$

and obtain the error

$$\boldsymbol{y}_{\text{err}} = \hat{\boldsymbol{y}}_{n+1} - \boldsymbol{y}_{n+1} = \Delta t_n \sum_{i=1}^{s} (\hat{b}_i - b_i) \dot{\boldsymbol{Y}}_{ni} \tag{4.122}$$

by pure function evaluation. Tab. 4.4 summarizes the time-adaptive, embedded DIRK-scheme.

Table 4.4: Time-adaptive, embedded DIRK-scheme

```
Given:
    • coefficients $c_i$, $a_{ij}$, $b_j$, $(i, j = 1, \ldots, s)$ of a stiffly-accurate DIRK-scheme
    • starting point $t_0$, initial step-size $\Delta t_0$
    • initial values $\boldsymbol{y}(t_0) \equiv \begin{Bmatrix} \boldsymbol{u}(t_0) \\ \boldsymbol{\Theta}(t_0) \\ \boldsymbol{q}(t_0) \end{Bmatrix} = \begin{Bmatrix} \boldsymbol{u}_0 \\ \boldsymbol{\Theta}_0 \\ \boldsymbol{q}_0 \end{Bmatrix} \equiv \boldsymbol{y}_0$
Loop over time-steps: $n = 0, \ldots, N$
    Repeat
        Loop over stages: $i = 1, \ldots, s$
            $T_{ni} = t_n + c_i \Delta t_n$
            $\boldsymbol{S}_{ni} = \boldsymbol{y}_n + \Delta t_n \sum_{j=1}^{i-1} a_{ij} \dot{\boldsymbol{Y}}_{nj}$
            solve: $\boldsymbol{F}\left(T_{ni}, \boldsymbol{Y}_{ni}, \frac{\boldsymbol{Y}_{ni} - \boldsymbol{S}_{ni}}{\Delta t_n \, a_{ii}}\right) = \boldsymbol{0}$ for $\boldsymbol{Y}_{ni} = \begin{Bmatrix} \boldsymbol{U}_{ni} \\ \boldsymbol{\Theta}_{ni} \\ \boldsymbol{Q}_{ni} \end{Bmatrix}$
            save: $\dot{\boldsymbol{Y}}_{ni} = \frac{\boldsymbol{Y}_{ni} - \boldsymbol{S}_{ni}}{\Delta t_n \, a_{ii}}$
        Error estimation according to (4.118), (4.119).
        Compute new step-size $\Delta t_{\text{neu}}$ according to (4.120).
        If time-step is accepted, put $\Delta t_n = \Delta t_{\text{new}}$.
    Until time-step accepted
    Update:
        $t_{n+1} = t_n + \Delta t_n$, $\Delta t_{n+1} = \Delta t_{\text{neu}}$, $\boldsymbol{y}_{n+1} = \boldsymbol{Y}_{ns}$
```

4.4 Multilevel-Newton Algorithm and Functional Matrices

The system of nonlinear equations, see (4.100) and (4.105), arising within the temporal discretization of the DAE-system (4.80) - (4.83) is solved by means of the Multilevel-Newton Algorithm which emerged in the context of large-scale electrical networks, see (Rabbat et al., 1979). If suitable conditions on the continuity and regularity of the Jacobian matrix are fulfilled, the algorithm is known to have local quadratic convergence. In (Ellsiepen and Hartmann, 2001) the MLNA is related to the consistent tangent operator developed in (Simo and Taylor, 1985). In the following section we omit the index ni for the sake of brevity. In (Quint, 2012), which discusses the application of the MLNA to the thermo-mechanically coupled problem, the short notations

$\boldsymbol{G}^{\mathrm{T}} := \{\boldsymbol{G}_{\mathrm{u}}^{\mathrm{T}}, \boldsymbol{G}_{\theta}^{\mathrm{T}}\}$ and $\boldsymbol{V}^{\mathrm{T}} := \{\boldsymbol{U}^{\mathrm{T}}, \boldsymbol{\Theta}^{\mathrm{T}}\}$ are introduced and so (4.105) can be reformulated as

$$\begin{Bmatrix} \boldsymbol{G}(\boldsymbol{V}, \boldsymbol{Q}) \\ \boldsymbol{L}(\boldsymbol{V}, \boldsymbol{Q}) \end{Bmatrix} = \boldsymbol{0}. \tag{4.123}$$

In this manner, the structure of the MLNA familiar from isothermal solid mechanics, see (Ellsiepen and Hartmann, 2001), for example, is preserved. The implicit function theorem states that if $\boldsymbol{L}(\boldsymbol{V}_0, \boldsymbol{Q}_0) = \boldsymbol{0}$ holds and if the function $\boldsymbol{L}$ is C^1 continuous in some neighborhood N of $(\boldsymbol{V}_0, \boldsymbol{Q}_0)$ with $\partial\boldsymbol{L}/\partial\boldsymbol{Q}$ regular, then there is a function $\boldsymbol{Q} = \hat{\boldsymbol{Q}}(\boldsymbol{V})$ in N, see (Burg et al., 1989). Inserting this function into the first part of (4.123) leads to

$$\boldsymbol{G}\Big(\boldsymbol{V}, \hat{\boldsymbol{Q}}(\boldsymbol{V})\Big) = \boldsymbol{0}. \tag{4.124}$$

Applying the classical Newton-Raphson scheme to equation (4.124) yields

$$\left[\frac{\partial \boldsymbol{G}}{\partial \boldsymbol{V}} + \frac{\partial \boldsymbol{G}}{\partial \boldsymbol{Q}} \frac{\mathrm{d}\hat{\boldsymbol{Q}}}{\mathrm{d}\boldsymbol{V}}\right]_{\boldsymbol{y}^{(m)}} \Delta \boldsymbol{V}^{(m)} = -\boldsymbol{G}\left(\boldsymbol{V}^{(m)}, \boldsymbol{Q}^{(m)}\right), \tag{4.125}$$

with m indicating the iteration number. The derivatives of the discretized weak form of the equilibrium condition and the discretized weak form of the heat equation with respect to the displacements and temperatures $\partial\boldsymbol{G}/\partial\boldsymbol{V}$ and the internal variables $\partial\boldsymbol{G}/\partial\boldsymbol{Q}$ can be stated explicitly. But since the function $\hat{\boldsymbol{Q}}(\boldsymbol{V})$ is not known, we employ the lower part of (4.123) in order to determine the unknown function value $\boldsymbol{Q}$ and the unknown derivative $\partial\hat{\boldsymbol{Q}}/\partial\boldsymbol{V}$. Based on its total derivative

$$\frac{\mathrm{d}\boldsymbol{L}}{\mathrm{d}\boldsymbol{V}} = \frac{\partial \boldsymbol{L}}{\partial \boldsymbol{V}} + \frac{\partial \boldsymbol{L}}{\partial \boldsymbol{Q}} \frac{\mathrm{d}\hat{\boldsymbol{Q}}}{\mathrm{d}\boldsymbol{V}} = \boldsymbol{0} \tag{4.126}$$

leads to a system of linear equations with several right-hand sides

$$\frac{\partial \boldsymbol{L}}{\partial \boldsymbol{Q}} \frac{\mathrm{d}\hat{\boldsymbol{Q}}}{\mathrm{d}\boldsymbol{V}} = -\frac{\partial \boldsymbol{L}}{\partial \boldsymbol{V}} \tag{4.127}$$

determining the consistent tangent operator $\partial\hat{\boldsymbol{Q}}/\partial\boldsymbol{V}$. The unknown function values of the internal variables are computed by solving the system of nonlinear equations $\boldsymbol{L}(\boldsymbol{V}, \boldsymbol{Q}) = \boldsymbol{0}$ for given $\boldsymbol{V}$ by applying the Newton-Raphson scheme. Since the evolution equations for the internal variables are decoupled from Gauss point to Gauss point, both the computation of the consistent tangent and the the evaluation of the function values of the internal variables are done at Gauss point level. On a global level, the linear system (4.125) is solved for the increment in the displacement and temperature coefficients $\Delta\boldsymbol{V}^{(m)}$ at each iteration. For this purpose, we divied the procedure into a local and a global part, see (Hartmann, 2005; Quint, 2012). The global iteration is stopped once a user-prescribed convergence criterion is fulfilled. The procedure is summarized in Tab. 4.5. Having described the Multilevel-Newton Algorithm in a rather general fashion, we will now proceed to discuss the arising quantities in more detail. Inserting the short notations

Table 4.5: Multilevel-Newton algorithm at the ith stage of the time-step from t_n to t_{n+1}

```
Given: $\boldsymbol{V}^{(0)}, \boldsymbol{Q}^{(0)}$ from initial iterate, $\Delta t_n$, $t_n + c_i \Delta t_n$, $a_{ii}$, $\boldsymbol{S}$
Repeat   $m = 0, \ldots$
    local (quadrature point) level
    given: $\boldsymbol{V}^{(m)}, \boldsymbol{y} := \left(\boldsymbol{U}^{(m)}, \boldsymbol{\Theta}^{(m)}, \boldsymbol{Q}^{(m)}\right)$
    local integration step
        $\boldsymbol{L}(\boldsymbol{V}^{(m)}, \boldsymbol{Q}^{(m)}) = \boldsymbol{0}$    $\rightsquigarrow \boldsymbol{Q}^{(m)}$
    consistent linearization
        $\left.\frac{\partial \boldsymbol{L}}{\partial \boldsymbol{Q}}\right|_{\boldsymbol{y}} \left.\frac{\mathrm{d}\hat{\boldsymbol{Q}}}{\mathrm{d}\boldsymbol{V}}\right|_{\boldsymbol{y}} = -\left.\frac{\partial \boldsymbol{L}}{\partial \boldsymbol{V}}\right|_{\boldsymbol{y}}$    $\rightsquigarrow \left.\frac{\mathrm{d}\boldsymbol{Q}}{\mathrm{d}\boldsymbol{V}}\right|_{\boldsymbol{y}}$
    global level
    solve linear system of equations
        $\left[\left.\frac{\partial \boldsymbol{G}}{\partial \boldsymbol{V}}\right|_{\boldsymbol{y}} + \left.\frac{\partial \boldsymbol{G}}{\partial \boldsymbol{Q}}\right|_{\boldsymbol{y}} \left.\frac{\mathrm{d}\hat{\boldsymbol{Q}}}{\mathrm{d}\boldsymbol{V}}\right|_{\boldsymbol{y}}\right] \Delta \boldsymbol{V} = -\boldsymbol{G}(\boldsymbol{y})$    $\rightsquigarrow \Delta \boldsymbol{V}$
    update of global variables
        $\boldsymbol{V}^{(m+1)} \leftarrow \boldsymbol{V}^{(m)} + \Delta \boldsymbol{V}$    $\rightsquigarrow \boldsymbol{V}^{(m+1)}$
until   the convergence criterion is fulfilled
```

$\boldsymbol{G}^{\mathrm{T}} := \{\boldsymbol{G}_{\mathrm{u}}^{\mathrm{T}}, \boldsymbol{G}_{\theta}^{\mathrm{T}}\}$ and $\boldsymbol{V}^{\mathrm{T}} := \{\boldsymbol{U}^{\mathrm{T}}, \boldsymbol{\Theta}^{\mathrm{T}}\}$ into (4.125) and (4.127) leads to

$$\begin{bmatrix} \dfrac{\mathrm{d}\boldsymbol{G}_{\mathrm{u}}}{\mathrm{d}\boldsymbol{U}} & \dfrac{\mathrm{d}\boldsymbol{G}_{\mathrm{u}}}{\mathrm{d}\boldsymbol{\Theta}} \\ \dfrac{\mathrm{d}\boldsymbol{G}_{\theta}}{\mathrm{d}\boldsymbol{U}} & \dfrac{\mathrm{d}\boldsymbol{G}_{\theta}}{\mathrm{d}\boldsymbol{\Theta}} \end{bmatrix} \begin{Bmatrix} \Delta \boldsymbol{U} \\ \Delta \boldsymbol{\Theta} \end{Bmatrix} = - \begin{Bmatrix} \boldsymbol{G}_{\mathrm{u}}(\boldsymbol{U}, \boldsymbol{\Theta}, \boldsymbol{Q}) \\ \boldsymbol{G}_{\theta}(\boldsymbol{U}, \boldsymbol{\Theta}, \boldsymbol{Q}) \end{Bmatrix} \tag{4.128}$$

and

$$\begin{bmatrix} \dfrac{\partial \boldsymbol{L}}{\partial \boldsymbol{Q}} \end{bmatrix} \begin{bmatrix} \dfrac{\partial \hat{\boldsymbol{Q}}}{\partial \boldsymbol{U}} & \dfrac{\partial \hat{\boldsymbol{Q}}}{\partial \boldsymbol{\Theta}} \end{bmatrix} = - \begin{bmatrix} \dfrac{\partial \boldsymbol{L}}{\partial \boldsymbol{U}} & \dfrac{\partial \boldsymbol{L}}{\partial \boldsymbol{\Theta}} \end{bmatrix}, \tag{4.129}$$

where the iteration counter has been omitted for brevity. The right-hand side of (4.128) is given by (4.101) and (4.102) whereas the necessary derivatives will be discussed below.

Derivation of $\partial \boldsymbol{G}_{\mathrm{u}}/\partial \boldsymbol{U}$

In order to derive $\partial \boldsymbol{G}_{\mathrm{u}}/\partial \boldsymbol{U}$ let us start with the internal virtual work

$$\pi_{\mathrm{u\,i}} = \int\limits_{\Omega} \tilde{\mathbf{T}} \cdot \delta\mathbf{E}\,\mathrm{d}V. \tag{4.130}$$

With the short notation $\mathrm{Grad}\,\delta\boldsymbol{u} = \delta\mathbf{H}$ the virtual Green strain tensor (3.30) results in

$$\delta\mathbf{E} = \frac{1}{2}(\mathbf{F}^{\mathrm{T}}\delta\mathbf{H} + \delta\mathbf{H}^{\mathrm{T}}\mathbf{F}). \tag{4.131}$$

Inserting (4.131) into (4.130) yields

$$\pi_{\mathrm{u\,i}} = \frac{1}{2}\int\limits_{\Omega} \left(\tilde{\mathbf{T}} \cdot \mathbf{F}^{\mathrm{T}}\delta\mathbf{H} + \tilde{\mathbf{T}}^{\mathrm{T}} \cdot \mathbf{F}^{\mathrm{T}}\delta\mathbf{H}\right)\mathrm{d}V = \int\limits_{\Omega} \mathbf{F}\tilde{\mathbf{T}} \cdot \delta\mathbf{H}\,\mathrm{d}V \tag{4.132}$$

where the definition of a transposition of a tensor and (2.61) are applied. Employing the Gateaux-derivative

$$\mathsf{D}_{\mathbf{A}}\,\mathbf{F}(\mathbf{A})[\mathbf{H}] = \frac{\mathrm{d}}{\mathrm{d}\lambda}\mathbf{F}\left(\mathbf{A} + \lambda\mathbf{H}\right)\bigg|_{\lambda=0} \tag{4.133}$$

to the virtual internal work and representing the stress state by $\tilde{\mathbf{T}} = \mathbf{h}\,(\boldsymbol{u}, \theta, \boldsymbol{q})$, (4.132) leads to

$$\mathsf{D}_{\boldsymbol{u}}\,\pi_{\mathrm{u\,i}}(\boldsymbol{u}, \theta)[\Delta\boldsymbol{u}] = \int\limits_{\Omega} \left(\mathbf{F}\mathsf{D}_{\boldsymbol{u}}\,\mathbf{h}(\boldsymbol{u}, \theta, \boldsymbol{q})[\Delta\boldsymbol{u}] + \mathsf{D}_{\boldsymbol{u}}\,\mathbf{F}(\boldsymbol{u})[\Delta\boldsymbol{u}]\,\mathbf{h}\,(\boldsymbol{u}, \theta, \boldsymbol{q})\right) \cdot \delta\mathbf{H}\,\mathrm{d}V \tag{4.134}$$

$$= \int\limits_{\Omega} \left(\mathbf{F}\tilde{\mathcal{C}}_{\mathrm{u}}\Delta\mathbf{E} + (\mathrm{Grad}\,\Delta\boldsymbol{u})\,\mathbf{h}\,(\boldsymbol{u}, \theta, \boldsymbol{q})\right) \cdot \delta\mathbf{H}\,\mathrm{d}V \tag{4.135}$$

$$= \int\limits_{\Omega} \left(\tilde{\mathcal{C}}_{\mathrm{u}}\Delta\mathbf{E} \cdot \mathbf{F}^{\mathrm{T}}\delta\mathbf{H} + (\mathrm{Grad}\,\Delta\boldsymbol{u})\,\mathbf{h}\,(\boldsymbol{u}, \theta, \boldsymbol{q}) \cdot \delta\mathbf{H}\right)\mathrm{d}V \tag{4.136}$$

$$= \int\limits_{\Omega} \left(\tilde{\mathcal{C}}_{\mathrm{u}}\Delta\mathbf{E} \cdot \delta\mathbf{E} + (\mathrm{Grad}\,\Delta\boldsymbol{u})\,\mathbf{h}\,(\boldsymbol{u}, \theta, \boldsymbol{q}) \cdot \delta\mathbf{H}\right)\mathrm{d}V \tag{4.137}$$

thus allowing (4.137) to be split into one part accounting for the material nonlinearity $\tilde{\mathcal{C}}_{\mathrm{u}}\Delta\mathbf{E} \cdot \delta\mathbf{E}$ and one part $(\mathrm{Grad}\,\Delta)\,\boldsymbol{u}\tilde{\mathbf{T}} \cdot \delta\mathbf{H}$ which is due to the geometrical nonlinearity. $\tilde{\mathcal{C}}_{\mathrm{u}}$ is a stiffness tensor of fourth order represented by

$$\tilde{\mathcal{C}}_{\mathrm{u}} = 2\left[\frac{\mathrm{d}\mathbf{h}}{\mathrm{d}\mathbf{C}} + \frac{\mathrm{d}\mathbf{h}}{\mathrm{d}\mathbf{q}}\frac{\mathrm{d}\mathbf{q}}{\mathrm{d}\mathbf{C}}\right], \tag{4.138}$$

the Gateaux-derivative is expressed by

$$\mathsf{D}_{\boldsymbol{u}}\,\mathbf{h}(\boldsymbol{u}, \theta, \boldsymbol{q}\,(\boldsymbol{u}))[\Delta\boldsymbol{u}] = \tilde{\mathcal{C}}_{\mathrm{u}}\Delta\mathbf{E} \tag{4.139}$$

and the incremental Green strain tensor is

$$\Delta \mathbf{E} = \mathsf{D}\,\mathbf{E}(\boldsymbol{u})[\Delta \boldsymbol{u}] = \frac{1}{2}\left(\left(\mathrm{Grad}^{\mathrm{T}}\,\Delta \boldsymbol{u}\right)\mathbf{F} + \mathbf{F}^{\mathrm{T}}\,\mathrm{Grad}\,\Delta \boldsymbol{u}\right). \tag{4.140}$$

The derivatives of the second Piola-Kirchhoff stress tensor with respect to the right Cauchy-Green tensor and the internal variables are given in Appendix A.6. The gradients of the incremental and virtual displacement vector, $\mathrm{Grad}\,\Delta\boldsymbol{u}$ and $\mathrm{Grad}\,\delta\boldsymbol{u}$ can be expressed as column matrices

$$\Delta \boldsymbol{H} = \tilde{\mathbf{L}}_{\mathrm{NL}}\mathbf{N}^{e}_{\mathrm{d}}\Delta\mathbf{u}^{\mathrm{e}} \quad \text{for} \quad \boldsymbol{X} \in \Omega_e \tag{4.141}$$

and

$$\delta \boldsymbol{H} = \tilde{\mathbf{L}}_{\mathrm{NL}}\mathbf{N}^{e}_{\mathrm{d}}\delta\mathbf{u}^{\mathrm{e}} \quad \text{for} \quad \boldsymbol{X} \in \Omega_e, \tag{4.142}$$

where use of the differential operator matrix

$$\tilde{\mathbf{L}}_{\mathrm{NL}} = \begin{bmatrix} \frac{\partial}{\partial X} & 0 & 0 \\ 0 & \frac{\partial}{\partial Y} & 0 \\ 0 & 0 & \frac{\partial}{\partial Z} \\ \frac{\partial}{\partial Y} & 0 & 0 \\ 0 & \frac{\partial}{\partial Z} & 0 \\ 0 & 0 & \frac{\partial}{\partial X} \\ \frac{\partial}{\partial Z} & 0 & 0 \\ 0 & \frac{\partial}{\partial X} & 0 \\ 0 & 0 & \frac{\partial}{\partial Y} \end{bmatrix} \tag{4.143}$$

and the hierarchic shape functions $\mathbf{N}^{e}_{\mathrm{d}}$ given by (4.34) is made. By rearranging the components of the second Piola-Kirchhoff stress tensor as

$$\mathbf{M}^{e}_{\tilde{\mathbf{T}}} = \begin{bmatrix} \tilde{t}_{11} & 0 & 0 & \tilde{t}_{12} & 0 & 0 & \tilde{t}_{31} & 0 & 0 \\ 0 & \tilde{t}_{22} & 0 & 0 & \tilde{t}_{23} & 0 & 0 & \tilde{t}_{12} & 0 \\ 0 & 0 & \tilde{t}_{33} & 0 & 0 & \tilde{t}_{31} & 0 & 0 & \tilde{t}_{23} \\ \tilde{t}_{12} & 0 & 0 & \tilde{t}_{22} & 0 & 0 & \tilde{t}_{23} & 0 & 0 \\ 0 & \tilde{t}_{32} & 0 & 0 & \tilde{t}_{33} & 0 & 0 & \tilde{t}_{31} & 0 \\ 0 & 0 & \tilde{t}_{31} & 0 & 0 & \tilde{t}_{11} & 0 & 0 & \tilde{t}_{12} \\ \tilde{t}_{31} & 0 & 0 & \tilde{t}_{23} & 0 & 0 & \tilde{t}_{33} & 0 & 0 \\ 0 & \tilde{t}_{12} & 0 & 0 & \tilde{t}_{31} & 0 & 0 & \tilde{t}_{11} & 0 \\ 0 & 0 & \tilde{t}_{23} & 0 & 0 & \tilde{t}_{12} & 0 & 0 & \tilde{t}_{22} \end{bmatrix}$$

it is possible to formulate the tangent resulting from the geometrical nonlinearity as follows:

$$\int\limits_{\Omega} \mathrm{Grad}\,\Delta\boldsymbol{u}\tilde{\mathbf{T}} \cdot \delta\mathbf{H}\,\mathrm{d}V \tag{4.144}$$

$$= \delta\boldsymbol{u}^{\mathrm{T}}\left[\sum_{e=1}^{n_{\mathrm{el}}} \boldsymbol{Z}^{e\mathrm{T}}_{\mathrm{d}}\left[\int\limits_{\Omega_e}\left(\tilde{\mathbf{L}}_{\mathrm{NL}}\mathbf{N}^{e}_{\mathrm{d}}\right)^{\mathrm{T}}\mathbf{M}^{e}_{\tilde{\mathbf{T}}}\tilde{\mathbf{L}}_{\mathrm{NL}}\mathbf{N}^{e}_{\mathrm{d}}\,\mathrm{d}V\right]\boldsymbol{Z}^{e}_{\mathrm{d}}\right]\Delta\boldsymbol{u}. \tag{4.145}$$

If the components of the virtual Green strain tensor are rearranged as

$$\delta \mathbf{E}^{e\,h} = \{\delta E_{11}, \delta E_{22}, \delta E_{33}, 2\delta E_{12}, 2\delta E_{23}, 2\delta E_{13}\}\,, \tag{4.146}$$

(4.131) can be approximated by

$$\delta \mathbf{E}^{e\,h}(\mathbf{X}, t) = \tilde{\mathbf{B}}^{e}_{\mathrm{d}}(\mathbf{u}^{e}(t), \mathbf{X})\ \delta \mathbf{u}^{\mathrm{e}}(t) \tag{4.147}$$

employing the matrix

$$\tilde{\mathbf{B}}^{e}_{\mathrm{d}}(\mathbf{u}^{e}(t), \mathbf{X}) = \left[\tilde{\mathbf{B}}^{e}_{\mathrm{d}\,1}(\mathbf{u}^{e}(t), \mathbf{X}) \ldots \tilde{\mathbf{B}}^{e}_{\mathrm{d}\,n_{\mathrm{em}}}(\mathbf{u}^{e}(t), \mathbf{X})\right] \in \mathbb{R}^{6 \times 3 n_{\mathrm{em}}}, \tag{4.148}$$

composed of the submatrices

$$\tilde{\mathbf{B}}^{e}_{\mathrm{d}\,a} = \begin{bmatrix} F^{e}_{11} n^{e}_{a,X} & F^{e}_{21} n^{e}_{a,X} & F^{e}_{31} n^{e}_{a,X} \\ F^{e}_{12} n^{e}_{a,Y} & F^{e}_{22} n^{e}_{a,Y} & F^{e}_{32} n^{e}_{a,Y} \\ F^{e}_{13} n^{e}_{a,Z} & F^{e}_{23} n^{e}_{a,Z} & F^{e}_{33} n^{e}_{a,Z} \\ F^{e}_{11} n^{e}_{a,Y} + F^{e}_{12} n^{e}_{a,X} & F^{e}_{21} n^{e}_{a,Y} + F^{e}_{22} n^{e}_{a,X} & F^{e}_{31} n^{e}_{a,Y} + F^{e}_{32} n^{e}_{a,X} \\ F^{e}_{12} n^{e}_{a,Z} + F^{e}_{13} n^{e}_{a,Y} & F^{e}_{22} n^{e}_{a,Z} + F^{e}_{23} n^{e}_{a,Y} & F^{e}_{32} n^{e}_{a,Z} + F^{e}_{33} n^{e}_{a,Y} \\ F^{e}_{13} n^{e}_{a,X} + F^{e}_{11} n^{e}_{a,Z} & F^{e}_{23} n^{e}_{a,X} + F^{e}_{21} n^{e}_{a,Z} & F^{e}_{33} n^{e}_{a,X} + F^{e}_{31} n^{e}_{a,Z} \end{bmatrix} \tag{4.149}$$

with $a = 1, ..., n_{\mathrm{em}}$. The F^{e}_{ij} indicate the components of the deformation gradient, see (2.7). n^{e}_{a} is a short notation for the shape functions employed in (4.34). Furthermore,

$$\Delta \mathbf{E}^{e\,h} = \tilde{\mathbf{B}}^{e}_{\mathrm{d}}(\mathbf{u}^{e}(t), \mathbf{X})\ \Delta \mathbf{u}^{\,e} \tag{4.150}$$

holds with the increment $\Delta \mathbf{E}^{e\,h}$ arranged as

$$\Delta \mathbf{E}^{e\,h} = \{\Delta E_{11}, \Delta E_{22}, \Delta E_{33}, 2\Delta E_{12}, 2\Delta E_{23}, 2\Delta E_{13}\}\,. \tag{4.151}$$

Rearranging the components of the stiffness tensor of fourth order given in (4.138) as a matrix

$$\tilde{\mathbf{C}}^{e}_{\mathrm{u}} = \begin{bmatrix} C_{1111} & C_{1122} & C_{1133} & \frac{1}{2}(C_{1112} + C_{1121}) & \frac{1}{2}(C_{1123} + C_{1132}) & \frac{1}{2}(C_{1131} + C_{1113}) \\ C_{2211} & C_{2222} & C_{2233} & \frac{1}{2}(C_{2212} + C_{2221}) & \frac{1}{2}(C_{2223} + C_{2232}) & \frac{1}{2}(C_{2231} + C_{2213}) \\ C_{3311} & C_{3322} & C_{3333} & \frac{1}{2}(C_{3312} + C_{3321}) & \frac{1}{2}(C_{3323} + C_{3332}) & \frac{1}{2}(C_{3331} + C_{3313}) \\ C_{1211} & C_{1222} & C_{1233} & \frac{1}{2}(C_{1212} + C_{1221}) & \frac{1}{2}(C_{1223} + C_{1232}) & \frac{1}{2}(C_{1231} + C_{1213}) \\ C_{2311} & C_{2322} & C_{2333} & \frac{1}{2}(C_{2312} + C_{2321}) & \frac{1}{2}(C_{2323} + C_{2332}) & \frac{1}{2}(C_{2331} + C_{2313}) \\ C_{3111} & C_{3122} & C_{3133} & \frac{1}{2}(C_{3112} + C_{3121}) & \frac{1}{2}(C_{3123} + C_{3132}) & \frac{1}{2}(C_{3131} + C_{3113}) \end{bmatrix}, \tag{4.152}$$

see (Hartmann, 2003), and making use of (4.147) and (4.150), the weak form of the equilibrium condition can be reformulated as

$$\int\limits_{\Omega} \tilde{\mathcal{C}}_{\mathrm{u}} \Delta \mathbf{E} \cdot \delta \mathbf{E} \,\mathrm{d}V = \delta \boldsymbol{u}^{\mathrm{T}} \left[\sum_{e=1}^{n_{\mathrm{el}}} \boldsymbol{Z}^{e\mathrm{T}}_{\mathrm{d}} \left[\int\limits_{\Omega_e} \tilde{\mathbf{B}}^{e\mathrm{T}}_{\mathrm{d}} \tilde{\mathbf{C}}^{e}_{\mathrm{u}} \tilde{\mathbf{B}}^{e}_{\mathrm{d}} \,\mathrm{d}V \right] \boldsymbol{Z}^{e}_{\mathrm{d}} \right] \Delta \boldsymbol{u}. \tag{4.153}$$

The tangents resulting from the physical and geometrical nonlinearity in material and spatial representation then read

$$\mathbf{k}^e_{\mathrm{UC}} = \int\limits_{\Omega_e} \tilde{\mathbf{B}}^{e\mathrm{T}}_{\mathrm{d}} \tilde{\mathbf{C}}^e_{\mathrm{u}} \tilde{\mathbf{B}}^e_{\mathrm{d}} \, \mathrm{d}V = \int\limits_{\omega_e} \mathbf{B}^{e\mathrm{T}}_{\mathrm{d}} \mathbf{C}^e_{\mathrm{u}} \mathbf{B}^e_{\mathrm{d}} \, \mathrm{d}v \tag{4.154}$$

with

$$\tilde{\mathbf{B}}^{e\mathrm{T}}_{\mathrm{d}} = \mathbf{B}^{e\mathrm{T}}_{\mathrm{d}} \mathbf{F}^e_{23} = \begin{bmatrix} \mathbf{B}^{e\mathrm{T}}_{\mathrm{d}1} \mathbf{F}^e_{23} \\ \vdots \\ \mathbf{B}^{e\mathrm{T}}_{\mathrm{d}n_{\mathrm{em}}} \mathbf{F}^e_{23} \end{bmatrix}, \quad \mathbf{C}^e_{\mathrm{u}} = \frac{1}{J} \mathbf{F}^e_{23} \tilde{\mathbf{C}}^e_{\mathrm{u}} \mathbf{F}^{e\mathrm{T}}_{23} \tag{4.155}$$

and

$$\mathbf{k}^e_{\mathrm{UG}} = \int\limits_{\Omega_e} \left(\tilde{\mathbf{L}}_{\mathrm{NL}} \mathbf{N}^e_{\mathrm{d}} \right)^{\mathrm{T}} \mathbf{M}^e_{\tilde{\mathbf{T}}} \tilde{\mathbf{L}}_{\mathrm{NL}} \mathbf{N}^e_{\mathrm{d}} \, \mathrm{d}V \tag{4.156}$$

$$= \int\limits_{\Omega_e} \frac{1}{J} \left(\mathbf{L}_{\mathrm{NL}} \mathbf{N}^e_{\mathrm{d}} \right)^{\mathrm{T}} \mathbf{M}^e_{\mathbf{S}} \mathbf{L}_{\mathrm{NL}} \mathbf{N}^e_{\mathrm{d}} \, \mathrm{d}v. \tag{4.157}$$

This is based on

$$\mathbf{M}^e_{\mathbf{S}} = \begin{bmatrix} S^e_{11} & 0 & 0 & S^e_{12} & 0 & 0 & S^e_{31} & 0 & 0 \\ 0 & S^e_{22} & 0 & 0 & S^e_{23} & 0 & 0 & S^e_{12} & 0 \\ 0 & 0 & S^e_{33} & 0 & 0 & S^e_{31} & 0 & 0 & S^e_{23} \\ S^e_{12} & 0 & 0 & S^e_{22} & 0 & 0 & S^e_{23} & 0 & 0 \\ 0 & S^e_{23} & 0 & 0 & S^e_{33} & 0 & 0 & S^e_{31} & 0 \\ 0 & 0 & S^e_{31} & 0 & 0 & S^e_{11} & 0 & 0 & S^e_{12} \\ S^e_{31} & 0 & 0 & S^e_{23} & 0 & 0 & S^e_{33} & 0 & 0 \\ 0 & S^e_{12} & 0 & 0 & S^e_{31} & 0 & 0 & S^e_{11} & 0 \\ 0 & 0 & S^e_{23} & 0 & 0 & S^e_{12} & 0 & 0 & S^e_{22} \end{bmatrix} \tag{4.158}$$

and

$$\mathbf{L}_{\mathrm{NL}} = \begin{bmatrix} \frac{\partial}{\partial x} & 0 & 0 \\ 0 & \frac{\partial}{\partial y} & 0 \\ 0 & 0 & \frac{\partial}{\partial z} \\ \frac{\partial}{\partial y} & 0 & 0 \\ 0 & \frac{\partial}{\partial z} & 0 \\ 0 & 0 & \frac{\partial}{\partial x} \\ \frac{\partial}{\partial z} & 0 & 0 \\ 0 & \frac{\partial}{\partial x} & 0 \\ 0 & 0 & \frac{\partial}{\partial y} \end{bmatrix}. \tag{4.159}$$

Moreover, in (4.154) the derivatives of the shape functions with respect to the current configuration

$$\mathbf{B}^{e\mathrm{T}}_{\mathrm{d}} = \left[\mathbf{B}^e_{\mathrm{d}\,1} \ldots \mathbf{B}^e_{\mathrm{d}\,n_{\mathrm{em}}} \right] \in \mathbb{R}^{6 \times 3 n_{\mathrm{em}}}, \tag{4.160}$$

containing the submatrices

$$\mathbf{B}^e_{\mathrm{d}\,a} = \begin{bmatrix} n^e_{a,x} & 0 & 0 \\ 0 & n^e_{a,y} & 0 \\ 0 & 0 & n^e_{a,z} \\ n^e_{a,y} & n^e_{a,x} & 0 \\ 0 & n^e_{a,z} & n^e_{a,y} \\ n^e_{a,z} & 0 & n^e_{a,x} \end{bmatrix} \tag{4.161}$$

with $a = 1, ..., n_{\text{em}}$, are necessary. The first part of (4.155) becomes apparent when considering

$$\tilde{\mathbf{B}}^e_{\mathrm{d}\,1} = \left[\mathbf{B}^{e\mathrm{T}}_{\mathrm{d}1} \mathbf{F}^e_{23}\right]^{\mathrm{T}} =$$

$$\begin{bmatrix} F^e_{11}\overbrace{F^e_{k1} n^e_{a,k}}^{\mathrm{d}n^e_a/\,\mathrm{d}X} & F^e_{21}F^e_{k1}n^e_{a,k} & F^e_{31}F^e_{k1}n^e_{a,k} \\ F^e_{12}F^e_{k2}n^e_{a,k} & F^e_{22}F^e_{k2}n^e_{a,k} & F^e_{32}F^e_{k2}n^e_{a,k} \\ F^e_{13}F^e_{k3}n^e_{a,k} & F^e_{23}F^e_{k3}n^e_{a,k} & F^e_{33}F^e_{k3}n^e_{a,k} \\ F^e_{11}F^e_{k2}n^e_{a,k} + F^e_{12}F^e_{k1}n^e_{a,k} & F^e_{21}F^e_{k2}n^e_{a,k} + F^e_{22}F^e_{k1}n^e_{a,k} & F^e_{31}F^e_{k2}n^e_{a,k} + F^e_{32}F^e_{k1}n^e_{a,k} \\ F^e_{12}F^e_{k3}n^e_{a,k} + F^e_{13}F^e_{k2}n^e_{a,k} & F^e_{22}F^e_{k3}n^e_{a,k} + F^e_{23}F^e_{k2}n^e_{a,k} & F^e_{32}F^e_{k3}n^e_{a,k} + F^e_{33}F^e_{k2}n^e_{a,k} \\ F^e_{13}F^e_{k1}n^e_{a,k} + F^e_{11}F^e_{k3}n^e_{a,k} & F^e_{23}F^e_{k1}n^e_{a,k} + F^e_{21}F^e_{k3}n^e_{a,k} & F^e_{33}F^e_{k1}n^e_{a,k} + F^e_{31}F^e_{k3}n^e_{a,k} \end{bmatrix}. \tag{4.162}$$

The index U refers to the discretized weak form of the equilibrium condition, G to the part of the tangent resulting from the geometrical nonlinearity and C to the part resulting from the constitutive model.

Since this thesis deals with deformation-dependent loads, it is necessary to differentiate the external work

$$\pi_{\mathrm{u\,e}} = \int\limits_{\partial\omega} \boldsymbol{s} \cdot \delta\boldsymbol{u} \,\mathrm{d}a \tag{4.163}$$

in terms of the displacements. The deformation-dependent loads under consideration are always normal to the deformed surface and have a constant magnitude, referred to as follower loading, see (Schweizerhof, 1982; Simo et al., 1991; Wriggers, 2008), for example. A discussion about the implementation of follower loading in the p-version of the finite element method can be found in (Yosibash et al., 2007), which looks at axisymmetric domains. The area of an infinitely small surface element in current configuration $\mathrm{d}a$ can be expressed as

$$\mathrm{d}a = \|\boldsymbol{x},_\xi \times \boldsymbol{x},_\eta\| \,\mathrm{d}\xi \,\mathrm{d}\eta. \tag{4.164}$$

Based on

$$\hat{\boldsymbol{n}} = \boldsymbol{x},_\xi \times \boldsymbol{x},_\eta \quad \text{and} \quad \boldsymbol{x} = \boldsymbol{X} + \boldsymbol{u} \tag{4.165}$$

the unit normal vector of the surface element $\mathrm{d}a$ reads

$$\boldsymbol{n} = \frac{\hat{\boldsymbol{n}}}{\|\hat{\boldsymbol{n}}\|} = \frac{(\boldsymbol{X},_\xi + \boldsymbol{u},_\xi) \times (\boldsymbol{X},_\eta + \boldsymbol{u},_\eta)}{\|(\boldsymbol{X},_\xi + \boldsymbol{u},_\xi) \times (\boldsymbol{X},_\eta + \boldsymbol{u},_\eta)\|}. \tag{4.166}$$

With the help of Cauchy's theorem

$$\boldsymbol{s} = p\boldsymbol{n} \tag{4.167}$$

and (4.164), (4.163) can be stated as

$$\pi_{\mathrm{u\,e}} = \int\limits_{\Omega^q_{st}} p\,[(\boldsymbol{X},_\xi + \boldsymbol{u},_\xi) \times (\boldsymbol{X},_\eta + \boldsymbol{u},_\eta)] \cdot \delta\boldsymbol{u}\,\mathrm{d}\xi\,\mathrm{d}\eta \tag{4.168}$$

$$= \int\limits_{\Omega^q_{st}} p\,[\boldsymbol{X},_\xi \times \boldsymbol{X},_\eta + \boldsymbol{X},_\xi \times \boldsymbol{u},_\eta + \boldsymbol{u},_\xi \times \boldsymbol{X},_\eta + \boldsymbol{u},_\xi \times \boldsymbol{u},_\eta] \cdot \delta\boldsymbol{u}\,\mathrm{d}\xi\,\mathrm{d}\eta. \tag{4.169}$$

Applying the Gateaux-derivative to (4.169) yields

$$\mathsf{D}_{\boldsymbol{u}}\,\pi_{\mathrm{u\,e}}(\boldsymbol{u})[\Delta\boldsymbol{u}] = \tag{4.170}$$

$$= \int\limits_{\Omega^h_{st}} p\,[\boldsymbol{X},_\xi \times \Delta\boldsymbol{u},_\eta + \Delta\boldsymbol{u},_\xi \times \boldsymbol{X},_\eta + \Delta\boldsymbol{u},_\xi \times \boldsymbol{u},_\eta + \boldsymbol{u},_\xi \times \Delta\boldsymbol{u},_\eta] \cdot \delta\boldsymbol{u}\,\mathrm{d}\xi\,\mathrm{d}\eta \tag{4.171}$$

$$= \int\limits_{\Omega^q_{st}} p\,[(\boldsymbol{X} + \boldsymbol{u}),_\xi \times \Delta\boldsymbol{u},_\eta + \Delta\boldsymbol{u},_\xi \times (\boldsymbol{X} + \boldsymbol{u}),_\eta] \cdot \delta\boldsymbol{u}\,\mathrm{d}\xi\,\mathrm{d}\eta \tag{4.172}$$

$$= \int\limits_{\Omega^q_{st}} p\,[\boldsymbol{x},_\xi \times \Delta\boldsymbol{u},_\eta + \Delta\boldsymbol{u},_\xi \times \boldsymbol{x},_\eta] \cdot \delta\boldsymbol{u}\,\mathrm{d}\xi\,\mathrm{d}\eta. \tag{4.173}$$

With the approximation for the displacements (4.20), the virtual displacements (4.21),

$$\Delta\boldsymbol{u}^h(\mathbf{X},t) = \boldsymbol{N}_{\mathrm{ad}}(\mathbf{X})\,\Delta\boldsymbol{u}(t) = \mathbf{N}^e_{\mathrm{d}}(\varphi^e(\mathbf{X}))\Delta\mathbf{u} \quad \text{for} \quad \mathbf{X} \in \Omega_e \tag{4.174}$$

and the skew symmetric matrix

$$\mathbf{M},_\alpha = \begin{bmatrix} 0 & z,_\alpha & -y,_\alpha \\ -z,_\alpha & 0 & x,_\alpha \\ y,_\alpha & -x,_\alpha & 0 \end{bmatrix}, \tag{4.175}$$

the cross products yield

$$\boldsymbol{x},_\xi \times \Delta\boldsymbol{u},_\eta = -\mathbf{M},_\xi\,\mathbf{N}^e_{\mathrm{d}},_\eta\,\Delta\mathbf{u}, \tag{4.176}$$

$$\Delta\boldsymbol{u},_\xi \times \boldsymbol{x},_\eta = \mathbf{M},_\eta\,\mathbf{N}^e_{\mathrm{d}},_\xi\,\Delta\mathbf{u}. \tag{4.177}$$

This is based on $()_{,\xi}$ denoting a differentiation with respect to ξ. Finally, the Gateaux-derivative of $\pi_{\mathrm{u\,e}}$ in direction of an increment in the displacements can be expressed by

$$\mathsf{D}_{\boldsymbol{u}}\,\pi_{\mathrm{u\,e}}(\boldsymbol{u})[\Delta\boldsymbol{u}] = \delta\boldsymbol{u}^{\mathrm{T}} \left[\sum_{e=1}^{n_{\mathrm{el}}} \boldsymbol{Z}^{e\mathrm{T}}_{\mathrm{d}} \left[\int\limits_{\Omega^q_{st}} p\mathbf{N}^{e\mathrm{T}}_{\mathrm{d}} \left(\mathbf{M},_\eta\,\mathbf{N}^e_{\mathrm{d},\xi} - \mathbf{M},_\xi\,\mathbf{N}^e_{\mathrm{d},\eta}\right) \mathrm{d}\xi\,\mathrm{d}\eta \right] \boldsymbol{Z}^e_{\mathrm{d}} \right] \Delta\boldsymbol{u}. \tag{4.178}$$

The components x, y and z populating the skew symmetric matrix given in (4.175) indicate the current position of a material point. The stiffness matrix resulting from the tangent of the follower load then reads

$$\mathbf{k}^e_{\mathrm{UF}} = \int\limits_{\Omega^q_{st}} p\mathbf{N}^{e\mathrm{T}}_{\mathrm{d}} \left(\mathbf{M},_\eta\,\mathbf{N}^e_{\mathrm{d},\xi} - \mathbf{M},_\xi\,\mathbf{N}^e_{\mathrm{d},\eta}\right) \mathrm{d}\xi\,\mathrm{d}\eta, \tag{4.179}$$

where the index F refers to follower loading. We can now write the derivative of the discretized weak form of the equilibrium condition as

$$\frac{\mathrm{d}\boldsymbol{G}_{\mathrm{u}}}{\mathrm{d}\boldsymbol{U}} = \sum_{e=1}^{n_{\mathrm{el}}} \boldsymbol{Z}_{\mathrm{d}}^{e\mathrm{T}} \left[\mathbf{k}_{\mathrm{UG}}^{e} + \mathbf{k}_{\mathrm{UC}}^{e} + \mathbf{k}_{\mathrm{UF}}^{e}\right] \boldsymbol{Z}_{\mathrm{d}}^{e}, \tag{4.180}$$

with $\mathbf{k}_{\mathrm{UG}}^{e}$, $\mathbf{k}_{\mathrm{UC}}^{e}$ and $\mathbf{k}_{\mathrm{UF}}^{e}$ provided in (4.157), (4.154) and (4.179).

Derivation of $\mathrm{d}\boldsymbol{G}_{\mathbf{u}}/\,\mathrm{d}\boldsymbol{\Theta}$

When contemplating fully coupled thermo-mechanical problems, the weak form of the balance of linear momentum also depends on the temperature so the derivative $\mathrm{d}\boldsymbol{G}_{\mathrm{u}}/\,\mathrm{d}\boldsymbol{\Theta}$ in (4.128) arises. Since the external forces are assumed to be independent of the temperature, only the internal virtual work, see (4.130),

$$\pi_{\mathrm{u\,i}}\left(\mathbf{u}, \theta, \boldsymbol{q}\right) = \delta\boldsymbol{u}^{\mathrm{T}} \sum_{e=1}^{n_{\mathrm{el}}} \boldsymbol{Z}_{\mathrm{d}}^{e\mathrm{T}} \left[\int_{\Omega_e} \tilde{\mathbf{B}}_{\mathrm{d}}^{e\mathrm{T}} \mathbf{h}\left(\mathbf{u}, \theta, \mathbf{q}^{e}\right) \mathrm{d}V\right], \tag{4.181}$$

cf. also (4.62) and (4.155), needs to be taken into account when deriving the tangent of the mechanical part with respect to the temperature yielding

$$\begin{aligned}
\mathsf{D}_{\boldsymbol{\Theta}}\, \pi_{\mathrm{u\,i}}(\mathbf{u}, \theta, \boldsymbol{q})[\Delta\boldsymbol{\Theta}] &= \delta\boldsymbol{u}^{\mathrm{T}} \sum_{e=1}^{n_{\mathrm{el}}} \boldsymbol{Z}_{\mathrm{d}}^{e\mathrm{T}} \left[\int_{\Omega_e} \tilde{\mathbf{B}}_{\mathrm{d}}^{e\mathrm{T}} \mathsf{D}_{\boldsymbol{\Theta}^e}\, \mathbf{h}((\mathbf{h}, \theta, \mathbf{q}^{e}))[\Delta\boldsymbol{\Theta}^{e}]\, \mathrm{d}V\right] && (4.182)\\
&= \delta\boldsymbol{u}^{\mathrm{T}} \sum_{e=1}^{n_{\mathrm{el}}} \boldsymbol{Z}_{\mathrm{d}}^{e\mathrm{T}} \left[\int_{\Omega_e} \tilde{\mathbf{B}}_{\mathrm{d}}^{e\mathrm{T}} \tilde{\mathbf{C}}_{\theta}^{e} \mathbf{N}_{\theta}^{e\mathrm{T}}\, \mathrm{d}V \Delta\boldsymbol{\Theta}^{e}\right] && (4.183)\\
&= \delta\boldsymbol{u}^{\mathrm{T}} \left[\sum_{e=1}^{n_{\mathrm{el}}} \boldsymbol{Z}_{\mathrm{d}}^{e\mathrm{T}} \left[\int_{\Omega_e} \tilde{\mathbf{B}}_{\mathrm{d}}^{e\mathrm{T}} \tilde{\mathbf{C}}_{\theta}^{e} \mathbf{N}_{\theta}^{e\mathrm{T}}\, \mathrm{d}V\right] \boldsymbol{Z}_{\theta}^{e}\right] \Delta\boldsymbol{\Theta} && (4.184)
\end{aligned}$$

based on

$$\mathsf{D}_{\boldsymbol{\Theta}^e}\, \mathbf{h}((\mathbf{C}, \theta, \mathbf{q}^{e}))[\Delta\boldsymbol{\Theta}^{e}] = \left\{\frac{\mathrm{d}\mathbf{h}}{\mathrm{d}\theta} + \frac{\mathrm{d}\mathbf{h}}{\mathrm{d}\mathbf{q}^{e}} \frac{\mathrm{d}\mathbf{q}^{e}}{\mathrm{d}\theta}\right\} \frac{\mathrm{d}\theta}{\mathrm{d}\boldsymbol{\Theta}^{e}} \Delta\boldsymbol{\Theta}^{e} = \tilde{\mathbf{C}}_{\theta}^{e} \mathbf{N}_{\theta}^{e\mathrm{T}} \Delta\boldsymbol{\Theta}^{e} \tag{4.185}$$

with $\theta = \mathbf{N}_{\theta}^{e\,\mathrm{T}} \boldsymbol{\Theta}^{e}$ and $\tilde{\mathbf{C}}_{\theta}^{e} = \left\{\frac{\mathrm{d}\mathbf{h}}{\mathrm{d}\theta} + \frac{\mathrm{d}\mathbf{h}}{\mathrm{d}\mathbf{q}^{e}} \frac{\mathrm{d}\mathbf{q}^{e}}{\mathrm{d}\theta}\right\}$. For the sake of brevity, we leave out the index h indicating a discretized quantity. The derivatives of the second Piola-Kirchhoff stress tensor with respect to the temperature θ and to the internal variables are given in Appendix A.6. With the short notation

$$\mathbf{k}_{\mathrm{U}\theta}^{e} = \int_{\Omega_e} \tilde{\mathbf{B}}_{\mathrm{d}}^{e\mathrm{T}} \tilde{\mathbf{C}}_{\theta}^{e} \mathbf{N}_{\theta}^{e\,\mathrm{T}}\, \mathrm{d}V \quad \in \mathbb{R}^{3n_{\mathrm{em}} \times n_{\mathrm{em}}} \tag{4.186}$$

the derivative $\mathrm{d}\boldsymbol{G}_\mathrm{u}/\,\mathrm{d}\boldsymbol{\Theta}$ can be formulated as

$$\frac{\mathrm{d}\boldsymbol{G}_\mathrm{u}}{\mathrm{d}\boldsymbol{\Theta}} = \sum_{e=1}^{n_\mathrm{el}} \boldsymbol{Z}_\mathrm{d}^{e\mathrm{T}} \mathbf{k}_{\mathrm{U}\theta}^{e} \boldsymbol{Z}_\theta^{e} \tag{4.187}$$

with the subscript θ referring to a differentiation with respect to the temperature.

Tangents of the Heat Equation

Having discussed the tangents of the mechanical part of (4.128), we will now proceed to address the tangents of the heat conduction equation. Grouping the summands of the heat conduction equation in reference configuration (3.34) as

$$\pi_\mathrm{c} = \int\limits_\Omega \varrho_\mathrm{R} c_\mathrm{d} \dot{\theta} \delta\theta \,\mathrm{d}V, \tag{4.188}$$

$$\pi_\mathrm{q} = -\int\limits_\Omega \boldsymbol{q}_\mathrm{R} \cdot \operatorname{Grad} \delta\theta \,\mathrm{d}V, \tag{4.189}$$

$$\pi_\mathrm{e} = \int\limits_{\partial_\mathrm{q}\Omega} f_\mathrm{q} \delta\theta \,\mathrm{d}A + \int\limits_{\partial_{\theta\mathrm{q}}\Omega} f_{\theta\mathrm{q}} \delta\theta \,\mathrm{d}A, \tag{4.190}$$

and

$$\pi_\mathrm{i} = -\int\limits_\Omega \varrho_\mathrm{R} (r + p + d) \delta\theta \,\mathrm{d}V, \tag{4.191}$$

where use of the Neumann-boundary conditions (3.9) and (3.10) is made, we write the resulting derivatives

$$\frac{\mathrm{d}\boldsymbol{G}_\theta}{\mathrm{d}\boldsymbol{U}} = \sum_{e=1}^{n_\mathrm{el}} \boldsymbol{Z}_\theta^{e\mathrm{T}} \left[\mathbf{k}_{\theta\,\mathrm{Uc}}^{e} + \mathbf{k}_{\theta\,\mathrm{Uq}}^{e} + \mathbf{k}_{\theta\,\mathrm{Ue}}^{e} + \mathbf{k}_{\theta\,\mathrm{Ui}}^{e} \right] \boldsymbol{Z}_\mathrm{d}^{e}, \tag{4.192}$$

$$\frac{\mathrm{d}\boldsymbol{G}_\theta}{\mathrm{d}\boldsymbol{\Theta}} = \sum_{e=1}^{n_\mathrm{el}} \boldsymbol{Z}_\theta^{e\mathrm{T}} \left[\mathbf{k}_{\theta\,\theta\,\mathrm{c}}^{e} + \mathbf{k}_{\theta\,\theta\,\mathrm{q}}^{e} + \mathbf{k}_{\theta\,\theta\,\mathrm{e}}^{e} + \mathbf{k}_{\theta\,\theta\,\mathrm{i}}^{e} \right] \boldsymbol{Z}_\theta^{e}. \tag{4.193}$$

π_c refers to heat storage, π_q to heat conduction, π_e to external heat supply and π_i to internal heat production.

Derivation of $\mathrm{d}\boldsymbol{G}_\theta/\,\mathrm{d}\boldsymbol{\Theta}$

Spatially discretizing (4.188) yields

$$\pi_\mathrm{c} = \delta\boldsymbol{\Theta}^\mathrm{T} \sum_{e=1}^{n_\mathrm{el}} \boldsymbol{Z}_\theta^{e\mathrm{T}} \left\{ \int\limits_{\Omega_e} \varrho_\mathrm{R} c_\mathrm{d}(\theta) \mathbf{N}_\theta^{e} \mathbf{N}_\theta^{e\mathrm{T}} \dot{\boldsymbol{\Theta}}^{e} \,\mathrm{d}V \right\}, \tag{4.194}$$

see also the first sum in (4.71). In order to derive the element stiffness contribution with respect to the temperature field, let us take a look at the Gateaux-derivative

$$
\begin{aligned}
&\mathsf{D}_{\boldsymbol{\Theta}}\,\pi_{\mathrm{c}}(\boldsymbol{\Theta})[\Delta\boldsymbol{\Theta}] \\
&= \delta\boldsymbol{\Theta}^{\mathrm{T}} \sum_{e=1}^{n_{\mathrm{el}}} \boldsymbol{Z}_{\theta}^{e\mathrm{T}} \\
&\left\{ \int\limits_{\Omega_e} \varrho_{\mathrm{R}} \left(\mathsf{D}_{\boldsymbol{\Theta}^e}\, c_{\mathrm{d}}(\theta)[\Delta\boldsymbol{\Theta}^e]\, \mathbf{N}_{\theta}^{e} \mathbf{N}_{\theta}^{e\mathrm{T}} \dot{\boldsymbol{\Theta}}^e \; + c_{\mathrm{d}}(\theta) \mathbf{N}_{\theta}^{e} \mathbf{N}_{\theta}^{e\mathrm{T}} \mathsf{D}_{\boldsymbol{\Theta}^e}\, \dot{\boldsymbol{\Theta}}^e(\boldsymbol{\Theta}^e)[\Delta\boldsymbol{\Theta}^e] \right) \mathrm{d}V \right\} && (4.195) \\
&= \delta\boldsymbol{\Theta}^{\mathrm{T}} \sum_{e=1}^{n_{\mathrm{el}}} \boldsymbol{Z}_{\theta}^{e\mathrm{T}} \left\{ \int\limits_{\Omega_e} \varrho_{\mathrm{R}} \left(\frac{\partial c_{\mathrm{d}}}{\partial\theta} \mathbf{N}_{\theta}^{e\mathrm{T}} \Delta\boldsymbol{\Theta}^e\, \mathbf{N}_{\theta}^{e} \dot{\theta} \; + \mathbf{N}_{\theta}^{e} \mathbf{N}_{\theta}^{e\mathrm{T}} \frac{c_{\mathrm{d}}(\theta)}{\Delta t_n a_{ii}} \Delta\boldsymbol{\Theta}^e \right) \mathrm{d}V \right\} && (4.196) \\
&= \delta\boldsymbol{\Theta}^{\mathrm{T}} \left[\sum_{e=1}^{n_{\mathrm{el}}} \boldsymbol{Z}_{\theta}^{e\mathrm{T}} \left[\int\limits_{\Omega_e} \varrho_{\mathrm{R}} \mathbf{N}_{\theta}^{e} \left(\frac{\partial c_{\mathrm{d}}}{\partial\theta}\, \dot{\theta} \; + \frac{c_{\mathrm{d}}(\theta)}{\Delta t_n a_{ii}} \right) \mathbf{N}_{\theta}^{e\mathrm{T}}\, \mathrm{d}V \right] \boldsymbol{Z}_{\theta}^{e} \right] \Delta\boldsymbol{\Theta} && (4.197)
\end{aligned}
$$

based on the relations

$$
\mathsf{D}_{\boldsymbol{\Theta}^e}\, c_{\mathrm{d}}(\theta)[\Delta\boldsymbol{\Theta}^e] = \frac{\partial c_{\mathrm{d}}}{\partial\theta} \mathbf{N}_{\theta}^{e\mathrm{T}} \Delta\boldsymbol{\Theta}^e \tag{4.198}
$$

and

$$
\mathsf{D}_{\boldsymbol{\Theta}^e}\, \dot{\boldsymbol{\Theta}}^e(\boldsymbol{\Theta}^e)[\Delta\boldsymbol{\Theta}^e] = \frac{\Delta\boldsymbol{\Theta}^e}{\Delta t_n a_{ii}} \tag{4.199}
$$

with

$$
\dot{\boldsymbol{\Theta}}^e = \boldsymbol{Z}_{\theta}^{e}\, \dot{\boldsymbol{\Theta}} + \overline{\boldsymbol{Z}}_{\theta}^{e}\, \dot{\overline{\boldsymbol{\Theta}}} = \boldsymbol{Z}_{\theta}^{e} \left\{ \frac{\boldsymbol{\Theta} - \boldsymbol{S}^{\boldsymbol{\Theta}}}{\Delta t_n\, a_{ii}} \right\} + \overline{\boldsymbol{Z}}_{\theta}^{e}\, \dot{\overline{\boldsymbol{\Theta}}}. \tag{4.200}
$$

In (4.200) the indices indicating the time-step and stage are omitted for brevity. As a result we are able to define the corresponding element stiffness contribution

$$
\begin{aligned}
\mathbf{k}_{\theta\,\theta\,\mathrm{c}}^{e} &= \int\limits_{\Omega_e} \varrho_{\mathrm{R}} \mathbf{N}_{\theta}^{e} \left(\frac{\partial c_{\mathrm{d}}}{\partial\theta} \dot{\theta} + \frac{c_{\mathrm{d}}}{\Delta t_n\, a_{ii}} \right) \mathbf{N}_{\theta}^{e\mathrm{T}}\, \mathrm{d}V \\
&= \int\limits_{\omega_e} \varrho_{\mathrm{R}} \frac{1}{J} \mathbf{N}_{\theta}^{e} \left(\frac{\partial c_{\mathrm{d}}}{\partial\theta} \dot{\theta} + \frac{c_{\mathrm{d}}}{\Delta t_n\, a_{ii}} \right) \mathbf{N}_{\theta}^{e\mathrm{T}}\, \mathrm{d}v.
\end{aligned}
$$

In addition, we also contemplate the Gateaux-derivative of π_{q} in direction of $\Delta\theta$

$$
\begin{aligned}
\mathsf{D}_{\theta}\,\pi_{\mathrm{q}}(\boldsymbol{u},\theta)[\Delta\theta] &= \int\limits_{\Omega} (\det\mathbf{F})\,\mathbf{F}^{-\mathrm{T}} \left(\frac{\partial\lambda}{\partial\theta} \Delta\theta\, \mathrm{Grad}\,\theta + \lambda\, \mathrm{Grad}\,\Delta\theta \right) \cdot \mathbf{F}^{-\mathrm{T}}\, \mathrm{Grad}\,\delta\theta\, \mathrm{d}V \\
&= \int\limits_{\omega} \left(\frac{\partial\lambda}{\partial\theta} \Delta\theta\, \mathrm{grad}\,\theta + \lambda\, \mathrm{grad}\,\Delta\theta \right) \cdot\, \mathrm{grad}\,\delta\theta\, \mathrm{d}v
\end{aligned}
$$

where (2.145) is employed in conjunction with (2.146). Spatial discretization yields

$$
\begin{aligned}
&\delta\boldsymbol{\Theta}^{\mathrm{T}} \sum_{e=1}^{n_{\mathrm{el}}} \boldsymbol{Z}_{\theta}^{e\mathrm{T}} \int\limits_{\omega_e} \begin{bmatrix} \mathbf{N}_{\theta}^{e\mathrm{T}}{}_{,x} \\ \mathbf{N}_{\theta}^{e\mathrm{T}}{}_{,y} \\ \mathbf{N}_{\theta}^{e\mathrm{T}}{}_{,z} \end{bmatrix}^{\mathrm{T}} \left\{ \tfrac{\partial\lambda}{\partial\theta} \mathbf{N}_{\theta}^{e\mathrm{T}} \Delta\boldsymbol{\Theta}^{e} \begin{Bmatrix} \theta_{,x} \\ \theta_{,y} \\ \theta_{,z} \end{Bmatrix} + \lambda \begin{bmatrix} \mathbf{N}_{\theta}^{e\mathrm{T}}{}_{,x} \\ \mathbf{N}_{\theta}^{e\mathrm{T}}{}_{,y} \\ \mathbf{N}_{\theta}^{e\mathrm{T}}{}_{,z} \end{bmatrix} \Delta\boldsymbol{\Theta}^{e} \right\} \mathrm{d}v \\
&= \delta\boldsymbol{\Theta}^{\mathrm{T}} \left[\sum_{e=1}^{n_{\mathrm{el}}} \boldsymbol{Z}_{\theta}^{e\mathrm{T}} \left[\int\limits_{\omega_e} \left[\mathbf{N}_{\theta}^{e}{}_{,x} \left\{ \tfrac{\partial\lambda}{\partial\theta} \theta_{,x} \mathbf{N}_{\theta}^{e\mathrm{T}} + \lambda \mathbf{N}_{\theta}^{e\mathrm{T}}{}_{,x} \right\} + \mathbf{N}_{\theta}^{e}{}_{,y} \left\{ \tfrac{\partial\lambda}{\partial\theta} \theta_{,y} \mathbf{N}_{\theta}^{e\mathrm{T}} + \lambda \mathbf{N}_{\theta}^{e\mathrm{T}}{}_{,y} \right\} \right.\right.\right. \\
&\qquad\qquad \left.\left.\left. + \mathbf{N}_{\theta}^{e}{}_{,z} \left\{ \tfrac{\partial\lambda}{\partial\theta} \theta_{,z} \mathbf{N}_{\theta}^{e\mathrm{T}} + \lambda \mathbf{N}_{\theta}^{e\mathrm{T}}{}_{,z} \right\} \right] \mathrm{d}v \right] \boldsymbol{Z}_{\theta}^{e} \right] \Delta\boldsymbol{\Theta}
\end{aligned}
$$

and then we can finally state the element stiffness contribution required in (4.193)

$$
\mathbf{k}_{\theta\,\theta\,\mathrm{q}}^{e} = \int\limits_{\omega_e} \left[\mathbf{N}_{\theta}^{e}{}_{,x} \left\{ \tfrac{\partial\lambda}{\partial\theta} \theta_{,x} \mathbf{N}_{\theta}^{e\mathrm{T}} + \lambda \mathbf{N}_{\theta}^{e\mathrm{T}}{}_{,x} \right\} + \mathbf{N}_{\theta}^{e}{}_{,y} \left\{ \tfrac{\partial\lambda}{\partial\theta} \theta_{,y} \mathbf{N}_{\theta}^{e\mathrm{T}} + \lambda \mathbf{N}_{\theta}^{e\mathrm{T}}{}_{,y} \right\} \right. \tag{4.201}
$$

$$
\left. + \mathbf{N}_{\theta}^{e}{}_{,z} \left\{ \tfrac{\partial\lambda}{\partial\theta} \theta_{,z} \mathbf{N}_{\theta}^{e\mathrm{T}} + \lambda \mathbf{N}_{\theta}^{e\mathrm{T}}{}_{,z} \right\} \right] \mathrm{d}v. \tag{4.202}
$$

In order to derive the element stiffness contributions resulting from the external heat supply, we derive the Gateaux-derivative of

$$
\pi_{\mathrm{e}} = \int\limits_{\partial_{\mathrm{q}}\omega} f_{\mathrm{q}} \delta\theta \,\mathrm{d}a + \int\limits_{\partial_{\theta\mathrm{q}}\omega} f_{\theta\mathrm{q}} \delta\theta \,\mathrm{d}a = \int\limits_{\Omega_{st}^{q}} \left(f_{\mathrm{q}} + f_{\theta\mathrm{q}} \right) \delta\theta \| \boldsymbol{x}_{,\xi} \times \boldsymbol{x}_{,\eta} \| \,\mathrm{d}\xi \,\mathrm{d}\eta \tag{4.203}
$$

in the direction of $\Delta\theta$

$$
\mathsf{D}_{\theta}\, \pi_{\mathrm{e}}(\boldsymbol{u}, \theta)[\Delta\theta] = \int\limits_{\Omega_{st}^{q}} \frac{\mathrm{d}f_{\theta\mathrm{q}}}{\mathrm{d}\theta} \Delta\theta \delta\theta \|\hat{\boldsymbol{n}}\| \,\mathrm{d}\xi \,\mathrm{d}\eta \tag{4.204}
$$

$$
= \delta\boldsymbol{\Theta}^{\mathrm{T}} \left[\sum_{e=1}^{n_{\mathrm{el}}} \boldsymbol{Z}_{\theta}^{e\mathrm{T}} \left[\int\limits_{\Omega_{st}^{q}} \mathbf{N}_{\theta}^{e} \mathbf{N}_{\theta}^{e\mathrm{T}} \frac{\mathrm{d}f_{\theta\mathrm{q}}}{\mathrm{d}\theta} \|\hat{\boldsymbol{n}}\| \,\mathrm{d}\xi \,\mathrm{d}\eta \right] \boldsymbol{Z}_{\theta}^{e} \right] \Delta\boldsymbol{\Theta} \tag{4.205}
$$

based on (4.165), and find

$$
\mathbf{k}_{\theta\,\theta\,\mathrm{e}}^{e} = \int\limits_{\Omega_{st}^{q}} \mathbf{N}_{\theta}^{e} \mathbf{N}_{\theta}^{e\mathrm{T}} \frac{\mathrm{d}f_{\theta\mathrm{q}}}{\mathrm{d}\theta} \|\hat{\boldsymbol{n}}\| \,\mathrm{d}\xi \,\mathrm{d}\eta. \tag{4.206}
$$

Summing up the thermoelastic coupling term and the inelastic dissipation $w = p + d$, the derivation of the coupling terms with respect to the temperature reads

$$
\begin{aligned}
&\mathsf{D}_\theta\, \pi_{\mathrm{i}}(\mathbf{C}, \mathbf{C}_{\mathrm{v}}, \theta)[\Delta\theta] \\
&= -\int\limits_{\Omega} \varrho_{\mathrm{R}} \mathsf{D}_\theta\, w(\mathbf{C}, \mathbf{C}_{\mathrm{v}}, \theta)[\Delta\theta]\delta\theta \,\mathrm{d}V \\
&= -\int\limits_{\Omega} \varrho_{\mathrm{R}} \frac{\mathrm{D}w}{\mathrm{D}\theta} \Delta\theta\delta\theta \,\mathrm{d}V,
\end{aligned}
\tag{4.207}
$$

where the short notation

$$
\frac{\mathrm{D}w}{\mathrm{D}\theta} = \frac{\partial w}{\partial \theta} + \frac{\partial w}{\partial \dot{\theta}} \frac{1}{\Delta t_n\, a_{ii}} + \left\{\frac{\partial \mathbf{q}^e}{\partial \theta}\right\}^{\mathrm{T}} \left\{\frac{\partial w}{\partial \mathbf{q}^e}\right\}
\tag{4.208}
$$

is employed. $\mathbf{q}^e$ denotes the internal variables which are evaluated at Gauss point level. Spatially discretizing (4.207) results in

$$
-\int\limits_{\Omega} \varrho_{\mathrm{R}} \frac{\mathrm{D}w}{\mathrm{D}\theta} \Delta\theta\delta\theta \,\mathrm{d}V = -\delta\boldsymbol{\Theta}^{\mathrm{T}} \left[\sum_{e=1}^{n_{\mathrm{el}}} \boldsymbol{Z}_\theta^{e\mathrm{T}} \left[\int\limits_{\Omega_e} \varrho_{\mathrm{R}} \frac{\mathrm{D}w}{\mathrm{D}\theta} \mathbf{N}_\theta^e \mathbf{N}_\theta^{e\mathrm{T}} \,\mathrm{d}V \right] \boldsymbol{Z}_\theta^e \right] \Delta\boldsymbol{\Theta}.
\tag{4.209}
$$

The required tangents are given in Appendix A.6.4 and A.6.5. Now the element stiffness contribution reads

$$
\mathbf{k}_{\theta\,\theta\,\mathrm{i}}^e = -\int\limits_{\Omega_e} \varrho_{\mathrm{R}} \frac{\mathrm{D}w}{\mathrm{D}\theta} \mathbf{N}_\theta^e \mathbf{N}_\theta^{e\mathrm{T}} \,\mathrm{d}V = -\int\limits_{\omega_e} \frac{\varrho_{\mathrm{R}}}{J} \frac{\mathrm{D}w}{\mathrm{D}\theta} \mathbf{N}_\theta^e \mathbf{N}_\theta^{e\mathrm{T}} \,\mathrm{d}v.
\tag{4.210}
$$

Derivation of $\mathrm{d}\boldsymbol{G}_\theta / \,\mathrm{d}\boldsymbol{U}$

Even though the heat storage is usually deformation-dependent, in many cases $c_{\mathrm{d}} = c_{\mathrm{d}}(\theta)$ is assumed, resulting in

$$
\mathsf{D}_{\boldsymbol{u}}\, \pi_{\mathrm{c}}(\boldsymbol{\Theta})[\Delta\boldsymbol{u}] = \boldsymbol{0}.
\tag{4.211}
$$

The element stiffness contribution accordingly reads

$$
\mathbf{k}_{\theta\,\mathrm{U}\,\mathrm{c}}^e = \mathbf{0}.
\tag{4.212}
$$

Inserting (2.145) with (2.146) into (4.189) yields

$$
\pi_{\mathrm{q}} = \int\limits_{\Omega} \lambda(\det \mathbf{F}) \mathbf{F}^{-1} \mathbf{F}^{-\mathrm{T}} \,\mathrm{Grad}\, \theta \cdot \,\mathrm{Grad}\, \delta\theta \,\mathrm{d}V
\tag{4.213}
$$

$$
= \int\limits_{\Omega} \lambda(\det \mathbf{F}) \mathbf{F}^{-\mathrm{T}} \,\mathrm{Grad}\, \theta \cdot \mathbf{F}^{-\mathrm{T}} \,\mathrm{Grad}\, \delta\theta \,\mathrm{d}V.
\tag{4.214}
$$

With the identities

$$\operatorname{grad}\Delta\boldsymbol{u} = (\operatorname{Grad}\Delta\boldsymbol{u})\,\mathbf{F}^{-1} = \Delta\mathbf{H}\mathbf{F}^{-1}, \tag{4.215}$$

$$\operatorname{grad}\theta = \mathbf{F}^{-\mathrm{T}}\operatorname{Grad}\theta, \tag{4.216}$$

and $\mathbf{F}^{-\mathrm{T}}\cdot\Delta\mathbf{H} = \mathbf{F}^{-\mathrm{T}}\cdot(\operatorname{grad}\Delta\boldsymbol{u})\,\mathbf{F} = \mathbf{1}\cdot\operatorname{grad}\Delta\boldsymbol{u} = \operatorname{tr}(\operatorname{grad}\Delta\boldsymbol{u}) = \operatorname{div}\Delta\boldsymbol{u}$ the Gateaux-derivative reads

$$\begin{aligned}\mathsf{D}_{\boldsymbol{u}}\,\pi_{\mathrm{q}}(\boldsymbol{u},\theta)[\Delta\boldsymbol{u}] = &\int\limits_{\Omega}\lambda\,(\det\mathbf{F})\,\mathbf{F}^{-\mathrm{T}}\operatorname{Grad}\theta\cdot\mathbf{F}^{-\mathrm{T}}\operatorname{Grad}\delta\theta\left(\mathbf{F}^{-\mathrm{T}}\cdot\Delta\mathbf{H}\right)\mathrm{d}V\\ &-\int\limits_{\Omega}\lambda\,(\det\mathbf{F})\,\mathbf{F}^{-\mathrm{T}}\Delta\mathbf{H}^{\mathrm{T}}\mathbf{F}^{-\mathrm{T}}\operatorname{Grad}\theta\cdot\mathbf{F}^{-\mathrm{T}}\operatorname{Grad}\delta\theta\,\mathrm{d}V\\ &-\int\limits_{\Omega}\lambda\,(\det\mathbf{F})\,\mathbf{F}^{-\mathrm{T}}\operatorname{Grad}\theta\cdot\mathbf{F}^{-\mathrm{T}}\Delta\mathbf{H}^{\mathrm{T}}\mathbf{F}^{-\mathrm{T}}\operatorname{Grad}\delta\theta\,\mathrm{d}V,\end{aligned}$$

based on

$$\mathsf{D}_{\boldsymbol{u}}\,\det\mathbf{F}(\boldsymbol{u})[\Delta\mathbf{H}] = (\det\mathbf{F})\,\mathbf{F}^{-\mathrm{T}}\cdot\Delta\mathbf{H}, \tag{4.217}$$

$$\mathsf{D}_{\boldsymbol{u}}\,\mathbf{F}^{-\mathrm{T}}(\boldsymbol{u})[\Delta\mathbf{H}] = -\mathbf{F}^{-\mathrm{T}}\Delta\mathbf{H}^{\mathrm{T}}\mathbf{F}^{-\mathrm{T}}. \tag{4.218}$$

This can be expressed by quantities operating on the current configuration yielding

$$\mathsf{D}_{\boldsymbol{u}}\,\pi_{\mathrm{q}}(\boldsymbol{u},\theta)[\Delta\boldsymbol{u}] = \int\limits_{\omega}\lambda\operatorname{grad}\theta\cdot\operatorname{grad}\delta\theta\;(\operatorname{div}\Delta\boldsymbol{u})\,\mathrm{d}v \tag{4.219}$$

$$-\int\limits_{\omega}\lambda\,(\operatorname{grad}\Delta\boldsymbol{u})\operatorname{grad}\delta\theta\cdot\operatorname{grad}\theta\,\mathrm{d}v \tag{4.220}$$

$$-\int\limits_{\omega}\lambda\,(\operatorname{grad}\Delta\boldsymbol{u})\operatorname{grad}\theta\cdot\operatorname{grad}\delta\theta\,\mathrm{d}v. \tag{4.221}$$

Spatially discretizing (4.219) yields

$$\int\limits_{\omega}\lambda\begin{Bmatrix}\delta\theta,_x\\ \delta\theta,_y\\ \delta\theta,_z\end{Bmatrix}^{\mathrm{T}}\begin{Bmatrix}\theta,_x\\ \theta,_y\\ \theta,_z\end{Bmatrix}(\Delta u_x,_x+\Delta u_y,_y+\Delta u_z,_z)\,\mathrm{d}v \tag{4.222}$$

$$= \delta\boldsymbol{\Theta}^{\mathrm{T}}\left[\sum_{e=1}^{n_{\mathrm{el}}}\boldsymbol{Z}_{\theta}^{e\mathrm{T}}\left[\int\limits_{\omega_e}\lambda\begin{bmatrix}\mathsf{N}_{\theta}^{e\,\mathrm{T}},_x\\ \mathsf{N}_{\theta}^{e\,\mathrm{T}},_y\\ \mathsf{N}_{\theta}^{e\,\mathrm{T}},_z\end{bmatrix}^{\mathrm{T}}\begin{Bmatrix}\theta,_x\\ \theta,_y\\ \theta,_z\end{Bmatrix}\left(\mathsf{N}_{\mathrm{d}}^{e1\,\mathrm{T}},_x+\mathsf{N}_{\mathrm{d}}^{e2\,\mathrm{T}},_y+\mathsf{N}_{\mathrm{d}}^{e3\,\mathrm{T}},_z\right)\mathrm{d}v\right]\boldsymbol{Z}_{\mathrm{d}}^{e}\right]\Delta\mathbf{u} \tag{4.223}$$

$$\begin{aligned}&= \delta\boldsymbol{\Theta}^{\mathrm{T}}\left[\sum_{e=1}^{n_{\mathrm{el}}}\boldsymbol{Z}_{\theta}^{e\mathrm{T}}\right.\\ &\left.\left[\int\limits_{\omega_e}\lambda\,(\theta,_x\,\mathsf{N}_{\theta}^{e},_x+\theta,_y\,\mathsf{N}_{\theta}^{e},_y+\theta,_z\,\mathsf{N}_{\theta}^{e},_z)\left(\mathsf{N}_{\mathrm{d}}^{e1\,\mathrm{T}},_x+\mathsf{N}_{\mathrm{d}}^{e2\,\mathrm{T}},_y+\mathsf{N}_{\mathrm{d}}^{e3\,\mathrm{T}},_z\right)\mathrm{d}v\right]\boldsymbol{Z}_{\mathrm{d}}^{e}\right]\Delta\boldsymbol{u}\end{aligned} \tag{4.224}$$

based on

$$\mathbf{N}^{e}_{\mathrm{d}},_{j} = \begin{bmatrix} \mathbf{N}^{e1\,\mathrm{T}}_{\mathrm{d}},_{j} \\ \mathbf{N}^{e2\,\mathrm{T}}_{\mathrm{d}},_{j} \\ \mathbf{N}^{e3\,\mathrm{T}}_{\mathrm{d}},_{j} \end{bmatrix} \quad \text{with} \quad \mathbf{N}^{e\,i}_{\mathrm{d}},_{j} = \begin{bmatrix} \mathbf{N}^{e\,i}_{\mathrm{d}\,1},_{j} \\ \vdots \\ \mathbf{N}^{e\,i}_{\mathrm{d}\,n_{\mathrm{em}}},_{j} \end{bmatrix} \in \mathbb{R}^{3n_{\mathrm{em}}} \quad \text{for} \quad i = 1, 2, 3 \tag{4.225}$$

and

$$\mathbf{N}^{e\,1\,\mathrm{T}}_{\mathrm{d}\,a},_{j} = \left\{ n^{e}_{a,j} \quad 0 \quad 0 \right\}, \quad \mathbf{N}^{e\,2\,\mathrm{T}}_{\mathrm{d}\,a},_{j} = \left\{ 0 \quad n^{e}_{a,j} \quad 0 \right\} \quad \text{and} \quad \mathbf{N}^{e\,3\,\mathrm{T}}_{\mathrm{d}\,a},_{j} = \left\{ 0 \quad 0 \quad n^{e}_{a,j} \right\} \tag{4.226}$$

with $a = 1, ..., n_{\mathrm{em}}$. $()_{,j}$ denotes a derivative with respect to x, y or z. Accordingly, the stiffness contribution can be expressed by

$$\mathbf{k}^{e}_{\theta\,\mathrm{U\,q\,1}} = \int\limits_{\omega_e} \lambda \left(\theta,_{x} \mathbf{N}^{e}_{\theta},_{x} + \theta,_{y} \mathbf{N}^{e}_{\theta},_{y} \, \theta,_{z} \mathbf{N}^{e}_{\theta},_{z}\right) \left(\mathbf{N}^{1\,\mathrm{T}}_{\mathrm{d}},_{y} + \mathbf{N}^{2\,\mathrm{T}}_{\mathrm{d}},_{y} + \mathbf{N}^{3\,\mathrm{T}}_{\mathrm{d}},_{z}\right) \mathrm{d}v. \tag{4.227}$$

The approximation of (4.220) yields

$$\begin{aligned}
&\int\limits_{\omega} \lambda \, \mathrm{grad}^{\mathrm{T}} \delta\theta \left(\mathrm{grad}^{\mathrm{T}} \Delta\mathbf{u}\right) \mathrm{grad}\,\theta \, \mathrm{d}v \\
&= \delta\boldsymbol{\Theta}^{\mathrm{T}} \sum_{e=1}^{n_{\mathrm{el}}} \boldsymbol{Z}^{e\mathrm{T}}_{\theta} \left[\int\limits_{\omega_e} \lambda \begin{bmatrix} \mathbf{N}^{e\mathrm{T}}_{\theta},_{x} \\ \mathbf{N}^{e\mathrm{T}}_{\theta},_{y} \\ \mathbf{N}^{e\mathrm{T}}_{\theta},_{z} \end{bmatrix}^{\mathrm{T}} \left[\begin{bmatrix} \mathbf{N}^{e\,1\mathrm{T}}_{\mathrm{d}},_{x} \\ \mathbf{N}^{e\,1\mathrm{T}}_{\mathrm{d}},_{y} \\ \mathbf{N}^{e\,1\mathrm{T}}_{\mathrm{d}},_{z} \end{bmatrix} \Delta\mathbf{u}^{e} \begin{bmatrix} \mathbf{N}^{e\,2\mathrm{T}}_{\mathrm{d}},_{x} \\ \mathbf{N}^{e\,2\mathrm{T}}_{\mathrm{d}},_{y} \\ \mathbf{N}^{e\,2\mathrm{T}}_{\mathrm{d}},_{z} \end{bmatrix} \Delta\mathbf{u}^{e} \begin{bmatrix} \mathbf{N}^{e\,3\mathrm{T}}_{\mathrm{d}},_{x} \\ \mathbf{N}^{e\,3\mathrm{T}}_{\mathrm{d}},_{y} \\ \mathbf{N}^{e\,3\mathrm{T}}_{\mathrm{d}},_{z} \end{bmatrix} \Delta\mathbf{u}^{e} \right] \begin{Bmatrix} \theta,_{x} \\ \theta,_{y} \\ \theta,_{z} \end{Bmatrix} \mathrm{d}v \right] \\
&= \delta\boldsymbol{\Theta}^{\mathrm{T}} \sum_{e=1}^{n_{\mathrm{el}}} \boldsymbol{Z}^{e\mathrm{T}}_{\theta} \left[\int\limits_{\omega_e} \lambda \begin{bmatrix} \mathbf{N}^{e\mathrm{T}}_{\theta},_{x} \\ \mathbf{N}^{e\mathrm{T}}_{\theta},_{y} \\ \mathbf{N}^{e\mathrm{T}}_{\theta},_{z} \end{bmatrix}^{\mathrm{T}} \begin{Bmatrix} \mathbf{N}^{e\,1\mathrm{T}}_{\mathrm{d}},_{x} \Delta\mathbf{u}^{e}\theta,_{x} + \mathbf{N}^{e\,2\mathrm{T}}_{\mathrm{d}},_{x} \Delta\mathbf{u}^{e}\theta,_{y} + \mathbf{N}^{e\,3\mathrm{T}}_{\mathrm{d}},_{x} \Delta\mathbf{u}^{e}\theta,_{z} \\ \mathbf{N}^{e\,1\mathrm{T}}_{\mathrm{d}},_{y} \Delta\mathbf{u}^{e}\theta,_{x} + \mathbf{N}^{e\,2\mathrm{T}}_{\mathrm{d}},_{y} \Delta\mathbf{u}^{e}\theta,_{y} + \mathbf{N}^{e\,3\mathrm{T}}_{\mathrm{d}},_{y} \Delta\mathbf{u}^{e}\theta,_{z} \\ \mathbf{N}^{e\,1\mathrm{T}}_{\mathrm{d}},_{z} \Delta\mathbf{u}^{e}\theta,_{x} + \mathbf{N}^{e\,2\mathrm{T}}_{\mathrm{d}},_{z} \Delta\mathbf{u}^{e}\theta,_{y} + \mathbf{N}^{e\,3\mathrm{T}}_{\mathrm{d}},_{z} \Delta\mathbf{u}^{e}\theta,_{z} \end{Bmatrix} \mathrm{d}v \right] \\
&= \delta\boldsymbol{\Theta}^{\mathrm{T}} \left[\sum_{e=1}^{n_{\mathrm{el}}} \boldsymbol{Z}^{e\mathrm{T}}_{\theta} \left[\int\limits_{\omega_e} \lambda \begin{bmatrix} \mathbf{N}^{e\mathrm{T}}_{\theta},_{x} \\ \mathbf{N}^{e\mathrm{T}}_{\theta},_{y} \\ \mathbf{N}^{e\mathrm{T}}_{\theta},_{z} \end{bmatrix}^{\mathrm{T}} \begin{Bmatrix} \mathbf{N}^{e\,1\mathrm{T}}_{\mathrm{d}},_{x} \theta,_{x} + \mathbf{N}^{e\,2\mathrm{T}}_{\mathrm{d}},_{x} \theta,_{y} + \mathbf{N}^{e\,3\mathrm{T}}_{\mathrm{d}},_{x} \theta,_{z} \\ \mathbf{N}^{e\,1\mathrm{T}}_{\mathrm{d}},_{y} \theta,_{x} + \mathbf{N}^{e\,2\mathrm{T}}_{\mathrm{d}},_{y} \theta,_{y} + \mathbf{N}^{e\,3\mathrm{T}}_{\mathrm{d}},_{y} \theta,_{z} \\ \mathbf{N}^{e\,1\mathrm{T}}_{\mathrm{d}},_{z} \theta,_{x} + \mathbf{N}^{e\,2\mathrm{T}}_{\mathrm{d}},_{z} \theta,_{y} + \mathbf{N}^{e\,3\mathrm{T}}_{\mathrm{d}},_{z} \theta,_{z} \end{Bmatrix} \mathrm{d}v \right] \boldsymbol{Z}^{e}_{\mathrm{d}} \right] \Delta\mathbf{u} \\
&= \delta\boldsymbol{\Theta}^{\mathrm{T}} \left[\sum_{e=1}^{n_{\mathrm{el}}} \boldsymbol{Z}^{e\mathrm{T}}_{\theta} \left[\int\limits_{\omega_e} \mathbf{k}^{e}_{\theta\,\mathrm{U\,q\,2}} \, \mathrm{d}v \right] \boldsymbol{Z}^{e}_{\mathrm{d}} \right] \Delta\mathbf{u}.
\end{aligned}$$

The corresponding contribution of the element stiffness matrix is given by

$$\mathbf{k}^{e}_{\theta\,\mathrm{U\,q\,2}} = \lambda \sum_{i=1}^{3} n^{e}_{k,i} \hat{\mathbf{b}}_{ij} \in \mathbb{R}^{n_{\mathrm{em}} \times 3n_{\mathrm{em}}} \quad \text{for} \quad k = 1, ..., n_{\mathrm{em}} \quad \text{and} \quad j = 1, ..., n_{\mathrm{em}} \tag{4.228}$$

with

$$\hat{\mathbf{b}}_{ij} = \sum_{k=1}^{3} \mathbf{N}^{e\,k\,\mathrm{T}}_{\mathrm{d}\,j},_{i} \theta,_{k} \qquad \in \mathbb{R}^{1\times 3}. \tag{4.229}$$

$\mathbf{N}_{\mathrm{d}j}^{e\,k\,\mathrm{T}},_i$ is given in (4.226) and $(.)\,,_i$ for $i = 1, 2, 3$ denotes a derivative with respect to the coordinates x, y and z. The components of the shape functions associated with the coefficients of the temperature field are denoted by n^e_k in order to simplify the notation and, accordingly, the matrix of the shape functions reads

$$\mathbf{N}_{\theta}^{e\mathrm{T}},_i = \left\{ n^e_{a,i} \quad \dots \quad n^e_{n_{\mathrm{em}},i} \right\}, \tag{4.230}$$

cf. (4.35). Eq. (4.221) results in

$$\begin{aligned}
&\int\limits_{\omega} \lambda \, \mathrm{grad}^{\mathrm{T}} \, \delta\theta \, (\mathrm{grad} \, \Delta\mathbf{u}) \, \mathrm{grad} \, \theta \, \mathrm{d}v \\
&= \delta\boldsymbol{\Theta}^{\mathrm{T}} \sum_{e=1}^{n_{\mathrm{el}}} \boldsymbol{Z}_{\theta}^{e\mathrm{T}} \left[\int\limits_{\omega_e} \lambda \begin{bmatrix} \mathbf{N}_{\theta}^{e\mathrm{T}},_x \\ \mathbf{N}_{\theta}^{e\mathrm{T}},_y \\ \mathbf{N}_{\theta}^{e\mathrm{T}},_z \end{bmatrix}^{\mathrm{T}} \left[\begin{bmatrix} \mathbf{N}_{\mathrm{d}}^{e\,1\mathrm{T}},_x \\ \mathbf{N}_{\mathrm{d}}^{e\,2\mathrm{T}},_x \\ \mathbf{N}_{\mathrm{d}}^{e\,3\mathrm{T}},_x \end{bmatrix} \Delta\mathbf{u}^e \begin{bmatrix} \mathbf{N}_{\mathrm{d}}^{e\,1\mathrm{T}},_y \\ \mathbf{N}_{\mathrm{d}}^{e\,2\mathrm{T}},_y \\ \mathbf{N}_{\mathrm{d}}^{e\,3\mathrm{T}},_y \end{bmatrix} \Delta\mathbf{u}^e \begin{bmatrix} \mathbf{N}_{\mathrm{d}}^{e\,1\mathrm{T}},_z \\ \mathbf{N}_{\mathrm{d}}^{e\,2\mathrm{T}},_z \\ \mathbf{N}_{\mathrm{d}}^{e\,3\mathrm{T}},_z \end{bmatrix} \Delta\mathbf{u}^e \right] \begin{Bmatrix} \theta,_x \\ \theta,_y \\ \theta,_z \end{Bmatrix} \mathrm{d}v \right] \\
&= \delta\boldsymbol{\Theta}^{\mathrm{T}} \sum_{e=1}^{n_{\mathrm{el}}} \boldsymbol{Z}_{\theta}^{e\mathrm{T}} \left[\int\limits_{\omega_e} \lambda \begin{bmatrix} \mathbf{N}_{\theta}^{e\mathrm{T}},_x \\ \mathbf{N}_{\theta}^{e\mathrm{T}},_y \\ \mathbf{N}_{\theta}^{e\mathrm{T}},_z \end{bmatrix}^{\mathrm{T}} \begin{Bmatrix} \mathbf{N}_{\mathrm{d}}^{e\,1\mathrm{T}},_x \Delta\mathbf{u}^e\theta,_x + \mathbf{N}_{\mathrm{d}}^{e\,1\mathrm{T}},_y \Delta\mathbf{u}^e\theta,_y + \mathbf{N}_{\mathrm{d}}^{e\,1\mathrm{T}},_z \Delta\mathbf{u}^e\theta,_z \\ \mathbf{N}_{\mathrm{d}}^{e\,2\mathrm{T}},_x \Delta\mathbf{u}^e\theta,_x + \mathbf{N}_{\mathrm{d}}^{e\,2\mathrm{T}},_y \Delta\mathbf{u}^e\theta,_y + \mathbf{N}_{\mathrm{d}}^{e\,2\mathrm{T}},_z \Delta\mathbf{u}^e\theta,_z \\ \mathbf{N}_{\mathrm{d}}^{e\,3\mathrm{T}},_x \Delta\mathbf{u}^e\theta,_x + \mathbf{N}_{\mathrm{d}}^{e\,3\mathrm{T}},_y \Delta\mathbf{u}^e\theta,_y + \mathbf{N}_{\mathrm{d}}^{e\,3\mathrm{T}},_z \Delta\mathbf{u}^e\theta,_z \end{Bmatrix} \mathrm{d}v \right] \\
&= \delta\boldsymbol{\Theta}^{\mathrm{T}} \left[\sum_{e=1}^{n_{\mathrm{el}}} \boldsymbol{Z}_{\theta}^{e\mathrm{T}} \left[\int\limits_{\omega_e} \lambda \begin{bmatrix} \mathbf{N}_{\theta}^{e\mathrm{T}},_x \\ \mathbf{N}_{\theta}^{e\mathrm{T}},_y \\ \mathbf{N}_{\theta}^{e\mathrm{T}},_z \end{bmatrix}^{\mathrm{T}} \begin{Bmatrix} \mathbf{N}_{\mathrm{d}}^{e\,1\mathrm{T}},_x \theta,_x + \mathbf{N}_{\mathrm{d}}^{e\,1\mathrm{T}},_y \theta,_y + \mathbf{N}_{\mathrm{d}}^{e\,1\mathrm{T}},_z \theta,_z \\ \mathbf{N}_{\mathrm{d}}^{e\,2\mathrm{T}},_x \theta,_x + \mathbf{N}_{\mathrm{d}}^{e\,2\mathrm{T}},_y \theta,_y + \mathbf{N}_{\mathrm{d}}^{e\,2\mathrm{T}},_z \theta,_z \\ \mathbf{N}_{\mathrm{d}}^{e\,3\mathrm{T}},_x \theta,_x + \mathbf{N}_{\mathrm{d}}^{e\,3\mathrm{T}},_y \theta,_y + \mathbf{N}_{\mathrm{d}}^{e\,3\mathrm{T}},_z \theta,_z \end{Bmatrix} \Delta\mathbf{u}^e \, \mathrm{d}v \right] \boldsymbol{Z}_{\mathrm{d}}^{e} \right] \Delta\mathbf{u} \\
&= \delta\boldsymbol{\Theta}^{\mathrm{T}} \left[\sum_{e=1}^{n_{\mathrm{el}}} \boldsymbol{Z}_{\theta}^{e\mathrm{T}} \left[\int\limits_{\omega_e} \mathbf{k}_{\theta\,\mathrm{U\,q\,3}}^{e} \, \mathrm{d}v \right] \boldsymbol{Z}_{\mathrm{d}}^{e} \right] \Delta\mathbf{u}.
\end{aligned}$$

We write the corresponding contribution of the element stiffness matrix as

$$\mathbf{k}_{\theta\,\mathrm{U\,q\,3}}^{e} = \lambda \sum_{i=1}^{3} n^e_{k,i} \bar{\mathbf{b}}_{ij} \in \mathbb{R}^{n_{\mathrm{em}} \times 3 n_{\mathrm{em}}} \quad \text{for} \quad k = 1, \dots, n_{\mathrm{em}} \quad \text{and} \quad j = 1, \dots, n_{\mathrm{em}} \tag{4.231}$$

with

$$\bar{\mathbf{b}}_{ij} = \sum_{k=1}^{3} \mathbf{N}_{\mathrm{d}j}^{e\,i\,\mathrm{T}},_k \theta,_k \qquad \in \mathbb{R}^{1\times 3}. \tag{4.232}$$

The tangent resulting from π_{q} with respect to an increment in the displacements $\Delta\boldsymbol{u}$ leads to the element stiffness contribution required in (4.192)

$$\mathbf{k}_{\theta\,\mathrm{Uq}}^{e} = \mathbf{k}_{\theta\,\mathrm{Uq1}}^{e} - \mathbf{k}_{\theta\,\mathrm{Uq2}}^{e} - \mathbf{k}_{\theta\,\mathrm{Uq3}}^{e}$$

with the stiffness contributions (4.227), (4.228) and (4.231).

Employing (4.176), (4.177) and (4.165), the Gateaux-derivative of (4.203) reads

$$
\begin{aligned}
&\mathsf{D}_\theta\, \pi_{\mathrm{e}}(\boldsymbol{u},\theta)[\Delta\boldsymbol{u}]\\
&= \int\limits_{\Omega^q_{st}} (f_{\mathrm{q}} + f_{\theta\mathrm{q}})\, \delta\theta \frac{1}{2\|\hat{\boldsymbol{n}}\|} \left(2\left(\Delta\boldsymbol{u},_\xi \times \boldsymbol{x},_\eta\right) \cdot \left(\boldsymbol{x},_\xi \times \boldsymbol{x},_\eta\right)\right.\\
&\qquad\qquad\qquad\qquad \left. +2\left(\boldsymbol{x},_\xi \times \Delta\boldsymbol{u},_\eta\right) \cdot \left(\boldsymbol{x},_\xi \times \boldsymbol{x},_\eta\right)\right) \mathrm{d}\xi\, \mathrm{d}\eta\\
&= \int\limits_{\Omega^q_{st}} (f_{\mathrm{q}} + f_{\theta\mathrm{q}})\, \delta\theta \frac{\hat{\boldsymbol{n}}}{\|\hat{\boldsymbol{n}}\|} \cdot \left(\boldsymbol{x},_\xi \times \Delta\boldsymbol{u},_\eta + \Delta\boldsymbol{u},_\xi \times \boldsymbol{x},_\eta\right) \mathrm{d}\xi\, \mathrm{d}\eta\\
&= \delta\boldsymbol{\Theta}^{\mathrm{T}} \left[\sum_{e=1}^{n_{\mathrm{el}}} \boldsymbol{Z}_\theta^{e\mathrm{T}} \left[\int\limits_{\Omega^q_{st}} (f_{\mathrm{q}} + f_{\theta\mathrm{q}})\, \mathbf{N}_\theta^e \left\{\frac{\hat{\boldsymbol{n}}}{\|\hat{\boldsymbol{n}}\|}\right\}^{\mathrm{T}} \left[\mathbf{M},_\eta \mathbf{N}_{\mathrm{d}}^e,_\xi - \mathbf{M},_\xi \mathbf{N}_{\mathrm{d}}^e,_\eta\right] \mathrm{d}\xi\, \mathrm{d}\eta\right] \boldsymbol{Z}_{\mathrm{d}}^e\right] \Delta\boldsymbol{u}
\end{aligned}
$$

and the element stiffness contribution accounting for the deformation dependence of the surface element $\mathrm{d}a$ reads

$$
\mathbf{k}^e_{\theta\,\mathrm{U\,e}} = \int\limits_{\Omega^q_{st}} (f_{\mathrm{q}} + f_{\theta\mathrm{q}})\, \mathbf{N}_\theta^e \left\{\frac{\hat{\boldsymbol{n}}}{\|\hat{\boldsymbol{n}}\|}\right\}^{\mathrm{T}} \left[\mathbf{M},_\eta \mathbf{N}_{\mathrm{d}}^e,_\xi - \mathbf{M},_\xi \mathbf{N}_{\mathrm{d}}^e,_\eta\right] \mathrm{d}\xi\, \mathrm{d}\eta. \tag{4.233}
$$

Next, we look at the internal heat production π_{i}. The derivative of the right Cauchy-Green tensor with respect to the displacement field

$$
\begin{aligned}
&\mathsf{D}_{\boldsymbol{u}}\, \mathbf{C}(\boldsymbol{u})[\Delta\boldsymbol{u}]\\
&= \operatorname{Grad}\Delta\boldsymbol{u} + \operatorname{Grad}^{\mathrm{T}}\Delta\boldsymbol{u} + \left(\operatorname{Grad}^{\mathrm{T}}\Delta\boldsymbol{u}\right)\operatorname{Grad}\boldsymbol{u} + \left(\operatorname{Grad}^{\mathrm{T}}\boldsymbol{u}\right)\operatorname{Grad}\Delta\boldsymbol{u}\\
&= \mathbf{F}^{\mathrm{T}}\operatorname{Grad}\Delta\boldsymbol{u} + \left(\operatorname{Grad}^{\mathrm{T}}\Delta\boldsymbol{u}\right)\mathbf{F}
\end{aligned} \tag{4.234}
$$

is expressed by means of the strain-displacement matrix

$$
\Delta\mathbf{C}^{e\,h} = 2\tilde{\mathbf{B}}^e_{\mathrm{d}}(\mathbf{u}^e(t),\mathbf{X})\; \Delta\mathbf{u}^e \tag{4.235}
$$

with

$$
\Delta\mathbf{C}^{e\,h} = \left\{\Delta C_{11}, \Delta C_{22}, \Delta C_{33}, 2\Delta C_{12}, 2\Delta C_{23}, 2\Delta C_{13}\right\}, \tag{4.236}
$$

cf. (4.150). The Gateaux-derivative of the internal heat production in the direction of an increment in the displacements reads

$$
\mathsf{D}_{\boldsymbol{u}}\, \pi_{\mathrm{i}}(\mathbf{C},\mathbf{C}_{\mathrm{v}},\theta)[\Delta\boldsymbol{u}] \tag{4.237}
$$

$$
= -\int\limits_{\Omega} \varrho_{\mathrm{R}} \mathsf{D}_{\boldsymbol{u}}\, w(\mathbf{C},\mathbf{C}_{\mathrm{v}},\theta)[\Delta\boldsymbol{u}]\delta\theta\, \mathrm{d}V \tag{4.238}
$$

$$
= -\delta\boldsymbol{\Theta}^{\mathrm{T}} \left\{\sum_{e=1}^{n_{\mathrm{el}}} \boldsymbol{Z}_\theta^{e\mathrm{T}} \left\{\int\limits_{\Omega_e} \varrho_{\mathrm{R}} \mathbf{N}_\theta^e \frac{\mathrm{D}w}{\mathrm{D}\mathbf{u}^e} \Delta\mathbf{u}^e\, \mathrm{d}V\right\}\right\}, \tag{4.239}
$$

$$
= -\delta\boldsymbol{\Theta}^{\mathrm{T}} \left[\sum_{e=1}^{n_{\mathrm{el}}} \boldsymbol{Z}_\theta^{e\mathrm{T}} \left[\int\limits_{\Omega_e} 2\varrho_{\mathrm{R}} \mathbf{N}_\theta^e \mathbf{w}_{\mathrm{c}}^{\mathrm{T}} \tilde{\mathbf{B}}^e_{\mathrm{d}}\, \mathrm{d}V\right] \boldsymbol{Z}_{\mathrm{d}}^e\right] \Delta\boldsymbol{u}, \tag{4.240}
$$

based on

$$\frac{\mathrm{D}w}{\mathrm{D}\mathbf{u}^e}\Delta\mathbf{u}^e = \left\{ \left\{\frac{\partial w}{\partial \mathbf{C}}\right\}^{\mathrm{T}} \left[\frac{\partial \mathbf{C}}{\partial \mathbf{U}}\right] + \left\{\frac{\mathrm{d}w}{\mathrm{d}\dot{\mathbf{C}}}\right\}^{\mathrm{T}} \left[\frac{\mathrm{d}\dot{\mathbf{C}}}{\mathrm{d}\mathbf{U}}\right] + \left\{\frac{\mathrm{d}w}{\mathrm{d}\mathbf{q}^e}\right\}^{\mathrm{T}} \left[\frac{\mathrm{d}\mathbf{q}^e}{\mathrm{d}\mathbf{C}}\right] \left[\frac{\mathrm{d}\mathbf{C}}{\mathrm{d}\mathbf{U}}\right] \right\} \Delta\mathbf{u}^e \tag{4.241}$$

$$= \left\{ 2\left\{\frac{\partial w}{\partial \mathbf{C}}\right\}^{\mathrm{T}} + 2\left\{\frac{\mathrm{d}w}{\mathrm{d}\dot{\mathbf{C}}}\right\}^{\mathrm{T}} \frac{1}{\Delta t_n a_{ii}} + 2\left\{\frac{\mathrm{d}w}{\mathrm{d}\mathbf{q}^e}\right\}^{\mathrm{T}} \left[\frac{\mathrm{d}\mathbf{q}^e}{\mathrm{d}\mathbf{C}}\right] \right\} \tilde{\mathbf{B}}^e_{\mathrm{d}} \Delta\mathbf{u}^e \tag{4.242}$$

$$= 2\mathbf{w}_{\mathrm{c}}^{\mathrm{T}} \tilde{\mathbf{B}}^e_{\mathrm{d}} \Delta\mathbf{u}^e \tag{4.243}$$

with

$$\mathbf{w}_{\mathrm{c}} = \frac{\partial w}{\partial \mathbf{C}} + \frac{1}{\Delta t_i a_{ii}} \frac{\mathrm{d}w}{\mathrm{d}\dot{\mathbf{C}}} + \left[\frac{\mathrm{d}\mathbf{q}^e}{\mathrm{d}\mathbf{C}}\right]^{\mathrm{T}} \left\{\frac{\mathrm{d}w}{\mathrm{d}\mathbf{q}^e}\right\} \qquad \mathbf{w}_{\mathrm{c}} \in \mathbb{R}^6. \tag{4.244}$$

The temporal derivative of the right Cauchy-Green tensor is expressed by means of

$$\dot{\mathbf{C}} = 2\tilde{\mathbf{B}}^e_{\mathrm{d}} \dot{\mathbf{u}}^e = 2\tilde{\mathbf{B}}^e_{\mathrm{d}} \left\{ \boldsymbol{Z}^e_{\mathrm{d}} \dot{\boldsymbol{U}} + \overline{\boldsymbol{Z}}^e_{\mathrm{d}} \dot{\overline{\boldsymbol{U}}} \right\} = 2\tilde{\mathbf{B}}^e_{\mathrm{d}} \left\{ \boldsymbol{Z}^e_{\mathrm{d}} \left\{ \frac{\boldsymbol{U}_{ni} - \boldsymbol{S}^u_{ni}}{\Delta t_n\, a_{ii}} \right\} + \overline{\boldsymbol{Z}}^e_{\mathrm{d}} \dot{\overline{\boldsymbol{U}}} \right\} \tag{4.245}$$

and its derivative with respect to the displacements reads

$$\frac{\mathrm{d}\dot{\mathbf{C}}}{\mathrm{d}\boldsymbol{U}_{ni}} = \frac{2}{\Delta t a_{ii}} \tilde{\mathbf{B}}^e_{\mathrm{d}}. \tag{4.246}$$

Thus, the element stiffness contribution reads

$$\mathbf{k}^e_{\theta\,\mathrm{U\,i}} = -\int\limits_{\Omega_e} 2\varrho_{\mathrm{R}} \mathbf{N}^e_\theta \mathbf{w}_{\mathrm{c}}^{\mathrm{T}} \tilde{\mathbf{B}}^e_{\mathrm{d}}\, \mathrm{d}V. \tag{4.247}$$

Stress Algorithm

Within the framework of the Multilevel-Newton algorithm the derivatives of the internal variables with respect to the right Cauchy-Green tensor $\mathrm{d}\mathbf{q}/\,\mathrm{d}\mathrm{C}$, and the derivative for the temperature $\mathrm{d}\mathbf{q}/\,\mathrm{d}\theta$, required in (4.138) and (4.185), respectively, are computed at local level as indicated in (4.129). It is therefore necessary to solve a system of linear equations with 7 right-hand sides at each Gauss point. We do not adopt the approach of reducing the stress algorithm for computing three unknowns, see (Hartmann, 2003). Besides these dervatives, we also look for the internal variables required for evaluating the discretized weak form of the balance of linear momentum, see (4.128), which depends on the internal variables via the stress state, see (4.59). It is now necessary to solve the system of nonlinear equations (4.103) for the internal variables. We deal with the solution of (4.103) using the Newton-Raphson algorithm below. For the sake of brevity, we omit the indices indicating the time-step and stage. Since the internal variables need to be determined for given displacements and temperatures, we assume that $\mathbf{V}$ is known. In order to solve the system of nonlinear equations

$$\mathbf{L}(\mathbf{V}, \mathbf{Q}^e) = \boldsymbol{0}, \tag{4.248}$$

L is linearized according to Taylor's series

$$\mathsf{L}(\mathsf{V}, \mathsf{Q}^{e\,(k)}) + \left[\frac{\mathrm{d}\mathsf{L}}{\mathrm{d}\mathsf{Q}^{e}}\right]\Bigg|_{\mathsf{Q}^{e}=\mathsf{Q}^{e\,(k)}} \Delta\mathsf{Q}^{e\,(k)} = \boldsymbol{0}. \tag{4.249}$$

Terms of higher order are disregarded, yielding a system of linear equations

$$\left[\frac{\mathrm{d}\mathsf{L}}{\mathrm{d}\mathsf{Q}^{e}}\right]\Bigg|_{\mathsf{Q}^{e}=\mathsf{Q}^{e\,(k)}} \Delta\mathsf{Q}^{e\,(k)} = -\mathsf{L}(\mathsf{V}, \mathsf{Q}^{e\,(k)}) \tag{4.250}$$

for the increment in the internal variables $\Delta\mathsf{Q}^{e\,(k)}$. The internal variables at the next iteration now read

$$\mathsf{Q}^{e\,(k+1)} = \mathsf{Q}^{e\,(k)} + \Delta\mathsf{Q}^{e\,(k)}. \tag{4.251}$$

The internal variables of the last time-step are chosen as the starting vector $\mathsf{Q}^{e\,(0)}$. This iterative procedure is continued until the convergence criteria

$$\|\boldsymbol{L}(\boldsymbol{V}, \boldsymbol{Q}^{(k)})\| < \mathrm{tol}_{\boldsymbol{Q}} \quad \text{and} \quad \|\Delta\boldsymbol{Q}^{(k)}\| < \mathrm{tol}_{\boldsymbol{Q}} \tag{4.252}$$

are fulfilled. Having computed the internal variables, it is now possible to evaluate the right-hand side belonging to the discretized equilibrium condition $\boldsymbol{G}_{\mathrm{u}}(\boldsymbol{U}, \boldsymbol{\Theta}, \boldsymbol{Q}) = \boldsymbol{0}$, see (4.128).

As we now know all the stiffness contributions used in (4.180), (4.187), (4.192) and (4.193), we can proceed to the evaluation of the tangent on the left-hand side of (4.128). Its right-hand side is given by the discretized principle of virtual displacements (4.101) and the discretized heat conduction equation (4.102) making it possible to evaluate the increment in the displacement and temperature coefficients according to (4.128). This process is repeated untill a user-specified tolerance criterion is reached.

4.5 Accelerating the Newton-like method

Since the solution of the nonlinear systems consumes a considerable part of the available computational resources, different approaches for accelerating this iterative procedure are discussed in the following section. Two efficient methods that have been discussed in the h-version finite-element context in (Quint, 2012) are the extrapolation of the initial iterate and the CMLNA.

4.5.1 Extrapolator

It is frequently suggested that the iterate from the previous time-step should be used as the inital one for the MLNA, see (Bathe, 1996; Belytschko et al., 2000; Wriggers, 2008). For DIRK-methods this approach means using the last stage quantity as the initial iterate. Apart from accuracy requirements, the step-size in implicit methods is restricted by the decreasing robustness of the Newton-like method, see (Belytschko et al., 2000). If the initial iterate is far from the solution, there will either be no quadratic convergence or the Newton-like method might even diverge. For this reason, the initial iterate clearly needs to be as close to the solution as possible.

Extrapolators, also referred to as predictors, as proposed in (Esche et al., 1997; Miller, 2005; Stricklin et al., 1973), can be applied for this purpose. To avoid confusion with the predictor-corrector scheme in time integration, we refrain from using this terminology in favour of the term extrapolator. (Hartmann et al., 2009a) proposes a linear extrapolation of the last two known solutions (nodal displacements) in the context of h-elements

$$\boldsymbol{u}_{(i)}^{(0)} = \frac{t_{(i)} - t_{(i-1)}}{t_{(i-1)} - t_{(i-2)}} (\boldsymbol{u}_{(i-1)} - \boldsymbol{u}_{(i-2)}) + \boldsymbol{u}_{(i-1)} \tag{4.253}$$

applied to isothermal problems. It is shown that choosing (4.253) instead of $\boldsymbol{u}_{n+1}^{(0)} = \boldsymbol{u}_n$ not only drastically decreases the number of iterations but also causes non-converging problems to incur just a few iterations. A discussion about the application of (4.253) in the context of p-version finite elements is given in (Netz et al., 2013a). Transferring this approach to thermo-mechanically coupled problems as applied in (Quint, 2012) for h-version finite elements yields

$$\boldsymbol{V}_{(i)}^{(0)} = \frac{t_{(i)} - t_{(i-1)}}{t_{(i-1)} - t_{(i-2)}} \left(\boldsymbol{V}_{(i-1)} - \boldsymbol{V}_{(i-2)}\right) + \boldsymbol{V}_{(i-1)}. \tag{4.254}$$

The times $t_{(i)}$ denote stage times which either belong to the current time-step or to previous time-steps. $\boldsymbol{V}_{(i)}$ contains the coefficients related to both the displacement and temperature fields. Since no information about previous time-steps is available in the first time-step, the prescribed step-size is multiplied by a factor of 10^{-3}. For the internal variables the extrapolation technique is not applied, see (Quint, 2012). The subsequent time-steps employ the extrapolation (4.254). Even though the additional computational time resulting from evaluating (4.254) is negligible, the extrapolation produces the aforementioned advantages. In the context of h-version finite elements several observations have been reported in (Quint, 2012). To begin with, in many cases it is possible to halve the number of iterations. Secondly, a significant stabilization of the MLNA can be observed. Frequently, if the extrapolation under consideration is not applied, the MLNA diverges and the step-size has to be reduced, whereas the application of the extrapolation results in the successful execution of the MLNA, leading to a larger step-size. According to the author's experience, these statements also hold true when p-version finite elements are employed.

4.5.2 CMLNA

Besides the approximation of the initial iterate of the Newton-method, enabling the application of a larger step-size, a further means of gaining efficiency is related to the notion of the Newton-Raphson-Chord method (NRC-method), see (Kelley, 1995), or the modified Newton-method, see (Belytschko et al., 2000). Instead of evaluating the derivative

$$\boldsymbol{K}^{(m)} = \left[\frac{\partial \boldsymbol{G}}{\partial \boldsymbol{V}} + \frac{\partial \boldsymbol{G}}{\partial \hat{\boldsymbol{Q}}} \frac{\mathrm{d}\hat{\boldsymbol{Q}}}{\mathrm{d}\boldsymbol{V}}\right]_{\boldsymbol{y}^{(m)}},$$

required in (4.125), at each iteration, it can remain constant for a given number of iterations. Based on the author's experience, it is useful to keep the matrix $\boldsymbol{K}^{(m)}$ constant, not only within each individual load-step but to fix it for a number of load-steps. Applying the CMLNA (Chord-Multilevel-Newton algorithm) produces a slower rate of convergence, so more iterations have to be conducted than in the standard Newton-method. When direct solvers are used, however, only one $\boldsymbol{LU}$-decomposition is required and only back-substitution steps are needed, which means that neither the derivative of the discretized principle of virtual displacements with respect to the displacement and temperature coefficients $\mathrm{d}\boldsymbol{G}/\,\mathrm{d}\boldsymbol{V}$ nor the derivative of the internal variables for the displacement and temperature coefficients $\mathrm{d}\hat{\boldsymbol{Q}}/\,\mathrm{d}\boldsymbol{V}$, resulting from the solution of the linear equations (4.127), have to be evaluated. This has a considerable impact on the p-FEM approach owing to the fact that, with the p-version, most of the computational time is spent on computing the element stiffness matrices. Moreover, the global convergence properties of the method can be improved by adding a line search such as the Armijo rule (see (Kelley, 1995, p.145)). It reduces the step length of the CMLNA, if necessary. The first step is to compute the search direction $\Delta\boldsymbol{V}^{(m)}$ using

$$\left[\frac{\partial\boldsymbol{G}}{\partial\boldsymbol{V}}+\frac{\partial\boldsymbol{G}}{\partial\boldsymbol{Q}}\frac{\mathrm{d}\hat{\boldsymbol{Q}}}{\mathrm{d}\boldsymbol{V}}\right]_{\boldsymbol{y}^{(0)}}\Delta\boldsymbol{V}^{(m)}=-\boldsymbol{G}\Big(\boldsymbol{V}^{(m)},\hat{\boldsymbol{Q}}\Big(\boldsymbol{V}^{(m)}\Big)\Big). \tag{4.255}$$

In order to keep the step from going too far, it is essential that

$$\Big\|\boldsymbol{G}\Big(\boldsymbol{V}^{(m)}+\omega\Delta\boldsymbol{V}^{(m)},\hat{\boldsymbol{Q}}\big(\boldsymbol{V}^{(m)}+\omega\Delta\boldsymbol{V}^{(m)}\big)\Big)\Big\|<\Big\|\boldsymbol{G}\Big(\boldsymbol{V}^{(m)},\hat{\boldsymbol{Q}}\big(\boldsymbol{V}^{(m)}\big)\Big)\Big\| \tag{4.256}$$

is fulfilled, using the step length ω. This involves searching for the smallest integer n so that for $\omega=2^{-n}$ the criterion (4.256) is satisfied, meaning that the step length is halved at each iteration step. The global variables for the next iteration are given by

$$\boldsymbol{V}^{(m+1)}=\boldsymbol{V}^{(m)}+\omega\Delta\boldsymbol{V}^{(m)}. \tag{4.257}$$

Employing the CMLNA in combination with the starting vector estimation considerably speeds up the solution of the system of nonlinear equations.

4.6 Solution of Linear Systems

At each iteration of the MLNA it is necessary to solve the linear system of equations (4.125) whose general form reads

$$\boldsymbol{K}\boldsymbol{w}=\boldsymbol{s},\quad \boldsymbol{s}\in\mathbb{R}^{n_{\text{eq}}} \tag{4.258}$$

with the global stiffness matrix $\boldsymbol{K}:=\mathrm{d}\boldsymbol{G}/\,\mathrm{d}\boldsymbol{V}|_{\boldsymbol{y}^{(m)}}\in\mathbb{R}^{n_{\text{eq}}\times n_{\text{eq}}}$, the residual of the global equation system $\boldsymbol{s}:=\boldsymbol{G}(\boldsymbol{y}^{(m)})\in\mathbb{R}^{n_{\text{eq}}}$ and the unknown vector $\boldsymbol{w}=\Delta\boldsymbol{V}^{(m)}\in\mathbb{R}^{n_{\text{eq}}}$. $\boldsymbol{s}$ is evaluated at the current approximation $\boldsymbol{y}^{(m)}=\big(\boldsymbol{U}^{(m)},\boldsymbol{\Theta}^{(m)},\boldsymbol{Q}^{(m)}\big)$. We take advantage of the fact that there are many zero entries in the global stiffness matrix by making use of the parallel direct sparse solver PARDISO 3.2, see (Schenk and Gärtner, 2004; Schenk et al., 1999). (Gould et al., 2007) compare PARDISO and ten other direct solvers for linear systems and PARDISO is shown to be among the fastest in different test scenarios. PARDISO is a high-performance, robust, and memory-efficient parallel solver which is optimized for shared memory multiprocessor architectures. It also takes advantage of the memory hierarchy on modern microprocessors to achieve a high floating-point performance. Its application in the h-version of the finite element method is discussed in (Hartmann et al., 2009a), for instance. To study the influence of applying different numbers of threads to the computational time used by PARDISO for solving a system of linear equations, let us take a look at the structure depicted in Fig. 5.13(b). It is discretized with 72 elements with a uniform polynomial degree of 8 making use of the trunk space, resulting in 19011 degrees of freedom. The time spent on solving the linear system (4.258) (also referred to as "computational time spent at global level") is plotted in Fig. 4.16(a) over the number of threads used by PARDISO. We can see that, if up to 4 threads are employed, the parallelization capabilities of PARDISO are very efficient. If we use 4 threads instead of one, the computational time takes only $1.35\,\mathrm{s}$ instead of $4.5\,\mathrm{s}$ yielding $1.35/4.5 = 30\,\%$ of the original computational time. But if 8 threads are used, the computational time is reduced to $1\,\mathrm{s}$, which amounts to $1/4.5 \approx 22\,\%$ of the original computational time for solving the linear system. Accordingly, we only gain another $8\,\%$ of computational time. [*] Taking a closer look at the computational time spent at both the local and the global level, we realize that the solution of (4.258) is not the bottleneck with the p-version of the finite element method, see (Krafczyk et al., 1997). In contrast to the h-version, where the solution of (4.258) consumes up to $90\,\%$ of the computational resources, the p-version's bottleneck is the computation of the element stiffness matrices. For the example under investigation,

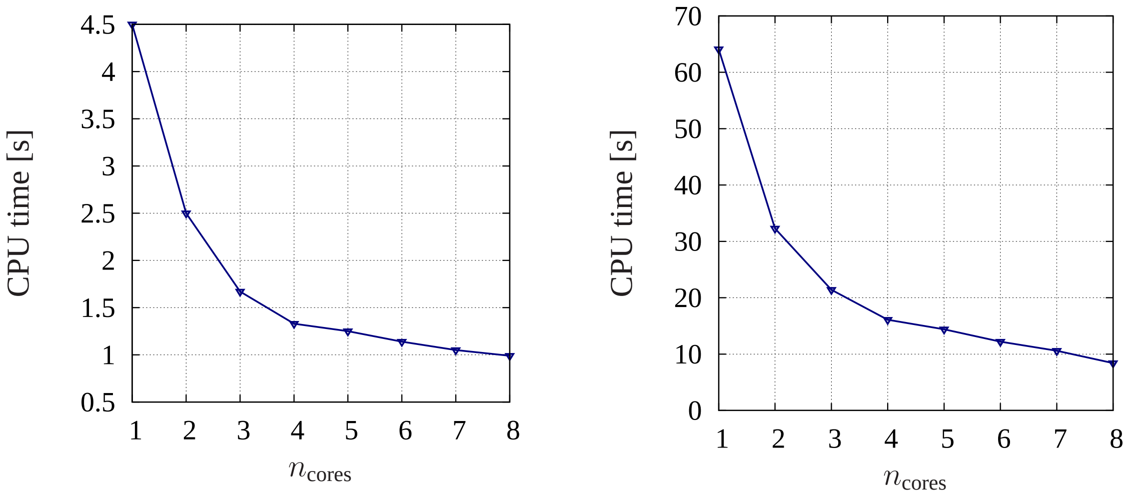

(a) Global computation time over n_{cores} (b) Local computation time over n_{cores}

Figure 4.16: Global and local computation time over n_{cores}

---

[*] In contrast to the decreasing efficiency of PARDISO, when using more than 4 threads, the parallelization of the computation of the element stiffness matrices (also referred to as "computational time spent at the local level") is very efficient, even if we use the total number of available threads (8). Fig. 4.16(b) shows the global computational time plotted over the number of threads involved for the above example.

only approximately $1.0\,$s is spent on solving the linear system (4.258) whereas roughly $8.4\,$s are spent on computing the element stiffness matrices and the corresponding assemblage procedure. Thus, in this case the quotient

$$b = \frac{\text{Computational time spent at the local level}}{\text{Computational time spent at the global level}} \tag{4.259}$$

yields $b \approx 8.3$ for the forementioned example. For computation purposes, we use a Dual Quad Core computer with $2.5\,$GHz with an Intel Xeon E5420 CPU processor. The linear system is solved using the linear solver PARDISO and the computation of the element stiffness matrices is done in parallel using all eight threads of the aforementioned computer. As ansatz space for the p-version we consider the trunk space without applying a condensation of the internal modes. Generally speaking, the higher the polynomial degree of the elements involved, the higher the ratio of the quotient b. This can be illustrated by the outcome of $b \approx 22.2$ for a fully coupled thermo-mechanical computation involving 112 elements, which have a uniform polynomial degree of 10, resulting in 79149 degrees of freedom.

5 Numerical Examples

We look at three different kinds of numerical examples. For the first examples, we assume hyperelastic material behavior. Here the p-version of the finite element method is compared with a mixed element formulation discretizing not only the displacement field but also the pressure and the volumetric deformation, see (Hartmann, 2002) and the literature cited therein. On top of that, we investigate several possibilities aimed at accelerating finite element computations, like predicting the initial iterate within the nonlinear solution procedure, the parallelization of the element assemblage as well as the solution of the arising linear systems and the CMLNA.

We also address the topic of verification. Code verification is carried out, on the one hand, by comparing the results of different p-version codes. For this purpose, the results discussed in Section 5.1.1 are compared with results obtained using the p-version code $AdhoC^4$, see (Düster et al., 2004). On the other hand, the results of finite element discretizations for a tube exposed to internal pressure are compared with an available semi-analytical solution.

In addition, we also take a look at isothermal rate-dependent material behavior, employing the p-version for the spatial discretization and DIRK-type integration schemes for the temporal discretization. The superior performance of DIRK-type integration schemes for problems of viscoelasticity has been addressed in several publications, see (Hartmann, 2003), for instance. This thesis demonstrates that the superior performance of high-order time integration schemes carries over to p-version finite elements. We also discuss time-adaptive computations. The blending function method allows almost arbitrarily shaped surfaces and curves to be included in the map mediating between the global and the local coordinates.

The final section deals with the application of the p-version in conjunction with high-order time integration schemes to problems of finite thermo-viscoelasticity. First of all, the implemented material model of finite thermo-viscoelasticity is verified by means of several effects that are characteristic for elastomers. Then, this approach is applied to fully three-dimensional structures. As well as investigating the high-order time integration schemes in question from the point of view of accuracy and efficiency, we also demonstrate time-adaptive computations. In the last example, we discuss the effect of the displacement-induced temperature increase caused by the elastic (2.212) and inelastic coupling terms (2.218). All p-version finite element computations are based on the trunk space.

5.1 Isothermal Considerations - Hyperelasticity

The following section investigates several examples which demonstrate that p-version finite elements based on hierarchic shape functions are robust under finite strains, while simultaneously studying the efficiency and accuracy for various element types. For the subsequent numerical

Table 5.1: Material parameters of constitutive model

K MPa	c_{10} MPa	c_{01} MPa	α MPa
1000	0.1788	0.1958	$3.67e$-02

investigations, we choose the material parameters given in Tab. 5.1. (Hartmann and Neff, 2003) identified c_{01}, c_{10} and α from the termination points of relaxation of a carbon black-filled elastomer which define the equilibrium stress state. The experimental data was published in (Haupt and Sedlan, 2001).

The computations are carried out using the direct solver PARDISO, see (Schenk et al., 1999) on a Dual Quad Core computer with 2.5GHz with an Intel Xeon E5420 CPU processor. All element formulations are implemented in the in-house code TASA-FEM.

5.1.1 Partially Loaded Plane Rubber Block

Taking the first example, we investigate the compression of a partially loaded plane rubber block, see Fig. 5.1, as proposed in (Reese, 2001; Reese et al., 1999; Reese and Wriggers, 2000). This benchmark problem is discretized with high-order finite elements in (Düster et al., 2003) demonstrating the fast convergence of a p-extension with respect to the displacement of one single point. This example is modified by introducing additional boundary conditions, meaning that the displacements on the left and right side are fixed horizontally. Due to these additional constraints, the deformation of the rubber block under compression is even more pronounced, leading to highly distorted finite elements. The horizontal displacements $\overline{u}_x$ of the upper surface

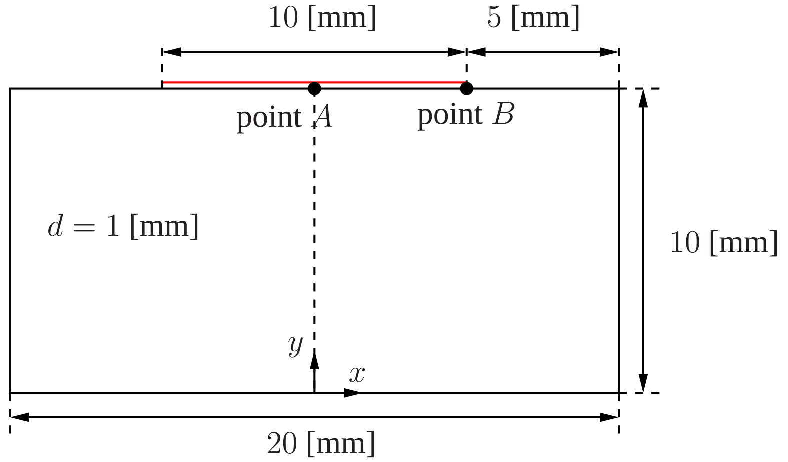

Figure 5.1: Geometry of partially loaded rubber block

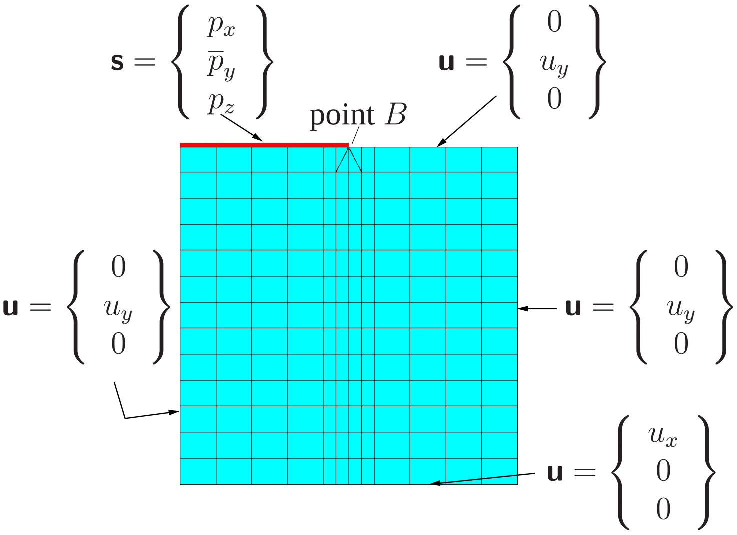

Figure 5.2: Mesh of reference solution

of the plate are suppressed and the rubber block is subjected to a pressure $\overline{p}_y$ [MPa], which is increased linearly. Plain strain assumptions are introduced by suppressing the displacements in z-direction on the front and reverse side of the 3D-mesh. Due to its symmetry, only one half of the system, see Fig. 5.1, is meshed. Fig. 5.3 shows a p-mesh and the deformations resulting from various loads $\overline{p}_y$. One layer of elements is applied in z-direction. The polynomial degree of the elements in z-direction is set to 1 and a polynomial degree of up to 9 is applied in the in-plane direction, taking advantage of the anisotropic element formulation presented in (Düster et al., 2001, 2007). In order to investigate the mixed and high-order finite elements' resilience to distortion, we investigate the error resulting from different load levels (5 MPa, 20 MPa, 100 MPa, 1000 MPa). The resulting deformations are given in Fig. 5.3. In order to compute relative error measures, we compare different h-version meshes, see Fig. 5.4, with the p-version mesh given in Fig. 5.3(a). The reference solution with a uniform polynomial degree of 10 in in-plane direction is based on the mesh given in Fig. 5.2. Both the reference solution and all the h- and p-version discretizations are evaluated for the error investigations at the points indicated by a background grid, see Fig. 5.5(a). Thus, having evaluated the displacement and stress field, it is possible to compute the relative error measures

$$\epsilon_{\text{rel}}(\boldsymbol{u}) = \sqrt{\frac{1}{n_{\text{NR}}} \sum_{k=1}^{n_{\text{NR}}} \sum_{i=1}^{3} \left(\frac{u_{ik}^{\text{ex}} - u_{ik}}{u_{ik}^{\text{ex}}} \right)^2}, \tag{5.1}$$

$$\epsilon_{\text{rel}}(\boldsymbol{T}) = \frac{1}{n_{\text{NR}}} \sum_{k=1}^{n_{\text{NR}}} \frac{\max |\sigma_{ik} - \sigma_{ik}^{\text{ex}}|}{|\sigma_{jk}^{\text{ex}}|} \quad \forall \quad i = 1, ..., 6. \tag{5.2}$$

n_{NR} represents the number of nodes in the background grid. The subscript (ex) refers to the reference solution. The subscript (k) indicates the node number of the evaluation grid. With regard to the error in the displacement field, the subscript (i) denotes the x-, y- and z-direction of the displacement field whereas the subscript (i) of the error in the stress field counts the

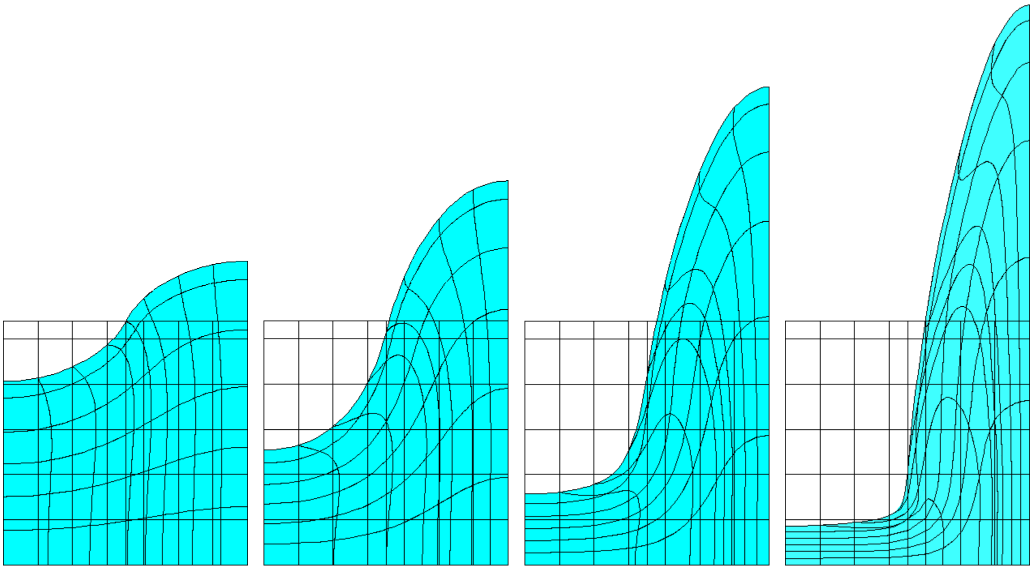

(a) $\overline{p}_y = 5\,\mathrm{MPa}$ with $p = 9$ (b) $\overline{p}_y = 20\,\mathrm{MPa}$ with $p = 9$ (c) $\overline{p}_y = 100\,\mathrm{MPa}$ with $p = 9$ (d) $\overline{p}_y = 1000\,\mathrm{MPa}$ with $p = 9$

Figure 5.3: Deformations for different load levels

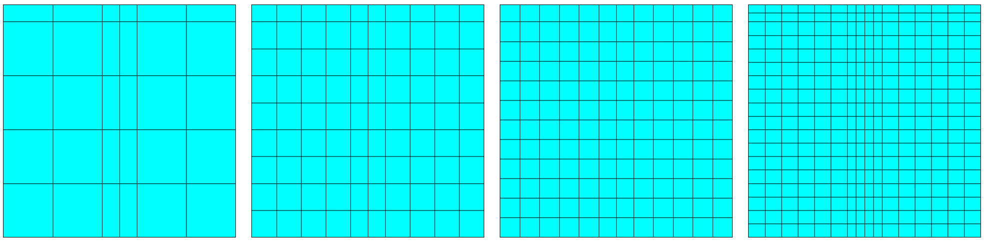

(a) M1 (b) M2 (c) M3 (d) M4

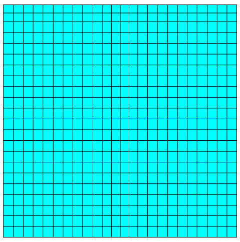

(e) M5

Figure 5.4: h-version meshes for partially loaded plane rubber block

components of the Cauchy stress tensor in Voigt notation, see (4.48). The subscript (j) equals the index (i) which results from evaluating $\max|\sigma_{ik} - \sigma^{\text{ex}}_{ik}|\,\forall\, i = 1, ..., 6$. The displacements and stresses near point B are disregarded, when computing the error measures, in order to exclude

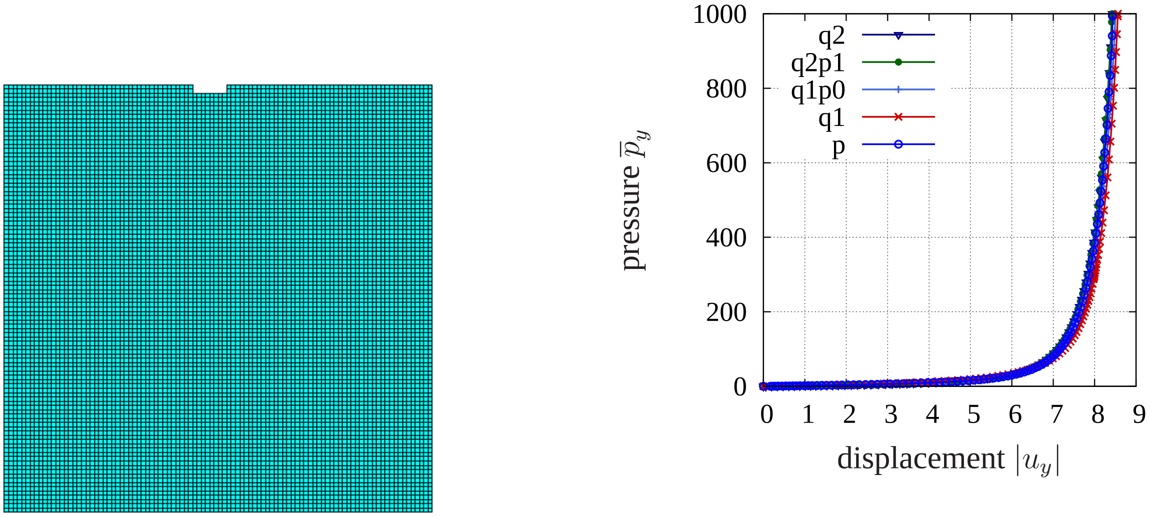

(a) Evaluation grid with 20374 nodes

(b) Load-deflection curve at point A for $p = 9$ and the finest h-discretization

Figure 5.5: Evaluation grid and load-deflection curve

non-physical results of h-version computations close to the singularity. It turns out that some extremely large deformations occur for certain meshes. Figs. 5.6, 5.7 and 5.8 show the relative error measures (5.1) and (5.2) for different load levels over the number of unknowns of the specific discretization, see Tab. 5.2 and 5.3. In the case of the Q1P0-elements, there is one additional degree of freedom for the volumetric strain and one for the pressure field per element, i.e. it has $24 + 2 = 26$ unknowns. On the element level these are, of course, eliminated by a static condensation technique. For the sake of the representation, however, it is important to sum

	M1	M2	M3	M4	M5
Q1	120	360	576	1152	2112
Q2	440	1332	2137	4287	7875
Q1P0	180	540	864	1728	3168
Q2P1	686	2062	3301	6607	12123

Table 5.2: Number of unknowns n_{nu} of the chosen meshes for partially loaded plane rubber block

p-level	1	2	3	4	5	6	7	8	9
n_{nu}	192	576	960	1534	2298	3252	4396	5730	7254

Table 5.3: p-level of rubber block with 25 elements and the number of unknowns n_{nu}

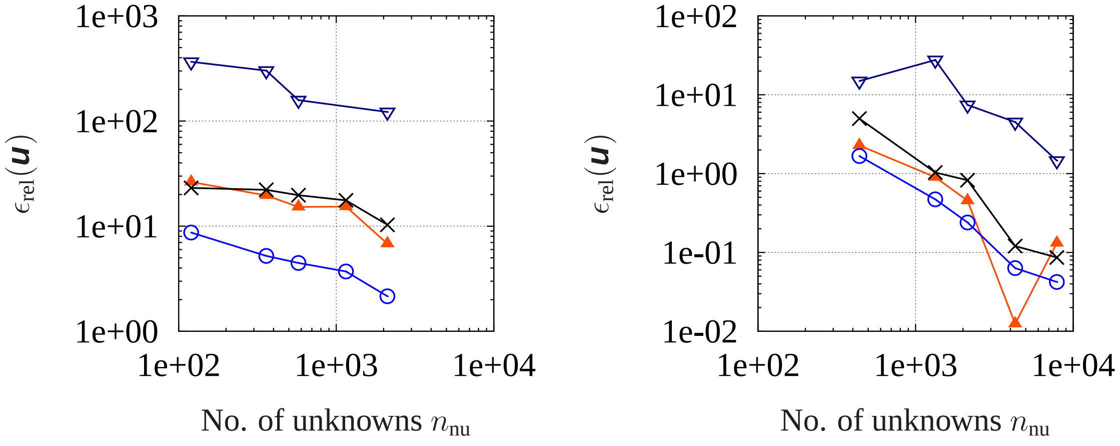

(a) Q1 (b) Q2

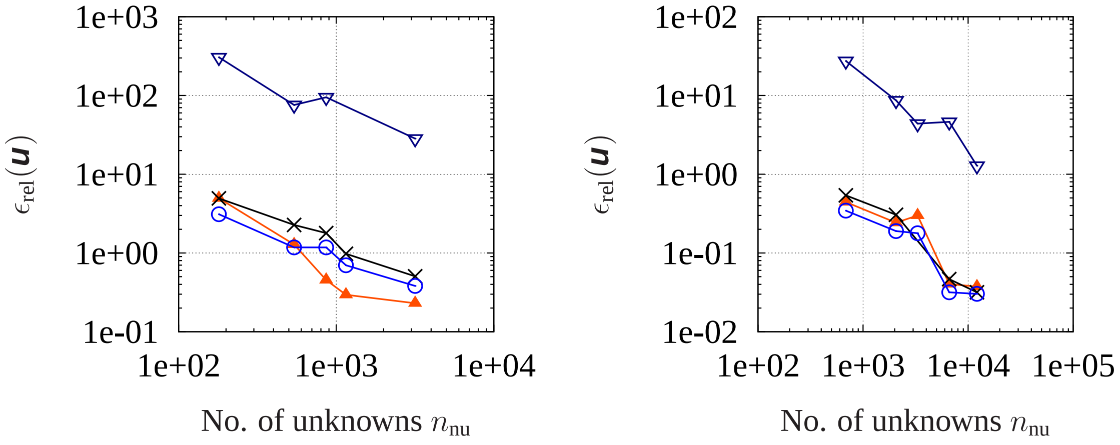

(c) Q1P0 (d) Q2P1

Figure 5.6: Relative error of displacement field of h-version elements (see Fig. 5.8(c) for key)

up all the unknowns. Since a linear ansatz is used for the volumetric strains and the pressure within the 20-noded Q2P1-elements, there are eight additional degrees of freedom per element $(60 + 8 = 68)$. Apart from the linear elements, it is possible to observe the tendency that the relative error in displacements increases in line with a growing load factor. In the h-version, the Q2P1-elements exhibit the best performance in terms of the error in stresses and displacements. Where the load factor is increased to $100\,\mathrm{MPa}$ and $1000\,\mathrm{MPa}$, however, the error in stresses and

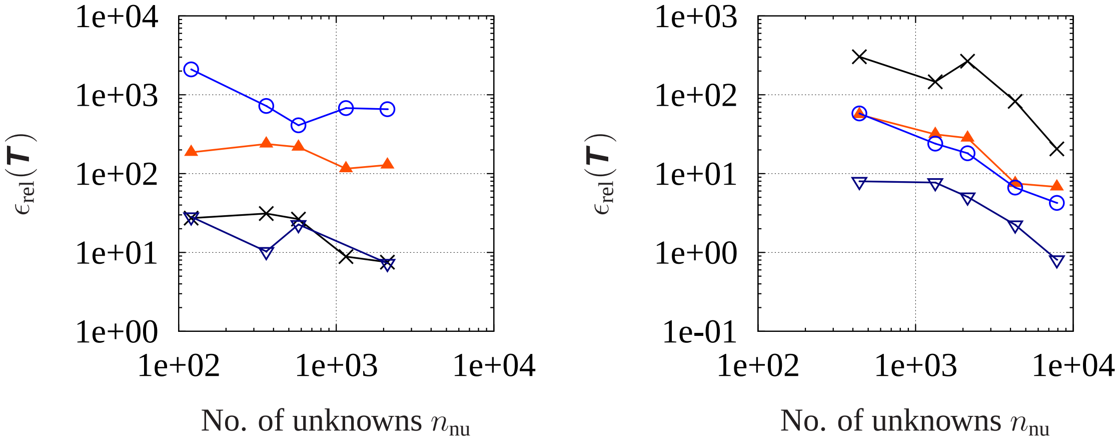

(a) Q1

(b) Q2

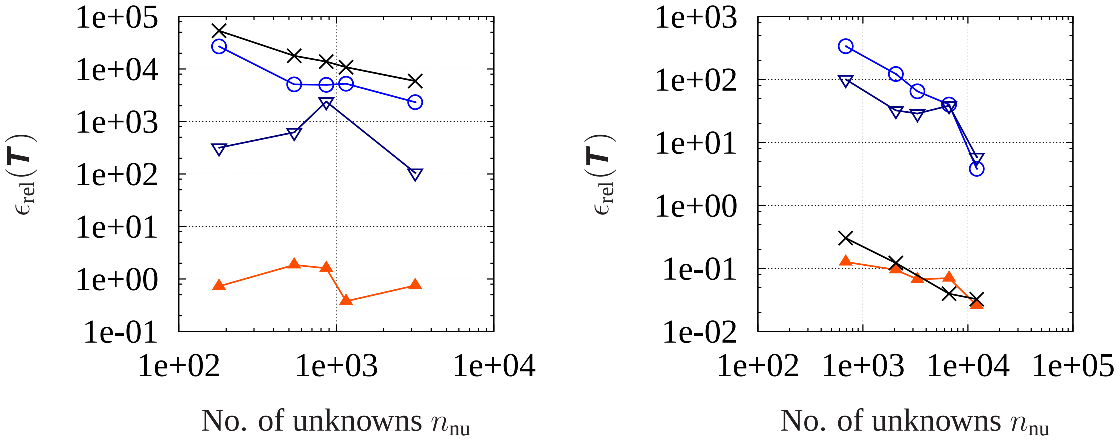

(c) Q1P0

(d) Q2P1

Figure 5.7: Relative error of stress field of h-version elements (see Fig. 5.8(c) for key)

displacements increases drastically. The extremely large relative error of the h-version meshes for high load levels in the stress field is caused by highly distorted elements. Within a finite element computation the stresses are evaluated at the Gauss points only, but for the evaluation of the error measures under consideration the deformation is assessed at each point given by the background grid, see Fig. 5.5(a). Since there are many times more evaluation points in every element than Gauss points, the deformation at some evaluation points can be very large, leading to extremely high stress values. Compared to the performance of the h-version, the p-version produces good results, particularly for high load levels, as shown in Fig. 5.8. When considering the relative error in the displacement field for the highest load level, we note that the error resulting from p-version discretizations is one order of magnitude smaller than the error resulting from computations with Q2P1-elements, see Figs. 5.8(a) and 5.6(d). Of the h-version elements, the Q2P1-elements yield the most accurate results. We can make similar observations with respect to the relative error in stresses. One major drawback of the h-version of the finite element method is that it is difficult to generate fine meshes that do not fail due to strongly distorted elements, especially when large deformations are considered. It is consistently a fairly complicated matter to obtain precise results using h-version finite elements. Although increasing the load factor generally has a negative effect on the performance of the p-version, a p-refinement still improves the quality of the solution without any difficulty, see Fig. 5.8. So it can be stated that high-order elements are highly resilient to distortion, enabling the analysis of problems with large strains without introducing the tedious task of remeshing. The p-version produces results that often prove to be superior to the h-version elements in terms of the relative error measures (5.1) and (5.2), particularly when large deformations are concerned. We accordingly conclude that, for verification purposes, the use of the p-version is more promising than using h-version

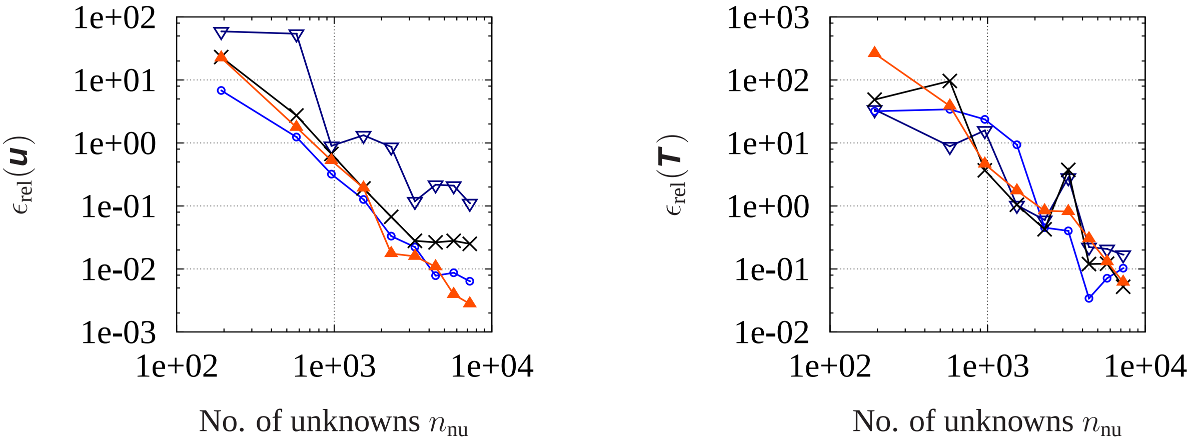

(a) Relative error of displacement field

(b) Relative error of stress field

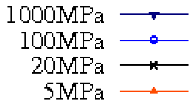

(c) Key

Figure 5.8: Relative error of the displacement and stress field of p-version elements for $p = 1, ..., 9$

elements.

For the purpose of code verification, we compare the results of the in-house code TASA-FEM with those obtained by means of the p-version code $AdhoC^4$, see (Düster et al., 2004). It turns out that at least the first ten digits of the nodal displacements are identical.

5.1.2 Tube under Internal Pressure

In this section, we compare a semi-analytic solution for a tube under internal pressure, see (Yosibash et al., 2007), with the results obtained by means of h- and p-version discretizations. See Fig. 5.9 for the boundary conditions and the p-version discretization. The internal and external radii are assumed to be 10.4mm and 20 mm, respectively. The height of the tube is 2.2 mm. The upper und lower parts of the tube are fixed in the z-direction. We prescribe symmetry boundary conditions for the planes defined by $x = 0$ and $y = 0$ and a follow-up load $\bar{\mathbf{s}}$ oriented normal to the surface in current configuration on the inside of the tube, see Section 4.4. Neo-Hookean material behavior with a bulk modulus of $K = 1000$ MPa and $c_{10} = 0.5$ MPa serves as basis for the comparison. The h-version meshes concerned are given in Fig. 5.10 and the resulting displacement field in Fig. 5.11. In order to assess the quality of the h- and p-version discretizations, we take a look at the relative error measure

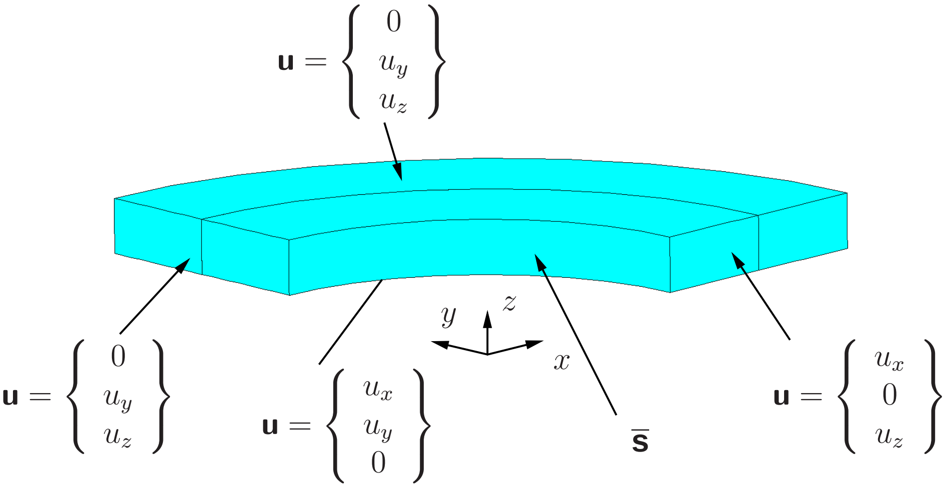

Figure 5.9: Tube discretized with two p-elements and applied boundary conditions

$$\text{reler} = \frac{1}{11} \sum_{i=1}^{11} \frac{|u_i^{\text{ex}} - u_i^{\text{fe}}|}{|u_i^{\text{ex}}|} \times 100. \tag{5.3}$$

u_i^{ex} with $i = 1, ..., 11$ denote the displacements of material points that are equally distributed in the radial direction and emanate from the semi-analytic solution. u_i^{fe} denote the corresponding displacements obtained by means of finite element discretizations. The number of unknowns for the h-version discretizations under investigation is given in Tab. 5.4 and Tab. 5.5 shows the

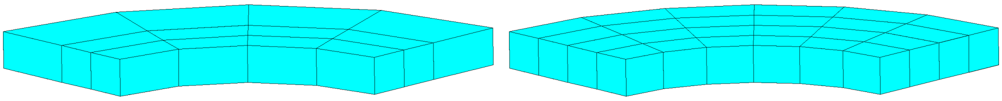

(a) Mesh 1: 12 elements (b) Mesh 2: 24 elements

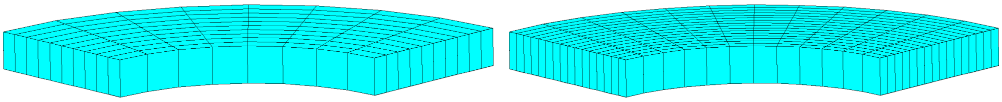

(c) Mesh 2: 80 elements (d) Mesh 2: 192 elements

Figure 5.10: h-version meshes

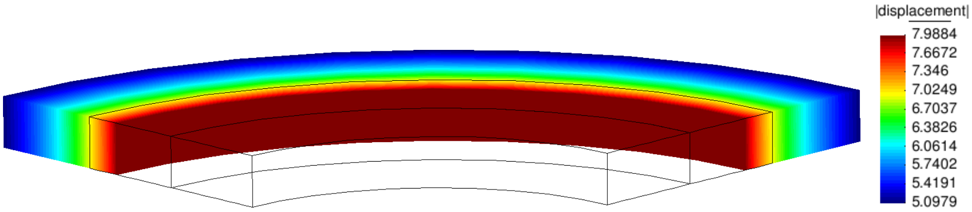

(a) $\sqrt{\boldsymbol{u} \cdot \boldsymbol{u}}$ displayed on deformed configuration ($p = 6$) (b) Key

Figure 5.11: Resulting displacement field displayed on deformed configuration (p=6)

number of unknowns associated with the p-version. Since the local η-direction of the p-elements coincides with the global z-direction, $p_\eta = 1$ holds for the polynomial degree associated with the local η-direction and only p_ξ and p_ζ are increased uniformly. First of all, we note that the linear h-version elements, referred to as Q1 in Fig. 5.12, exhibit the poorest performance. When mixed elements based on a linear ansatz for the displacement field and a constant ansatz for the pressures (Q1P0) are employed, we observe a better performance. For a given number of unknowns the result corresponding to Q1P0-elements is one order of magnitude more precise than the result obtained with Q1-elements. If we contemplate h-version elements based on a quadratic ansatz for the displacement field (Q2), or their mixed counterparts with an additional linear ansatz for the pressure (Q2P1), we gain another order of magnitude in accuracy. But when h-version elements are compared with the p-version, we observe that the p-version delivers results which are as precise as those produced by quadratic mixed elements, even though this discretization contains 70 times as many unknowns as the number required with the p-version, see Tab. 5.4 and Tab. 5.5. We also note that, for a polynomial degree greater than five, the error resulting from p-discretizations remains constant. This can be explained by having a closer look at the manner in which the geometry is prescribed. The geometric modeling package GiD, see (Ribo et al., 2008), defines the surface contours needed in the map (4.1), by means of B-splines, see (Rogers, 2001). Furthermore, a quasi-regional mapping is employed, which approximates the surface description using Lagrange polynomials. At this point we choose a polynomial degree of 7, thus introducing an error that limits the accuracy attainable with the p-version implementation. (Bröker, 2001, p. 72) investigates the accuracy of p-version discretizations of a sphere under external pressure. On the one hand the map is carried out on the basis of the exact geometry

	Mesh 1	Mesh 2	Mesh 3	Mesh 4
Q1	64	120	352	816
Q2	399	765	2373	5577
Q1P0	88	168	512	1200
Q2P1	495	957	3013	7113

Table 5.4: Number of unknowns n_{nu} of the meshes chosen for the tube under internal pressure

p-level	1	2	3	4	5	6	7	8	9
n_{nu}	12	32	52	80	116	160	212	272	340

Table 5.5: p-level of tube with 2 elements and the number of unknowns n_{nu}

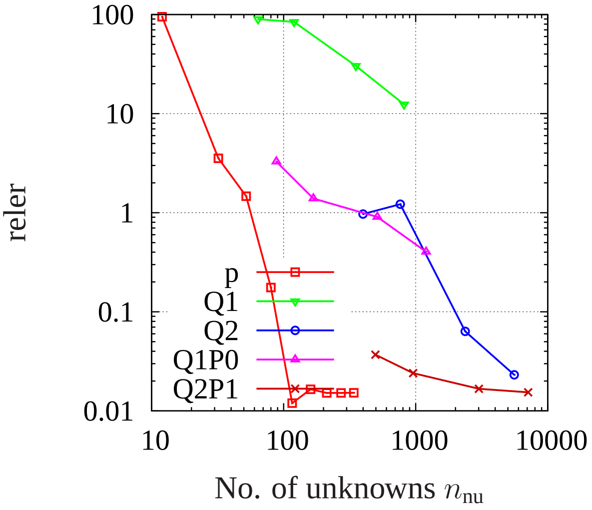

Figure 5.12: Error versus number of unknown diagram for tube

and on the other hand quasi-regional mapping, i.e. an approximation of the exact geometry, is employed. It is demonstrated that, if quasi-regional mapping is employed, the accuracy of p-version computations is limited by the inaccurate geometry description. Starting with a particular polynomial degree, there is no indication that an increase in the polynomial degree diminishes the error. In other words, the higher the polynomial degree for the ansatz of the displacement field, the more dominant the error introduced by the inaccurate geometry description becomes. This limitation in accuracy only disappears in case the computation is based on the exact geometry. This example nevertheless demonstrates the superior convergence properties of the p-version, which ends with a polynomial degree of 6. (Bröker, 2001) and (Heisserer et al., 2008b; Yosibash et al., 2007) demonstrate that, if the computation is based on an exact description of the geometry, superior convergence characteristics become apparent regardless of the size of the polynomial degree that is used for approximating the displacement field. The latter references address the case of axisymmetric problems. We can therefore conclude that the p-version, employed for the spatial discretization, is generally suitable for verification purposes. But this example also highlights the importance of correctly describing the geometry when carrying out finite element computations.

5.1.3 Cantilever

In the following example, error investigations are carried out using a cantilever beam proposed in (Bathe, 2002) which is extended here to 3D. Fig. 5.13(a) shows the geometry of the cantilever and Fig. 5.13(b) the boundary conditions. The prescribed displacements $\overline{u}_y$ on the right-hand side increase linearly in time up to 10 mm.

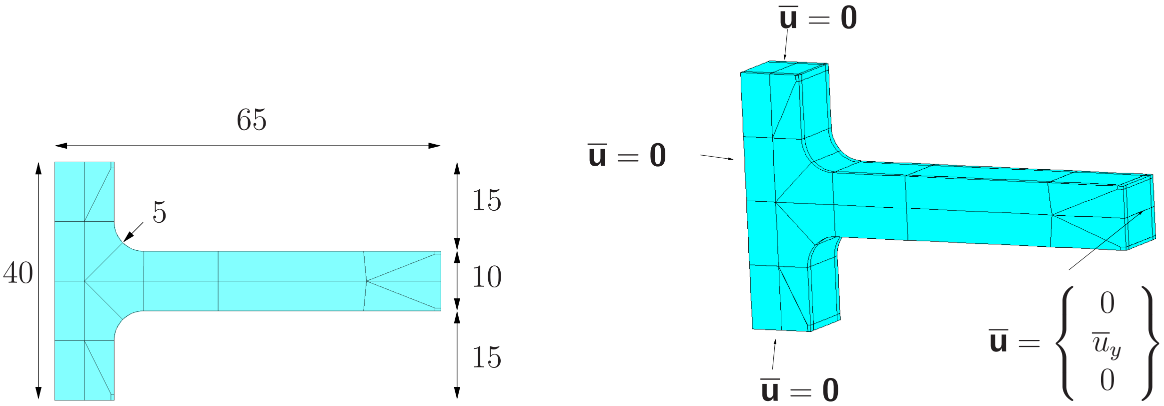

(a) Cantilever with thickness 10 mm

(b) p-FEM mesh and boundary conditions

Figure 5.13: Geometry and p-FEM mesh for comparison purposes with boundary conditions

In order to compare the errors, we evaluate the displacements and the stresses at spatial points. To this end a background grid serves as a function evaluation grid, see Fig. 5.15(b). While the cantilever is discretized with p-version finite elements, uniformly varying the polynomial degree from 2 to 8, as shown in Fig. 5.13(b), we also employ different kinds of h-version meshes based on Q1, Q2, Q1P0, Q2P1 and T2 elements. The h-element meshes are depicted in Fig. 5.14. Tab. 5.6 shows the number of unknowns for classical h-version elements and Tab. 5.7 those for p-elements.

	M1	M2	M3	M4	M5	M6	M7	M8
Q1	1500	6282	16440	46167				
Q2	10563	46167	123435	352737				
Q1P0	2256	9782	26044	74167				
Q2P1	13587	60167	161851	464737				
T2					10563	46167	123435	352737

Table 5.6: No. of unknowns n_{nu} of the chosen meshes

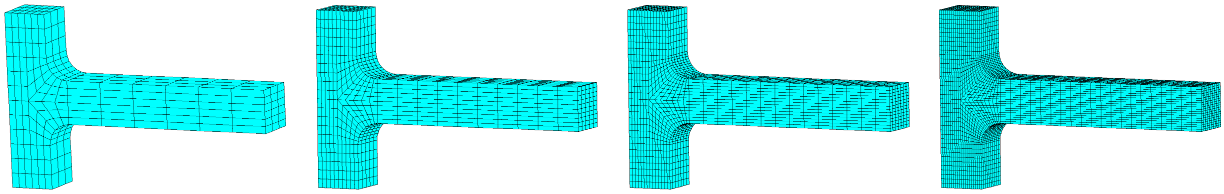

(a) Mesh 1: 378 elements (b) Mesh 2: 1750 elements (c) Mesh 3: 4802 elements (d) Mesh 4: 14000 elements

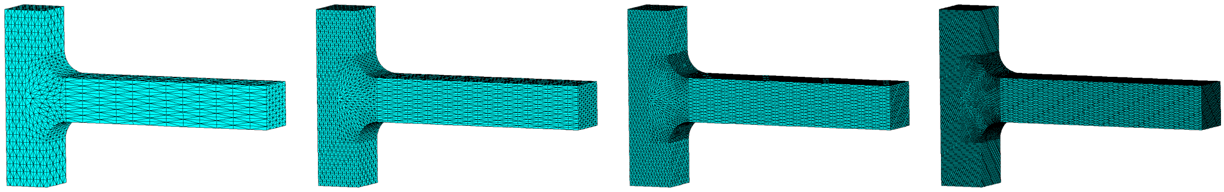

(e) Mesh 5: 2268 elements (f) Mesh 6: 10500 elements (g) Mesh 7: 28812 elements (h) Mesh 8: 84000 elements

Figure 5.14: h-version meshes

p-level	2	3	4	5	6	7	8
n_{nu}	1092	1896	3429	5691	8898	13266	19011

Table 5.7: p-level of cantilever beam with 72 elements and the number of unknowns n_{nu}

5.1.3.1 Accuracy Considerations

Initial investigations serve to ascertain the degree of accuracy that can be obtained. A computation based on the mesh shown in Fig. 5.15(a) is performed by way of a reference solution using 176 elements with $p = 10$. In order to assess the different discretizations, we compare the displacement fields resulting from the reference with all the other discretizations at the coordinates given by the background grid, which is depicted in Fig. 5.15(b). Having evaluated the

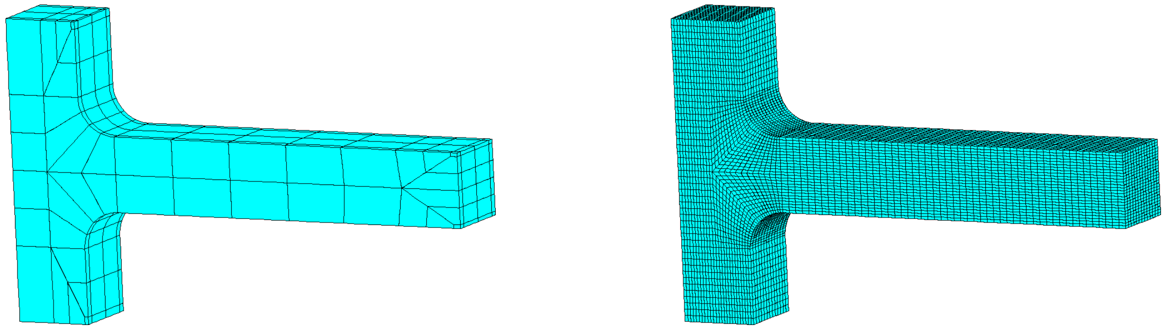

(a) Mesh of reference solution using 176 elements with $p = 10$

(b) Evaluation grid with 42210 nodes

Figure 5.15: Reference mesh and evaluation grid

displacement field at the coordinates of the background grid, we proceed to calculate the errors in displacements and Cauchy stresses using the error measures

$$\epsilon(\boldsymbol{u}) = \frac{1}{n_{\mathrm{NR}}}\sqrt{\sum_{k=1}^{n_{\mathrm{NR}}}(\boldsymbol{u}_k - \boldsymbol{u}_{\mathrm{ex}k})^T(\boldsymbol{u}_k - \boldsymbol{u}_{\mathrm{ex}k})}, \qquad \epsilon(\boldsymbol{T}) = \frac{1}{n_{\mathrm{NR}}}\sum_{k=1}^{n_{\mathrm{NR}}}\max|\boldsymbol{T}_k - \boldsymbol{T}_{\mathrm{ex}k}|. \quad (5.4)$$

n_{NR} represents the number of nodes of the background grid. $\max|.|$ denotes the maximum of the absolute difference between the 6 entities of the Cauchy stress tensor $\boldsymbol{T}$ at an evaluation point between the reference solution and the underlying computation. These values are summed up over all the nodes of the evaluation grid and the results are plotted in Fig. 5.16. Linear displacement approximations exhibit the poorest behavior from the point of view of accuracy versus the number of equations, see Figs. 5.16(a) and 5.16(b). If a quadratic ansatz is chosen instead of a linear one, the error in both the displacement field and the stress field decreases faster in terms of the number of unknowns when compared to the linear elements. Mixed element formulations are a much better choice for overcoming the volumetric locking effect. The stress error is very low, but this is restricted to the low slope, see Fig. 5.16(b), whereas the error is reduced much faster by increasing the polynomial degree. For details concerning volumetric locking phenomena of p-elements see (Düster et al., 2003; Heisserer et al., 2008b; Yosibash et al., 2007). When increasing the polynomial degree of the p-version from 2 to 8, the error decreases much faster than that obtained with the h-version element formulations under consideration. However, the Q2P1-elements yield similarly good results for the error in the displacements, although the number of unknowns is greater.

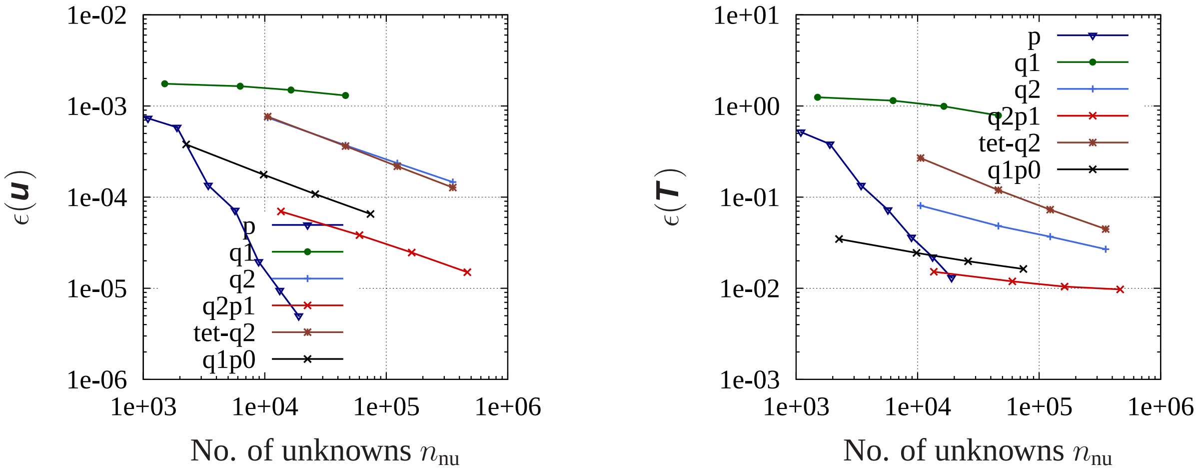

(a) Global error of displacements

(b) Global error of stresses

Figure 5.16: Error versus number of unknown diagrams

5.1.3.2 Efficiency Considerations

The number of equations is not an indication of the interesting behavior displayed by the computational time required for such computations. This is shown in Figs. 5.17(a)-5.17(b), where

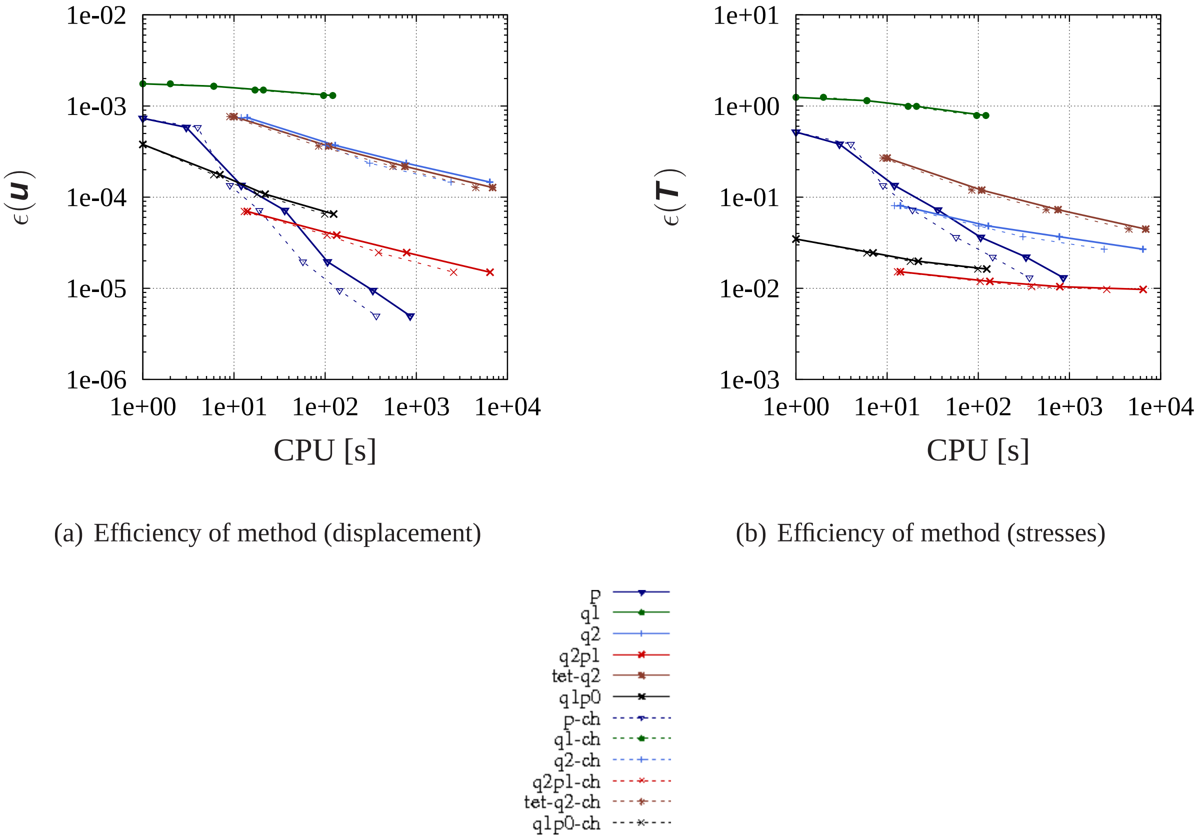

(a) Efficiency of method (displacement)

(b) Efficiency of method (stresses)

Figure 5.17: Error versus computational time diagrams for cantilever

further investigations are provided. Faster and more accurate results are only obtainable for $p \geq 7$ using p-elements. If we take another look at the stresses, however, we see that the p-elements and mixed element formulations are favorable, see Fig. 5.17(b). The NRC-method, see Section 4.5.2, has a considerable impact in the p-version of the finite element method, where the computational input at element level is larger than in the case of h-elements, due to the greater effort involved in computing the triple product given in (4.154) and (4.157) at each Gauss point. However, the (global) linear system in the Newton-Raphson method is smaller than in the case of h-elements for the same degree of accuracy. Thus, with the h-version the computational costs are mainly influenced by the solution of the linear equation system, whereas the contribution afford by setting up the element stiffness matrix is relatively small. Fig. 5.17 shows that the computational time can be further decreased by employing the Newton-Raphson-Chord method for element formulations with considerable computational costs at Gauss point level, such as hierarchical shape function formulations and mixed elements. For the p-version, employing a polynomial degree of $p = 8$ saves 57% of the computational time and in the case of Q2P1 elements (M4) as much as 60% can be saved. In both cases, the assemblage procedure of the stiffness matrix and the solution of the linear equation systems are done in parallel using eight cores. We also investigate the acceleration of the solution process caused by parallel computing. The aforementioned discretizations (setting up the stiffness matrix and solving the resulting linear equation) are carried out on 2, 4, 6 and 8 cores. In this case, the linear solver PARDISO makes use of different numbers of processors (cores) and the element assemblage assigns $n_{\text{el}}/n_{\text{cores}}$-elements to each core ($n_{\text{el}}$ is the number of elements and n_{cores} symbolizes the number of cores). In this context OpenMP is applied. The computational times are plotted against the number of cores for the p-version and for Q1P0- and Q2P1-discretizations in Figs. 5.18 and 5.19. As it happens, the p-version benefits particularly from parallel computing in view of the considerable computational time spent at element level, see also (Krafczyk et al., 1997). If we compare the ratios of the computation time for the Q2P1-elements for 2 or 8 cores respectively, we obtain the factor 0.45 (a saving of 55%) and 0.276 for the p-version, in other words a saving of 72% of the computational time. Further information on parallel computing with the p-version can be found in (Dong and Yosibash, 2008; Rank et al., 2001).

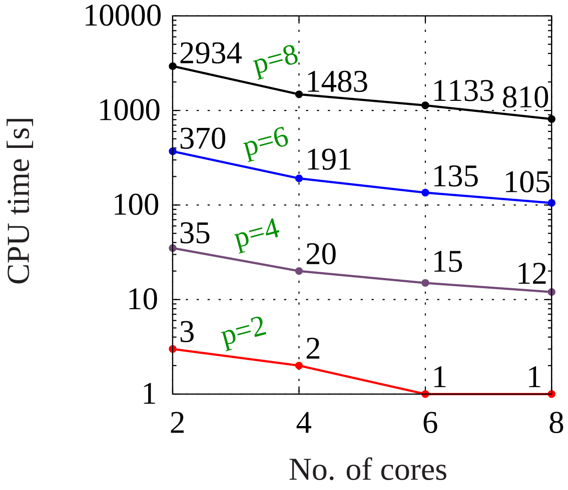

Figure 5.18: Parallelization of assemblage procedure for p-version using 2, 4, 6 and 8 cores for cantilever. The numbers at the points indicate the computational time in seconds.

5.2 Isothermal Considerations - Finite Strain Viscoelasticity

This section discusses two examples based on isothermal material behavior, see Section 2.3.4. The material parameters employed here and summarized in Tab. 5.8 were developed in (Hartmann, 2002) and (Hartmann and Neff, 2003).

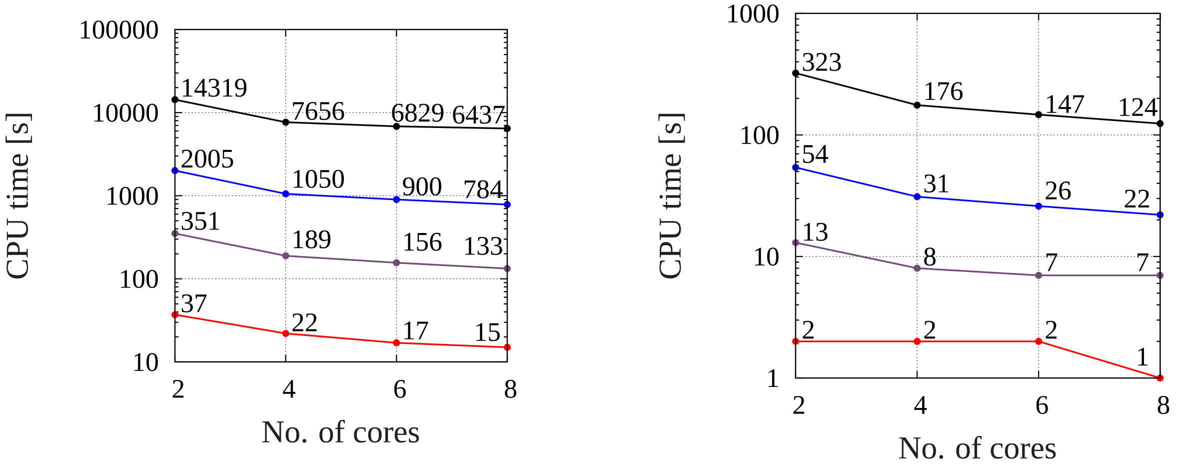

(a) Q2P1 meshes M1 - M4 (b) Q1P0 meshes M1 - M4

Figure 5.19: Parallelization of assemblage procedure for h-version mixed elements using 2, 4, 6 and 8 cores for cantilever. The numbers at the points indicate the computational time in seconds.

Table 5.8: Material parameters of constitutive model

K MPa	c_{10} MPa	c_{01} MPa	α MPa	μ MPa	η_0 MPa s	s MPa^{-1}
1000	0.1788	0.1958	$3.67e$-02	0.2	180	$1.0e$-03

5.2.1 Distance Spacer

We begin by contemplating the distance spacer given in Fig. 5.20.

5.2.1.1 Investigation of the Spatial Discretization

In order to assess the quality of the spatial discretization, we begin by assuming hyperelastic material behavior, based on a strain-energy function given in (2.118), see (Hartmann and Neff, 2003). Clamping its lower side, we apply symmetry boundary conditions on both the left and right-hand side. We prescribe displacement boundary conditions, increasing linearly in time $\overline{u}_y(t) = -at$ with $a = 1\,\text{mm/s}$ on the red part of the upper side of the distance spacer, see also Fig. 5.20. We investigate two different kinds of discretizations with respect to the error measures given by Eq. (5.4): elements with a linear ansatz for the displacement field (Q1) or a linear ansatz for the displacement field *and* a constant ansatz for the pressure and the volumetric strains (Q1P0) on the one hand and the p-version of the finite element method (P) on the other. The mesh given in Fig. 5.20 serves as basis for constructing p-discretizations with a uniform polynomial degree varying from 1 to 8. The h-version discretizations are given in Fig. 5.21.

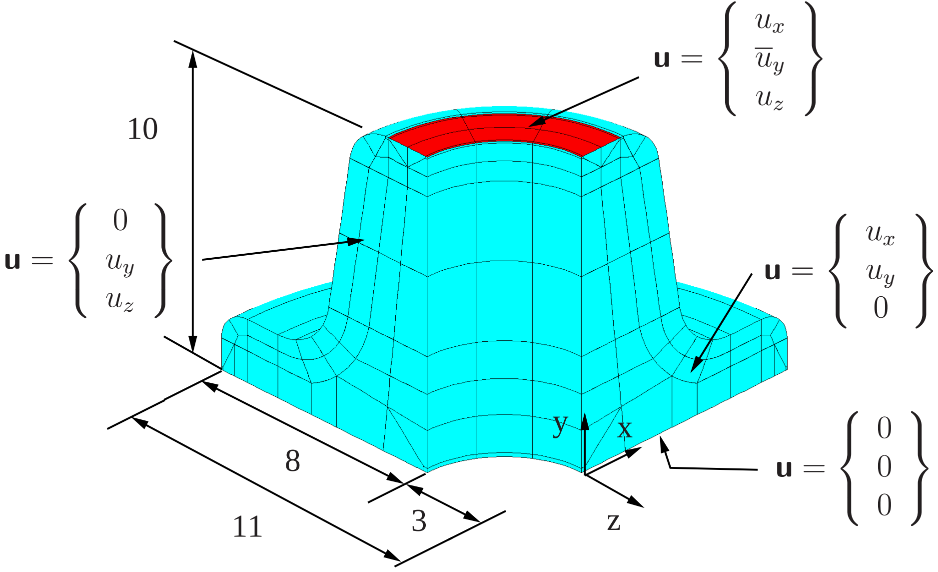

Figure 5.20: p-version discretization and boundary conditions

The number of degrees of freedom for the h-version vs. p-version discretizations is given in

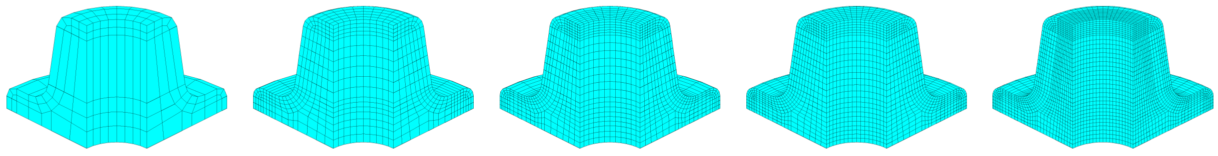

(a) Mesh 1 (b) Mesh 2 (c) Mesh 3 (d) Mesh 4 (e) Mesh 5

Figure 5.21: h-discretizations of distance spacer

Tabs. 5.9 and 5.10. We obtain the reference solution by means of the mesh shown in Fig. 5.22(b) using 195 elements with $p = 10$ yielding 94054 degrees of freedom. In order to compare the different discretizations, we evaluate both the reference and all the other discretizations at the coordinates of the background grid given in Fig. 5.22(a). Having evaluated the displacement field, we compute the error in displacements and stresses using the error measures given in (5.4). The spatial errors depicted in Fig. 5.23 show that the p-version discretizations exhibit a faster convergence in the forementioned norm with respect to the number of degrees of freedom for this structure, so it is more effective regardless of whether we contemplate the global error in displacements or in stresses, see (5.4). A polynomial degree of 6 yields an error in displacements $\epsilon(\boldsymbol{u})$ which is considered to be sufficiently small, since it is almost two orders of magnitude lower than the error achieved by making use of the h-version. For this polynomial degree the error $\epsilon(\boldsymbol{T})$ resulting from the p-version is also superior to the error of the h-version. The following

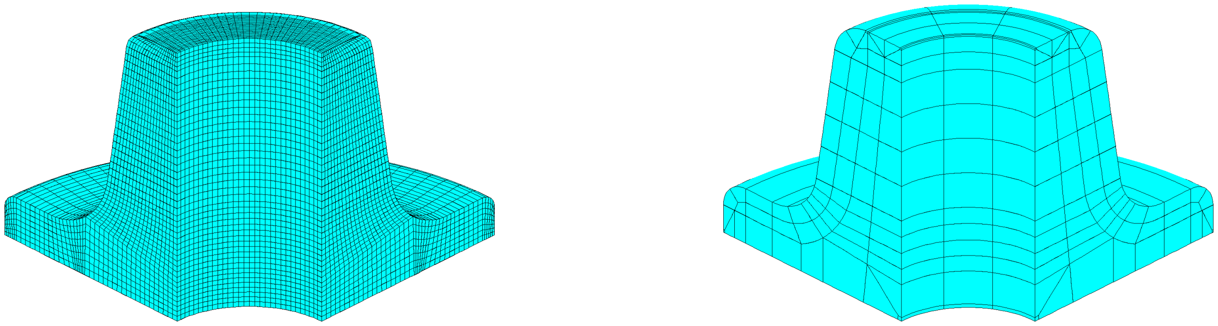

(a) Evaluation grid with 35991 nodes

(b) Reference solution with 195 elements and uniform $p = 10$

Figure 5.22: Background grid and reference mesh for distance spacer

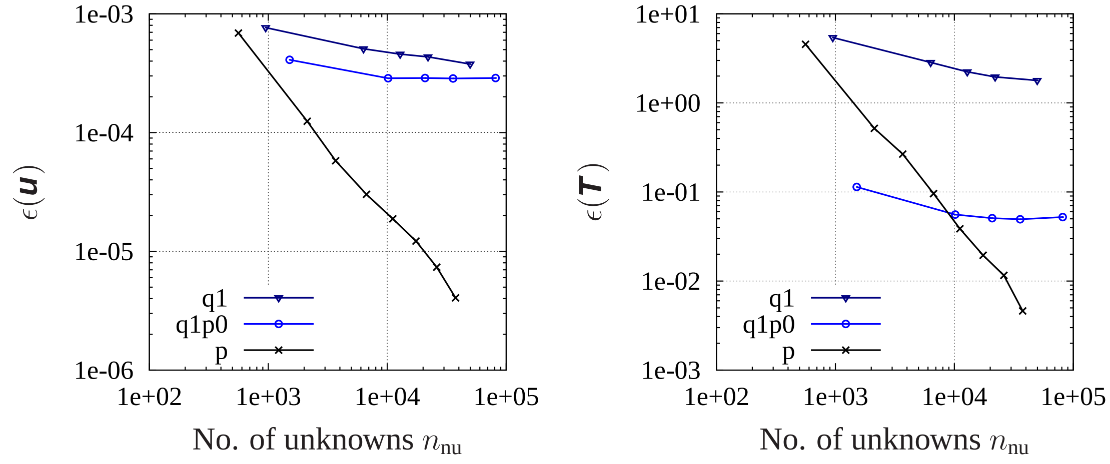

(a) Global error of displacements

(b) Global error of stresses

Figure 5.23: Error versus number of unknown diagrams

p-level	1	2	3	4	5	6	7	8
n_{nu}	561	2123	3685	6688	11132	17458	26107	37520

Table 5.9: p-level of distance spacer with 147 elements and the number of unknowns n_{nu}

investigations of the temporal discretization schemes are accordingly based on p-discretizations with a uniform polynomial degree of 6. See Fig. 5.24 for the von Mises stress distribution displayed on the deformed configuration.

Mesh	1	2	3	4	5
Q1 n_{nu}	950	6324	12839	22001	49715
Q1P0 n_{nu}	1510	10164	20807	35761	81515
n_{el}	280	1920	3984	6880	15900
n_{Q}	13440	92160	191232	330240	763200

Table 5.10: Number of unknowns n_{nu}, elements n_{el} and internal variables n_{Q} for distance spacer

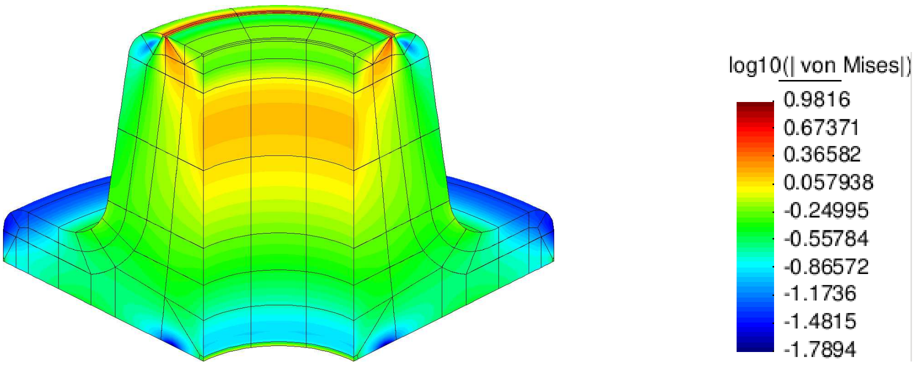

(a) Deformed configuration and von Mises stress distribution (here, $\log_{10}\sqrt{3/2\mathbf{T}^D \cdot \mathbf{T}^D}$ is introduced to provide a better insight)

(b) Key

Figure 5.24: Deformed configuration von Mises stress disribution displayed on deformed configuration

5.2.1.2 Investigation of Temporal Discretization Schemes

We will now proceed to discuss the temporal error for the finite viscoelasticity model described above, see Section 2.3.4 and (Hartmann, 2002). In order to judge different time discretization schemes, we introduce

$$\text{abserrq} := \max_n \left(\|\boldsymbol{q}_n^{\text{ref}} - \boldsymbol{q}_n\| \right), \qquad \text{abserru} := \max_n \left(\|\boldsymbol{u}_n^{\text{ref}} - \boldsymbol{u}_n\| \right), \tag{5.5}$$

i.e. for all time-steps the maximum error is computed. The highly accurate solution (reference solution $\boldsymbol{q}_n^{\text{ref}}$ and $\boldsymbol{u}_n^{\text{ref}}$) is done using the 4th order method proposed by Hairer, see (Hairer and Wanner, 1996) with a constant step-size of $\Delta t_n = 0.5 \times 10^{-4}$ s. In this example we apply a displacement of 1 mm within 0.4 s yielding $\overline{u}_y(t) = -at$ with $a = 2.5$ mm/s, see Fig. 5.20. In Fig. 5.25(a) and 5.25(b) the error in internal variables and displacements (5.5) are plotted against the step-size for time discretization schemes of first, second and third order. The method of first order is the frequently applied Backward-Euler method, the method of second order is called Ellsiepen's method, see (Ellsiepen, 1999; Ellsiepen and Hartmann, 2001), the method of third order is known as Alexander's method, see (Alexander, 1977). For the sake of simplicity, we compute the error in displacements using the nodal degrees of freedom of the p-discretization only. We achieve the anticipated order of the investigated time discretization schemes for both

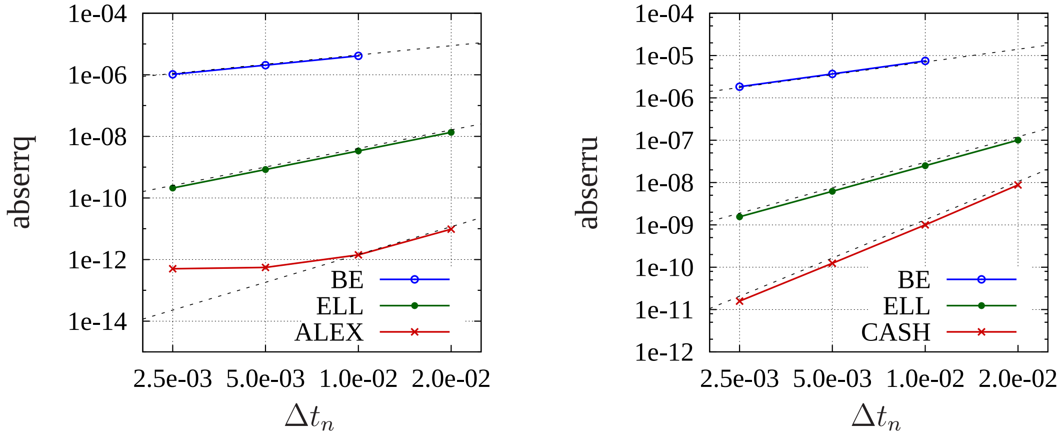

(a) Error in internal variables

(b) Error in displacements

Figure 5.25: Error versus step-size for distance spacer

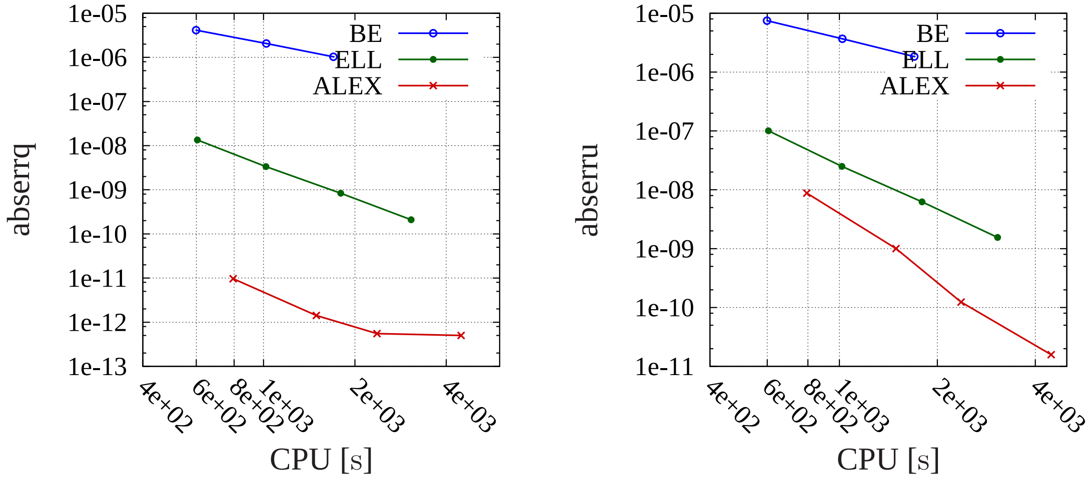

(a) Error in internal variables

(b) Error in displacements

Figure 5.26: Efficiency considerations for distance spacer

kinds of errors. The Backward-Euler method failed for the largest step-size, since the root of the system of nonlinear equations could not be found in this case. Figs. 5.26(a) and 5.26(b) plot the error in displacements and internal variables respectively over the total CPU time. For a given computational effort the method of second order yields an error which is approximately two orders of magnitude lower than the error resulting from the Backward-Euler method, regardless of whether we consider the error in displacements or internal variables. The method of third order is even more efficient, so we observe not only superior accuracy but also greater efficiency in the time discretization schemes of high order for the problem in question.

5.2.1.3 Time-Adaptivity

This section deals with the automatic step-size control of diagonally-implicit Runge-Kutta methods of first, second and third order. The time-adaptive third order method proposed by Cash, see (Cash, 1979), is an extension of Alexander's 3rd order method, see (Alexander, 1977). We again choose the model of finite strain viscoelasticity, applying the load as depicted in Fig. 5.27(a). In the case of the Backward-Euler method, we employ a load-step control using the number of iterations. If the number of iterations required for solving the global equation system is less than or equal to 4, the time-step size is increased by about $20\,\%$. If the number of iterations exceeds 15, the step-size is decreased by about $15\,\%$. Otherwise the step-size remains constant. This procedure makes use of the non-linearity of the problem to determine Δt_{new}. It does not control the local integration error, however. If methods of higher order are applied, we employ the embedded technique shown in Section 4.3.3, see (Hartmann, 2003). The new step-size is computed according to (4.120) with the error measure $\mathrm{e}_{\text{max}} = \max(e_u, e_q)$ which is based on the first part of (4.118) and (4.119). ϵ^u_{a}, ϵ^u_{r}, ϵ^q_{a} and ϵ^q_{r} are user-defined relative and absolute error tolerances, given in Tab. 5.11. The factors $f_{\text{min}} = 0.3$, $f_{\text{safety}} = 0.85$ and $f_{\text{max}} = 2.5$ are chosen. $\hat{p}$ denotes the order of the embedded time integration method. Fig. 5.27(b) depicts the step-size behavior of the aforementioned time discretization schemes and the prescribed displacements are given

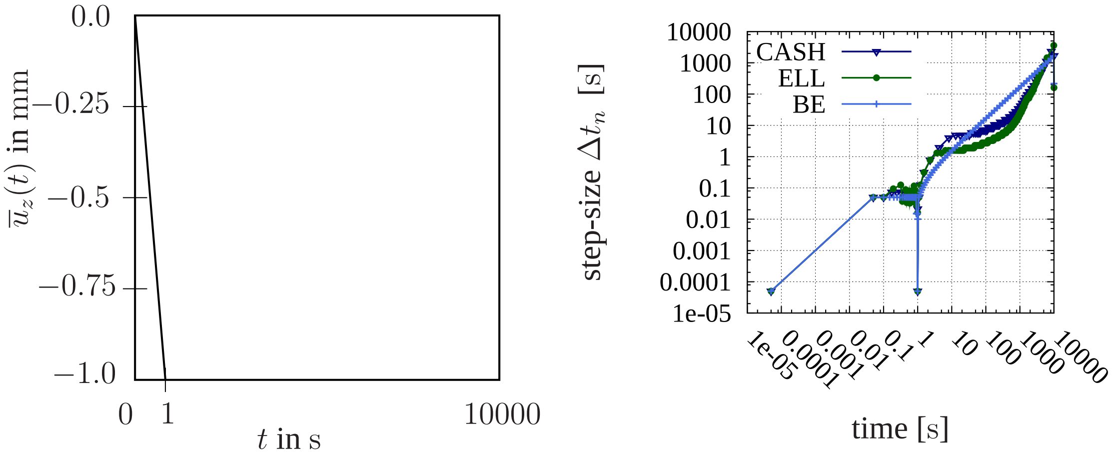

(a) Prescribed displacements for time-adaptive computations

(b) Step-size for distance spacer

Figure 5.27: Displacement prescribed at the red part of the upper side of the distance spacer

Table 5.11: Error tolerances for the step-size control technique

$\epsilon_{\mathrm{a}}^{q}$	$\epsilon_{\mathrm{r}}^{q}$	$\epsilon_{\mathrm{a}}^{u}$	$\epsilon_{\mathrm{r}}^{u}$
10^{-5}	10^{-5}	10^{-3}	10^{-3}

in Fig. 5.27(a). It turns out that the step-size increases drastically when the prescribed displacements remain constant. The computational time spent on the time-adaptive computations are 1075 s for Backward-Euler, 3899 s for Ellsiepen's method and 3435 s for Cash's method. The computations are carried out on a double quadcore computer with an Intel Xeon E5420 cpu with 2.5 GHz. Without the application of adaptive time integration schemes, the computation of problems with different time scales calls for plenty of computation time, which renders such computations practically impossible. Even though the computational cost of the Backward-Euler method is less than that required for Ellsiepen's and Cash's methods, we should bear in mind that its integration error is not monitored. Moreover, depending on the tolerances chosen for the time-adaptive methods of higher order, these can also be more effective in terms of the computational input than the Backward-Euler method, see (Hartmann and Bier, 2008).

5.2.2 Exhaust Pipe Mounting Bracket

The next example is the exhaust pipe mounting bracket whose geometry and dimensioning is given in Fig. 5.28. Due to the symmetry of the structure the finite element mesh is based on one eighth of the exhaust pipe mounting bracket only. The applied boundary conditions are depicted in Fig. 5.29. This example serves to compare the spatial error with the temporal error. For this purpose, we initially investigate the spatial and the temporal discretizations separately before comparing the influence that increasing the p-level has on the error of the displacement field with the influence of a more accurate time integration scheme.

5.2.2.1 Investigation of the Spatial Discretization

In order to carry out the spatial discretization of the structure under consideration, we take a look at the p-version of the finite element method as well as the Q1-, Q1P0-elements. The mesh on which the p-version discretization is based is given in Fig. 5.29, while the h-version discretization can be found in Fig. 5.21. In order to judge the quality of the spatial discretization, we investigate the error in displacements $\epsilon(\boldsymbol{u})$ for hyperelastic material behavior for Q1-, Q1P0- and p-elements, see Fig. 5.31. The h-discretizations on whose basis the aforementioned error is computed are depicted in Fig. 5.32, the corresponding number of unknowns can be found in Tab. 5.12. Tab. 5.13 shows the number of unknowns of the p-version discretizations and Fig. 5.33(a) depicts the deformed and original configuration, while the colors indicate von Mises stresses. In order to determine the errors in displacements, we evaluate the displacements at the node coordinates of the background grid given in Fig. 5.30(a). For the reference solution,

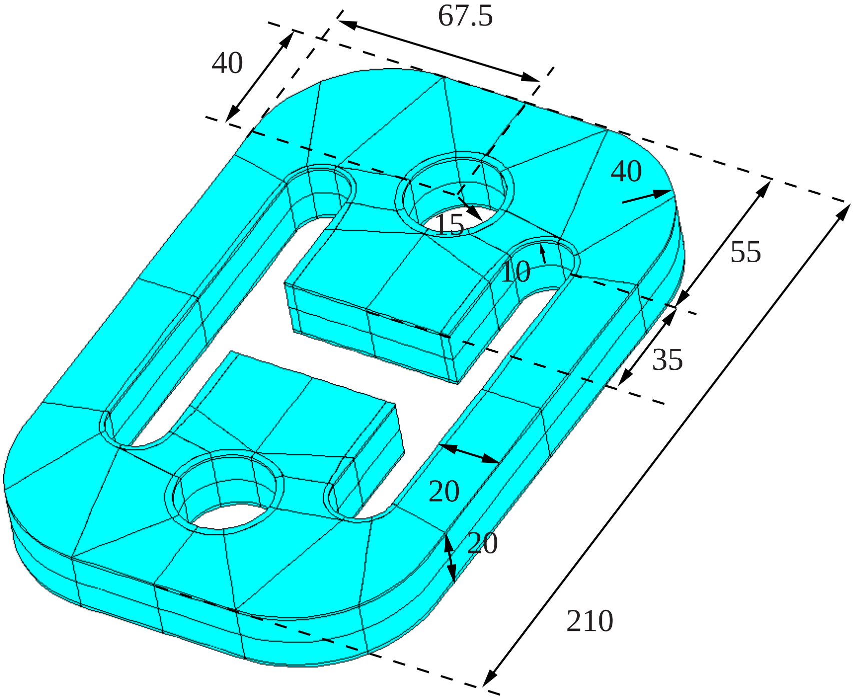

Figure 5.28: Geometry and dimensioning of exhaust pipe mounting bracket

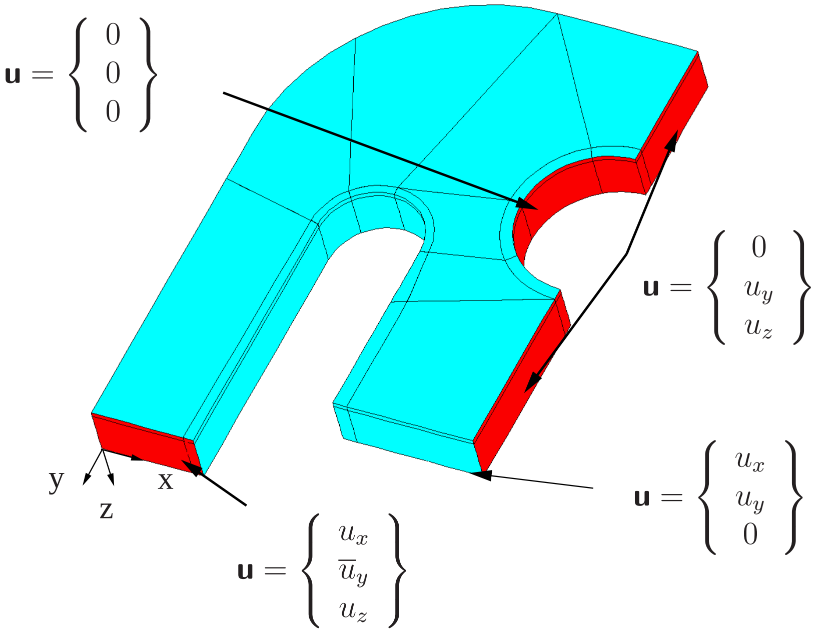

Figure 5.29: p-version mesh and boundary conditions

which is performed on the basis of the discretization given in Fig. 5.30(b), we also evaluate

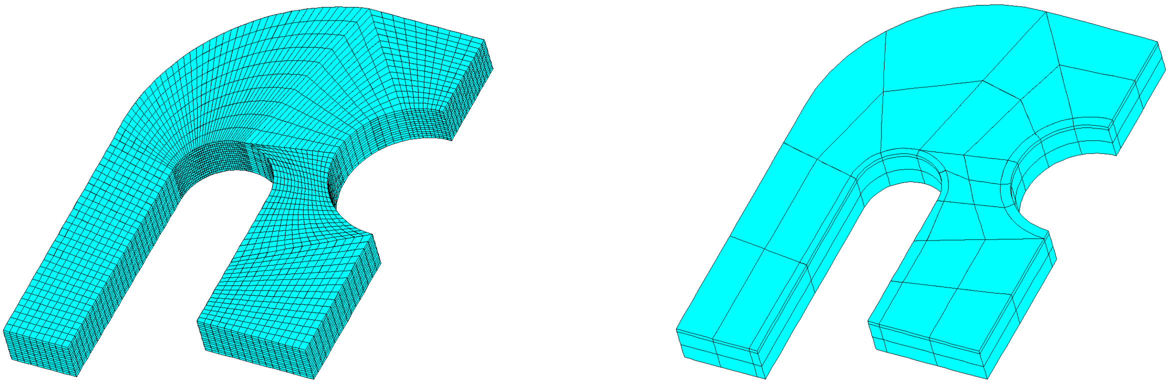

(a) Evaluation grid with 26085 nodes

(b) Reference solution with 117 elements and uniform $p = 10$

Figure 5.30: Background grid and reference mesh for exhaust pipe mounting bracket

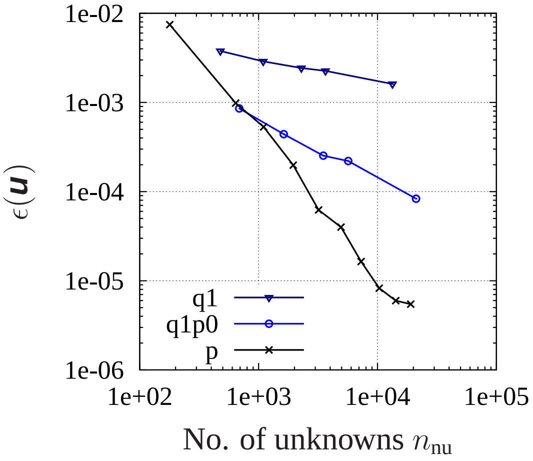

Figure 5.31: Global error of displacements for exhaust pipe mounting bracket ($p = 1, \ldots, 10$)

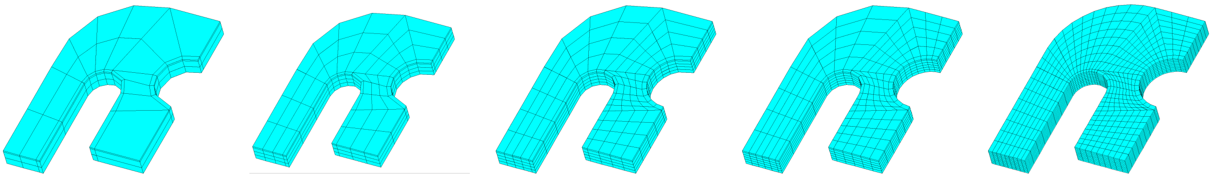

(a) Mesh 1

(b) Mesh 2

(c) Mesh 3

(d) Mesh 4

(e) Mesh 5

Figure 5.32: h-discretizations of exhaust pipe mounting bracket

the displacements at the coordinates given by the background grid. Once we know the reference

Mesh	1	2	3	4	5
Q1 n_{nu}	477	1092	2289	3653	13359
Q1P0 n_{nu}	687	1628	3499	5669	21117
n_{el}	105	268	605	1008	3879
n_{Q}	5040	12864	29040	48384	186192

Table 5.12: Number of unknowns n_{nu}, elements n_{el} and internal variables n_{Q} for exhaust pipe mounting bracket

p-level	1	2	3	4	5	6	7	8	9	10
n_{nu}	179	641	1103	1955	3197	4937	7283	10343	14225	19037

Table 5.13: p-level of exhaust pipe mounting bracket with 36 elements and the number of unknowns n_{nu}

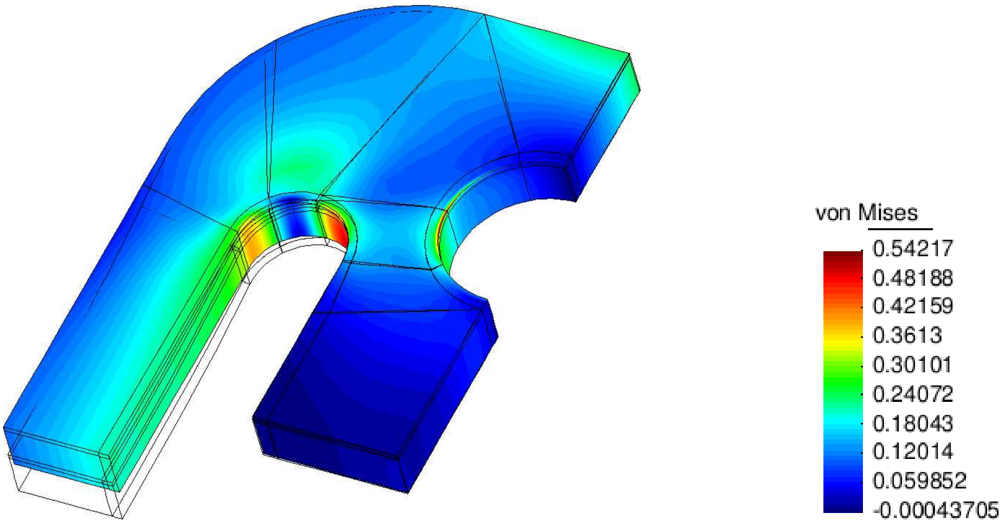

(a) Original and deformed configuration of exhaust pipe mounting bracket, colors indicating von Mises stresses ($p = 8$)

(b) Legend

Figure 5.33: Von Misese stress distribution displayed on deformed configuration of exhaust pipe mounting bracket

solution, we can compute the error according to (5.4). Again, the error in displacements resulting from p-version discretizations proves to be superior to what can be achieved using linear mixed elements where the polynomial degree of the p-version is greater than or equal to 5. We therefore assume a polynomial degree of 6 when taking the temporal error into account.

5.2.2.2 Investigation of Temporal Discretization Schemes

Having discussed the spatial discretization of the exhaust pipe mounting bracket, we shall now proceed to describe the temporal discretization. According to Fig. 5.34(a), which plots the error in internal variables resulting from different time discretization schemes with respect to the step-size, all time integration schemes attain their anticipated order. We not only investigate the error resulting from a given time-step size but also the efficiency of the time integration schemes, see Fig. 5.34(b), depicting the error with respect to the computation time. Here again, the superiority of high-order DIRK-methods over the Backward-Euler method, in terms of error with respect to computation time, becomes obvious. For the given computation, time high-order methods produce results that are several orders of magnitude more accurate than those obtained with the Backward-Euler method.

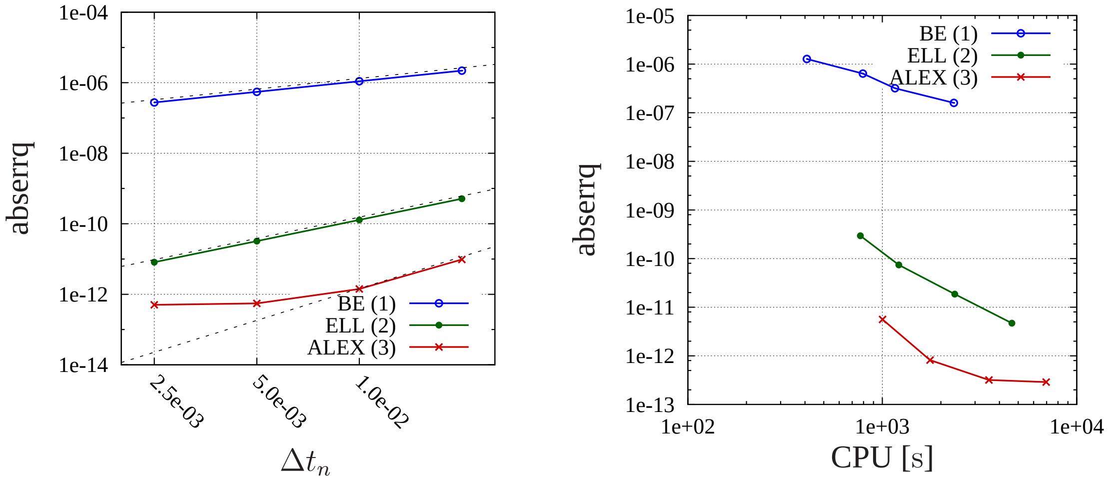

(a) Error in internal variables with respect to the step-size Δt_n

(b) Error in internal variables with respect to the computational time

Figure 5.34: Error versus step-size and versus CPU time for exhaust pipe mounting bracket

The investigations presented so far demonstrate that the p-version is a very effective option for carrying out the spatial discretization. With respect to verification purposes, p-discretizations exhibit characteristics that are often superior to those of h-version finite elements. It is also demonstrated that the superiority of high-order time integration schemes over the Backward-Euler method investigated in the context of h-version finite elements in (Hartmann, 2002), for example, carries over to the p-version. With this approach it is accordingly possible to compute very precise results for isothermal problems. In addition, we also describe the successful application of embedded techniques for time-step control.

Rosenbrock-type methods have recently been studied in the context of small strain (Hartmann and Wensch, 2007) and large strain viscoelasticity (Hamkar et al., 2012; Hartmann and Hamkar, 2010). This is based on a mixed element formulation for the spatial discretization, meaning that quadratic shape functions are chosen for the displacements and linear ones for the pressure and the volumetric deformation, see (Hartmann, 2002). A discussion on the application of Rosenbrock-type methods for the temporal discretization and the p-version for the spatial discretization can be found in (Netz et al., 2013b, 2011).

5.2.2.3 Error in Space Compared to Error in Time

Having discussed the error in space and time separately, the influence of a refinement in the temporal and spatial discretization on the error remains to be investigated. For this purpose, we contemplate the discretization of the exhaust pipe mounting bracket, given in Fig. 5.29, which is assumed to be made of viscoelastic material. The displacement $\overline{u}_y$ is increased linearly from $0.4\,\mathrm{s}$ to $5\,\mathrm{mm}$ $\overline{u}_y(t) = 12.5t\,\mathrm{mm}$. In order to compute an error, we conduct a reference solution based on Fig. 5.30(b) with a uniform polynomial degree of 10 in each element. Since a high-precision reference solution needs to be computed for both the spatial and for the temporal domain, we employ Alexander's method with a step-size of $\Delta t_n = 2.5 \times 10^{-3}\,\mathrm{s}$ because the resulting temporal error is less than $\Delta t_n = 1.0 \times 10^{-12}\,\mathrm{s}$, see Fig. 5.34(a). With the aid of this reference solution, we compare several p-discretizations, whose polynomial degrees are varied from 1 to 9. We use three different time integration schemes for the temporal discretization, see (Alexander, 1977; Ellsiepen, 1999), choosing a step-size of 1.0e-01 for each time integration method. The error in the displacement field $\epsilon(\boldsymbol{u})$ is computed according to (5.4) based on the polynomial coefficients of the last time-step. Refining the temporal discretization by employing a method of second or third order instead of a Backward-Euler step produces a slightly more accurate result for this smooth problem. Since an improvement in the spatial discretization reduces the error by several orders of magnitude more than the decrease caused by a finer temporal discretization, there is no visible difference between the three time discretization schemes under consideration, see Fig. 5.35. The main advantage of high-order time integrations schemes in this example is the possibility of performing time-adaptive computations *and* of controlling the local integration error. When dealing with non smooth problems, such as problems of elasto-plasticity, the application of high-order time integration schemes might be more effective than in the case of a smooth problem, see (Hartmann et al., 2008a). In this case the superior characteristics of high-order time integration schemes should be more pronounced.

5.3 Thermo-Mechanically Coupled Problems

This section starts with several one-dimensional examples, whose purpose is to verify the implemented material model. We begin by comparing the constitutive equations of the equilibrium part of the material model with the corresponding analytical solution for several temperature levels before undertaking the code verification using the Gough-Joule effect and the thermo-elastic inversion effect. We then proceed to investigate a fully three-dimensional structure from the point of view of the error resulting from different spatial discretization schemes as well as several high-order time integration schemes. The final example deals with the reaction force of a structure subjected to different weather conditions, finishing off by demonstrating the displacement-

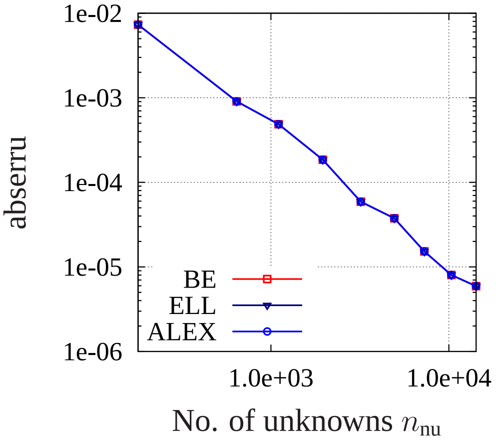

Figure 5.35: Error in displacements for different temporal discretization schemes with respect to n_{nu} for exhaust pipe mounting bracket exhibiting finite viscoelastic material behavior ($p = 1, \dots, 10$)

induced temperature increase. The unit system employed for all thermo-mechanically coupled computations is given in Tab. 5.36.

Measure	**Dim**	**SI**	**Factor**	**Units**
Length	L	m	10^3	mm
Mass	M	kg	10^{-3}	t
Time	T	s	1	s
Temperature	θ	K	1	K
Density	M/L^3	$\mathrm{kg/m^3}$	10^{-12}	$\mathrm{t/mm^3}$
Force	ML/T^2	N	1	N
Stress	M/(L T)^2	Pa	10^{-6}	MPa
Energy	ML^2/T^2	J	10^3	$\mathrm{tmm^2/s^2}$
Power	ML^2/T^3	W	10^3	$\mathrm{tmm^2/s^3}$
Heat capacity	L^2/(T$^2\theta$)	$\mathrm{J/(kgK)}$	10^6	$\mathrm{mm^2/(s^2K)}$
Thermal conductivity	ML/(T$^3\theta$)	$\mathrm{W/(mK)}$	1	$\mathrm{tmm/(s^3K)}$
Heat transfer coefficient	M/(T$^3\theta$)	$\mathrm{W/(m^2K)}$	10^{-3}	$\mathrm{t/(s^3K)}$
Stefan–Boltzmann constant	M/(T$^3\theta^4$)	$\mathrm{W/(m^2K^4)}$	10^{-3}	$\mathrm{t/(s^3K^4)}$

Figure 5.36: Unit system for thermo-mechanically coupled computations

5.3.1 Simple Tension - Finite Thermo-Elasticity

For the purpose of code verification, we take a look at several examples for which analytic solutions are available, beginning with the temperature dependence of the material model in question and comparing it with the analytical solution. We employ the Gough-Joule effect and the thermo-elastic inversion, see (Holzapfel, 2008), for code verification purposes, assuming thermo-hyperelastic material behavior for these investigations. In this section we choose the material parameters of the mechanical subproblem $K = 1000$ MPa, $c_{10} = 0.1788$ MPa, $c_{01} = 0.1958$ MPa and $\alpha = $ 3.67e-03 MPa. These material parameters have been identified at room temperature from the termination points of relaxation of a carbon black-filled elastomer in (Hartmann and Neff, 2003). The experimental data was published in (Haupt and Sedlan, 2001). The material parameters of the thermal subproblem, which were identified in (Heimes, 2005), are summarized in Tab. 5.14.

Table 5.14: Thermal material parameters of constitutive model for elastomer

c_{d0} $\text{mm}^2/(\text{s}^2\,\text{K})$	c_{dk} K^{-1}	λ $\text{t}\,\text{mm}/(\text{s}^3\,\text{K})$	α_θ K^{-1}	θ_0 K	ϱ_{R} t/mm^3
$1.539e$+09	$3.75e$-03	0.2595	$2.06e$-04	20	$1.12e$-09

5.3.1.1 Temperature Dependence of Stress-Strain Relation

In order to demonstrate the explicit temperature dependence of the material model and to verify the code, we consider the process of a uniaxial tension of a volume element, which is characterized by the deformation gradient

$$\mathbf{F} = \lambda \boldsymbol{e}_x \otimes \boldsymbol{e}_x + \lambda_Q \boldsymbol{e}_y \otimes \boldsymbol{e}_y + \lambda_Q \boldsymbol{e}_z \otimes \boldsymbol{e}_z. \tag{5.6}$$

Inserting (5.6) into the stress-strain relation of the equilibrium stresses

$$\tilde{\mathbf{T}}_{\text{eq}} = \tilde{\mathbf{T}}_{\text{eq}}^{\text{vol}} + \tilde{\mathbf{T}}_{\text{eq}}^{\text{iso}} \tag{5.7}$$

yields with $\tilde{T}_{22} = 0$ a system of nonlinear equations

$$\tilde{T}_{11} = \varrho_{\text{R}} f(\lambda, \lambda_Q, \theta) \tag{5.8}$$

$$0 = g(\lambda, \lambda_Q, \theta) \tag{5.9}$$

with

$$
\begin{aligned}
f(\lambda,\lambda_Q,\theta) \equiv{}& \frac{\theta}{\theta_0}\frac{J}{\varphi}U'(J/\varphi)\lambda^{-2} \\
&+ 2\frac{\theta}{\theta_0}J^{-2/3}\left(w_1 + w_2\mathrm{I}_{\bar{\mathbf{C}}} - w_2\lambda^2 J^{-2/3} - \frac{1}{3}(w_1\mathrm{I}_{\bar{\mathbf{C}}} + 2w_2\mathrm{II}_{\bar{\mathbf{C}}})\lambda^{-2}J^{2/3}\right), \\
g(\lambda,\lambda_Q,\theta) \equiv{}& \frac{\theta}{\theta_0}\frac{J}{\varphi}U'(J/\varphi)\lambda_Q^{-2} \\
&+ 2\frac{\theta}{\theta_0}J^{-2/3}\left(w_1 + w_2\mathrm{I}_{\bar{\mathbf{C}}} - w_2\lambda_Q^2 J^{-2/3} - \frac{1}{3}(w_1\mathrm{I}_{\bar{\mathbf{C}}} + 2w_2\mathrm{II}_{\bar{\mathbf{C}}})\lambda_Q^{-2}J^{2/3}\right)
\end{aligned}
$$

and

$$\varphi(\theta) = 1 + \alpha_\theta\,(\theta - \theta_0)\,,$$

which, for the given stretch λ and temperature θ, has to be solved for the unknown lateral stretch λ_Q and the unknown component of the second Piola-Kirchhoff stress tensor $\tilde{T}_{11}$. $\mathrm{I}_{\bar{\mathbf{C}}}$ and $\mathrm{II}_{\bar{\mathbf{C}}}$ are given by (2.26) and (2.27), respectively. For the finite-element computation, the volume element, whose edges are all 1 mm long, is discretized with one element with a linear ansatz for the displacement and the temperature field. The corresponding boundary conditions, based on

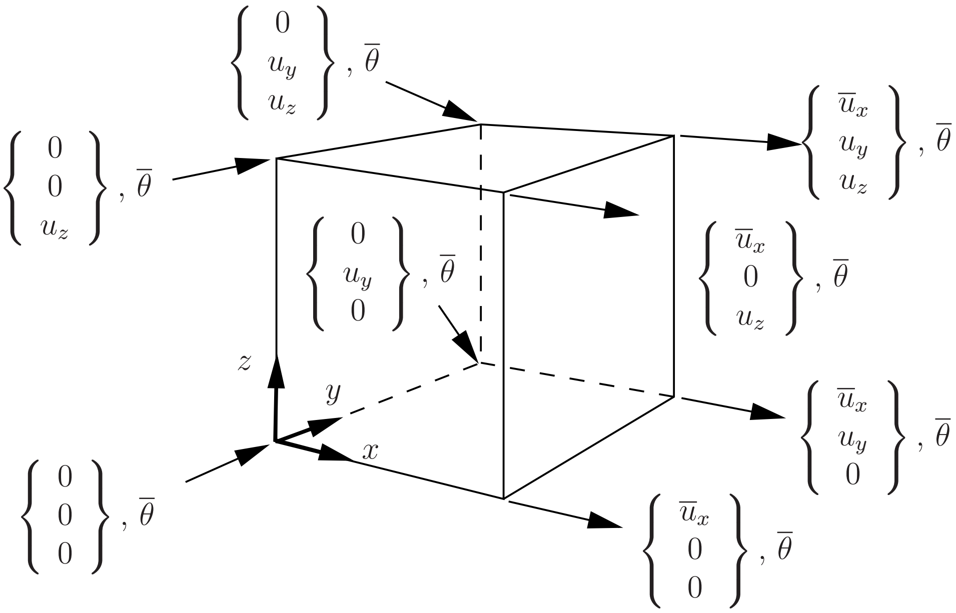

Figure 5.37: Boundary conditions for a volume element exposed to uniaxial tension

$$
\overline{u}_x = \begin{cases} 0 \quad \text{if} \quad 0\,\mathrm{s} \le t \le 1\,\mathrm{s} \\ (t - 1\,\mathrm{s})2\,\mathrm{s}^{-1}\mathrm{mm} \quad \text{if} \quad 1\,\mathrm{s} < t \le 2\,\mathrm{s} \end{cases}
$$

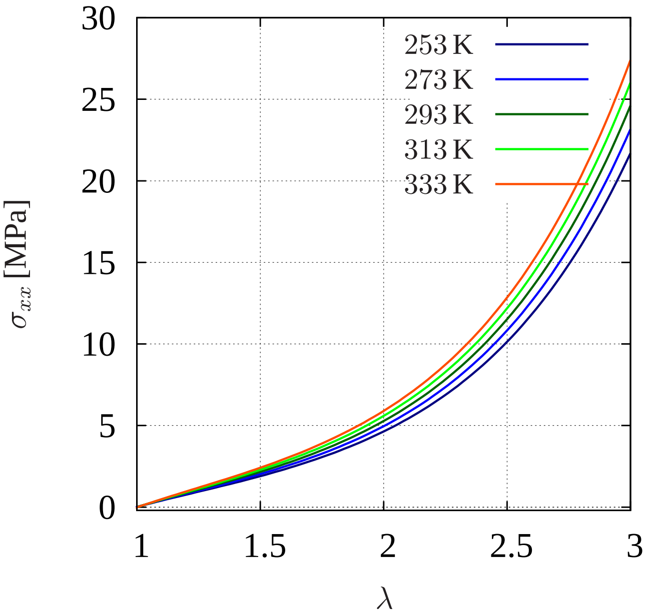

Figure 5.38: Stress-strain relations of equilibrium stresses for different temperature levels, see also (Hamkar, 2013)

and

$$\bar{\theta} = \begin{cases} (\theta_k - 293.15\,\mathrm{K})\, t\, \mathrm{s}^{-1} + 293.15\,\mathrm{K} \quad \text{if} \quad 0\,\mathrm{s} \le t \le 1\,\mathrm{s} \\ \theta_k \quad \text{if} \quad 1\,\mathrm{s} < t \le 2\,\mathrm{s} \end{cases}$$

are depicted in Fig. 5.37, which means that the temperature of the volume element is shifted to $\theta_k = 253\,\mathrm{K} \ldots 333\,\mathrm{K}$ within the first second of the process. The volume element is subsequently elongated linearly in time until a stretch of $\lambda = 3$ is reached. The resulting Cauchy stress is given for several temperature levels in Fig. 5.38. We ascertain firstly that the solutions of (5.8) and (5.9) produce the same results for all temperature levels under consideration as the finite-element computation, with an accuracy of at least 10^{-12} and secondly that the equilibrium stresses (5.7) are dependent on the temperature. The higher the temperature of the volume element, the higher the absolute value of the axial stress. This property is typical for rubber-like materials. The force required to keep a tensile bar made of rubber-like material at constant length, whilst the temperature is increased, rises approximately in line with the temperature, see (Lion, 2000).

5.3.1.2 Gough-Joule Effect

(Treloar, 1975) presents investigations into butadiene-acrylonitrile rubber showing that elastomers that are subjected to a reversible tensile test, heat up if the prescribed stretch is above a specific range. A further characteristic property of elastomers is that they cool down when the prescribed stretch is below this range. Depending on the material, this range may extend to $10\,\%$, see (Heimes, 2005). We next derive an analytic solution for an adiabatic reversible tensile test which is to be compared with a finite-element computation. A reversible process is characterized by $s = 0$, see (Lion, 2000, p. 32), leading to

$$s = -\frac{\partial \psi}{\partial \theta} + \frac{1}{\varrho_{\mathrm{R}}} \frac{\varphi'}{3\varphi^{1/3}} \mathbf{1} \cdot \mathbf{S}_{\mathrm{M}} = 0. \tag{5.10}$$

Inserting $\bar{\psi}^{\mathrm{ov}}_{\mathrm{M}} = 0$ into the strain-energy function (2.116) we arrive at

$$\psi\left(\mathbf{E}_{\mathrm{M}}, \check{\mathbf{\Gamma}}_{\mathrm{e}}, \theta\right) = \frac{\theta}{\theta_0}\left[U(J_{\mathrm{M}}) + \bar{v}(\bar{\mathbf{C}})\right] + \psi_\theta \tag{5.11}$$

based on the identity (2.121). The derivative of the strain energy with respect to the temperature necessary in (5.10) reads

$$\frac{\partial \psi}{\partial \theta} = \frac{1}{\theta_0}\left(U\left(J_{\mathrm{M}}\right) + w\left(\mathrm{I}_{\bar{\mathbf{C}}}, \mathrm{II}_{\bar{\mathbf{C}}}\right)\right) + \frac{\mathrm{d}\psi_\theta}{\mathrm{d}\theta} \tag{5.12}$$

based on

$$\frac{\mathrm{d}\psi_\theta}{\mathrm{d}\theta} = c_{\mathrm{d0}}\left(\left(-\ln\frac{\theta}{\theta_0}\right)(1 - c_{\mathrm{dk}}\theta_0) - c_{\mathrm{dk}}\left(\theta - \theta_0\right)\right). \tag{5.13}$$

Since $\mathbf{S}^{\mathrm{ov}}_{\mathrm{M}} = \mathbf{0}$ holds in this case, we only need the weighted Cauchy stress tensor $\mathbf{S}^{\mathrm{eq}}_{\mathrm{M}}$ operating on the mechanical intermediate configuration. It is expressed in terms of the Cauchy stress tensor $\mathbf{T}_{\mathrm{eq}}$ by

$$\mathbf{S}^{\mathrm{eq}}_{\mathrm{M}} = J\mathbf{F}_\theta^{-1}\mathbf{T}_{\mathrm{eq}}\mathbf{F}_\theta^{-\mathrm{T}} = \varphi^{-2/3}J\mathbf{T}_{\mathrm{eq}}. \tag{5.14}$$

In the purely thermo-hyperelastic case the Cauchy stress tensor reads

$$\mathbf{T}_{\mathrm{eq}} = \varrho_{\mathrm{R}}\frac{\theta}{\theta_0}\varphi^{-1}U'(J/\varphi)\mathbf{1} + 2\varrho_{\mathrm{R}}\frac{\theta}{\theta_0}J^{-1}\left(\frac{\mathrm{d}\bar{v}}{\mathrm{d}\bar{\mathbf{B}}}\bar{\mathbf{B}}\right)^{\mathrm{D}} \tag{5.15}$$

with

$$\left(\frac{\mathrm{d}\bar{v}}{\mathrm{d}\bar{\mathbf{B}}}\bar{\mathbf{B}}\right)^{\mathrm{D}} = \left(\left(w_1 + w_2\mathrm{I}_{\bar{\mathbf{B}}}\right)\bar{\mathbf{B}}^{\mathrm{D}} - w_2\left(\bar{\mathbf{B}}\bar{\mathbf{B}}\right)^{\mathrm{D}}\right), \tag{5.16}$$

$$w_1 = \frac{\mathrm{d}w}{\mathrm{d}\mathrm{I}_{\bar{\mathbf{B}}}} = (1/\varrho_{\mathrm{R}})\left(c_{10} + 3\alpha\mathrm{I}_{\bar{\mathbf{B}}}\right) \tag{5.17}$$

and

$$w_2 = \frac{\mathrm{d}w}{\mathrm{d}\mathrm{II}_{\bar{\mathbf{B}}}} = \frac{3}{2\varrho_{\mathrm{R}}}\mathrm{II}_{\bar{\mathbf{B}}}^{1/2}c_{10}. \tag{5.18}$$

With the deformation gradient (5.6) the unimodular left Cauchy-Green tensor can be expressed by

$$\bar{\mathbf{B}} = J^{-2/3}\mathbf{F}\mathbf{F}^{\mathrm{T}} = \lambda^{4/3}\lambda_Q^{-4/3}\boldsymbol{e}_x \otimes \boldsymbol{e}_x + \lambda^{-2/3}\lambda_Q^{2/3}\boldsymbol{e}_y \otimes \boldsymbol{e}_y + \lambda^{-2/3}\lambda_Q^{2/3}\boldsymbol{e}_z \otimes \boldsymbol{e}_z. \tag{5.19}$$

Inserting the unimodular left Cauchy-Green tensor (5.19) into (5.15) results in

$$\begin{aligned} f(\lambda, \lambda_Q, \theta) =& \frac{\theta}{\theta_0}\varphi^{-1}U'\left(J/\varphi\right) + 2\frac{\theta}{\theta_0}J^{-1} \\ & \left[\frac{2}{3}\left(w_1 + w_2 \mathrm{I}_{\bar{\mathbf{B}}}\right)\left(\left(\frac{\lambda}{\lambda_Q}\right)^{4/3} - \left(\frac{\lambda_Q}{\lambda}\right)^{2/3}\right) - \frac{2}{3}w_2\left(\left(\frac{\lambda}{\lambda_Q}\right)^{8/3} - \left(\frac{\lambda_Q}{\lambda}\right)^{4/3}\right)\right] \end{aligned} \tag{5.20}$$

and

$$\begin{aligned} g(\lambda, \lambda_Q, \theta) =& \frac{\theta}{\theta_0}\varphi^{-1}U'\left(J/\varphi\right) + 2\frac{\theta}{\theta_0}J^{-1} \\ & \left[\frac{1}{3}\left(w_1 + w_2 \mathrm{I}_{\bar{\mathbf{B}}}\right)\left(\left(\frac{\lambda_Q}{\lambda}\right)^{2/3} - \left(\frac{\lambda}{\lambda_Q}\right)^{4/3}\right) - \frac{1}{3}w_2\left(\left(\frac{\lambda_Q}{\lambda}\right)^{4/3} - \left(\frac{\lambda}{\lambda_Q}\right)^{8/3}\right)\right]. \end{aligned} \tag{5.21}$$

Based on (5.12) - (5.16) and (5.19) from the entropy (5.10), it follows that

$$\begin{aligned} h(\lambda, \lambda_Q, \theta, \sigma_{xx}) =& -\frac{1}{\theta_0}\left(U\left(J_{\mathrm{M}}\right) + w\left(\mathrm{I}_{\bar{\mathbf{C}}}, \mathrm{II}_{\bar{\mathbf{C}}}\right)\right) \\ & - c_{\mathrm{d}0}\left(-\ln\frac{\theta}{\theta_0}(1 - c_{\mathrm{dk}}\theta_0) - c_{\mathrm{dk}}\left(\theta - \theta_0\right)\right) + \frac{J}{3\varrho_{\mathrm{R}}}\frac{\varphi'}{\varphi}\sigma_{xx}. \end{aligned} \tag{5.22}$$

For given stretch λ the system of nonlinear equations consisting of

$$\sigma_{xx} = \varrho_{\mathrm{R}} f(\lambda, \lambda_Q, \theta) \tag{5.23}$$

$$0 = g(\lambda, \lambda_Q, \theta) \tag{5.24}$$

$$0 = h(\lambda, \lambda_Q, \theta, \sigma_{xx}) \tag{5.25}$$

is solved for the unknowns λ_Q, θ and σ_{xx}. The boundary conditions belonging to the finite-element computation are depicted in Fig. 5.39. $\overline{u}_x$ indicates a prescribed displacement which evolves according to the stretch λ. 0 indicates a fixed displacement degree of freedom and u_x, u_y and u_z correspond to unknown displacements. Fig. 5.40(b) compares this semi-analytic solution with the solution resulting from a finite-element computation showing that the relative error is less than $0.01\,\%$. While the chosen material describes the Gough-Joule effect both solution procedures are in agreement. Fig. 5.40(a) illustrates the temperature increase caused by an elongation of the volume element. In order to demonstrate the Gough-Joule effect Fig. 5.41 exhibits the temperature increase taking place when employing a maximum stretch of 10 %. Here, we observe that the temperature of the volume element decreases before it heats.

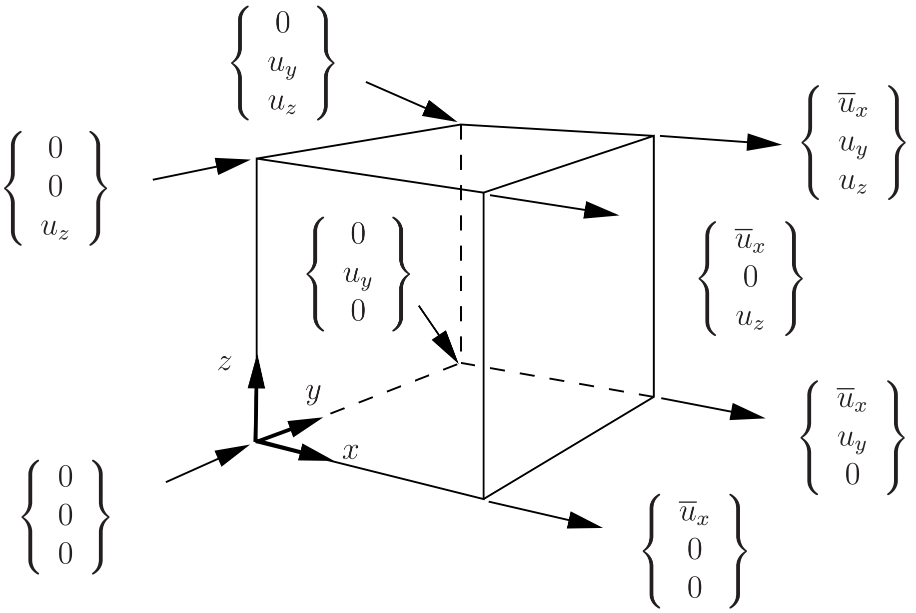

Figure 5.39: Boundary conditions for a volume element exposed to reversible adiabatic uniaxial tension ($q_\mathrm{n} = 0$ holds for the surface of the volume element)

5.3.1.3 Thermo-Elastic Inversion

Besides the linear dependence of the stresses on the temperature, as discussed in Section 5.3.1.1, we also investigate the behavior of the stresses induced by a change in temperature, as follows. To this end, we consider one element with a linear ansatz for the displacement and temperature field whose boundary conditions are given in Fig. 5.37. The first step is to increase the displacement $\overline{u}_x$ and decrease the temperature from $293.13\,\mathrm{K}$ to $273.13\,\mathrm{K}$ and the second step is to increase the temperature while keeping $\overline{u}_x$ constant according to

$$\overline{u}_x = \begin{cases} t\overline{u}_k\,\mathrm{s}^{-1} & \text{if} \quad 0\,\mathrm{s} \leq t \leq 1\,\mathrm{s} \\ \overline{u}_k \quad \text{if} \quad 1\,\mathrm{s} < t \leq 2\,\mathrm{s} \end{cases}$$

and

$$\overline{\theta} = \begin{cases} 293.15\,\mathrm{K} - 20t\,\mathrm{s}^{-1}\,\mathrm{K} & \text{if} \quad 0\,\mathrm{s} \leq t \leq 1\,\mathrm{s} \\ 273.15\,\mathrm{K} + 100t\,\mathrm{s}^{-1}\,\mathrm{K} & \text{if} \quad 1\,\mathrm{s} < t \leq 2\,\mathrm{s} \end{cases} .$$

We choose $\overline{u}_k = 0.01\,\mathrm{mm}, 0.03\,\mathrm{mm}, 0.06\,\mathrm{mm}, 0.1\,\mathrm{mm}$ and $0.2\,\mathrm{mm}$ for the prescribed displacements resulting in the stretches $\lambda = 1.01, 1.03, 1.06, 1.1, 1.2$. Fig. 5.42(a) plots the resulting Cauchy stress component σ_{xx} over the temperature θ. In order to conduct further code verification, we derive an analytic solution for the thermo-elastic inversion effect, see (Holzapfel, 2008). For this purpose (5.8) and (5.9) are solved for the given stretch λ and the given temperature θ

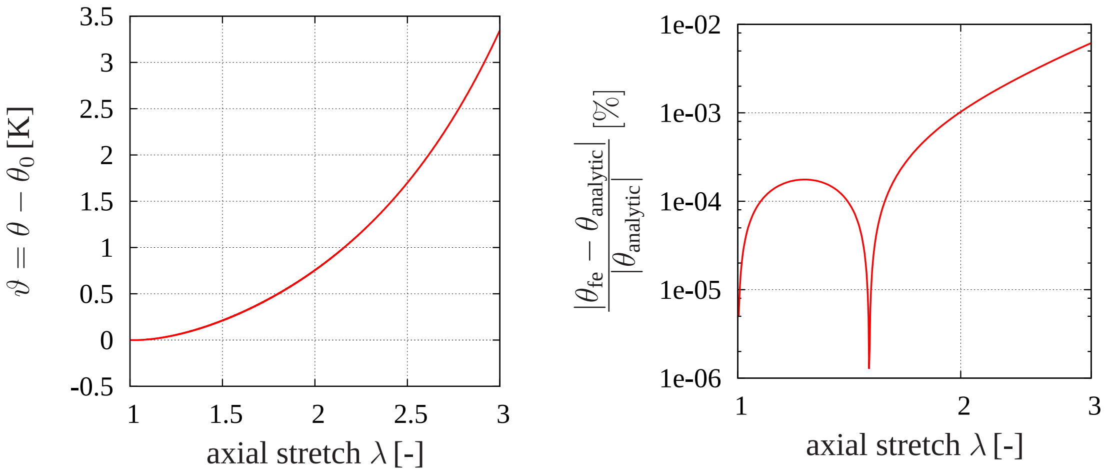

(a) Temperature increase induced by thermoelastic coupling

(b) Relative error

Figure 5.40: Temperature increase due to thermo-elastic coupling and the corresponding relative error

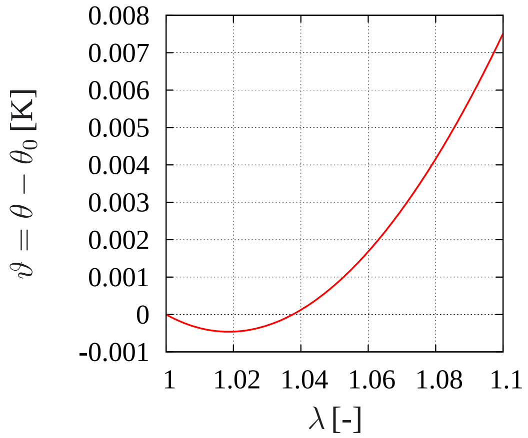

Figure 5.41: Gough-Joule effect, see e.g. (Hamkar, 2013; Holzapfel, 2008)

yielding the lateral stretch λ_Q and the stress $\tilde{T}_{11}$. By means of (2.167) $\tilde{T}_{11}$ is transformed to the current configuration and compared to the analytical solution with the outcome that both results coincide with an accuracy of at least 10^{-12}.

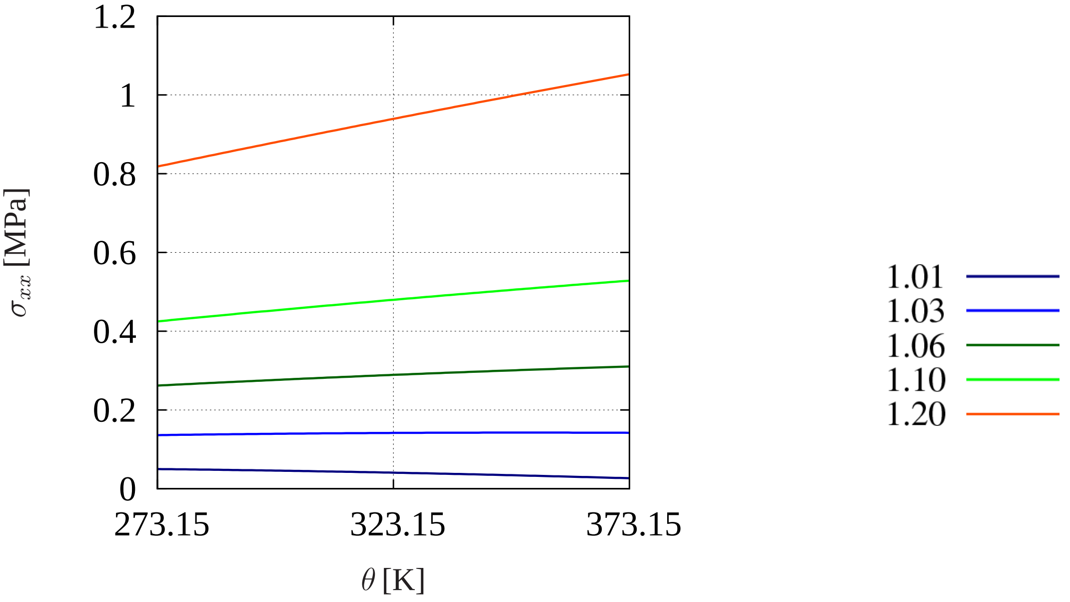

(a) Thermo-elastic inversion effect

(b) Key indicating the applied stretch λ

Figure 5.42: Thermo-elastic inversion effect, see (Hamkar, 2013; Holzapfel, 2008), for instance

5.3.2 Rod

Table 5.15: Mechanical material parameters of constitutive model (overstress part) for elastomer

μ MPa	$\bar{\eta}_0$ MPa s	$\bar{s}_0$ MPa	s_∞ MPa	κ K	ω_s K^{-1}	r_0 1
0.2	180	$1.0e$-03	$1.5e$-03	$8e$+03	$8e$-02	4

The first purpose of this section is to investigate the spatial discretization schemes applied to the thermo-mechanically coupled problem. For this purpose, we look at the structure which is given in Fig. 5.43 and assumed to be thermo-elastic. On the one hand, we study two versions of the h-version (Q1,Q2) and on the other hand the p-version of the finite element method from the point of view of accuracy and computational efficiency. We will also demonstrate another implication of the thermo-elastic inversion effect discussed above as well as investigating different temporal discretization schemes of DIRK-type. For this purpose, we assume thermo-viscoelastic material behavior. The material parameters employed for the equilibrium part are stated in Section 5.3.1. Tab. 5.15 gives the material parameters for the overstress part of the mechanical subproblem. The material parameters related to the temperature-dependent viscosity $\bar{s}_0$, s_∞, κ and ω_s are chosen according to (Lion, 2000). The parameters $\bar{\eta}_0$ and μ were developed in (Hartmann, 2002) based on experimental data published in (Haupt and Sedlan, 2001). All computations are based on the trunk space, see Section A.1.3, and the thermal material parameters given in Tab. 5.14 are employed.

5.3.2.1 Finite Thermo-Elasticity

In order to study the influence of different space discretization schemes, let us contemplate the structure given in Fig. 5.43. Both its displacement and the temperature degrees of freedom on the plane denoted by $z = 200$ are fixed. On its opposite plane, the stress in z-direction and the temperature, both increasing linearly in time, are prescribed according to

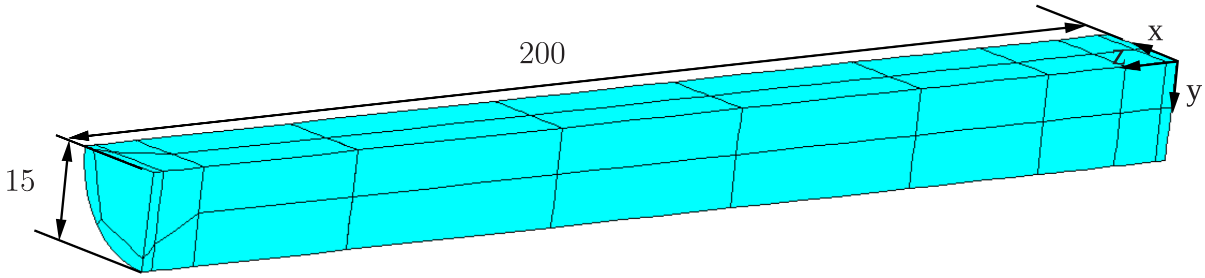

Figure 5.43: Geometry and dimensioning of rod discretized with 30 p-elements

$$\bar{p}_z = -(t/t_\mathrm{e})\,\mathrm{MPa}, \tag{5.26}$$

$$\bar{\theta}_1 = 293.15\,\mathrm{K}, \tag{5.27}$$

$$\bar{\theta}_2 = 293.15\,\mathrm{K} + (t/t_\mathrm{e})80\,\mathrm{K}, \tag{5.28}$$

with $t_\mathrm{e} = 1000\,\mathrm{s}$, see Figs. 5.45 and 5.44. With the exception of the planes defined by $z = 0$ and $z = 200$, where a temperature is prescribed, the surface of the structure is considered to be adiabatic ($q_\mathrm{n} = 0$). We will proceed to investigate the p-version and the h-version of the finite element method. p-discretizations employing a polynomial degree from 1 to 9 are constructed on the basis of the mesh given in Fig. 5.43. Tab. 5.16 gives the corresponding number of unknowns. Fig. 5.46 depicts the h-version meshes while Tab. 5.17 indicates the corresponding number of unknowns. Besides the boundary conditions, Fig. 5.45 also illustrates the reference mesh, which

p-level	1	2	3	4	5	6	7	8	9
$n_\mathrm{nu} + n_{\mathrm{n}\theta}$	213	744	1275	2243	3648	5610	8249	11658	16038

Table 5.16: p-level of rod with 30 elements and the number of unknowns n_nu

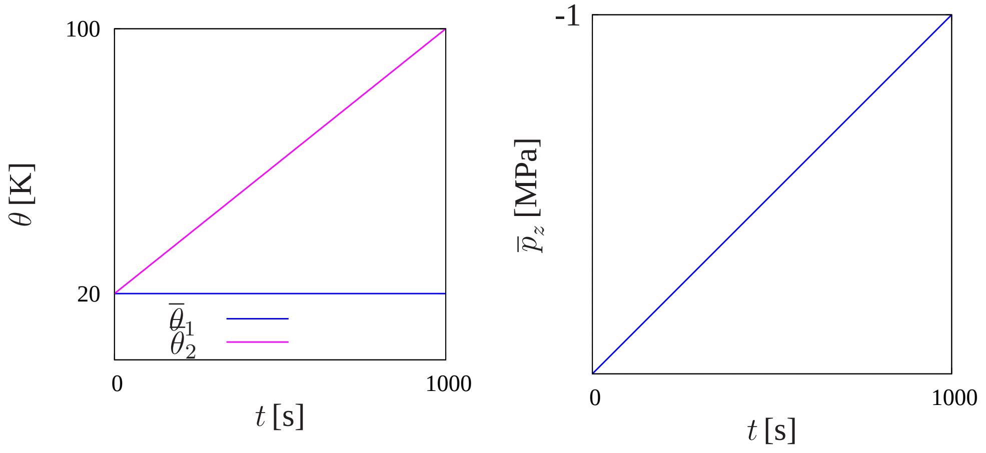

(a) Prescribed temperature plotted over time (b) Prescribed pressure plotted over time

Figure 5.44: Prescribed displacement boundary conditions

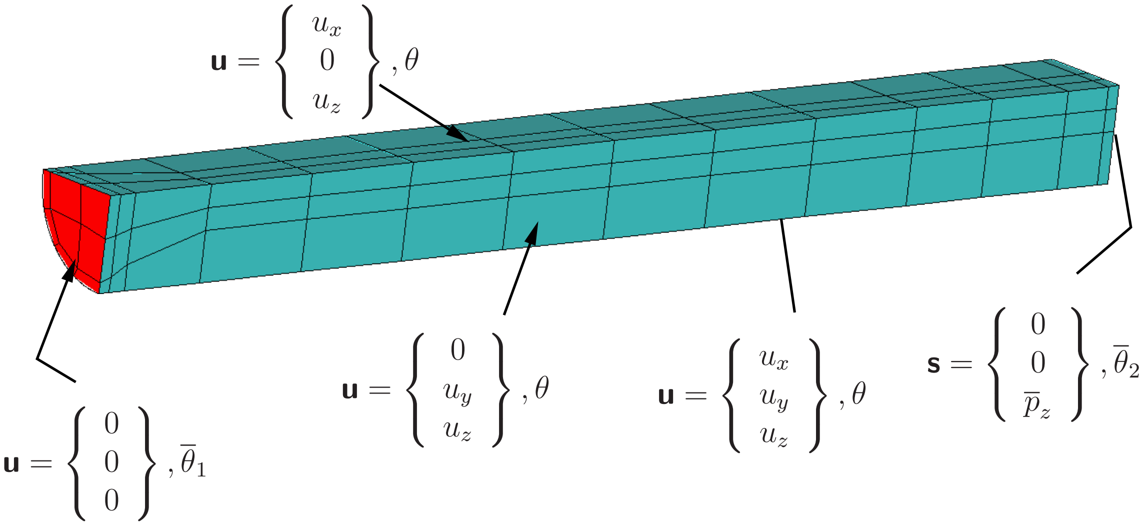

Figure 5.45: Reference solution with 112 p-elements and boundary conditions

	M1	M2	M3	M4	M5	M6
Q1	971	1301	2643	3313	3983	10109
Q2	3611	4831	10060	12600	15104	38891

Table 5.17: Number of unknowns $n_{\text{nu}} + n_{\text{n}\theta}$ of the chosen meshes

is used for comparing the results stemming from the h- and p-version discretizations. The ref-

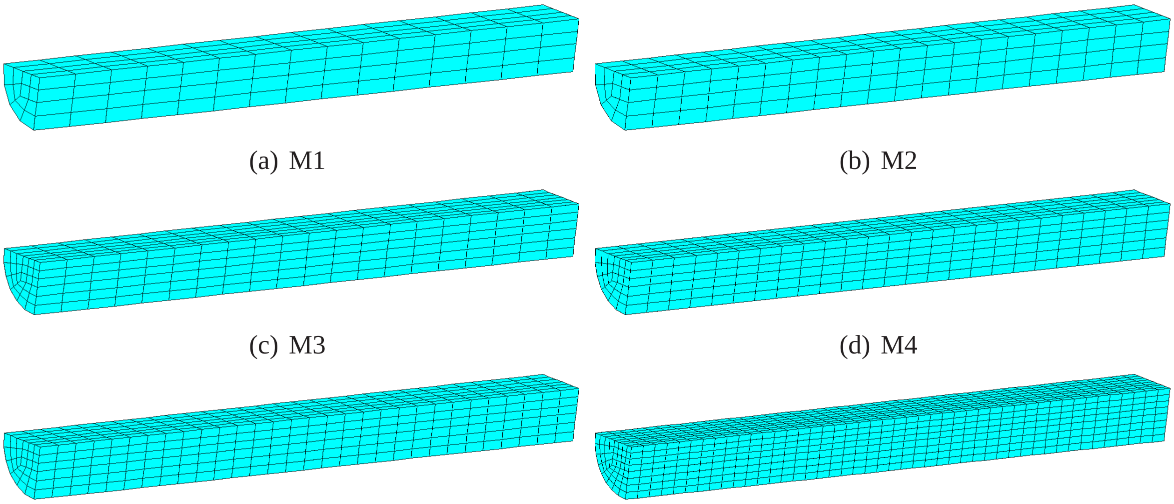
(a) M1
(b) M2
(c) M3
(d) M4
(e) M5
(f) M6

Figure 5.46: h-version meshes

erence mesh contains 112 hexahedrals with a uniform polynomial degree of 10 yielding 74865 unknowns. For the temporal discretization, we apply the second order accurate method proposed by Ellsiepen, see (Ellsiepen, 1999), for each discretization with an embedded step-size control. For the displacements we use the absolute error $\epsilon_{\mathrm{a}}^{u} = 10^{-4}$ and the relative error $\epsilon_{\mathrm{r}}^{u} = 10^{-6}$ and for the temperatures and the internal variables we employ the tolerances $\epsilon_{\mathrm{a}}^{\theta} = 10^{-3}$, $\epsilon_{\mathrm{r}}^{\theta} = 10^{-5}$, $\epsilon_{\mathrm{a}}^{q} = 10^{-5}$ and $\epsilon_{\mathrm{r}}^{q} = 10^{-5}$. In order to assess the quality of the discretization schemes, we make use of the error measures

$$\epsilon(\boldsymbol{\Theta}) = \frac{1}{n_{\mathrm{NR}}} \sum_{k=1}^{n_{\mathrm{NR}}} |\theta_k - \theta_{\mathrm{ex}k}| \tag{5.29}$$

and (5.4). The sum of the absolute differences in the temperature field of the reference solution $\theta_{\mathrm{ex}k}$ and the approximate solution θ_k, both evaluated at the nodes given by the background grid, see Fig. 5.47, correlates to the number of nodes in the background grid n_{NR}. Since this investigation is based on finite thermo-elastic material behavior implicating $\tilde{\mathbf{T}}_{\mathrm{ov}} = \mathbf{0}$, the stress state at a given node of the evaluation grid only depends on the temperature and the displacement at the node in question. Having completed this evaluation, we can derive the corresponding stress state

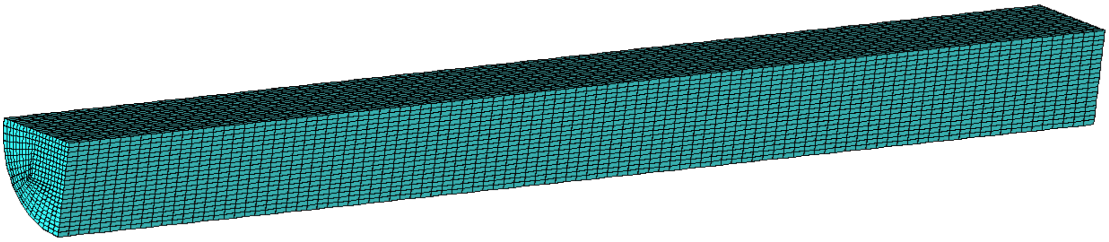

Figure 5.47: Evaluation grid with 33431 points

and thus compute not only the error in the displacement and temperature field, but also the error in the stress field. Figs. 5.49 and 5.48 show the resulting displacement field in z- and y-direction displayed on the deformed configuration. The increase in the absolute value of the y-component of the displacement field near $z = 0$ results from the prescribed temperature at $z = 0$. Figs. 5.50 and 5.51 display the stress state and the temperature distribution. All displayed quantities stem from a computation with a uniform polynomial degree of $p = 6$. For the errors in the displacement field with respect to the number of unknowns and the CPU time see Fig. 5.52. The errors in the temperature- and stress field can be found in Figs. 5.53 and 5.54. No matter which error measure is taken into consideration, the linear elements exhibit the poorest behavior. This holds for both accuracy and efficiency considerations, meaning that the error for a given number of unknowns or a given CPU time, is much larger if linear elements are used instead of quadratic ones. The best choice among all the discretizations under consideration is the p-version, which not only exhibits a steeper slope, especially for the error in the displacement and the stress field, but also produces the smallest absolute value of all error measures concerned for a given number of unknowns and a given CPU time. We accordingly observe a superior accuracy and efficiency of the p-version for this example.

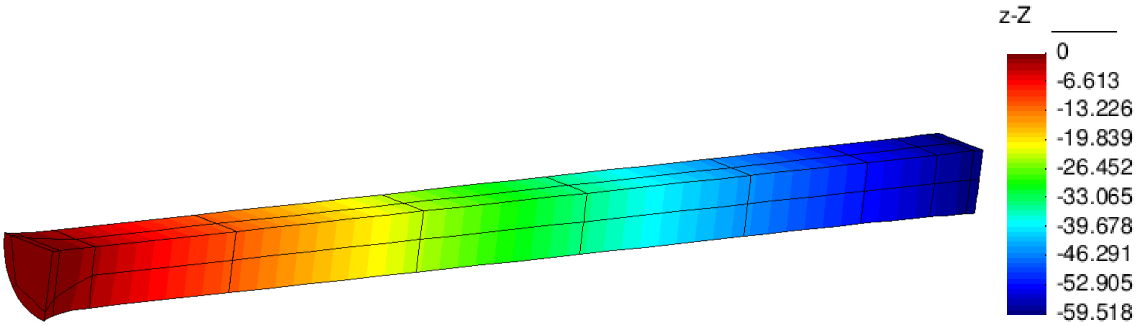

(a) Deformed configuration displaying displacement field in z-direction and undeformed configuration ($p = 6$)

(b) Key

Figure 5.48: Displacement field in z-direction (axial direction), $t = 1000\,\mathrm{s}$

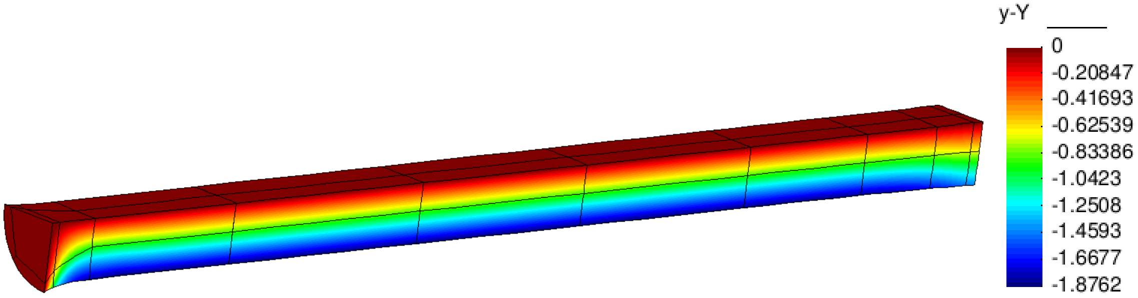

(a) Displacement field in y-direction ($p = 6$)

(b) Key

Figure 5.49: Displacement field in y-direction (lateral direction), $t = 1000\,\mathrm{s}$

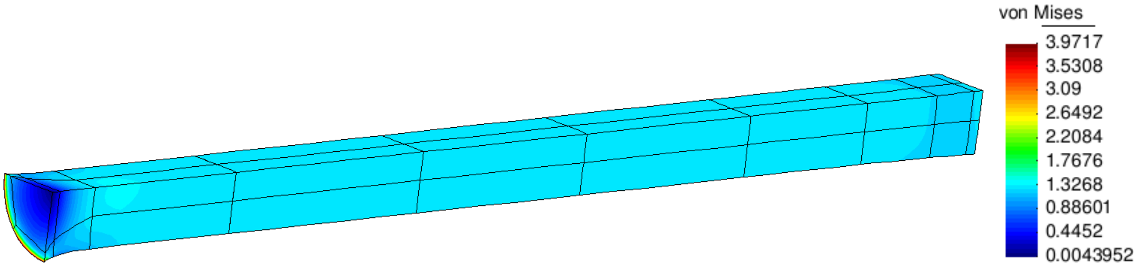

(a) von Mises stress distribution (b) Key

Figure 5.50: von Mises stress distribution displayed on deformed configuration ($p = 6$), $t = 1000\,\mathrm{s}$

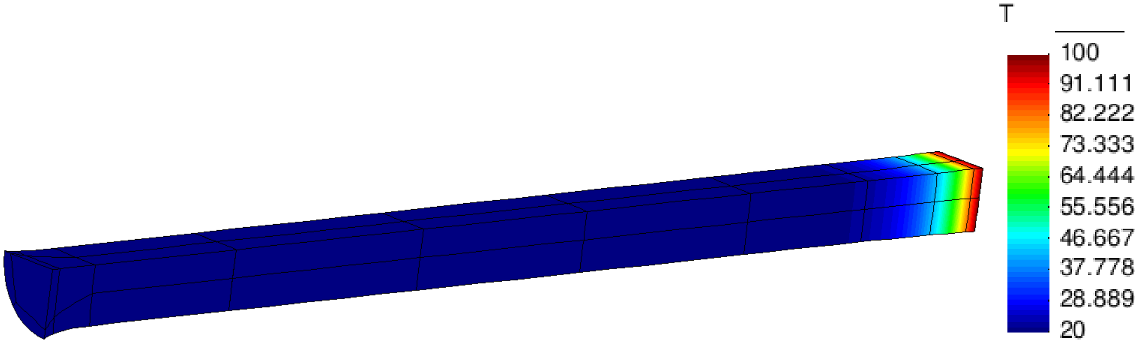

(a) Temperature distribution (b) Key

Figure 5.51: Temperature distribution ($p = 6$), $t = 1000\,\mathrm{s}$

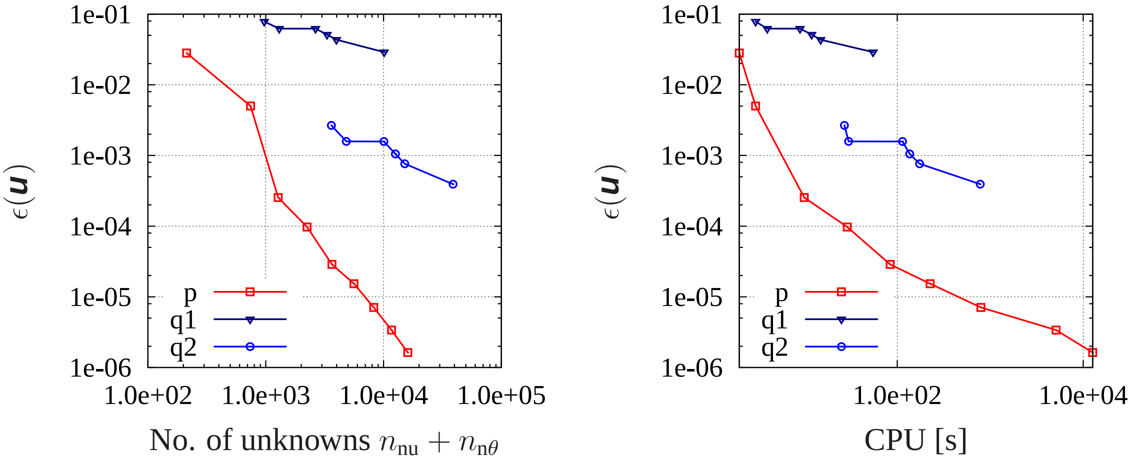

(a) Error in displacement field (b) Error in displacement field over CPU time

Figure 5.52: Error in displacement field for rod ($p = 1, ..., 9$)

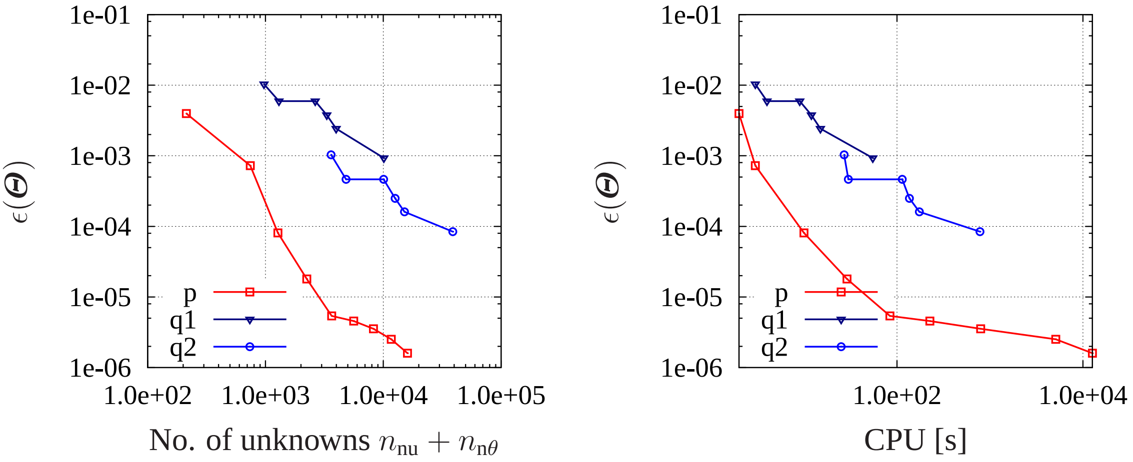

(a) Error in temperature field

(b) Error in temperature field over CPU time

Figure 5.53: Error in temperature field for rod ($p = 1, ..., 9$)

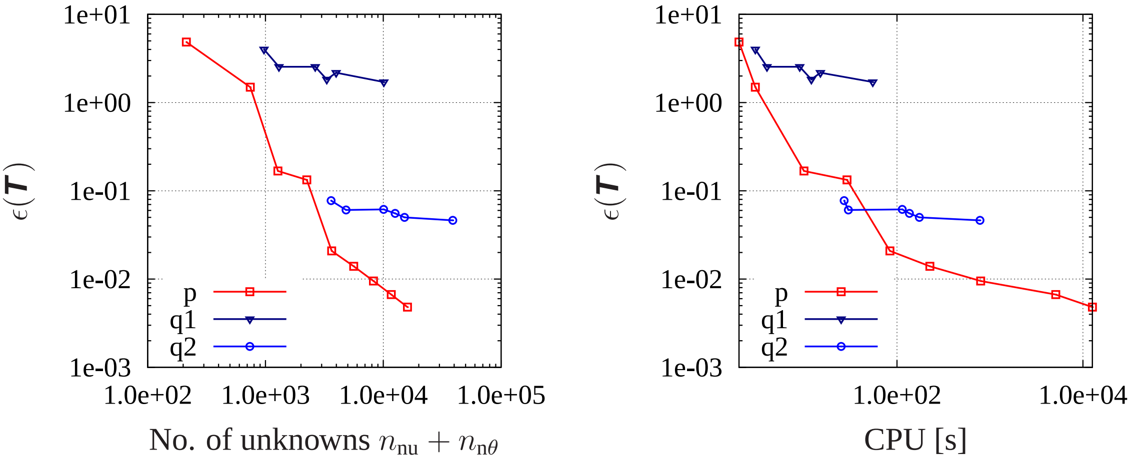

(a) Error in stress field

(b) Error in stress field over CPU time

Figure 5.54: Error in stress field for rod ($p = 1, ..., 9$)

5.3.2.2 Thermo-Elastic Inversion of Rod

We also investigate another implication of the thermo-elastic inversion effect. For this purpose, we assume finite thermo-elastic material behavior and use the material parameters given in Section 5.3.1. Section 5.3.1.3 demonstrates that increasing the temperature results in an increase in the resulting stress, if the stretch exceeds a certain value and we are contemplating an adiabatic reversible process. This means that, if we fix a specimen at one end and apply a given load at the other, it retracts when we simultaneously apply localized heat. In order to demonstrate this effect, let us look at the boundary conditions depicted in Fig. 5.45. The temperature at the plane indicated by $z = 200$ is fixed throughout the entire process at $293.15\,\mathrm{K}$ so we write $\overline{\theta}_1 = 293.15\,\mathrm{K}$. Within the first second of the process, we apply a load of $-8\,\mathrm{MPa}$ to the plane given by $z = 0$, increasing linearly in time. The prescribed load remains constant during all subsequent periods. During the next period from $t = 2\,\mathrm{s}$ to $t = 10\,\mathrm{s}$ we raise the temperature at the plane indicated by $z = 0$ linearly in time until it reaches $373.15\,\mathrm{K}$. During the third period, both the prescribed load and the prescribed temperature remain constant. We can accordingly write

$$\overline{p}_z = -8t\,\mathrm{s}^{-1}\,\mathrm{MPa} \quad \text{for} \quad 0 \le t \le 1\,\mathrm{s} \quad \text{else} \quad \overline{p}_z = -8\,\mathrm{MPa}, \tag{5.30}$$

$$\overline{\theta}_1 = 293.15\,\mathrm{K}, \tag{5.31}$$

$$\overline{\theta}_2 = 293.15\,\mathrm{K} \quad \text{for} \quad 0\,\mathrm{s} \le t \le 1\,\mathrm{s},$$

and

$$\overline{\theta}_2 = 293.15\,\mathrm{K} + 8.\overline{8}\mathrm{s}^{-1}(t - 1\,\mathrm{s})\,\mathrm{K} \quad \text{for} \quad 1\,\mathrm{s} < t \le 10\,\mathrm{s} \quad \text{else} \quad \overline{\theta}_2 = 373.15\,\mathrm{K}. \tag{5.32}$$

Following the loading process, we observe a maximal displacement of the plane specified by $z = 0$ of $388\,\mathrm{mm}$, which decreases once the temperature $\overline{\theta}_2$ is increased, even though the prescribed load remains constant. The shortening of the rod is given in Fig. 5.55. At the beginning of the process, we notice a significant change in the length of the specimen. Contraction stops once the thermal equilibrium is reached, see Fig. 5.56. The resulting displacement field is given in Fig. 5.57. A very similar investigation based on a slightly different geometry and finite thermo-viscoelastic material behavior can be found in (Suwannachit, 2012).

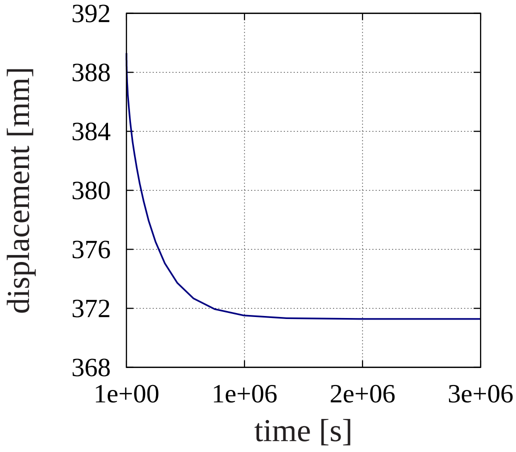

Figure 5.55: Shortening of rod due to a temperature increase on plane $z = 0$ ($p = 6$)

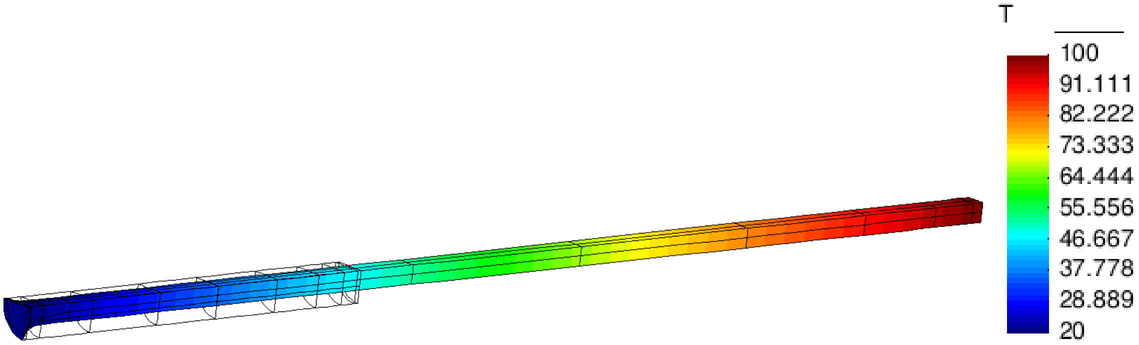

(a) Temperature distribution at the end of the process (b) Key

Figure 5.56: Temperature field ($p = 6$)

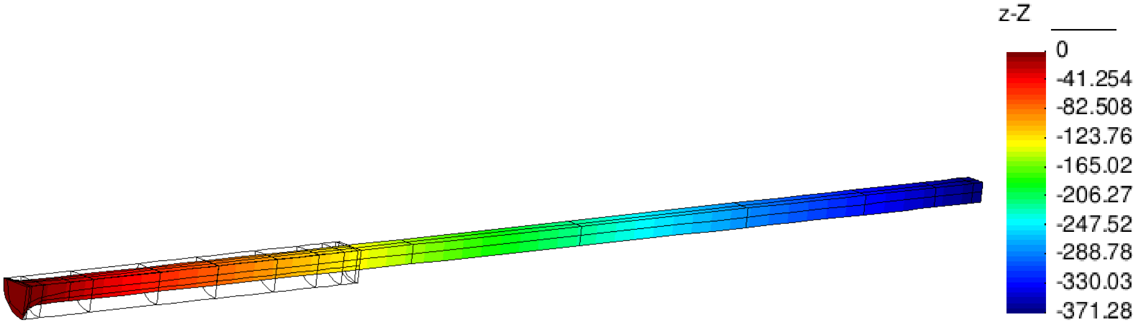

(a) Displacement field and the end of the process (b) Key

Figure 5.57: Displacement field ($p = 6$)

5.3.2.3 Finite Thermo-Viscoelasticity

This section is devoted to applying different temporal discretization schemes of DIRK-type to the thermo-viscoelastic problem. The material parameters are given in Tabs. 5.14, 5.15 and in Section 5.3.1. We employ the boundary conditions given in Fig. 5.58. The prescribed Dirichlet boundary conditions read

$$\overline{u}_z = -0.5t\,\mathrm{s}^{-1}\,\mathrm{mm} \quad \text{for} \quad 0 \leq t \leq 40\,\mathrm{s} \tag{5.33}$$

and

$$\overline{\theta} = 293.15\,\mathrm{K} + t\,\mathrm{s}^{-1}\mathrm{K} \quad \text{for} \quad 0 \leq t \leq 40\,\mathrm{s}. \tag{5.34}$$

Due to the elastic (2.212) and inelastic production term (2.218), there is also an evolution in the temperature field. As regards the discussion of the spatial discretization schemes set out in the last section, we choose a polynomial degree of $p = 6$ for investigating the behavior of the temporal discretization schemes of first, second and third order as this is considered to be sufficiently accurate, see Figs. 5.52, 5.53 and 5.54, see Section 5.2.2.2 and 5.2.1.2 for isothermal considerations. In order to assess the quality of the temporal discretization schemes, we adopt the error measures (5.5) and

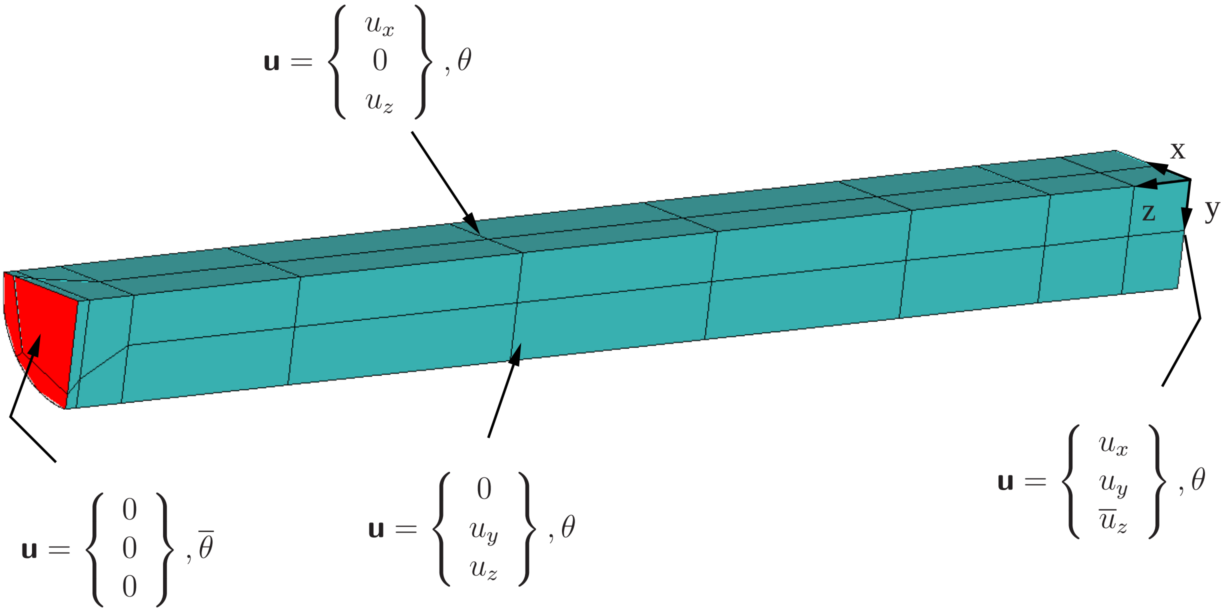

Figure 5.58: Boundary conditions of problem of finite thermo-viscoelasticity

$$\text{abserrt} := \max_{n} \left(\| \boldsymbol{\Theta}_n^{\text{ref}} - \boldsymbol{\Theta}_n \| \right). \tag{5.35}$$

The highly accurate solution (reference solution $\boldsymbol{q}_n^{\text{ref}}$, $\boldsymbol{u}_n^{\text{ref}}$ and $\boldsymbol{\Theta}_n^{\text{ref}}$) is carried out by means of the 3rd order method proposed by Alexander, see (Alexander, 1977), with a constant step-size of

$\Delta t_n = 0.25 \times 10^{-2}$ s. We investigate both the accuracy and the efficiency of the time integration schemes, the level of accuracy being based on the errors in displacements, temperatures and internal variables plotted over the step-size, see Figs. 5.59(a), 5.60(a) and 5.61(a). The first observation is that all methods attain their anticipated order. With respect to a given step-size Δt_n the second order accurate method proposed by Ellsiepen is several times more accurate than the commonly applied Backward-Euler scheme. The most accurate results, however, are obtained using Alexander's third order accurate method. To assess the efficiency, we consider the errors in displacements, temperatures and internal variables in terms of the computational effort, see Figs. 5.59(b), 5.60(b) and 5.61(b). Again, the time integration schemes of higher order prove to be more efficient than the Backward-Euler scheme. If we compare the errors in the quantities under investigation for the Backward-Euler method with $\Delta t_n = 1.25e\text{-}01$ s with those resulting from computations based on Ellsiepen's and Alexander's method employing the coarsest step-size $\Delta t_n = 1.0e\text{-}00$ s, we see that high-order time integration methods deliver a higher accuracy while simultaneously reducing the error, see Tab. 5.18.

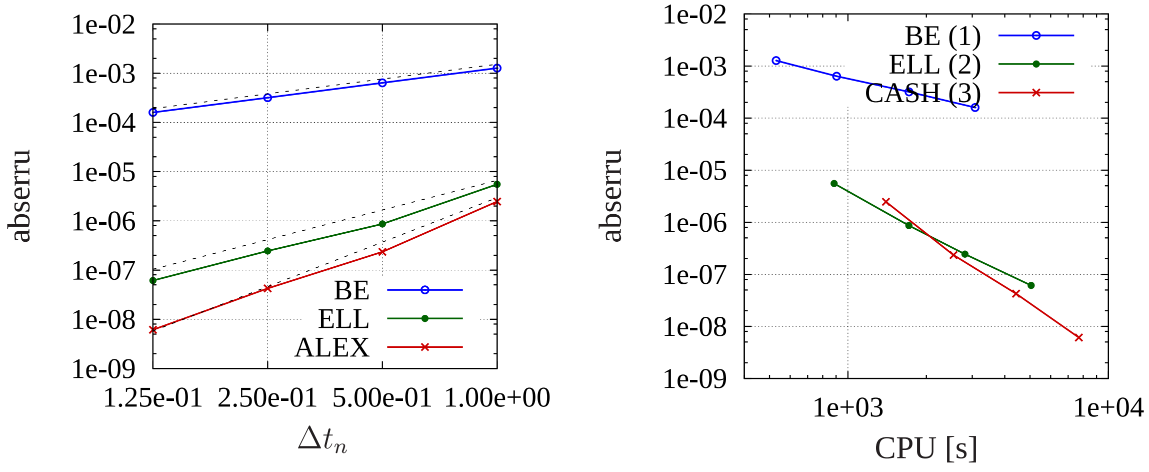

(a) Error in displacements

(b) Error in displacements

Figure 5.59: Error in displacements with respect to the step-size Δt_n and computation time

Table 5.18: Comparison between Backward-Euler (BE) and higher order DIRK-methods

name	order	stages	abserru	abserrt	abserrq	CPU s	CPU %
ELL	2	2	5.6e-06	3.5e-03	3.3e-07	885	28.8
ALEX	3	3	2.5e-06	1.2e-03	1.2e-08	1399	45.5
BE	1	1	1.6e-04	3.9e-02	7.7e-05	3077	100

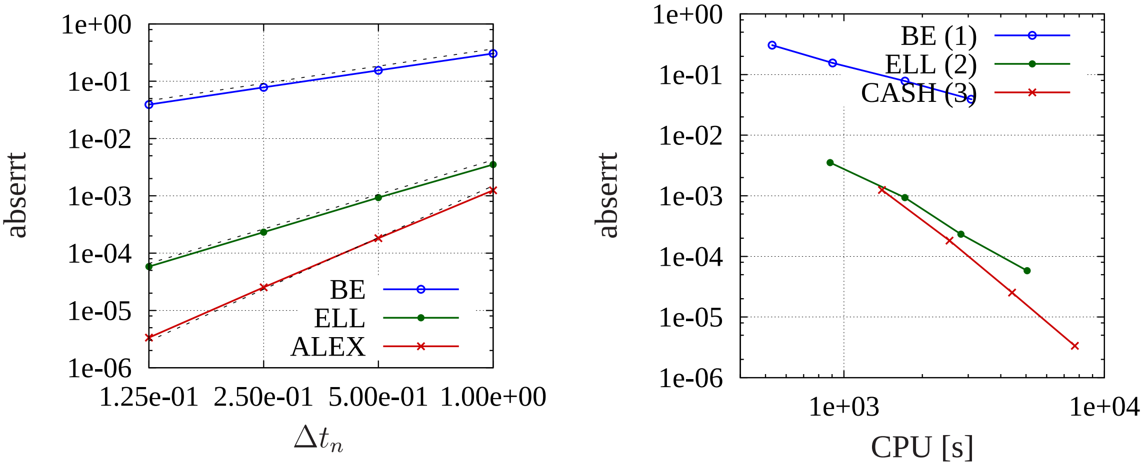

(a) Error in temperatures (b) Error in temperatures

Figure 5.60: Error in temperatures with respect to the step-size Δt_n and computation time

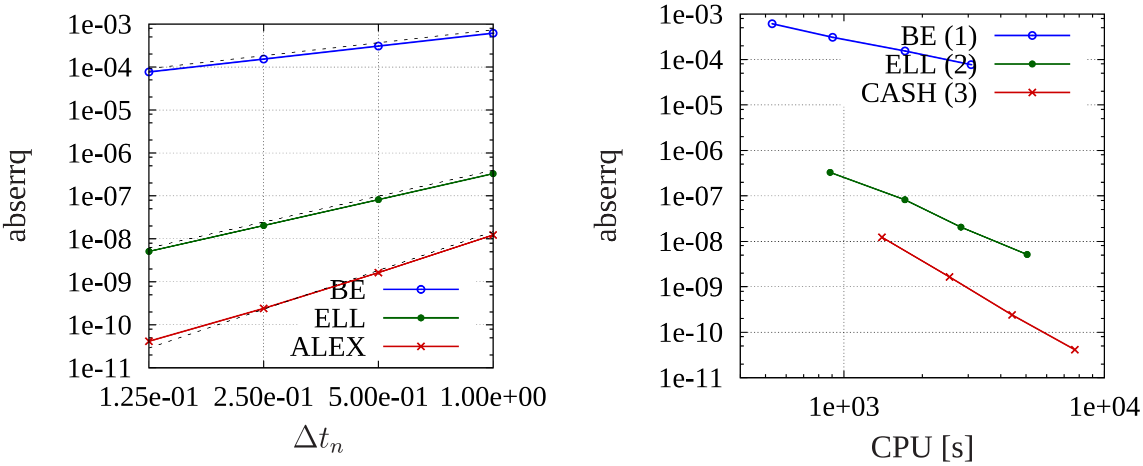

(a) Error in internal variables (b) Error in internal variables

Figure 5.61: Error in internal variables with respect to the step-size Δt_n and computation time

So far, we have discussed accuracy and efficiency aspects of thermo-mechanically coupled problems. It turns out that the beneficial characteristics of the approach under consideration carry over from the isothermal case to the thermo-mechanically coupled case. The p-version proves to be very competitive in terms of the spatial error while the high-order methods prove to be superior to the commonly applied Backward-Euler method with respect to the temporal discretization. Combining the p-version for the spatial discretization with high-order time integration schemes of DIRK-type accordingly appears to be a highly favorable approach when highly accurate solutions of thermo-mechanically coupled problems are sought. We therefore conclude that this approach is adequate for verification purposes.

5.3.3 Bearing

This section deals with a more practical example, whose focus lies in describing the physical effects like the influence of different weather conditions on the behavior of the bearing. The bearing that we consider in this section consists of two layers of steel dyed cyan and one of elastomeric material dyed blue, see Fig. 5.62. Figs. 5.63 and 5.64 illustrate the dimensioning. The elastomeric material is modeled using the finite viscoelasticity material model, see Section 2.3,

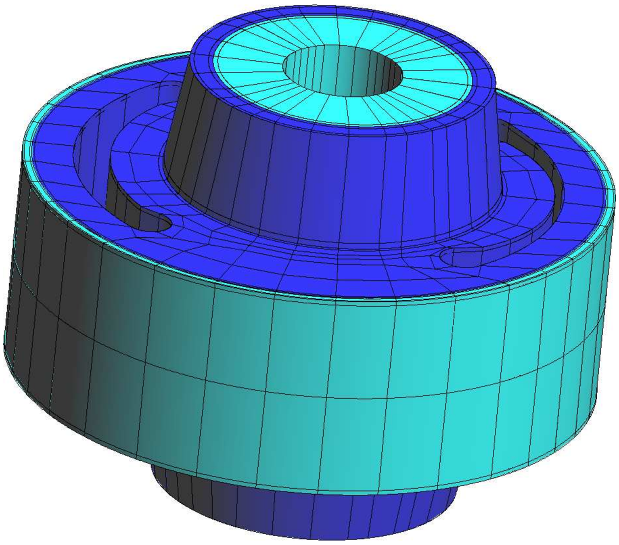

Figure 5.62: Bearing

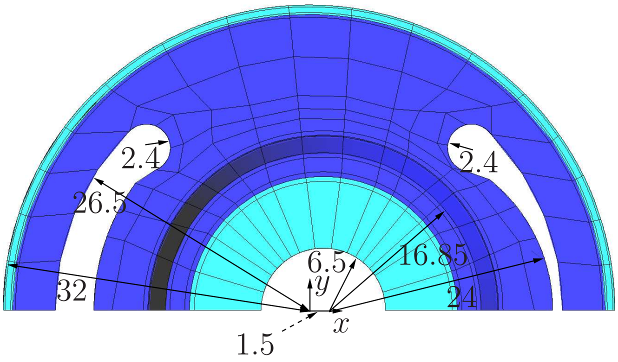

Figure 5.63: Dimensioning of bearing in x-y-plane (540 elements)

and Section 5.3.1 for the corresponding material parameters, Tabs. 5.14 and 5.15 in particular. We use a temperature-dependent elastic material model for 51CrV4 for the steel layers, as proposed in (Quint et al., 2011). The corresponding material parameters, summarized in Tab. 5.19, are taken from (Quint, 2012). Since the yield stress is not reached within the steel layers, no plastification occurs. Based on (Quint, 2012), we choose the free energy

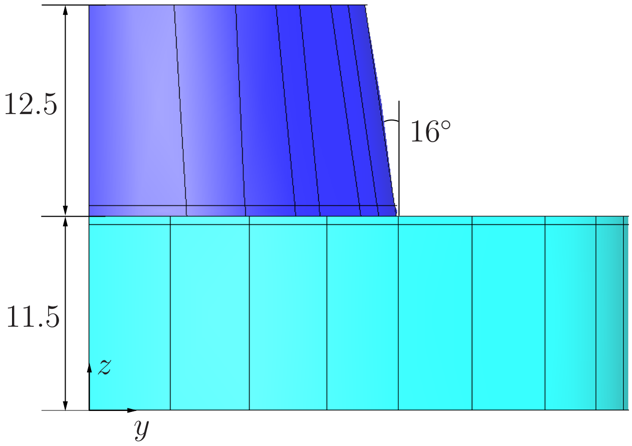

Figure 5.64: Dimensioning of bearing in y-z-plane (540 elements)

Table 5.19: Material parameters of constitutive model for steel taken from (Quint, 2012)

K_0 GPa	c_k MPa/K	G_0 GPa	c_g MPa/K	λ_0 tmm/(s^3K)	c_{d0} mm^2/(s^{2}K)	α_θ 1/K	ϱ_R t/mm^3
167	-91	76.9	-42	35	$6e$+08	$1.2e$-05	$7.815e$-09

$$\varrho_R \psi = U(J_M, \theta) + \bar{v}(I_{\bar{C}}, \theta) \tag{5.36}$$

with the specific parts

$$U(J_M, \theta) = \frac{K(\theta)}{50\varrho_R}(J_M^5 + J_M^{-5} - 2) \quad \text{and} \quad \bar{v}(I_{\bar{C}}, \theta) = \frac{G(\theta)}{2\varrho_R}(I_{\bar{C}} - 3) \tag{5.37}$$

with

$$I_{\bar{C}} = \mathbf{1} \cdot \bar{\mathbf{C}} = J_M^{-\frac{2}{3}} \mathbf{C} \cdot \mathbf{1}. \tag{5.38}$$

The temperature-dependent bulk and shear moduli are assumed to be

$$K(\theta) = K_0 + c_k(\theta - \theta_0) \quad \text{and} \quad G(\theta) = G_0 + c_g(\theta - \theta_0). \tag{5.39}$$

Making use of the derivatives of the free energy which is related to a volumetric deformation in terms of the right Cauchy-Green tensor

$$2\varrho_{\mathrm{R}}\frac{\mathrm{d}U}{\mathrm{d}\mathbf{C}} = \tilde{\mathbf{T}}_{\mathrm{eq}}^{\mathrm{vol}} = \varrho_{\mathrm{R}}\frac{J}{\varphi}U'(J/\varphi)\mathbf{C}^{-1} = \varrho_{\mathrm{R}}J_{\mathrm{M}}U'(J/\varphi)\mathbf{C}^{-1},$$

its derivative with respect to the determinant of the mechanical deformation gradient

$$U'(J_{\mathrm{M}}) = \frac{K(\theta)}{10\varrho_{\mathrm{R}}}\left(J_{\mathrm{M}}^{4} - J_{\mathrm{M}}^{-6}\right),$$

and the derivative of the free energy related to a volume-preserving deformation in terms of the right Cauchy-green tensor

$$\begin{aligned}\tilde{\mathbf{T}}_{\mathrm{eq}}^{\mathrm{iso}} &= 2\varrho_{\mathrm{R}}\frac{\mathrm{d}\bar{v}}{\mathrm{d}\mathbf{C}} = G(\theta)\left(-\frac{2}{3}\right)J_{\mathrm{M}}^{-\frac{5}{3}}\frac{1}{2}J_{\mathrm{M}}\left(\mathbf{1}\cdot\mathbf{C}\right)\mathbf{C}^{-1} + J_{\mathrm{M}}^{-\frac{2}{3}}\mathbf{1}\\ &= G(\theta)J_{\mathrm{M}}^{-\frac{2}{3}}\left(\mathbf{1} - \frac{1}{3}\left(\mathbf{1}\cdot\mathbf{C}\right)\mathbf{C}^{-1}\right),\end{aligned}$$

the stress tensor in reference configuration reads

$$\tilde{\mathbf{T}} = 2\varrho_{\mathrm{R}}\frac{\partial\psi}{\partial\mathbf{C}} = \tilde{\mathbf{T}}_{\mathrm{eq}}^{\mathrm{vol}} + \tilde{\mathbf{T}}_{\mathrm{eq}}^{\mathrm{iso}}.$$

5.3.3.1 Investigation of Bearing Subjected to Different Thermal Boundary Conditions

We now proceed to the behavior of a bearing exposed to different weather conditions. In order to simulate the cooling or heating of the bearing, we apply a heat flux to its surface. The heat flux is modeled as a linear combination of convection and radiation. Linear dependence is often assumed for pure convection, see (3.12). We also take a look at the net rate of heat transfer that is induced by thermal radiation, based on (3.13). For the surface of the structure under consideration, where a heat flux is prescribed, see Fig. 5.65, either a linear combination of heat convection and radiation

$$q_{\mathrm{n}} = \overline{q}_{\mathrm{con}} + \overline{q}_{\mathrm{rad}} \tag{5.40}$$

or $q_{\mathrm{n}} = 0$ is assumed. The thermal boundary conditions are depicted in Fig. 5.65 and the mechanical boundary conditions can be taken from Fig. 5.66. During the whole process the bearing is subjected to a thermal load given by (5.40), see also (3.12) and (3.13). We prescribe $\theta_\infty = 253.15\,\mathrm{K}$ and $\theta_{\mathrm{f}} = 253.15\,\mathrm{K}$ for the cooling and $\theta_\infty = 323.15\,\mathrm{K}$ and $\theta_{\mathrm{f}} = 323.15\,\mathrm{K}$ for the heating, assuming an emissivity of $\epsilon = \epsilon_{\mathrm{r}} = 0.95$ for the rubber, see (Banic et al., 2012), and $\epsilon = \epsilon_{\mathrm{s}} = 0.2$ for the steel, see (Quint, 2012). The heat transfer coefficient amounts to $h_{\mathrm{c}} = 2.5 \times 10^{-2}\mathrm{t}/(\mathrm{s}^3\mathrm{K})$. After a period of $1000\,\mathrm{s}$, we apply displacement boundary conditions

$$\begin{aligned}\overline{u}_x &= 0\,\mathrm{mm} && \text{for} \quad 0\,\mathrm{s} \le t \le 1000\,\mathrm{s},\\ \overline{u}_x &= -1.25\,\mathrm{s}^{-1}(t - 1000\,\mathrm{s})\,\mathrm{mm} && \text{for} \quad 1000\,\mathrm{s} < t \le 1002\,\mathrm{s},\\ \overline{u}_x &= -2.5\,\mathrm{mm} - 0.5\sin\left(\omega_{\mathrm{bearing}}\left(t - 1002\,\mathrm{s}\right)\right)\mathrm{mm} && \text{for} \quad 1002\,\mathrm{s} < t \le 1100\,\mathrm{s},\end{aligned} \tag{5.41}$$

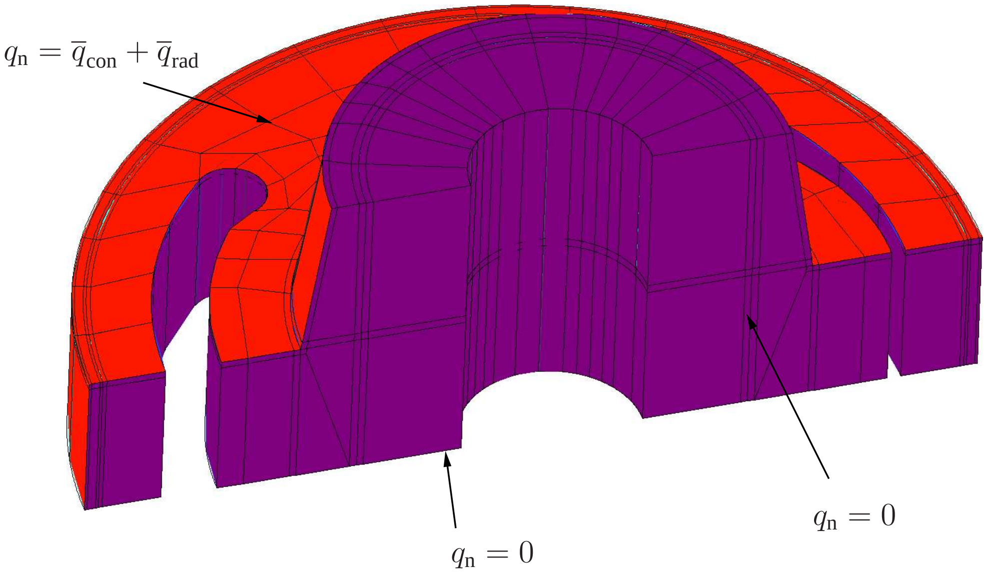

Figure 5.65: Thermal boundary conditions

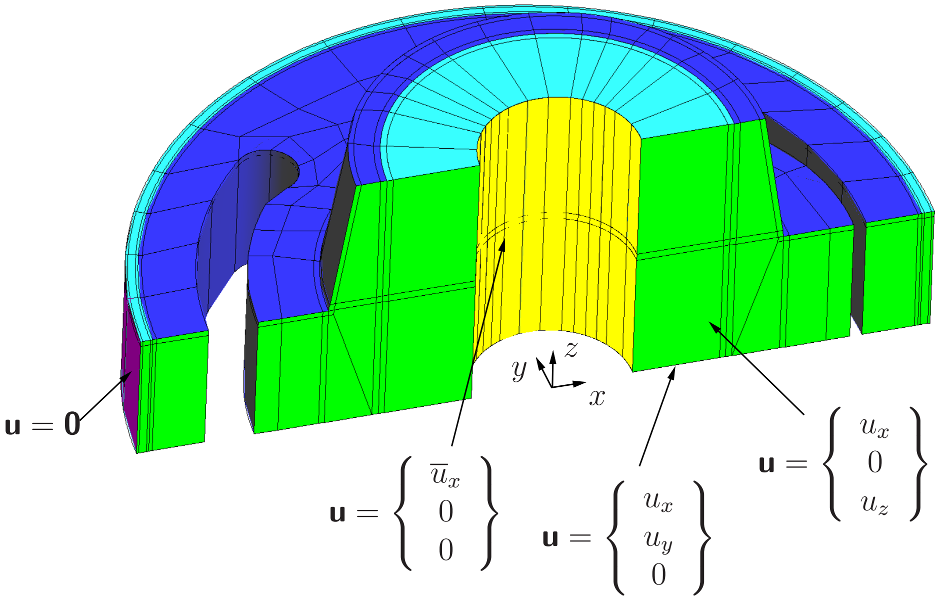

Figure 5.66: Mechanical boundary conditions

see also Figs. 5.66 and Fig. 5.67. Besides an ongoing cooling or heating of the bearing, we run 30 sinosoidal cycles for $98\,\mathrm{s}$ resulting in a frequency of $\mathrm{f}_\mathrm{bearing} = 0.306\mathrm{s}^{-1}$ and an angular frequency of $\omega_\mathrm{bearing} = 1.92\mathrm{s}^{-1}$. We use Ellsiepen's method with an embedded step-size control for the temporal discretization, employing the tolerances $\epsilon_\mathrm{a}^{u} = 10^{-4}$, $\epsilon_\mathrm{r}^{u} = 10^{-6}$, $\epsilon_\mathrm{a}^{\theta} = 10^{-3}$, $\epsilon_\mathrm{r}^{\theta} = 10^{-5}$, $\epsilon_\mathrm{a}^{q} = 10^{-4}$ and $\epsilon_\mathrm{r}^{q} = 10^{-6}$. The temperature and displacement fields, following

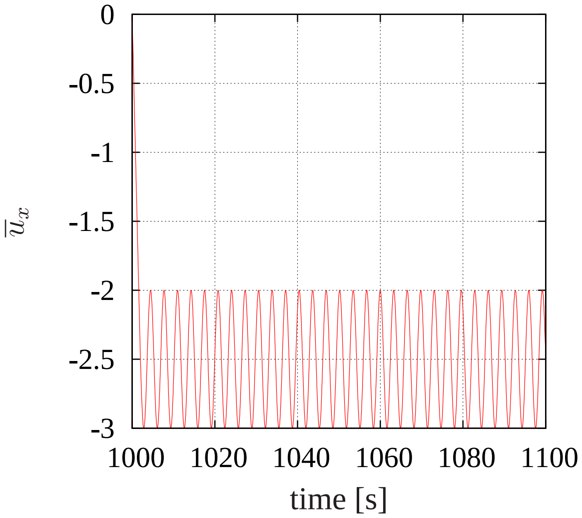

Figure 5.67: Displacement applied to bearing

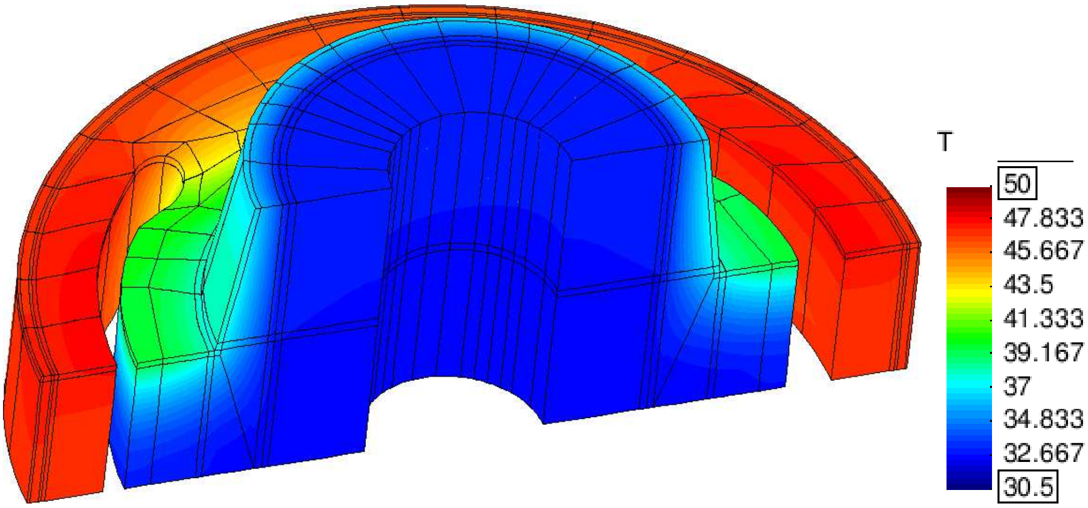

(a) Heating

(b) Key for heating

Figure 5.68: Temperature distribution in bearing after 1020 s displayed on deformed configuration ($p = 6$)

the application of the heat flux and linearly increasing the displacements on the inner radius of the bearing, are given in Figs. 5.68, 5.69 and 5.70. The resulting force can be taken from Fig. 5.71(a). At the beginning of the process, the reaction force of the bearing subjected to a heatflux resulting in a temperature increase is approximately 50 N greater than the reaction force resulting from the cooling process. At room temperature the reaction force is somewhere in

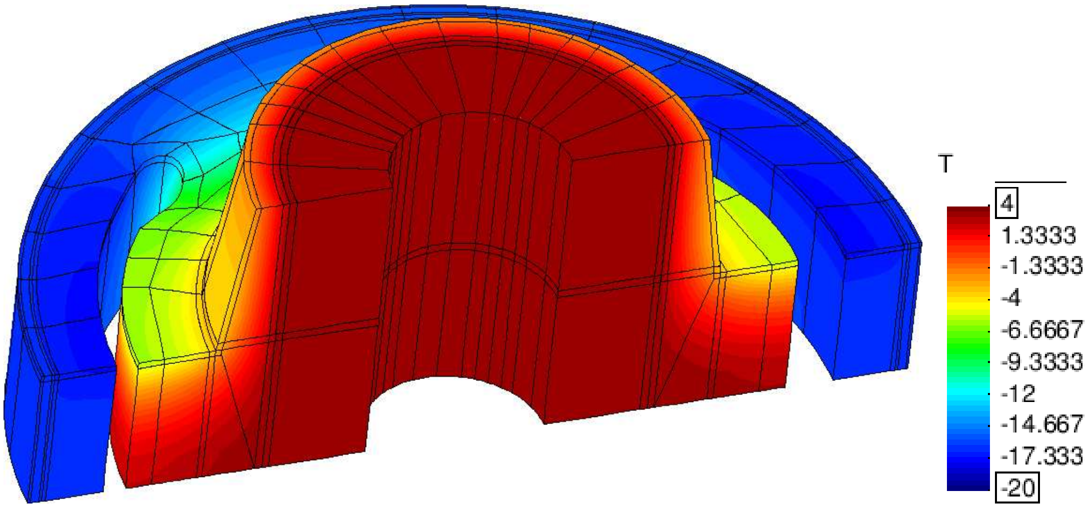

(a) Cooling (b) Key for cooling

Figure 5.69: Temperature distribution in bearing after $1020\,\text{s}$ displayed on deformed configuration ($p = 6$)

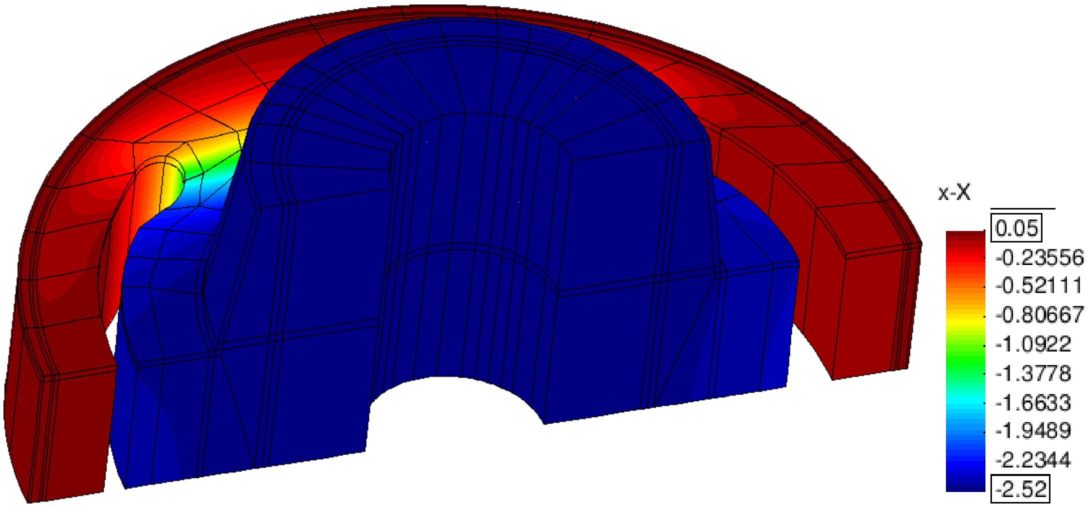

(a) Heating (b) Key

Figure 5.70: Displacement field in bearing after $1020\,\text{s}$ displayed on deformed configuration ($p = 6$)

between. The chosen step-sizes are given in Fig. 5.71(b). For the first $1000\,\text{s}$ of the process, the step-sizes chosen for the process taking place at room temperature are by far the largest, because there is no evolution either in the temperature (both the bearing and its surroundings measure $293.15\,\text{K}$) or in the displacement field. It also emerges that the heating process requires a smaller step-size than the cooling process, a circumstance that applies to the cyclic loading period,too.

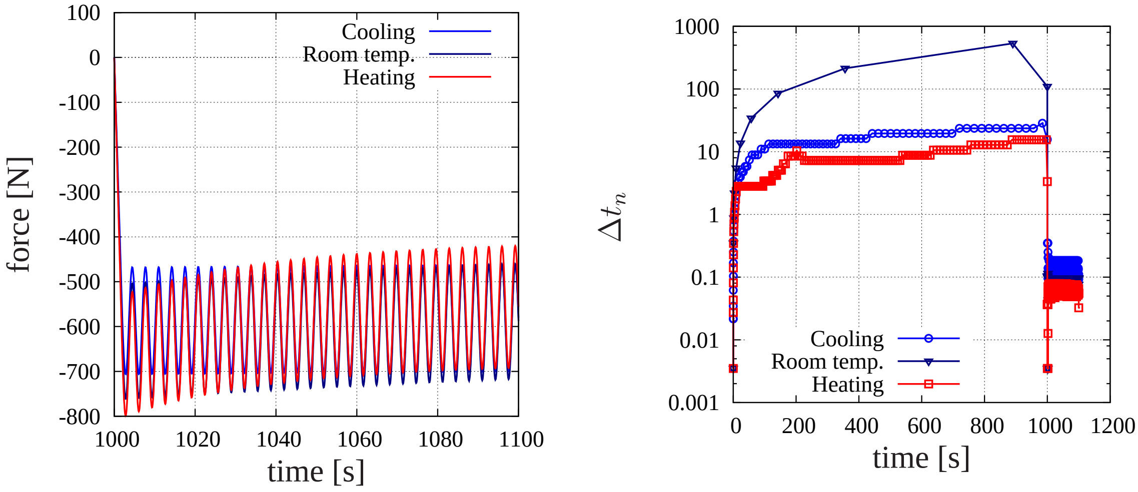

(a) Reaction forces for different temperature levels

(b) Corresponding step-size behavior

Figure 5.71: Reaction force of bearing for different temperature levels and corresponding step-size behavior

As soon as the cyclic loading commences, the step-size of the process taking place at room temperature decreases drastically, because an evolution takes place in both the displacement an the temperature field.

5.3.3.2 Investigation of Thermo-Mechanical Coupling

In order to study the coupling of the mechanical and the thermal field, we investigate the temperature increase in the bearing resulting from a change in the mechanical field for different values of the parameter μ which mainly influences the temperature evolution. It is of interest to investigate the contribution made by the coupling terms to the evolution in the temperature field, because, depending on the purpose of the computation and the desired accuracy requirements, it might not be necessary to account for them. See (2.212) and (2.218) for the thermo-elastic and inelastic coupling terms responsible for a displacement-induced evolution of the temperature field. The mechanical boundary conditions are given by

$$\overline{u}_x = -1.25\,\mathrm{s}^{-1} t\,\mathrm{mm} \qquad \text{for} \quad 0\,\mathrm{s} < t \leq 2\,\mathrm{s}, \tag{5.42}$$

and

$$\overline{u}_x = -2.5\,\mathrm{mm} - 0.5\sin\left(\omega_{\text{bearing}}\left(t - 2\,\mathrm{s}\right)\right)\mathrm{mm} \qquad \text{for} \quad 2\,\mathrm{s} < t \leq 20\,\mathrm{s}, \tag{5.43}$$

see also Fig. 5.66. We accordingly conduct 40 sinusoidal cycles over the space of $18\,\mathrm{s}$ yielding $\mathrm{f}_{\text{bearing}} = 2.\overline{2}\,\mathrm{s}^{-1}$ and $\omega_{\text{bearing}} = 13.96\,\mathrm{s}^{-1}$. For the thermal boundary conditions see Fig. 5.72

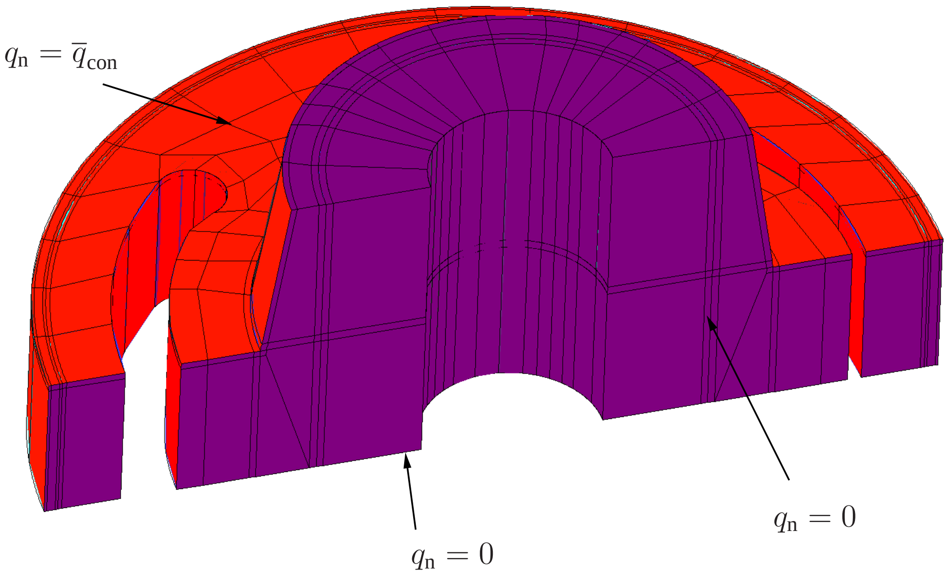

Figure 5.72: Thermal boundary conditions

with $q_{\mathrm{n}}{=}\bar{q}_{\mathrm{con}}$ evolving according to (3.12), based on the heat transfer coefficient $h_{\mathrm{c}} = 2.5e$-02 $\mathrm{t}/(\mathrm{s}^3\mathrm{K})$ and $\theta_{\mathrm{f}} = 293.15\,\mathrm{K}$. We use Ellsiepen's method with an embedded step-size control for the computation. The tolerances we employ are $\epsilon_{\mathrm{a}}^{u} = 10^{-3}$, $\epsilon_{\mathrm{r}}^{u} = 10^{-5}$, $\epsilon_{\mathrm{a}}^{\theta} = 10^{-4}$, $\epsilon_{\mathrm{r}}^{\theta} = 10^{-6}$, $\epsilon_{\mathrm{a}}^{q} = 10^{-5}$ and $\epsilon_{\mathrm{r}}^{q} = 10^{-5}$ and the resulting step-size behavior is given in Fig. 5.76. The

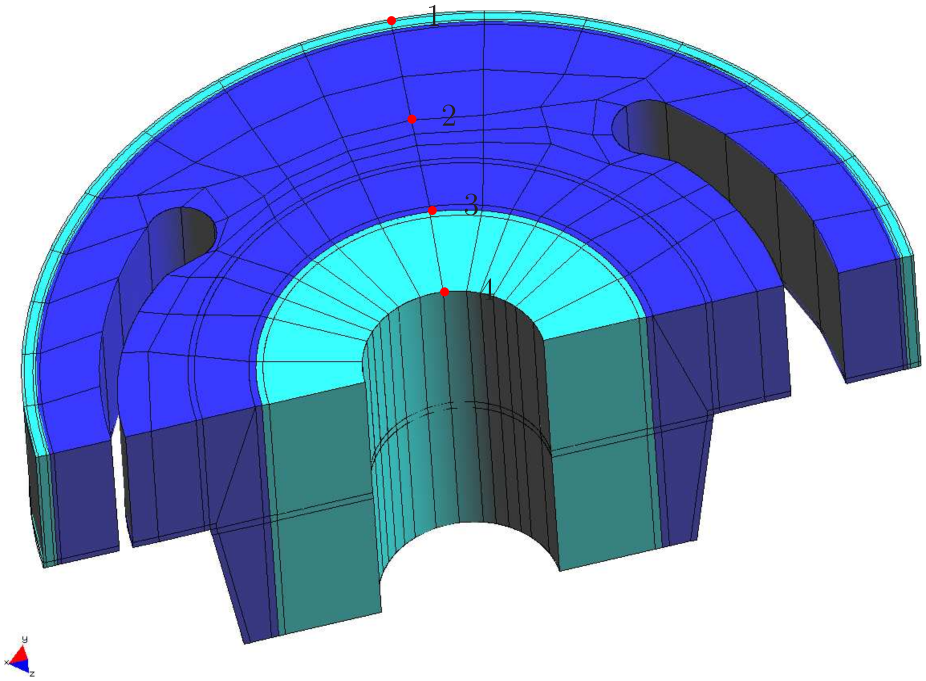

Figure 5.73: Evaluation points of temperature field for parameter study

temperature evolution is investigated at the points given in Fig. 5.73 for large strain thermo-elastic and thermo-viscoelastic material behavior. For the latter case the material parameter μ is varied from $\mu = 0.2\,\mathrm{MPa}$ until the physically insignificent value of $\mu = 32\,\mathrm{MPa}$. The resulting temperature evaluation is given in Figs. 5.74 and 5.75. The first observation that can be made is

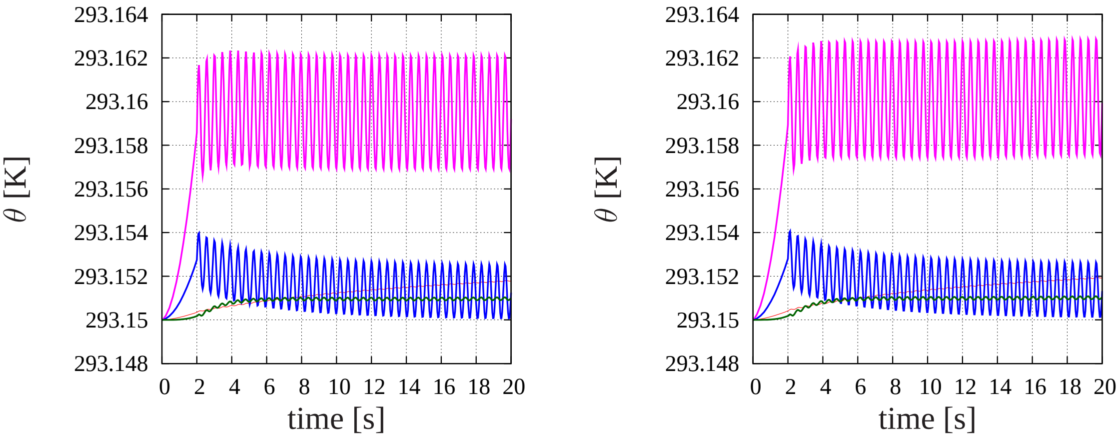

(a) $\mu = 0\,\mathrm{MPa}$ (finite thermo-elasticity)

(b) $\mu = 0.2\,\mathrm{MPa}$

Figure 5.74: Temperature evolution of bearing at the points given in Fig. 5.73 for finite thermo-elasticity and finite viscoelasticity ($p = 6$). The corresponding legend is given in Fig. 5.75(c).

that the temperature increase related to a purely thermo-elastic material behavior is the smallest, as would be expected. We can also state that the main temperature increase takes place at point 2, which is not surprising, because it is here that the largest strains and accordingly the highest strain rate occur. Since hardly any deformation is apparent in the steel layers, its contribution to the mechanically induced evolution in the temperature field is not taken into account. Since point 3 belongs to both the elastomer and the steel layer, smaller strains and strain rates occur, resulting in a lesser increase in the temperature. The temperature increase at points 1 and 4 is caused by convection so hardly any oscillation takes place. Due to the inelastic coupling term (2.218) just a very small increase in the temperature occurs when contemplating a physically meaningful value of the material parameter μ, see Figs. 5.74(a) and 5.74(b). A considerable increase in the temperature field only occurs if μ is assigned an extremely high value, see Figs. 5.75(a) and 5.75(b).

Depending on the purpose of the computation and the chosen material parameters, it might be adequate to disregard the temperature evolution caused by the inelastic coupling term d. Another feature is that the higher the value of the parameter μ, the smaller the chosen step-size becomes. Disregarding the inelastic coupling term accordingly proves to be beneficial for the step-size behavior, too.

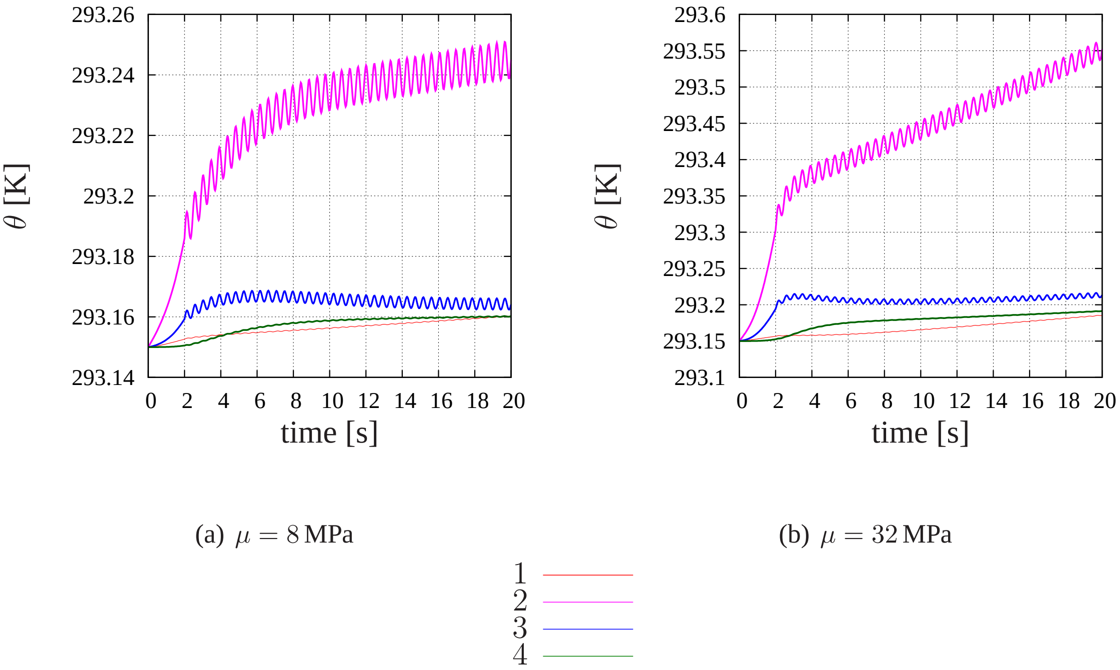

(a) $\mu = 8\,\text{MPa}$

(b) $\mu = 32\,\text{MPa}$

(c) Key

Figure 5.75: Temperature evolution of bearing at the points given in Fig. 5.73 for finite viscoelasticity ($p = 6$)

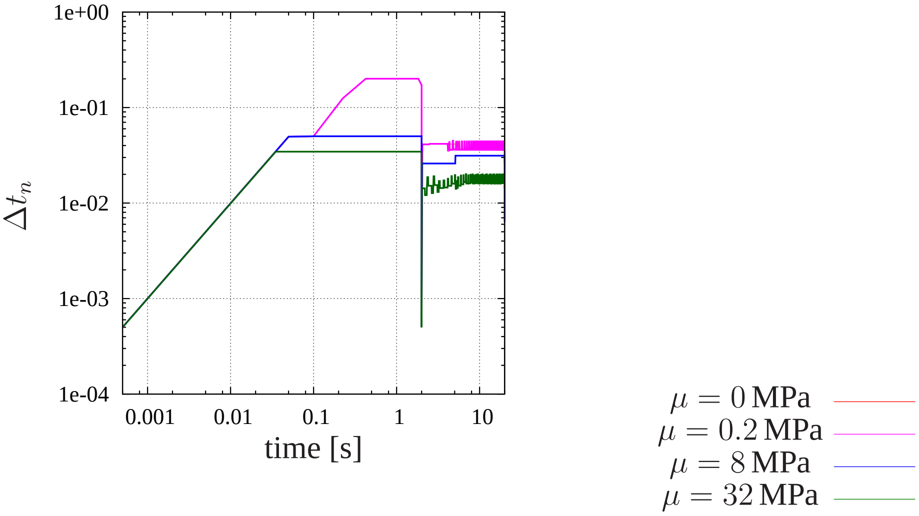

(a) Step-size

(b) Key

Figure 5.76: Step-size behavior of the displacement-induced increase in bearing's temperature field for different values of μ

6 Conclusions and Outlook

The purpose of this thesis is to investigate the p-version of the finite element method in conjunction with high-order time integration schemes of DIRK-type in the context of quasistatic, geometrically and physically nonlinear, thermo-mechanically-coupled problems employing constitutive equations of evolutionary type. Due to the higher order rates of convergence in both the DIRK-type time integration schemes and the p-version, this approach delivers highly accurate results at reasonable costs.

For the isothermal case, we compare the p-version with mixed element formulations making use of a linear/quadratic ansatz for the displacement and a constant/linear ansatz for the volumetric strains and the pressure (Q1P0/Q2P1). This procedure reveals the outstanding properties of the p-version, particularly when large deformations are considered. With respect to the error measures concerned, the results attained with p-version discretizations are superior to those based on h-version discretizations, regardless of whether efficiency or accuracy aspects are addressed. In accordance with (Rank et al., 2001) it has to be emphasized that the parallelization of the set-up of the element stiffness matrices and the right-hand sides results in a considerable speeding up of the computational time for both the h-version and for the p-version. But the increase in efficiency due to a parallelization of the set-up of the element stiffness matrices is more pronounced for the p-version than for the h-version. This can be explained by the following line of thought. While for the p-version the quotient of the computational time spent on local and global level exceeds that of the h-version, the parallelization of the computation of the element stiffness matrices is more efficient than the parallelization of the solution of the global equation system, see Figs. 4.16(a) and 4.16(b), which explains the aforementioned relation. In addition to making use of the parallel architecture of modern computers, there is more potential for accelerating the solution process. Since the convergence behavior of Newton-type iteration schemes depends on the quality of the initial iterate, the number of iterations required for solving a system of nonlinear equations can be reduced by employing a skilled guess. A common approach in the context of nonlinear finite elements is to use the solution of the previous time-step as the initial iterate. Instead, we use a linear extrapolator, which takes information from previous time stages of the DIRK-method, in order to guess the initial iterate, see (Quint, 2012) and the literature cited therein. This approach also renders the Newton-type iteration scheme more robust, allowing a larger time step-size, which is of course limited by accuracy considerations of the time integration schemes. Another means of accelerating the solution process is to use the CMLNA (Chord-Multilevel-Newton Algorithm), meaning that the global stiffness matrix is kept constant over several iterations.

Moreover, the topic of verification is addressed by means of comparing results for a tube under internal pressure stemming from p-version and h-version finite element computations with a semi-analytical solution derived in (Yosibash et al., 2007). It turns out that the p-version elements converge faster to the semi-analytical solution than the h-version elements. But due to the inexact geometry description of the tube, the p-version's error remains constant, starting with a polynomial degree of 6. At this juncture the importance of correctly describing the geometry emerges. Further code verification is carried out by comparing results from different p-version codes. To this end, we compare the in-house code TASA-FEM, see (Hartmann, 2006), on whose basis the computations discussed in this work are carried out, with $AdhoC^4$, see (Düster et al., 2004). Both codes deliver at least ten identical decimal places for the displacement field of the example given in Section 5.1.1.

We also investigate problems of isothermal finite viscoelasticity, where the corresponding high-order time integration schemes of first, second and third order achieve their theoretical rates of convergence for the rate-dependent problems concerned. We accordingly demonstrate that, based on the p-version for the spatial discretization, applying high-order time integration schemes of DIRK-type produces a result that is several orders of magnitude more accurate than that of the Backward-Euler method for a given computational effort. On top of gaining accuracy *and* reducing the computational effort, high-order time integration schemes also allow the application of an adaptive time step-size control, maintaining a defined level of error at each time-step. In this context, we wish to mention the second order accurate method proposed by Ellsiepen. When considering problems of finite viscoelasticity, the gain in accuracy resulting from an improvement in the spatial discretization is several times greater than that resulting from a more precise temporal approximation. Nevertheless, there is still the advantage of being able to compute processes with different time-scales making use of the embedded time step-size control.

Besides isothermal problems, we also contemplate thermo-mechanically coupled problems. For the purpose of code verification, we look at several effects for which analytical solutions are available, first comparing the analytical solution for simple tension at different temperature levels with results obtained by means of finite element compuations. Secondly, there is the Joule-Gough effect, addressing a marginal temperature decrease, which is followed by a temperature increase, when a specimen is exposed to a tensile test. Thirdly, code verification is done by means of the analytic solution for the thermoelastic inversion effect, which is associated with a decrease in the stress state of a specimen subjected to a slight elongation when it is heated. If the elongation exceeds a certain value, however, the stress state increases.

The favorable characteristics of the combination of p-version finite elements employed for the spatial discretization and DIRK-type time integration schemes pass from the isothermal to the thermo-mechanically coupled case. We observe the superiority of the p-version over the h-version for the spatial discretization, regardless of whether we choose a linear or a quadratic ansatz for the displacement and temperature field, while also being able to use the advantages of the high-order time integration schemes mentioned above. For fully coupled problems, the high-order time integration schemes of first, second and third order under consideration also attain their theoretical order for the applications concerned. They prove to be superior to the Backward-Euler method in terms of both accuracy and efficiency. We also demonstrate the successful application of the embedded step-size control of high-order time integration schemes. With respect to the coupling terms yielding an increase in the temperature field, which is induced by a change in the displacement field, we wish to point out that their effect on the temperature field is relatively small for the considered material model and for physically meaningful material parameters.

We therefore conclude that the combination of high-order time and space discretization schemes is not only suitable but also very efficient and precise for both isothermal and thermo-mechanically coupled problems, so it is safe to say that the approach in question is ideally suited for verification purposes.

In order to further exploit the superior properties of high-order DIRK-type time integration schemes, we should take a look at problems of finite plasticity, where the superior accuracy of high-order time integration schemes should be more pronounced than in the case of a relatively smooth problem like that of finite viscoelasticity. Applying Rosenbrock-type methods, see (Hamkar and Hartmann, 2012; Hartmann and Hamkar, 2010; Netz et al., 2013b), for example, to problems of finite plasticity in conjunction with the p-version should also be considered. Rosenbrock-type methods result in a completely iteration-free approach, even though they obtain higher order accuracy, which leads to a substantial decrease in the number of function and derivative evaluations. Since the evaluation of the stiffness matrix involves a great deal of computational input in the case of the p-version, this approach is very promising. Besides options of accelerating the solution process even further, an adaptivity of the spatial discretization might be investigated.

A Appendix

A.1 Ansatz Spaces for the Spatial Discretization

This section specifies the shape functions for the trunk and for the tensor product space for two- and three-dimensional regions, see (Düster, 2001) and (Szabo and Babuska, 1991).

A.1.1 The Trunk Space $\mathcal{S}_{ts}^{p_\xi,p_\eta}(\Omega_{st}^q)$ for Quadrilateral Elements

The **nodal modes** associated with the nodes of an element are given by

$$N_{1,1}^{N_i} = \frac{1}{4}(1+\xi_i\xi)(1+\eta_i\eta), \quad i = 1, ..., 4. \tag{A.1}$$

Altogether, there are $2((p_\xi - 1) + (p_\eta - 1))$ **edge modes**. The $2(p_\xi - 1)$ edge modes belonging to the ξ-direction read

$$N_{i,1}^{E_1}(\xi,\eta) = \frac{1}{2}(1-\eta)\phi_i(\xi), \quad i = 2, ..., p_\xi, \tag{A.2}$$

$$N_{i,1}^{E_3}(\xi,\eta) = \frac{1}{2}(1+\eta)\phi_i(\xi), \quad i = 2, ..., p_\xi \tag{A.3}$$

and the $2(p_\eta - 1)$ edge modes belonging to the η-direction are

$$N_{1,j}^{E_2}(\xi,\eta) = \frac{1}{2}(1+\xi)\phi_i(\eta), \quad i = 2, ..., p_\xi, \tag{A.4}$$

$$N_{1,j}^{E_4}(\xi,\eta) = \frac{1}{2}(1-\xi)\phi_i(\eta), \quad i = 2, ..., p_\eta. \tag{A.5}$$

In addition, there are **internal modes** which are given by

$$N_{i,j}^{int}(\xi,\eta) = \phi_i(\xi)\phi_j(\eta), \quad i = 2, ..., p_\xi - 4, j = 2, ..., p_\eta - 4, i+j = 4, ..., \max(p_\xi, p_\eta)\,. \tag{A.6}$$

$\phi_i(\xi)$ is given in (4.25).

A.1.2 The Tensor Product Space $\mathcal{S}_{ps}^{p_\xi,p_\eta}(\Omega_{st}^q)$ for Quadrilateral Elements

The **nodal** and **edge modes** are those used for the trunk space, see Section A.1.1. For quadrilateral elements only the shape functions associated with the interior of the element differ from those of the trunk space. The **internal modes** read

$$N_{i,j}^{int}(\xi,\eta) = \phi_i(\xi)\phi_j(\eta), \quad i = 2, ..., p_\xi, j = 2, ..., p_\eta. \tag{A.7}$$

A.1.3 The Trunk Space $\mathcal{S}_{ts}^{p_\xi,p_\eta,p_\zeta}(\Omega_{st}^h)$ for Hexahedral Elements

There are 8 **nodal modes** given by

$$N_{1,1,1}^{N_i}(\xi,\eta,\zeta) = \frac{1}{8}(1+\xi_i\xi)(1+\eta_i\eta), \quad i = 1, ..., 8.$$

Altogether, there are $4((p_\xi - 1) + (p_\eta - 1) + (p_\zeta - 1))$ **edge modes**. The $4(p_\xi - 1)$ edge modes belonging to the ξ-direction read

$$N_{i,1,1}^{E_1}(\xi,\eta,\zeta) = \frac{1}{4}(1-\eta)(1-\zeta)\phi_i(\xi), \quad i = 2, ..., p_\xi, \tag{A.8}$$

$$N_{i,1,1}^{E_3}(\xi,\eta,\zeta) = \frac{1}{4}(1+\eta)(1-\zeta)\phi_i(\xi), \quad i = 2, ..., p_\xi, \tag{A.9}$$

$$N_{i,1,1}^{E_9}(\xi,\eta,\zeta) = \frac{1}{4}(1-\eta)(1+\zeta)\phi_i(\xi), \quad i = 2, ..., p_\xi, \tag{A.10}$$

$$N_{i,1,1}^{E_{11}}(\xi,\eta,\zeta) = \frac{1}{4}(1+\eta)(1+\zeta)\phi_i(\xi), \quad i = 2, ..., p_\xi, \tag{A.11}$$

the $4(p_\eta - 1)$ edge modes belonging to the η-direction are

$$N_{1,j,1}^{E_2}(\xi,\eta,\zeta) = \frac{1}{4}(1+\xi)(1-\zeta)\phi_i(\eta), \quad i = 2, ..., p_\eta, \tag{A.12}$$

$$N_{1,j,1}^{E_4}(\xi,\eta,\zeta) = \frac{1}{4}(1-\xi)(1-\zeta)\phi_i(\eta), \quad i = 2, ..., p_\eta, \tag{A.13}$$

$$N_{1,j,1}^{E_{10}}(\xi,\eta,\zeta) = \frac{1}{4}(1+\xi)(1+\zeta)\phi_i(\eta), \quad i = 2, ..., p_\eta, \tag{A.14}$$

$$N_{1,j,1}^{E_{12}}(\xi,\eta,\zeta) = \frac{1}{4}(1-\xi)(1+\zeta)\phi_i(\eta), \quad i = 2, ..., p_\eta, \tag{A.15}$$

and the $4(p_\zeta - 1)$ edge modes belonging to the ζ-direction are given by

$$N_{1,1,k}^{E_5}(\xi,\eta,\zeta) = \frac{1}{4}(1-\xi)(1-\eta)\phi_i(\zeta), \quad i = 2, ..., p_\zeta, \tag{A.16}$$

$$N_{1,1,k}^{E_6}(\xi,\eta,\zeta) = \frac{1}{4}(1+\xi)(1-\eta)\phi_i(\zeta), \quad i = 2, ..., p_\zeta, \tag{A.17}$$

$$N_{1,1,k}^{E_7}(\xi,\eta,\zeta) = \frac{1}{4}(1+\xi)(1+\eta)\phi_i(\zeta), \quad i = 2, ..., p_\zeta, \tag{A.18}$$

$$N_{1,1,k}^{E_8}(\xi,\eta,\zeta) = \frac{1}{4}(1-\xi)(1+\eta)\phi_i(\zeta), \quad i = 2, ..., p_\zeta. \tag{A.19}$$

The **face modes** associated with a hexahedral element are given by

$$\begin{aligned}
N^{F_1}_{i,j,1}(\xi,\eta,\zeta) =& \frac{1}{2}(1-\zeta)\phi_i(\xi)\phi_j(\eta), \\
& i=2,...,p_\xi-2, j=2,...,p_\eta-2, i+j=4,...,\max\left(p_\xi,p_\eta\right), \qquad \text{(A.20)} \\
N^{F_2}_{i,1,k}(\xi,\eta,\zeta) =& \frac{1}{2}(1-\eta)\phi_i(\xi)\phi_k(\zeta), \\
& i=2,...,p_\xi-2, k=2,...,p_\zeta-2, i+k=4,...,\max\left(p_\xi,p_\zeta\right), \qquad \text{(A.21)} \\
N^{F_3}_{1,j,k}(\xi,\eta,\zeta) =& \frac{1}{2}(1+\xi)\phi_j(\eta)\phi_k(\zeta), \\
& j=2,...,p_\eta-2, k=2,...,p_\zeta-2, j+k=4,...,\max\left(p_\eta,p_\zeta\right), \qquad \text{(A.22)} \\
N^{F_4}_{i,1,k}(\xi,\eta,\zeta) =& \frac{1}{2}(1+\eta)\phi_i(\xi)\phi_k(\zeta), \\
& i=2,...,p_\xi-2, k=2,...,p_\zeta-2, i+k=4,...,\max\left(p_\xi,p_\zeta\right), \qquad \text{(A.23)} \\
N^{F_5}_{1,j,k}(\xi,\eta,\zeta) =& \frac{1}{2}(1-\xi)\phi_j(\eta)\phi_k(\zeta), \\
& j=2,...,p_\eta-2, k=2,...,p_\zeta-2, j+k=4,...,\max\left(p_\eta,p_\zeta\right), \qquad \text{(A.24)} \\
N^{F_6}_{i,j,1}(\xi,\eta,\zeta) =& \frac{1}{2}(1+\zeta)\phi_i(\xi)\phi_j(\eta), \\
& i=2,...,p_\xi-2, j=2,...,p_\eta-2, i+j=4,...,\max\left(p_\xi,p_\eta\right), \qquad \text{(A.25)}
\end{aligned}$$

and the **internal modes** read

$$\begin{aligned}
N^{int}_{i,j,k}(\xi,\eta) =& \phi_i(\xi)\phi_j(\eta)\phi_k(\zeta), \\
& i=2,...,p_\xi-4, j=2,...,p_\eta-4, k=2,...,p_\zeta-4, \\
& i+j+k=6,...,\max\left(p_\xi,p_\eta,p_\zeta\right). \qquad \text{(A.26)}
\end{aligned}$$

A.1.4 The Tensor Product Space $\mathcal{S}^{p_\xi,p_\eta,p_\zeta}_{ps}(\Omega^h_{st})$ for Hexahedral Elements

The **nodal** and **edge modes** of the tensor product space are those of the trunk space, see Section A.1.3. Altogether, there are $2\left[(p_\xi-1)(p_\eta-1)+(p_\xi-1)(p_\zeta-1)+(p_\eta-1)(p_\zeta-1)\right]$ **face modes**, given by

$$N^{F_1}_{i,j,1}(\xi,\eta,\zeta) = \frac{1}{2}(1-\zeta)\phi_i(\xi)\phi_j(\eta), \quad i=2,...,p_\xi, \quad j=2,...,p_\eta, \tag{A.27}$$

$$N^{F_2}_{i,1,k}(\xi,\eta,\zeta) = \frac{1}{2}(1-\eta)\phi_i(\xi)\phi_k(\zeta), \quad i=2,...,p_\xi, \quad k=2,...,p_\zeta, \tag{A.28}$$

$$N^{F_3}_{1,j,k}(\xi,\eta,\zeta) = \frac{1}{2}(1+\xi)\phi_j(\eta)\phi_k(\zeta), \quad i=2,...,p_\eta, \quad k=2,...,p_\zeta, \tag{A.29}$$

$$N^{F_4}_{i,1,k}(\xi,\eta,\zeta) = \frac{1}{2}(1+\eta)\phi_i(\xi)\phi_k(\zeta), \quad i=2,...,p_\xi, \quad k=2,...,p_\zeta, \tag{A.30}$$

$$N^{F_5}_{1,j,k}(\xi,\eta,\zeta) = \frac{1}{2}(1-\xi)\phi_j(\eta)\phi_k(\zeta), \quad j=2,...,p_\eta, \quad k=2,...,p_\zeta, \tag{A.31}$$

$$N^{F_6}_{i,j,1}(\xi,\eta,\zeta) = \frac{1}{2}(1+\zeta)\phi_i(\xi)\phi_j(\eta), \quad i=2,...,p_\xi, \quad j=2,...,p_\eta, \tag{A.32}$$

and $(p_\xi - 1)(p_\eta - 1)(p_\zeta - 1)$ **internal modes**, given by

$$N^{int}_{i,j,k}(\xi,\eta,\zeta) = \phi_i(\xi)\phi_j(\eta)\phi_k(\zeta), \quad i=2,...,p_\xi, \quad j=2,...,p_\eta, \quad k=2,...,p_\zeta. \tag{A.33}$$

A.2 Blending Functions for Hexahedral Elements

The blending function terms, see (Bröker, 2001; Düster, 2001) are either associated with the edges or the faces of the unit element. The edge-blending terms are given in Tab. A.1 and the face-blending terms in Tab. A.2.

Table A.1: Edge-Blending Terms

$$\begin{aligned}
\boldsymbol{e}_1(\xi,\eta,\zeta) &:= \left(\boldsymbol{E}_1(\xi) - \frac{(1-\xi)\boldsymbol{X}_1 + (1+\xi)\boldsymbol{X}_2}{2}\right)\left(\frac{1-\eta}{2}\right)\left(\frac{1-\zeta}{2}\right)\\
\boldsymbol{e}_2(\xi,\eta,\zeta) &:= \left(\boldsymbol{E}_2(\eta) - \frac{(1-\eta)\boldsymbol{X}_2 + (1+\eta)\boldsymbol{X}_2}{2}\right)\left(\frac{1+\xi}{2}\right)\left(\frac{1-\zeta}{2}\right)\\
\boldsymbol{e}_3(\xi,\eta,\zeta) &:= \left(\boldsymbol{E}_3(\xi) - \frac{(1-\xi)\boldsymbol{X}_4 + (1+\xi)\boldsymbol{X}_3}{2}\right)\left(\frac{1+\eta}{2}\right)\left(\frac{1-\zeta}{2}\right)\\
\boldsymbol{e}_4(\xi,\eta,\zeta) &:= \left(\boldsymbol{E}_4(\eta) - \frac{(1-\eta)\boldsymbol{X}_1 + (1+\eta)\boldsymbol{X}_4}{2}\right)\left(\frac{1-\xi}{2}\right)\left(\frac{1-\zeta}{2}\right)\\
\boldsymbol{e}_5(\xi,\eta,\zeta) &:= \left(\boldsymbol{E}_5(\zeta) - \frac{(1-\zeta)\boldsymbol{X}_1 + (1+\zeta)\boldsymbol{X}_5}{2}\right)\left(\frac{1-\xi}{2}\right)\left(\frac{1-\eta}{2}\right)\\
\boldsymbol{e}_6(\xi,\eta,\zeta) &:= \left(\boldsymbol{E}_6(\zeta) - \frac{(1-\zeta)\boldsymbol{X}_2 + (1+\zeta)\boldsymbol{X}_6}{2}\right)\left(\frac{1+\xi}{2}\right)\left(\frac{1-\eta}{2}\right)\\
\boldsymbol{e}_7(\xi,\eta,\zeta) &:= \left(\boldsymbol{E}_7(\zeta) - \frac{(1-\zeta)\boldsymbol{X}_3 + (1+\zeta)\boldsymbol{X}_7}{2}\right)\left(\frac{1+\xi}{2}\right)\left(\frac{1+\eta}{2}\right)\\
\boldsymbol{e}_8(\xi,\eta,\zeta) &:= \left(\boldsymbol{E}_8(\zeta) - \frac{(1-\zeta)\boldsymbol{X}_4 + (1+\zeta)\boldsymbol{X}_8}{2}\right)\left(\frac{1-\xi}{2}\right)\left(\frac{1+\eta}{2}\right)\\
\boldsymbol{e}_9(\xi,\eta,\zeta) &:= \left(\boldsymbol{E}_9(\xi) - \frac{(1-\xi)\boldsymbol{X}_5 + (1+\xi)\boldsymbol{X}_6}{2}\right)\left(\frac{1-\eta}{2}\right)\left(\frac{1+\zeta}{2}\right)\\
\boldsymbol{e}_{10}(\xi,\eta,\zeta) &:= \left(\boldsymbol{E}_{10}(\eta) - \frac{(1-\eta)\boldsymbol{X}_6 + (1+\eta)\boldsymbol{X}_7}{2}\right)\left(\frac{1+\xi}{2}\right)\left(\frac{1+\zeta}{2}\right)\\
\boldsymbol{e}_{11}(\xi,\eta,\zeta) &:= \left(\boldsymbol{E}_{11}(\xi) - \frac{(1-\xi)\boldsymbol{X}_8 + (1+\xi)\boldsymbol{X}_7}{2}\right)\left(\frac{1+\eta}{2}\right)\left(\frac{1+\zeta}{2}\right)\\
\boldsymbol{e}_{12}(\xi,\eta,\zeta) &:= \left(\boldsymbol{E}_{12}(\eta) - \frac{(1-\eta)\boldsymbol{X}_5 + (1+\eta)\boldsymbol{X}_8}{2}\right)\left(\frac{1-\xi}{2}\right)\left(\frac{1+\zeta}{2}\right)
\end{aligned}$$

Table A.2: Face-Blending Terms

$$\begin{aligned}
\boldsymbol{f}_1(\xi,\eta,\zeta) \;&:=\; (\boldsymbol{F}_1(\xi,\eta) - \frac{1}{4}((1-\xi)(1-\eta)\boldsymbol{X}_1 + (1+\xi)(1-\eta)\boldsymbol{X}_2\\
&+\; (1+\xi)(1+\eta)\boldsymbol{X}_3 + (1-\xi)(1+\eta)\boldsymbol{X}_4))\left(\frac{1-\zeta}{2}\right)
\end{aligned}$$

$$\begin{aligned}
\boldsymbol{f}_2(\xi,\eta,\zeta) \;&:=\; (\boldsymbol{F}_2(\xi,\zeta) - \frac{1}{4}((1-\xi)(1-\zeta)\boldsymbol{X}_1 + (1+\xi)(1-\zeta)\boldsymbol{X}_2\\
&+\; (1+\xi)(1+\zeta)\boldsymbol{X}_6 + (1-\xi)(1+\zeta)\boldsymbol{X}_5))\left(\frac{1-\eta}{2}\right)
\end{aligned}$$

$$\begin{aligned}
\boldsymbol{f}_3(\xi,\eta,\zeta) \;&:=\; (\boldsymbol{F}_3(\eta,\zeta) - \frac{1}{4}((1-\eta)(1-\zeta)\boldsymbol{X}_2 + (1+\eta)(1-\zeta)\boldsymbol{X}_3\\
&+\; (1+\eta)(1+\zeta)\boldsymbol{X}_7 + (1-\eta)(1+\zeta)\boldsymbol{X}_6))\left(\frac{1+\xi}{2}\right)
\end{aligned}$$

$$\begin{aligned}
\boldsymbol{f}_4(\xi,\eta,\zeta) \;&:=\; (\boldsymbol{F}_4(\xi,\zeta) - \frac{1}{4}((1-\xi)(1-\zeta)\boldsymbol{X}_4 + (1+\xi)(1-\zeta)\boldsymbol{X}_3\\
&+\; (1+\xi)(1+\zeta)\boldsymbol{X}_7 + (1-\xi)(1+\zeta)\boldsymbol{X}_8))\left(\frac{1+\eta}{2}\right)
\end{aligned}$$

$$\begin{aligned}
\boldsymbol{f}_5(\xi,\eta,\zeta) \;&:=\; (\boldsymbol{F}_5(\eta,\zeta) - \frac{1}{4}((1-\eta)(1-\zeta)\boldsymbol{X}_1 + (1+\eta)(1-\zeta)\boldsymbol{X}_4\\
&+\; (1+\eta)(1+\zeta)\boldsymbol{X}_8 + (1-\eta)(1+\zeta)\boldsymbol{X}_5))\left(\frac{1-\xi}{2}\right)
\end{aligned}$$

$$\begin{aligned}
\boldsymbol{f}_6(\xi,\eta,\zeta) \;&:=\; (\boldsymbol{F}_6(\eta,\zeta) - \frac{1}{4}((1-\xi)(1-\eta)\boldsymbol{X}_5 + (1+\xi)(1-\eta)\boldsymbol{X}_6 +\\
&+\; (1+\xi)(1+\eta)\boldsymbol{X}_7 + (1-\xi)(1+\eta)\boldsymbol{X}_8))\left(\frac{1+\zeta}{2}\right)
\end{aligned}$$

A.3 Abscissas and Weight Factors for Gaussian Integration

The abscissas and weights for the Gaussian integration are summarized in Tabs. A.3 and A.4.

Table A.3: Abscissas and weight factors for Gaussian integration

order	abscissa	weight factor
1	0.0000000000000000	2.0000000000000000
2	0.5773502691896258	1.000000000000000
	−0.5773502691896258	1.000000000000000
3	0.7745966692414834	0.5555555555555556
	0.0000000000000000	0.8888888888888889
	−0.7745966692414834	0.5555555555555556
4	0.8611363115940526	0.3478548451374539
	0.3399810435848563	0.6521451548625461
	−0.3399810435848563	0.6521451548625461
	−0.8611363115940526	0.3478548451374539
5	0.9061798459386640	0.2369268850561891
	0.5384693101056831	0.4786286704993665
	0.0000000000000000	0.5688888888888889
	−0.5384693101056831	0.4786286704993665
	−0.9061798459386640	0.2369268850561891
6	0.9324695142031520	0.1713244923791703
	0.6612093864662645	0.3607615730481386
	0.2386191860831969	0.4679139345726910
	−0.2386191860831969	0.4679139345726910
	−0.6612093864662645	0.3607615730481386
	−0.9324695142031520	0.1713244923791703
7	0.9491079123427585	0.1294849661688697
	0.7415311855993944	0.2797053914892767
	0.4058451513773972	0.3818300505051189
	0.0000000000000000	0.4179591836734694
	−0.4058451513773972	0.3818300505051189
	−0.7415311855993944	0.2797053914892767
	−0.9491079123427585	0.1294849661688697
8	0.9602898564975362	0.1012285362903763
	0.7966664774136267	0.2223810344533745
	0.5255324099163290	0.3137066458778873
	0.1834346424956498	0.3626837833783620
	−0.1834346424956498	0.3626837833783620
	−0.5255324099163290	0.3137066458778873
	−0.7966664774136267	0.2223810344533745
	−0.9602898564975362	0.1012285362903763
9	0.9681602395076261	0.08127438836157441
	0.8360311073266358	0.1806481606948574
	0.6133714327005904	0.2606106964029355
	0.3242534234038089	0.3123470770400028
	0.0000000000000000	0.3302393550012598
	−0.3242534234038089	0.3123470770400028
	−0.6133714327005904	0.2606106964029355
	−0.8360311073266358	0.1806481606948574
	−0.9681602395076261	0.08127438836157441

Table A.4: Abscissas and weight factors for Gaussian integration

order	abscissa	weight factor
10	0.9739065285171717	0.06667134430868814
	0.8650633666889845	0.1494513491505806
	0.6794095682990244	0.2190863625159820
	0.4333953941292472	0.2692667193099964
	0.1488743389816312	0.2955242247147529
	−0.1488743389816312	0.2955242247147529
	−0.4333953941292472	0.2692667193099964
	−0.6794095682990244	0.2190863625159820
	−0.8650633666889845	0.1494513491505806
	−0.9739065285171717	0.06667134430868814
11	0.9782286581460570	0.05566856711617367
	0.8870625997680953	0.1255803694649046
	0.7301520055740493	0.1862902109277343
	0.5190961292068118	0.2331937645919905
	0.2695431559523450	0.2628045445102467
	0.0000000000000000	0.2729250867779006
	−0.2695431559523450	0.2628045445102467
	−0.5190961292068118	0.2331937645919905
	−0.7301520055740493	0.1862902109277343
	−0.8870625997680953	0.1255803694649046
	−0.9782286581460570	0.05566856711617367

A.4 Chen-Babuska Points

The Chen-Babuska points, see (Chen and Babuska, 1995), on whose basis the geometry approximation is carried out are given in Tabs. A.5 and A.6.

Table A.5: Babuska-Chen points

order	abscissa
3	−1.0000000000000000
	−0.4177913013559897
	0.4177913013559897
	1.0000000000000000
4	−1.0000000000000000
	−0.6209113046899123
	0.0000000000000000
	0.6209113046899123
	1.0000000000000000
5	−1.0000000000000000
	−0.7341266671891752
	−0.2689070447719729
	0.2689070447719729
	0.7341266671891752
	1.0000000000000000
6	−1.0000000000000000
	−0.8034402382691066
	−0.5674306027472533
	0.00000000000000000
	0.5674306027472533
	0.8034402382691066
	1.0000000000000000

Table A.6: Babuska-Chen points

order	abscissa
7	−1.0000000000000000
	−0.8488719610366557
	−0.5674306027472533
	−0.1992877299056662
	0.1992877299056662
	0.5674306027472533
	0.8488719610366557
	1.0000000000000000
8	−1.0000000000000000
	−0.8802308527184540
	−0.6535334790799030
	−0.3477879716116667
	0.0000000000000000
	0.3477879716116667
	0.6535334790799030
	0.8802308527184540
	1.0000000000000000
9	−1.0000000000000000
	−0.9027709752917726
	−0.7166138606253078
	−0.4601498259228992
	−0.1585652886576400
	0.1585652886576400
	0.4601498259228992
	0.7166138606253078
	0.9027709752917726
	1.0000000000000000
10	−1.0000000000000000
	−0.9195087517942991
	−0.7640984545671450
	−0.5466676961746040
	−0.2848880010669259
	0.0000000000000000
	0.2848880010669259
	0.5466676961746040
	0.7640984545671450
	0.9195087517942991
	1.0000000000000000

A.5 Butcher Arrays of Embedded DIRK-Methods

Tab. A.7 contains the high-order time integration schemes that are employed in this thesis. They range from second to fourth order.

Table A.7: Butcher arrays of embedded DIRK-methods

(a) Ellsiepen's method (Ellsiepen, 1999) ($s = 2, p = 2, \hat{p} = 1$)

$$\begin{array}{c|cc} \alpha & \alpha & \\ 1 & 1-\alpha & \alpha \\ \hline & 1-\alpha & \alpha \\ & 1-\hat{\alpha} & \hat{\alpha} \end{array} \qquad \alpha = 1 - \tfrac{1}{2}\sqrt{2}, \qquad \hat{\alpha} = 2 - \tfrac{5}{4}\sqrt{2}$$

(b) Cash's method (Cash, 1979) ($s = 3, p = 3, \hat{p} = 2$)

$$\begin{array}{c|ccc} \gamma & \gamma & & \\ \delta & \tau-\gamma & \gamma & \\ 1 & \alpha & \beta & \gamma \\ \hline & \alpha & \beta & \gamma \\ & \hat{\alpha} & \hat{\beta} & 0 \end{array} \qquad \begin{aligned} \gamma &= 0.4358665215084580 \\ \tau-\gamma &= 0.2820667392457705 \\ \alpha &= 1.2084966491760101 \\ \beta &= -0.6443631706844691 \\ \delta &= 0.7179332607542295 \\ \hat{\alpha} &= 0.7726301276675511 \\ \hat{\beta} &= 0.2273698723324489 \end{aligned}$$

(d) Hairer & Wanner's method (Hairer and Wanner, 1996) ($s = 5, p = 4, \hat{p} = 3$)

$$\begin{array}{c|ccccc} \frac{1}{4} & \frac{1}{4} & & & & \\ \frac{3}{4} & \frac{1}{2} & \frac{1}{4} & & & \\ \frac{11}{20} & \frac{17}{50} & -\frac{1}{25} & \frac{1}{4} & & \\ \frac{1}{2} & \frac{371}{1360} & -\frac{137}{2720} & \frac{15}{544} & \frac{1}{4} & \\ 1 & \frac{25}{24} & -\frac{49}{48} & \frac{125}{16} & -\frac{85}{12} & \frac{1}{4} \\ \hline & \frac{25}{24} & -\frac{49}{48} & \frac{125}{16} & -\frac{85}{12} & \frac{1}{4} \\ & \frac{59}{48} & -\frac{17}{96} & \frac{225}{32} & -\frac{85}{12} & 0 \end{array}$$

A.6 Tangents of Thermo-Viscoelastic Material Model

A.6.1 $\tilde{\mathrm{T}}$ with Respect to C

The tangent $\tilde{\mathcal{C}} = 2\frac{\mathrm{d}\tilde{\mathbf{T}}}{\mathrm{d}\mathbf{C}}$ needed in (4.138) is composed of

$$\tilde{\mathcal{C}} = \tilde{\mathcal{C}}_{\text{vol}} + \tilde{\mathcal{C}}^{\text{iso}}_{\text{eq}} + \tilde{\mathcal{C}}_{\text{ov}}. \tag{A.34}$$

The parts of the tangent resulting from the equilibrium stresses read

$$\begin{aligned} \tilde{\mathcal{C}}_{\text{vol}} &= 2\frac{\mathrm{d}\tilde{\mathbf{T}}^{\text{vol}}_{\text{eq}}}{\mathrm{d}\mathbf{C}} \\ &= \varrho_{\mathrm{R}}\frac{J}{\varphi}\frac{\theta}{\theta_0}\left[\left(U'(J/\varphi) + \frac{J}{\varphi}U''(J/\varphi)\right)\mathbf{C}^{-1}\otimes\mathbf{C}^{-1} - 2U'(J/\varphi)\left[\mathbf{C}^{-1}\otimes\mathbf{C}^{-1}\right]^{T_{23}}\right] \end{aligned} \tag{A.35}$$

and

$$\begin{aligned} \tilde{\mathcal{C}}^{\text{iso}}_{\text{eq}} = 2\frac{\mathrm{d}\tilde{\mathbf{T}}^{\text{iso}}_{\text{eq}}}{\mathrm{d}\mathbf{C}} &= 4\varrho_{\mathrm{R}}J^{-4/3}\frac{\theta}{\theta_0}\left[\mathcal{I} - \frac{1}{3}\overline{\mathbf{C}}^{-1}\otimes\overline{\mathbf{C}}\right]\frac{\mathrm{d}^2\overline{v}}{\mathrm{d}\overline{\mathbf{C}}\;\mathrm{d}\overline{\mathbf{C}}}\left[\mathcal{I} - \frac{1}{3}\overline{\mathbf{C}}\otimes\overline{\mathbf{C}}^{-1}\right] - \\ &- \frac{2J^{-2/3}}{3}\left[\tilde{\mathbf{T}}^{\text{iso}}_{\text{eq}}\otimes\overline{\mathbf{C}}^{-1} + \overline{\mathbf{C}}^{-1}\otimes\tilde{\mathbf{T}}^{\text{iso}}_{\text{eq}}\right] + \\ &+ \frac{4\varrho_{\mathrm{R}}J^{-4/3}}{3}\left(\overline{\mathbf{C}}\cdot\frac{\mathrm{d}\overline{v}}{\mathrm{d}\overline{\mathbf{C}}}\right)\left[\left[\overline{\mathbf{C}}^{-1}\otimes\overline{\mathbf{C}}^{-1}\right]^{T_{23}} - \frac{1}{3}\overline{\mathbf{C}}^{-1}\otimes\overline{\mathbf{C}}^{-1}\right], \end{aligned} \tag{A.36}$$

based on

$$\begin{aligned} \frac{\mathrm{d}\overline{v}}{\mathrm{d}\overline{\mathbf{C}}} &= (w_1 + w_2\mathrm{I}_{\bar{\mathbf{C}}})\,\mathbf{I} - w_2\overline{\mathbf{C}}, \\ \frac{\mathrm{d}^2\overline{v}}{\mathrm{d}\overline{\mathbf{C}}\;\mathrm{d}\overline{\mathbf{C}}} &= \left(w_{11} + 2w_{12}\mathrm{I}_{\bar{\mathbf{C}}} + w_{22}\mathrm{I}^2_{\bar{\mathbf{C}}} + w_2\right)\mathbf{I}\otimes\mathbf{I} \\ &\quad - (w_{12} + \mathrm{I}_{\bar{\mathbf{C}}}w_{22})\left[\mathbf{I}\otimes\overline{\mathbf{C}} + \overline{\mathbf{C}}\otimes\mathbf{I}\right] - -w_2\mathcal{I} + w_{22}\overline{\mathbf{C}}\otimes\overline{\mathbf{C}}, \\ w_{k1} = \frac{\partial w_k}{\partial\mathrm{I}_{\bar{\mathbf{C}}}} &\quad\text{and}\quad w_{k2} = \frac{\partial w_k}{\partial\mathrm{II}_{\bar{\mathbf{C}}}}\quad\text{for}\quad k = 1, 2. \end{aligned} \tag{A.37}$$

With the relation for the overstresses

$$\tilde{\mathbf{T}}_{\text{ov}} = 2\varrho_{\mathrm{R}}\mu J^{-\frac{2}{3}}(\mathbf{C}\cdot\mathbf{C}^{-1}_{\mathrm{v}})\mathbf{C}^{-1} \tag{A.38}$$

the Gateaux-derivative yields

$$\begin{aligned}
&\mathsf{D}_{\mathbf{C}}\,\tilde{\mathbf{T}}_{\mathrm{ov}}(\mathbf{C},\mathbf{C}_{\mathrm{v}})[\Delta\mathbf{C}]\\
&= -\frac{2}{3}\varrho_{\mathrm{R}}\mu J^{-\frac{2}{3}}\mathbf{C}^{-1}\cdot\Delta\mathbf{C}\left(\mathbf{C}_{\mathrm{v}}^{-1}-\frac{1}{3}(\mathbf{C}\cdot\mathbf{C}_{\mathrm{v}}^{-1})\mathbf{C}^{-1}\right)\\
&+ 2\varrho_{\mathrm{R}}\mu J^{-\frac{2}{3}}\left(-\frac{1}{3}\left(\Delta\mathbf{C}\cdot\mathbf{C}_{\mathrm{v}}^{-1}\right)\mathbf{C}^{-1}+\frac{1}{3}(\mathbf{C}\cdot\mathbf{C}_{\mathrm{v}}^{-1})\left[\mathbf{C}^{-1}\otimes\mathbf{C}^{-1}\right]^{T_{23}}\Delta\mathbf{C}\right)\\
&= -\frac{2}{3}\varrho_{\mathrm{R}}\mu J^{-\frac{2}{3}}\Bigg[\left[\mathbf{C}_{\mathrm{v}}^{-1}\otimes\mathbf{C}^{-1}\right]-\frac{1}{3}\left(\mathbf{C}\cdot\mathbf{C}_{\mathrm{v}}^{-1}\right)\left[\mathbf{C}^{-1}\otimes\mathbf{C}^{-1}\right]\\
&+\left[\mathbf{C}^{-1}\otimes\mathbf{C}_{\mathrm{v}}^{-1}\right]-\left(\mathbf{C}\cdot\mathbf{C}_{\mathrm{v}}^{-1}\right)\left[\mathbf{C}^{-1}\otimes\mathbf{C}^{-1}\right]^{T_{23}}\Bigg]\Delta\mathbf{C}
\end{aligned}\tag{A.39}$$

resulting in the tangent

$$\begin{aligned}
\tilde{\mathcal{C}}_{\mathrm{ov}} = 2\frac{\mathrm{d}\tilde{\mathbf{T}}_{\mathrm{ov}}}{\mathrm{d}\mathbf{C}} = -\frac{4}{3}\varrho_{\mathrm{R}}\mu J^{-\frac{2}{3}}\Bigg[&\mathbf{C}_{\mathrm{v}}^{-1}\otimes\mathbf{C}^{-1}+\mathbf{C}^{-1}\otimes\mathbf{C}_{\mathrm{v}}^{-1}\\
&-\frac{1}{3}\left(\mathbf{C}\cdot\mathbf{C}_{\mathrm{v}}^{-1}\right)\left(\mathbf{C}^{-1}\otimes\mathbf{C}^{-1}+3\left[\mathbf{C}^{-1}\otimes\mathbf{C}^{-1}\right]^{T_{23}}\right)\Bigg].
\end{aligned}\tag{A.40}$$

A.6.2 $\tilde{\mathrm{T}}$ with Respect to C_{v}

With (A.38) we write

$$\mathsf{D}_{\mathbf{C}_{\mathrm{v}}}\,\tilde{\mathbf{T}}_{\mathrm{ov}}(\mathbf{C},\mathbf{C}_{\mathrm{v}})[\Delta\mathbf{C}] = \frac{2}{3}\varrho_{\mathrm{R}}\mu J^{-\frac{2}{3}}\left[\mathbf{C}^{-1}\otimes\mathbf{C}-3\mathcal{I}\right]\left[\mathbf{C}_{\mathrm{v}}^{-1}\otimes\mathbf{C}_{\mathrm{v}}^{-1}\right]^{T_{23}}\Delta\mathbf{C}\tag{A.41}$$

and so the derivative of the overstresses with respect to the viscous right Cauchy-Green tensor needed in (4.138) and (4.185) reads

$$\frac{\mathrm{d}\tilde{\mathbf{T}}}{\mathrm{d}\mathbf{C}_{\mathrm{v}}} = \frac{\mathrm{d}\tilde{\mathbf{T}}_{\mathrm{ov}}}{\mathrm{d}\mathbf{C}_{\mathrm{v}}} = \frac{2}{3}\varrho_{\mathrm{R}}\mu J^{-\frac{2}{3}}\left[\mathbf{C}^{-1}\otimes\mathbf{C}-3\mathcal{I}\right]\left[\mathbf{C}_{\mathrm{v}}^{-1}\otimes\mathbf{C}_{\mathrm{v}}^{-1}\right]^{T_{23}}.\tag{A.42}$$

A.6.3 $\tilde{\mathrm{T}}$ with Respect to θ

The derivative of $\tilde{\mathbf{T}}$ with respect to the temperature θ reads

$$\frac{\mathrm{d}\tilde{\mathbf{T}}}{\mathrm{d}\theta} = \frac{\mathrm{d}\tilde{\mathbf{T}}_{\mathrm{eq}}^{\mathrm{vol}}}{\mathrm{d}\theta}+\frac{\mathrm{d}\tilde{\mathbf{T}}_{\mathrm{eq}}^{\mathrm{iso}}}{\mathrm{d}\theta}+\frac{\mathrm{d}\tilde{\mathbf{T}}_{\mathrm{ov}}}{\mathrm{d}\theta}.\tag{A.43}$$

With the stress state

$$\tilde{\mathbf{T}}_{\mathrm{eq}}^{\mathrm{vol}} = \varrho_{\mathrm{R}}\frac{\theta}{\theta_0}\frac{J}{\varphi}U'(J/\varphi)\mathbf{C}^{-1},\tag{A.44}$$

the determinant of the deformation gradient

$$J = \det\mathbf{F},\tag{A.45}$$

the volumetric expansion

$$\varphi(\theta) = 1 + \alpha_\theta(\theta - \theta_0), \tag{A.46}$$

its derivative with respect to θ

$$\varphi' = \alpha_\theta, \tag{A.47}$$

the strain energy function with its derivatives

$$\begin{aligned}
U(J/\varphi) &= \frac{K}{50}((J/\varphi)^5 + (J/\varphi)^{-5} - 2), &\text{(A.48)}\\
U'(J/\varphi) &= \frac{K}{10}((J/\varphi)^4 - (J/\varphi)^{-6}), &\text{(A.49)}\\
U''(J/\varphi) &= \frac{K}{10}(4(J/\varphi)^3 + 6(J/\varphi)^{-7}), &\text{(A.50)}\\
U'''(J/\varphi) &= \frac{K}{10}(12(J/\varphi)^2 - 42(J/\varphi)^{-8}), &\text{(A.51)}
\end{aligned}$$

and the derivation of U' with respect to θ

$$\begin{aligned}
\frac{\mathrm{d}U'}{\mathrm{d}\theta} &= \frac{K}{10}\left(-4J^4\varphi^{-5}\alpha_\theta - 6J^{-6}\varphi^5\alpha_\theta\right) &\text{(A.52)}\\
&= -\frac{\alpha_\theta K}{10\varphi}\left(4(J/\varphi)^4 + 6(J/\varphi)^{-6}\right) &\text{(A.53)}\\
&= -\frac{\alpha_\theta}{\varphi}\frac{J}{\varphi}U''(J/\varphi), &\text{(A.54)}
\end{aligned}$$

the first derivative in (A.43) yields

$$\begin{aligned}
\frac{\mathrm{d}\tilde{\mathbf{T}}_{\mathrm{eq}}^{\mathrm{vol}}}{\mathrm{d}\theta} &= \varrho_{\mathrm{R}}\frac{1}{\theta_0}\frac{J}{\varphi}U'(J/\varphi)\mathbf{C}^{-1} - \varrho_{\mathrm{R}}\frac{\theta}{\theta_0}\frac{J}{\varphi^2}\alpha_\theta U'(J/\varphi)\mathbf{C}^{-1} - \varrho_{\mathrm{R}}\frac{\theta}{\theta_0}\frac{\alpha_\theta}{\varphi}\left(\frac{J}{\varphi}\right)^2 U''(J/\varphi)\mathbf{C}^{-1} \\
&= \frac{\varrho_{\mathrm{R}}}{\theta_0}\frac{J}{\varphi}\left[\left(1 - \frac{\theta\alpha_\theta}{\varphi}\right)U'(J/\varphi) - \theta\frac{\alpha_\theta J}{\varphi^2}U''(J/\varphi)\right]\mathbf{C}^{-1} &\text{(A.55)}\\
&= \frac{\varrho_{\mathrm{R}}}{\theta_0}\frac{J}{\varphi}\frac{\theta\alpha_\theta}{\varphi}\left[\left(\frac{\varphi}{\theta\alpha_\theta} - 1\right)U'(J/\varphi) - \frac{J}{\varphi}U''(J/\varphi)\right]\mathbf{C}^{-1} &\text{(A.56)}\\
&= \varrho_{\mathrm{R}}J\beta\mathbf{C}^{-1}, &\text{(A.57)}
\end{aligned}$$

based on the abbreviation

$$\beta = \frac{\theta}{\theta_0}\frac{\varphi'}{\varphi^2}\left(\left(\frac{\varphi}{\theta\alpha_\theta} - 1\right)U'(J/\varphi) - \frac{J}{\varphi}U''(J/\varphi)\right). \tag{A.58}$$

In the current configuration, we write

$$(1/J)\mathbf{F}\frac{\mathrm{d}\tilde{\mathbf{T}}_{\mathrm{eq}}^{\mathrm{vol}}}{\mathrm{d}\theta}\mathbf{F}^{\mathrm{T}} = \varrho_{\mathrm{R}}\beta\mathbf{1}. \tag{A.59}$$

Due to the linear dependence of $\tilde{\mathbf{T}}_{\text{eq}}^{\text{iso}}$ in θ

$$\frac{\mathrm{d}\tilde{\mathbf{T}}_{\text{eq}}^{\text{iso}}}{\mathrm{d}\theta} = \frac{1}{\theta}\tilde{\mathbf{T}}_{\text{eq}}^{\text{iso}} \tag{A.60}$$

follows in the reference or

$$(1/J)\mathbf{F}\frac{\mathrm{d}\tilde{\mathbf{T}}_{\text{eq}}^{\text{iso}}}{\mathrm{d}\theta}\mathbf{F}^{\,\mathrm{T}} = \frac{1}{\theta J}\mathbf{S}_{\text{eq}}^{\text{iso}} \tag{A.61}$$

in current configuration, based on the isochoric Kirchhoff stress tensor

$$\mathbf{S}_{\text{eq}}^{\text{iso}} = 2\varrho_{\mathrm{R}}\frac{\theta}{\theta_0}\left(\left(w_1 + w_2\mathrm{I}_{\bar{\mathbf{B}}}\right)\bar{\mathbf{B}}^{\mathrm{D}} - w_2\left(\bar{\mathbf{B}}\bar{\mathbf{B}}\right)^{\mathrm{D}}\right).$$

Since there is no explicit dependence of $\tilde{\mathbf{T}}_{\text{ov}}$ in the temperature, we obtain

$$\frac{\mathrm{d}\tilde{\mathbf{T}}_{\text{ov}}}{\mathrm{d}\theta} = \mathbf{0} \tag{A.62}$$

and (A.43) yields

$$\frac{\mathrm{d}\tilde{\mathbf{T}}}{\mathrm{d}\theta} = \varrho_{\mathrm{R}}J\beta\mathbf{C}^{-1} + \frac{1}{\theta}\tilde{\mathbf{T}}_{\text{eq}}^{\text{iso}} \tag{A.63}$$

in the reference configuration and

$$(1/J)\mathbf{F}\frac{\mathrm{d}\tilde{\mathbf{T}}}{\mathrm{d}\theta}\mathbf{F} = \varrho_{\mathrm{R}}\beta\mathbf{1} + \frac{1}{\theta J}\mathbf{S}_{\text{eq}}^{\text{iso}} \tag{A.64}$$

in the current configuration.

A.6.4 Tangents of the Thermo-Elastic coupling term p

The thermo-elastic coupling term can be expressed by means of quantities operating on either the current or the reference configuration

$$p(\mathbf{C},\dot{\mathbf{C}},\theta) = \frac{1}{2}\left(\theta\beta(\theta,J)J\mathbf{C}^{-1} + \frac{1}{\varrho_{\mathrm{R}}}\tilde{\mathbf{T}}_{\text{eq}}^{\text{iso}}\right)\cdot\dot{\mathbf{C}} \tag{A.65}$$

$$= \frac{1}{2}\left(\theta\beta(\theta,J)J\mathbf{1} + \frac{1}{\varrho_{\mathrm{R}}}\mathbf{S}_{\text{eq}}^{\text{iso}}\right)\cdot\mathbf{F}^{\,-\mathrm{T}}\dot{\mathbf{C}}\mathbf{F}^{-1}. \tag{A.66}$$

Its derivative with respect to $\mathbf{C}$ can be expressed by means of

$$\frac{\mathrm{d}p}{\mathrm{d}\mathbf{C}} = \frac{\partial p}{\partial\mathbf{C}} + \left\{\frac{\mathrm{d}\dot{\mathbf{C}}}{\mathrm{d}\mathbf{C}}\right\}^{\mathrm{T}}\frac{\mathrm{d}p}{\mathrm{d}\dot{\mathbf{C}}}. \tag{A.67}$$

The approximation of $\dot{\mathbf{C}} = 2\dot{\mathbf{E}}$ is carried out according to (4.245). For the purposes of deriving tangents, this approximation is not considered due to notational simplicity.

Making use of the derivative of the inverse of a tensor which can be computed via

$$\mathsf{D}_{\mathbf{C}}\,\mathbf{C}\mathbf{C}^{-1}(\mathbf{C})[\Delta\mathbf{C}] = \Delta\mathbf{C}\mathbf{C}^{-1} + \mathbf{C}\mathsf{D}_{\mathbf{C}}\,\mathbf{C}^{-1}(\mathbf{C})[\Delta\mathbf{C}] = 0 \tag{A.68}$$

yielding

$$\mathsf{D}\,\mathbf{C}^{-1}(\mathbf{C})[\Delta\mathbf{C}] = -\mathbf{C}^{-1}\Delta\mathbf{C}\mathbf{C}^{-1} = -\left[\mathbf{C}^{-1}\otimes\mathbf{C}^{-1}\right]^{T_{23}}\Delta\mathbf{C} \tag{A.69}$$

the Gateaux-derivative

$$\begin{aligned}
\mathsf{D}_{\mathbf{C}}\,p(\mathbf{C},\dot{\mathbf{C}},\theta)[\Delta\mathbf{C}] = \Bigg[&\theta\frac{\mathrm{d}\beta}{\mathrm{d}J}\frac{\mathrm{d}J}{\mathrm{d}\mathbf{C}}\cdot\Delta\mathbf{C}J\mathbf{C}^{-1} + \theta\beta\mathsf{D}_{\mathbf{C}}\,J(\mathbf{C})[\Delta\mathbf{C}]\mathbf{C}^{-1} && \text{(A.70)}\\
&+\theta\beta J\mathsf{D}_{\mathbf{C}}\,\mathbf{C}^{-1}(\mathbf{C})[\Delta\mathbf{C}] + \frac{1}{\varrho_{\mathrm{R}}}\mathsf{D}_{\mathbf{C}}\,\tilde{\mathbf{T}}^{\mathrm{iso}}_{\mathrm{eq}}(\mathbf{C})[\Delta\mathbf{C}]\Bigg]\cdot\dot{\mathbf{E}} && \text{(A.71)}
\end{aligned}$$

yields with

$$\begin{aligned}
\frac{\mathrm{d}\beta}{\mathrm{d}J} &= \frac{\theta}{\theta_0}\frac{\alpha_\theta}{\varphi^2}\left(\left(\frac{\varphi}{\theta\alpha_\theta}-1\right)\frac{\partial U'(J/\varphi)}{\partial J} - \frac{J}{\varphi}\frac{\partial U''(J/\varphi)}{\partial J} - \frac{1}{\varphi}U''(J/\varphi)\right) && \text{(A.72)}\\
&= \frac{\theta}{\theta_0}\frac{\alpha_\theta}{\varphi^2}\left[\left(\frac{\varphi}{\theta\alpha_\theta}-2\right)\frac{1}{\varphi}U''(J/\varphi) - \frac{1}{\varphi}\frac{J}{\varphi}U'''(J/\varphi)\right], && \text{(A.73)}
\end{aligned}$$

$$\frac{\partial U'(J/\varphi)}{\partial J} = \frac{K}{5\varphi}\left(2(J/\varphi)^3 + 3(J/\varphi)^{-7}\right) = \frac{1}{\varphi}U'', \tag{A.74}$$

$$\frac{\partial U''(J/\varphi)}{\partial J} = \frac{3K}{5\varphi}\left(2(J/\varphi)^2 - 7(J/\varphi)^{-8}\right) = \frac{1}{\varphi}U''', \tag{A.75}$$

$$\mathsf{D}_{\mathbf{C}}\,J(\mathbf{C})[\Delta\mathbf{C}] = \frac{\partial J}{\partial\mathbf{C}}\cdot\Delta\mathbf{C} = (1/2)J\mathbf{C}^{-1}\cdot\Delta\mathbf{C}, \tag{A.76}$$

and

$$\mathsf{D}_{\mathbf{C}}\,\tilde{\mathbf{T}}^{\mathrm{iso}}_{\mathrm{eq}}(\mathbf{C})[\Delta\mathbf{C}] = \frac{\mathrm{d}\tilde{\mathbf{T}}^{\mathrm{iso}}_{\mathrm{eq}}}{\mathrm{d}\mathbf{C}}\Delta\mathbf{C} = \frac{1}{2}\tilde{\mathcal{C}}^{\mathrm{iso}}_{\mathrm{eq}}\Delta\mathbf{C} \tag{A.77}$$

$$\begin{aligned}
\mathsf{D}_{\mathbf{C}}\,p(\mathbf{C},\theta)[\Delta\mathbf{C}] &= \Bigg[\theta\frac{\mathrm{d}\beta}{\mathrm{d}J}(1/2)J\mathbf{C}^{-1}\cdot\Delta\mathbf{C}J\mathbf{C}^{-1} + \theta\beta(1/2)J\mathbf{C}^{-1}\cdot\Delta\mathbf{C}\mathbf{C}^{-1}\\
&\quad -\theta\beta J\left[\mathbf{C}^{-1}\otimes\mathbf{C}^{-1}\right]^{T_{23}}\Delta\mathbf{C} + \frac{1}{2\varrho_{\mathrm{R}}}\tilde{\mathcal{C}}^{\mathrm{iso}}_{\mathrm{eq}}\Delta\mathbf{C}\Bigg]\cdot\dot{\mathbf{E}}\\
&= \Bigg[\frac{1}{2}\theta J\left(\frac{\mathrm{d}\beta}{\mathrm{d}J}J+\beta\right)\left[\mathbf{C}^{-1}\otimes\mathbf{C}^{-1}\right]\\
&\quad -\theta\beta J\left[\mathbf{C}^{-1}\otimes\mathbf{C}^{-1}\right]^{T_{23}} + \frac{1}{2\varrho_{\mathrm{R}}}\tilde{\mathcal{C}}^{\mathrm{iso}}_{\mathrm{eq}}\Bigg]\Delta\mathbf{C}\cdot\dot{\mathbf{E}}\\
&= \Bigg[\frac{1}{2}\theta J\left(\frac{\mathrm{d}\beta}{\mathrm{d}J}J+\beta\right)\left[\mathbf{C}^{-1}\otimes\mathbf{C}^{-1}\right]\\
&\quad -\theta\beta J\left[\mathbf{C}^{-1}\otimes\mathbf{C}^{-1}\right]^{T_{23}} + \frac{1}{2\varrho_{\mathrm{R}}}\tilde{\mathcal{C}}^{\mathrm{iso}}_{\mathrm{eq}}\Bigg]\dot{\mathbf{E}}\cdot\Delta\mathbf{C}.
\end{aligned}$$

With the short notation

$$\tilde{\mathcal{C}}_p = J\left[\left(\frac{\mathrm{d}\beta}{\mathrm{d}J}J+\beta\right)\left[\mathbf{C}^{-1}\otimes\mathbf{C}^{-1}\right] - 2\beta\left[\mathbf{C}^{-1}\otimes\mathbf{C}^{-1}\right]^{T_{23}}\right] \tag{A.78}$$

we obtain

$$\frac{\partial p}{\partial \mathbf{C}} = \frac{1}{2}\left(\theta\tilde{\mathcal{C}}_p + \frac{1}{\varrho_{\mathrm{R}}}\tilde{\mathcal{C}}^{\mathrm{iso}}_{\mathrm{eq}}\right)\dot{\mathbf{E}}. \tag{A.79}$$

Applying the push forward operator $\frac{1}{J}\mathbf{F}\,(.)\,\mathbf{F}^{\mathrm{T}}$ to the terms of the derivative and making use of

$$\begin{aligned}
\mathbf{F}^{-\mathrm{T}}\dot{\mathbf{E}}\mathbf{F}^{-1} &= \frac{1}{2}\mathbf{F}^{-\mathrm{T}}\dot{\mathbf{C}}\mathbf{F}^{-1} = \frac{1}{2}\mathbf{F}^{-\mathrm{T}}\left(\dot{\mathbf{F}}^{\mathrm{T}}\mathbf{F}+\mathbf{F}^{\mathrm{T}}\dot{\mathbf{F}}\right)\mathbf{F}^{-1} && \text{(A.80)}\\
&= \frac{1}{2}\left(\mathbf{F}^{-\mathrm{T}}\dot{\mathbf{F}}^{\mathrm{T}}+\dot{\mathbf{F}}\mathbf{F}^{-1}\right) = \frac{1}{2}\left(\mathbf{L}^{\mathrm{T}}+\mathbf{L}\right) = \mathbf{D} && \text{(A.81)}
\end{aligned}$$

subsequently yields

$$\begin{aligned}
\frac{1}{J}\mathbf{F}\left[\mathbf{C}^{-1}\otimes\mathbf{C}^{-1}\right]\dot{\mathbf{E}}\mathbf{F}^{\mathrm{T}} &= \frac{1}{J}\mathbf{F}\mathbf{C}^{-1}\mathbf{F}^{\mathrm{T}}\left(\mathbf{C}^{-1}\cdot\dot{\mathbf{E}}\right) = \frac{1}{J}\left(\mathbf{C}^{-1}\cdot\dot{\mathbf{E}}\right)\mathbf{1}\\
&= \frac{1}{J}\left(\mathbf{1}\cdot\mathbf{F}^{-\mathrm{T}}\dot{\mathbf{E}}\mathbf{F}^{-1}\right)\mathbf{1} = \frac{1}{J}\left(\mathbf{1}\cdot\mathbf{D}\right)\mathbf{1}\\
&= \frac{1}{J}\left[\mathbf{1}\otimes\mathbf{1}\right]\mathbf{D}, && \text{(A.82)}
\end{aligned}$$

$$\frac{1}{J}\mathbf{F}\left[\mathbf{C}^{-1}\otimes\mathbf{C}^{-1}\right]^{T_{23}}\dot{\mathbf{E}}\mathbf{F}^{\mathrm{T}} = \frac{1}{J}\mathbf{F}\mathbf{C}^{-1}\dot{\mathbf{E}}\mathbf{C}^{-\mathrm{T}}\mathbf{F}^{\mathrm{T}} = \frac{1}{J}\mathbf{F}^{-\mathrm{T}}\dot{\mathbf{E}}\mathbf{F}^{-1} = \frac{1}{J}\mathcal{I}\mathbf{D} \tag{A.83}$$

and

$$\begin{aligned}
\tilde{\mathcal{C}}^{\mathrm{iso}}_{\mathrm{eq}}\dot{\mathbf{E}} &= J\left[\mathbf{F}^{-1}\otimes\mathbf{F}^{-1}\right]^{T_{23}}\mathcal{C}^{\mathrm{iso}}_{\mathrm{eq}}\left[\mathbf{F}^{-\mathrm{T}}\otimes\mathbf{F}^{-\mathrm{T}}\right]^{T_{23}}\dot{\mathbf{E}}\\
&= J\left[\mathbf{F}^{-1}\otimes\mathbf{F}^{-1}\right]^{T_{23}}\mathcal{C}^{\mathrm{iso}}_{\mathrm{eq}}\mathbf{F}^{-\mathrm{T}}\dot{\mathbf{E}}\mathbf{F}^{-1}\\
&= J\mathbf{F}^{-1}\mathcal{C}^{\mathrm{iso}}_{\mathrm{eq}}\mathbf{D}\mathbf{F}^{-\mathrm{T}} \qquad \longrightarrow \frac{1}{J}\mathbf{F}\tilde{\mathcal{C}}^{\mathrm{iso}}_{\mathrm{eq}}\dot{\mathbf{E}}\mathbf{F}^{\mathrm{T}} = \mathcal{C}^{\mathrm{iso}}_{\mathrm{eq}}\mathbf{D}
\end{aligned}$$

and we accordingly write

$$\frac{1}{J}\mathbf{F}\frac{\partial p}{\partial \mathbf{C}}\mathbf{F}^{\mathrm{T}} = \frac{1}{2}\left[\theta\mathcal{C}_p + \frac{1}{\varrho_{\mathrm{R}}}\mathcal{C}^{\mathrm{iso}}_{\mathrm{eq}}\right]\mathbf{D} \tag{A.84}$$

with

$$\mathcal{C}_p = \left(\frac{\partial\beta}{\partial J}J+\beta\right)\left[\mathbf{1}\otimes\mathbf{1}\right] - 2\beta\mathcal{I}. \tag{A.85}$$

Moreover, we also need the differentiation of the thermoelastic coupling term with respect to $\dot{\mathbf{C}}$

$$\frac{\partial p}{\partial \dot{\mathbf{C}}} = \frac{1}{2}\left(\theta\beta(\theta,J)J\mathbf{C}^{-1} + \frac{1}{\varrho_{\mathrm{R}}}\tilde{\mathbf{T}}^{\mathrm{iso}}_{\mathrm{eq}}\right). \tag{A.86}$$

Its representation based on quantities of the current configuration reads

$$\frac{1}{J}\mathbf{F}\frac{\partial p}{\partial \dot{\mathbf{C}}}\mathbf{F}^{\mathrm{T}} = \frac{1}{2}\left(\theta\beta(\theta, J)\mathbf{1} + \frac{1}{J\varrho_{\mathrm{R}}}\mathbf{S}_{\mathrm{eq}}^{\mathrm{iso}}\right). \tag{A.87}$$

The tangent of the thermoelastic coupling term with respect to θ reads

$$\frac{\mathrm{d}p}{\mathrm{d}\theta} = \left(\beta(\theta, J)J\mathbf{C}^{-1} + \theta\frac{\mathrm{d}\beta}{\mathrm{d}\theta}J\mathbf{C}^{-1} + \frac{1}{\varrho_{\mathrm{R}}}\frac{\partial\tilde{\mathbf{T}}_{\mathrm{eq}}^{\mathrm{iso}}}{\partial\theta}\right)\cdot\dot{\mathbf{E}} \tag{A.88}$$

based on the derivatives

$$\begin{aligned}\frac{\mathrm{d}\beta}{\mathrm{d}\theta} &= \left(\frac{1}{\theta_0}\frac{\alpha_\theta}{\varphi^2} - 2\frac{\theta}{\theta_0}\frac{\alpha_\theta^2}{\varphi^3}\right)\left(\left(\frac{\varphi}{\theta\alpha_\theta} - 1\right)U'(J/\varphi) - \frac{J}{\varphi}U''(J/\varphi)\right)\\ &\quad + \frac{\theta}{\theta_0}\frac{\alpha_\theta}{\varphi^2}\left(\left(\frac{1}{\theta} - \frac{\varphi}{\theta^2\alpha_\theta}\right)U' + \left(\frac{\varphi}{\theta\alpha_\theta} - 1\right)\frac{\partial U'}{\partial\theta} + \frac{J\alpha_\theta}{\varphi^2}U'' - \frac{J}{\varphi}\frac{\partial U''}{\partial\theta}\right)\\ &= \frac{\theta\varphi'}{\theta_0\varphi^2}\left[\left(\frac{2\varphi'}{\varphi} - \frac{2}{\theta}\right)U'(J/\varphi) + \left(4\frac{\varphi'}{\varphi} - \frac{2}{\theta}\right)\frac{J}{\varphi}U''(J/\varphi) + \frac{\varphi'}{\varphi}\frac{J^2}{\varphi^2}U'''(J/\varphi)\right]\end{aligned} \tag{A.89}$$

with

$$\frac{\partial U'}{\partial\theta} = \frac{-KJ\varphi'}{10\varphi^2}\left(4(J/\varphi)^3 + 6(J/\varphi)^{-7}\right) = -\frac{J\varphi'}{\varphi^2}U'', \tag{A.90}$$

$$\frac{\partial U''}{\partial\theta} = \frac{-KJ\varphi'}{10\varphi^2}\left(12(J/\varphi)^2 - 42(J/\varphi)^{-8}\right) = -\frac{J\varphi'}{\varphi^2}U''' \tag{A.91}$$

and

$$\frac{\mathrm{d}\tilde{\mathbf{T}}_{\mathrm{eq}}^{\mathrm{iso}}}{\mathrm{d}\theta} = \frac{1}{\theta}\tilde{\mathbf{T}}_{\mathrm{eq}}^{\mathrm{iso}}. \tag{A.92}$$

With quantities of the current configuration, we obtain

$$\frac{\mathrm{d}p}{\mathrm{d}\theta} = \left((\beta(\theta, J) + \theta\frac{\mathrm{d}\beta}{\mathrm{d}\theta})J\mathbf{1} + \frac{1}{\varrho_{\mathrm{R}}}\frac{\partial\mathbf{S}_{\mathrm{eq}}^{\mathrm{iso}}}{\partial\theta}\right)\cdot\mathbf{F}^{-\mathrm{T}}\dot{\mathbf{E}}\mathbf{F}^{-1} \tag{A.93}$$

$$= \left((\beta(\theta, J) + \theta\frac{\mathrm{d}\beta}{\mathrm{d}\theta})J\mathbf{1} + \frac{1}{\varrho_{\mathrm{R}}}\frac{\partial\mathbf{S}_{\mathrm{eq}}^{\mathrm{iso}}}{\partial\theta}\right)\cdot\mathbf{D}. \tag{A.94}$$

A.6.5 Tangents of the Internal Dissipation d

The tangents of the internal dissipation

$$d(\mathbf{C}, \mathbf{C}_{\mathrm{v}}, \dot{\mathbf{C}}_{\mathrm{v}}, \theta) = \frac{\mu}{\varrho_{\mathrm{R}}}J^{-\frac{2}{3}}\left[\mathbf{C}_{\mathrm{v}}^{-1}\otimes\mathbf{C}_{\mathrm{v}}^{-1}\right]^{T_{23}}\mathbf{C}\cdot\dot{\mathbf{C}}_{\mathrm{v}} \tag{A.95}$$

required for the MLNA are given below. The tangent of the internal dissipation with respect to $\mathbf{C}$ reads

$$\frac{\mathrm{d}d}{\mathrm{d}\mathbf{C}} = \frac{\partial d}{\partial \mathbf{C}} + \left\{ \frac{\mathrm{d}\tilde{\boldsymbol{r}}}{\mathrm{d}\mathbf{C}} \right\}^{\mathrm{T}} \frac{\mathrm{d}d}{\mathrm{d}\dot{\mathbf{C}}_{\mathrm{v}}} \tag{A.96}$$

with

$$\frac{\partial d}{\partial \mathbf{C}} = \frac{\mu}{\varrho_{\mathrm{R}}} J^{-\frac{2}{3}} \left(\left[\mathbf{C}_{\mathrm{v}}^{-1} \otimes \mathbf{C}_{\mathrm{v}}^{-1} \right]^{T_{23}} \dot{\mathbf{C}}_{\mathrm{v}} - \frac{1}{3} \left(\left[\mathbf{C}_{\mathrm{v}}^{-1} \otimes \mathbf{C}_{\mathrm{v}}^{-1} \right]^{T_{23}} \mathbf{C} \cdot \dot{\mathbf{C}}_{\mathrm{v}} \right) \mathbf{C}^{-1} \right) \tag{A.97}$$

and

$$\frac{\mathrm{d}d}{\mathrm{d}\dot{\mathbf{C}}_{\mathrm{v}}} = \frac{\mu}{\varrho_{\mathrm{R}}} J^{-\frac{2}{3}} \left[\mathbf{C}_{\mathrm{v}}^{-1} \otimes \mathbf{C}_{\mathrm{v}}^{-1} \right]^{T_{23}} \mathbf{C}. \tag{A.98}$$

In order to derive the tangent of $\tilde{\boldsymbol{r}}$ with respect to $\mathbf{C}$ the Gateaux-derivative of the evolution equation, we consider

$$\begin{aligned} \mathsf{D}_{\mathbf{C}}\, \tilde{\boldsymbol{r}}(\mathbf{C}, \theta, \mathbf{C}_{\mathrm{v}})[\Delta \mathbf{C}] = {} & 4\mu \mathsf{D}_{\mathbf{C}}\, \eta^{-1}(\mathbf{C}, \mathbf{C}_{\mathrm{v}}^{-1})[\Delta \mathbf{C}] \varphi^{-2/3} J^{-\frac{2}{3}} \left(\mathbf{C} - \frac{1}{3} \left(\mathbf{C}_{\mathrm{v}}^{-1} \cdot \mathbf{C} \right) \mathbf{C}_{\mathrm{v}} \right) \\ & + 4 \frac{\mu}{\eta} \varphi^{-2/3} \mathsf{D}_{\mathbf{C}}\, \left(\det \mathbf{C} \right)^{-1/3} (\mathbf{C})[\Delta \mathbf{C}] \left(\mathbf{C} - \frac{1}{3} \left(\mathbf{C}_{\mathrm{v}}^{-1} \cdot \mathbf{C} \right) \mathbf{C}_{\mathrm{v}} \right) \\ & + 4 \frac{\mu}{\eta} \varphi^{-2/3} J^{-\frac{2}{3}} \left(\Delta \mathbf{C} - \frac{1}{3} \left(\mathbf{C}_{\mathrm{v}}^{-1} \cdot \Delta \mathbf{C} \right) \mathbf{C}_{\mathrm{v}} \right) \end{aligned} \tag{A.99}$$

with

$$\eta \left(\mathbf{C}, \mathbf{C}_{\mathrm{v}} \right) = \eta_0 e^{\alpha(\mathbf{C}, \mathbf{C}_{\mathrm{v}})}, \tag{A.100}$$

$$\alpha \left(\mathbf{C}, \mathbf{C}_{\mathrm{v}} \right) = - \frac{\| \varphi^{-\frac{2}{3}} \mathbf{C} \tilde{\mathbf{T}}_{\mathrm{ov}} \|}{s_0 \left(\frac{1}{\sqrt{3}} \| \mathbf{C}_{\mathrm{v}}^{-1} \| \right)^{r_0}} = - \frac{2 \mu \varphi^{-\frac{2}{3}} J^{-\frac{2}{3}} \sqrt{\tau}}{s_0 \left(\det \mathbf{C} \right)^{1/3} \left(\sqrt{\frac{1}{3} \mathbf{C}_{\mathrm{v}}^{-1} \cdot \mathbf{C}_{\mathrm{v}}^{-1}} \right)^{r_0}} \tag{A.101}$$

and

$$\tau = \mathbf{C} \mathbf{C}_{\mathrm{v}}^{-1} \cdot \mathbf{C}_{\mathrm{v}}^{-1} \mathbf{C} - \frac{1}{3} \left(\mathbf{C} \cdot \mathbf{C}_{\mathrm{v}}^{-1} \right)^2. \tag{A.102}$$

With the derivatives

$$\mathsf{D}_{\mathbf{C}}\, \left(\det \mathbf{C} \right)^{-1/3} (\mathbf{C})[\Delta \mathbf{C}] = - \frac{1}{3} \left(\det \mathbf{C} \right)^{-1/3} \mathbf{C}^{-1} \cdot \Delta \mathbf{C}, \tag{A.103}$$

and

$$\mathsf{D}_{\mathbf{C}}\, \alpha(\mathbf{C}, \mathbf{C}_{\mathrm{v}})[\Delta \mathbf{C}] = \alpha \left(\tau^{-1} \mathcal{L}_{\mathrm{v}} \mathbf{C} - \frac{1}{3} \mathbf{C}^{-1} \right) \cdot \Delta \mathbf{C}, \tag{A.104}$$

based on the relations

$$\mathcal{L}_{\mathrm{v}} = \left[\mathbf{C}_{\mathrm{v}}^{-1} \otimes \mathbf{C}_{\mathrm{v}}^{-1} \right]^{T_{23}} - \frac{1}{3} \left[\mathbf{C}_{\mathrm{v}}^{-1} \otimes \mathbf{C}_{\mathrm{v}}^{-1} \right] \tag{A.105}$$

and

$$\frac{\mathrm{d}\tau^{1/2}}{\mathrm{d}\mathbf{C}} = \tau^{-1/2} \mathcal{L}_{\mathrm{v}} \mathbf{C}, \tag{A.106}$$

we can state the derivative

$$\frac{\mathrm{d}\eta^{-1}}{\mathrm{d}\mathbf{C}} = -\eta^{-1}\alpha\left(\tau^{-1}\mathcal{L}_{\mathrm{v}}\mathbf{C} - \frac{1}{3}\mathbf{C}^{-1}\right). \tag{A.107}$$

Now (A.99) can be expressed as

$$\begin{aligned}
&\mathsf{D}_{\mathbf{C}}\,\tilde{\boldsymbol{r}}(\mathbf{C},\theta,\mathbf{C}_{\mathrm{v}})[\Delta\mathbf{C}] \\
&= 4\frac{\mu}{\eta}\varphi^{-2/3}J^{-\frac{2}{3}}\Bigg[-\left(\mathbf{C}_{\mathrm{v}}^{-1}\cdot\mathbf{C}\right)\left(\frac{\alpha}{3\tau}\left[\mathbf{C}_{\mathrm{v}}\otimes\mathcal{L}_{\mathrm{v}}\mathbf{C}\right] + \left(\alpha+\frac{1}{3}\right)\frac{1}{3}\left[\mathbf{C}_{\mathrm{v}}\otimes\mathbf{C}^{-1}\right]\right) \\
&\qquad + (1-\alpha)\frac{1}{3}\left[\mathbf{C}\otimes\mathbf{C}^{-1}\right] + \frac{\alpha}{\tau}\left[\mathbf{C}\otimes\mathcal{L}_{\mathrm{v}}\mathbf{C}\right] + \mathcal{I} - \left[\mathbf{C}_{\mathrm{v}}\otimes\mathbf{C}_{\mathrm{v}}^{-1}\right]\Bigg]\Delta\mathbf{C},
\end{aligned} \tag{A.108}$$

and the corresponding tangent reads

$$\begin{aligned}
\frac{\mathrm{d}\tilde{\boldsymbol{r}}}{\mathrm{d}\mathbf{C}} =& 4\frac{\mu}{\eta}\varphi^{-2/3}J^{-\frac{2}{3}}\Bigg[-\left(\mathbf{C}_{\mathrm{v}}^{-1}\cdot\mathbf{C}\right)\left(\frac{\alpha}{3\tau}\left[\mathbf{C}_{\mathrm{v}}\otimes\mathcal{L}_{\mathrm{v}}\mathbf{C}\right] + \left(\alpha+\frac{1}{3}\right)\frac{1}{3}\left[\mathbf{C}_{\mathrm{v}}\otimes\mathbf{C}^{-1}\right]\right) \\
&\qquad + (1-\alpha)\frac{1}{3}\left[\mathbf{C}\otimes\mathbf{C}^{-1}\right] + \frac{\alpha}{\tau}\left[\mathbf{C}\otimes\mathcal{L}_{\mathrm{v}}\mathbf{C}\right] + \mathcal{I} - \left[\mathbf{C}_{\mathrm{v}}\otimes\mathbf{C}_{\mathrm{v}}^{-1}\right]\Bigg].
\end{aligned} \tag{A.109}$$

The tangent with respect to $\mathbf{C}_{\mathrm{v}}$ reads

$$\frac{\mathrm{d}d}{\mathrm{d}\mathbf{C}_{\mathrm{v}}} = \frac{\partial d}{\partial\mathbf{C}_{\mathrm{v}}} + \left\{\frac{\mathrm{d}\tilde{\boldsymbol{r}}}{\mathrm{d}\mathbf{C}_{\mathrm{v}}}\right\}^{\mathrm{T}}\frac{\mathrm{d}d}{\mathrm{d}\dot{\mathbf{C}}_{\mathrm{v}}}. \tag{A.110}$$

By means of the Gateaux-derivative

$$\begin{aligned}
&\mathsf{D}_{\mathbf{C}_{\mathrm{v}}}\,d(\mathbf{C},\mathbf{C}_{\mathrm{v}},\theta)[\Delta\mathbf{C}] \\
&= -\frac{\mu}{\varrho_{\mathrm{R}}}J^{-\frac{2}{3}}\left(\mathbf{C}_{\mathrm{v}}^{-1}\Delta\mathbf{C}\mathbf{C}_{\mathrm{v}}^{-1}\mathbf{C}\mathbf{C}_{\mathrm{v}}^{-1} + \mathbf{C}_{\mathrm{v}}^{-1}\mathbf{C}\mathbf{C}_{\mathrm{v}}^{-1}\Delta\mathbf{C}\mathbf{C}_{\mathrm{v}}^{-1}\right)\cdot\dot{\mathbf{C}}_{\mathrm{v}} \\
&= -\frac{\mu}{\varrho_{\mathrm{R}}}J^{-\frac{2}{3}}\left(\left[\mathbf{C}_{\mathrm{v}}^{-1}\otimes\mathbf{C}_{\mathrm{v}}^{-1}\mathbf{C}\mathbf{C}_{\mathrm{v}}^{-1}\right]^{T_{23}}\Delta\mathbf{C} + \left[\mathbf{C}_{\mathrm{v}}^{-1}\mathbf{C}\mathbf{C}_{\mathrm{v}}^{-1}\otimes\mathbf{C}_{\mathrm{v}}^{-1}\right]^{T_{23}}\Delta\mathbf{C}\right)\cdot\dot{\mathbf{C}}_{\mathrm{v}} \\
&= -\frac{\mu}{\varrho_{\mathrm{R}}}J^{-\frac{2}{3}}\left(\left[\mathbf{C}_{\mathrm{v}}^{-1}\mathbf{C}\mathbf{C}_{\mathrm{v}}^{-1}\otimes\mathbf{C}_{\mathrm{v}}^{-1}\right]^{T_{23}}\dot{\mathbf{C}}_{\mathrm{v}} + \left[\mathbf{C}_{\mathrm{v}}^{-1}\otimes\mathbf{C}_{\mathrm{v}}^{-1}\mathbf{C}\mathbf{C}_{\mathrm{v}}^{-1}\right]^{T_{23}}\dot{\mathbf{C}}_{\mathrm{v}}\right)\cdot\Delta\mathbf{C}
\end{aligned}$$

we compute the tangent

$$\frac{\partial d}{\partial\mathbf{C}_{\mathrm{v}}} = -\frac{\mu}{\varrho_{\mathrm{R}}}J^{-\frac{2}{3}}\left(\left[\mathbf{C}_{\mathrm{v}}^{-1}\mathbf{C}\mathbf{C}_{\mathrm{v}}^{-1}\otimes\mathbf{C}_{\mathrm{v}}^{-1}\right]^{T_{23}}\dot{\mathbf{C}}_{\mathrm{v}} + \left[\mathbf{C}_{\mathrm{v}}^{-1}\otimes\mathbf{C}_{\mathrm{v}}^{-1}\mathbf{C}\mathbf{C}_{\mathrm{v}}^{-1}\right]^{T_{23}}\dot{\mathbf{C}}_{\mathrm{v}}\right). \tag{A.111}$$

$\dfrac{\mathrm{d}d}{\mathrm{d}\dot{\mathbf{C}}_{\mathrm{v}}}$ is given in (A.98). The following section outlines the derivation of

$$\tilde{\boldsymbol{r}}\left(\mathbf{C},\theta,\mathbf{C}_{\mathrm{v}}\right) = 4\mu\frac{\varphi^{-2/3}}{(\det\mathbf{C})^{1/3}}\eta^{-1}(\mathbf{C},\mathbf{C}_{\mathrm{v}})\mathbf{g}(\mathbf{C},\mathbf{C}_{\mathrm{v}}) \quad \text{with} \quad \mathbf{g}(\mathbf{C},\mathbf{C}_{\mathrm{v}}) = \mathbf{C} - \frac{1}{3}(\mathbf{C}_{\mathrm{v}}^{-1}\cdot\mathbf{C})\mathbf{C}_{\mathrm{v}}, \tag{A.112}$$

in direction of $\mathbf{C}_{\mathrm{v}}$. The derivative of the inverse of the viscosity yields

$$\frac{\mathrm{d}\eta^{-1}}{\mathrm{d}\mathbf{C}_{\mathrm{v}}} = -\,\eta^{-1}\left[\mathbf{C}_{\mathrm{v}}^{-1}\otimes\mathbf{C}_{\mathrm{v}}^{-1}\right]^{T_{23}}\left(\frac{r_0\alpha}{\|\mathbf{C}_{\mathrm{v}}^{-1}\|}\mathbf{C}_{\mathrm{v}}^{-1} + \frac{\alpha}{3\tau}\left(\mathbf{C}\cdot\mathbf{C}_{\mathrm{v}}^{-1}\right)\mathbf{C} - \frac{\alpha}{\tau}\left[\mathbf{C}\otimes\mathbf{C}\right]^{T_{23}}\mathbf{C}_{\mathrm{v}}^{-1}\right) \tag{A.113}$$

Making use of

$$\frac{\mathrm{d}\left(\phi(\mathbf{B})\mathbf{A}(\mathbf{B})\right)}{\mathrm{d}\mathbf{B}} = \mathbf{A}\otimes\frac{\mathrm{d}\phi}{\mathrm{d}\mathbf{B}} + \phi\frac{\mathrm{d}\mathbf{A}}{\mathrm{d}\mathbf{B}}, \tag{A.114}$$

see (Holzapfel, 2008), and

$$\frac{\mathrm{d}\mathbf{g}}{\mathrm{d}\mathbf{C}_{\mathrm{v}}} = \frac{1}{3}(\mathbf{C}_{\mathrm{v}}^{-1}\cdot\mathbf{C})\left[\mathcal{I} - \frac{1}{3}\mathbf{C}_{\mathrm{v}}\otimes\mathbf{C}_{\mathrm{v}}^{-1}\mathbf{C}\mathbf{C}_{\mathrm{v}}^{-1}\right], \tag{A.115}$$

we obtain the derivative of the evolution equation with respect to $\mathbf{C}_{\mathrm{v}}$

$$\frac{\mathrm{d}\tilde{\boldsymbol{r}}}{\mathrm{d}\mathbf{C}_{\mathrm{v}}} = 4\mu\frac{\varphi^{-2/3}}{(\det\mathbf{C})^{1/3}}\left(\mathbf{g}(\mathbf{C},\mathbf{C}_{\mathrm{v}})\otimes\frac{\mathrm{d}\eta^{-1}(\mathbf{C},\mathbf{C}_{\mathrm{v}})}{\mathrm{d}\mathbf{C}_{\mathrm{v}}} + \eta^{-1}(\mathbf{C},\mathbf{C}_{\mathrm{v}})\frac{\mathrm{d}\mathbf{g}}{\mathrm{d}\mathbf{C}_{\mathrm{v}}}\right). \tag{A.116}$$

The derivative of the dissipation with respect to the temperature yields

$$\frac{\mathrm{d}d}{\mathrm{d}\theta} = \left\{\frac{\mathrm{d}d}{\mathrm{d}\dot{\mathbf{C}}_{\mathrm{v}}}\right\}^{\mathrm{T}}\frac{\mathrm{d}\tilde{\boldsymbol{r}}}{\mathrm{d}\theta}, \tag{A.117}$$

based on (A.98) and

$$\begin{aligned}\frac{\mathrm{d}\tilde{\boldsymbol{r}}}{\mathrm{d}\theta} &= 4\frac{\mu}{(\det\mathbf{C})^{1/3}}\mathbf{g}(\mathbf{C},\mathbf{C}_{\mathrm{v}})\left(\frac{\mathrm{d}\varphi^{-2/3}}{\mathrm{d}\theta}\eta^{-1} + \varphi^{-2/3}\frac{\mathrm{d}\eta^{-1}}{\mathrm{d}\theta}\right) &\text{(A.118)}\\ &= 4\frac{\mu\varphi^{-2/3}}{(\det\mathbf{C})^{1/3}\,\eta}\mathbf{g}(\mathbf{C},\mathbf{C}_{\mathrm{v}})\left(\alpha s_0^{-1}\omega_s(\bar{s}_0 - s_\infty)e^{-\omega_s(\theta-\theta_0)} + \kappa\theta^{-2} - \frac{2}{3}\varphi^{-1}\varphi'(\alpha+1)\right) &\text{(A.119)}\end{aligned}$$

with

$$\frac{\mathrm{d}\varphi^{-2/3}}{\mathrm{d}\theta} = -\frac{2}{3}\varphi^{-5/3}\varphi' \tag{A.120}$$

and

$$\frac{\mathrm{d}\eta^{-1}}{\mathrm{d}\theta} = \eta^{-1}\left(\kappa\theta^{-2} - \alpha\left(\frac{2}{3}\varphi^{-1}\varphi' - s_0^{-1}\omega_s(\bar{s}_0 - s_\infty)e^{-\omega_s(\theta-\theta_0)}\right)\right). \tag{A.121}$$

B List of symbols

B.1 Scalars

A_i	i th Lagrange polynomial
α	Curve parameter, material parameter
α_θ	Coefficient of linear thermal expansion
Δt_n	Time step-size of intervall reaching from t_n until t_{n+1}
a_{ij}, b_i, c_i	Coefficients of a Runge-Kutta method
$\hat{b}_i$	Weighting coefficients of an embedded Runge-Kutta method
c_{ij}	Material parameters of generalized polynomial elasticity
C_{ijkl}	Component of fourth order tensor
$c_{\mathrm{d0}}, c_{\mathrm{dk}}$	Coefficients determining heat capacity
c_{d}	Heat capacity
$c_{\mathrm{d}}^{\mathrm{h}}$	Discretized heat capacity
ϱ	Density in current configuration
ϱ_{R}	Density in reference configuration
$\mathrm{d}V$	Material volume element in reference configuration
$\mathrm{d}v$	Material volume element in current configuration
d	Internal dissipation
d^{h}	Discretized internal dissipation
δE_{ij}	Component of virtual Green strain tensor
ΔE_{ij}	Component of incremental virtual Green strain tensor
$\delta\theta$	Virtual temperature
$\delta\theta^h$	Approximated virtual temperature
E_{ij}	Components of Green strain tensors given as vector
$E(\mathcal{B}, t)$	Internal energy
e	Mass specific internal energy
e_u	Error norm for displacement coefficients
e_θ	Error norm for temperature coefficients
e_q	Error norm for internal variables
$\mathrm{e}_{\max}$	Maximum of e_u, e_θ and e_q
ϵ_r, ϵ_a	Relative and absolute error tolerances
ϵ_{r}^u,ϵ_{a}^u	Relative and absolute error tolerances for displacements
$\epsilon_{\mathrm{r}}^\theta$, $\epsilon_{\mathrm{a}}^\theta$	Relative and absolute error tolerances for temperatures
ϵ_{r}^q, ϵ_{a}^q	Relative and absolute error tolerances for internal variables
η	Viscosity of material body

η_0	Initial viscosity
F_{ij}	Components of deformation gradient
f_{q}, $f_{\theta\mathrm{q}}$	Prescribed heat flux
$f_{\min}$	Factor in step-size control algorithm
$f_{\max}$	Factor in step-size control algorithm
f_{safety}	Factor in step-size control algorithm
G	Shear modulus
γ	Entropy production density
$\Gamma(\mathcal{B},t)$	Volume-distributed entropy production
$H(\mathcal{B},t)$	Entropy exchange
$\mathrm{I}_{\mathbf{C}}$	First invariant of tensor $\mathbf{C}$
$\mathrm{II}_{\mathbf{C}}$	Second invariant of tensor $\mathbf{C}$
$\mathrm{III}_{\mathbf{C}}$	Third invariant of tensor $\mathbf{C}$
J	Determinant of deformation gradient
J_{M}	Mechanical part of deformation gradient
K	Bulk modulus
$K(\mathcal{B},t)$	Kinetic energy
κ	Material parameter related to viscosity
λ	Isotropic thermal conductivity
λ^{h}	Discretized isotropic thermal conductivity
λ, λ_Q	Stretches
$L(\mathcal{B},t)$	Power of external forces
L_i	i th Legendre polynomial
$m(\mathcal{B},t)$	Mass of a material body
μ	Material parameter associated with overstresses
$N_{i,1}^{E_1}$	Shape function with $p_\xi = i$ and $p_\eta = 1$ belonging to edge E_1 (2-D)
$N_{i,1,1}^{E_1}$	Shape function with $p_\xi = i$, $p_\eta = 1$ and $p_\zeta = 1$ belonging to edge E_1 (3-D)
$N_{i,j,1}^{F_1}$	Shape function with $p_\xi = i$, $p_\eta = j$ and $p_\zeta = 1$ belonging to face F_1 (3-D)
$N_{i,j}^{int}(\xi,\eta)$	Shape function with $p_\xi = i$ and $p_\eta = j$ belonging to the interior of an element (2-D)
$N_{i,j,k}^{int}$	Shape function with $p_\xi = i$, $p_\eta = j$ and $p_\zeta = k$ belonging the interior of an element (3-D)
N_i	Linear shape function belonging to node N_i (1-D)
$N_{1,1}^{N_i}$	Linear shape function belonging to node N_i (2-D)
$N_{1,1,1}^{N_i}$	Linear shape function belonging to node N_i (3-D)
n_{modes}	Number of modes with which the displacement or the temperature field within a domain is discretized
n_{eq}	Number of equations
n_{nu}	Number of unknown displacement coefficients
n_{pu}	Number of prescribed displacement coefficients
$n_{\mathrm{n}\theta}$	Number of unknown temperature coefficients
$n_{\mathrm{p}\theta}$	Number of prescribed displacement coefficients

n_{em}	Number of modes belonging to an element
n_{ip}	Number of integration points within an element
n_{el}	Number of elements discretizing the domain
n_{q}	Number of internal variables at a Gauss point
n_{Q}	Number of all internal variables of a structure
n_{ov}	Number of Maxwell elements associated with overstresses
n_{edges}	Number of modes associated with the edges of an element
n_{faces}	Number of modes associated with the surfaces of an element
n_{ext}	Number of modes associated with the exterior of an element
n_{int}	Number of modes associated with the interior of an element
n_{cores}	Number of cores
n_{NR}	Number of nodes of background grid
ω	Step length in line search
p_ξ, p_η, p_ζ	Polynomial degree of finite element in ξ-, η- and ζ-direction
ψ	Helmholtz free energy
$\psi_{\mathrm{M}}, \psi_\theta$	Mechanical and thermal part of Helmholtz free energy
$\bar{\psi}^{\mathrm{eq}}_{\mathrm{M}}$, $\bar{\psi}^{\mathrm{ov}}_{\mathrm{M}}$	Equilibrium and overstress part of mechanical free energy
U, $\bar{v}$, $\bar{w}_{\mathrm{ov}}$	Free energies related to volumetric, isochoric and inelastic deformations
φ	Isotropic thermal expansion
ϕ_j	Integrated Legendre polynomial
p	Thermoelastic coupling term
p^{h}	Discretized thermoelastic coupling term
q_k	Components of $\boldsymbol{q}$
$q_{\mathrm{err},k}$	Components of $\boldsymbol{q}_{\mathrm{err}}$
$Q(\mathcal{B}, t)$	Non-mechanical energy
p, $\hat{p}$	Order of Runge-Kutta method
p^{h}	Discretized volume-distributed heat supply
r_0	Material parameter related to viscosity
σ	Volume-distributed entropy supply
σ_{xx}	Component of $\mathbf{T}$
S^e_{11}	Component of $\mathbf{S}$
$S_{i,k}$, $R_{j,l}$	Normalized B-spline basis functions
$s_\infty, \bar{s}_0$	Material parameter related to viscosity
s	Mass specific entropy
s	Number of stages of a Runge-Kutta method
$S(\mathcal{B}, t)$	Entropy content of a material body
r	Volume-distributed heat supply
θ	Absolute temperature
θ_{G}	Glass transition temperature
θ^h	Approximated absolute temperature
θ_0	Temperature of surroundings
θ_{f}	Temperature of surrounding fluid
θ_l	Components of $\boldsymbol{\Theta}$

$\theta_{\mathrm{err},l}$	Components of $\boldsymbol{\Theta}_{\mathrm{err}}$
t	Time
t_{i}	Starting time of a process
T_{ni}	Time at stage i of time step n
$\tilde{t}_{11}$	Component of $\tilde{\mathbf{T}}$
t_{e}	End time of a process
$\mathrm{tol}_{\boldsymbol{Q}}$	Convergence criterion for internal variables
u_l	Unknown displacement coefficients (components of $\boldsymbol{u}$)
$u_{\mathrm{err},l}$	Components of $\boldsymbol{u}_{\mathrm{err}}$
w_s	Material parameter related to viscosity
$w_{i,j}$	Weights associated with the control vertices $\boldsymbol{P}_{i,j}$
w_i	Weights associated with the control vertices $\boldsymbol{P}_i$
X, Y, Z	Component of coordinates of material point in reference configuration
x, y, z	Component of coordinates of material point in current configuration
z_{R}	Production density of physical quantity in reference configuration
z	Production density of physical quantity in current configuration
ξ, η, ζ	Components of the vector $\boldsymbol{\xi}$

B.2 Vector Valued Quantities

$\boldsymbol{\chi}$	Arbitrary configuration of material body
$\boldsymbol{\chi}_t$	Current configuration of material body
$\boldsymbol{\chi}_{\mathrm{R}}$	Motion of a material body
$\boldsymbol{\chi}^e$	Mapping from unit element to reference configuration
$\delta\boldsymbol{u}$	Virtual displacements
$\mathrm{d}\boldsymbol{X}$	Material line element in reference configuration
$\mathrm{d}\boldsymbol{x}$	Material line element in current configuration
$\mathrm{d}\boldsymbol{A}$	Material surface element in reference configuration
$\mathrm{d}\boldsymbol{a}$	Material surface element in current configuration
$\boldsymbol{e}_x$,$\boldsymbol{e}_y$,$\boldsymbol{e}_z$	Base vectors of cartesian coordinates
$\boldsymbol{e}_i$	Part of map $\boldsymbol{\chi}^e$ associated with the edges of a hexahedral element
$\boldsymbol{E}_i$	Parametric curve description for curve i of the reference element
$\boldsymbol{f}_i$	Part of map $\boldsymbol{\chi}^e$ associated with the surfaces of a hexahedral element
$\boldsymbol{F}_i$	Parametric surface description for surface i of the reference element
$\boldsymbol{g}_i$	Tangent vector belonging to a material surface element in current configuration
$\boldsymbol{G}^j$	Gradient vector belonging to a material surface element in reference configuration
$\boldsymbol{k}$	Volume-distributed external force (usually gravitational forces)
$\boldsymbol{m}(\mathcal{B}, t)$	Rotational momentum
$\boldsymbol{n}_{\mathrm{R}}$	Surface unit normal in reference configuration

$\boldsymbol{n}$	Surface unit normal in current configuration
$\hat{\boldsymbol{n}}$	Surface normal in current configuration
$\boldsymbol{\phi}$	Entropy flux vector
$\boldsymbol{p}(\mathcal{B}, t)$	Linear momentum
$\boldsymbol{P}_i$	Control vertices of a curve
$\boldsymbol{P}_{i,j}$	Control vertices of a surface
$\boldsymbol{q}$	Cauchy heat flux vector
$\boldsymbol{q}_{\mathrm{R}}$	Piola-Kirchhoff heat flux vector
$\boldsymbol{r}$	Residual vector corresponding to terms of higher order in Taylor expansion
$\bar{\boldsymbol{s}}$, $\hat{\boldsymbol{s}}$	Prescribed stresses
$\boldsymbol{t}$	Cauchy stress vector
$\boldsymbol{t}_{\mathrm{R}}$	Piola stress vector
$\boldsymbol{u}$	Displacement of material point
$\boldsymbol{v}$	Velocity of material point with respect to the current configuration
$\boldsymbol{x}$	Position of a material point at time t
$\boldsymbol{X}$	Position of a material point in reference configuration
$\boldsymbol{X}_0$	Position of a specific material point in reference configuration
$\boldsymbol{\xi}$	Coordinates of the reference element

B.3 Second and Higher Order Tensor Quantities

$\mathbf{B}$	Left Cauchy-Green tensor
$\bar{\mathbf{B}}$	Volume-preserving part of left Cauchy-Green tensor
$\bar{\mathbf{B}}_{\mathrm{M}}$	Mechanical, volume-preserving part of left Cauchy-Green tensor
$\bar{\mathbf{B}}_{\mathrm{e}}$	Volume-preserving part of $\mathbf{B}$ operating on intermediate configuration
$\mathbf{C}$	Right Cauchy-Green tensor
$\bar{\mathbf{C}}$	Volume-preserving part of right Cauchy-Green tensor
$\mathbf{C}_{\mathrm{M}}$	Mechanical part of right Cauchy-Green tensor
$\bar{\mathbf{C}}_{\mathrm{M}}$	Mechanical, volume-preserving part of right Cauchy-Green tensor
$\check{\mathbf{C}}_{\mathrm{e}}$	Elastic part of right Cauchy-Green tensor operating on intermediate configuration
$\mathbf{C}_{\mathrm{v}}$	Viscous right Cauchy-Green tensor
$\tilde{\mathcal{C}}_{\mathrm{u}}$	Tangent operator (mechanical part) with respect to reference configuration
$\tilde{\mathbf{C}}_{\theta}$	Tangent operator
$\mathbf{D}$	Symmetric part of spatial velocity gradient
$\delta\mathbf{E}$	Virtual Green strain tensor
$\mathbf{E}$	Green strain tensor
$\mathbf{E}_{\mathrm{M}}$	Mechanical part of Green strain tensor
$\mathbf{E}_{\theta}$	Thermal part of Green strain tensor
$\delta\mathbf{H}$	Virtual displacement gradient
$\mathbf{F}$	Deformation gradient

$\hat{\mathbf{F}}$	Isochoric part of deformation gradient
$\bar{\mathbf{F}}$	Volume-changing part deformation gradient
$\mathbf{F}_\theta$	Thermal part of deformation gradient
$\mathbf{F}_\mathrm{M}$	Mechanical part of deformation gradient
$\hat{\mathbf{F}}_\mathrm{M}$	Mechanical, volume-changing part of deformation gradient
$\bar{\mathbf{F}}_\mathrm{M}$	Mechanical, volume-preserving part of deformation gradient
$\bar{\mathbf{F}}_\mathrm{e}$	Isochoric elastic part of deformation gradient
$\bar{\mathbf{F}}_\mathrm{v}$	Isochoric inelastic part of deformation gradient
$\check{\mathbf{F}}_\mathrm{e}$	Elastic part of deformation gradient operating on intermediate configuration
$\check{\mathbf{\Gamma}}_\mathrm{e}$	Strain tensor operating on elastic intermediate configuration
$\overset{\triangle}{\mathbf{\Gamma}}, \overset{\triangle}{\mathbf{\Gamma}}_\mathrm{M}, \overset{\triangle}{\mathbf{\Gamma}}_\theta$	Strain rate tensors in intermediate configuration
$\overset{\triangle}{\check{\mathbf{\Gamma}}}_\theta, \overset{\triangle}{\check{\mathbf{\Gamma}}}_\mathrm{e}, \overset{\triangle}{\bar{\mathbf{\Gamma}}}_\mathrm{v}$	Strain rate tensors in intermediate configuration
$\mathbf{H}$	Displacement gradient
$\mathbf{1}$	Second order identity tensor
$\mathcal{I}$	$= [\mathbf{1} \otimes \mathbf{1}]^{T_{23}}$, fourth order identity tensor
$\mathbf{L}$, $\mathbf{L}_\mathrm{v}$	Spatial velocity gradients
$\boldsymbol{\lambda}$, $\boldsymbol{\lambda}_\mathrm{R}$	Thermal conductivity tensor with respect to current or reference configuration
$\mathbf{\mathsf{q}}$	Vector of internal variables at a material point
S	Weighted Cauchy stress tensor, Kirchhoff stress tensor
S_M	Mechanical part of Kirchhoff stress tensor
$\mathsf{S}_\mathrm{M}^\mathrm{eq}$	Equilibrium part of mechanical weighted Cauchy stresses
$\check{\mathsf{S}}_\mathrm{ov}$	Overstress part of Kirchhoff stress tensor operating on intermediate configuration
$\mathbf{T}$	Cauchy stress tensor
$\mathbf{T}_\mathrm{eq}$	Cauchy stress tensor of equilibrium part
$\mathbf{T}_\mathrm{R}$	First Piola-Kirchhoff stress tensor
$\tilde{\mathbf{T}}$	Second Piola-Kirchhoff stress tensor
$\tilde{\mathbf{T}}_\mathrm{eq}$	Equilibrium part of second Piola-Kirchhoff stress tensor
$\tilde{\mathbf{T}}_\mathrm{ov}$	Overstress part of second Piola-Kirchhoff stress tensor
$\mathbf{W}$	Skew symmetric part of spatial velocity gradient

B.4 Matrices and Column Matrices

$\boldsymbol{A}$	$\in \mathbb{R}^{s\times s}$, contains coefficients a_{ij} of Runge-Kutta method
$\boldsymbol{b}$	$\in \mathbb{R}^{s}$, contains coefficients b_i of Runge-Kutta method
$\hat{\boldsymbol{b}}$	$\in \mathbb{R}^{s}$, contains coefficients $\hat{b}_i$ of Runge-Kutta method
$\mathbf{B}_\mathrm{d}^e$	$\in \mathbb{R}^{6\times 3n_\mathrm{em}}$, strain-displacement matrix
$\mathbf{B}_{\mathrm{d}\,i}^e$	$\in \mathbb{R}^{6\times 3}$, strain-displacement matrix for element mode i
$\tilde{\mathbf{B}}_\mathrm{d}^e$	$\in \mathbb{R}^{6\times 3n_\mathrm{em}}$, strain-displacement matrix (reference configuration)

$\tilde{\mathbf{B}}^{e}_{\mathrm{d}\,i}$	$\in \mathbb{R}^{3\times 3}$, strain-displacement matrix for element mode i (reference configuration)
$\mathbf{B}^{e}_{\theta}$	$\in \mathbb{R}^{3\times n_{\mathrm{em}}}$, matrix relating temperatures to temperature gradients
$\mathbf{C}$	$\in \mathbb{R}^{6}$, components of the right Cauchy-Green tensor ordered in a column matrix
$\mathbf{C}_{ni}$	$\in \mathbb{R}^{6}$, $\mathbf{C}$ at time step n of stage i
$\mathbf{C}^{\boldsymbol{u}}_{ni}$	$\in \mathbb{R}^{6}$, starting value of $\mathbf{C}$ in DIRK-method
$\tilde{\mathbf{C}}^{e}_{\mathrm{u}}$	$\in \mathbb{R}^{6\times 6}$, tangent operator (mechanical part) arranged as matrix
$\tilde{\mathbf{C}}^{e}_{\theta}$	$\in \mathbb{R}^{6}$, tangent operatur (thermal part) arranged as column matrix
$\mathbf{C}_{\mathrm{d}}$	$\in \mathbb{R}^{n_{\mathrm{modes}}\times n_{\mathrm{modes}}}$, capacity matrix
$\boldsymbol{C}_{\lambda}$	$\in \mathbb{R}^{n_{\mathrm{modes}}\times n_{\mathrm{modes}}}$, conductivity matrix
$\boldsymbol{c}$	$\in \mathbb{R}^{s}$, contains coefficients c_i of Runge-Kutta method
$\boldsymbol{\delta}$, $\hat{\boldsymbol{\delta}}$	$\in \mathbb{R}^{n}$, local integration error
$\delta\mathbf{E}^{e\,h}$	$\in \mathbb{R}^{6}$, virtual Green strain tensor arranged as column matrix
$\Delta\mathbf{E}^{e\,h}$	$\in \mathbb{R}^{6}$, increment in virtual Green strain tensor arranged as column matrix
$\delta\boldsymbol{\Theta}$	$\in \mathbb{R}^{n_{\mathrm{n}\theta}}$, column matrix containing unknown virtual temperature coefficients
$\delta\boldsymbol{\Theta}_{\mathrm{a}}$	$\in \mathbb{R}^{n_{\mathrm{modes}}}$, column matrix containing all virtual temperature coefficients
$\delta\boldsymbol{u}_{\mathrm{a}}$	$\in \mathbb{R}^{3n_{\mathrm{modes}}}$, column matrix containing all virtual displacement coefficients
$\delta\boldsymbol{u}^{h}$	$\in \mathbb{R}^{3}$, approximated virtual displacement
$\delta\boldsymbol{u}$	$\in \mathbb{R}^{n_{\mathrm{nu}}}$, column matrix containing the coefficients associated with unknown virtual displacement coefficients
$\delta\overline{\boldsymbol{u}}$	$\in \mathbb{R}^{n_{\mathrm{pu}}}$, column matrix containing the coefficients associated with prescribed virtual displacement coefficients
$\delta\boldsymbol{\Theta}^{e}$	$\in \mathbb{R}^{n_{\mathrm{em}}}$, virtual temperature coefficients of an element
$\delta\mathbf{u}^{\mathrm{e}}$	$\in \mathbb{R}^{3n_{\mathrm{em}}}$, virtual displacement coefficients of an element
$\Delta\mathbf{u}^{e}_{\mathrm{a}}$	$\in \mathbb{R}^{3n_{\mathrm{ext}}}$, unknown vector corresponding to exterior modes
$\Delta\mathbf{u}^{e}_{\mathrm{b}}$	$\in \mathbb{R}^{3n_{\mathrm{int}}}$, unknown vector corresponding to interior modes
$\Delta\mathbf{u}^{e}$	$\in \mathbb{R}^{3n_{\mathrm{em}}}$, unknown vector corresponding to all displacement coefficients of an element
$\mathbf{F}^{e}_{23}$	$\in \mathbb{R}^{6\times 6}$, matrix notation of push forward operator $\left[\mathbf{F}\otimes\mathbf{F}\right]^{\mathrm{T}_{23}}$
$\boldsymbol{G}_{\mathrm{u}}$, $\boldsymbol{G}_{\mathrm{u}\,ni}$	$\in \mathbb{R}^{n_{\mathrm{nu}}}$, system of nonlinear equations (mechanical part of DAE-system)
$\boldsymbol{G}_{\theta}$, $\boldsymbol{G}_{\theta\;ni}$	$\in \mathbb{R}^{n_{\mathrm{n}\theta}}$, system of nonlinear equations (thermal part of DAE-system)
$\mathbf{g}^{e}_{\mathrm{a}}$	$\in \mathbb{R}^{3n_{\mathrm{ext}}}$, right hand side of element corresponding to exterior modes
$\mathbf{g}^{e}_{\mathrm{b}}$	$\in \mathbb{R}^{3n_{\mathrm{int}}}$, right hand side of element corresponding to interior modes
$\mathbf{J}_{e}$	$\in \mathbb{R}^{3\times 3}$, gradient of coordinates of the reference configuration with respect to coordinates of the reference element
$\mathbf{j}_{e}$	$\in \mathbb{R}^{3\times 3}$, gradient of coordinates of the current configuration with respect to coordinates of the reference element
$\boldsymbol{g}$	$\in \mathbb{R}^{n_{\mathrm{nu}}}$, algebraic equations of DAE-system
$\boldsymbol{K}^{(m)}$	$\in \mathbb{R}^{n_{\mathrm{eq}}\times n_{\mathrm{eq}}}$, global stiffness matrix in iteration m
$\boldsymbol{K}$	$\in \mathbb{R}^{n_{\mathrm{eq}}\times n_{\mathrm{eq}}}$, global stiffness matrix
$\mathbf{k}^{e}_{\mathrm{UC}}$	$\in \mathbb{R}^{3n_{\mathrm{em}}\times 3n_{\mathrm{em}}}$, elemental stiffness contribution

	resulting from physical nonlinearity
$\mathbf{k}^{e}_{\mathrm{UG}}$	$\in \mathbb{R}^{3n_{\mathrm{em}}\times 3n_{\mathrm{em}}}$, elemental stiffness contribution resulting from gemetric nonlinearity
$\mathbf{k}^{e}_{\mathrm{UF}}$	$\in \mathbb{R}^{3n_{\mathrm{em}}\times 3n_{\mathrm{em}}}$, elemental stiffness contribution resulting from follower load
$\mathbf{k}^{e}_{\mathrm{U}\theta}$	$\in \mathbb{R}^{3n_{\mathrm{em}}\times n_{\mathrm{em}}}$, elemental stiffness contribution (derivative of principle of virtual displacements with respect to temperature)
$\mathbf{k}^{e}_{\theta\,\mathrm{U\,c}}$	$\in \mathbb{R}^{n_{\mathrm{em}}\times 3n_{\mathrm{em}}}$, part of elemental stiffness contribution
$\mathbf{k}^{e}_{\theta\,\mathrm{U\,q}}$	$\in \mathbb{R}^{n_{\mathrm{em}}\times 3n_{\mathrm{em}}}$, part of elemental stiffness contribution
$\mathbf{k}^{e}_{\theta\,\mathrm{U\,q\,1}}$	$\in \mathbb{R}^{n_{\mathrm{em}}\times 3n_{\mathrm{em}}}$, part of elemental stiffness contribution
$\mathbf{k}^{e}_{\theta\,\mathrm{U\,q\,2}}$	$\in \mathbb{R}^{n_{\mathrm{em}}\times 3n_{\mathrm{em}}}$, part of elemental stiffness contribution
$\mathbf{k}^{e}_{\theta\,\mathrm{U\,q\,3}}$	$\in \mathbb{R}^{n_{\mathrm{em}}\times 3n_{\mathrm{em}}}$, part of elemental stiffness contribution
$\mathbf{k}^{e}_{\theta\,\mathrm{U\,e}}$	$\in \mathbb{R}^{n_{\mathrm{em}}\times 3n_{\mathrm{em}}}$, part of elemental stiffness contribution
$\mathbf{k}^{e}_{\theta\,\mathrm{U\,i}}$	$\in \mathbb{R}^{n_{\mathrm{em}}\times 3n_{\mathrm{em}}}$, part of elemental stiffness contribution
$\mathbf{k}^{e}_{\theta\,\theta\,\mathrm{c}}$	$\in \mathbb{R}^{n_{\mathrm{em}}\times n_{\mathrm{em}}}$, part of elemental stiffness contribution
$\mathbf{k}^{e}_{\theta\,\theta\,\mathrm{q}}$	$\in \mathbb{R}^{n_{\mathrm{em}}\times n_{\mathrm{em}}}$, part of elemental stiffness contribution
$\mathbf{k}^{e}_{\theta\,\theta\,\mathrm{e}}$	$\in \mathbb{R}^{n_{\mathrm{em}}\times n_{\mathrm{em}}}$, part of elemental stiffness contribution
$\mathbf{k}^{e}_{\theta\,\theta\,\mathrm{i}}$	$\in \mathbb{R}^{n_{\mathrm{em}}\times n_{\mathrm{em}}}$, part of elemental stiffness contribution
$\boldsymbol{L}$, $\boldsymbol{L}_{ni}$	$\in \mathbb{R}^{n_{\mathrm{Q}}}$, nonlinear equations (differential part of DAE-system)
$\mathbf{M}^{e}_{\tilde{\mathbf{T}}}$	$\in \mathbb{R}^{9\times 9}$, components of $\tilde{\mathbf{T}}$ arranged as matrix associated with element e
$\mathbf{M}^{e}_{\mathbf{S}}$	$\in \mathbb{R}^{9\times 9}$, components of $\mathbf{S}$ arranged as matrix
$\boldsymbol{N}_{\mathrm{ad}}$	$\in \mathbb{R}^{3\times n_{\mathrm{modes}}}$, matrix containing all shape functions for displacement field
$\boldsymbol{N}_{\mathrm{d}}$	$\in \mathbb{R}^{3\times n_{\mathrm{nu}}}$, matrix containing shape functions corresponding to unknown displacement coefficients
$\overline{\boldsymbol{N}}_{\mathrm{d}}$	$\in \mathbb{R}^{3\times n_{\mathrm{pu}}}$ matrix containing shape functions corresponding to prescribed displacement coefficients
$\boldsymbol{N}_{\mathrm{a}\theta}$	$\in \mathbb{R}^{n_{\mathrm{modes}}}$, column matrix containing all shape functions for the temperature field
$\boldsymbol{N}_{\theta}$	$\in \mathbb{R}^{n_{\mathrm{n}\theta}}$, column matrix containing shape functions corresponding to unknown temperature coefficients
$\overline{\boldsymbol{N}}_{\theta}$	$\in \mathbb{R}^{n_{\mathrm{p}\theta}}$, column matrix containing shape functions corresponding to prescribed temperature coefficients
$\mathbf{N}^{e}_{\mathrm{d}}$	$\in \mathbb{R}^{3\times 3n_{\mathrm{em}}}$, shape functions of one element approximating the displacement field
$\mathbf{N}^{e}_{\theta}$	$\in \mathbb{R}^{n_{\mathrm{em}}}$, shape functions of one element approximating the temperature field
$\mathbf{N}^{e\mathrm{N}}_{\mathrm{d}}$	$\in \mathbb{R}^{3\times 24}$, linear shape functions for the displacement field
$\mathbf{N}^{e\mathrm{N}}_{\theta}$	$\in \mathbb{R}^{8}$, linear shape functions for the temperature field
$\mathbf{N}^{e\mathrm{E}}_{\mathrm{d}}$	$\in \mathbb{R}^{3\times 3n_{\mathrm{edges}}}$, shape functions associated with the edges of an element for the displacement field
$\mathbf{N}^{e\mathrm{E}}_{\theta}$	$\in \mathbb{R}^{n_{\mathrm{edges}}}$, shape functions associated with the edges of an element for the temperature field
$\mathbf{N}^{e\mathrm{F}}_{\mathrm{d}}$	$\in \mathbb{R}^{3\times 3n_{\mathrm{faces}}}$, shape functions associated with the faces of an element for the displacement field
$\mathbf{N}^{e\mathrm{F}}_{\theta}$	$\in \mathbb{R}^{n_{\mathrm{faces}}}$, shape functions associated with the faces of an element

	for the temperature field
$\mathbf{N}_\mathrm{d}^{e\mathrm{I}}$	$\in \mathbb{R}^{3\times 3n_\mathrm{int}}$, shape functions associated with the interior of an element for the displacement field
$\mathbf{N}_\theta^{e\mathrm{I}}$	$\in \mathbb{R}^{n_\mathrm{int}}$, shape functions associated with the interior of an element for the temperature field
$\mathbf{N}_\mathrm{d}^{i}$	$\in \mathbb{R}^{3n_\mathrm{em}}$, ith row of $\mathbf{N}_\mathrm{d}^{e}$
$\boldsymbol{Q}$	$\in \mathbb{R}^{n_\mathrm{Q}}$, column matrix of internal variables
$\boldsymbol{Q}^{(k)}$	$\in \mathbb{R}^{n_\mathrm{Q}}$, column matrix of internal variables in iteration k
$\boldsymbol{Q}_{ni}$	$\in \mathbb{R}^{n_\mathrm{Q}}$, stage values of internal variables
$\boldsymbol{q}$	$\in \mathbb{R}^{n_\mathrm{Q}}$, contains all internal variables of a structure
$\boldsymbol{q}_0$	$\in \mathbb{R}^{n_\mathrm{Q}}$, contains the initial conditions of the internal variables
$\boldsymbol{q}_\mathrm{err}$	$\in \mathbb{R}^{n_\mathrm{Q}}$, vector of local integration error in internal variables
$\boldsymbol{q}_n$	$\in \mathbb{R}^{n_\mathrm{Q}}$, differential variable of DAE-system at time t_n
$\mathbf{q}^e$	$\in \mathbb{R}^{n_\mathrm{ip}\cdot n_\mathrm{q}}$, column matrix of internal variables belonging to an element
$\mathbf{q}^e(\boldsymbol{\xi}_i, t)$	$\in \mathbb{R}^{n_\mathrm{q}}$, column matrix of internal variables at Gauss point i
$\boldsymbol{\Phi}$, $\hat{\boldsymbol{\Phi}}$	$\in \mathbb{R}^{n}$, increment function of Runge-Kutta method
$\mathbf{S}^e$	$\in \mathbb{R}^{6}$, components of weighted Cauchy stress tensor ordered as column matrix
$\tilde{\mathbf{T}}^e$	$\in \mathbb{R}^{6}$, components of $\tilde{\mathbf{T}}$ ordered as column matrix
$\boldsymbol{R}_\Theta$, $\boldsymbol{R}_\Theta^\mathrm{ext}$	$\in \mathbb{R}^{n_\mathrm{modes}}$, right hand sides of heat conduction equation
$\boldsymbol{r}$	$\in \mathbb{R}^{n_\mathrm{Q}}$, right hand side of differential part of equation system corresponding to internal variables
$\boldsymbol{r}_\theta$	$\in \mathbb{R}^{n_{\mathrm{n}\theta}}$, right hand side of differential part of equation system corresponding to heat conduction
$\boldsymbol{S}_{ni}$	$\in \mathbb{R}^{n}$, starting values in DIRK-method
$\boldsymbol{S}_{ni}^{q}$	$\in \mathbb{R}^{n_\mathrm{Q}}$, starting value of internal variables
$\boldsymbol{S}^{u}$	$\in \mathbb{R}^{n_\mathrm{nu}}$, starting value of displacement coefficients in DIRK-method
$\boldsymbol{S}_{ni}^{\boldsymbol{\Theta}}$	$\in \mathbb{R}^{n_{\mathrm{n}\theta}}$, starting value of temperature coefficients in DIRK-method
$\boldsymbol{s}$	$\in \mathbb{R}^{n_\mathrm{eq}}$, general right hand side
$\mathbf{s}^e$	$\in \mathbb{R}^{3}$, surface tractions
$\boldsymbol{\Theta}$	$\in \mathbb{R}^{n_{\mathrm{n}\theta}}$, column matrix containing unknown temperature coefficients
$\boldsymbol{\Theta}_\mathrm{a}$	$\in \mathbb{R}^{n_\mathrm{modes}}$, column matrix containing all temperature coefficients
$\boldsymbol{\Theta}_\mathrm{err}$	$\in \mathbb{R}^{n_{\mathrm{n}\theta}}$, vector of local integration error in temperature coefficients
$\boldsymbol{\Theta}_0$	$\in \mathbb{R}^{n_{\mathrm{n}\theta}}$, initial conditions for temperature coefficients
$\boldsymbol{\Theta}_n$	$\in \mathbb{R}^{n_{\mathrm{n}\theta}}$, column matrix of unknown temperature coefficients at time t_n
$\boldsymbol{\Theta}_{ni}$	$\in \mathbb{R}^{n_{\mathrm{n}\theta}}$, stage values of temperature coefficients
$\overline{\boldsymbol{\Theta}}$	$\in \mathbb{R}^{n_{\mathrm{p}\theta}}$, column matrix containing prescribed temperature coefficients
$\boldsymbol{u}_\mathrm{err}$	$\in \mathbb{R}^{n_\mathrm{nu}}$, vector of local integration error in displacement coefficients
$\boldsymbol{\Theta}^e$	$\in \mathbb{R}^{n_\mathrm{em}}$, temperature coefficients of an element
$\boldsymbol{U}$	$\in \mathbb{R}^{n_\mathrm{nu}}$, vector of displacement coefficients
$\boldsymbol{U}_{ni}$	$\in \mathbb{R}^{n_\mathrm{nu}}$, stage values of displacement coefficients
$\boldsymbol{u}_\mathrm{a}$	$\in \mathbb{R}^{3n_\mathrm{modes}}$, column matrix containing all displacement coefficients
$\boldsymbol{u}$	$\in \mathbb{R}^{n_\mathrm{nu}}$, column matrix containing the coefficients associated with unknown

	displacement coefficients
$\boldsymbol{u}^{h}$	$\in \mathbb{R}^3$, approximated displacement of a material point
$\overline{\boldsymbol{u}}$	$\in \mathbb{R}^{n_{\text{pu}}}$, column matrix containing the coefficients associated with prescribed displacement coefficients
$\boldsymbol{u}_0$	$\in \mathbb{R}^{n_{\text{nu}}}$, initial conditions for displacement coefficients
$\boldsymbol{u}_n$	$\in \mathbb{R}^{n_{\text{nu}}}$, column matrix of unknown displacement coefficients at time t_n
$\boldsymbol{u}_{n+1}^{(0)}$	$\in \mathbb{R}^{n_{\text{nu}}}$, unknown displacement coefficients at time t_{n+1} in iteration 0
$\mathbf{u}^{\text{e}}$	$\in \mathbb{R}^{3n_{\text{em}}}$, displacement coefficients of an element
$\boldsymbol{V}$	$\in \mathbb{R}^{n_{\text{nu}}+n_{\text{n}\theta}}$, contains displacement and temperature coefficients
$\boldsymbol{V}^{(m)}$	$\in \mathbb{R}^{n_{\text{nu}}+n_{\text{n}\theta}}$, $\boldsymbol{V}$ at iteration m
$\boldsymbol{w}$	$\in \mathbb{R}^{n_{\text{eq}}}$, general unknown vector
$\mathbf{w}_{\text{c}}$	$\in \mathbb{R}^6$, derivative of internal heat production with respect to right Cauchy-Green tensor
$\boldsymbol{\xi}_i$	$\in \mathbb{R}^3$, cordinate of Gauss point i in unit element
$\boldsymbol{y}$	$\in \mathbb{R}^n$, vector of unknowns
$\boldsymbol{y}_0$	$\in \mathbb{R}^n$, vector of initial conditions
$\boldsymbol{y}_n$	$\in \mathbb{R}^n$, vector of unknowns at time t_n
$\boldsymbol{y}_{n+1}$	$\in \mathbb{R}^n$, vector of unknowns at time t_{n+1}
$\boldsymbol{Y}_{ni}$	$\in \mathbb{R}^n$, stage value of Runge-Kutta method
$\dot{\boldsymbol{Y}}_{ni}$	$\in \mathbb{R}^n$, stage derivatives of Runge-Kutta method
$\boldsymbol{Z}_{\text{d}}^{e}$	$\in \mathbb{R}^{3n_{\text{em}}\times 3n_{\text{modes}}}$, coincidence matrix
$\mathbf{Z}_{\text{q}}^{e}$	$\in \mathbb{R}^{n_{\text{q}}\times n_{\text{Q}}}$, coincidence matrix
$\boldsymbol{Z}_{\theta}^{e}$	$\in \mathbb{R}^{n_{\text{modes}}\times n_{\text{em}}}$, coincidence matrix
$\boldsymbol{z}$	$\in \mathbb{R}^{n_{\text{eq}}}$, general unknown vector

B.5 Mathematical Operators

$\det$	Determinant of a second order tensor
div	Divergence with respect to coordinates of the current configuration
Div	Divergence with respect to coordinates of the reference configuration
grad	$= \frac{\partial ()^i}{\partial x^j} \boldsymbol{e}_i \otimes \boldsymbol{e}^j$, gradient of a vector field with respect to coordinates of the current configuration
Grad	$= \frac{\partial ()^i}{\partial X^j} \boldsymbol{e}_i \otimes \boldsymbol{e}^j$, gradient of a vector field with respect to coordinates of the reference configuration
$\lVert$expr.$\rVert$	Norm of expr.
$\mathbf{A} \cdot \mathbf{B}$	Inner product of two second order tensors
$\mathbf{A} \otimes \mathbf{B}$	Dyadic product of two second order tensors
$\operatorname{tr} \mathbf{A}$	Trace of a second order tensor
$\mathbf{A}^{\text{D}}$	$= \mathbf{A} - \frac{1}{3} \left(\operatorname{tr} \mathbf{A}\right) \mathbf{1}$, deviator of a second order tensor
$\mathbf{A}^{-1}$	Invers of a second order tensor

L_d	Differential operator matrix
L_t	Differential operator matrix
L_NL	Differential operator matrix
$\dfrac{\partial x}{\partial y}$	Partial derivative of x with respect to y
$\dfrac{\mathrm{d}x}{\mathrm{d}y}$	Total derivative of x with respect to y

B.6 Short Notations

CMLNA	Chord-Multilevel-Newton Algorithm
CAD	Computer Aided Design
CSC	Compressed sparse column storage format
CSR	Compressed sparse row storage format
DAE	Differential-algebraic equations
DIRK	Diagonally implicit Runge-Kutta methods
FEM	Finite element method
IBVP	Initial boundary value problem
MLNA	Multilevel-Newton algorithm
MOL	Method of lines
ODE	Ordinary differential equations

B.7 Miscellaneous

$\mathcal{B}$	Material body
$\partial\mathcal{B}$	Surface of a material body
π_θ^h	Weak form of discretized heat conduction equation
π_u	Energy functional (principle of virtual displacements)
$\pi_\mathrm{u}^\mathrm{h}$	Discretized principle of virtual displacements
π_c	Part of heat conduction equation related to heat storage
π_q	Part of heat conduction equation related to heat conduction
π_e	Part of heat conduction equation related to external heat supply
π_i	Part of heat conduction equation related to internal heat production
$\varphi(\boldsymbol{x}, t)$	Production density of physical quantity in current configuration
$\varphi_\mathrm{R}(\boldsymbol{X}, t)$	Production density of physical quantity in reference configuration
$\boldsymbol{\Psi}$	Physical quantity in current configuration
$\boldsymbol{\Psi}_\mathrm{R}$	Physical quantity in reference configuration
$\boldsymbol{\Phi}$	Flux of physical quantity in current configuration
$\boldsymbol{\Phi}_\mathrm{R}$	Flux of physical quantity in reference configuration
$\partial_\mathrm{q}\Omega_e$, $\partial_\mathrm{q}\omega_e$	Boundary of an element with prescribed heat flux

$\partial_{\mathrm{s}}\Omega_e$, $\partial_{\mathrm{s}}\omega_e$	Boundary of an element with prescribed stresses
$\partial\Omega$	Boundary of a body in reference configuration
$\partial\omega$	Boundary of a body in current configuration
$\partial_{\mathrm{u}}\Omega, \partial_{\mathrm{u}}\omega$	Boundary with prescribed displacements
$\partial_{\mathrm{s}}\Omega, \partial_{\mathrm{s}}\omega$	Boundary with prescribed stresses
$\partial_{\theta}\Omega, \partial_{\theta}\omega$	Boundary with prescribed temperatures
$\partial_{\mathrm{q}}\Omega, \partial_{\mathrm{q}}\omega$	Boundary with prescribed heat fluxes
$\partial_{\theta\mathrm{q}}\Omega, \partial_{\theta\mathrm{q}}\omega$	Boundary with prescribed combination of temperatures and heat fluxes
Ω	Discretized volume (reference configuration)
$\overline{\Omega}$	Closed set of body $\overline{\Omega} = \Omega \cup \partial\Omega$
Ω_e	Volume of element e (reference configuration)
Ω_{st}^h	Volume of unit element (3-D)
Ω_{st}^q	Area of unit element (2-D)
ω	Discretized volume (current configuration)
ω_e	Volume of element e (current configuration)
$\mathcal{P}$	Material point or particle
$\boldsymbol{\mathcal{S}}_{ps}^{p_\xi,p_\eta}(\Omega_{st}^q)$	Tensor product space (2-D)
$\boldsymbol{\mathcal{S}}_{ps}^{p_\xi,p_\eta,p_\zeta}(\Omega_{st}^h)$	Tensor product space (3-D)
$\boldsymbol{\mathcal{S}}_{ts}^{p_\xi,p_\eta}(\Omega_{st}^q)$	Trunk space (2-D)
$\boldsymbol{\mathcal{S}}_{ts}^{p_\xi,p_\eta,p_\zeta}(\Omega_{st}^h)$	Trunk space (3-D)
$\mathcal{K}$	Set of configurations
$\boldsymbol{\mathcal{R}}$	Reference configuration of material body
$\boldsymbol{\mathcal{S}}_{u,t}$	Set of displacement trial functions
$\mathcal{S}_{\theta,t}$	Set of temperature trial functions
$\boldsymbol{\mathcal{V}}_u$	Set of displacement test functions, variations
$\mathcal{V}_\theta$	Set of temperature test functions, variations

Bibliography

Actis, R., Szabo, B., and Schwab, C. Hierarchic models for laminated plates and shells. *Computer Methods in Applied Mechanics and Engineering*, 172:79–107, 1999.

Al-Kinani, R., Hartmann, S., and Netz, T. Anisotropic finite strain hyperelasticity based on the multiplicative decomposition of the deformation gradient. *Proceedings in Applied Mathematics and Mechanics*, 12:295–206, 2012.

Alexander, R. Diagonally implicit Runge-Kutta methods for stiff O.D.E.'s. *SIAM Journal on Numerical Analysis*, 14:1006–1021, 1977.

Andelfinger, U. and Ramm, E. EAS-elements for two-dimensional, three-dimensional, plate and shell structures and their equivalence to hr-elements. *International Journal for Numerical Methods in Engineering*, 36:1311–1337, 1993.

Armero, F. and Simo, C. A new unconditionally stable fractional step method for non-linear coupled thermomechanical problems. *International Journal for Numerical Methods in Engineering*, 35:737–766, 1992.

Armero, F. and Simo, J. C. A priori stability estimates and unconditionally stable product formula algorithms for nonlinear coupled thermoplasticity. *International Journal of Plasticity*, 9(6):749–782, 1993.

Babuska, I., Nobile, F., and Tempone, R. Reliability of compuational science. *Numerical Methods for Partial Differential Equations*, 23:753–784, 2007.

Babuska, I. and Oden, J. V & V in Computational Engineering and Science. Part I: Basic Concepts. Technical report, Institute for Computational Engineering and Scineces, The University of Texas at Austin, 2003.

Babuska, I. and Oden, J. The reliability of computer predictions: Can they be trusted? *International Journal for Numerical Analysis and Modeling*, 1:1–18, 2005.

Babuska, I. and Strouboulis, T. *The finite element method and its reliability*. Oxford University Press, 2001.

Babuska, I. and Suri, M. Locking effects in the finite-element approximation of elasticity problems. *Numerische Mathematik*, 62:439–463, 1992.

Babuska, I. and Szabo, B. On the rates of convergence of the finite element method. *International Journal for Numerical Methods in Engineering*, 18:323:341, 1982.

Banic, M., Dusan, S., Vojislav, D. M., Milosevic, M., Miltenovic, A., Djekic, P., and Rackov, M. Prediction of heat generation in rubber or rubber-metal springs. *Thermal Science*, 16:527–539, 2012.

Bathe, K. *Finite-Elemente-Methode*. Springer-Verlag Berlin, 2002.

Bathe, K.-J. *Finite Element Procedures*. Prentice Hall, New Jersey, 1996.

Belytschko, T., Liu, W., and Moran, B. *Nonlinear finite elements for continua and structures*. John Wiley & Sons, Chichester, 2000.

Belytschko, T., Ong, J., and Liu, W. Hourglass control in linear and nonlinear problems. *Computer Methods in Applied Mechanics and Engineering*, 43:251–276, 1984.

Bier, W. *A Constitutve Model for Metal Powder and its Numerical Treatment using Finite Elements*. Ph.D. thesis, University of Kassel, 2007.

Bonet, J. and Wood, R. *Nonlinear Continuum Mechanics for Finite Element Analysis*. Cambridge University Press, 2000.

Brink, U. and Stein, E. On some mixed finite elment methods for incompressible and nearly incompressible finite elasticity. *Computational Mechanics*, 19:105–119, 1996.

Bröker, H. *Integration von geometrischer Modellierung und Berechnung nach der p-Version der FEM*. Ph.D. thesis, Technische Universität München, 2001.

Burg, Haf, and Wille. *Höhere Mathematik für Ingenieure - Band I Analysis*. B.G. Teubner Stuttgart, 1989.

Cash, J. Diagonally implicit Runge-Kutta formulae with error estimates. *Journal of the Institute of Mathematics and its Applications*, 24:293–301, 1979.

Caylak, I. *Stabilized Mixed Triangular and Tetrahedral Finite Elemetns with Volume and Area Bubble Functions*. Ph.D. thesis, Universität Paderborn, 2011.

Chen, Q. and Babuska, I. Approximate optimal points for polynomial interpolation of real functions in an interval and in a triangle. *Computer Methods in Applied Mechanics and Engineering*, 128:405–417, 1995.

Chen, Q. and Babuska, I. The optimal symmetrical points for polynomial interpolation of real functions in the tetrahedron. *Computer Methods in Applied Mechanics and Engineering*, 137:89–94, 1996.

Diebels, S., Ellsiepen, P., and Ehlers, W. Error-Controlled Runge-Kutta Time Integration of a Viscoplastic Hybrid Two-Phase Model. *Technische Mechanik*, 19:19–27, 1998.

Dong, S. and Yosibash, Z. A parallel spectral element method for dynamic three-dimensional nonlinear elasticity problems. *Computers and Structures*, 87:59–72, 2008.

Düster, A. *High order finite elements for three-dimensional, thin-walled nonlinear continua*. Ph.D. thesis, Lehrstuhl für Bauinformatik, Fakultät für Bauingenieur- und Vermessungswesen, Technische Universität München, 2001.

Düster, A., Bröker, H., Heidkamp, H., Heisserer, U., Kollmannsberger, S., Krause, R., Muthler, A., Niggl, A., Nübel, V., Rücker, M., and Scholz, D. $AdhoC^4$ *- User's Guide*. Lehrstuhl für Bauinformatik, TU München, 2004.

Düster, A., Bröker, H., and Rank, E. The p-version of the finite element method for three-dimensional curved thin walled structures. *International Journal for Numerical Methods in Engineering*, 52:673–703, 2001.

Düster, A., Hartmann, S., and Rank, E. p-fem applied to finite isotropic hyperelastic bodies. *Computer Methods in Applied Mechanics and Engineering*, 192:5147–5166, 2003.

Düster, A., Niggl, A., Nübel, V., and Rank, E. A numerical investigation of high-order finite elements for problems of elastoplasticity. *Journal of Scientific Computing*, 17:397–404, 2002.

Düster, A. and Rank, E. The p-version of the finite element method compared to an adaptive h-version for the deformation theory of plasticity. *Computer Methods in Applied Mechanics and Engineering*, 190:1925–1935, 2001.

Düster, A. and Rank, E. A p-version finite element approach for two- and three-dimensional problems of the J_2 flow theory with non-linear isotropic hardening. *International Journal for Numerical Methods in Engineering*, 53:49–63, 2002.

Düster, A., Scholz, D., and Rank, E. pq-adaptive solid finite elements for three-dimensional plates and shells. *Computer Methods in Applied Mechanics and Engineering*, 197:243–254, 2007.

Eckert, S., Baaser, H., Gross, D., and Scherf, O. A bdf2 integration method with step size control for elasto-plasticity. *Computational Mechanics*, 34:377–386, 2004.

Ellsiepen, P. *Zeit- und ortsadaptive Verfahren angewandt auf Mehrphasenprobleme poröser Medien*. Ph.D. thesis, Institute of Mechanics II, University of Stuttgart, 1999.

Ellsiepen, P. and Hartmann, S. Remarks on the interpretation of current non-linear finite-element-analyses as differential-algebraic equations. *International Journal for Numerical Methods in Engineering*, 51:679–707, 2001.

Erbts, P. and Düster, A. Accelerated staggered coupling schemes for problems of thermoelasticity at finite strains. *Computers and Mathematics with Applications*, 64:2408–2430, 2012.

Esche, S. K., Kinzel, G., and Altan, T. Issues in convergence improvements for non-linear finite element programs. *International Journal for Numerical Methods in Engineering*, 40:4577–4594, 1997.

Felippa, C. and Park, K. Staggered transient analysis procedures for coupled mechanical systems: formulation. *Computer Methods in Applied Mechanics and Engineering*, 24:61–111, 1980.

Flanagan, D. and Belytschko, T. A uniform strain hexahedron and quadrilateral with orthogonal hourglass control. *International Journal for Numerical Methods in Engineering*, 17:679–706, 1981.

Flory, P. Thermodynamic relations for high elastic materials. *Transaction of the Farady Societay*, 57:829–838, 1961.

Fritzen, P. *Numerische Behandlung nichlinearer Probleme der Elastizitäts- und Plastizitätstheorie*. Ph.D. thesis, Department of Mathematics, University of Darmstadt, 1997.

Garcia-Donore, D., Garcia-Castillo, L., and Gomez-Revuelto, I. An interface between an hp-adaptive finite element package and the pre- and post-processor GiD. *Finite Elements in Analysis and Design*, 46:328–338, 2010.

Glaser, S. *Berechnung gekoppelter thermomechanischer Prozesse*. Ph.D. thesis, Universität Stuttgart, 1992.

Glaser, S. and Armero, F. On the formulation of enhanced strain finite elements in finite deformations. *Engineering Computations*, 14:759–791, 1997.

Gordon, W. and Hall, C. Construction of curvilinear co-ordinate systems and applications to mesh generation. *International Journal for Numerical Methods in Engineering*, 7:461–477, 1973a.

Gordon, W. and Hall, C. Transfinite element methods: Blending-function interpolation over arbitrary curved element domains. *Numerische Mathematik*, 21:109–129, 1973b.

Gould, N. I. M., Scott, J. A., and Hu, Y. A numerical evaluation of sparse direct solvers for the solution of large sparse symmetric linear systems of equations. *ACM Transactions on Mathematical Software*, 33:10, 2007.

Großmann, C. and Roos, H.-G. *Numerische Behandlung partieller Differentialgleichungen*. Teubner, Stuttgart, 2005.

Hairer, E., Lubich, C., and Roche, M. *The Numerical Solution of Differential-Algebraic Systems by Runge-Kutta Methods*. Lecture Notes in Mathematics. Springer-Verlag, Berlin, 1988.

Hairer, E., Norsett, S., and Wanner, G. *Solving Ordinary Differential Equations I*. Springer-Verlag, Berlin, 2nd revised edition, 1993.

Hairer, E. and Wanner, G. *Solving Ordinary Differential Equations II*. Springer-Verlag, Berlin, 2nd revised edition, 1996.

Hamkar, A.-W. *Eine iterationsfreie Lösungsprozedur im Rahmen finiter Thermoviskoelastizität*. Ph.D. thesis, TU Clausthal, 2013. Submitted to.

Hamkar, A.-W. and Hartmann, S. Theoretical and numerical aspects in weak-compressible finite strain thermo-elasticity. *Journal of Theoretical and Applied Mechanics*, 50:3–22, 2012.

Hamkar, A.-W., Hartmann, S., and Rang, J. A stiffly accurate Rosenbrock-type method of order 2 applied to FE-analyses in finite strain viscoelasticity. *Applied Numerical Mathematics*, 62:1837 – 1848, 2012.

Hartmann, S. Zur Berechnung inelastischer Festkörper mit der Methode der finiten Elemente. In Hartmann, S., Haupt, P., and Ulbricht, V., editors, *Modellierung und Identifikation*, pages 119–130. Gesamthochschul-Bibliothek, Kassel, 1998.

Hartmann, S. Computation in finite-strain viscoelasticity: Finite elements based on the interpretation as differential-algebraic equations. *Computer Methods in Applied Mechanics and Engineering*, 191:1439–1470, 2002.

Hartmann, S. *Finite-Element Berechnung inelastischer Kontinua. Interpretation als Algebro-Differentialgleichungssysteme*. Habilitationsschrift, Universität Kassel, Institut für Mechanik, 2003.

Hartmann, S. A remark on the application of the Newton-Raphson method in non-linear fininte element analysis. *Comput Mech*, 36:100–116, 2005.

Hartmann, S. TASA-FEM: Ein Finite-Elemente Programm für raum-zeitadaptive gekoppelte Strukturberechnungen, Version 1.0. Mitteilung des Instituts für Mechanik 1/ 06, Institut für Mechanik, Universität Kassel, 2006.

Hartmann, S. and Bier, W. High-order time integration applied to metal powder plasticity. *International Journal of Plasticity*, 24:17–54, 2008.

Hartmann, S., Duintjer Tebbens, J., Quint, K., and Meister, A. Iterative solvers within sequences of large linear systems in non-linear structural mechanics. *Zeitschrift für Angewandte Mathematik und Mechanik*, 89:711–728, 2009a.

Hartmann, S. and Hamkar, A.-W. Rosenbrock-type methods applied to finite element computations within finite strain viscoelasticity. *Computer Methods in Applied Mechanics and Engineering*, 199:1455–1470, 2010.

Hartmann, S., Haupt, P., and Tschöpe, T. Parameter identification with a direct search method using finite elements. In Besdo, D., Schuster, R., and Ihlemann, J., editors, *Constitutive Models for Rubber II*, pages 249–256. Balkema Pulb., Lisse, 2001.

Hartmann, S., Kuhl, D., and Quint, K. Time-adaptive computation of thermoviscoplastic structures. In Steinhoff, K., Maier, H. J., and Biermann, D., editors, *Functionally graded materials in industrial mass production*, pages 269–282. Verlag Wissenschaftliche Scripten, 2009b.

Hartmann, S. and Neff, P. Polyconvexity of generalized polynomial-type hyperelastic strain energy functions for near-incompressibility. *International Journal of Solids and Structures*, 40:2767–2791, 2003.

Hartmann, S., Quint, K., and Arnold, M. On plastic incompressibility within time-adaptive finite elements combined with projection techniques. *Computer Methods in Applied Mechanics and Engineering*, 198:178–193, 2008a.

Hartmann, S., Quint, K. J., and Hamkar, A.-W. Displacement control in time-adaptive non-linear finite-element analysis. *Journal of Applied Mathematics and Mechanics*, 88:342–364, 2008b.

Hartmann, S. and Rothe, S. A rigorous application of the method of vertical lines to coupled systems in finite element analysis. In Ansorge, R., Bijl, H., Meister, A., and Sonar, T., editors, *Recent Developments in the Numerics of Nonlinear Hyperbolic Conservation Laws*, volume 120 of *Notes on Numerical Fluid Mechanics and Multidisciplinary Design*, pages 161–175. Springer Berlin / Heidelberg, 2013.

Hartmann, S., Tschöpe, T., Schreiber, L., and Haupt, P. Finite deformations of a carbon black-filled rubber. Experiment, optical measurement and material parameter identifications using finite elements. *European Journal of Mechanics*, 22:309–324, 2003.

Hartmann, S. and Wensch, J. Finite element analysis of viscoelastic structures using Rosenbrock-type methods. *Computational Mechanics*, 40:383–398, 2007.

Haupt, P. *Continuum Mechanics and Theory of Materials*. Springer-Verlag Berlin Heidelberg, 2000.

Haupt, P. and Sedlan, K. Viscoplasticity of elastomeric materials: experimental facts and constitutive modelling. *Archive of Applied Mechanics*, 71:89–109, 2001.

Haupt, P. and Tsakmakis, C. On the application of dual variables in continuum mechanics. *Journal of Continuum Mechanics and Thermodynamics*, 1:165–196, 1989.

Haupt, P. and Tsakmakis, C. Stress tensors associated with deformation tensors via duality. *Archives of Mechanics*, 48:347–384, 1996.

Heimes, T. *Finite Thermoinelastizität: Experimente, Materialmodellierung und Implementierung in die FEM am Beispiel einer technischen Gummimischung*. Ph.D. thesis, Institut für Mechanik, Fakultät für Luft- und Raumfahrttechnik, Universität der Bundeswehr München, 2005.

Heisserer, U. *High-order finite elements for material and geometric nonlinear finite strain problems*. Ph.D. thesis, Technische Universität München, 2007.

Heisserer, U., Hartmann, S., Düster, A., Bier, W., Yosibash, Z., and Rank, E. p-fem for finite deformation powder compaction. *Computer Methods in Applied Mechanics and Engineering*, 197:727–740, 2008a.

Heisserer, U., Hartmann, S., Düster, A., and Yosibash, Z. On volumetric locking-free behaviour of p-version finite elements under finite deformations. *Communications in Numerical Methods in Engineering*, 24:1019–1032, 2008b.

Hinnant, H. A fast method of numerical quadrature for p-version finite element matrices. *International Journal for Numerical Methods in Engineering*, 37:3723–3750, 1994.

Holzapfel, G. *Nonlinear Solid Mechanics: A Continuum Approach for Engineering*. John Wiley & Sons, 5th edition, 2008.

Holzapfel, G. and Simo, J. Entropy elasticity of isotropic rubber-like solids at finite strains. *Computer Methods in Applied Mechanics and Engineering*, 132:17–44, 1996a.

Holzapfel, G. and Simo, J. A new viscoelastic constitutive model for continuous media at finite thermomechanical changes. *International Journal of Solids and Structures*, 33:3019–3034, 1996b.

Holzapfel, G. A. and Reiter, G. Fully coupled thermomechanical behaviour of viscoelastic solids treated with finite elements. *International Journal for Engineering Science*, 33:1037–1058, 1995.

Holzer, S. Modellierung und Berechnung mit der p-verion der FEM. Technical report, Informationsverarbeitung im Konstruktiven Ingenierubau, Universität Stuttgart, 1999.

Holzer, S. and Yosibash, Z. The p-version of the finite element method in incremental elastoplastic analysis. *International Journal for Numerical Methods in Engineering*, 39:1859–1878, 1996.

Hughes, T. *The Finite Element Method*. Mineola, NY: Dover Publications, 2000.

Incropera, F. P., DeWitt, D. P., Bergman, T. L., and Lavine, A. S. *Fundamentals of Heat and Mass Transfer*. John Wiley & Sons, Hoboken, NJ, 6th edition, 2007.

Jakobsen, B. and Rosendahl, F. The Sleipner Platform Accident. *Structural Engineering International*, 4:190–193, 1994.

Jansohn, W. *Formulierung und Integration von Stoffgesetzen zur Beschreibung großer Deformationen in der Thermoplastizität und -viskoplastizität*. Ph.D. thesis, Forschungszentrum Karlsruhe, Institut für Materialforschung, 1997.

Jeltsch-Fricker, R. *Variationsrechnung - Skript zur Vorlesung in den Technikstudiengängen der Universität Kassel*. Kassel: AG Ingenieur-Mathematik, 2002.

Jeremic, B. and Xenophontos, C. Application of the p-version of the finite element method to elastoplasticity with localization of deformation. *Communications in Numerical Methods in Engineering*, 15:867–876, 1999.

Kelley, C. T. *Iterative methods for linear and nonlinear equations*. SIAM Society for Industrial and Applied Mathematics, Philadelphia, Philadelphia, 1995.

Kim, C. and Suri, M. On the p-Version of the Finite Element Method in the Presence of Numerical Integration. *Numerical Methods for Partial Differential Equations*, 9:593–629, 1993.

Kiralyfalvi, G. and Szabo, B. Quasi-regional mapping for the p-version of the finite element method. *Finite Elements in Analysis and Design*, 27:85–97, 1997.

Koschnick, F. *Geometrische Locking-Effekte bei Finiten Elementen und ein allgemeines Konzept zu ihrer Vermeidung*. Ph.D. thesis, Lehrstuhl für Statik der Technischen Universität München, 2004.

Krafczyk, M., Rank, E., Rücker, M., and Düster, A. The inside project: Some remarkts concerning control flow in 'real life' parallel software and the parallelization of the p-version of fem. Technical report, TU München, Lehrstuhl für Bauinformatik, 1997.

Krause, R., Mücke, R., and Rank, E. hp-version finite elements for geometrically non-linear problem. *Communications in Numerical Methods in Engineering*, 11:887–897, 1995.

Lion, A. On the large deformation behaviour of reinfored rubber at different temperatures. *Journal of the Mechanics and Physics of Solids*, 45:1805–1834, 1997.

Lion, A. Thermomechanik von Elastomeren: Experimente und Materialtheorie. Habilitationsschrift, Universität Kassel, Institut für Mechanik, 2000.

Liu, C., Hofstetter, G., and Mang, H. 3D finite element analysis of rubber-like materials at finite strains. *Engineering Computations*, 11:111–128, 1994.

Lu, S. and Pister, K. Decomposition of deformation and representation of the free energy function for isotropic thermoelastic solids. *International Journal of Solids and Structures*, 11:927–934, 1975. Siehe Ordner.

Lübbing, C. *Zur Stabilität von gestaffelten Finite-Elemente Berechnungen*. Ph.D. thesis, Universität Stuttgart, 1997.

Lubliner, J. A model of rubber viscoelasticity. *Mechanics Research Communications*, 12:93–99, 1985.

Malkus, D. and Hughes, T. Mixed finite element methods - reduced and selective integration techniques: a unification of concepts. *Computer Methods in Applied Mechanics and Engineering*, 15:68–81, 1978.

Martins-Wagner, M. On efficient numerical integration of p-version finite element stiffness matrices. Technical report, Universität der Bundeswehr München - Institut für Mathematik und Bauinformatik, 2003.

Miehe, C. *Zur numerischen Behandlung thermomechanischer Prozesse*. Ph.D. thesis, Universität Hannover, 1988.

Miehe, C. *Kanonische Modelle multiplikativer Elasto-Plastizität. Thermodynamische Formulierung und numerische Implementation*. Ph.D. thesis, Universität Hannover, 1993.

Miehe, C. Entropic thermoelasticity at finite strains: Aspects of the formulation and numerical implementation. *Computer Methods in Applied Mechanics and Engineering*, 120:243–269, 1995a.

Miehe, C. A theory of large-strain isotropic thermoplasticity based on metric transformation tensors. *Archive of Applied Mechanics*, 66(1–2):45–64, 1995b.

Miehe, C. Multisurface thermoplasticity for single crystals at large strains in terms of Eulerian vector updates. *International Journal of Solids and Structures*, 33(20-22):3103–3130, 1996.

Miller, K. Nonlinear Krylov and moving nodes in the method of lines. *Journal of Computational and Applied Mathematics*, 183:275–287, 2005.

Netz, T., Düster, A., and Hartmann, S. High-order finite elements compared to low-order mixed element formulations. *Zeitschrift für Angewandte Mathematik und Mechanik*, 93:163–176, 2013a.

Netz, T., Hamkar, A.-W., and Hartmann, S. High-order quasi-static finite element analysis in space and time with application to finite strain viscoelasticity. *Computers and Mathematics with Applications*, 2013b. Accepted for publication.

Netz, T. and Hartmann, S. High-order time integration in the p-version of finite elements. *Proceedings in Applied Mathematics and Mechanics*, 10:201–202, 2010.

Netz, T., Hartmann, S., and Hamkar, A.-W. Applications of Rosenbrock-type methods to the p-version of finite elements. *Proceedings in Applied Mathematics and Mechanics*, 11:255–256, 2011.

Noel, A. and Szabo, B. Formulation of geometrically non-linear problems in the spatial reference frame. *International Journal for Numerical Methods in Engineering*, 40:1263–1280, 1997.

Nübel, A., V.and Düster and Rank, E. Die Methode Vektorintegration bei der p-Version der Finite-Elemente-Methode. Technical report, Technische Unversität München - Lehrstuhl für Bauinformatik, 2000.

Nübel, V. *Die adaptive rp-Methode für elastoplastische Probleme*. Ph.D. thesis, Technische Universität München, 2005.

Park, K. Partitioned transient analysis procedures for coupled-field problems: Stability analysis. *Journal of Applied Mechanics*, 47:370–376, 1980.

Park, K. and Felippa, C. Partitioned transient analysis procedures for coupled-field problems: Accuracy analysis. *Journal of Applied Mechanics*, 47:919–926, 1980.

Peano, A. Hierarchies of conforming finite elements for plane elasticity and plate bending. *Computers and Mathematics with Applications*, 2:211–224, 1976.

Quint, K. *Thermomechanically Coupled Processes for Functionally Graded Products: Experiments, Modelling, and Finite Element Analysis using High-Order DIRK-Methods*. Ph.D. thesis, Clausthal University of Technology, 2012.

Quint, K., Hartmann, S., S.and Rothe, Saba, N., and Steinhoff, K. Experimental validation of high-order time integration for non-linear heat transfer problems. *Comput Mech*, 48:81–96, 2011.

Rabbat, N., Sangiovanni-Vincentelli, and Hsieh, H. A multilevel Newton algorithm with macromodeling and latency for the analysis of large-scale nonlinear circuits in the time domain. *IEEE Transactions on Circuits and Systems*, 26:733–740, 1979.

Rank, E., Düster, A., Nübel, V., Preusch, K., and Bruhns, O. High order finite elements for shells. *Computer Methods in Applied Mechanics and Engineering*, 194:2494–1512, 2005.

Rank, E., Krause, R., and Preusch, K. On the accuracy of p-version elements for the Reissner-mindlin plate problem. *International Journal for Numerical Methods in Engineering*, 43:51–67, 1998.

Rank, E., Rücker, M., Düster, A., and Bröker, H. The efficiency of the p-version finite element method in a distributed computing environment. *International Journal for Numerical Methods in Engineering*, 52:589–604, 2001.

Reese, S. Thermomechanische Modellierung gummiartiger Polymer-Strukturen. Habilitationsschrift, Universität Hannover, Institut für Baumechanik und Numerische Mechanik, 2001. Report No. F01/4.

Reese, S. On a consistent hourglass stabilization technique to treat large inelastic deformations and thermo-mechanical coupling in plane strain problems. *International Journal for Numerical Methods in Engineering*, 57:1095–1127, 2003.

Reese, S. and Govindjee, S. Theoretical and numerical aspects in the thermo-viscoelastic material behaviour of rubber-like polymers. *Mechanics of Time-Dependent Materials*, 1:357–396, 1998.

Reese, S., Küssner, M., and Reddy, B. A new stabilization technique for finite elements in non-linear elasticity. *International Journal for Numerical Methods in Engineering*, 44:1617–1652, 1999.

Reese, S. and Wriggers, P. A stabilization technique to avoid hourglassing in finite elasticity. *International Journal for Numerical Methods in Engineering*, 48:79–109, 2000.

Reese, S. and Wriggers, P. On a physically stabilized one point finite element formulation for three-dimensional finite elasto-plasticity. *Computer Methods in Applied Mechanics and Engineering*, 194:4685–4715, 2005.

Reese, S., Wriggers, P., and Reddy, B. A new locking-free brick element technique for large deformation problems in elasticity. *Computers and Structures*, 75:291–304, 2000.

Ribo, R., de Riera, M. P., Tercero, E. E., Ronda, J. S. P., Sans, A. C., Ribera, A. M., and Horcas, S. G. GiD. The personal pre and postprocessor. The universal, adaptive and userfriendly pre- and post-processing system for computer analysis in science and engineering. Reference Manual. Version 9, 2008.

Rogers, D. *An Introduction to NURBS: with historical perspective*. Academic Press, 2001.

Rothe, S., Hamkar, A.W., Quint, and K.J. Hartmann, S. Comparison of diagonal-implicit, linear-implicit and half-explicit Runge-Kutta methods in non-linear finite element analyses. *Archive of Applied Mechanics,* 82:1057–1074, 2012.

Schenk, O. and Gärtner, K. Solving unsymmetric sparse systems of linear equations with pardiso. *Future Generation Computer Systems,* 20:475–487, 2004.

Schenk, O., Gärtner, K., and Fichtner, W. Efficient sparse LU factorization with left-right looking strategy on shared memory multiprocessors. *BIT Numerical Mathematics*, 40:158–176, 1999.

Schiesser, W. E. *The Numerical Method of Lines: Integration of Partial Differential Equations*. Academic Press Inc, San Diego, CA, 1991.

Schwarz, H. and Köckler, N. *Numerische Mathematik*. Teubner-Verlag, 2004.

Schweizerhof, K. Nichtlineare Berechnung von Tragwerken unter verformungsabhängiger Belastung mit finiten Elementen. Technical report, Institut für Baustatik, Universität Stuttgart, 1982.

Schwer, L. An overview of the PTC 60 V & V 10 Guide for Verification and Validation in Computational Solid Mechanics. 2007.

Sedlan, K. *Viskoelastisches Materialverhalten von Elastomerwerkstoffen: Experimentelle Untersuchung und Modellbildung*. Ph.D. thesis, Universität Gesamthochschule Kassel, Institut für Mechanik, 2000.

Selby, R., Vecchio, F., and Collins, M. The failure of an offshore platform. *Concrete International*, 19:28–35, 1997.

Simo, J. and Armero, F. Geometrically nonlinear enhanced strain mixed methods and the method of incompatible modes. *International Journal for Numerical Methods in Engineering*, 33:1413–1449, 1992.

Simo, J. and Miehe, C. Associative coupled thermoplasticity at finite strains: Formulation, numerical analysis and implementation. *Computer Methods in Applied Mechanics and Engineering*, 98:41–104, 1992.

Simo, J. and Rifai, S. A class of mixed assumed strain methods and the method of incompatible modes. *International Journal for Numerical Methods in Engineering*, 29:1595–1638, 1990.

Simo, J. and Taylor, R. Consistent tangent operators for rate-independent elastoplasticity. *Computer Methods in Applied Mechanics and Engineering*, 48:101–118, 1985.

Simo, J. and Taylor, R. Quasi-incompressible finite elasticity in principal stretches. *Computer Methods in Applied Mechanics and Engineering*, 85:273–310, 1991.

Simo, J., Taylor, R., and Pister, K. Variational and projection methods for the volume constraint in finite deformation elasto-plasticity. *Computer Methods in Applied Mechanics and Engineering*, 51:177–208, 1985.

Simo, J., Taylor, R., and Wriggers, P. A note on finite-element implementation of pressure boundary loading. *Communications in Applied Numerical Methods*, 7:513–525, 1991.

Strehmel, K. and Weiner, R. *Numerik gewöhnlicher Differentialgleichungen*. Teubner Verlag, Stuttgart, 1995.

Stricklin, J., Haisler, W., and von Riesemann, W. Evaluation of solution procedures for material and for geometrically nonlinear structural analysis. *American Institute of Aeronautics and Astronautics*, 11:292–299, 1973.

Suri, M. Analytical and computational assessment of locking in the hp finite element method. *Computer Methods in Applied Mechanics and Engineering*, 133:347–371, 1996.

Suwannachit, A. *Constitutive Modeling of Tire Rubber Compounds with Application to Rolling Contact Problems*. Ph.D. thesis, Leibniz Universität Hannover, 2012.

Szabo, B. Some recent developments in fininte element analysis. *Comput. Math. Appl.*, 5:99–115, 1979.

Szabo, B. Mesh design for the p-version of the finite element method. *Computer Methods in Applied Mechanics and Engineering*, 55:181–197, 1986.

Szabo, B. and Actis, R. On the role of hierarchic spaces and models in verfication and validation. *Computer Methods in Applied Mechanics and Engineering*, 198:1273.1280, 2009.

Szabo, B., Actis, R., and Holzer, S. Solution of elastic-plastic stress analysis problems by the p-version of the finite element method. Technical report, Washington University, Center for Computational Mechanics, 1993.

Szabo, B. and Babuska, I. *Finite Element Analysis*. John Wiley & Sons, 1991.

Szabo, B., Babuska, I., and Chayapathy, B. Stress computations for nearly incompressible materials by the p-version of the finite element method. *International Journal for Numerical Methods in Engineering*, 28:2175–2190, 1989.

Szabo, B., Babuska, I., and Pitkaranta. The problem of verification with reference to the Girkmann problem. *Engineering with Computers*, 26:171–183, 2010.

Szabo, B., Düster, A., and Rank, E. The p-version of the finite element method. In *Encyclopedia of Computational Mechanics*, chapter 5, pages 119–139. John Wiley & Sons, 2004.

Taylor, R., Beresford, P., and Wilson, E. A non-conforming element for stress analysis. *International Journal for Numerical Methods in Engineering*, 10:1211–1219, 1976.

Treloar, L. *The Physics of Rubber Elasticity*. Oxford University Press, 1975.

Turska, E. and Schrefler, B. On convergence conditions of partitioned solution procedures for consolidation problems. *Computer Methods in Applied Mechanics and Engineering*, 106:51–63, 1993.

Vogelius, M. An analysis of the p-version of the finite element method for nearly incompressible materials - uniformly valid, optimal error estimates. *Numerische Mathematik*, 41:39–53, 1983.

von Karman, T. Collapse of the Tacoma Narrows Bridge. *Resonance*, 10:97–1002, 2005.

Wittekindt, J. *Die numerische Lösung von Anfangs-Randwertproblemen zur Bescheibung inelastischen Werkstoffverhaltens*. Ph.D. thesis, Department of Mathematics, University of Darmstadt, 1991.

Wriggers, P. *Nonlinear Finite Element Methods*. Springer-Verlag, 2008.

Yosibash, Z., Hartmann, S., Heisserer, U., Düster, E., A.and Rank, and Szanto, M. Axisymmetric pressure boundary loading for finite deformation analysis using p-fem. *Computer Methods in Applied Mechanics and Engineering*, 196:1261–1277, 2007.

Yosibash, Z. and Priel, E. Artery active mechanial response: High order finite element implementation and investigation. *Computer Methods in Applied Mechanics and Engineering*, 237-240:51–66, 2012.

Zienkiewicz, O., Taylor, R., and Too, J. Reduced integration technique in general analysis of plates and shells. *International Journal for Numerical Methods in Engineering*, 3:275–290, 1971.

Curriculum Vitae

Persönliche Daten

Name	Torben Netz, Dipl.-Ing.
geboren am	11.08.1983 in Wolfhagen
Familienstand	ledig

Schulausbildung

09. 1989 bis 06. 1993	Christine-Brückner-Schule, Bad Emstal Sand
09. 1993 bis 07. 2003	König-Heinrich-Schule, Fritzlar Appolinaire-Preis der Robert Bosch Stiftung für außerordentliche Leistungen im Abiturfach Französisch

Studium

10. 2003 bis 06. 2007	Studium des Maschinenbaus an der Universität Kassel Diplom I: *Strukturoptimierung Smarter Systeme mittels Neuronalen Netzen* Auszeichnung für das zweitbeste Diplom I im SS 2007
10. 2006 bis 03. 2007	Praktikant im L-Lab in Paderborn (Forschungsinstitut für Lichttechnik und Mechatronik, getragen von der Hella KGaA und der Universität Paderborn)
07. 2007 bis 07. 2008	Diplom II: *Untersuchung der Effizienzsteigerung bei Elementroutinen physikalisch und geometrisch nichtlinearer Problemstellungen* Auszeichnung für das zweitbeste Diplom II im SS 2008

Berufliche Tätigkeiten

09. 2008 bis 05. 2013	Wissenschaftlicher Mitarbeiter am Institut für Technische Mechanik der Technischen Universität Clausthal
seit 07. 2013	Berechnungsingenieur in der Abteilung Technische Berechnung der ThyssenKrupp Rothe Erde GmbH in Lippstadt